# Transition Metal Dichalcogenides: Part II

Yury Holubeu *

August 31, 2026

This draft is not aimed for distribution.

## Contents

**Preface** **5**

**VII Other Articles and Theories in a Nutshell** **6**

**7 Other articles in a Nutshell** **6**
7.1 Other Articles About Calculations in a Nutshell . . . 6
7.1.1 Essence of "First principles investigation of $TaS_2$" by Jung Kim et al. . . . 6
7.1.2 Essence of "Dynamical control of Coulomb int. 1T-$TaS_2$" by Notter et al. . . . 8
7.2 Other Articles About Experiments in a Nutshell . . . 8
7.2.1 Essence of "Dualistic insulator states in 1T-TaS $_2$ crystals" by Wang et al. . . . 8

**VIII Other My Theories** **12**
7.2.2 Taking into account dimensinality . . . 12

**IX Calculations from First Principles** **13**

**8 First principles investigation of $TaS_2$ by Jung Kim et al.** **13**
8.1 Article . . . 13
8.1.1 Introduction . . . 13
8.1.2 Results and Discussion . . . 17
8.1.3 Method Details . . . 27
8.2 Discussion . . . 29
8.2.1 My conclusion about the article . . . 29
8.2.2 Questions About the Methods, Calculations . . . 30
8.2.3 Questions About the Meaning of Methods, Materials: Less Important . . . 35
8.2.4 Questions about Correct Summarization and Takeaways . . . 38

**9 First principles investigation of $TaS_2$ by Jung Kim et al.** **48**
9.1 Article . . . 48
9.1.1 Introduction . . . 49
9.1.2 Results and Discussion . . . 52
9.1.3 Method Details . . . 62
9.2 Discussion . . . 64
9.2.1 My conclusion about the article . . . 64
9.2.2 Questions About the Methods, Calculations . . . 65
9.2.3 Questions About the Meaning of Methods, Materials: Less Important . . . 70
9.2.4 Questions about Correct Summarization and Takeaways . . . 73

*https://yuriholubeu.github.io/, yuri.holubev@gmail.com

**10 Controlling magnetic frustration in 1T-$TaS_2$ via Coulomb engineered long-range interactions by Chen, Rösner, Lado** **83**
10.0.1 Introduction . . . 83
10.0.2 Effective model for monolayer 1T-$TaS_2$ . . . 85
10.0.3 Coulomb engineering of the spin Hamiltonian of 1T-$TaS_2$ . . . 86
10.0.4 Discussion . . . 88
10.0.5 Conclusions . . . 89

**11 Ab initio theory of magnetism in two-dimensional $1T$-$TaS_2$ by Pasquier, Yazyev** **92**
11.1 Article . . . 92
11.2 My Discussion . . . 100

**X Other Explanations of Typical Theory** **101**

**12 Theoretical Modeling of Amorphous State in 1T-$TaS_2$ by Vodeb et al.** **101**
12.1 Introduction . . . 101
12.2 The Model . . . 102
12.3 Monte Carlo Method . . . 103
12.4 Tiling . . . 103
12.5 Results . . . 104
12.6 Discussion . . . 107
12.7 Conclusion . . . 108

**13 Band insulator to Mott insulator transition in $1T - TaS_2$ (2020)** **109**

**14 Dynamical control of Coulomb interactions and bands in 1T-$TaS_2$ by Notter et al.** **120**
14.1 Article . . . 120
14.1.1 Introduction . . . 120
14.1.2 Results . . . 122
14.1.3 Discussion . . . 127
14.1.4 SM . . . 128
14.2 My Discussion . . . 130
14.2.1 My Conclusion and Analysis of the article . . . 130
14.2.2 Questions about Assumed Knowledge . . . 133
14.2.3 Questions about Reproduction of Results . . . 139
14.2.4 Things That I Maybe Understood Wrongly . . . 143
14.2.5 Potential Future Research Directions . . . 148

**15 Orbital-driven Mottness collapse in 1T-$TaS_{2-x}Se_x$ transition metal dichalcogenide by Qiao et al. (2016)** **149**
15.1 INTRODUCTION . . . 149
15.2 EXPERIMENT AND CALCULATION METHODS . . . 150
15.3 ORBITAL TEXTURES IN PRISTINE $TaS_2$ . . . 151
15.3.1 Structural and electronic properties . . . 151
15.3.2 Low-energy orbital textures and their origin . . . 151
15.4 MOTTNESS COLLAPSE UPON $Se$ SUBSTITUTION . . . 152
15.4.1 Phase transitions . . . 153
15.4.2 Topographic change . . . 154
15.4.3 Electronic inhomogeneity . . . 154
15.4.4 Orbital shifts . . . 155
15.5 THEORETICAL FORMALISM . . . 156
15.6 CONCLUSION . . . 158

## XI Other Experiments and Simulations 159

**16 Possible origin of nonlinear conductivity and large dielectric constant in CCDW of $1T - TaS_2$ by Ma, Hou et al. 159**
16.0.1 I. INTRODUCTION . . . 159
16.0.2 II. EXPERIMENT . . . 160
16.0.3 III. RESULTS AND DISCUSSION . . . 161
16.0.4 IV. SUMMARY . . . 171
16.1 My Discussion . . . 171
16.1.1 My Conclusion . . . 171
16.1.2 My Left Questions . . . 171
16.1.3 Things That I Maybe Understood Wrongly . . . 171
16.1.4 Potential Future Research Directions . . . 171

**17 Real-time imaging of quasiparticle dynamics at a topological defect in an electronic crystal by Vaskivskyi, Vodeb, Vaskivskyi, Mihailovic 171**
17.1 Article . . . 172

## XII Other Explanations of a Typical Theories 202

**18 Theoretical Modeling of Amorphous State in 1T-$TaS_2$ by Vodeb et al. 202**
18.1 Introduction . . . 202
18.2 The Model . . . 203
18.3 Monte Carlo Method . . . 204
18.4 Tiling . . . 204
18.5 Results . . . 205
18.6 Discussion . . . 208
18.7 Conclusion . . . 209

**19 Band insulator to Mott insulator transition in $1T - TaS_2$ (2020) 210**

**20 Dynamical control of Coulomb interactions and bands in 1T-$TaS_2$ by Notter et al. 221**
20.1 Article . . . 221
20.1.1 Introduction . . . 221
20.1.2 Results . . . 223
20.1.3 Discussion . . . 228
20.1.4 SM . . . 229
20.2 My Discussion . . . 231
20.2.1 My Conclusion and Analysis of the article . . . 231
20.2.2 Questions about Assumed Knowledge . . . 234
20.2.3 Questions about Reproduction of Results . . . 240
20.2.4 Things That I Maybe Understood Wrongly . . . 244
20.2.5 Potential Future Research Directions . . . 249

**21 Orbital-driven Mottness collapse in 1T-$TaS_{2-x}Se_x$ transition metal dichalcogenide by Qiao et al. (2016) 250**
21.1 INTRODUCTION . . . 250
21.2 EXPERIMENT AND CALCULATION METHODS . . . 251
21.3 ORBITAL TEXTURES IN PRISTINE $TaS_2$ . . . 252
21.3.1 Structural and electronic properties . . . 252
21.3.2 Low-energy orbital textures and their origin . . . 252
21.4 MOTTNESS COLLAPSE UPON $Se$ SUBSTITUTION . . . 253
21.4.1 Phase transitions . . . 254
21.4.2 Topographic change . . . 255

21.4.3 Electronic inhomogeneity . . . 255
21.4.4 Orbital shifts . . . 256
21.5 THEORETICAL FORMALISM . . . 257
21.6 CONCLUSION . . . 259

**XIII Potential Applications 260**

**22 Charge Configuration Memory Devices: Energy Efficiency and Switching Speed by Mraz et al. (2022) 260**

**XIV Exotic Effects 269**

**23 Quantum billiards by Ravnik et al. 269**
23.0.1 Results . . . 271
23.1 SM . . . 277

**24 Band insulator to Mott insulator transition in a bilayer Hubbard model by Kancharla, Okamoto 287**
24.1 Article . . . 288

**25 Ultrafast Electronic Structure Engineering in 1$T$-TaS$_2$: Role of Doping and Amplitude Mode Dynamics by Jayabalan et al. 293**

**26 Filling-dependent intertwined electronic and atomic orders in the flat-band state of 1T-TaS$_2$ by Geng 306**
26.0.1 Results and Discussion . . . 307
26.0.2 Conclusion . . . 311
26.0.3 Methods . . . 311
26.0.4 References: . . . 312

**27 Dualistic insulator states in 1T-TaS $_2$ crystals (2023) by Wang et al. 321**
27.1 Article . . . 321
27.1.1 Introduction . . . 321
27.1.2 Results . . . 323
27.1.3 Discussion . . . 333
27.1.4 Methods . . . 334
27.2 My Discussion . . . 337
27.2.1 My Conclusion ans Summary . . . 337
27.2.2 My Main questions . . . 338
27.2.3 What I Understood Wrongly (Maybe) . . . 343

**28 Distinguishing a Mott Insulator from a Trivial Insulator with Atomic Adsorbates by Lee et al. 350**

**XV Appendix 356**
.1 Appendix . . . 356
.1.1 Literature . . . 356

**Bibliography 357**
.2 References from Generally Main Articles . . . 357
.3 References from Main Articles about Experiments . . . 453
.4 References from Main Articles about Applications . . . 454

# Preface to part 2

Other My Theories

Main experiments

Other Special Theories, Models

Another Explanations of a Typical Theories

Other Experiments and Simulations

### Amazing facts

(I'll reveal it later)

### Puzzles for motivation

(I'll reveal it later)

# Part VII
# Other Articles and Theories in a Nutshell

## 7 Other articles in a Nutshell

### 7.1 Other Articles About Calculations in a Nutshell

#### 7.1.1 Essence of "First principles investigation of $TaS_2$" by Jung Kim et al.

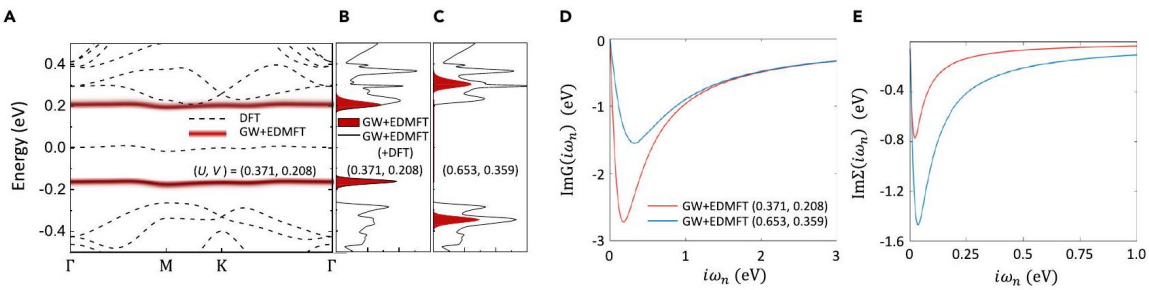


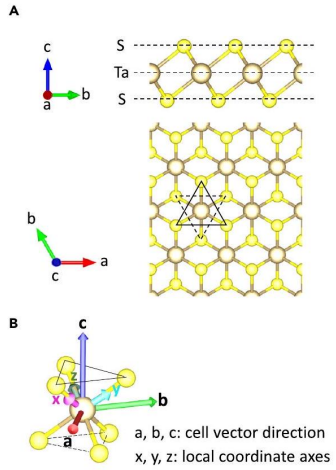


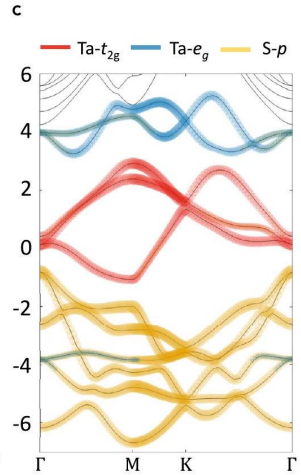


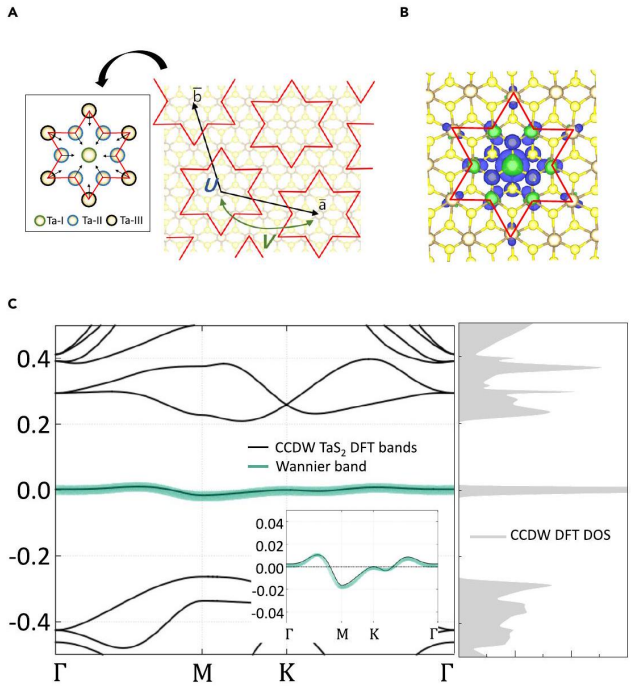


normal phase CDW, but without U and V

Extended Hubbard model

$$H = -\sum_{ij\sigma} t_{ij} c^\dagger_{i\sigma} c_{j\sigma} + U \sum_i n_{i\uparrow} n_{i\downarrow} + V \sum_{\langle ij \rangle} n_i n_j - \mu \sum_i n_i.$$

The calculated $t$, $U$, and $V$ define the many-body model.

Effective SOD interactions

$$U_{\mathbf{R}-\mathbf{R}'} = \frac{1}{N_q} \sum_{\mathbf{q}} U_{\mathbf{q}} e^{i\mathbf{q}\cdot(\mathbf{R}-\mathbf{R}')}.$$

$$U = \frac{1}{13^2} \sum_{\mathbf{R},\mathbf{R}'\in\mathrm{SOD}} U_{\mathbf{R}-\mathbf{R}'}, \qquad V = \frac{1}{13^2} \sum_{\substack{\mathbf{R}\in\mathrm{SOD}_1 \\ \mathbf{R}'\in\mathrm{SOD}_2}} U_{\mathbf{R}-\mathbf{R}'}.$$

These formulas give the effective local interaction $U$ and nearest-neighbor interaction $V$ between SOD molecular orbitals.

Interacting Green function

$$G(\mathbf{k}, i\omega_n) = \left[i\omega_n - t(\mathbf{k}) + \mu - \Sigma(\mathbf{k}, i\omega_n)\right]^{-1}.$$

Dynamically screened interaction

$$W(\mathbf{q}, i\Omega_m) = v(\mathbf{q}) \left[1 - v(\mathbf{q}) P(\mathbf{q}, i\Omega_m)\right]^{-1}.$$

EDMFT Weiss fields

$$\mathcal{G} = \left[G_{\mathrm{loc}}^{-1} + \Sigma_{\mathrm{loc}}\right]^{-1}, \qquad \mathcal{U} = \left[W_{\mathrm{loc}}^{-1} + P_{\mathrm{loc}}\right]^{-1}.$$

EDMFT impurity problem

$$S_{\mathrm{imp}} = -\iint d\tau\, d\tau'\, \bar{c}(\tau) \mathcal{G}^{-1}(\tau - \tau') c(\tau') + \frac{1}{2} \iint d\tau\, d\tau'\, \mathcal{U}(\tau - \tau') n(\tau) n(\tau').$$

GW contribution

$$\Sigma^{GW}(k, i\omega_n) = -\sum_{q, i\Omega_m} G(k+q, i\omega_n + i\Omega_m) W(q, i\Omega_m),$$

$$P^{GW}(q, i\Omega_m) = 2 \sum_{k, i\omega_n} G(k+q, i\omega_n + i\Omega_m) G(k, i\omega_n).$$

GW+EDMFT

$$\Sigma = \Sigma_{\mathrm{imp}} + \Sigma_{\mathrm{nonloc}}^{GW}, \qquad P = P_{\mathrm{imp}} + P_{\mathrm{nonloc}}^{GW}.$$

Spectral function

$$A(\mathbf{k}, \omega) = -\frac{1}{\pi} \operatorname{Im} G^R(\mathbf{k}, \omega).$$

Charge susceptibility

$$\chi(\mathbf{q}) = \left. \frac{-P(\mathbf{q}, i\Omega_m)}{1 - v(\mathbf{q}) P(\mathbf{q}, i\Omega_m)} \right|_{\Omega_m = 0}.$$

### 7.1.2 Essence of "Dynamical control of Coulomb int. 1T-$TaS_2$" by Notter et al.

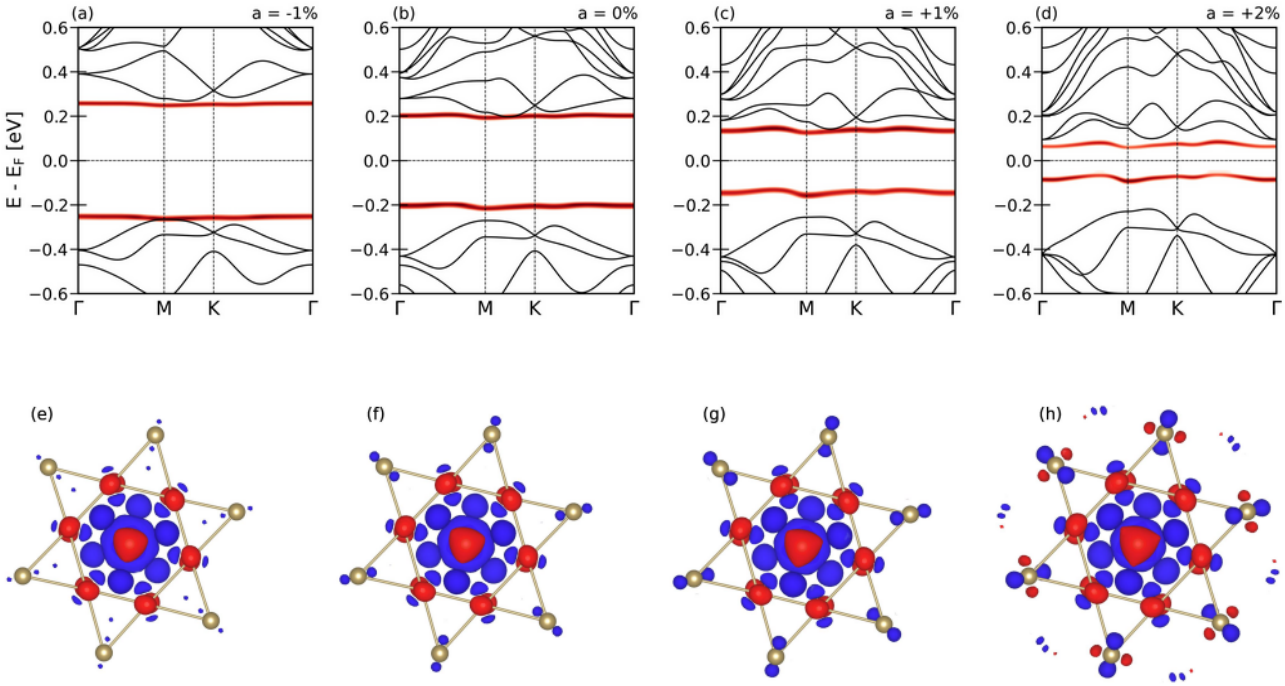


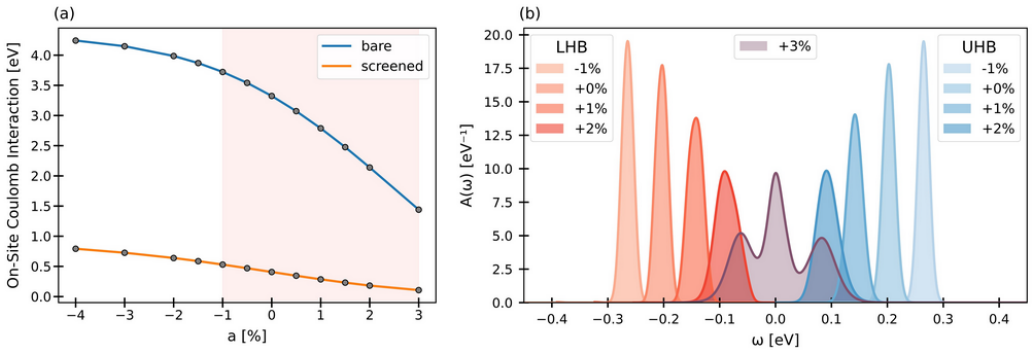


$W = (1 - V\chi_0)^{-1}V$

$$U = W(1 + \chi_0^t W)^{-1}, \tag{7.1}$$

$$\chi_0^t(\mathbf{r}, \mathbf{r}') = 2 \sum_{nn' \in t} \sum_{\mathbf{qk}} \frac{f_{n'\mathbf{k}+\mathbf{q}} - f_{n\mathbf{k}}}{\epsilon_{n'\mathbf{k}+\mathbf{q}} - \epsilon_{n\mathbf{k}}} \psi^*_{n\mathbf{k}}(\mathbf{r})\psi_{n'\mathbf{k}+\mathbf{q}}(\mathbf{r})\psi^*_{n'\mathbf{k}+\mathbf{q}}(\mathbf{r}')\psi_{n\mathbf{k}}(\mathbf{r}'), \tag{7.2}$$

$$\hat{H}_a = \sum_{ij,\sigma} H_a^{(\mathbf{R}_i - \mathbf{R}_j)} \hat{c}^\dagger_{i\sigma}\hat{c}_{j\sigma} + U_a \sum_i \hat{n}_{i\uparrow}\hat{n}_{i\downarrow}, \tag{7.3}$$

## 7.2 Other Articles About Experiments in a Nutshell

### 7.2.1 Essence of "Dualistic insulator states in 1T-TaS $_2$ crystals" by Wang et al.

(I'll write my summary text later)

laddering sliding → weaker interlayer overlap → suppressed SoD dimerization

$\rightarrow\downarrow t_\perp$, $\downarrow$ screening $\rightarrow\uparrow U/t_\perp$ → Mott-insulating behavior,

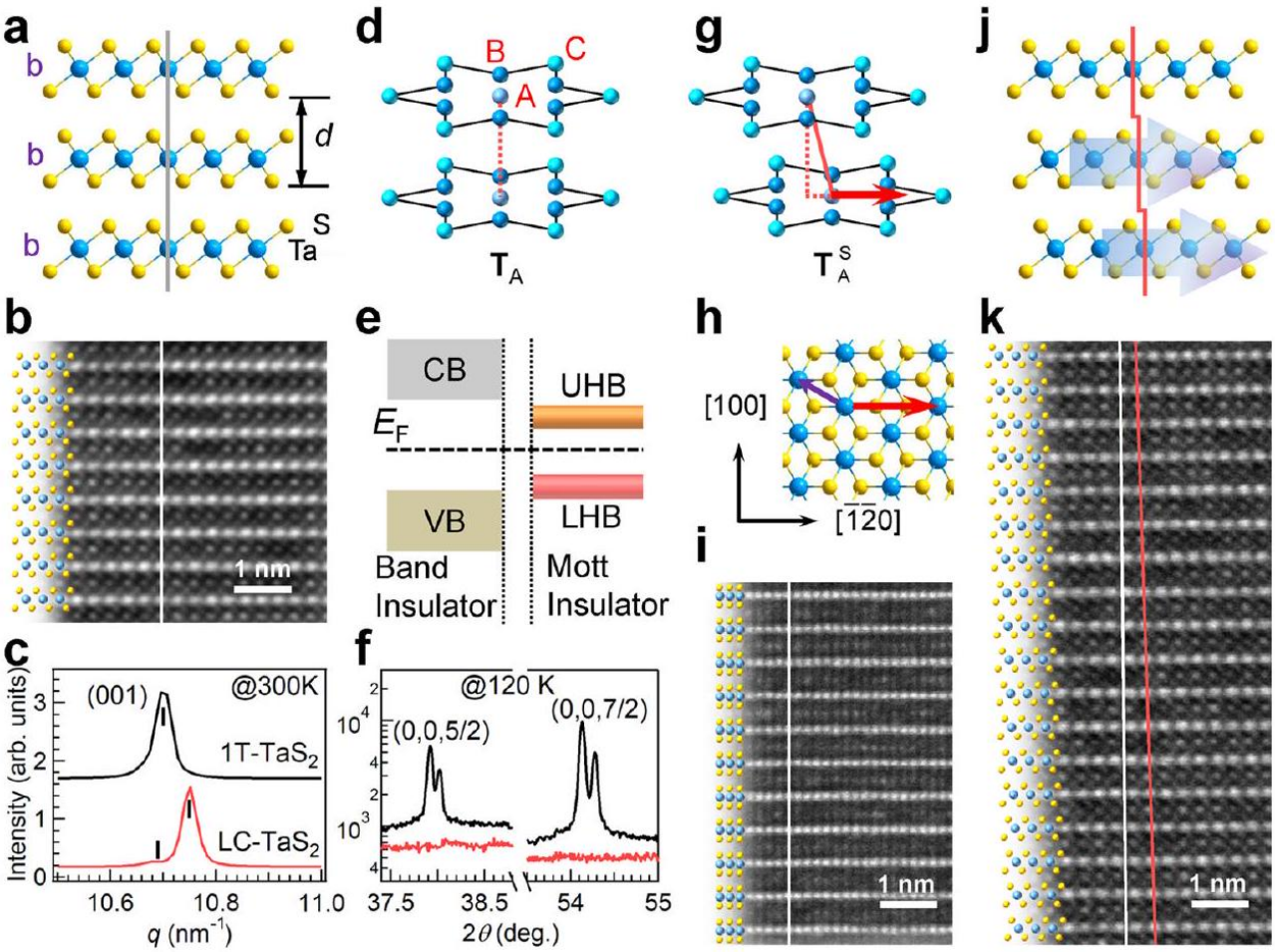

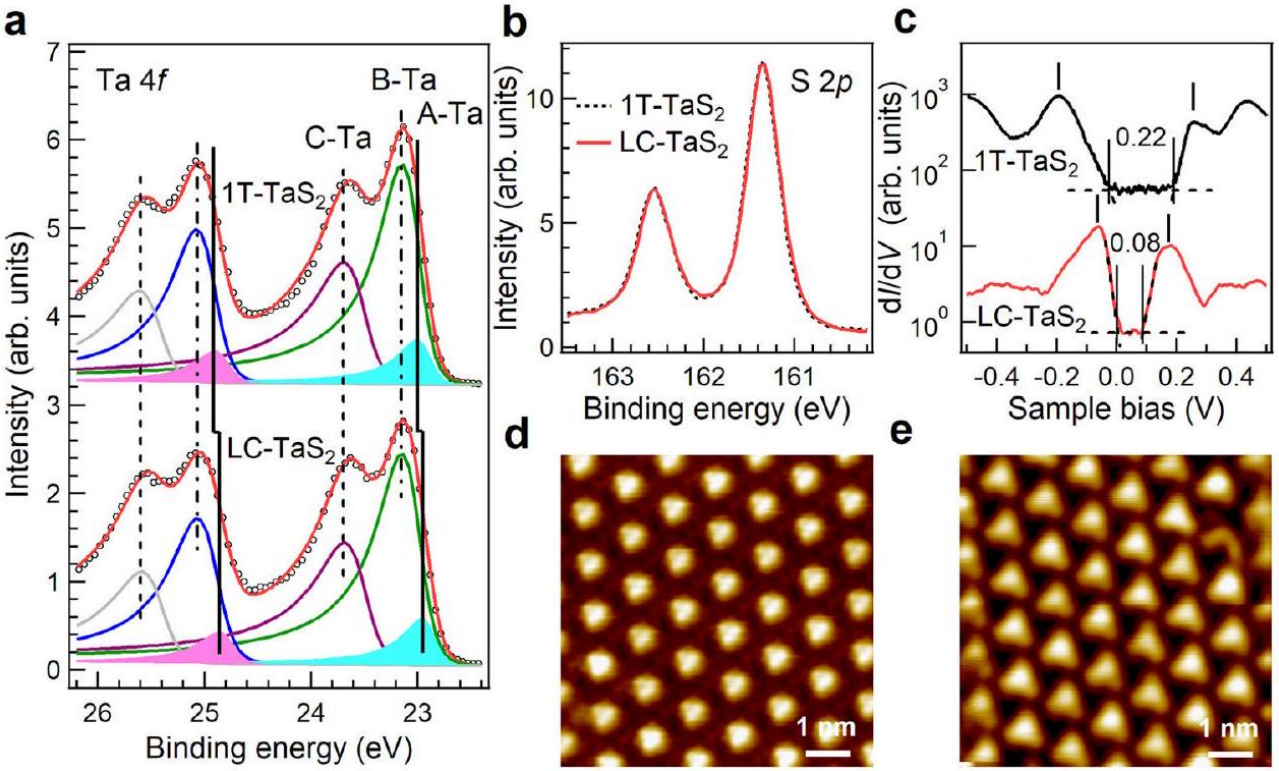
a
Ta 4f
B-Ta
A-Ta
C-Ta
1T-TaS2
LC-TaS2
Intensity (arb. units)
Binding energy (eV)
b
S 2p
1T-TaS2
LC-TaS2
Intensity (arb. units)
Binding energy (eV)
c
1T-TaS2
LC-TaS2
0.22
0.08
dI/dV (arb. units)
Sample bias (V)
d
1 nm
e
1 nm

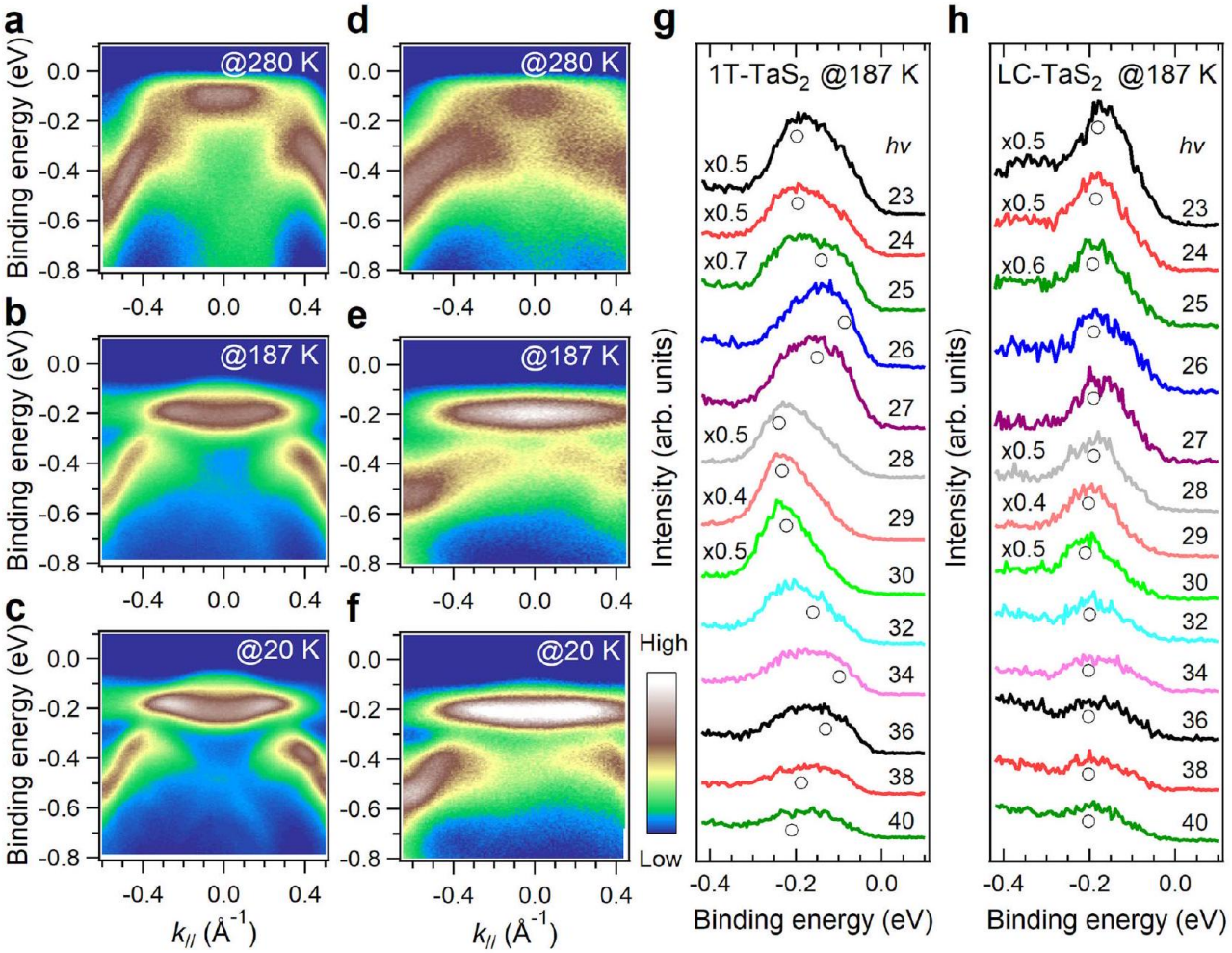
a
@280 K
b
@187 K
c
@20 K
d
@280 K
e
@187 K
f
@20 K
Binding energy (eV)
$k_{//}$ (Å$^{-1}$)
High
Low
g
1T-TaS2 @187 K
h
LC-TaS2 @187 K
hv
Intensity (arb. units)
Binding energy (eV)

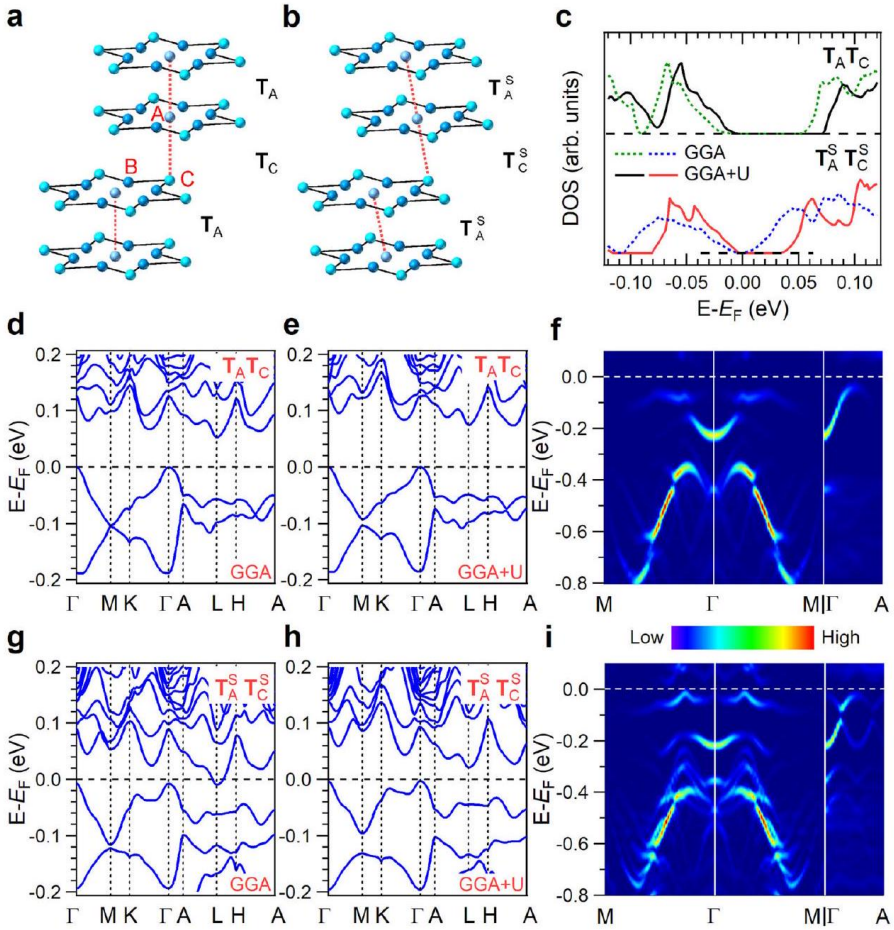
a
b
c
A
B
C
$T_A$
$T_C$
$T_A^S$
$T_C^S$
DOS (arb. units)
GGA
GGA+U
E-$E_F$ (eV)
d
e
f
g
h
i
E-$E_F$ (eV)
Γ M K Γ A L H A
M Γ M|Γ A
Low
High

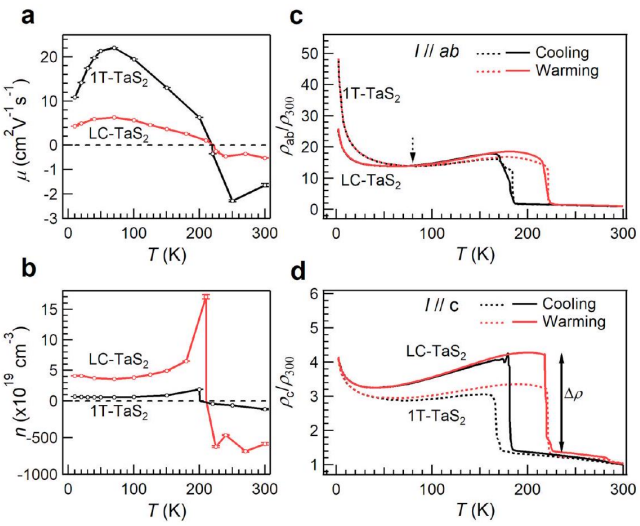
a
b
c
d
1T-TaS$_2$
LC-TaS$_2$
$\mu$ (cm$^2$V$^{-1}$s$^{-1}$)
$n$ (x10$^{19}$ cm$^{-3}$)
$\rho_{ab}/\rho_{300}$
$\rho_c/\rho_{300}$
$I$ // $ab$
$I$ // c
Cooling
Warming
$\Delta\rho$
$T$ (K)

# Part VIII
# Other My Theories

### 7.2.2 Taking into account dimensinality

(??? how to do it??? revise Rossnagel, what did he write about it?)

# Part IX
# Calculations from First Principles

## 8 First principles investigation of screened Coulomb interaction and electronic structure of low-temperature phase $TaS_2$ by Jung Kim, Yong Jeong, Joon Han (2022)

**Abstract**

By means of ab initio computation schemes, we examine the electronic screening(formula for electronic screening?) , Coulomb interaction strength (final formula for Coulomb interaction strength for exactly this material?) , and the electronic structure(that plot of bands below) of a quantum spin liquid candidate monolayer TaS2 in its low-temperature commensurate chargedensity-wave phase.

Not only local (U) but non-local (V) correlations (non-local (V) correlations?) are estimated within random phase approximation based on two different screening models (which different screening models?) .

Using GW + EDMFT (GW plus extended dynamical mean-field theory) method(what is this method?) , we investigate the detailed electronic structure by increasing the level of non-local approximation from DMFT ($V = 0$) to EDMFT and GW + EDMFT.

### 8.1 Article

(BY THE WAY, WHAT IS HARD IN JUST INPUTTING A VALUES TO THE CODE???? I HAVE NEVER UNDERSTOOD THIS)

(the article obtains:

$$t \to 0 \quad \Longrightarrow \quad W \to 0 \quad \Longrightarrow \quad E(k) \approx \epsilon_0,$$

for the

$$H = -\sum_{ij\sigma} t_{ij} c^\dagger_{i\sigma} c_{j\sigma} + U \sum_i n_{i\uparrow} n_{i\downarrow} + V \sum_{\langle ij \rangle} n_i n_j - \mu \sum_i n_i \tag{7}$$

this is the main its value. )

#### 8.1.1 Introduction

(just abstract intro) Understanding the effect of Coulombic interaction between electrons in solid has long been a central theme of condensed matter physics.

[1] Notably, the relevant material systems are being extended to include various two-dimensional (2D) van der Waals materials (what is the van der Waals material?) [2–9] and more recently their twisted combinations.

(summary of Hubbard model, I'll think later about it) [10–18] The local on-site interaction (conventionally represented by U in Hubbard model) can induce electron localization, magnetic moment and thereby leading to metal-to-insulator and magnetic phase transition.

[1,19–21] Many of most intriguing phenomena have been explored within this picture such as unconventional superconductivity and quantum spin liquid. [21–26] (interesting but most likely irrelevant effects)

Non-local Coulomb interaction (denoted by $V$ in extended Hubbard model) also plays an important role. (origin of non-local Coulomb interaction?)

For example, it can enhance the itinerancy (=traveling from place to place) of electrons by screening Coulomb interactions or broadening the effective bandwidth. [27,28] (learn why later)

(intro to phase transitions) Out of its competition and cooperation with electron hoppings and local correlations, various instabilities can be induced toward the charge-ordered or charge density wave (CDW) phase and many others including high angular momentum superconductivity. [27–37] (I am assured that high angular momentum SC is irrelevant)

(just some citations about $V$, they could be just in the one before previous sentence) Recently, the effect of non-local Coulomb interaction receives increasing attention in 2D material. [6,38–41]

(intro to TaS2) Among many correlated van der Waals materials, $TaS_2$ provides an intriguing case by displaying multiple ordered phases and their transitions. [42–45]

(typical property of TaS2) At high temperature, $TaS_2$ is known to be metallic and has 1 T structure shown in Figure 1A.

(typical property of TaS2) As temperature is lowered, it exhibits so-called 'nearly commensurate CDW (NCCDW)', and then finally becomes insulating. [46,47]

(typical property of TaS2) Superconductivity is also observed below $T_C \approx 2-5$ K by applying pressure, doping or electric field (check the electric field, didn't know about it) . [42–44]

(here is a bad formulation of the fact that there is also a PLD of a David star form) Importantly, the stabilization of the low temperature insulating phase is accompanied by commensurate CDW (CCDW) transition for which the long-range 'star of David (SOD)' (SOD will be used in this article a lot) pattern of atomic rearrangement is well identified in both experiments and simulations (see Figures 2A and 2B). [46–50]

This phase hosts a flat band in the close vicinity of chemical potential because of the reduced hopping integral in between SOD molecular orbitals (for example, $E(k) = \epsilon_0 - 2t\cos(ka)$, so if $t$ is lower than the band is flatter) .

(the hopping integral diminishes, because orbitals are more localized, so they overlap less and this is directly seen in the hopping integral)

(just "our study is important" promise:) Therefore, unveiling (=reveal something for the first time) the electronic property of CCDW SOD phase is important to understand the metal-insulator transition and the other related phases observed or suggested in this material at low temperature. [42–45,51–53]

Given that Ta atom has the 4+ formal valance ($Ta^{4+}(S^{2-})_2$) , the SOD unit cell should have odd number of electrons (i.e., $13 = 5\ d^1 \times 13$), and CCDW- $TaS_2$ is expected to be metallic according to the standard band picture.

(GPT: The formal ionic picture of $TaS_2$ is $Ta^{4+}(S^{2-})_2$. Neutral Ta has the approximate valence-electron configuration Ta : $[\mathrm{Xe}]\,4f^{14}5d^3 6s^2$, so formally removing four electrons gives $Ta^{4+} : 5d^1$. Thus, each Ta atom contributes one $d$ electron to the relevant low-energy electronic states.)

(GPT: In the formal ionic picture, each Ta atom contributes one $5d$ electron. Therefore, a Star-of-David (SOD) cluster containing 13 Ta atoms has 13 $d$ electrons.)

(GPT: In the CCDW phase, six bonding molecular orbitals are completely filled by 12 electrons, leaving one electron in the isolated SOD-derived band near $E_F$. Since this band can accommodate two electrons per SOD due to spin degeneracy, it is half-filled.)

(GPT: In the standard non-interacting band picture, a half-filled band has the Fermi energy inside the band and therefore corresponds to a metallic state. Thus, 13 $d$ electrons $\rightarrow$ 12 electrons in filled bonding states + one electron in a half-filled band $\rightarrow$ metallic CCDW-$TaS_2$.)

(GPT: Experimentally, however, CCDW-$TaS_2$ is insulating, indicating the importance of physics beyond the standard band picture, such as strong electronic correlations and Mott localization.)

It is however in a sharp contrast to experiments. [54] (and what was wrong in this reasoning?)

Several recent studies focusing on this issue suggested that either Mott mechanism or interlayer dimerization(interlayer dimerization?) is responsible for metal-to-insulator transition. [45,55–61](learn this methods!)

The important challenge here is to estimate the strengths of Coulomb interactions. [62] (so these Coulomb interactions somehow should help explain PT, since the standard reasoning is not working)

Another intriguing possibility in this material is quantum spin liquid (QSL). (where is it in phase diagram?)

(there is a spin in TaS2, so it might be a QSL) By noting that the low-temperature CCDW phase forms a triangular lattice and carries nominally S = $\frac{1}{2}$ local moment(how is it, carries S = $\frac{1}{2}$ local moment? why is it so???) , the low temperature $TaS_2$ was suggested as a QSL candidate. [51]

(some good for QSL effects are also present) This idea is supported by the absence of long-range magnetic order down to low temperature and the gapless spin excitations. [51–53](what are these effects?)

Notably, a recent study highlights the effect of non-local Coulomb interaction ($V$) (non-local Coulomb interaction???) on the magnetic nature related to QSL. [63] (it is just a motivation to study Coulomb interactions, because maybe they can be used in QSL)

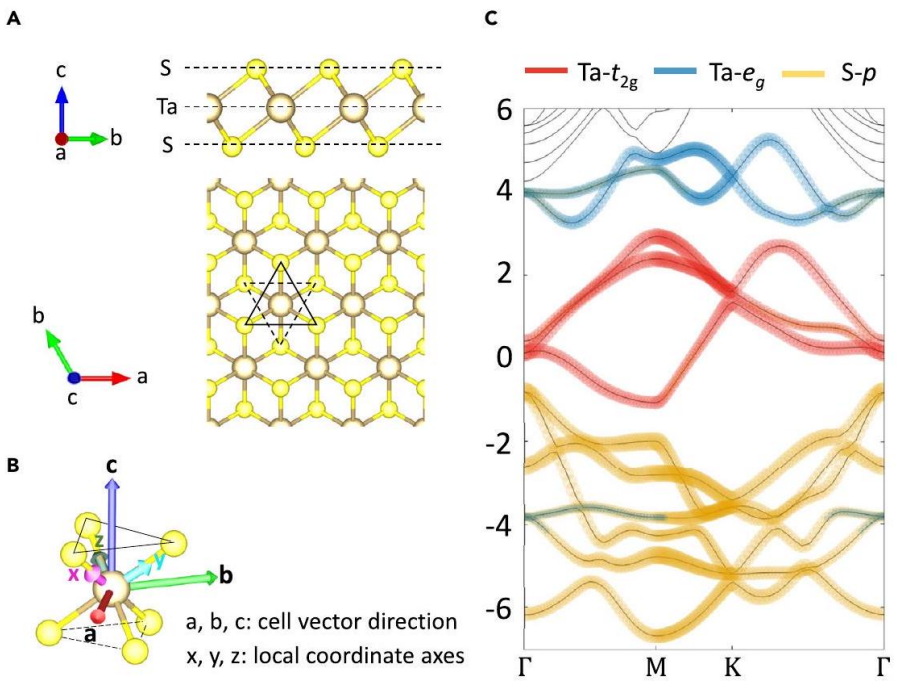


Figure 1. Crystal and electronic structure of $\mathbf{1T-TaS_2}$
(obvious description of 1a: ) (A) Crystal structure of monolayer 1 $T-TaS_2$. The side and top view is presented above and below, respectively. As shown in the side view, a layer consists of S-Ta-S layer. In the top view, the triangle (solid line) and inverted triangle (dotted line) indicates the S atoms around Ta in the upper and the lower layers, respectively.
(B) The local environment(local environment?) around Ta.
The Ta atom is surrounded by six S atoms forming the octahedral structure with slight trigonal distortion.
The red, green, and blue arrow (a, b, and c vectors) indicates the three cell vectors shown in (A).
The magenta, cyan, and olive colored arrow shows the local coordinate axes for Ta-d orbital projection.
Local axes point to the octahedral directions by neglecting the small trigonal distortion.
(C) The orbital-projected band structure of 1T-TaS2 (it is meant at normal state, since fig. 2 will be at CDW state) . Blue and red color shows the $Ta-t_{2\ g}$ and $Ta-e_g$ orbital contribution (why exactly such contributions?) , respectively, and yellow refers to the $p$ orbital contribution of $S$ atoms. (what are the units on Y axes, $E-E_F$???)

(repetition of a title) In this paper, we examine the detailed electronic behaviors of monolayer $TaS_2$.

Based on two different models, the electronic screenings are taken into account within random phase approximation (RPA). (what is exactly RPA here?)

Correlation strengths (Correlation strengths?) , in terms of both on-site $U$ and inter-site V, are successfully quantified for the low-temperature CCDW phase.

(repetition of an abstract) By adopting GW + EDMFT, [32,64–69] we calculate the electronic structure with three different levels of approximation (DMFT, extended GW+EDMFT, GW+GW+EDMFT) for inter-site correlation (learn later, what is the meaning of them?) .

Although the Mott gap is mainly governed by the local interaction (why Mott gap is mainly governed by the local interaction?) , non-local Coulomb interaction is also sizable (=has some influence on bands) .

(some effects will be discussed =) Its effect on the electronic screening, band dispersion and

another possibility toward charge-ordered phase are discussed.

### 8.1.2 Results and Discussion

**Non-interacting band structure and tight-binding parameters**

Figures 1A and 1B shows the crystal structure of 1 T $-$ $TaS_2$ and the local $TaS_6$ unit, respectively. ($TaS_6$ is a molecular unit cell)

The corresponding non-interacting band structure within generalized gradient approximation (GGA; i.e., $U = V = 0$eV) (generalized gradient approximation???) is presented in Figure 1C where different colors represent the different orbital characters as projected onto the local coordinates (projected onto the local coordinates???) as defined in Figure 1B.

(look at the red bands from the plot) Ta- $t_{2\ g}$(why exactly them?) states dominate the near Fermi energy ($E_F$) region and the $t^1_{2\ g}$ configuration is well identified ($t^1_{2\ g}$ configuration is well identified?) .

The higher energy bands above +3 eV and below -1 eV are mainly composed of Ta-$e_g$ and S-p character (why exactly them?) , respectively, whereas the greenish bands reflect the mixture of Ta $-$ $e_g$ and S $-$ $p$ (how can it be that greenish bands are the mixtures?) .

The overall electronic feature is in good agreement with previous studies. [56,70−72] (check some of them later!)

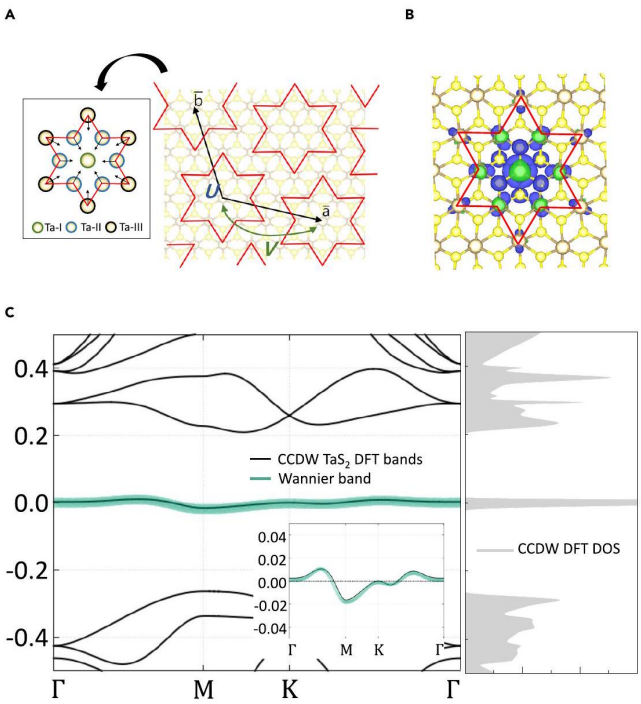


Figure 2. Crystal and electronic structure of CCDW-$TaS_2$
(A) Crystal structure of CCDW phase of $TaS_2$.
Twelve Ta atoms move toward the central Ta, forming a SOD unit (inset) and a molecular orbital at around the center.(so totally we have a 13 atom molecule)
$U$ and $V$ refers to the on-site and the inter-site Coulomb interaction of the molecular orbital, respectively.
$\bar{a}$ and $\bar{b}$ are the unit cell vectors corresponding to CCDW phase.
(B) The calculated MLWF (maximally localized Wannier function) for the SOD molecular orbital in $CCDW - TaS_2$. (I guess that blue means a region where there is a big density of electrons, green - the biggest) Red line depicts the SOD unit. (maybe this quantity is used later for calculation of bands)
(magic results of DMFT:) (C) The calculated DFT band structure (left; black line) and its density of state (right).
The overlaid green line shows the band structure of MLWF for SOD molecular orbital.(so the results fully coincide)
The inset shows the zoom-in figure near $E_F$.

(reminder about TaS2) By lowering temperature, $1\ T - TaS_2$ is known to undergo CDW structural transitions.

(reminder about TaS2) So-called nearly commensurate charge density wave (NCCDW) phase is stabilized below $T \approx 350$ K and followed by CCDW at $T \approx 180$ K. [46–48]

(there is a PLD=) Figure 2A depicts the CCDW structure, so-called SOD pattern, in which twelve Ta atoms move toward the central one forming a 13-Ta-atom unit cluster. [46,47,73,74]

(intro to spectra) In this phase, the band structure also changes accordingly. [55,56,75,76] (check this literature!)

As shown in Figure 2C, a well-separated single electron band is solely responsible for the low energy region near $E_F$(since only it will be partly occupied, so the physics will be because of it) whereas six bonding orbital states are fully occupied by twelve Ta-d electrons well below $E_F$(I guess we don't see them, they are below the bottom of the plot) .

It is noted that the near $E_F$ band is fairly flat and nondispersive. (was it so before? I can't

compare, because fig. 1 has strange units on Y axes)

It is therefore prone to metal-to-insulator transition and other exotic possibilities such as quantum spin liquid phase when interactions come in to play. [55,56,75,76](why do we need a flat band for it???)

(Fig. 2c - bands with another method) The green-colored line in Figure 2C shows the band produced by maximally localized Wannier function (MLWF) [77,78] based on which we estimated a reliable set of parameters for the low energy effective (non-interacting) Hamiltonian of CCDW-$TaS_2$. (and how did they estimate them?)

Its real space visualization is given in Figure 2B. (how to calculate the fig. 2b?)

The calculated TB parameters are as follow: the first and the second neighbor hopping is $|t_1| = 1.812$ and $|t_2| = 0.814$meV, respectively, well compared with the previous reports. (why are they such???)

[63,79] It is interesting to note that the third neighbor hopping $|t_3| = 1.785$meV is larger than $|t_2|$ and comparable with $|t_1|$.[63] (why is it so, it is so strange??? what are the orbitals for it? can we see it on fig. 2b?)

### The estimation of on-site and inter-site correlation

Now we try to calculate the interaction parameters from first-principles. (maybe it is about finding TB parameters)

(abstract useless intro) Quantitative information of correlation strength(correlation strength?) is often crucial for exploring the possible exotic quantum phases and understanding their properties.

In the debate over the band gap origin of $TaS_2$, [45,55−61] for example, the size of on-site $U$ is of key importance. (connection btw $U$ and the gap?)

Non-local $V$ is of particular interest in the systems close to the CDW instability as it can induce charge-ordering instability(charge-ordering instability??? how?) in the extended Hubbard systems. [27,32,80]

In general, the constructed phase diagrams can be qualitatively different depending on the non-local term. (are there examples? with this $V$ we get this phase diagram, with another - another?)

As such, there have been several attempts to directly estimate the interaction strengths of various transition metal dichalcogenides (TMDs). [2,55,81−85] (check how they tried to estimate the parameters???)

(calculations ar hard, we know it) However, ab initio calculation of these parameters corresponding to CDW phase is challenging especially for non-local $V$.

We calculate both $U$ and $V$ for CCDW- $TaS_2$ based RPA/cRPA method. (what is this method?)

(we wanted to use only cRPA) Ideally, it is desirable to compute these parameters from the direct cRPA calculation of CCDW unitcell.

(but cRPA was too slow for this problem) However, a difficulty arises from the demanding computation cost in dealing with the large cell size.

Here we extract the interaction parameters from the undistorted 1 T-structure(because only geometry is changed, so it will be taken into account below) , [55,86] and consider two different approaches (which approaches?) .

First, the CCDW $U$ value can be estimated as the average of atomic Coulomb interactions of 1 T structure whose screening process can be considered within RPA. (formula below is assumed)

This first way of computation gives rise to:

$$U = \frac{1}{13^2} \sum_{R,R' \in \star} U_{R-R'} \tag{1}$$

(why $\frac{1}{13^2}$?)

where $U_{R-R'}$ is the Fourier transformed leading eigenvalue of RPA-screened Coulomb matrix (RPA-screened Coulomb matrix???) .

Namely, $U_{R-R'} = \frac{1}{N_q} \sum_q U_q e^{iq\cdot(R-R')}$ where $U_q = \max \lambda_q$, and $\lambda_q$ is the eigenvalue of RPA-screened Coulomb matrix $\mathcal{W}_{\mathrm{II}}^{\mathcal{RA}}$ represented in the eigenbasis of bare Coulomb matrix. [86] (see the citation, it is a big formalism, it should be explained there?)

The screened Coulomb matrix is calculated for $t_{2\ g}$ manifold; namely, the red-colored bands in Figure 1C. (see the cited paper to understand what is meant here?)

R and R′ are the lattice cell vectors corresponding to 1T structure, and q is the lattice momentum.

$N_q$ is the grid number of lattice momentum.

The white-star symbol represents the $\star$ indices of Ta atoms in the same SOD (which is composed of 13 Ta atoms; see Figure 2A).

In this first approach, the inter-site correlation V is also computed within the same spirit:

$$V = \frac{1}{13^2} \sum_{R \in \star, R' \in \star} U_{R-R'} \tag{2}$$

where the black-star symbol $\star$ refers to the indices of Ta atoms belonging to the nearest-neighboring SOD (indicated by the unit cell vector $\bar{a}$ and $\bar{b}$ in Figure 2A). (I guess it is meant that R' and R belong to different stars)

The calculated $U$ and $V$ following this first approach are presented in Table 1; referred to as '3 bands (RPA)'.

Table 1. Estimated Coulomb interactions for CCDW-$TaS_2$

| | 3 bands (RPA) | 5 bands (cRPA) |
|---|---|---|
| $U$(eV) | 0.371 | 0.653 |
| V (eV) | 0.208 | 0.359 |

The calculated on-site ( $U$) and inter-site Coulomb interaction ($V$) corresponding to the SOD CDW phase. The parameters are estimated from two different approaches as discussed in the main text.

The second approach considers the weights of Ta atoms by projecting them onto the CCDW molecular orbital. (what is going on here?)

This idea itself is not necessarily combined with (c)RPA but can go with any other method of computing atomic Coulomb interaction $\bar{U}^{\mathrm{LR}}$.[55] (atomic Coulomb interaction $\bar{U}^{\mathrm{LR}}$???) (this idea improves other idea, this is what is written?)

The molecular orbital U then can be estimated from the atomic $\mathrm{Ta}-d\overline{\mathrm{U}}^{\mathrm{LR}}$ : By calculating the projected weights of Ta-d orbitals ($|\mathrm{d_a}\rangle$) with respect to CCDW molecular orbitals ($|\Psi\rangle$), (this is this second method, some weights.. see cited paper about it)

$$\frac{U}{\overline{U}^{LR}} = \sum_{a \in \star} |\langle\ \mathrm{d_a}\ |\ \Psi\rangle|^4 \tag{3}$$

(how to use this formula at all????)

where $a$ is the atomic Ta index.

Ta atoms are classified into three different types considering their symmetry (see the inset of Figure 2A).

Our calculations give rise to $|\langle d_{\mathrm{a}} \mid \Psi\rangle|^2 = 0.229, 0.064$ and 0.035 for Ta-I, Ta-II, and Ta-III, respectively. (how to calculate it???)

U and V are obtained as follow: (these are the expressions in scope of approach 2, if you understand it, you'll understand these formulas:)

$$U = \sum_{R,R'\in\star} |\langle d_R \mid \Psi\rangle|^2 \, |\langle d_{R'} \mid \Psi\rangle|^2 \, \bar{U}_{R-R'} \tag{4}$$

$$V = \sum_{R\in\star,R'\in\star} |\langle d_R \mid \Psi\rangle|^2 \, |\langle d_{R'} \mid \Psi\rangle|^2 \, \bar{U}_{R-R'} \tag{5}$$

Here we calculate $\bar{U}_{R-R'}$ based on cRPA.

Table 1. Estimated Coulomb interactions for CCDW-TaS $_2$

| | 3 bands (RPA) | 5 bands (cRPA) |
|---|---|---|
| $U$(eV) | 0.371 | 0.653 |
| V (eV) | 0.208 | 0.359 |

The calculated on-site ( $U$) and inter-site Coulomb interaction ($V$) corresponding to the SOD CDW phase. The parameters are estimated from two different approaches as discussed in the main text.

In Table 1, this set of results are denoted by ' 5 bands (cRPA)' as 5-band model of 1 $\mathrm{T-TaS_2}$ (both $\mathrm{t_{2\ g}}$ and $\mathrm{e_g}$) is adopted.

(why are they called 3-band and 5-band???)

The calculation results are summarized in Table 1.

The $U$ values are different in two different approaches: $U = 0.371$eV from '3-band RPA' and 0.653 eV from ' 5 -band cRPA'. (which value is the correct???)

It is not surprising but rather expected because different 'models' shall take care of different screenings. (where are the screenings in the models?)

For example, the weaker correlation in the former model is naturally attributed to the more screening channels taken into account (what is known about number of channels taken into account?) .

Both results ('3-band RPA' and ' 5 -band cRPA') therefore carry useful information for further study whereas the larger supercell of CCDW phase is not directly computable within cRPA (Performing their cRPA calculation directly using this full 13-Ta Star-of-David unit cell would be computationally impossible) .

(so basically it is written here again, that $U$ and $V$ are calculated in the undistorted phase)

(below, it is about another work, which gave different results and some vague ideas about the reasons)

It is also noted that our results are considerably larger than that of a previous study based on linear response calculation; $U = 0.180$eV. [55] (learn this another calculation)

(here is just a link to another study, I'll look at it If I decide understand better the second approach here) From the point of view of the extracting method of CCDW- $U$ value from 1T structure, the previous study by Darancet et al. [55] is the same with our second approach (i.e., 'five-band model').

Thus the ∼0.5 eV difference certainly reflects the difference between the linear response adopted by Darancet et al. [55] and our RPA method whereas only the latter takes the electronic

screenings into account directly. (I guess, it is a very hard question, why the results of two methods that make sense differ?)

(another quantity in another calculation method does not coincide again with this one) Interestingly, however, the calculated atomic $U$ itself (that is, corresponding to Ta-d on-site interaction) is larger in the linear response calculation, $\bar{U}^{\mathrm{LR}} = 2.27\mathrm{eV}$, [55] than our cRPA $\bar{U}_{R-R'=0} = 1.83\mathrm{eV}$.

(the difference is in the model, not only in the method) It is therefore indicative of that the difference is not simply attributed to the difference between cRPA and linear response.

We presume that the projection also plays an important role. (projection???)

As shown in Equation 4, our projection method not just takes all of Equation 3 portions into account but it also includes some inter-site contributions(inter-site contributions???) between different Ta atoms in an SOD molecular orbital.

(below, some vague ideas about comparison with another material)

It is also useful to compare the correlation strength of $TaS_2$ to that of $NbSe_2$. (why do we need to compare them?)

A previous study of Kamil et al. [86] reports $U = 0.3\mathrm{eV}$ for $NbSe_2$ and their estimation was based on RPA and three-band model, corresponding to our first approach. (check how did they do it, with the similar approach?)

It is noted that $U$ for $\mathrm{CCDW} - TaS_2$ is significantly larger than $\mathrm{CCDW} - NbSe_2$ by about 0.07 eV (see Table 1), which is likely attributed to the different screenings (why screenings?) as discussed in the previous studies on the comparison of $TaSe_2$ with $TaS_2$.[85,87] (check this comparison, looks informative)

Here we also note that a recent ARPES study suggests the weaker correlation for $NbSe_2$ than $TaSe_2$. [88] (how is it, weaker correlation?)

Table 1 also presents the inter-site correlation strength $V$ which can be important for understanding the possible exotic phases relevant to this system, but has not been quantitatively estimated before.

(we got big V) First of all, sizable V value is noticed; ∼50% of on-site correlation in both models.

(we'll use Hubbard model written in appendix) It can therefore be important to take this effect into account within the extended Hubbard model.

It is obvious that Hubbard-type correlation is indispensable for overcoming the DFT-GGA (Generalized Gradient Approximation) limitation which gives rise to metallic band structure. [54]

(actually, this calculations were done before (but without V)) Previous theoretical studies showed that the inclusion of on-site correlation within DFT+ $U$ and single-site DMFT (single-site DMFT??) indeed well reproduces the insulating state even though the former incorrectly predicts the magnetically ordered ground state (magnetically ordered ground state??) . [55,56]

(so local on-site correlations U are sufficient to turn CCDW-TaS2 from the metallic state predicted by ordinary DFT into an insulating state)

(check that papers!!! they are maybe one step before this paper, so they will help to understand it)

According to the DMFT calculation, Mott transition starts to occur at $U \sim 0.7\mathrm{eV}$ in bulk $TaS_2$. [56] (why is it so? I'll look later to this paper)

Note that both sets of our results in Table 1 provide the large enough interaction $U$ with respect to the bandwidth $W \sim 9|t| \sim 0.02\mathrm{eV}$ (from where do we take a bandwidth???) .

Importantly, however, the effect of non-local $V$ has remained unexplored. (why???)

### GW + EDMFT electronic structure

To see the effect of both local $U$ and non-local $V$ on the electronic structure, one needs to go beyond the single-site DMFT. (and what are the plots for the case without V and U?)

Here we adopt GW + EDMFT for that purpose. (are there alternatives?)

Computation details are given in STAR Methods.

In Figures 3A-3C, we present the calculated spectral functions as obtained by analytic continuation of Matsubara Green function using maximum entropy method. [89–91] (learn this method! how to do it? I heard of it, but it is informative to see these articles)

In sharp contrast to the metallic DFT-GGA band structure(see, you can do a very hard calculation, but then there will be another method of calculations which will give purely another results) , GW + EDMFT result clearly shows the insulating gap being consistent with experiment, DFT+ $U$ and single-site DMFT.

(so why the DFT-GGA is so wrong?)

In the case of DFT+ $U$, the long-range spin order naturally comes in as the ground state configuration. [55] (do we touch somewhere here the long-range spin order?)

With our first set of interaction parameters ($U = 0.371$eV, $V = 0.208$eV; shown in Figures 3A and 3B), the upper and the lower Hubbard peak (I think, it is meant Hubbard band) is observed at about $\pm 0.2$eV, respectively, which is well compared with a recent STM experiment of monolayer $TaS_2$.[54,69] (check this plot from experiment!)

Another set of 5-band model produces a slightly larger gap as presented in Figure 3C.

Although this stronger correlation set of parameters also reproduces the insulting phase as expected (= we got the gap in DOS) , the notable difference is the position of Hubbard bands which are in this case found inside the uncorrelated states (thin black line). (The calculation is done with U and without U (no correlation). In both cases the system is insulating, but the positions of the Hubbard bands tells us that with U is a more realistic case.)

(what is the more realistic model???? with which V??? with which U??? why???)

The detailed spectroscopic characterization of the valence and conduction band can therefore be useful to determine the correlation strength (that U parameter) whereas the band gap size itself is probably too small to be precisely compared. (and how to find U from bands?)

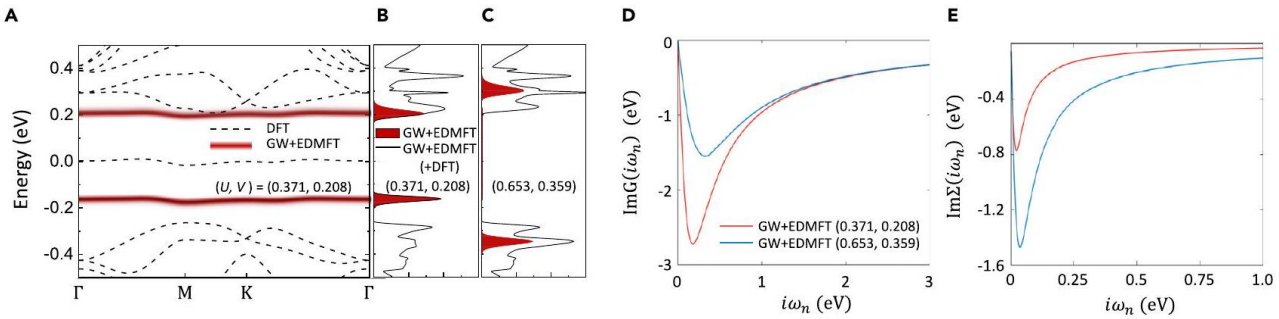


Figure 3. Results of GW + EDMFT calculations
(GPT: Figure 3 shows the interacting electronic structure of the CCDW phase: unlike Figure 2, where $U$ and $V$ are not included, here the extended Hubbard model with the calculated $U$ and $V$ is solved using GW+EDMFT. The narrow half-filled SOD band is split into lower and upper Hubbard bands, producing a Mott gap. Both estimated $(U, V)$ parameter sets give an insulating state, although they predict different Hubbard-band positions. Figures 3D and 3E additionally confirm the Mott character through the vanishing low-energy spectral weight and quasiparticle weight $Z \simeq 0$.)
(A) The momentum-dependent spectral function calculated by DFT-GGA (dashed lines) and GW + EDMFT (red line).
The estimated Coulomb interaction parameters from 3-band model were used as given in parentheses $(U, V)$.
(B and C) The momentum-integrated spectral function of GW + EDMFT.
Coulomb interactions are estimated by (B) 3-band and (C) 5-band model.
The red colored data represent the density of states (DOS) of GW + EDMFT, and the black lines show the DOS sum of GW + EDMFT and DFT.
(D and E) The calculated imaginary part of local (D) Green function and (E) self-energy of GW + EDMFT.
The red and blue color refers to the two different interaction parameter sets as given in the parentheses.

To unveil the other aspects of electronic correlations, we present the imaginary part of local Green function in Figure 3D.

(some sentences below argue that fig. 3d, 3e give us knowledge about the existence of the gap)

With both parameter sets, it is clearly observed that $\mathrm{Im\,G}\,(\mathrm{i}\omega_\mathrm{n})$ goes to zero as $\mathrm{i}\omega_\mathrm{n} \to 0$, indicative of the zero spectral weight at $\mathrm{E_F}$, namely, the insulating phase. (can we expect this or it is only from calculations?)

From the fact that minimum frequency point is lower in the 3-band-model case (red line) (I guess it is still afout fig. 3D) , it also confirms the observed gap size difference in Figures 3A-3C. (I don't understand these connections, fig. 3D and 3A)

The calculated self-energies highlight the same feature: In Figure 3E, the slope of $\partial\,\mathrm{Im}\,\Sigma/\partial\omega_n$ at $\mathrm{i}\omega_n \to 0$ shows the vanishing quasiparticle weight $Z = \left[1 - \frac{\partial\,\mathrm{Im}\,\Sigma}{\partial\omega_n}\right]^{-1} \approx 0$, indicating Mott phase. (why Z is such?) (why does it indicate a Mott phase?)

**Further examination of screened Coulomb interactions**

(SUMMARY: the results of dependence on V is presented, there is an phase transition on a very nonphysical V. All this is pointless, because the V is fixed, they have already told us their value/)

To gain further insights on the electronic correlations, we investigate the screened Coulomb interaction and the charge susceptibility. (I thought that it was already screened before?)

Figure 4A shows the real part of screened Coulomb interaction $\mathrm{W_{loc}}$ . (what is the formula for it?)

The effect of non-local Coulomb interaction can be systematically examined by changing the level of approximations (changing method of calculation, EDMFT, GW+EDMFT, only thems) .

Here we fix the value of on-site interaction $U = 0.371$eV, and compare the results of two different inter-site $V = 0$ and 0.208 eV. (why such two values? then, it is written, V=0.565...)

GW self-energy can also be taken into account on top of that. (how?? how to use GW on top?)

In high-frequency limit, the effective Coulomb interaction approaches to its 'bare' value $U = 0.371$eV in all three cases. (why high-frequency limit??? Isn't it a constant?)

In low frequency limit, $\mathrm{W_{loc}}$ gradually decreases as the more non-local interactions get involved. (influence of non-local interaction on W???)

It is a general feature of extended Hubbard model [27,32](reminder to learn Hubbard model) although the screening effect by $V$ is not significant as the charge fluctuation is largely suppressed in Mott phase.

Figure 4B also shows that $\mathrm{W}\,(\mathrm{i}\Omega_\mathrm{m} = 0)$ gradually decreases as $V$ increases (in the low V limit) whereas it does not vary much when $V$ is small.

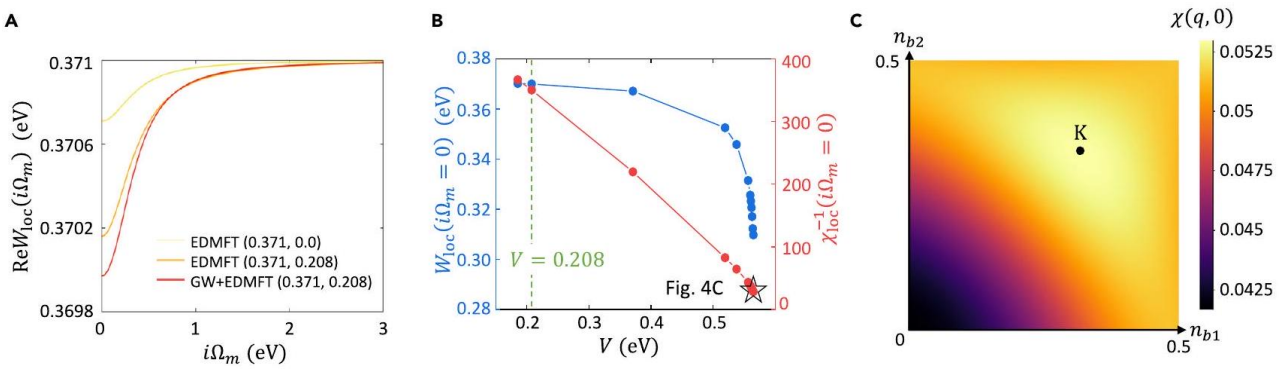


Figure 4. Bosonic (why bosonic?) quantities from GW + EDMFT
(A) The screened Coulomb interaction $W$ calculated by DMFT (yellow; $V = 0$), EDMFT (orange), and GW + EDMFT (red).
(B) The static part of $\mathrm{W}_{(loc)}\,(\mathrm{i}\Omega_m = 0)$ (blue-colored; left yaxis) and $\chi^{-1}_{\mathrm{loc}}$ (red-colored; right yaxis) as a function of $V$.
The 3-band RPA estimation of $V$ is indicated by vertical green-dotted line.
(C) The momentum-dependent charge susceptibility $\chi\,(\mathrm{q}, \mathrm{i}\Omega_m = 0)$ in the vicinity of charge-ordered phase.
The calculation has been conducted with $(U, V) = (0.371\mathrm{eV}, 0.565\mathrm{eV})$ indicated by black-star symbol in (B). ($\mathrm{n_b}$ is just a coordinate along $q_x$ or $q_y$) (K point on c) plot is a point of the maximum)

In large $V$ limit, on the other hand, its effect can become pronounced. (why intuitively it is so?)

(here is an interpretation of fig. 4B, V is charge hopping = fluctuations, which "screen" reduction of W) As shown in Figure 4B, the screened Coulomb interaction is significantly reduced, indicating that charge fluctuations caused by V further screen the Coulomb interactions. [27,32]

In this regime of V $\gtrsim$ 0.5eV, $W_{(loc)}$ gets rapidly reduced, and simultaneously, the local charge susceptibility diverges (red line): [27,32] (check cited papers!)

$$\chi_{\mathrm{loc}}^{-1} \to 0 \tag{6}$$

(why is it so from formulas?)

where $\chi_{\mathrm{loc}} = \frac{1}{\mathrm{N_q}} \sum_{\mathrm{q}} \chi(\mathrm{q})$ and (why there is a such def?) $\chi(\mathrm{q}) = \left(-\mathrm{P}\left(\mathrm{q}, \mathrm{i}\Omega_m\right)\left[1 - \mathrm{v}(\mathrm{q})\mathrm{P}\left(\mathrm{q}, \mathrm{i}\Omega_m\right)\right]^{-1}\right)_{\mathrm{i}\Omega_m=0}$. (and why $\chi$ is such???)

To perform the detailed investigation of this limit, we calculate the momentum-dependent static charge susceptibility at $V = 0.565$eV which is deemed (=regard something in a specific way) a point close enough to the charge-ordering-type instability (corresponding to the black star point in Figure 4B).

In Figure 4C, a diverging feature is clearly identified at $(\mathrm{n_{b_1}}, \mathrm{n_{b_2}}) = (0.333, 0.333)$ indicative of a charge-ordering instability (another hypothetical phase transition like a Pereles model) ($\mathrm{n_{b_i}}$ is fractional coordinate of reciprocal lattice vector $\mathrm{b_i}$). (what is this $\mathrm{n_b}$????)

Although it implies the further charge instability over the CCDW phase (= another CDW on top of well-known CDW!!!) , the critical $V$ value is far from being realistic in the current system. (but for some reason it is not physical)

### Conclusions

(repetition of an intro) We investigated the electronic screening and the spectral property of monolayer $TaS_2$ by the combination of DFT, RPA, MLWF and GW + EDMFT.

(repetition of an intro) Both on-site and inter-site correlation strengths are estimated based on two different ab initio RPA approaches.

(repetition of an intro, it is not clear what exactly is meant) Although its Mott insulating gap is mainly determined by on-site interaction, the inter-site $V$ is also found to be sizable.

The comparison of DMFT, EDMFT, and GW + EDMFT exhibits a systematic change of the electronic behavior because the levels of non-local self-energy computations are varied. (why exactly levels of non-local self-energy computations are varied? and why it gives such impact?)

Our work provides useful information and insight for understanding $TaS_2$ and the other related systems. (what useful it gives? how one can use it?)

### Limitations of the study

(repetition of the intro) Our computations of screened Coulomb interaction are based on random phase approximation.

(repetition of the intro) The electronic structure calculations take account of non-local as well as dynamical self-energy(dynamical self-energy??? is it dynamical?) within GW + EDMFT.

The singlet formation(singlet formation???) caused by interlayer dimerization [57,59,92,93] could not be considered in our calculation setups.

### 8.1.3 Method Details

| Method | SOURCE | IDENTIFIER |
|---|---|---|
| Software and algorithms | | |
| VASP | Georg Kresse et al. [94,95] | https://www.vasp.at/ |
| ComDMFT | Sangkook Choi et al. [96] | https://github.com/comscope/ComDMFT |
| RESPACK | Kazuma Nakamura et al. [97] | https://sites.google.com/view/kazuma7k6r |

#### DFT and extended Hubbard model construction

We performed DFT calculations of monolayer 1T- and CCDW- $TaS_2$ with Vienna Ab initio Simulation Package (VASP). [94,95] (is it a popular one code?)

(reminder to learn 1T and 2H phases, why they are such?)

The cell parameters and the internal coordinates were optimized with the force criterion of 0.1 meV/Å (optimization with the force criterion?) .

The GGA-PBE functional [98] (GGA-PBE functional?) was used and the 25Å vacuum (vacuum?) taken into account to simulate the monolayer.

$21 \times 21 \times 1 (8 \times 8 \times 1)$ k-grid and 500 eV (400 eV) cutoff energy were adopted for $1\ \mathrm{T} - \mathrm{TaS_2}$ $(\mathrm{CCDW} - \mathrm{TaS_2})$. (I guess it is not very important, why exactly such values?)

To describe the effect of electronic correlations of low-energy state in CCDW- $TaS_2$, we consider the single-band extended Hubbard model: (reminder to learn the Hubbard model)

$$H = -\sum_{ij\sigma} t_{ij} c^{\dagger}_{i\sigma} c_{j\sigma} + U \sum_{i} n_{i\uparrow} n_{i\downarrow} + V \sum_{\langle ij \rangle} n_i n_j - \mu \sum_{i} n_i \tag{7}$$

(why there is a minus in the first term?)

where $c^{\dagger}_{i\sigma}$ and $c_{i\sigma}$ is the creation and annihilation operator of electron, respectively, with spin $\sigma = \{\uparrow, \downarrow\}$ at site $i$.$\mathrm{n_i} = c^{\dagger}_{i\sigma} \mathrm{c_{i\sigma}}$ is the electron number operator at site $i$, and $\sum_{\langle ij \rangle}$ denotes the nearest-neighbor summation.

The hopping amplitude $\mathrm{t_{ij}}$ between two site $i$ and $j$ was calculated with the MLWF method. [77,78]

$U$ and $V$ is the local and non-local Coulomb interaction, respectively. (as was discussed in the article)

The realistic estimation of these two interaction parameters is one of the main issues of current study. (write how they were obtained here)

For this purpose, we used (c)RPA method as implemented in RESPACK code. [97] (and how it was used? maybe I'll try to reproduce it)

#### GW + EDMFT

(write somewhere the GW+EDMFT, I don't understand this method)

(GW + EDMFT code works like this: ) The Hamiltonian is solved within GW + EDMFT whose standard self-consistent loop can be briefly summarized as below. [27,32]

(i) Calculate the lattice green function $G$ and the screened Coulomb interaction $W$:

$$\mathrm{G}\left(\mathrm{k}, \mathrm{i}\omega_{\mathrm{n}}\right) = \left[\mathrm{i}\omega_{\mathrm{n}} - \mathrm{t}(\mathrm{k}) + \mu - \Sigma\left(\mathrm{k}, \mathrm{i}\omega_{\mathrm{n}}\right)\right]^{-1},$$
$$\mathrm{W}\left(\mathrm{q}, \mathrm{i}\Omega_m\right) = \mathrm{v}(\mathrm{q})\left[1 - \mathrm{v}(\mathrm{q})\mathrm{P}\left(\mathrm{q}, \mathrm{i}\Omega_m\right)\right]^{-1},$$

where k and q are the crystal momentum vectors. $\mathrm{i}\omega_\mathrm{n}$ and $\mathrm{i}\Omega_\mathrm{m}$ refers to the fermionic and bosonic Matsubara frequency, respectively.

The momentum space t(k) corresponds to the Fourier transformed $\mathrm{t_{ij}}$.

$\Sigma\left(\mathrm{k}, \mathrm{i}\omega_n\right)$ and $\mathrm{P}\left(\mathrm{q}, \mathrm{i}\Omega_m\right)$ represents the electron self-energy and the polarization function, respectively. (what is the formula for them?)

The bare Coulomb interaction v(q) is given by $\mathrm{v(q)} = 2\ \mathrm{V}\left[\cos\left(\mathrm{q_x}\right) + \cos\left(\frac{1}{2}\mathrm{q_x} + \frac{\sqrt{3}}{2}\mathrm{q_y}\right) + \cos\left(-\frac{1}{2}\mathrm{q_x} + \frac{\sqrt{3}}{2}\mathrm{q_y}\right)\right]$. (why is it so?)

In practice, we start the first loop from $\Sigma\left(\mathrm{k}, \mathrm{i}\omega_\mathrm{n}\right) = \mathrm{P}\left(\mathrm{q}, \mathrm{i}\Omega_\mathrm{m}\right) = 0$.

($\mu$=???? )

(ii) Compute the fermionic and bosonic Wiess fields (I guess the name "Wiess fields" is not that important?) $\mathcal{G}$ and $\mathcal{U}$:

$$\mathcal{G}\left(\mathrm{i}\omega_n\right) = \left[\mathrm{G_{loc}}\left(\mathrm{i}\omega_n\right)^{-1} + \Sigma_{\mathrm{loc}}\left(\mathrm{i}\omega_n\right)\right]^{-1},$$
$$\mathcal{U}\left(\mathrm{i}\Omega_m\right) = \left[\mathrm{W_{loc}}\left(\mathrm{i}\Omega_n\right)^{-1} + \mathrm{P_{loc}}\left(\mathrm{i}\Omega_m\right)\right]^{-1},$$

(it was a typo here, it was written "$\mathrm{W_{loc}}\left(\mathrm{i}\omega_n\right)$") where $A_{\mathrm{loc}}\ \left(i\omega_n\right) = \frac{1}{N_k}\sum_k A\left(k, i\omega_n\right)$ for any $A$ , and $N_k$ is the number of $k$-points.

(iii) Solve the following impurity model(impurity model???) to obtain the impurity self-energy $\Sigma_{\mathrm{imp}}\left(\mathrm{i}\omega_\mathrm{n}\right)$ and polarization $P_{\mathrm{imp}}\ \left(i\Omega_m\right)$ (get somehow $\Sigma_{\mathrm{imp}}\left(\mathrm{i}\omega_\mathrm{n}\right)$ and $P_{\mathrm{imp}}\ \left(i\Omega_m\right)$ from this action) (and how to get them???) :

$$\mathrm{S_{imp}} = \iint_0^\beta \mathrm{d}\tau\ \mathrm{d}\tau'\overline{\mathrm{c}}(\tau)\left[-\mathcal{G}^{-1}\left(\tau - \tau'\right)\right]\mathrm{c}\left(\tau'\right) + \frac{1}{2}\iint_0^\beta \mathrm{d}\tau\ \mathrm{d}\tau'\mathcal{U}\left(\tau - \tau'\right)\mathrm{n}(\tau)\mathrm{n}\left(\tau'\right)$$

where $\mathrm{A}(\tau)$ is the Fourier transormation of $\mathrm{A}\left(\mathrm{i}\omega_\mathrm{n}\right)$(for example, $A$ can be W or P) , and $\overline{\mathrm{c}}(\tau)$ and $\mathrm{c}(\tau)$ are the Grassmann field for electrons.

(why at all the method and formula here is such???)

(are there somewhere explicit calculations of this method?)

Here we took the continuous-time hybridization expansion quantum Monte Carlo impurity solver as implemented in ComDMFT package. [96] (quantum Monte Carlo impurity solver??? how does it work at all???)

(iv) Construct the new self-energy and polarization function from the calculated $\Sigma_{\mathrm{imp}}\left(\mathrm{i}\omega_\mathrm{n}\right)$ and $\mathrm{P_{imp}}\left(\mathrm{i}\Omega_m\right)$:

$$\Sigma\left(\mathrm{k}, \mathrm{i}\omega_n\right) = \Sigma_{\mathrm{imp}}\ \left(\mathrm{i}\omega_n\right) + \Sigma^{\mathrm{GW}}_{\mathrm{nonloc}}\ \left(\mathrm{k}, \mathrm{i}\omega_n\right),$$
$$\mathrm{P}\left(\mathrm{q}, \mathrm{i}\Omega_m\right) = \mathrm{P_{imp}}\ \left(\mathrm{i}\Omega_m\right) + \mathrm{P}^{\mathrm{GW}}_{\mathrm{nonloc}}\ \left(\mathrm{q}, i\Omega_m\right),$$

where

$$\Sigma^{\mathrm{GW}}\left(\mathrm{k}, \mathrm{i}\omega_\mathrm{n}\right) = -\sum_{\mathrm{q}, \mathrm{i}\Omega_m}\mathrm{G}\left(\mathrm{k}+\mathrm{q}, \mathrm{i}\omega_\mathrm{n} + \mathrm{i}\Omega_m\right)\mathrm{W}\left(\mathrm{q}, i\Omega_m\right),$$
$$\mathrm{P}^{\mathrm{GW}}\left(\mathrm{q}, \mathrm{i}\Omega_m\right) = 2\sum_{\mathrm{k}, \mathrm{i}\omega_\mathrm{n}}\mathrm{G}\left(\mathrm{k}+\mathrm{q}, \mathrm{i}\omega_\mathrm{n} + \mathrm{i}\Omega_m\right)\mathrm{G}\left(\mathrm{k}, \mathrm{i}\omega_\mathrm{n}\right),$$

and

$$A_{\mathrm{nonloc}}\ \left(k, i\omega_n\right) = A\left(k, i\omega_n\right) - A_{\mathrm{loc}}\ \left(i\omega_n\right).$$

(v) Go back to the step (i) and repeat the calculations until $\mathrm{G}\left(\mathrm{k}, \mathrm{i}\omega_\mathrm{n}\right)$ and $\mathrm{W}\left(\mathrm{q}, i\Omega_m\right)$ are converged.

(give example of this calculation, looks very complicated!!!!)

## 8.2 Discussion

### 8.2.1 My conclusion about the article

#### My conclusion

The main idea is that they use also a V parameter (not only U) in the Hubbard model and check which bands appear because of it. And they claim that the comparison to experiment is better.

Also, they use many advanced methods.

#### When can the intersite interaction $V$ be neglected?

(think about it, it is important to understand!!! GPT:)

Although previous calculations found a sizable Coulomb interaction $V$ between neighbouring Star-of-David clusters, its effect on the electronic spectrum is expected to be small in the deep Mott-insulating regime. At half-filling, strong local repulsion suppresses charge fluctuations and approximately fixes one electron on every cluster,

$$\langle \hat{n}_i \rangle \simeq 1. \tag{8.1}$$

Consequently, the intersite term

$$\hat{H}_V = V \sum_{\langle ij \rangle} \hat{n}_i \hat{n}_j \tag{8.2}$$

is approximately constant because

$$\hat{n}_i \hat{n}_j \simeq 1. \tag{8.3}$$

It therefore produces mainly an overall energy shift without qualitatively modifying the equilibrium Mott spectrum. This explains why extended-Hubbard calculations have found that the insulating state of monolayer $1T$-$TaS_2$ is primarily controlled by the local interaction $U$, despite the non-negligible magnitude of $V$.

Nevertheless, the omission of $V$ may become less reliable close to the distortion-driven metal–insulator transition considered in the article. As the Star-of-David Wannier orbital becomes more delocalized, the bandwidth increases and the local interaction decreases,

$$W(a) \uparrow, \qquad U(a) \downarrow, \tag{8.4}$$

which enhances local and intersite charge fluctuations,

$$\left\langle (\hat{n}_i - \langle \hat{n}_i \rangle)^2 \right\rangle \uparrow . \tag{8.5}$$

In this regime, $\hat{n}_i \hat{n}_j$ is no longer approximately constant, and $V$ can modify the energies of charge excitations. For example, an inter-cluster hopping process,

$$(1,1) \longrightarrow (0,2), \tag{8.6}$$

has an approximate interaction-energy cost

$$\Delta E \sim U - V, \tag{8.7}$$

rather than $U$ alone. Nonlocal interactions may therefore shift the Hubbard bands, provide additional screening, and change the critical distortion at which the metallic state appears. Furthermore, $V$ should itself depend on the structural coordinate,

$$V_{ij}(a) = \int d\mathbf{r}\, d\mathbf{r}'\, |w_{ia}(\mathbf{r})|^2 W_a^r(\mathbf{r}, \mathbf{r}') |w_{ja}(\mathbf{r}')|^2, \tag{8.8}$$

particularly because the Wannier orbitals become substantially more extended as the distortion changes. Thus, neglecting $V$ is probably reasonable for describing the qualitative equilibrium Mott-insulating state, but its inclusion would be necessary to test quantitatively the predicted Hubbard-band shifts and the precise position of the distortion-driven metal–insulator transition.

### 8.2.2 Questions About the Methods, Calculations

**How are the effective $U$ and $V$ obtained in the cRPA approach?**

(GPT:)

The low-energy electronic state of one Star-of-David (SOD) is a molecular orbital spread over the 13 Ta atoms,

$$|\Psi_{\mathrm{SOD}}\rangle = \sum_i c_i |d_i\rangle, \qquad w_i = |c_i|^2 = |\langle d_i|\Psi_{\mathrm{SOD}}\rangle|^2, \qquad \sum_i w_i = 1.$$

Here $|d_i\rangle$ denotes an atomic Ta-$d$ orbital and $w_i$ gives its weight in the SOD molecular orbital. The cRPA calculation provides the screened Coulomb interactions $\bar{U}_{ij}$ between these atomic orbitals. To obtain the effective interaction of the whole SOD orbital, these atomic interactions are projected onto $|\Psi_{\mathrm{SOD}}\rangle$. For two electrons on the same SOD,

$$U = \sum_{i,j\in\mathrm{SOD}} w_i w_j \bar{U}_{ij},$$

while for electrons on two neighboring SODs $A$ and $B$,

$$V = \sum_{\substack{i\in\mathrm{SOD}_A \\ j\in\mathrm{SOD}_B}} w_i w_j \bar{U}_{ij}.$$

Thus, $U$ is the effective Coulomb repulsion within one SOD molecular orbital, whereas $V$ is the effective repulsion between neighboring SOD molecular orbitals. The simpler expression

$$U = \frac{1}{13^2} \sum_{i,j\in\mathrm{SOD}} U_{ij}$$

corresponds to assuming equal weight $w_i = 1/13$ on every Ta atom, since $w_i w_j = 1/13^2$. Therefore, schematically,

$$\mathrm{cRPA} \to \bar{U}_{ij}, \qquad \mathrm{DFT/Wannier} \to w_i, \qquad (\bar{U}_{ij}, w_i) \to U, V,$$

and the resulting $U$ and $V$ are then used as parameters of the extended Hubbard model.

**Example of how the effective $U$ and $V$ are obtained.**

(GPT:)

Consider, for simplicity, a molecular orbital distributed over only three atomic Ta-$d$ orbitals instead of the 13 Ta atoms of the real SOD. Suppose that 60% of the electron probability is on atom 1, 30% on atom 2, and 10% on atom 3. A quantum state is written in terms of probability amplitudes $c_i$, while the probabilities are $w_i = |c_i|^2$. Therefore, to obtain probabilities $w_1 = 0.6$, $w_2 = 0.3$, and $w_3 = 0.1$, we write

$$|\Psi\rangle = \sqrt{0.6}|d_1\rangle + \sqrt{0.3}|d_2\rangle + \sqrt{0.1}|d_3\rangle,$$

since $|\sqrt{0.6}|^2 = 0.6$, etc., and $0.6 + 0.3 + 0.1 = 1$. Suppose that cRPA gives the screened Coulomb interactions between these atomic orbitals as

$$\bar{U}_{ij} = \begin{pmatrix} 1.0 & 0.4 & 0.2 \\ 0.4 & 1.0 & 0.4 \\ 0.2 & 0.4 & 1.0 \end{pmatrix} \text{eV}.$$

For example, $\bar{U}_{11} = 1.0$ eV is the screened interaction associated with charge on atomic orbital 1, while $\bar{U}_{12} = 0.4$ eV is the interaction between charge on atomic orbitals 1 and 2. We want to replace these three atomic orbitals by one effective molecular orbital and therefore calculate its effective interaction

$$U_{\text{eff}} = \sum_{i,j} w_i w_j \bar{U}_{ij}.$$

For the chosen example,

$$\begin{aligned} U_{\text{eff}} &= (0.6)^2(1.0) + (0.3)^2(1.0) + (0.1)^2(1.0) \\ &\quad + 2(0.6)(0.3)(0.4) + 2(0.6)(0.1)(0.2) + 2(0.3)(0.1)(0.4) = 0.652 \text{ eV}. \end{aligned}$$

Thus, many atomic interaction matrix elements $\bar{U}_{ij}$ are converted into one effective Hubbard parameter $U_{\text{eff}}$ for the molecular orbital. For the real SOD the same idea is applied to its Ta-$d$ orbital weights,

$$U = \sum_{i,j \in \text{SOD}} w_i w_j \bar{U}_{ij}.$$

To calculate $V$, the same procedure is used, but $i$ belongs to one SOD and $j$ to a neighboring SOD,

$$V = \sum_{\substack{i \in \text{SOD}_A \\ j \in \text{SOD}_B}} w_i w_j \bar{U}_{ij}.$$

Therefore, $U$ describes the effective interaction within one SOD molecular orbital, while $V$ describes the interaction between two neighboring SOD molecular orbitals.

### Comments about structure of TaS2

(GPT:)

The formal ionic picture of $TaS_2$ is

$$\text{Ta}^{4+}(\text{S}^{2-})_2.$$

This is important electronically. Neutral Ta has the approximate valence-electron configuration

$$\text{Ta} : [\text{Xe}]\, 4f^{14} 5d^3 6s^2.$$

Formally removing four electrons gives approximately

$$\text{Ta}^{4+} : 5d^1.$$

Thus, each Ta atom contributes one $d$ electron to the relevant low-energy electronic states.

**What is the difference between fig. 2 and 3? Why in fig. 3 there are more parameters?**

(GPT)

Figure 2C and Figure 3A both describe the electronic structure, but they show different quantities. In Figure 2C, the curves are ordinary non-interacting DFT/MLWF energy bands,

$$E_n(\mathbf{k}),$$

where the many-body effects of $U$ and $V$ are not included. In Figure 3A, $U$ and $V$ are included using GW+EDMFT, and the plotted quantity is the interacting spectral function

$$A(\mathbf{k},\omega) = -\frac{1}{\pi}\,\mathrm{Im}\,G^R(\mathbf{k},\omega).$$

It plays a role similar to an interacting band structure and shows the formation of the lower and upper Hubbard bands.

Figures 2 and 3B,C both contain a density of states, but it is calculated differently. For the non-interacting case,

$$D(E) = \frac{1}{N_k}\sum_{n,\mathbf{k}} \delta(E - E_{n\mathbf{k}}),$$

whereas for the interacting case,

$$D(\omega) = \frac{1}{N_k}\sum_{\mathbf{k}} A(\mathbf{k},\omega).$$

Thus, Figures 3B,C show the interacting DOS for the two different $(U, V)$ parameter sets. Both give a gap and therefore an insulating state, but the positions of the Hubbard bands are different.

Figure 3D shows $\mathrm{Im}\,G(i\omega_n)$. For both parameter sets,

$$\mathrm{Im}\,G(i\omega_n) \to 0 \qquad \text{as } \omega_n \to 0,$$

which confirms the absence of spectral weight at the Fermi energy and therefore the insulating state.

Figure 3E shows the self-energy $\Sigma(i\omega_n)$. From its low-frequency behavior, the quasiparticle weight is estimated as

$$Z = \left[1 - \frac{\partial\,\mathrm{Im}\,\Sigma(i\omega_n)}{\partial\omega_n}\right]^{-1} \simeq 0.$$

The vanishing quasiparticle weight confirms that the insulating state is a Mott state produced by strong electronic correlations.

Thus, the figures can be summarized as

| | | |
|---|---|---|
| Fig. 2C | : | $E_n(\mathbf{k})$ non-interacting DFT/MLWF bands, |
| Fig. 3A | : | $A(\mathbf{k},\omega)$ interacting spectrum, |
| Fig. 3B,C | : | $D(\omega)$ interacting DOS and Hubbard bands, |
| Fig. 3D | : | $G$ confirms zero spectral weight at $E_F$, |
| Fig. 3E | : | $\Sigma,\ Z \simeq 0$ confirms the Mott character. |

### What are Hubbard bands?

(GPT:)

Hubbard bands are correlation-induced electronic states that appear when the Hubbard interaction $U$ becomes strong compared with the bandwidth. In the non-interacting CCDW calculation of Figure 2, there is one narrow half-filled SOD band near $E_F$. When $U$ and $V$ are included and the system is treated with GW+EDMFT in Figure 3, the spectral weight of this band is redistributed into a Lower Hubbard Band (LHB) and an Upper Hubbard Band (UHB), separated by a Mott gap:

$$\text{narrow half-filled SOD band} \xrightarrow{\text{strong } U} \text{LHB} \mid \text{Mott gap} \mid \text{UHB}.$$

Roughly, the LHB corresponds to electron-removal excitations and the UHB to electron-addition excitations. Unlike an ordinary band described by a sharp dispersion $E_n(\mathbf{k})$, a Hubbard band is a region of large spectral weight in $A(\mathbf{k}, \omega)$ and can therefore appear as a broadened or "smeared" band. Thus, the red features in Figure 3 are Hubbard bands: they are correlation-induced descendants of the narrow SOD band in Figure 2 and are absent from the corresponding non-interacting calculation.

### What is the meaning of fig. 4c?

(GPT:)

Figure 4C shows the static momentum-dependent charge susceptibility $\chi(\mathbf{q}, i\Omega_m = 0)$ close to the charge-ordering instability.

The axes $n_{b_1}$ and $n_{b_2}$ are simply the fractional coordinates of the momentum $\mathbf{q}$ in the reciprocal-lattice basis:

$$\mathbf{q} = n_{b_1}\mathbf{b}_1 + n_{b_2}\mathbf{b}_2,$$

where $\mathbf{b}_1$ and $\mathbf{b}_2$ are primitive reciprocal-lattice vectors.

Thus,

$$(n_{b_1}, n_{b_2}) = \left(\frac{1}{3}, \frac{1}{3}\right)$$

means

$$\mathbf{q} = \frac{1}{3}\mathbf{b}_1 + \frac{1}{3}\mathbf{b}_2.$$

The point marked $K$ is the corresponding high-symmetry point of the Brillouin zone. The calculation shows that $\chi(\mathbf{q})$ becomes very large near

$$\mathbf{q} = K,$$

which means that the system is close to developing a charge modulation with this wavevector.

Therefore, Figure 4B shows that a charge-ordering instability is approached, while Figure 4C shows at which momentum it occurs:

$$\mathbf{Q} = K.$$

The value $V = 0.565$ eV used in Figure 4C is larger than the realistic estimated $V$, so this additional charge-ordered state is not expected for the realistic parameters of the material.

### What is the GGA?

(GPT:)

An example of the Generalized Gradient Approximation (GGA) is the PBE functional (Perdew–Burke–Ernzerhof), which is also used in this paper. In GGA, the exchange-correlation energy depends not only on the local electron density $n(\mathbf{r})$, but also on its spatial gradient $\nabla n(\mathbf{r})$:

$$E_{\mathrm{xc}}^{\mathrm{GGA}}[n] = \int d^3r\, n(\mathbf{r})\, \varepsilon_{\mathrm{xc}}\left(n(\mathbf{r}), \nabla n(\mathbf{r})\right).$$

Thus, in contrast to LDA, $E_{\mathrm{xc}}^{\mathrm{LDA}}[n] = \int d^3r\, n(\mathbf{r})\varepsilon_{\mathrm{xc}}(n(\mathbf{r}))$, GGA takes into account spatial variations of the electron density.

### What is the GW that adds to DMFT?

(??????? it is a big topic, I'll think later)

### What is the EDMFT (Extended Dynamical Mean-Field Theory)?

(GPT:)

EDMFT (Extended Dynamical Mean-Field Theory) is an extension of DMFT that allows non-local Coulomb interactions $V$ to be included in addition to the local Hubbard interaction $U$.

For the extended Hubbard model,

$$H = -\sum_{ij\sigma} t_{ij} c_{i\sigma}^{\dagger} c_{j\sigma} + U \sum_{i} n_{i\uparrow} n_{i\downarrow} + V \sum_{\langle ij \rangle} n_i n_j - \mu \sum_{i} n_i,$$

DMFT mainly describes local electronic correlations caused by $U$, while EDMFT additionally accounts for the effects of $V$ through a dynamically screened effective interaction $\mathcal{U}(i\Omega)$.

Thus, the hierarchy used in the paper can be summarized as: DMFT $\rightarrow$ local correlations from $U$; EDMFT $\rightarrow$ adds the effects of non-local $V$ and dynamical screening; GW+EDMFT $\rightarrow$ additionally includes a non-local, momentum-dependent contribution to the electronic self-energy, $\Sigma(\mathbf{k}, i\omega) = \Sigma_{\mathrm{imp}}(i\omega) + \Sigma_{\mathrm{nonloc}}^{GW}(\mathbf{k}, i\omega)$.

### What is the single-site DMFT?

(GPT:)

The central approximation of single-site DMFT is that the electronic self-energy is local, i.e. momentum independent:

$$\Sigma(\mathbf{k}, i\omega_n) \approx \Sigma_{\mathrm{loc}}(i\omega_n).$$

The interacting lattice Green's function is therefore

$$G(\mathbf{k}, i\omega_n) = \frac{1}{i\omega_n + \mu - \varepsilon_{\mathbf{k}} - \Sigma_{\mathrm{loc}}(i\omega_n)},$$

and the local Green's function is obtained by averaging over momentum,

$$G_{\mathrm{loc}}(i\omega_n) = \frac{1}{N_k} \sum_{\mathbf{k}} G(\mathbf{k}, i\omega_n).$$

DMFT maps the lattice problem onto a single interacting impurity coupled to an effective bath. The corresponding Weiss Green's function is determined self-consistently from

$$\mathcal{G}_0^{-1}(i\omega_n) = G_{\mathrm{loc}}^{-1}(i\omega_n) + \Sigma_{\mathrm{loc}}(i\omega_n).$$

The impurity model contains the local Hubbard interaction $U$, schematically

$$S_{\text{imp}} = -\sum_{\sigma,n} c^{\dagger}_{\sigma n}\mathcal{G}_0^{-1}(i\omega_n)c_{\sigma n} + U\int_0^{\beta} d\tau\, n_{\uparrow}(\tau)n_{\downarrow}(\tau).$$

Solving the impurity problem gives a new local self-energy,

$$\Sigma_{\text{imp}}(i\omega_n) = \mathcal{G}_0^{-1}(i\omega_n) - G_{\text{imp}}^{-1}(i\omega_n),$$

and single-site DMFT imposes the self-consistency conditions

$$\Sigma_{\text{loc}} = \Sigma_{\text{imp}}, \qquad G_{\text{loc}} = G_{\text{imp}}.$$

Thus, single-site DMFT treats the local interaction $U$ dynamically and non-perturbatively, but neglects the spatial dependence of the electronic self-energy.

**What is meant by the limitation related to interlayer dimerization and singlet formation?**

(GPT:)

The authors state that their calculation does not include singlet formation caused by interlayer dimerization. Their main calculation describes the correlation-driven mechanism,

$$\text{strong } U, V \longrightarrow \text{Mott localization} \longrightarrow \text{insulating state.}$$

However, another mechanism has been proposed for bulk $TaS_2$. SOD orbitals belonging to neighboring layers can hybridize strongly and form interlayer dimers. Since each SOD has approximately one electron in its low-energy orbital, two neighboring SODs can form a spin singlet,

$$|\text{singlet}\rangle = \frac{1}{\sqrt{2}}\left(|\uparrow\downarrow\rangle - |\downarrow\uparrow\rangle\right), \qquad S = 0.$$

Interlayer hopping $t_{\perp}$ can split the corresponding states into bonding and antibonding states,

$$E_{\pm} \sim \varepsilon_0 \pm t_{\perp},$$

so that the two electrons can occupy the lower bonding state and an insulating gap can appear. Thus, an alternative mechanism is

$$\text{interlayer } t_{\perp} \longrightarrow \text{dimerization and singlet formation} \longrightarrow \text{bonding–antibonding splitting} \longrightarrow \text{insulating}$$

The present calculation does not include this mechanism and therefore cannot determine the relative importance of Mott correlations and interlayer dimerization in bulk $TaS_2$. This limitation is less relevant to an isolated monolayer, where interlayer dimerization is absent.

### 8.2.3 Questions About the Meaning of Methods, Materials: Less Important

**What is the meaning of screening?**

(????? I have no idea, since they do not explain. what should we understand about the screening to understand the paper?)

**How to see that if we go to non CDW phase, then V goes to 0?**

(GPTs opinion, which is most likely useless:)

We do not expect $V$ to become zero in the non-CDW phase. $V$ is the non-local Coulomb interaction and exists also in the normal phase. The values of $U$ and $V$ calculated in the paper are effective interactions for the low-energy SOD model of the CCDW phase; when the SOD structure disappears, that particular effective model and its $U, V$ parameters are no longer applicable.

**What is the value of $\mu$ in the Hamiltonian? 0?**

(GPTs opinion, which is most likely useless:)

$\mu$ is chosen to obtain the required filling, here one electron per effective SOD orbital (half filling). It can sometimes be absorbed into the choice of the zero of energy, but it should not generally be assumed that $\mu = 0$.

**How exactly $t$ change if we go from normal to CDW state?**

(GPTs opinion, which is most likely useless:)

The CDW distortion changes the Ta–Ta distances and orbital overlaps, so the hopping integrals change. After formation of the SOD, the relevant low-energy hoppings are no longer simply hoppings between individual Ta atoms but effective hoppings between SOD molecular orbitals, characterized by $t_1, t_2, t_3, \ldots$

**Comparison of spectra with experiments (???) They are not like in fig. 7 in Rossnagel paper.**

(GPTs opinion, which is most likely useless:)

Figure 3 should not be compared directly with the full experimental spectrum in Rossnagel because the GW+EDMFT calculation describes mainly the isolated low-energy SOD band. The relevant comparison is primarily the Mott gap and positions of the lower and upper Hubbard bands; the paper notes Hubbard peaks around $\pm 0.2$ eV for the weaker interaction set, in reasonable agreement with STM.

**What is wrong in reasoning that TaS2 is a conductor?**

(GPTs opinion, which is most likely useless:)

Within the non-interacting CCDW band picture the reasoning is correct: the remaining SOD band is half-filled and therefore metallic. What is missing is strong electron correlation: sufficiently large $U/W$ splits this band into lower and upper Hubbard bands and produces a Mott insulating state.

**What is the intuitive understanding of W?**

(GPTs opinion, which is most likely useless:)

Here $W$ in $W \sim 9|t|$ is the bandwidth: the energy range over which an electron can disperse because of hopping,

$$W = E_{\max} - E_{\min}.$$

Large hopping generally means a large $W$ and more delocalized electrons; large $U/W$ favors localization.

**Which effects are there from V? exactly in which ways it improves the plot for the case without V?**

(GPTs opinion, which is most likely useless:)

$V$ introduces Coulomb interaction between neighboring SODs and therefore non-local charge fluctuations and dynamical screening. Compared with the $V = 0$ DMFT calculation, including $V$ changes the effective screened interaction and the spectral positions/shape of the Hubbard features; it also allows the charge-ordering instability studied in Figure 4.

**Are the a and b (unit cell vectors) discussed? what if we ahve a different ones?**

(GPTs opinion, which is most likely useless:)

The choice of primitive vectors is not unique. Different valid primitive vectors describe the same lattice; the formulas for $\mathbf{k}$, $\mathbf{q}$ and reciprocal vectors change their coordinate representation, but physical quantities such as the spectrum and susceptibility do not.

**How do we know the a and b vectors? (from ab into calculations)???**

(GPTs opinion, which is most likely useless:)

They are determined from the crystal structure. From the real-space primitive vectors $\mathbf{a}_1, \mathbf{a}_2$, reciprocal vectors $\mathbf{b}_1, \mathbf{b}_2$ are defined by

$$\mathbf{a}_i \cdot \mathbf{b}_j = 2\pi\delta_{ij}.$$

They are then used to represent momenta, for example $\mathbf{q} = n_{b_1}\mathbf{b}_1 + n_{b_2}\mathbf{b}_2$.

**We calculate U from what, from absence of U or from cycle that takes U into account? or do we plug into U only a non distorted configuration?**

(GPTs opinion, which is most likely useless:)

$U$ is calculated before the GW+EDMFT cycle using (c)RPA screening and then used as an input of the Hubbard model. For the effective CCDW model, the interaction is projected onto the SOD molecular orbital associated with the distorted CCDW structure; it is not obtained self-consistently from the later GW+EDMFT cycle.

**Does just W obtained from t or also we need to take U into account?**

(GPTs opinion, which is most likely useless:)

If $W$ means the bandwidth in $W \sim 9|t|$, it is obtained from the non-interacting dispersion and therefore from the hopping parameters $t$; $U$ is not included. This is precisely why the ratio $U/W$ is useful for comparing interaction strength with kinetic energy.

**W=|t|, but what is t? we have t1, t2, t3.**

(GPTs opinion, which is most likely useless:)

Strictly, $W \neq |t|$. For the nearest-neighbor triangular-lattice model,

$$W = 9|t|.$$

With $t_1, t_2, t_3$, the full dispersion $\varepsilon(\mathbf{k})$ contains all three hoppings and

$$W = \max_{\mathbf{k}} \varepsilon(\mathbf{k}) - \min_{\mathbf{k}} \varepsilon(\mathbf{k}).$$

The paper's $W \sim 9|t|$ is an approximate nearest-neighbor estimate.

**If we work with Matsubara GF, what is the temperature?**

(GPTs opinion, which is most likely useless:)

The Matsubara frequencies explicitly contain the temperature,

$$\omega_n = (2n+1)\pi T, \qquad \Omega_m = 2m\pi T,$$

with $k_B = 1$. Therefore a Matsubara GW+EDMFT calculation is performed at a finite specified temperature; the temperature determines the spacing of the Matsubara frequencies.

**Does large $V$ lead to additional charge ordering?**

Yes, but it is unphysical.

(GPT:)

Yes. The CCDW phase is already included in the effective model, where each Star-of-David (SOD) cluster acts as one effective lattice site. If the inter-SOD Coulomb interaction $V$ becomes sufficiently large, it becomes energetically favorable to develop an additional modulation of the charge density between different SODs. This instability is signaled by a divergence of the charge susceptibility $\chi(\mathbf{Q})$ at $\mathbf{Q} = K$. In the calculations it appears for $V \gtrsim 0.5$ eV, with Figure 4C showing the system close to the instability at $V = 0.565$ eV. However, the realistic 3-band RPA estimate is only $V = 0.208$ eV. Therefore, the paper does not predict this additional charge ordering for realistic CCDW-$TaS_2$; it demonstrates a possible instability of the model at unrealistically large $V$.

### 8.2.4 Questions about Correct Summarization and Takeaways

(some very complicated questions will be here)

**How to calculate from first principles band structure of TaS2?**

(??????????? I didn't yet still understand it....)

**What are the main equations of the paper?**

(below all is from GPT, check it!!!! I am not sure that it is a high quality theory!!!!)

The calculation can be divided into several stages. The important point is that the output of one stage often becomes the input of another stage:

$$\text{DFT} \to \begin{cases} \text{MLWF} \to t_{ij}, \\ \text{RPA/cRPA} \to U, V, \end{cases} \to \text{extended Hubbard model} \to \text{GW+EDMFT} \to G, \Sigma, W, P \to \text{spectral functions and charge response.}$$

**1. DFT calculation**

(below all is from GPT, check it!!!! I am not sure that it is a high quality theory!!!!)

**Input:** the crystal structure, atomic positions, and the choice of exchange-correlation functional (GGA-PBE in this work).

The Kohn-Sham problem is schematically

$$\left[-\frac{\nabla^2}{2} + V_{\text{ion}} + V_H[n] + V_{\text{xc}}[n]\right]\psi_{n\mathbf{k}} = \epsilon_{n\mathbf{k}}\psi_{n\mathbf{k}}.$$

**Output:**

$$\epsilon_{n\mathbf{k}}, \qquad \psi_{n\mathbf{k}}.$$

Here $\epsilon_{n\mathbf{k}}$ are the non-interacting DFT band energies and $\psi_{n\mathbf{k}}$ are the corresponding Kohn-Sham wave functions.

**Used later for:**

- plotting the DFT band structure;
- constructing maximally localized Wannier functions;
- constructing the polarization and screened Coulomb interaction in RPA/cRPA.

**2. MLWF calculation**

(below all is from GPT, check it!!!! I am not sure that it is a high quality theory!!!!)

**Input:**

$$\epsilon_{n\mathbf{k}}, \qquad \psi_{n\mathbf{k}}$$

from DFT, in particular the isolated low-energy SOD-derived band.

A localized Wannier orbital is constructed,

$$|w_i\rangle,$$

and the tight-binding hopping amplitudes are obtained as

$$t_{ij} = \langle w_i|\hat{H}_{\mathrm{DFT}}|w_j\rangle.$$

The momentum-space hopping is

$$t(\mathbf{k}) = \sum_{\mathbf{R}} t(\mathbf{R}) e^{i\mathbf{k}\cdot\mathbf{R}}.$$

**Output:**

$$t_{ij}, \qquad t(\mathbf{k}),$$

as well as the real-space SOD molecular orbital $|w_i\rangle$.

For this material the relevant reported values are

$$|t_1| = 1.812 \text{ meV}, \qquad |t_2| = 0.814 \text{ meV}, \qquad |t_3| = 1.785 \text{ meV}.$$

**Used later for:**

$$t_{ij} \longrightarrow H_{\mathrm{Hubbard}},$$

and

$$t(\mathbf{k}) \longrightarrow G(\mathbf{k}, i\omega_n)$$

in the GW+EDMFT calculation.

Thus the MLWF calculation provides the kinetic-energy part of the effective low-energy model.

**3. RPA/cRPA screening calculation**

(below all is from GPT, check it!!!! I am not sure that it is a high quality theory!!!!)

**Input:** DFT electronic states and the bare Coulomb interaction.

The standard screening relation is

$$W(\mathbf{q}, \omega) = v(\mathbf{q}) \left[1 - v(\mathbf{q}) P(\mathbf{q}, \omega)\right]^{-1},$$

where

$$v$$

is the bare Coulomb interaction and

$$P$$

is the electronic polarization.

In cRPA, the total polarization is conceptually separated as

$$P = P_{\text{low}} + P_{\text{rest}},$$

and the low-energy screening processes that will later be treated explicitly by the Hubbard model are excluded. Therefore,

$$W^{\text{cRPA}} = v\left[1 - vP_{\text{rest}}\right]^{-1}.$$

**Output:**

$$W^{\text{RPA}} \quad \text{or} \quad W^{\text{cRPA}}.$$

$W^{\text{cRPA}}$ is a partially screened Coulomb interaction. It is *not* yet the final quantity plotted in Figure 4.

**Used later for:**

Matrix elements of $W^{\text{RPA/cRPA}}$ are projected onto atomic or SOD orbitals in order to obtain the effective model parameters

$$U \quad \text{and} \quad V.$$

Thus,

$$W^{\text{RPA/cRPA}} \longrightarrow U, V \longrightarrow H_{\text{Hubbard}}.$$

The RPA/cRPA calculation is therefore mainly a method for constructing the interaction parameters of the low-energy model.

**4. First interaction estimate: 3-band RPA**

(below all is from GPT, check it!!!! I am not sure that it is a high quality theory!!!!)

The RPA-screened interaction in real space is written as

$$U_{\mathbf{R}-\mathbf{R}'} = \frac{1}{N_q}\sum_{\mathbf{q}} U_{\mathbf{q}} e^{i\mathbf{q}\cdot(\mathbf{R}-\mathbf{R}')}.$$

The effective interaction inside one SOD is estimated as

$$U = \frac{1}{13^2}\sum_{\mathbf{R},\mathbf{R}'\in\text{SOD}} U_{\mathbf{R}-\mathbf{R}'}.$$

The interaction between two neighboring SODs is

$$V = \frac{1}{13^2}\sum_{\substack{\mathbf{R}\in\text{SOD}_1\\ \mathbf{R}'\in\text{SOD}_2}} U_{\mathbf{R}-\mathbf{R}'}.$$

**Output:**

$$U = 0.371 \text{ eV}, \qquad V = 0.208 \text{ eV}.$$

**Used later for:**

These numbers are inserted into the extended Hubbard model and are used as one of the two parameter sets in the GW+EDMFT calculation:

$$(U, V) = (0.371, 0.208) \text{ eV}.$$

**5. Second interaction estimate: 5-band cRPA**

(below all is from GPT, check it!!!! I am not sure that it is a high quality theory!!!!)
**Input:** the atomic cRPA interaction

$$\bar{U}_{\mathbf{R}-\mathbf{R}'}$$

and the weights of the Ta-$d$ orbitals in the SOD molecular orbital

$$w_{\mathbf{R}} = |\langle d_{\mathbf{R}}|\Psi\rangle|^2 .$$

The effective on-SOD interaction is

$$U = \sum_{\mathbf{R},\mathbf{R}'\in\mathrm{SOD}} w_{\mathbf{R}} w_{\mathbf{R}'} \bar{U}_{\mathbf{R}-\mathbf{R}'} .$$

The effective nearest-neighbor SOD interaction is

$$V = \sum_{\substack{\mathbf{R}\in\mathrm{SOD}_1 \\ \mathbf{R}'\in\mathrm{SOD}_2}} w_{\mathbf{R}} w_{\mathbf{R}'} \bar{U}_{\mathbf{R}-\mathbf{R}'} .$$

**Output:**

$$U = 0.653 \text{ eV}, \qquad V = 0.359 \text{ eV}.$$

**Used later for:**
This gives the second parameter set used in the GW+EDMFT calculation:

$$(U, V) = (0.653, 0.359) \text{ eV}.$$

Thus the 3-band RPA and 5-band cRPA calculations do not directly give the final spectrum. They give two possible sets of interaction parameters $(U, V)$ which are then inserted into the same many-body model.

**6. Extended Hubbard model**

(below all is from GPT, check it!!!! I am not sure that it is a high quality theory!!!!)
**Input:**

$$t_{ij} \quad \text{from MLWF}, \qquad U, V \quad \text{from RPA/cRPA}.$$

The effective Hamiltonian is

$$H = -\sum_{ij\sigma} t_{ij} c^\dagger_{i\sigma} c_{j\sigma} + U \sum_i n_{i\uparrow} n_{i\downarrow} + V \sum_{\langle ij\rangle} n_i n_j - \mu \sum_i n_i .$$

**Output:**
The Hamiltonian itself is not yet a numerical observable. It defines the many-body problem to be solved.
**Used later for:**

$$H \longrightarrow \text{DMFT/EDMFT/GW+EDMFT}.$$

**7. DMFT**

(below all is from GPT, check it!!!! I am not sure that it is a high quality theory!!!!)
**Input:**

$$t(\mathbf{k}), \qquad U, \qquad V = 0.$$

The main DMFT approximation is

$$\Sigma(\mathbf{k}, i\omega_n) \approx \Sigma_{\text{loc}}(i\omega_n).$$

The interacting lattice Green function is

$$G(\mathbf{k}, i\omega_n) = \left[i\omega_n + \mu - t(\mathbf{k}) - \Sigma_{\text{loc}}(i\omega_n)\right]^{-1}.$$

The local Green function is

$$G_{\text{loc}}(i\omega_n) = \frac{1}{N_k} \sum_{\mathbf{k}} G(\mathbf{k}, i\omega_n).$$

**Output:**

$$G_{\text{loc}}(i\omega_n), \qquad \Sigma_{\text{loc}}(i\omega_n).$$

**Used later for:**
$G$ is used to calculate the electronic spectral function, while $\Sigma$ characterizes the correlation-induced modification of the electrons.
In this paper ordinary DMFT is mainly used as a reference calculation with

$$V = 0.$$

**8. EDMFT: lattice quantities**

(below all is from GPT, check it!!!! I am not sure that it is a high quality theory!!!!)
**Input:**

$$t(\mathbf{k}), \qquad U, \qquad V,$$

together with an initial approximation for

$$\Sigma(\mathbf{k}, i\omega_n), \qquad P(\mathbf{q}, i\Omega_m).$$

The electron Green function is

$$G(\mathbf{k}, i\omega_n) = \left[i\omega_n - t(\mathbf{k}) + \mu - \Sigma(\mathbf{k}, i\omega_n)\right]^{-1}.$$

The dynamically screened Coulomb interaction is

$$W(\mathbf{q}, i\Omega_m) = v(\mathbf{q}) \left[1 - v(\mathbf{q}) P(\mathbf{q}, i\Omega_m)\right]^{-1}.$$

**Output:**

$$G(\mathbf{k}, i\omega_n), \qquad W(\mathbf{q}, i\Omega_m).$$

Here

$$G$$

describes propagation of interacting electrons, whereas

$$W$$

is the Coulomb interaction after screening by the interacting system.

**Used later for:**

$$G, W \longrightarrow G_{\text{loc}}, W_{\text{loc}} \longrightarrow \mathcal{G}, \mathcal{U} \longrightarrow \text{impurity problem.}$$

Note that this $W$ is different from the cRPA $W^{\text{cRPA}}$ used earlier.

The earlier

$$W^{\text{cRPA}}$$

is used to construct the model parameters $U, V$.

The present

$$W(\mathbf{q}, i\Omega_m)$$

is a many-body quantity calculated *after* the Hubbard model has been constructed and is one of the physical outputs studied in Figure 4.

**9. Momentum-space interaction $v(\mathbf{q})$**

(below all is from GPT, check it!!!! I am not sure that it is a high quality theory!!!!)

For nearest-neighbor interaction $V$ on the triangular SOD lattice,

$$v(\mathbf{q}) = 2V\left[\cos q_x + \cos\left(\frac{q_x}{2} + \frac{\sqrt{3}q_y}{2}\right) + \cos\left(-\frac{q_x}{2} + \frac{\sqrt{3}q_y}{2}\right)\right].$$

**Output:**

$$v(\mathbf{q}).$$

**Used later in:**

$$W(\mathbf{q}, i\Omega_m) = \frac{v(\mathbf{q})}{1 - v(\mathbf{q})P(\mathbf{q}, i\Omega_m)},$$

and also in the charge susceptibility.

**10. Local quantities**

(below all is from GPT, check it!!!! I am not sure that it is a high quality theory!!!!)

For any momentum-dependent quantity $A$,

$$A_{\text{loc}} = \frac{1}{N}\sum_{\mathbf{k}} A(\mathbf{k}).$$

In particular,

$$G_{\text{loc}}(i\omega_n) = \frac{1}{N_k}\sum_{\mathbf{k}} G(\mathbf{k}, i\omega_n),$$

and

$$W_{\text{loc}}(i\Omega_m) = \frac{1}{N_q}\sum_{\mathbf{q}} W(\mathbf{q}, i\Omega_m).$$

**Output:**

$$G_{\text{loc}}, \qquad W_{\text{loc}}.$$

**Used later for:**

They define the effective impurity environment in EDMFT.

**11. Fermionic and bosonic Weiss fields**

(below all is from GPT, check it!!!! I am not sure that it is a high quality theory!!!!)
The effective fermionic bath is

$$\mathcal{G}(i\omega_n) = \left[G_{\text{loc}}^{-1}(i\omega_n) + \Sigma_{\text{loc}}(i\omega_n)\right]^{-1}.$$

The effective dynamical interaction is

$$\mathcal{U}(i\Omega_m) = \left[W_{\text{loc}}^{-1}(i\Omega_m) + P_{\text{loc}}(i\Omega_m)\right]^{-1}.$$

**Output:**

$$\mathcal{G}(i\omega_n), \qquad \mathcal{U}(i\Omega_m).$$

$\mathcal{G}$ describes the effective electronic environment seen by one SOD, while $\mathcal{U}$ describes the effective frequency-dependent interaction seen by that SOD.
**Used later for:**
They are the input of the EDMFT impurity model.

**12. EDMFT impurity model**

(below all is from GPT, check it!!!! I am not sure that it is a high quality theory!!!!)
**Input:**

$$\mathcal{G}, \qquad \mathcal{U}.$$

The impurity action is

$$S_{\text{imp}} = -\iint d\tau d\tau' \, \bar{c}(\tau)\mathcal{G}^{-1}(\tau-\tau')c(\tau') + \frac{1}{2}\iint d\tau d\tau' \, \mathcal{U}(\tau-\tau')n(\tau)n(\tau').$$

This problem is solved numerically using the CT-HYB quantum Monte Carlo impurity solver.
**Output:**

$$\Sigma_{\text{imp}}(i\omega_n), \qquad P_{\text{imp}}(i\Omega_m).$$

$\Sigma_{\text{imp}}$ is the local electronic self-energy caused by strong local correlations.
$P_{\text{imp}}$ is the local polarization associated with charge fluctuations.
**Used later for:**
They provide the local parts of the full GW+EDMFT self-energy and polarization.

**13. GW calculation**

(below all is from GPT, check it!!!! I am not sure that it is a high quality theory!!!!)
**Input:**

$$G, \qquad W.$$

The GW electronic self-energy is

$$\Sigma^{GW}(\mathbf{k}, i\omega_n) = -\sum_{\mathbf{q}, i\Omega_m} G(\mathbf{k}+\mathbf{q}, i\omega_n + i\Omega_m)W(\mathbf{q}, i\Omega_m).$$

The GW polarization is

$$P^{GW}(\mathbf{q}, i\Omega_m) = 2\sum_{\mathbf{k}, i\omega_n} G(\mathbf{k}+\mathbf{q}, i\omega_n + i\Omega_m)G(\mathbf{k}, i\omega_n).$$

**Output:**

$$\Sigma^{GW}, \qquad P^{GW}.$$

**Used later for:**
Only their non-local parts are added to the local EDMFT result.

**14. Separation of local and non-local parts**

For any quantity $A$,

$$A_{\text{nonloc}} = A - A_{\text{loc}}.$$

Thus,

$$\Sigma^{GW}_{\text{nonloc}} = \Sigma^{GW} - \Sigma^{GW}_{\text{loc}},$$

and

$$P^{GW}_{\text{nonloc}} = P^{GW} - P^{GW}_{\text{loc}}.$$

**Output:**

$$\Sigma^{GW}_{\text{nonloc}}, \qquad P^{GW}_{\text{nonloc}}.$$

**Used later for:**
They are combined with the local EDMFT quantities.

**15. GW+EDMFT combination**

The full electronic self-energy is

$$\Sigma(\mathbf{k}, i\omega_n) = \Sigma_{\text{imp}}(i\omega_n) + \Sigma^{GW}_{\text{nonloc}}(\mathbf{k}, i\omega_n).$$

The full polarization is

$$P(\mathbf{q}, i\Omega_m) = P_{\text{imp}}(i\Omega_m) + P^{GW}_{\text{nonloc}}(\mathbf{q}, i\Omega_m).$$

**Output:**

$$\Sigma(\mathbf{k}, i\omega_n), \qquad P(\mathbf{q}, i\Omega_m).$$

**Used later for:**
They are inserted back into

$$G^{-1} = i\omega_n + \mu - t - \Sigma$$

and

$$W = v(1 - vP)^{-1}.$$

Therefore the calculation is iterative.

**16. GW+EDMFT self-consistency**

The loop is

$$\Sigma, P \to G, W \to G_{\text{loc}}, W_{\text{loc}} \to \mathcal{G}, \mathcal{U} \to \Sigma_{\text{imp}}, P_{\text{imp}} \to \Sigma, P.$$

It is repeated until

$$G^{(n+1)} \simeq G^{(n)}, \qquad W^{(n+1)} \simeq W^{(n)}.$$

The converged quantities

$$G, \qquad \Sigma, \qquad W, \qquad P$$

are the principal outputs of the GW+EDMFT calculation.

**17. Spectral function**

**Input:**

$$G(\mathbf{k}, i\omega_n)$$

from the converged GW+EDMFT calculation.

After analytic continuation,

$$i\omega_n \to \omega + i0^+,$$

one obtains the retarded Green function

$$G^R(\mathbf{k}, \omega).$$

The spectral function is

$$A(\mathbf{k}, \omega) = -\frac{1}{\pi} \operatorname{Im} G^R(\mathbf{k}, \omega).$$

**Output:**

$$A(\mathbf{k}, \omega).$$

**Used for:**

This is the interacting band-like spectrum shown in Figure 3A.

The momentum-integrated spectrum is

$$A(\omega) = \frac{1}{N_k} \sum_{\mathbf{k}} A(\mathbf{k}, \omega),$$

which gives the interacting DOS shown in Figures 3B and 3C.

**18. Quasiparticle weight**

**Input:**

$$\Sigma(i\omega_n).$$

The quasiparticle weight is estimated as

$$Z = \left[1 - \frac{\partial \operatorname{Im} \Sigma(i\omega_n)}{\partial \omega_n}\right]^{-1}_{\omega_n \to 0}.$$

**Output:**

$$Z.$$

**Interpretation:**

For a coherent metal,

$$0 < Z \leq 1,$$

while for the Mott insulating state,

$$Z \to 0.$$

Thus $Z$ is a diagnostic of whether coherent quasiparticles survive.

**19. Screened interaction shown in Figure 4**

**Input:**

$$P(\mathbf{q}, i\Omega_m)$$

from the converged EDMFT or GW+EDMFT calculation.

Calculate

$$W(\mathbf{q}, i\Omega_m) = \frac{v(\mathbf{q})}{1 - v(\mathbf{q})P(\mathbf{q}, i\Omega_m)}.$$

Then

$$W_{\text{loc}}(i\Omega_m) = \frac{1}{N_q} \sum_{\mathbf{q}} W(\mathbf{q}, i\Omega_m).$$

**Output:**

$$W_{\text{loc}}(i\Omega_m).$$

**Used for:**

This is the quantity plotted in Figure 4A to compare DMFT, EDMFT and GW+EDMFT and to see how $V$ changes dynamical screening.

**20. Charge susceptibility**

**Input:**

$$P(\mathbf{q}, i\Omega_m), \qquad v(\mathbf{q}).$$

The static charge susceptibility is

$$\chi(\mathbf{q}) = \left. \frac{-P(\mathbf{q}, i\Omega_m)}{1 - v(\mathbf{q})P(\mathbf{q}, i\Omega_m)} \right|_{\Omega_m=0}.$$

The local susceptibility is

$$\chi_{\text{loc}} = \frac{1}{N_q} \sum_{\mathbf{q}} \chi(\mathbf{q}).$$

**Output:**

$$\chi(\mathbf{q}), \qquad \chi_{\text{loc}}.$$

**Used for:**

$\chi_{\text{loc}}^{-1}$ is plotted in Figure 4B as a function of $V$.

The momentum dependence

$$\chi(\mathbf{q})$$

is plotted in Figure 4C.

A charge-ordering instability is indicated by

$$\chi(\mathbf{Q}) \to \infty,$$

or equivalently by

$$\chi_{\text{loc}}^{-1} \to 0.$$

**Summary of the mathematical outputs**

The important distinction between the quantities called "screened interaction" at different stages is

$$W^{\mathrm{cRPA}} \longrightarrow U, V \longrightarrow H_{\mathrm{Hubbard}} \longrightarrow W^{\mathrm{EDMFT/GW+EDMFT}}.$$

Thus,

$$W^{\mathrm{cRPA}}$$

is an auxiliary first-principles quantity used to construct $U$ and $V$, whereas

$$W(\mathbf{q}, i\Omega_m)$$

in GW+EDMFT is a physical many-body output describing the dynamical screening inside the already constructed interacting Hubbard model.

The main chain of quantities is therefore

$$\epsilon_{n\mathbf{k}}, \psi_{n\mathbf{k}} \longrightarrow \begin{cases} t_{ij}, \\ U, V, \end{cases} \longrightarrow H \longrightarrow \Sigma, P \longrightarrow G, W \longrightarrow \begin{cases} A(\mathbf{k}, \omega), \\ Z, \\ W_{\mathrm{loc}}(i\Omega), \\ \chi(\mathbf{q}). \end{cases}$$

# 9 First principles investigation of screened Coulomb interaction and electronic structure of low-temperature phase $TaS_2$ by Jung Kim, Yong Jeong, Joon Han (2022)

**Abstract**

By means of ab initio computation schemes, we examine the electronic screening(formula for electronic screening?) , Coulomb interaction strength (final formula for Coulomb interaction strength for exactly this material?) , and the electronic structure(that plot of bands below) of a quantum spin liquid candidate monolayer TaS2 in its low-temperature commensurate chargedensity-wave phase.

Not only local (U) but non-local (V) correlations (non-local (V) correlations?) are estimated within random phase approximation based on two different screening models (which different screening models?) .

Using GW + EDMFT (GW plus extended dynamical mean-field theory) method(what is this method?) , we investigate the detailed electronic structure by increasing the level of non-local approximation from DMFT ($V = 0$) to EDMFT and GW + EDMFT.

## 9.1 Article

(BY THE WAY, WHAT IS HARD IN JUST INPUTTING A VALUES TO THE CODE???? I HAVE NEVER UNDERSTOOD THIS)

(the article obtains:

$$t \to 0 \quad \Longrightarrow \quad W \to 0 \quad \Longrightarrow \quad E(k) \approx \epsilon_0,$$

for the

$$H = -\sum_{ij\sigma} t_{ij} c^\dagger_{i\sigma} c_{j\sigma} + U \sum_i n_{i\uparrow} n_{i\downarrow} + V \sum_{\langle ij \rangle} n_i n_j - \mu \sum_i n_i \tag{7}$$

this is the main its value. )

### 9.1.1 Introduction

(just abstract intro) Understanding the effect of Coulombic interaction between electrons in solid has long been a central theme of condensed matter physics.

[1] Notably, the relevant material systems are being extended to include various two-dimensional (2D) van der Waals materials (what is the van der Waals material?) [2–9] and more recently their twisted combinations.

(summary of Hubbard model, I'll think later about it) [10–18] The local on-site interaction (conventionally represented by U in Hubbard model) can induce electron localization, magnetic moment and thereby leading to metal-to-insulator and magnetic phase transition.

[1,19–21] Many of most intriguing phenomena have been explored within this picture such as unconventional superconductivity and quantum spin liquid. [21–26] (interesting but most likely irrelevant effects)

Non-local Coulomb interaction (denoted by $V$ in extended Hubbard model) also plays an important role. (origin of non-local Coulomb interaction?)

For example, it can enhance the itinerancy (=traveling from place to place) of electrons by screening Coulomb interactions or broadening the effective bandwidth. [27,28] (learn why later)

(intro to phase transitions) Out of its competition and cooperation with electron hoppings and local correlations, various instabilities can be induced toward the charge-ordered or charge density wave (CDW) phase and many others including high angular momentum superconductivity. [27–37] (I am assured that high angular momentum SC is irrelevant)

(just some citations about $V$, they could be just in the one before previous sentence) Recently, the effect of non-local Coulomb interaction receives increasing attention in 2D material. [6,38–41]

(intro to TaS2) Among many correlated van der Waals materials, $TaS_2$ provides an intriguing case by displaying multiple ordered phases and their transitions. [42–45]

(typical property of TaS2) At high temperature, $TaS_2$ is known to be metallic and has 1 T structure shown in Figure 1A.

(typical property of TaS2) As temperature is lowered, it exhibits so-called 'nearly commensurate CDW (NCCDW)', and then finally becomes insulating. [46,47]

(typical property of TaS2) Superconductivity is also observed below $T_C \approx 2-5$ K by applying pressure, doping or electric field (check the electric field, didn't know about it) . [42–44]

(here is a bad formulation of the fact that there is also a PLD of a David star form) Importantly, the stabilization of the low temperature insulating phase is accompanied by commensurate CDW (CCDW) transition for which the long-range 'star of David (SOD)' (SOD will be used in this article a lot) pattern of atomic rearrangement is well identified in both experiments and simulations (see Figures 2A and 2B). [46–50]

This phase hosts a flat band in the close vicinity of chemical potential because of the reduced hopping integral in between SOD molecular orbitals (for example, $E(k) = \epsilon_0 - 2t\cos(ka)$, so if $t$ is lower than the band is flatter) .

(the hopping integral diminishes, because orbitals are more localized, so they overlap less and this is directly seen in the hopping integral)

(just "our study is important" promise:) Therefore, unveiling (=reveal something for the first time) the electronic property of CCDW SOD phase is important to understand the metal-insulator transition and the other related phases observed or suggested in this material at low temperature. [42–45,51–53]

Given that Ta atom has the 4+ formal valance ($Ta^{4+}(S^{2-})_2$) , the SOD unit cell should have odd number of electrons (i.e., $13 = 5\ d^1 \times 13$), and CCDW- $TaS_2$ is expected to be metallic according to the standard band picture.

(GPT: The formal ionic picture of $TaS_2$ is $Ta^{4+}(S^{2-})_2$. Neutral Ta has the approximate valence-electron configuration Ta : $[Xe]\,4f^{14}5d^3 6s^2$, so formally removing four electrons gives $Ta^{4+} : 5d^1$. Thus, each Ta atom contributes one $d$ electron to the relevant low-energy electronic states.)

(GPT: In the formal ionic picture, each Ta atom contributes one $5d$ electron. Therefore, a Star-of-David (SOD) cluster containing 13 Ta atoms has 13 $d$ electrons.)

(GPT: In the CCDW phase, six bonding molecular orbitals are completely filled by 12 electrons, leaving one electron in the isolated SOD-derived band near $E_F$. Since this band can accommodate two electrons per SOD due to spin degeneracy, it is half-filled.)

(GPT: In the standard non-interacting band picture, a half-filled band has the Fermi energy inside the band and therefore corresponds to a metallic state. Thus, 13 $d$ electrons $\rightarrow$ 12 electrons in filled bonding states + one electron in a half-filled band $\rightarrow$ metallic CCDW-$TaS_2$.)

(GPT: Experimentally, however, CCDW-$TaS_2$ is insulating, indicating the importance of physics beyond the standard band picture, such as strong electronic correlations and Mott localization.)

It is however in a sharp contrast to experiments. [54] (and what was wrong in this reasoning?)

Several recent studies focusing on this issue suggested that either Mott mechanism or interlayer dimerization(interlayer dimerization?) is responsible for metal-to-insulator transition. [45,55–61](learn this methods!)

The important challenge here is to estimate the strengths of Coulomb interactions. [62] (so these Coulomb interactions somehow should help explain PT, since the standard reasoning is not working)

Another intriguing possibility in this material is quantum spin liquid (QSL). (where is it in phase diagram?)

(there is a spin in TaS2, so it might be a QSL) By noting that the low-temperature CCDW phase forms a triangular lattice and carries nominally $S = \frac{1}{2}$ local moment(how is it, carries $S = \frac{1}{2}$ local moment? why is it so???) , the low temperature $TaS_2$ was suggested as a QSL candidate. [51]

(some good for QSL effects are also present) This idea is supported by the absence of long-range magnetic order down to low temperature and the gapless spin excitations. [51–53](what are these effects?)

Notably, a recent study highlights the effect of non-local Coulomb interaction ($V$) (non-local Coulomb interaction???) on the magnetic nature related to QSL. [63] (it is just a motivation to study Coulomb interactions, because maybe they can be used in QSL)

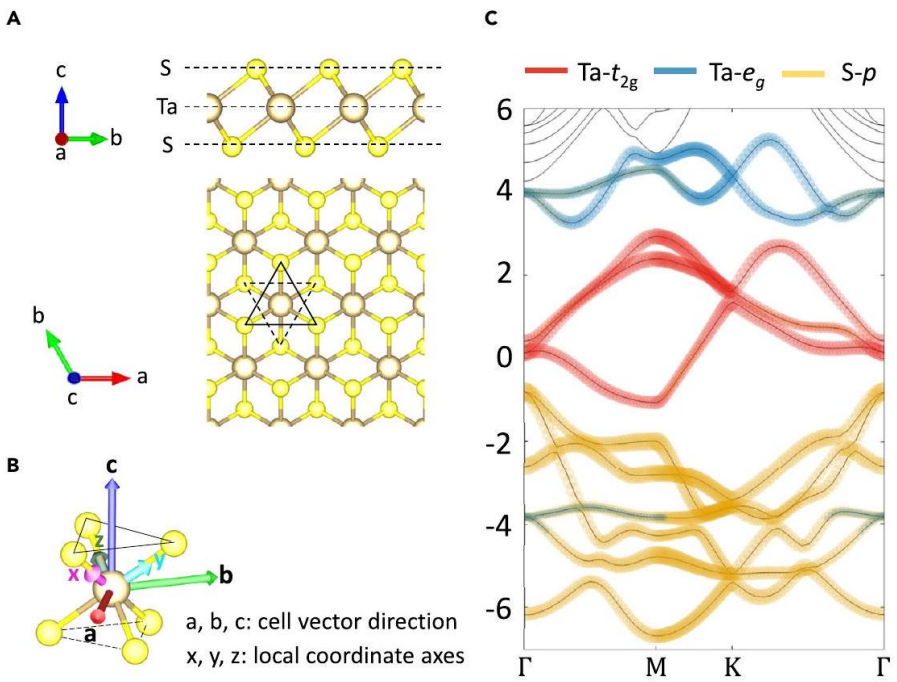


Figure 1. Crystal and electronic structure of $\mathbf{1T-TaS_2}$
(obvious description of 1a: ) (A) Crystal structure of monolayer 1 $T-TaS_2$. The side and top view is presented above and below, respectively. As shown in the side view, a layer consists of S-Ta-S layer. In the top view, the triangle (solid line) and inverted triangle (dotted line) indicates the S atoms around Ta in the upper and the lower layers, respectively.
(B) The local environment(local environment?) around Ta.
The Ta atom is surrounded by six S atoms forming the octahedral structure with slight trigonal distortion.
The red, green, and blue arrow (a, b, and c vectors) indicates the three cell vectors shown in (A).
The magenta, cyan, and olive colored arrow shows the local coordinate axes for Ta-d orbital projection.
Local axes point to the octahedral directions by neglecting the small trigonal distortion.
(C) The orbital-projected band structure of 1T-TaS2 (it is meant at normal state, since fig. 2 will be at CDW state) . Blue and red color shows the $Ta-t_{2\ g}$ and $Ta-e_g$ orbital contribution (why exactly such contributions?) , respectively, and yellow refers to the $p$ orbital contribution of $S$ atoms. (what are the units on Y axes, $E-E_F$???)

(repetition of a title) In this paper, we examine the detailed electronic behaviors of monolayer $TaS_2$.

Based on two different models, the electronic screenings are taken into account within random phase approximation (RPA). (what is exactly RPA here?)

Correlation strengths (Correlation strengths?) , in terms of both on-site $U$ and inter-site V, are successfully quantified for the low-temperature CCDW phase.

(repetition of an abstract) By adopting GW + EDMFT, [32,64–69] we calculate the electronic structure with three different levels of approximation (DMFT, extended GW+EDMFT, GW+GW+EDMFT) for inter-site correlation (learn later, what is the meaning of them?) .

Although the Mott gap is mainly governed by the local interaction (why Mott gap is mainly governed by the local interaction?) , non-local Coulomb interaction is also sizable (=has some influence on bands) .

(some effects will be discussed =) Its effect on the electronic screening, band dispersion and

another possibility toward charge-ordered phase are discussed.

### 9.1.2 Results and Discussion

#### Non-interacting band structure and tight-binding parameters

Figures 1A and 1B shows the crystal structure of 1 T $-$ $TaS_2$ and the local $TaS_6$ unit, respectively. ($TaS_6$ is a molecular unit cell)

The corresponding non-interacting band structure within generalized gradient approximation (GGA; i.e., $U = V = 0$eV) (generalized gradient approximation???) is presented in Figure 1C where different colors represent the different orbital characters as projected onto the local coordinates (projected onto the local coordinates???) as defined in Figure 1B.

(look at the red bands from the plot) Ta- $t_{2\ g}$(why exactly them?) states dominate the near Fermi energy ($E_F$) region and the $t^1_{2\ g}$ configuration is well identified ($t^1_{2\ g}$ configuration is well identified?) .

The higher energy bands above +3 eV and below -1 eV are mainly composed of Ta-$e_g$ and S-p character (why exactly them?) , respectively, whereas the greenish bands reflect the mixture of Ta $-$ $e_g$ and S $-$ $p$ (how can it be that greenish bands are the mixtures?) .

The overall electronic feature is in good agreement with previous studies. [56,70−72] (check some of them later!)

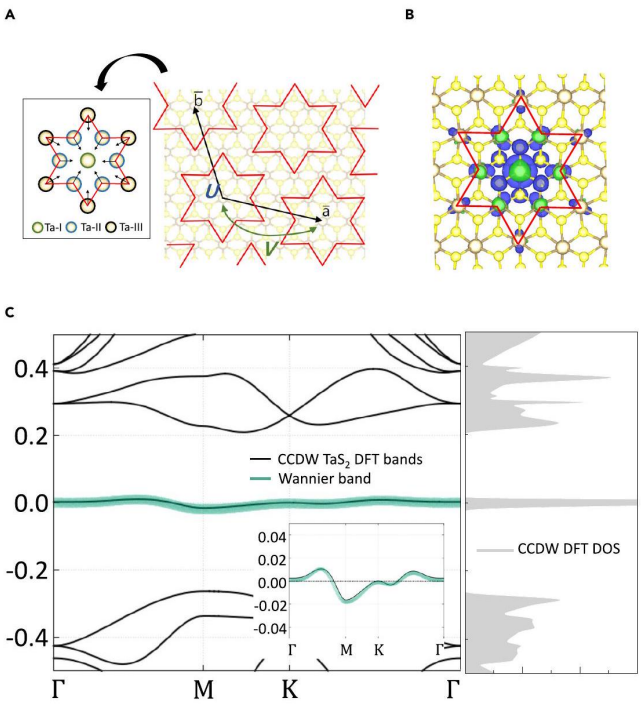


Figure 2. Crystal and electronic structure of CCDW-$TaS_2$
(A) Crystal structure of CCDW phase of $TaS_2$.
Twelve Ta atoms move toward the central Ta, forming a SOD unit (inset) and a molecular orbital at around the center.(so totally we have a 13 atom molecule)
$U$ and $V$ refers to the on-site and the inter-site Coulomb interaction of the molecular orbital, respectively.
$\bar{a}$ and $\bar{b}$ are the unit cell vectors corresponding to CCDW phase.
(B) The calculated MLWF (maximally localized Wannier function) for the SOD molecular orbital in $CCDW - TaS_2$. (I guess that blue means a region where there is a big density of electrons, green - the biggest) Red line depicts the SOD unit. (maybe this quantity is used later for calculation of bands)
(magic results of DMFT:) (C) The calculated DFT band structure (left; black line) and its density of state (right).
The overlaid green line shows the band structure of MLWF for SOD molecular orbital.(so the results fully coincide)
The inset shows the zoom-in figure near $E_F$.

(reminder about TaS2) By lowering temperature, $1\ T - TaS_2$ is known to undergo CDW structural transitions.

(reminder about TaS2) So-called nearly commensurate charge density wave (NCCDW) phase is stabilized below $T \approx 350$ K and followed by CCDW at $T \approx 180$ K. [46–48]

(there is a PLD=) Figure 2A depicts the CCDW structure, so-called SOD pattern, in which twelve Ta atoms move toward the central one forming a 13-Ta-atom unit cluster. [46,47,73,74]

(intro to spectra) In this phase, the band structure also changes accordingly. [55,56,75,76] (check this literature!)

As shown in Figure 2C, a well-separated single electron band is solely responsible for the low energy region near $E_F$(since only it will be partly occupied, so the physics will be because of it) whereas six bonding orbital states are fully occupied by twelve Ta-d electrons well below $E_F$(I guess we don't see them, they are below the bottom of the plot) .

It is noted that the near $E_F$ band is fairly flat and nondispersive. (was it so before? I can't

compare, because fig. 1 has strange units on Y axes)

It is therefore prone to metal-to-insulator transition and other exotic possibilities such as quantum spin liquid phase when interactions come in to play. [55,56,75,76](why do we need a flat band for it???)

(Fig. 2c - bands with another method) The green-colored line in Figure 2C shows the band produced by maximally localized Wannier function (MLWF) [77,78] based on which we estimated a reliable set of parameters for the low energy effective (non-interacting) Hamiltonian of CCDW-$TaS_2$. (and how did they estimate them?)

Its real space visualization is given in Figure 2B. (how to calculate the fig. 2b?)

The calculated TB parameters are as follow: the first and the second neighbor hopping is $|t_1| = 1.812$ and $|t_2| = 0.814$meV, respectively, well compared with the previous reports. (why are they such???)

[63,79] It is interesting to note that the third neighbor hopping $|t_3| = 1.785$meV is larger than $|t_2|$ and comparable with $|t_1|$.[63] (why is it so, it is so strange??? what are the orbitals for it? can we see it on fig. 2b?)

### The estimation of on-site and inter-site correlation

Now we try to calculate the interaction parameters from first-principles. (maybe it is about finding TB parameters)

(abstract useless intro) Quantitative information of correlation strength(correlation strength?) is often crucial for exploring the possible exotic quantum phases and understanding their properties.

In the debate over the band gap origin of $TaS_2$, [45,55−61] for example, the size of on-site $U$ is of key importance. (connection btw $U$ and the gap?)

Non-local $V$ is of particular interest in the systems close to the CDW instability as it can induce charge-ordering instability(charge-ordering instability??? how?) in the extended Hubbard systems. [27,32,80]

In general, the constructed phase diagrams can be qualitatively different depending on the non-local term. (are there examples? with this $V$ we get this phase diagram, with another - another?)

As such, there have been several attempts to directly estimate the interaction strengths of various transition metal dichalcogenides (TMDs). [2,55,81−85] (check how they tried to estimate the parameters???)

(calculations ar hard, we know it) However, ab initio calculation of these parameters corresponding to CDW phase is challenging especially for non-local $V$.

We calculate both $U$ and $V$ for CCDW- $TaS_2$ based RPA/cRPA method. (what is this method?)

(we wanted to use only cRPA) Ideally, it is desirable to compute these parameters from the direct cRPA calculation of CCDW unitcell.

(but cRPA was too slow for this problem) However, a difficulty arises from the demanding computation cost in dealing with the large cell size.

Here we extract the interaction parameters from the undistorted 1 T-structure(because only geometry is changed, so it will be taken into account below) , [55,86] and consider two different approaches (which approaches?) .

First, the CCDW $U$ value can be estimated as the average of atomic Coulomb interactions of 1 T structure whose screening process can be considered within RPA. (formula below is assumed)

This first way of computation gives rise to:

$$U = \frac{1}{13^2} \sum_{R,R' \in \star} U_{R-R'} \tag{1}$$

(why $\frac{1}{13^2}$?)

where $U_{R-R'}$ is the Fourier transformed leading eigenvalue of RPA-screened Coulomb matrix (RPA-screened Coulomb matrix???) .

Namely, $U_{R-R'} = \frac{1}{N_q} \sum_q U_q e^{iq\cdot(R-R')}$ where $U_q = \max \lambda_q$, and $\lambda_q$ is the eigenvalue of RPA-screened Coulomb matrix $\mathcal{W}_{\mathrm{II}}^{\mathcal{RA}}$ represented in the eigenbasis of bare Coulomb matrix. [86] (see the citation, it is a big formalism, it should be explained there?)

The screened Coulomb matrix is calculated for $t_{2\ g}$ manifold; namely, the red-colored bands in Figure 1C. (see the cited paper to understand what is meant here?)

R and R′ are the lattice cell vectors corresponding to 1T structure, and q is the lattice momentum.

$N_q$ is the grid number of lattice momentum.

The white-star symbol represents the $\star$ indices of Ta atoms in the same SOD (which is composed of 13 Ta atoms; see Figure 2A).

In this first approach, the inter-site correlation V is also computed within the same spirit:

$$V = \frac{1}{13^2} \sum_{R \in \star, R' \in \star} U_{R-R'} \tag{2}$$

where the black-star symbol $\star$ refers to the indices of Ta atoms belonging to the nearest-neighboring SOD (indicated by the unit cell vector $\bar{a}$ and $\bar{b}$ in Figure 2A). (I guess it is meant that R' and R belong to different stars)

The calculated $U$ and $V$ following this first approach are presented in Table 1; referred to as '3 bands (RPA)'.

Table 1. Estimated Coulomb interactions for CCDW-$TaS_2$

| | 3 bands (RPA) | 5 bands (cRPA) |
|---|---|---|
| $U$(eV) | 0.371 | 0.653 |
| V (eV) | 0.208 | 0.359 |

The calculated on-site ( $U$) and inter-site Coulomb interaction ($V$) corresponding to the SOD CDW phase. The parameters are estimated from two different approaches as discussed in the main text.

The second approach considers the weights of Ta atoms by projecting them onto the CCDW molecular orbital. (what is going on here?)

This idea itself is not necessarily combined with (c)RPA but can go with any other method of computing atomic Coulomb interaction $\bar{U}^{\mathrm{LR}}$.[55] (atomic Coulomb interaction $\bar{U}^{\mathrm{LR}}$???) (this idea improves other idea, this is what is written?)

The molecular orbital U then can be estimated from the atomic $\mathrm{Ta}-d\overline{\mathrm{U}}^{\mathrm{LR}}$ : By calculating the projected weights of Ta-d orbitals ($|\mathrm{d_a}\rangle$) with respect to CCDW molecular orbitals ($|\Psi\rangle$), (this is this second method, some weights.. see cited paper about it)

$$\frac{U}{\overline{U}^{LR}} = \sum_{a \in \star} |\langle\ \mathrm{d_a}\ |\ \Psi\rangle|^4 \tag{3}$$

(how to use this formula at all????)

where $a$ is the atomic Ta index.

Ta atoms are classified into three different types considering their symmetry (see the inset of Figure 2A).

Our calculations give rise to $|\langle d_{\mathrm{a}} \mid \Psi\rangle|^2 = 0.229, 0.064$ and 0.035 for Ta-I, Ta-II, and Ta-III, respectively. (how to calculate it???)

U and V are obtained as follow: (these are the expressions in scope of approach 2, if you understand it, you'll understand these formulas:)

$$U = \sum_{R,R'\in\star} |\langle d_R \mid \Psi\rangle|^2 \, |\langle d_{R'} \mid \Psi\rangle|^2 \, \bar{U}_{R-R'} \tag{4}$$

$$V = \sum_{R\in\star,R'\in\star} |\langle d_R \mid \Psi\rangle|^2 \, |\langle d_{R'} \mid \Psi\rangle|^2 \, \bar{U}_{R-R'} \tag{5}$$

Here we calculate $\bar{U}_{R-R'}$ based on cRPA.

Table 1. Estimated Coulomb interactions for CCDW-TaS $_2$

| | 3 bands (RPA) | 5 bands (cRPA) |
|---|---|---|
| $U$(eV) | 0.371 | 0.653 |
| V (eV) | 0.208 | 0.359 |

The calculated on-site ( $U$) and inter-site Coulomb interaction ($V$) corresponding to the SOD CDW phase. The parameters are estimated from two different approaches as discussed in the main text.

In Table 1, this set of results are denoted by ' 5 bands (cRPA)' as 5-band model of 1 $\mathrm{T-TaS_2}$ (both $\mathrm{t_{2\ g}}$ and $\mathrm{e_g}$) is adopted.

(why are they called 3-band and 5-band???)

The calculation results are summarized in Table 1.

The $U$ values are different in two different approaches: $U = 0.371$eV from '3-band RPA' and 0.653 eV from ' 5 -band cRPA'. (which value is the correct???)

It is not surprising but rather expected because different 'models' shall take care of different screenings. (where are the screenings in the models?)

For example, the weaker correlation in the former model is naturally attributed to the more screening channels taken into account (what is known about number of channels taken into account?) .

Both results ('3-band RPA' and ' 5 -band cRPA') therefore carry useful information for further study whereas the larger supercell of CCDW phase is not directly computable within cRPA (Performing their cRPA calculation directly using this full 13-Ta Star-of-David unit cell would be computationally impossible) .

(so basically it is written here again, that $U$ and $V$ are calculated in the undistorted phase)

(below, it is about another work, which gave different results and some vague ideas about the reasons)

It is also noted that our results are considerably larger than that of a previous study based on linear response calculation; $U = 0.180$eV. [55] (learn this another calculation)

(here is just a link to another study, I'll look at it If I decide understand better the second approach here) From the point of view of the extracting method of CCDW- $U$ value from 1T structure, the previous study by Darancet et al. [55] is the same with our second approach (i.e., 'five-band model').

Thus the ∼0.5 eV difference certainly reflects the difference between the linear response adopted by Darancet et al. [55] and our RPA method whereas only the latter takes the electronic

screenings into account directly. (I guess, it is a very hard question, why the results of two methods that make sense differ?)

(another quantity in another calculation method does not coincide again with this one) Interestingly, however, the calculated atomic $U$ itself (that is, corresponding to Ta-d on-site interaction) is larger in the linear response calculation, $\bar{U}^{\mathrm{LR}} = 2.27\mathrm{eV}$, [55] than our cRPA $\bar{U}_{R-R'=0} = 1.83\mathrm{eV}$.

(the difference is in the model, not only in the method) It is therefore indicative of that the difference is not simply attributed to the difference between cRPA and linear response.

We presume that the projection also plays an important role. (projection???)

As shown in Equation 4, our projection method not just takes all of Equation 3 portions into account but it also includes some inter-site contributions(inter-site contributions???) between different Ta atoms in an SOD molecular orbital.

(below, some vague ideas about comparison with another material)

It is also useful to compare the correlation strength of $TaS_2$ to that of $NbSe_2$. (why do we need to compare them?)

A previous study of Kamil et al. [86] reports $U = 0.3\mathrm{eV}$ for $NbSe_2$ and their estimation was based on RPA and three-band model, corresponding to our first approach. (check how did they do it, with the similar approach?)

It is noted that $U$ for $\mathrm{CCDW} - TaS_2$ is significantly larger than $\mathrm{CCDW} - NbSe_2$ by about 0.07 eV (see Table 1), which is likely attributed to the different screenings (why screenings?) as discussed in the previous studies on the comparison of $TaSe_2$ with $TaS_2$.[85,87] (check this comparison, looks informative)

Here we also note that a recent ARPES study suggests the weaker correlation for $NbSe_2$ than $TaSe_2$. [88] (how is it, weaker correlation?)

Table 1 also presents the inter-site correlation strength $V$ which can be important for understanding the possible exotic phases relevant to this system, but has not been quantitatively estimated before.

(we got big V) First of all, sizable V value is noticed; ∼50% of on-site correlation in both models.

(we'll use Hubbard model written in appendix) It can therefore be important to take this effect into account within the extended Hubbard model.

It is obvious that Hubbard-type correlation is indispensable for overcoming the DFT-GGA (Generalized Gradient Approximation) limitation which gives rise to metallic band structure. [54]

(actually, this calculations were done before (but without V)) Previous theoretical studies showed that the inclusion of on-site correlation within DFT+ $U$ and single-site DMFT (single-site DMFT??) indeed well reproduces the insulating state even though the former incorrectly predicts the magnetically ordered ground state (magnetically ordered ground state??) . [55,56]

(so local on-site correlations U are sufficient to turn CCDW-TaS2 from the metallic state predicted by ordinary DFT into an insulating state)

(check that papers!!! they are maybe one step before this paper, so they will help to understand it)

According to the DMFT calculation, Mott transition starts to occur at $U \sim 0.7\mathrm{eV}$ in bulk $TaS_2$. [56] (why is it so? I'll look later to this paper)

Note that both sets of our results in Table 1 provide the large enough interaction $U$ with respect to the bandwidth $W \sim 9|t| \sim 0.02\mathrm{eV}$ (from where do we take a bandwidth???) .

Importantly, however, the effect of non-local $V$ has remained unexplored. (why???)

### GW + EDMFT electronic structure

To see the effect of both local $U$ and non-local $V$ on the electronic structure, one needs to go beyond the single-site DMFT. (and what are the plots for the case without V and U?)

Here we adopt GW + EDMFT for that purpose. (are there alternatives?)

Computation details are given in STAR Methods.

In Figures 3A-3C, we present the calculated spectral functions as obtained by analytic continuation of Matsubara Green function using maximum entropy method. [89–91] (learn this method! how to do it? I heard of it, but it is informative to see these articles)

In sharp contrast to the metallic DFT-GGA band structure(see, you can do a very hard calculation, but then there will be another method of calculations which will give purely another results) , GW + EDMFT result clearly shows the insulating gap being consistent with experiment, DFT+ $U$ and single-site DMFT.

(so why the DFT-GGA is so wrong?)

In the case of DFT+ $U$, the long-range spin order naturally comes in as the ground state configuration. [55] (do we touch somewhere here the long-range spin order?)

With our first set of interaction parameters ($U = 0.371$eV, $V = 0.208$eV; shown in Figures 3A and 3B), the upper and the lower Hubbard peak (I think, it is meant Hubbard band) is observed at about $\pm 0.2$eV, respectively, which is well compared with a recent STM experiment of monolayer $TaS_2$.[54,69] (check this plot from experiment!)

Another set of 5-band model produces a slightly larger gap as presented in Figure 3C.

Although this stronger correlation set of parameters also reproduces the insulting phase as expected (= we got the gap in DOS) , the notable difference is the position of Hubbard bands which are in this case found inside the uncorrelated states (thin black line). (The calculation is done with U and without U (no correlation). In both cases the system is insulating, but the positions of the Hubbard bands tells us that with U is a more realistic case.)

(what is the more realistic model???? with which V??? with which U??? why???)

The detailed spectroscopic characterization of the valence and conduction band can therefore be useful to determine the correlation strength (that U parameter) whereas the band gap size itself is probably too small to be precisely compared. (and how to find U from bands?)

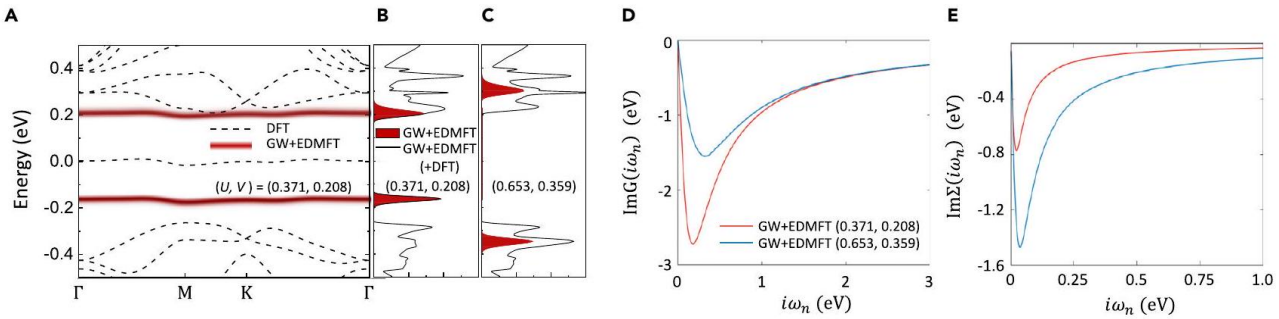


Figure 3. Results of GW + EDMFT calculations
(GPT: Figure 3 shows the interacting electronic structure of the CCDW phase: unlike Figure 2, where $U$ and $V$ are not included, here the extended Hubbard model with the calculated $U$ and $V$ is solved using GW+EDMFT. The narrow half-filled SOD band is split into lower and upper Hubbard bands, producing a Mott gap. Both estimated $(U, V)$ parameter sets give an insulating state, although they predict different Hubbard-band positions. Figures 3D and 3E additionally confirm the Mott character through the vanishing low-energy spectral weight and quasiparticle weight $Z \simeq 0$.)
(A) The momentum-dependent spectral function calculated by DFT-GGA (dashed lines) and GW + EDMFT (red line).
The estimated Coulomb interaction parameters from 3-band model were used as given in parentheses $(U, V)$.
(B and C) The momentum-integrated spectral function of GW + EDMFT.
Coulomb interactions are estimated by (B) 3-band and (C) 5-band model.
The red colored data represent the density of states (DOS) of GW + EDMFT, and the black lines show the DOS sum of GW + EDMFT and DFT.
(D and E) The calculated imaginary part of local (D) Green function and (E) self-energy of GW + EDMFT.
The red and blue color refers to the two different interaction parameter sets as given in the parentheses.

To unveil the other aspects of electronic correlations, we present the imaginary part of local Green function in Figure 3D.

(some sentences below argue that fig. 3d, 3e give us knowledge about the existence of the gap)

With both parameter sets, it is clearly observed that $\mathrm{Im\,G}\,(\mathrm{i}\omega_\mathrm{n})$ goes to zero as $\mathrm{i}\omega_\mathrm{n} \to 0$, indicative of the zero spectral weight at $\mathrm{E_F}$, namely, the insulating phase. (can we expect this or it is only from calculations?)

From the fact that minimum frequency point is lower in the 3-band-model case (red line) (I guess it is still afout fig. 3D) , it also confirms the observed gap size difference in Figures 3A-3C. (I don't understand these connections, fig. 3D and 3A)

The calculated self-energies highlight the same feature: In Figure 3E, the slope of $\partial\,\mathrm{Im}\,\Sigma/\partial\omega_n$ at $\mathrm{i}\omega_n \to 0$ shows the vanishing quasiparticle weight $Z = \left[1 - \frac{\partial\,\mathrm{Im}\,\Sigma}{\partial\omega_n}\right]^{-1} \approx 0$, indicating Mott phase. (why Z is such?) (why does it indicate a Mott phase?)

**Further examination of screened Coulomb interactions**

(SUMMARY: the results of dependence on V is presented, there is an phase transition on a very nonphysical V. All this is pointless, because the V is fixed, they have already told us their value/)

To gain further insights on the electronic correlations, we investigate the screened Coulomb interaction and the charge susceptibility. (I thought that it was already screened before?)

Figure 4A shows the real part of screened Coulomb interaction $W_{loc}$ . (what is the formula for it?)

The effect of non-local Coulomb interaction can be systematically examined by changing the level of approximations (changing method of calculation, EDMFT, GW+EDMFT, only thems) .

Here we fix the value of on-site interaction $U = 0.371$eV, and compare the results of two different inter-site $V = 0$ and 0.208 eV. (why such two values? then, it is written, V=0.565...)

GW self-energy can also be taken into account on top of that. (how?? how to use GW on top?)

In high-frequency limit, the effective Coulomb interaction approaches to its 'bare' value $U = 0.371$eV in all three cases. (why high-frequency limit??? Isn't it a constant?)

In low frequency limit, $W_{loc}$ gradually decreases as the more non-local interactions get involved. (influence of non-local interaction on W???)

It is a general feature of extended Hubbard model [27,32](reminder to learn Hubbard model) although the screening effect by $V$ is not significant as the charge fluctuation is largely suppressed in Mott phase.

Figure 4B also shows that $W(i\Omega_m = 0)$ gradually decreases as $V$ increases (in the low V limit) whereas it does not vary much when $V$ is small.

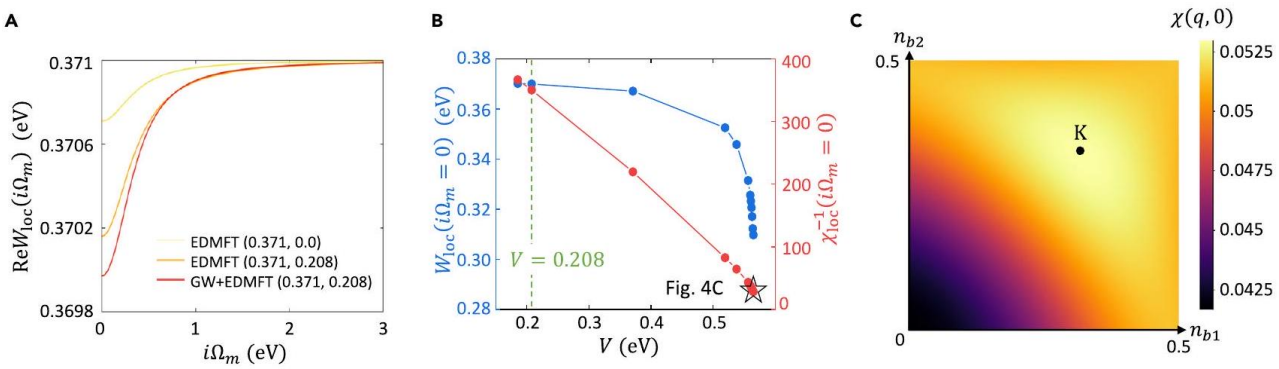


Figure 4. Bosonic (why bosonic?) quantities from GW + EDMFT
(A) The screened Coulomb interaction $W$ calculated by DMFT (yellow; $V = 0$), EDMFT (orange), and GW + EDMFT (red).
(B) The static part of $W_{(loc)}(i\Omega_m = 0)$ (blue-colored; left yaxis) and $\chi^{-1}_{\mathrm{loc}}$ (red-colored; right yaxis) as a function of $V$.
The 3-band RPA estimation of $V$ is indicated by vertical green-dotted line.
(C) The momentum-dependent charge susceptibility $\chi(\mathrm{q}, i\Omega_m = 0)$ in the vicinity of charge-ordered phase.
The calculation has been conducted with $(U, V) = (0.371\mathrm{eV}, 0.565\mathrm{eV})$ indicated by black-star symbol in (B). ($n_b$ is just a coordinate along $q_x$ or $q_y$) (K point on c) plot is a point of the maximum)

In large $V$ limit, on the other hand, its effect can become pronounced. (why intuitively it is so?)

(here is an interpretation of fig. 4B, V is charge hopping = fluctuations, which "screen" reduction of W) As shown in Figure 4B, the screened Coulomb interaction is significantly reduced, indicating that charge fluctuations caused by V further screen the Coulomb interactions. [27,32]

In this regime of V $\gtrsim$ 0.5eV, $W_{(loc)}$ gets rapidly reduced, and simultaneously, the local charge susceptibility diverges (red line): [27,32] (check cited papers!)

$$\chi_{\mathrm{loc}}^{-1} \to 0 \tag{6}$$

(why is it so from formulas?)

where $\chi_{\mathrm{loc}} = \frac{1}{\mathrm{N_q}} \sum_{\mathrm{q}} \chi(\mathrm{q})$ and (why there is a such def?) $\chi(\mathrm{q}) = \left(-\mathrm{P}\left(\mathrm{q}, \mathrm{i}\Omega_m\right)\left[1 - \mathrm{v}(\mathrm{q})\mathrm{P}\left(\mathrm{q}, \mathrm{i}\Omega_m\right)\right]^{-1}\right)_{\mathrm{i}\Omega_m=0}$. (and why $\chi$ is such???)

To perform the detailed investigation of this limit, we calculate the momentum-dependent static charge susceptibility at $V = 0.565$eV which is deemed (=regard something in a specific way) a point close enough to the charge-ordering-type instability (corresponding to the black star point in Figure 4B).

In Figure 4C, a diverging feature is clearly identified at $(\mathrm{n_{b_1}}, \mathrm{n_{b_2}}) = (0.333, 0.333)$ indicative of a charge-ordering instability (another hypothetical phase transition like a Pereles model) ($\mathrm{n_{b_i}}$ is fractional coordinate of reciprocal lattice vector $\mathrm{b_i}$). (what is this $\mathrm{n_b}$????)

Although it implies the further charge instability over the CCDW phase (= another CDW on top of well-known CDW!!!) , the critical $V$ value is far from being realistic in the current system. (but for some reason it is not physical)

### Conclusions

(repetition of an intro) We investigated the electronic screening and the spectral property of monolayer $TaS_2$ by the combination of DFT, RPA, MLWF and GW + EDMFT.

(repetition of an intro) Both on-site and inter-site correlation strengths are estimated based on two different ab initio RPA approaches.

(repetition of an intro, it is not clear what exactly is meant) Although its Mott insulating gap is mainly determined by on-site interaction, the inter-site $V$ is also found to be sizable.

The comparison of DMFT, EDMFT, and GW + EDMFT exhibits a systematic change of the electronic behavior because the levels of non-local self-energy computations are varied. (why exactly levels of non-local self-energy computations are varied? and why it gives such impact?)

Our work provides useful information and insight for understanding $TaS_2$ and the other related systems. (what useful it gives? how one can use it?)

### Limitations of the study

(repetition of the intro) Our computations of screened Coulomb interaction are based on random phase approximation.

(repetition of the intro) The electronic structure calculations take account of non-local as well as dynamical self-energy(dynamical self-energy??? is it dynamical?) within GW + EDMFT.

The singlet formation(singlet formation???) caused by interlayer dimerization [57,59,92,93] could not be considered in our calculation setups.

### 9.1.3 Method Details

| Method | SOURCE | IDENTIFIER |
|---|---|---|
| Software and algorithms | | |
| VASP | Georg Kresse et al. [94,95] | https://www.vasp.at/ |
| ComDMFT | Sangkook Choi et al. [96] | https://github.com/comscope/ComDMFT |
| RESPACK | Kazuma Nakamura et al. [97] | https://sites.google.com/view/kazuma7k6r |

#### DFT and extended Hubbard model construction

We performed DFT calculations of monolayer 1T- and CCDW- $TaS_2$ with Vienna Ab initio Simulation Package (VASP). [94,95] (is it a popular one code?)

(reminder to learn 1T and 2H phases, why they are such?)

The cell parameters and the internal coordinates were optimized with the force criterion of 0.1 meV/Å (optimization with the force criterion?) .

The GGA-PBE functional [98] (GGA-PBE functional?) was used and the 25Å vacuum (vacuum?) taken into account to simulate the monolayer.

$21 \times 21 \times 1 (8 \times 8 \times 1)$ k-grid and 500 eV (400 eV) cutoff energy were adopted for $1\ \mathrm{T} - \mathrm{TaS_2}$ $(\mathrm{CCDW} - \mathrm{TaS_2})$. (I guess it is not very important, why exactly such values?)

To describe the effect of electronic correlations of low-energy state in CCDW- $TaS_2$, we consider the single-band extended Hubbard model: (reminder to learn the Hubbard model)

$$H = -\sum_{ij\sigma} t_{ij} c^{\dagger}_{i\sigma} c_{j\sigma} + U \sum_{i} n_{i\uparrow} n_{i\downarrow} + V \sum_{\langle ij \rangle} n_i n_j - \mu \sum_{i} n_i \tag{7}$$

(why there is a minus in the first term?)

where $c^{\dagger}_{i\sigma}$ and $c_{i\sigma}$ is the creation and annihilation operator of electron, respectively, with spin $\sigma = \{\uparrow, \downarrow\}$ at site $i$.$\mathrm{n_i} = c^{\dagger}_{i\sigma} \mathrm{c_{i\sigma}}$ is the electron number operator at site $i$, and $\sum_{\langle ij \rangle}$ denotes the nearest-neighbor summation.

The hopping amplitude $\mathrm{t_{ij}}$ between two site $i$ and $j$ was calculated with the MLWF method. [77,78]

$U$ and $V$ is the local and non-local Coulomb interaction, respectively. (as was discussed in the article)

The realistic estimation of these two interaction parameters is one of the main issues of current study. (write how they were obtained here)

For this purpose, we used (c)RPA method as implemented in RESPACK code. [97] (and how it was used? maybe I'll try to reproduce it)

#### GW + EDMFT

(write somewhere the GW+EDMFT, I don't understand this method)

(GW + EDMFT code works like this: ) The Hamiltonian is solved within GW + EDMFT whose standard self-consistent loop can be briefly summarized as below. [27,32]

(i) Calculate the lattice green function $G$ and the screened Coulomb interaction $W$:

$$\mathrm{G}\left(\mathrm{k}, \mathrm{i}\omega_{\mathrm{n}}\right) = \left[\mathrm{i}\omega_{\mathrm{n}} - \mathrm{t}(\mathrm{k}) + \mu - \Sigma\left(\mathrm{k}, \mathrm{i}\omega_{\mathrm{n}}\right)\right]^{-1},$$
$$\mathrm{W}\left(\mathrm{q}, \mathrm{i}\Omega_m\right) = \mathrm{v}(\mathrm{q})\left[1 - \mathrm{v}(\mathrm{q})\mathrm{P}\left(\mathrm{q}, \mathrm{i}\Omega_m\right)\right]^{-1},$$

where k and q are the crystal momentum vectors. $\mathrm{i}\omega_\mathrm{n}$ and $\mathrm{i}\Omega_\mathrm{m}$ refers to the fermionic and bosonic Matsubara frequency, respectively.

The momentum space t(k) corresponds to the Fourier transformed $\mathrm{t_{ij}}$.

$\Sigma\left(\mathrm{k}, \mathrm{i}\omega_n\right)$ and $\mathrm{P}\left(\mathrm{q}, \mathrm{i}\Omega_m\right)$ represents the electron self-energy and the polarization function, respectively. (what is the formula for them?)

The bare Coulomb interaction v(q) is given by $\mathrm{v(q)} = 2\ \mathrm{V}\left[\cos\left(\mathrm{q_x}\right) + \cos\left(\frac{1}{2}\mathrm{q_x} + \frac{\sqrt{3}}{2}\mathrm{q_y}\right) + \cos\left(-\frac{1}{2}\mathrm{q_x} + \frac{\sqrt{3}}{2}\mathrm{q_y}\right)\right]$. (why is it so?)

In practice, we start the first loop from $\Sigma\left(\mathrm{k}, \mathrm{i}\omega_\mathrm{n}\right) = \mathrm{P}\left(\mathrm{q}, \mathrm{i}\Omega_\mathrm{m}\right) = 0$.

($\mu$=???? )

(ii) Compute the fermionic and bosonic Wiess fields (I guess the name "Wiess fields" is not that important?) $\mathcal{G}$ and $\mathcal{U}$:

$$\mathcal{G}\left(\mathrm{i}\omega_n\right) = \left[\mathrm{G_{loc}}\left(\mathrm{i}\omega_n\right)^{-1} + \Sigma_{\mathrm{loc}}\left(\mathrm{i}\omega_n\right)\right]^{-1},$$
$$\mathcal{U}\left(\mathrm{i}\Omega_m\right) = \left[\mathrm{W_{loc}}\left(\mathrm{i}\Omega_n\right)^{-1} + \mathrm{P_{loc}}\left(\mathrm{i}\Omega_m\right)\right]^{-1},$$

(it was a typo here, it was written "$\mathrm{W_{loc}}\left(\mathrm{i}\omega_n\right)$") where $A_{\mathrm{loc}}\ \left(i\omega_n\right) = \frac{1}{N_k}\sum_k A\left(k, i\omega_n\right)$ for any $A$ , and $N_k$ is the number of $k$-points.

(iii) Solve the following impurity model(impurity model???) to obtain the impurity self-energy $\Sigma_{\mathrm{imp}}\left(\mathrm{i}\omega_\mathrm{n}\right)$ and polarization $P_{\mathrm{imp}}\ \left(i\Omega_m\right)$ (get somehow $\Sigma_{\mathrm{imp}}\left(\mathrm{i}\omega_\mathrm{n}\right)$ and $P_{\mathrm{imp}}\ \left(i\Omega_m\right)$ from this action) (and how to get them???) :

$$\mathrm{S_{imp}} = \iint_0^\beta \mathrm{d}\tau\ \mathrm{d}\tau'\overline{\mathrm{c}}(\tau)\left[-\mathcal{G}^{-1}\left(\tau - \tau'\right)\right]\mathrm{c}\left(\tau'\right) + \frac{1}{2}\iint_0^\beta \mathrm{d}\tau\ \mathrm{d}\tau'\mathcal{U}\left(\tau - \tau'\right)\mathrm{n}(\tau)\mathrm{n}\left(\tau'\right)$$

where $\mathrm{A}(\tau)$ is the Fourier transormation of $\mathrm{A}\left(\mathrm{i}\omega_\mathrm{n}\right)$(for example, $A$ can be W or P) , and $\overline{\mathrm{c}}(\tau)$ and $\mathrm{c}(\tau)$ are the Grassmann field for electrons.

(why at all the method and formula here is such???)

(are there somewhere explicit calculations of this method?)

Here we took the continuous-time hybridization expansion quantum Monte Carlo impurity solver as implemented in ComDMFT package. [96] (quantum Monte Carlo impurity solver??? how does it work at all???)

(iv) Construct the new self-energy and polarization function from the calculated $\Sigma_{\mathrm{imp}}\left(\mathrm{i}\omega_\mathrm{n}\right)$ and $\mathrm{P_{imp}}\left(\mathrm{i}\Omega_m\right)$:

$$\Sigma\left(\mathrm{k}, \mathrm{i}\omega_n\right) = \Sigma_{\mathrm{imp}}\ \left(\mathrm{i}\omega_n\right) + \Sigma^{\mathrm{GW}}_{\mathrm{nonloc}}\ \left(\mathrm{k}, \mathrm{i}\omega_n\right),$$
$$\mathrm{P}\left(\mathrm{q}, \mathrm{i}\Omega_m\right) = \mathrm{P_{imp}}\ \left(\mathrm{i}\Omega_m\right) + \mathrm{P}^{\mathrm{GW}}_{\mathrm{nonloc}}\ \left(\mathrm{q}, i\Omega_m\right),$$

where

$$\Sigma^{\mathrm{GW}}\left(\mathrm{k}, \mathrm{i}\omega_\mathrm{n}\right) = -\sum_{\mathrm{q}, \mathrm{i}\Omega_m}\mathrm{G}\left(\mathrm{k}+\mathrm{q}, \mathrm{i}\omega_\mathrm{n} + \mathrm{i}\Omega_m\right)\mathrm{W}\left(\mathrm{q}, i\Omega_m\right),$$
$$\mathrm{P}^{\mathrm{GW}}\left(\mathrm{q}, \mathrm{i}\Omega_m\right) = 2\sum_{\mathrm{k}, \mathrm{i}\omega_\mathrm{n}}\mathrm{G}\left(\mathrm{k}+\mathrm{q}, \mathrm{i}\omega_\mathrm{n} + \mathrm{i}\Omega_m\right)\mathrm{G}\left(\mathrm{k}, \mathrm{i}\omega_\mathrm{n}\right),$$

and

$$A_{\mathrm{nonloc}}\ \left(k, i\omega_n\right) = A\left(k, i\omega_n\right) - A_{\mathrm{loc}}\ \left(i\omega_n\right).$$

(v) Go back to the step (i) and repeat the calculations until $\mathrm{G}\left(\mathrm{k}, \mathrm{i}\omega_\mathrm{n}\right)$ and $\mathrm{W}\left(\mathrm{q}, i\Omega_m\right)$ are converged.

(give example of this calculation, looks very complicated!!!!)

## 9.2 Discussion

### 9.2.1 My conclusion about the article

#### My conclusion

The main idea is that they use also a V parameter (not only U) in the Hubbard model and check which bands appear because of it. And they claim that the comparison to experiment is better.

Also, they use many advanced methods.

#### When can the intersite interaction $V$ be neglected?

(think about it, it is important to understand!!! GPT:)

Although previous calculations found a sizable Coulomb interaction $V$ between neighbouring Star-of-David clusters, its effect on the electronic spectrum is expected to be small in the deep Mott-insulating regime. At half-filling, strong local repulsion suppresses charge fluctuations and approximately fixes one electron on every cluster,

$$\langle \hat{n}_i \rangle \simeq 1. \tag{9.1}$$

Consequently, the intersite term

$$\hat{H}_V = V \sum_{\langle ij \rangle} \hat{n}_i \hat{n}_j \tag{9.2}$$

is approximately constant because

$$\hat{n}_i \hat{n}_j \simeq 1. \tag{9.3}$$

It therefore produces mainly an overall energy shift without qualitatively modifying the equilibrium Mott spectrum. This explains why extended-Hubbard calculations have found that the insulating state of monolayer $1T$-$TaS_2$ is primarily controlled by the local interaction $U$, despite the non-negligible magnitude of $V$.

Nevertheless, the omission of $V$ may become less reliable close to the distortion-driven metal–insulator transition considered in the article. As the Star-of-David Wannier orbital becomes more delocalized, the bandwidth increases and the local interaction decreases,

$$W(a) \uparrow, \qquad U(a) \downarrow, \tag{9.4}$$

which enhances local and intersite charge fluctuations,

$$\left\langle (\hat{n}_i - \langle \hat{n}_i \rangle)^2 \right\rangle \uparrow . \tag{9.5}$$

In this regime, $\hat{n}_i \hat{n}_j$ is no longer approximately constant, and $V$ can modify the energies of charge excitations. For example, an inter-cluster hopping process,

$$(1,1) \longrightarrow (0,2), \tag{9.6}$$

has an approximate interaction-energy cost

$$\Delta E \sim U - V, \tag{9.7}$$

rather than $U$ alone. Nonlocal interactions may therefore shift the Hubbard bands, provide additional screening, and change the critical distortion at which the metallic state appears. Furthermore, $V$ should itself depend on the structural coordinate,

$$V_{ij}(a) = \int d\mathbf{r}\, d\mathbf{r}'\, |w_{ia}(\mathbf{r})|^2 W_a^r(\mathbf{r}, \mathbf{r}') |w_{ja}(\mathbf{r}')|^2, \tag{9.8}$$

particularly because the Wannier orbitals become substantially more extended as the distortion changes. Thus, neglecting $V$ is probably reasonable for describing the qualitative equilibrium Mott-insulating state, but its inclusion would be necessary to test quantitatively the predicted Hubbard-band shifts and the precise position of the distortion-driven metal–insulator transition.

### 9.2.2 Questions About the Methods, Calculations

**How are the effective $U$ and $V$ obtained in the cRPA approach?**

(GPT:)

The low-energy electronic state of one Star-of-David (SOD) is a molecular orbital spread over the 13 Ta atoms,

$$|\Psi_{\mathrm{SOD}}\rangle = \sum_i c_i |d_i\rangle, \qquad w_i = |c_i|^2 = |\langle d_i|\Psi_{\mathrm{SOD}}\rangle|^2, \qquad \sum_i w_i = 1.$$

Here $|d_i\rangle$ denotes an atomic Ta-$d$ orbital and $w_i$ gives its weight in the SOD molecular orbital. The cRPA calculation provides the screened Coulomb interactions $\bar{U}_{ij}$ between these atomic orbitals. To obtain the effective interaction of the whole SOD orbital, these atomic interactions are projected onto $|\Psi_{\mathrm{SOD}}\rangle$. For two electrons on the same SOD,

$$U = \sum_{i,j\in\mathrm{SOD}} w_i w_j \bar{U}_{ij},$$

while for electrons on two neighboring SODs $A$ and $B$,

$$V = \sum_{\substack{i\in\mathrm{SOD}_A \\ j\in\mathrm{SOD}_B}} w_i w_j \bar{U}_{ij}.$$

Thus, $U$ is the effective Coulomb repulsion within one SOD molecular orbital, whereas $V$ is the effective repulsion between neighboring SOD molecular orbitals. The simpler expression

$$U = \frac{1}{13^2} \sum_{i,j\in\mathrm{SOD}} U_{ij}$$

corresponds to assuming equal weight $w_i = 1/13$ on every Ta atom, since $w_i w_j = 1/13^2$. Therefore, schematically,

$$\mathrm{cRPA} \to \bar{U}_{ij}, \qquad \mathrm{DFT/Wannier} \to w_i, \qquad (\bar{U}_{ij}, w_i) \to U, V,$$

and the resulting $U$ and $V$ are then used as parameters of the extended Hubbard model.

**Example of how the effective $U$ and $V$ are obtained.**

(GPT:)

Consider, for simplicity, a molecular orbital distributed over only three atomic Ta-$d$ orbitals instead of the 13 Ta atoms of the real SOD. Suppose that 60% of the electron probability is on atom 1, 30% on atom 2, and 10% on atom 3. A quantum state is written in terms of probability amplitudes $c_i$, while the probabilities are $w_i = |c_i|^2$. Therefore, to obtain probabilities $w_1 = 0.6$, $w_2 = 0.3$, and $w_3 = 0.1$, we write

$$|\Psi\rangle = \sqrt{0.6}|d_1\rangle + \sqrt{0.3}|d_2\rangle + \sqrt{0.1}|d_3\rangle,$$

since $|\sqrt{0.6}|^2 = 0.6$, etc., and $0.6 + 0.3 + 0.1 = 1$. Suppose that cRPA gives the screened Coulomb interactions between these atomic orbitals as

$$\bar{U}_{ij} = \begin{pmatrix} 1.0 & 0.4 & 0.2 \\ 0.4 & 1.0 & 0.4 \\ 0.2 & 0.4 & 1.0 \end{pmatrix} \text{eV}.$$

For example, $\bar{U}_{11} = 1.0$ eV is the screened interaction associated with charge on atomic orbital 1, while $\bar{U}_{12} = 0.4$ eV is the interaction between charge on atomic orbitals 1 and 2. We want to replace these three atomic orbitals by one effective molecular orbital and therefore calculate its effective interaction

$$U_{\text{eff}} = \sum_{i,j} w_i w_j \bar{U}_{ij}.$$

For the chosen example,

$$\begin{aligned} U_{\text{eff}} &= (0.6)^2(1.0) + (0.3)^2(1.0) + (0.1)^2(1.0) \\ &\quad + 2(0.6)(0.3)(0.4) + 2(0.6)(0.1)(0.2) + 2(0.3)(0.1)(0.4) = 0.652 \text{ eV}. \end{aligned}$$

Thus, many atomic interaction matrix elements $\bar{U}_{ij}$ are converted into one effective Hubbard parameter $U_{\text{eff}}$ for the molecular orbital. For the real SOD the same idea is applied to its Ta-$d$ orbital weights,

$$U = \sum_{i,j \in \text{SOD}} w_i w_j \bar{U}_{ij}.$$

To calculate $V$, the same procedure is used, but $i$ belongs to one SOD and $j$ to a neighboring SOD,

$$V = \sum_{\substack{i \in \text{SOD}_A \\ j \in \text{SOD}_B}} w_i w_j \bar{U}_{ij}.$$

Therefore, $U$ describes the effective interaction within one SOD molecular orbital, while $V$ describes the interaction between two neighboring SOD molecular orbitals.

### Comments about structure of TaS2

(GPT:)

The formal ionic picture of $TaS_2$ is

$$\text{Ta}^{4+}(\text{S}^{2-})_2.$$

This is important electronically. Neutral Ta has the approximate valence-electron configuration

$$\text{Ta} : [\text{Xe}]\, 4f^{14} 5d^3 6s^2.$$

Formally removing four electrons gives approximately

$$\text{Ta}^{4+} : 5d^1.$$

Thus, each Ta atom contributes one $d$ electron to the relevant low-energy electronic states.

**What is the difference between fig. 2 and 3? Why in fig. 3 there are more parameters?**

(GPT)

Figure 2C and Figure 3A both describe the electronic structure, but they show different quantities. In Figure 2C, the curves are ordinary non-interacting DFT/MLWF energy bands,

$$E_n(\mathbf{k}),$$

where the many-body effects of $U$ and $V$ are not included. In Figure 3A, $U$ and $V$ are included using GW+EDMFT, and the plotted quantity is the interacting spectral function

$$A(\mathbf{k},\omega) = -\frac{1}{\pi}\,\mathrm{Im}\,G^R(\mathbf{k},\omega).$$

It plays a role similar to an interacting band structure and shows the formation of the lower and upper Hubbard bands.

Figures 2 and 3B,C both contain a density of states, but it is calculated differently. For the non-interacting case,

$$D(E) = \frac{1}{N_k}\sum_{n,\mathbf{k}} \delta(E - E_{n\mathbf{k}}),$$

whereas for the interacting case,

$$D(\omega) = \frac{1}{N_k}\sum_{\mathbf{k}} A(\mathbf{k},\omega).$$

Thus, Figures 3B,C show the interacting DOS for the two different $(U, V)$ parameter sets. Both give a gap and therefore an insulating state, but the positions of the Hubbard bands are different.

Figure 3D shows $\mathrm{Im}\,G(i\omega_n)$. For both parameter sets,

$$\mathrm{Im}\,G(i\omega_n) \to 0 \qquad \text{as } \omega_n \to 0,$$

which confirms the absence of spectral weight at the Fermi energy and therefore the insulating state.

Figure 3E shows the self-energy $\Sigma(i\omega_n)$. From its low-frequency behavior, the quasiparticle weight is estimated as

$$Z = \left[1 - \frac{\partial\,\mathrm{Im}\,\Sigma(i\omega_n)}{\partial\omega_n}\right]^{-1} \simeq 0.$$

The vanishing quasiparticle weight confirms that the insulating state is a Mott state produced by strong electronic correlations.

Thus, the figures can be summarized as

| | | |
|---|---|---|
| Fig. 2C | : | $E_n(\mathbf{k})$ non-interacting DFT/MLWF bands, |
| Fig. 3A | : | $A(\mathbf{k},\omega)$ interacting spectrum, |
| Fig. 3B,C | : | $D(\omega)$ interacting DOS and Hubbard bands, |
| Fig. 3D | : | $G$ confirms zero spectral weight at $E_F$, |
| Fig. 3E | : | $\Sigma$, $Z \simeq 0$ confirms the Mott character. |

**What are Hubbard bands?**

(GPT:)

Hubbard bands are correlation-induced electronic states that appear when the Hubbard interaction $U$ becomes strong compared with the bandwidth. In the non-interacting CCDW calculation of Figure 2, there is one narrow half-filled SOD band near $E_F$. When $U$ and $V$ are included and the system is treated with GW+EDMFT in Figure 3, the spectral weight of this band is redistributed into a Lower Hubbard Band (LHB) and an Upper Hubbard Band (UHB), separated by a Mott gap:

$$\text{narrow half-filled SOD band} \xrightarrow{\text{strong } U} \text{LHB} \mid \text{Mott gap} \mid \text{UHB}.$$

Roughly, the LHB corresponds to electron-removal excitations and the UHB to electron-addition excitations. Unlike an ordinary band described by a sharp dispersion $E_n(\mathbf{k})$, a Hubbard band is a region of large spectral weight in $A(\mathbf{k}, \omega)$ and can therefore appear as a broadened or "smeared" band. Thus, the red features in Figure 3 are Hubbard bands: they are correlation-induced descendants of the narrow SOD band in Figure 2 and are absent from the corresponding non-interacting calculation.

**What is the meaning of fig. 4c?**

(GPT:)

Figure 4C shows the static momentum-dependent charge susceptibility $\chi(\mathbf{q}, i\Omega_m = 0)$ close to the charge-ordering instability.

The axes $n_{b_1}$ and $n_{b_2}$ are simply the fractional coordinates of the momentum $\mathbf{q}$ in the reciprocal-lattice basis:

$$\mathbf{q} = n_{b_1}\mathbf{b}_1 + n_{b_2}\mathbf{b}_2,$$

where $\mathbf{b}_1$ and $\mathbf{b}_2$ are primitive reciprocal-lattice vectors.

Thus,

$$(n_{b_1}, n_{b_2}) = \left(\frac{1}{3}, \frac{1}{3}\right)$$

means

$$\mathbf{q} = \frac{1}{3}\mathbf{b}_1 + \frac{1}{3}\mathbf{b}_2.$$

The point marked $K$ is the corresponding high-symmetry point of the Brillouin zone. The calculation shows that $\chi(\mathbf{q})$ becomes very large near

$$\mathbf{q} = K,$$

which means that the system is close to developing a charge modulation with this wavevector.

Therefore, Figure 4B shows that a charge-ordering instability is approached, while Figure 4C shows at which momentum it occurs:

$$\mathbf{Q} = K.$$

The value $V = 0.565$ eV used in Figure 4C is larger than the realistic estimated $V$, so this additional charge-ordered state is not expected for the realistic parameters of the material.

### What is the GGA?

(GPT:)

An example of the Generalized Gradient Approximation (GGA) is the PBE functional (Perdew–Burke–Ernzerhof), which is also used in this paper. In GGA, the exchange-correlation energy depends not only on the local electron density $n(\mathbf{r})$, but also on its spatial gradient $\nabla n(\mathbf{r})$:

$$E_{\mathrm{xc}}^{\mathrm{GGA}}[n] = \int d^3r\, n(\mathbf{r})\, \varepsilon_{\mathrm{xc}}\left(n(\mathbf{r}), \nabla n(\mathbf{r})\right).$$

Thus, in contrast to LDA, $E_{\mathrm{xc}}^{\mathrm{LDA}}[n] = \int d^3r\, n(\mathbf{r})\varepsilon_{\mathrm{xc}}(n(\mathbf{r}))$, GGA takes into account spatial variations of the electron density.

### What is the GW that adds to DMFT?

(??????? it is a big topic, I'll think later)

### What is the EDMFT (Extended Dynamical Mean-Field Theory)?

(GPT:)

EDMFT (Extended Dynamical Mean-Field Theory) is an extension of DMFT that allows non-local Coulomb interactions $V$ to be included in addition to the local Hubbard interaction $U$.

For the extended Hubbard model,

$$H = -\sum_{ij\sigma} t_{ij} c_{i\sigma}^{\dagger} c_{j\sigma} + U \sum_{i} n_{i\uparrow} n_{i\downarrow} + V \sum_{\langle ij \rangle} n_i n_j - \mu \sum_{i} n_i,$$

DMFT mainly describes local electronic correlations caused by $U$, while EDMFT additionally accounts for the effects of $V$ through a dynamically screened effective interaction $\mathcal{U}(i\Omega)$.

Thus, the hierarchy used in the paper can be summarized as: DMFT $\rightarrow$ local correlations from $U$; EDMFT $\rightarrow$ adds the effects of non-local $V$ and dynamical screening; GW+EDMFT $\rightarrow$ additionally includes a non-local, momentum-dependent contribution to the electronic self-energy, $\Sigma(\mathbf{k}, i\omega) = \Sigma_{\mathrm{imp}}(i\omega) + \Sigma_{\mathrm{nonloc}}^{GW}(\mathbf{k}, i\omega)$.

### What is the single-site DMFT?

(GPT:)

The central approximation of single-site DMFT is that the electronic self-energy is local, i.e. momentum independent:

$$\Sigma(\mathbf{k}, i\omega_n) \approx \Sigma_{\mathrm{loc}}(i\omega_n).$$

The interacting lattice Green's function is therefore

$$G(\mathbf{k}, i\omega_n) = \frac{1}{i\omega_n + \mu - \varepsilon_{\mathbf{k}} - \Sigma_{\mathrm{loc}}(i\omega_n)},$$

and the local Green's function is obtained by averaging over momentum,

$$G_{\mathrm{loc}}(i\omega_n) = \frac{1}{N_k} \sum_{\mathbf{k}} G(\mathbf{k}, i\omega_n).$$

DMFT maps the lattice problem onto a single interacting impurity coupled to an effective bath. The corresponding Weiss Green's function is determined self-consistently from

$$\mathcal{G}_0^{-1}(i\omega_n) = G_{\mathrm{loc}}^{-1}(i\omega_n) + \Sigma_{\mathrm{loc}}(i\omega_n).$$

The impurity model contains the local Hubbard interaction $U$, schematically

$$S_{\text{imp}} = -\sum_{\sigma,n} c^{\dagger}_{\sigma n}\mathcal{G}_0^{-1}(i\omega_n)c_{\sigma n} + U\int_0^{\beta} d\tau\, n_{\uparrow}(\tau)n_{\downarrow}(\tau).$$

Solving the impurity problem gives a new local self-energy,

$$\Sigma_{\text{imp}}(i\omega_n) = \mathcal{G}_0^{-1}(i\omega_n) - G_{\text{imp}}^{-1}(i\omega_n),$$

and single-site DMFT imposes the self-consistency conditions

$$\Sigma_{\text{loc}} = \Sigma_{\text{imp}}, \qquad G_{\text{loc}} = G_{\text{imp}}.$$

Thus, single-site DMFT treats the local interaction $U$ dynamically and non-perturbatively, but neglects the spatial dependence of the electronic self-energy.

**What is meant by the limitation related to interlayer dimerization and singlet formation?**

(GPT:)

The authors state that their calculation does not include singlet formation caused by interlayer dimerization. Their main calculation describes the correlation-driven mechanism,

$$\text{strong } U, V \longrightarrow \text{Mott localization} \longrightarrow \text{insulating state.}$$

However, another mechanism has been proposed for bulk $TaS_2$. SOD orbitals belonging to neighboring layers can hybridize strongly and form interlayer dimers. Since each SOD has approximately one electron in its low-energy orbital, two neighboring SODs can form a spin singlet,

$$|\text{singlet}\rangle = \frac{1}{\sqrt{2}}\left(|\uparrow\downarrow\rangle - |\downarrow\uparrow\rangle\right), \qquad S = 0.$$

Interlayer hopping $t_{\perp}$ can split the corresponding states into bonding and antibonding states,

$$E_{\pm} \sim \varepsilon_0 \pm t_{\perp},$$

so that the two electrons can occupy the lower bonding state and an insulating gap can appear. Thus, an alternative mechanism is

$$\text{interlayer } t_{\perp} \longrightarrow \text{dimerization and singlet formation} \longrightarrow \text{bonding–antibonding splitting} \longrightarrow \text{insulating}$$

The present calculation does not include this mechanism and therefore cannot determine the relative importance of Mott correlations and interlayer dimerization in bulk $TaS_2$. This limitation is less relevant to an isolated monolayer, where interlayer dimerization is absent.

### 9.2.3 Questions About the Meaning of Methods, Materials: Less Important

**What is the meaning of screening?**

(????? I have no idea, since they do not explain. what should we understand about the screening to understand the paper?)

**How to see that if we go to non CDW phase, then V goes to 0?**

(GPTs opinion, which is most likely useless:)

We do not expect $V$ to become zero in the non-CDW phase. $V$ is the non-local Coulomb interaction and exists also in the normal phase. The values of $U$ and $V$ calculated in the paper are effective interactions for the low-energy SOD model of the CCDW phase; when the SOD structure disappears, that particular effective model and its $U, V$ parameters are no longer applicable.

**What is the value of $\mu$ in the Hamiltonian? 0?**

(GPTs opinion, which is most likely useless:)

$\mu$ is chosen to obtain the required filling, here one electron per effective SOD orbital (half filling). It can sometimes be absorbed into the choice of the zero of energy, but it should not generally be assumed that $\mu = 0$.

**How exactly $t$ change if we go from normal to CDW state?**

(GPTs opinion, which is most likely useless:)

The CDW distortion changes the Ta–Ta distances and orbital overlaps, so the hopping integrals change. After formation of the SOD, the relevant low-energy hoppings are no longer simply hoppings between individual Ta atoms but effective hoppings between SOD molecular orbitals, characterized by $t_1, t_2, t_3, \ldots$

**Comparison of spectra with experiments (???) They are not like in fig. 7 in Rossnagel paper.**

(GPTs opinion, which is most likely useless:)

Figure 3 should not be compared directly with the full experimental spectrum in Rossnagel because the GW+EDMFT calculation describes mainly the isolated low-energy SOD band. The relevant comparison is primarily the Mott gap and positions of the lower and upper Hubbard bands; the paper notes Hubbard peaks around $\pm 0.2$ eV for the weaker interaction set, in reasonable agreement with STM.

**What is wrong in reasoning that TaS2 is a conductor?**

(GPTs opinion, which is most likely useless:)

Within the non-interacting CCDW band picture the reasoning is correct: the remaining SOD band is half-filled and therefore metallic. What is missing is strong electron correlation: sufficiently large $U/W$ splits this band into lower and upper Hubbard bands and produces a Mott insulating state.

**What is the intuitive understanding of W?**

(GPTs opinion, which is most likely useless:)

Here $W$ in $W \sim 9|t|$ is the bandwidth: the energy range over which an electron can disperse because of hopping,

$$W = E_{\max} - E_{\min}.$$

Large hopping generally means a large $W$ and more delocalized electrons; large $U/W$ favors localization.

**Which effects are there from V? exactly in which ways it improves the plot for the case without V?**

(GPTs opinion, which is most likely useless:)

$V$ introduces Coulomb interaction between neighboring SODs and therefore non-local charge fluctuations and dynamical screening. Compared with the $V = 0$ DMFT calculation, including $V$ changes the effective screened interaction and the spectral positions/shape of the Hubbard features; it also allows the charge-ordering instability studied in Figure 4.

**Are the a and b (unit cell vectors) discussed? what if we ahve a different ones?**

(GPTs opinion, which is most likely useless:)

The choice of primitive vectors is not unique. Different valid primitive vectors describe the same lattice; the formulas for $\mathbf{k}$, $\mathbf{q}$ and reciprocal vectors change their coordinate representation, but physical quantities such as the spectrum and susceptibility do not.

**How do we know the a and b vectors? (from ab into calculations)???**

(GPTs opinion, which is most likely useless:)

They are determined from the crystal structure. From the real-space primitive vectors $\mathbf{a}_1, \mathbf{a}_2$, reciprocal vectors $\mathbf{b}_1, \mathbf{b}_2$ are defined by

$$\mathbf{a}_i \cdot \mathbf{b}_j = 2\pi\delta_{ij}.$$

They are then used to represent momenta, for example $\mathbf{q} = n_{b_1}\mathbf{b}_1 + n_{b_2}\mathbf{b}_2$.

**We calculate U from what, from absence of U or from cycle that takes U into account? or do we plug into U only a non distorted configuration?**

(GPTs opinion, which is most likely useless:)

$U$ is calculated before the GW+EDMFT cycle using (c)RPA screening and then used as an input of the Hubbard model. For the effective CCDW model, the interaction is projected onto the SOD molecular orbital associated with the distorted CCDW structure; it is not obtained self-consistently from the later GW+EDMFT cycle.

**Does just W obtained from t or also we need to take U into account?**

(GPTs opinion, which is most likely useless:)

If $W$ means the bandwidth in $W \sim 9|t|$, it is obtained from the non-interacting dispersion and therefore from the hopping parameters $t$; $U$ is not included. This is precisely why the ratio $U/W$ is useful for comparing interaction strength with kinetic energy.

**W=|t|, but what is t? we have t1, t2, t3.**

(GPTs opinion, which is most likely useless:)

Strictly, $W \neq |t|$. For the nearest-neighbor triangular-lattice model,

$$W = 9|t|.$$

With $t_1, t_2, t_3$, the full dispersion $\varepsilon(\mathbf{k})$ contains all three hoppings and

$$W = \max_{\mathbf{k}} \varepsilon(\mathbf{k}) - \min_{\mathbf{k}} \varepsilon(\mathbf{k}).$$

The paper's $W \sim 9|t|$ is an approximate nearest-neighbor estimate.

**If we work with Matsubara GF, what is the temperature?**

(GPTs opinion, which is most likely useless:)

The Matsubara frequencies explicitly contain the temperature,

$$\omega_n = (2n+1)\pi T, \qquad \Omega_m = 2m\pi T,$$

with $k_B = 1$. Therefore a Matsubara GW+EDMFT calculation is performed at a finite specified temperature; the temperature determines the spacing of the Matsubara frequencies.

**Does large $V$ lead to additional charge ordering?**

Yes, but it is unphysical.

(GPT:)

Yes. The CCDW phase is already included in the effective model, where each Star-of-David (SOD) cluster acts as one effective lattice site. If the inter-SOD Coulomb interaction $V$ becomes sufficiently large, it becomes energetically favorable to develop an additional modulation of the charge density between different SODs. This instability is signaled by a divergence of the charge susceptibility $\chi(\mathbf{Q})$ at $\mathbf{Q} = K$. In the calculations it appears for $V \gtrsim 0.5$ eV, with Figure 4C showing the system close to the instability at $V = 0.565$ eV. However, the realistic 3-band RPA estimate is only $V = 0.208$ eV. Therefore, the paper does not predict this additional charge ordering for realistic CCDW-$TaS_2$; it demonstrates a possible instability of the model at unrealistically large $V$.

### 9.2.4 Questions about Correct Summarization and Takeaways

(some very complicated questions will be here)

**How to calculate from first principles band structure of TaS2?**

(??????????? I didn't yet still understand it....)

**What are the main equations of the paper?**

(below all is from GPT, check it!!!! I am not sure that it is a high quality theory!!!!)

The calculation can be divided into several stages. The important point is that the output of one stage often becomes the input of another stage:

$$\text{DFT} \to \begin{cases} \text{MLWF} \to t_{ij}, \\ \text{RPA/cRPA} \to U, V, \end{cases} \to \text{extended Hubbard model} \to \text{GW+EDMFT} \to G, \Sigma, W, P \to \text{spectral functions and charge response.}$$

**1. DFT calculation**

(below all is from GPT, check it!!!! I am not sure that it is a high quality theory!!!!)

**Input:** the crystal structure, atomic positions, and the choice of exchange-correlation functional (GGA-PBE in this work).

The Kohn-Sham problem is schematically

$$\left[-\frac{\nabla^2}{2} + V_{\text{ion}} + V_H[n] + V_{\text{xc}}[n]\right]\psi_{n\mathbf{k}} = \epsilon_{n\mathbf{k}}\psi_{n\mathbf{k}}.$$

**Output:**

$$\epsilon_{n\mathbf{k}}, \qquad \psi_{n\mathbf{k}}.$$

Here $\epsilon_{n\mathbf{k}}$ are the non-interacting DFT band energies and $\psi_{n\mathbf{k}}$ are the corresponding Kohn-Sham wave functions.

**Used later for:**

- plotting the DFT band structure;
- constructing maximally localized Wannier functions;
- constructing the polarization and screened Coulomb interaction in RPA/cRPA.

**2. MLWF calculation**

(below all is from GPT, check it!!!! I am not sure that it is a high quality theory!!!!)

**Input:**

$$\epsilon_{n\mathbf{k}}, \qquad \psi_{n\mathbf{k}}$$

from DFT, in particular the isolated low-energy SOD-derived band.

A localized Wannier orbital is constructed,

$$|w_i\rangle,$$

and the tight-binding hopping amplitudes are obtained as

$$t_{ij} = \langle w_i|\hat{H}_{\mathrm{DFT}}|w_j\rangle.$$

The momentum-space hopping is

$$t(\mathbf{k}) = \sum_{\mathbf{R}} t(\mathbf{R}) e^{i\mathbf{k}\cdot\mathbf{R}}.$$

**Output:**

$$t_{ij}, \qquad t(\mathbf{k}),$$

as well as the real-space SOD molecular orbital $|w_i\rangle$.

For this material the relevant reported values are

$$|t_1| = 1.812 \text{ meV}, \qquad |t_2| = 0.814 \text{ meV}, \qquad |t_3| = 1.785 \text{ meV}.$$

**Used later for:**

$$t_{ij} \longrightarrow H_{\mathrm{Hubbard}},$$

and

$$t(\mathbf{k}) \longrightarrow G(\mathbf{k}, i\omega_n)$$

in the GW+EDMFT calculation.

Thus the MLWF calculation provides the kinetic-energy part of the effective low-energy model.

**3. RPA/cRPA screening calculation**

(below all is from GPT, check it!!!! I am not sure that it is a high quality theory!!!!)

**Input:** DFT electronic states and the bare Coulomb interaction.

The standard screening relation is

$$W(\mathbf{q}, \omega) = v(\mathbf{q}) \left[1 - v(\mathbf{q}) P(\mathbf{q}, \omega)\right]^{-1},$$

where

$$v$$

is the bare Coulomb interaction and

$$P$$

is the electronic polarization.

In cRPA, the total polarization is conceptually separated as

$$P = P_{\text{low}} + P_{\text{rest}},$$

and the low-energy screening processes that will later be treated explicitly by the Hubbard model are excluded. Therefore,

$$W^{\text{cRPA}} = v\left[1 - vP_{\text{rest}}\right]^{-1}.$$

**Output:**

$$W^{\text{RPA}} \quad \text{or} \quad W^{\text{cRPA}}.$$

$W^{\text{cRPA}}$ is a partially screened Coulomb interaction. It is *not* yet the final quantity plotted in Figure 4.

**Used later for:**

Matrix elements of $W^{\text{RPA/cRPA}}$ are projected onto atomic or SOD orbitals in order to obtain the effective model parameters

$$U \quad \text{and} \quad V.$$

Thus,

$$W^{\text{RPA/cRPA}} \longrightarrow U, V \longrightarrow H_{\text{Hubbard}}.$$

The RPA/cRPA calculation is therefore mainly a method for constructing the interaction parameters of the low-energy model.

**4. First interaction estimate: 3-band RPA**

(below all is from GPT, check it!!!! I am not sure that it is a high quality theory!!!!)

The RPA-screened interaction in real space is written as

$$U_{\mathbf{R}-\mathbf{R}'} = \frac{1}{N_q}\sum_{\mathbf{q}} U_{\mathbf{q}} e^{i\mathbf{q}\cdot(\mathbf{R}-\mathbf{R}')}.$$

The effective interaction inside one SOD is estimated as

$$U = \frac{1}{13^2}\sum_{\mathbf{R},\mathbf{R}'\in\text{SOD}} U_{\mathbf{R}-\mathbf{R}'}.$$

The interaction between two neighboring SODs is

$$V = \frac{1}{13^2}\sum_{\substack{\mathbf{R}\in\text{SOD}_1\\ \mathbf{R}'\in\text{SOD}_2}} U_{\mathbf{R}-\mathbf{R}'}.$$

**Output:**

$$U = 0.371 \text{ eV}, \qquad V = 0.208 \text{ eV}.$$

**Used later for:**

These numbers are inserted into the extended Hubbard model and are used as one of the two parameter sets in the GW+EDMFT calculation:

$$(U, V) = (0.371, 0.208) \text{ eV}.$$

**5. Second interaction estimate: 5-band cRPA**

(below all is from GPT, check it!!!! I am not sure that it is a high quality theory!!!!)
**Input:** the atomic cRPA interaction

$$\bar{U}_{\mathbf{R}-\mathbf{R}'}$$

and the weights of the Ta-$d$ orbitals in the SOD molecular orbital

$$w_{\mathbf{R}} = |\langle d_{\mathbf{R}}|\Psi\rangle|^2 .$$

The effective on-SOD interaction is

$$U = \sum_{\mathbf{R},\mathbf{R}'\in\mathrm{SOD}} w_{\mathbf{R}} w_{\mathbf{R}'} \bar{U}_{\mathbf{R}-\mathbf{R}'} .$$

The effective nearest-neighbor SOD interaction is

$$V = \sum_{\substack{\mathbf{R}\in\mathrm{SOD}_1 \\ \mathbf{R}'\in\mathrm{SOD}_2}} w_{\mathbf{R}} w_{\mathbf{R}'} \bar{U}_{\mathbf{R}-\mathbf{R}'} .$$

**Output:**

$$U = 0.653 \text{ eV}, \qquad V = 0.359 \text{ eV}.$$

**Used later for:**
This gives the second parameter set used in the GW+EDMFT calculation:

$$(U, V) = (0.653, 0.359) \text{ eV}.$$

Thus the 3-band RPA and 5-band cRPA calculations do not directly give the final spectrum. They give two possible sets of interaction parameters $(U, V)$ which are then inserted into the same many-body model.

**6. Extended Hubbard model**

(below all is from GPT, check it!!!! I am not sure that it is a high quality theory!!!!)
**Input:**

$$t_{ij} \quad \text{from MLWF}, \qquad U, V \quad \text{from RPA/cRPA}.$$

The effective Hamiltonian is

$$H = -\sum_{ij\sigma} t_{ij} c^\dagger_{i\sigma} c_{j\sigma} + U \sum_i n_{i\uparrow} n_{i\downarrow} + V \sum_{\langle ij\rangle} n_i n_j - \mu \sum_i n_i .$$

**Output:**
The Hamiltonian itself is not yet a numerical observable. It defines the many-body problem to be solved.
**Used later for:**

$$H \longrightarrow \text{DMFT/EDMFT/GW+EDMFT}.$$

**7. DMFT**

(below all is from GPT, check it!!!! I am not sure that it is a high quality theory!!!!)
**Input:**

$$t(\mathbf{k}), \qquad U, \qquad V = 0.$$

The main DMFT approximation is

$$\Sigma(\mathbf{k}, i\omega_n) \approx \Sigma_{\text{loc}}(i\omega_n).$$

The interacting lattice Green function is

$$G(\mathbf{k}, i\omega_n) = \left[i\omega_n + \mu - t(\mathbf{k}) - \Sigma_{\text{loc}}(i\omega_n)\right]^{-1}.$$

The local Green function is

$$G_{\text{loc}}(i\omega_n) = \frac{1}{N_k} \sum_{\mathbf{k}} G(\mathbf{k}, i\omega_n).$$

**Output:**

$$G_{\text{loc}}(i\omega_n), \qquad \Sigma_{\text{loc}}(i\omega_n).$$

**Used later for:**
$G$ is used to calculate the electronic spectral function, while $\Sigma$ characterizes the correlation-induced modification of the electrons.
In this paper ordinary DMFT is mainly used as a reference calculation with

$$V = 0.$$

**8. EDMFT: lattice quantities**

(below all is from GPT, check it!!!! I am not sure that it is a high quality theory!!!!)
**Input:**

$$t(\mathbf{k}), \qquad U, \qquad V,$$

together with an initial approximation for

$$\Sigma(\mathbf{k}, i\omega_n), \qquad P(\mathbf{q}, i\Omega_m).$$

The electron Green function is

$$G(\mathbf{k}, i\omega_n) = \left[i\omega_n - t(\mathbf{k}) + \mu - \Sigma(\mathbf{k}, i\omega_n)\right]^{-1}.$$

The dynamically screened Coulomb interaction is

$$W(\mathbf{q}, i\Omega_m) = v(\mathbf{q}) \left[1 - v(\mathbf{q}) P(\mathbf{q}, i\Omega_m)\right]^{-1}.$$

**Output:**

$$G(\mathbf{k}, i\omega_n), \qquad W(\mathbf{q}, i\Omega_m).$$

Here

$$G$$

describes propagation of interacting electrons, whereas

$$W$$

is the Coulomb interaction after screening by the interacting system.

**Used later for:**

$$G, W \longrightarrow G_{\text{loc}}, W_{\text{loc}} \longrightarrow \mathcal{G}, \mathcal{U} \longrightarrow \text{impurity problem.}$$

Note that this $W$ is different from the cRPA $W^{\text{cRPA}}$ used earlier.

The earlier

$$W^{\text{cRPA}}$$

is used to construct the model parameters $U, V$.

The present

$$W(\mathbf{q}, i\Omega_m)$$

is a many-body quantity calculated *after* the Hubbard model has been constructed and is one of the physical outputs studied in Figure 4.

**9. Momentum-space interaction $v(\mathbf{q})$**

(below all is from GPT, check it!!!! I am not sure that it is a high quality theory!!!!)

For nearest-neighbor interaction $V$ on the triangular SOD lattice,

$$v(\mathbf{q}) = 2V\left[\cos q_x + \cos\left(\frac{q_x}{2} + \frac{\sqrt{3}q_y}{2}\right) + \cos\left(-\frac{q_x}{2} + \frac{\sqrt{3}q_y}{2}\right)\right].$$

**Output:**

$$v(\mathbf{q}).$$

**Used later in:**

$$W(\mathbf{q}, i\Omega_m) = \frac{v(\mathbf{q})}{1 - v(\mathbf{q})P(\mathbf{q}, i\Omega_m)},$$

and also in the charge susceptibility.

**10. Local quantities**

(below all is from GPT, check it!!!! I am not sure that it is a high quality theory!!!!)

For any momentum-dependent quantity $A$,

$$A_{\text{loc}} = \frac{1}{N}\sum_{\mathbf{k}} A(\mathbf{k}).$$

In particular,

$$G_{\text{loc}}(i\omega_n) = \frac{1}{N_k}\sum_{\mathbf{k}} G(\mathbf{k}, i\omega_n),$$

and

$$W_{\text{loc}}(i\Omega_m) = \frac{1}{N_q}\sum_{\mathbf{q}} W(\mathbf{q}, i\Omega_m).$$

**Output:**

$$G_{\text{loc}}, \qquad W_{\text{loc}}.$$

**Used later for:**

They define the effective impurity environment in EDMFT.

**11. Fermionic and bosonic Weiss fields**

(below all is from GPT, check it!!!! I am not sure that it is a high quality theory!!!!)
The effective fermionic bath is

$$\mathcal{G}(i\omega_n) = \left[G_{\text{loc}}^{-1}(i\omega_n) + \Sigma_{\text{loc}}(i\omega_n)\right]^{-1}.$$

The effective dynamical interaction is

$$\mathcal{U}(i\Omega_m) = \left[W_{\text{loc}}^{-1}(i\Omega_m) + P_{\text{loc}}(i\Omega_m)\right]^{-1}.$$

**Output:**

$$\mathcal{G}(i\omega_n), \qquad \mathcal{U}(i\Omega_m).$$

$\mathcal{G}$ describes the effective electronic environment seen by one SOD, while $\mathcal{U}$ describes the effective frequency-dependent interaction seen by that SOD.
**Used later for:**
They are the input of the EDMFT impurity model.

**12. EDMFT impurity model**

(below all is from GPT, check it!!!! I am not sure that it is a high quality theory!!!!)
**Input:**

$$\mathcal{G}, \qquad \mathcal{U}.$$

The impurity action is

$$S_{\text{imp}} = -\iint d\tau d\tau' \, \bar{c}(\tau)\mathcal{G}^{-1}(\tau-\tau')c(\tau') + \frac{1}{2}\iint d\tau d\tau' \, \mathcal{U}(\tau-\tau')n(\tau)n(\tau').$$

This problem is solved numerically using the CT-HYB quantum Monte Carlo impurity solver.
**Output:**

$$\Sigma_{\text{imp}}(i\omega_n), \qquad P_{\text{imp}}(i\Omega_m).$$

$\Sigma_{\text{imp}}$ is the local electronic self-energy caused by strong local correlations.
$P_{\text{imp}}$ is the local polarization associated with charge fluctuations.
**Used later for:**
They provide the local parts of the full GW+EDMFT self-energy and polarization.

**13. GW calculation**

(below all is from GPT, check it!!!! I am not sure that it is a high quality theory!!!!)
**Input:**

$$G, \qquad W.$$

The GW electronic self-energy is

$$\Sigma^{GW}(\mathbf{k}, i\omega_n) = -\sum_{\mathbf{q}, i\Omega_m} G(\mathbf{k}+\mathbf{q}, i\omega_n + i\Omega_m)W(\mathbf{q}, i\Omega_m).$$

The GW polarization is

$$P^{GW}(\mathbf{q}, i\Omega_m) = 2\sum_{\mathbf{k}, i\omega_n} G(\mathbf{k}+\mathbf{q}, i\omega_n + i\Omega_m)G(\mathbf{k}, i\omega_n).$$

**Output:**

$$\Sigma^{GW}, \qquad P^{GW}.$$

**Used later for:**
Only their non-local parts are added to the local EDMFT result.

**14. Separation of local and non-local parts**

For any quantity $A$,

$$A_{\text{nonloc}} = A - A_{\text{loc}}.$$

Thus,

$$\Sigma^{GW}_{\text{nonloc}} = \Sigma^{GW} - \Sigma^{GW}_{\text{loc}},$$

and

$$P^{GW}_{\text{nonloc}} = P^{GW} - P^{GW}_{\text{loc}}.$$

**Output:**

$$\Sigma^{GW}_{\text{nonloc}}, \qquad P^{GW}_{\text{nonloc}}.$$

**Used later for:**
They are combined with the local EDMFT quantities.

**15. GW+EDMFT combination**

The full electronic self-energy is

$$\Sigma(\mathbf{k}, i\omega_n) = \Sigma_{\text{imp}}(i\omega_n) + \Sigma^{GW}_{\text{nonloc}}(\mathbf{k}, i\omega_n).$$

The full polarization is

$$P(\mathbf{q}, i\Omega_m) = P_{\text{imp}}(i\Omega_m) + P^{GW}_{\text{nonloc}}(\mathbf{q}, i\Omega_m).$$

**Output:**

$$\Sigma(\mathbf{k}, i\omega_n), \qquad P(\mathbf{q}, i\Omega_m).$$

**Used later for:**
They are inserted back into

$$G^{-1} = i\omega_n + \mu - t - \Sigma$$

and

$$W = v(1 - vP)^{-1}.$$

Therefore the calculation is iterative.

**16. GW+EDMFT self-consistency**

The loop is

$$\Sigma, P \to G, W \to G_{\text{loc}}, W_{\text{loc}} \to \mathcal{G}, \mathcal{U} \to \Sigma_{\text{imp}}, P_{\text{imp}} \to \Sigma, P.$$

It is repeated until

$$G^{(n+1)} \simeq G^{(n)}, \qquad W^{(n+1)} \simeq W^{(n)}.$$

The converged quantities

$$G, \qquad \Sigma, \qquad W, \qquad P$$

are the principal outputs of the GW+EDMFT calculation.

**17. Spectral function**

**Input:**

$$G(\mathbf{k}, i\omega_n)$$

from the converged GW+EDMFT calculation.

After analytic continuation,

$$i\omega_n \to \omega + i0^+,$$

one obtains the retarded Green function

$$G^R(\mathbf{k}, \omega).$$

The spectral function is

$$A(\mathbf{k}, \omega) = -\frac{1}{\pi} \operatorname{Im} G^R(\mathbf{k}, \omega).$$

**Output:**

$$A(\mathbf{k}, \omega).$$

**Used for:**

This is the interacting band-like spectrum shown in Figure 3A.

The momentum-integrated spectrum is

$$A(\omega) = \frac{1}{N_k} \sum_{\mathbf{k}} A(\mathbf{k}, \omega),$$

which gives the interacting DOS shown in Figures 3B and 3C.

**18. Quasiparticle weight**

**Input:**

$$\Sigma(i\omega_n).$$

The quasiparticle weight is estimated as

$$Z = \left[1 - \frac{\partial \operatorname{Im} \Sigma(i\omega_n)}{\partial \omega_n}\right]^{-1}_{\omega_n \to 0}.$$

**Output:**

$$Z.$$

**Interpretation:**

For a coherent metal,

$$0 < Z \leq 1,$$

while for the Mott insulating state,

$$Z \to 0.$$

Thus $Z$ is a diagnostic of whether coherent quasiparticles survive.

**19. Screened interaction shown in Figure 4**

**Input:**

$$P(\mathbf{q}, i\Omega_m)$$

from the converged EDMFT or GW+EDMFT calculation.

Calculate

$$W(\mathbf{q}, i\Omega_m) = \frac{v(\mathbf{q})}{1 - v(\mathbf{q})P(\mathbf{q}, i\Omega_m)}.$$

Then

$$W_{\text{loc}}(i\Omega_m) = \frac{1}{N_q} \sum_{\mathbf{q}} W(\mathbf{q}, i\Omega_m).$$

**Output:**

$$W_{\text{loc}}(i\Omega_m).$$

**Used for:**

This is the quantity plotted in Figure 4A to compare DMFT, EDMFT and GW+EDMFT and to see how $V$ changes dynamical screening.

**20. Charge susceptibility**

**Input:**

$$P(\mathbf{q}, i\Omega_m), \qquad v(\mathbf{q}).$$

The static charge susceptibility is

$$\chi(\mathbf{q}) = \left. \frac{-P(\mathbf{q}, i\Omega_m)}{1 - v(\mathbf{q})P(\mathbf{q}, i\Omega_m)} \right|_{\Omega_m=0}.$$

The local susceptibility is

$$\chi_{\text{loc}} = \frac{1}{N_q} \sum_{\mathbf{q}} \chi(\mathbf{q}).$$

**Output:**

$$\chi(\mathbf{q}), \qquad \chi_{\text{loc}}.$$

**Used for:**

$\chi_{\text{loc}}^{-1}$ is plotted in Figure 4B as a function of $V$.

The momentum dependence

$$\chi(\mathbf{q})$$

is plotted in Figure 4C.

A charge-ordering instability is indicated by

$$\chi(\mathbf{Q}) \to \infty,$$

or equivalently by

$$\chi_{\text{loc}}^{-1} \to 0.$$

**Summary of the mathematical outputs**

The important distinction between the quantities called "screened interaction" at different stages is

$$W^{\mathrm{cRPA}} \longrightarrow U, V \longrightarrow H_{\mathrm{Hubbard}} \longrightarrow W^{\mathrm{EDMFT/GW+EDMFT}}.$$

Thus,

$$W^{\mathrm{cRPA}}$$

is an auxiliary first-principles quantity used to construct $U$ and $V$, whereas

$$W(\mathbf{q}, i\Omega_m)$$

in GW+EDMFT is a physical many-body output describing the dynamical screening inside the already constructed interacting Hubbard model.

The main chain of quantities is therefore

$$\epsilon_{n\mathbf{k}}, \psi_{n\mathbf{k}} \longrightarrow \begin{cases} t_{ij}, \\ U, V, \end{cases} \longrightarrow H \longrightarrow \Sigma, P \longrightarrow G, W \longrightarrow \begin{cases} A(\mathbf{k}, \omega), \\ Z, \\ W_{\mathrm{loc}}(i\Omega), \\ \chi(\mathbf{q}). \end{cases}$$

# 10 Controlling magnetic frustration in 1T-$TaS_2$ via Coulomb engineered long-range interactions by Chen, Rösner, Lado

**Abstract**

Magnetic frustrations in two-dimensional materials provide a rich playground to engineer unconventional phenomena. However, despite intense efforts, a realization of tunable frustrated magnetic order in two-dimensional materials remains an open challenge. Here we propose Coulomb engineering as a versatile strategy to tailor magnetic ground states in layered materials. Using the frustrated van der Waals monolayer 1T-$TaS_2$ as an example, we show how long-range Coulomb interactions renormalize the low energy nearly flat band structure, leading to a Heisenberg model which depends on the Coulomb interactions. Based on this, we show that superexchange couplings in the material can be precisely tailored by means of environmental dielectric screening, ultimately allowing to externally drive the material towards a tunable frustrated regime. Our results put forward Coulomb engineering as a powerful tool to manipulate magnetic properties of van der Waals materials.

### 10.0.1 Introduction

Magnetic frustration in quantum systems represents one of the fundamental ingredient to stabilize exotic magnetic order and, ultimately, quantum spin-liquid (QSL) states[1, 2, 3, 4, 5]. Interest in quantum-spin-liquids has been fueled by their potential emergent Majorana physics[6], high-temperature superconductivity[7, 8], and use for topological quantum computing[9]. A variety of materials have been proposed as QSL candidates[10, 11, 12, 13, 14, 15, 16, 17, 18, 19, 20, 21, 22, 23], yet observing their QSL state is found to be highly sensitive to details of their Hamiltonian. While natural QSL materials are rare and require very precise fine-tuning, engineered materials allow to drastically overcome such challenges. Interestingly,

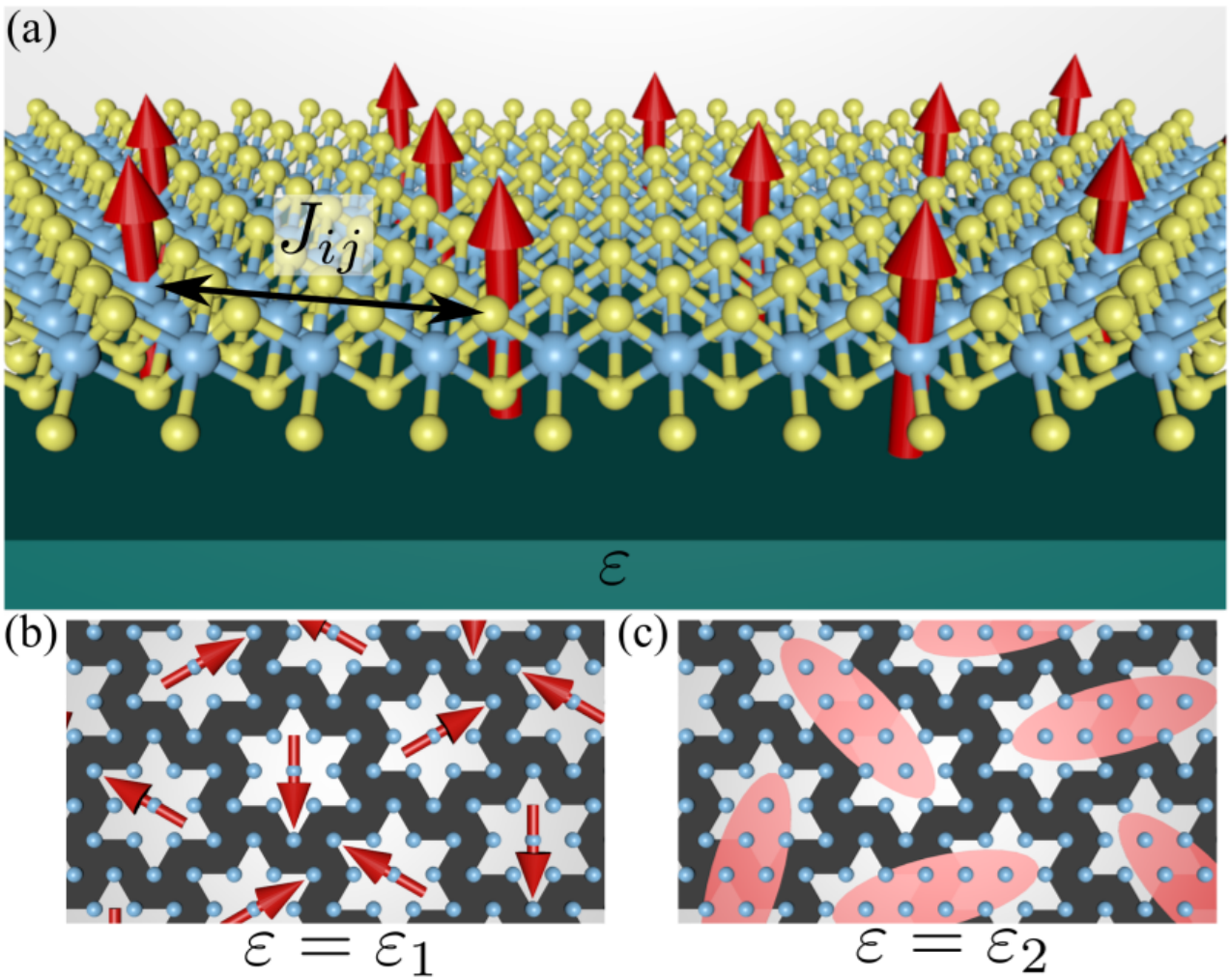


Figure 10.1: (a) Sketch of 1T-$TaS_2$ Coulomb engineered by a substrate with dielectric constant $\varepsilon$. The red arrows represent the local magnetic moments in the SOD unit cell. The superexchange couplings $J_{ij}$ between these magnetic moments can be tuned with Coulomb engineering. (b) Sketch of the helical spiral ground state in 1T-$TaS_2$. The red arrows represent the direction of the local magnetic moment. (c) Sketch of the QSL ground state in 1T-$TaS_2$.

van der Waals QSL candidates such as $TaS_2$[19, 25, 26] and $TaSe_2$[27] provide versatile platforms for a variety of quantum engineering methods such as straining[28, 29], twisting[30, 31, 32], impurity engineering[33, 34, 35] as well as Coulomb engineering, that could potentially promote QSL behavior in these materials.

Coulomb engineering[36, 37, 38] refers to a strategy to tailor many-body interactions by means of dielectric environments, which is particularly efficient for low-dimensional materials. This is due to the pronounced role of non-local Coulomb interactions, which decisively define many-body properties in low-dimensional systems and which can be simultaneously efficiently externally modified. In this way band gaps[39, 38, 40, 41, 42, 43, 44] as well as excitonic[38, 45, 43] or plasmonic[46, 47] excitations and even topological properties[48] can be precisely tailored in 2D and 1D systems with the help of (structured) dielectric substrates. Furthermore, Coulomb interactions also play a crucial role in magnetic van der Waals materials, affecting the magnetic exchange between localized magnetic moments. However, up to date, controlling magnetic properties of van der Waals materials via Coulomb engineering has been limited to the example of $CrI_3$[49].

Here, we put forward Coulomb engineering as a powerful tool to manipulate the ground states of magnetic van der Waals materials. Using the frustrated van der Waals magnet 1T-

$TaS_2$ as a prototypical example, we show how substrate screening renormalizes its low-energy electronic dispersion and how this controls the internal magnetic superexchange interactions. Together with direct exchange interactions, this allows to externally and non-invasively tailor the magnetic ground state in the material via changes to its dielectric environment. Importantly, beyond the case of 1T-$TaS_2$ analyzed here, our proposal provides a starting point towards the engineering of artificial magnets via tailored electronic interactions. Ultimately, these results put forward the control of long-range Coulomb interactions as a versatile strategy for quantum matter design.

### 10.0.2 Effective model for monolayer 1T-$TaS_2$

We now elaborate on the material we will focus on in our discussion, 1T-$TaS_2$. 1T-$TaS_2$ hosts a charge-density-wave (CDW) instability leading to the formation of the Star-of-David (SOD) unit cell with 13 Ta atoms at low temperature[19, 18, 51, 52, 53, 31]. The CDW as well as spin-orbit coupling (SOC) result in a half-filled narrow band at the Fermi energy, with a bandwidth of a few 10meV[55]. Together with sizable Coulomb interactions[56] this renders 1T-$TaS_2$ a correlated insulator rather than a simple metal. The electrons form local magnetic moments with $S = 1/2$ at each SOD, and interact via exchange and superexchange coupling (Fig. 10.1(a)), resulting in potential helical spiral and QSL ground states, as illustrated in Fig. 10.1(b) and (c), respectively.

We capture the low energy physics of 1T-$TaS_2$ with a single Wannier orbital model including long-range electronic interactions:

$$\begin{aligned} H = &\sum_{i,j,\sigma} t_{ij} c^\dagger_{i,\sigma} c_{j,\sigma} + U \sum_i n_{i,\uparrow} n_{i,\downarrow} \\ &+ \sum_{i,j,\sigma,\sigma'} \frac{V_{ij}}{2} n_{i,\sigma} n_{j,\sigma'}, \end{aligned} \tag{10.1}$$

where $\sigma$ and $\sigma'$ are spin indices, and $n_{i,\sigma} = c^\dagger_{i,\sigma} c_{i,\sigma}$. The hoppings $t_{ij}$ are fitted to DFT data[56] where we find hoppings up to the $14^{\text{th}}$ neighbor. The hoppings exhibit an oscillating behavior in addition to a decay with distance. This oscillating behavior stems from the nature of the Wannier wavefunctions of this material, and is inherited from the electronic structure from first principles calculations. We parameterize the long-range Coulomb interactions $V_{ij}$ via a modified Yukawa potential of the form

$$V_{ij} = \frac{U}{\sqrt{1 + \left(\frac{4\pi\varepsilon_0 U r_{ij}}{e^2}\right)^2}} e^{-r_{ij}/r_{\text{TF}}}, \tag{10.2}$$

where $U$ is the on-site Coulomb interaction and $r_{ij}$ the distance between sites $i$ and $j$. The included Ohno potential[57, 44] results in a $r^{-1}$ long-wavelength behavior, which is further suppressed by the exponential term controlled by an effective screening length $r_{\text{TF}}$. This way, the non-local Coulomb interaction is fully parameterized by the local interaction $U$ and the screening length $r_{\text{TF}}$. It is worth noting that environmental screening to layered materials, such as resulting from dielectric substrates, is strongly non-local[58, 36, 37] such that long-ranged interactions $V_{ij}$ are stronger reduced than the local one $U$. To fully characterize this model we, however, treat $U$ and $r_{\text{TF}}$ as independent parameters in the following, understanding that any environmental screening will reduce both simultaneously.

The interacting model of Eq. (10.1) is analyzed in two steps. In the limit $U \gg V_{ij}$, we can first integrate out the long-range interactions $V_{ij}$, leading to a renormalized dispersion for the

low-energy band[59, 60]. The resulting Hamiltonian $\tilde{H}$ takes the form

$$\tilde{H} = \sum_{i,j,\sigma} \tilde{t}_{ij} c^{\dagger}_{i,\sigma} c_{j,\sigma} + U \sum_{i} n_{i,\uparrow} n_{i,\downarrow}, \tag{10.3}$$

where $\tilde{t}_{ij}$ are the renormalized hoppings derived from Eq. (10.1) using a Hatree-Fock variational wavefunction enforcing time-reversal symmetry.

For $U$ between 100 and 500 meV as estimated for 1T metallic TMDCs [56, 61, 62] and several choices of $r_{\mathrm{TF}}$, the corresponding long-range Coulomb interactions $V_n$ and renormalized hoppings $\tilde{t}_n$ are shown in Figs. 10.2(a,b), where $V_n$ denotes $n_{\mathrm{th}}$ neighbor Coulomb interaction and similarly for $\tilde{t}_n$. We see that $V_n$ is increased by increasing $U$ and $r_{\mathrm{TF}}$, which mostly affects $\tilde{t}_1$ for $r_{\mathrm{TF}} < a$ ($a$ is the CDW lattice constant), while the long-range interaction with $r_{\mathrm{TF}} = a$ also modulates hoppings up to $\tilde{t}_5$. In Figs. 10.2(c-f) we show the bare electronic dispersion after integrating out long-range Coulomb interactions $V_n$, corresponding to the band structure of $\tilde{H}_{\mathrm{bare}} = \sum_{i,j,\sigma} \tilde{t}_{ij} c^{\dagger}_{i,\sigma} c_{j,\sigma}$. For $r_{\mathrm{TF}} = 0.3a$ (with $V_{n>1} \approx 0$) the renormalized bare bandwidth is not significantly affected and we find only modifications to the dispersion around $\Gamma$ upon changing $U$, c.f. Figs. 10.2(c,d). Increasing $r_{\mathrm{TF}} > 0.3a$ yields $V_{n>1} > 0$, which decisively affects both, the renormalized bare bandwidth and the overall dispersion, c.f. Figs. 10.2(e,f). As maintaining the Mott regime requires that the bandwidth renormalization should not be too large, we focus on $r_{\mathrm{TF}} \leq 0.4a$ in the following. In addition to the bandwidth renormalization, we observe a Coulomb controlled Lifshitz transition: as $U$ and $r_{\mathrm{TF}}$ increase, the electron pocket at $\Gamma$ vanishes, as depicted in the insets of Figs. 10.2(c-f). This transition results in different dependencies of superexchange couplings on the Coulomb interactions as we discuss in the following. We note that the renormalized bare dispersions shown in Fig. 10.2(c-f) do not explicitly take the local Coulomb interaction $U$ into account as in the Hamiltonian $\tilde{H}$ from Eq. (10.3). To obtain the electronic dispersion of $\tilde{H}$ including the effects of $U$, dynamical mean field theory (DMFT)[61, 44, 56, 62] calculations are required. We show that this is not needed to analyze the magnetic properties of $\tilde{H}$ in the following.

### 10.0.3 Coulomb engineering of the spin Hamiltonian of 1T-$TaS_2$

We now analyze the Hamiltonian from Eq. (10.3) in the strong coupling limit, i.e. $U \gg \tilde{t}_{ij}$, using the Schrieffer-Wolf transformation, leading to an effective model for spin-degrees of freedom:

$$\mathcal{H} = \sum_{i,j} J_{ij} \mathbf{S}_i \cdot \mathbf{S}_j, \tag{10.4}$$

with $J_{ij} = 2\frac{\tilde{t}^2_{ij}}{U}$. Due to the renormalization of $t_{ij}$ by $V_{ij}$, the magnetic superexchange interactions $J_{ij}$ are controlled by changes to $U$ and $r_{\mathrm{TF}}$ as well. In particular, we show in Fig. 10.3(a) the renormalized $n^{\mathrm{th}}$ neighbor exchange $J_n$. We see that $J_1$ exhibits a strong dependence on $U$ and $r_{\mathrm{TF}}$, stemming from the significant renormalization of $\tilde{t}_1$. In Fig. 10.3(b) we depict the full $U$ and $r_{\mathrm{TF}}$ dependencies of $J_1$ in units of $J^0_1 = 0.1$meV, where $J^0_1$ is the typical magnitude of $J_1$ in our regime. We find two regimes [separated by the white dashed line in Fig. 10.3(b)] stemming from the Coulomb driven Lifshitz transition of the Hamiltonian of Eq. (10.1). In the upper regime $V_n$ has a long-range character yielding renormalized band structures with unoccupied and rather flat dispersions around $\Gamma$, while in the lower regime the Coulomb interaction is short-ranged ($U$ and $V_1$) and we find occupied electron pockets (with positive effective mass) around $\Gamma$. $J_1$ is correspondingly larger in the upper regime and strongly dependent on $r_{\mathrm{TF}}$. In the lower regime $J_1$ is reduced and mostly dependent on $U$.

The model of Eq. (10.4) thus realizes a long-range Heisenberg model with tunable frustration controlled by the local and non-local Coulomb interactions. While a full calculation of the

phase diagram would require exactly solving the two-dimensional quantum many-body model, e.g. with tensor-network[63, 64] or neural network quantum states[65, 66], here we will focus on highlighting the physical regime where the frustration of the system is maximal. A frustrated magnetic system has competing magnetic exchange interactions whose energies cannot be simultaneously minimized by any magnetic configuration[67]. As a consequence, classical magnetic ground states of a frustrated magnetic system exhibit a high degree of degeneracy, preventing the system from magnetic ordering and promoting a QSL state. We may thus characterize the frustration of a magnetic system by the degeneracy of classical magnetic ground states. We consider different non-collinear magnetic configurations characterized by a vector $\mathbf{q}$[68, 69] and compute their energy $\omega(\mathbf{q})$ from the extended Hubbard model Eq. (10.1). The resulting $\omega(\mathbf{q})$ is then shifted and scaled: $\tilde{\omega}(\mathbf{q}) = (\omega(\mathbf{q}) - \omega_0)/(\omega_1 - \omega_0)$ with $\omega_0 = \min(\omega(\mathbf{q}))$ and $\omega_1 = \max(\omega(\mathbf{q}))$. The shifted ground state energy is 0, and the scaling allows comparison between systems with different magnitudes of magnetic exchange interactions. Finally, the degeneracy of the states at a given shifted and scaled energy $\omega$ can be given by

$$\tilde{\rho}(\omega) = \int_{\mathbf{q}\in\mathrm{BZ}} \frac{\mathrm{d}^2\mathbf{q}}{(2\pi)^2} \delta(\tilde{\omega}(\mathbf{q}) - \omega). \tag{10.5}$$

In particular, $\tilde{\rho}(0)$ characterizes the ground state degeneracy of a magnetic system, and a more frustrated system is characterized by larger $\tilde{\rho}(0)$.

The computation of $\omega(\mathbf{q})$ can be done by solving Eq. (10.1) self-consistently assuming the solution of a non-collinear magnetic state characterized by the vector $\mathbf{q}$, where without loss of generality we take the magnetization to be in $y$-$z$ plane. Alternatively, we can perform a unitary transformation that aligns the magnetization on every site to $z$ axis[68, 70, 69]: $H_{\mathbf{q}} = U_{\mathbf{q}}^\dagger H U_{\mathbf{q}}$ with $U_{\mathbf{q}} = \prod_i e^{-\frac{i}{2}\mathbf{q}\cdot\mathbf{r}_i\sigma_{x,i}}$, and solve it self-consistently assuming ferromagnetism in $z$ direction. The transformed $H_{\mathbf{q}}$ is:

$$\begin{aligned} H_{\mathbf{q}} = &\sum_{i,j,\sigma,\sigma'} t_{ij,\sigma\sigma'}(\mathbf{q}) c_{i,\sigma}^\dagger c_{j,\sigma'} + U \sum_i n_{i,\uparrow} n_{i,\downarrow} \\ &+ \sum_{i,j,\sigma,\sigma'} \frac{V_{ij}}{2} n_{i,\sigma} n_{j,\sigma'}, \end{aligned} \tag{10.6}$$

where $t_{ij,\sigma\sigma'}(\mathbf{q}) = t_{ij} e^{\frac{i}{2}\mathbf{q}\cdot(\mathbf{r}_i - \mathbf{r}_j)(\sigma_x)_{\sigma\sigma'}}$. In the limit $U \gg V_{ij}$, we can first integrate out $V_{ij}$ as we did for Eq. (10.1), leading to

$$\tilde{H}_{\mathbf{q}} = \sum_{i,j,\sigma,\sigma'} \tilde{t}_{ij,\sigma\sigma'}(\mathbf{q}) c_{i,\sigma}^\dagger c_{j,\sigma'} + U \sum_i n_{i,\uparrow} n_{i,\downarrow}, \tag{10.7}$$

where $\tilde{t}_{ij,\sigma\sigma'}(\mathbf{q}) = \tilde{t}_{ij} e^{\frac{i}{2}\mathbf{q}\cdot(\mathbf{r}_i - \mathbf{r}_j)(\sigma_x)_{\sigma\sigma'}}$ [1]. With the assumption of ferromagnetism along $z$ direction: $\langle n_{i,\uparrow}\rangle = 1$, $\langle n_{i,\downarrow}\rangle = 0$, Eq. (10.7) reduces to

$$H_{\mathbf{q}}^{\mathrm{MF}} = \sum_{i,j,\sigma,\sigma'} \tilde{t}_{ij,\sigma\sigma'}(\mathbf{q}) c_{i,\sigma}^\dagger c_{j,\sigma'} + \frac{U}{2} \sum_i (n_{i,\downarrow} - n_{i,\uparrow}) \tag{10.8}$$

up to a constant, and $\omega(\mathbf{q})$ can be computed by summing over occupied states in Eq. (10.8).

Now we move on to compute $\tilde{\rho}(0)$ for our model with different $U$ and $r_{\mathrm{TF}}$. We find that, $\tilde{\rho}(0)$ takes large values close to the Lifshitz transition and smaller values at other places

[1] We can perform a change of basis to Eq. (10.6): $d_{i,\uparrow}^\dagger = \cos\theta c_{i,\uparrow}^\dagger + i\sin\theta c_{i,\downarrow}^\dagger$ and $d_{i,\downarrow}^\dagger = i\sin\theta c_{i,\uparrow}^\dagger + \cos\theta c_{i,\downarrow}^\dagger$. This does not change the $V_{ij}$ term, and the Hamiltonian becomes Eq. 10.1 with only changes in the $U$ term. The resulting $\tilde{t}_{ij}$ after integrating out $V_{ij}$ is thus given by Eq. 10.3. Transforming back to the original basis results in Eq. (10.7).

(Fig.10.3(c)). In particular, below the Lifshitz transition, $\tilde{\omega}(\mathbf{q})$ exhibits a minima between $\Gamma$ and K (Fig.10.3(e)). As we approach the Lifshitz transition, $J_1$ increases, lowering $\tilde{\omega}(\mathbf{q})$ around $\mathbf{q} = \mathrm{K}$, eventually this results in an almost flat dispersion of $\tilde{\omega}(\mathbf{q})$ in the region between $\Gamma$ and K. Above the Lifshitz transition, $J_1$ further increases and starts to dominate other exchanges. This results in the stabilization of the helical spiral state with $\mathbf{q} = \mathrm{K}$, where $\tilde{\omega}(\mathbf{q})$ takes its minimum. We have thus found that by tuning the substrate-screening of 1T-$TaS_2$, we can enhance the magnetic frustration and make the QSL ground state more favorable.

We note that the extended Hubbard model Eq. (10.1) and the Heisenberg model Eq. (10.4) consider only superexchange couplings stemming from the local repulsion. Apart from that, it is important to note that direct exchange stemming from the overlap of Wannier centers would also appear in the effective Heisenberg model[56, 72]. In particular, strong direct exchange interactions promote a ferromagnetic ground state in 1T-$TaS_2$[56]. To account for this, we now include the direct exchange term $J_{\mathrm{DX}} \sum_{\langle i,j \rangle} \mathbf{S}_i \cdot \mathbf{S}_j$, which results from Hund's exchange interaction and can thus be assumed to be independent of the environmental screening [49]. The existence of a finite direct exchange merely cancels with the superexchange $J_1$. Thus the most frustrated regime appears at larger $J_1$, which for fixed $U$ appears at larger $r_{\mathrm{TF}}$ (Fig.10.3(d)). For smaller $r_{\mathrm{TF}}$, $\tilde{\omega}(\mathbf{q})$ has a minimum along $\Gamma$-K (Fig.10.3(f)), which would approach $\Gamma$ for sufficiently small $r_{\mathrm{TF}}$ or sufficiently large $J_{\mathrm{DX}}$. Thus we find that the existence of finite direct exchange does not influence our main result. We have thus demonstrated the potential of Coulomb engineering to tailor the magnetic ground state and the magnetic frustration. In practice this can be achieved by exposing the monolayer to different substrates, such as $SiO_2$, $SrTiO_3$, or hBN, or by embedding it in a tunable dielectric environment[73, 74], where the effective dielectric constant can be controlled by the thickness of the substrate and by gating the substrate.

### 10.0.4 Discussion

Finally, we comment on several aspects that should be addressed in future work. First, the exact dependence of the parameters $U$ and $r_{\mathrm{TF}}$ on the substrate dielectric constant can be solved with ab initio calculations in specific experimental setups. Second, our analysis focuses on a spin-isotropic model, where potentially anisotropic terms stemming from spin-orbit coupling are not included, which is motivated by recent DFT study[56]. The inclusion of spin-orbit coupling in the low-energy model would give rise to spin-dependent hoppings, which in turn could induce anisotropic exchange in the spin model generating an even richer phase diagram. Third, we used a Hatree-Fock variational wavefunction to capture the bandwidth renormalization induced by $V_{ij}$, while a more accurate approach would be extensions of the Peierls-Feynman-Bogoliubov variational principle [59, 75, 76] taking the full non-local Coulomb and nearest-neighbor exchange interactions into account. Yet for long-range $V_{ij}$ up to 3$^{\mathrm{rd}}$ neighbor, such an approach involves heavy computation that would go beyond the scope of this work. Fourth, we note that a more sophisticated description of the frustration can be performed by exactly solving the many-body system and analyzing the mathematical structure of the associated reduced density matrices[67]. Fifth, our analysis focused on the bilinear spin interactions of the spin-Hamiltonian, yet at intermediate interactions the strength biquadratic and four-spin ring-exchange couplings can have sizable contributions[77]. Finally, although we used the 1T-$TaS_2$ band structure as an example here, the same methodology can be applied to other van der Waals materials such as 1T-$NbSe_2$[78, 61, 79, 80], 1T-$NbS_2$[81, 82], 1T-$TaSe_2$[83], as well as other 1T-dichalcogenide alloys, and potentially twisted graphene multilayers[84, 85], where non-local Coulomb interactions are not negligible. As an outlook, Coulomb engineering can also be performed with spatially structured[39, 38, 42, 48, 47] or anisotropic[86, 87] screening environments giving rise to spatially dependent exchange interactions, that potentially leads to

coexisting ground states of different character within the same, homogeneous layered material.

### 10.0.5 Conclusions

To summarize, we have put forward a strategy to control the magnetic ground state of strongly correlated layered materials, which shows the potential to drive a two-dimensional magnetic material to a tunable frustrated regime by means of Coulomb engineering. Taking as a starting point the Wannier model for the nearly flat band structure in 1T-$TaS_2$, we demonstrated that tunable screening drastically impacts the low-energy spin model of the system. In particular, we showed that the long-range Coulomb interactions result in bandwidth renormalization at the Hatree-Fock level. The renormalized bandwidth, together with the long-range nature of the Wannier model gives rise in the strongly interacting limit to a screening-dependent frustrated Heisenberg model. Finally, we showed how tuning the long-range Coulomb interaction via screening can bring the system to a highly degenerate regime by analyzing the frustration of the spin system. Our proposal demonstrates how substrate-dependent screening, widely present in studies of van der Waals heterostructures, provides a powerful strategy to stabilize unconventional correlated states of matter. Ultimately, our results provide a starting point towards tailoring frustrated quantum magnetism via Coulomb engineering, potentially allowing to stabilize tunable frustrated states in a variety of van der Waals magnets.

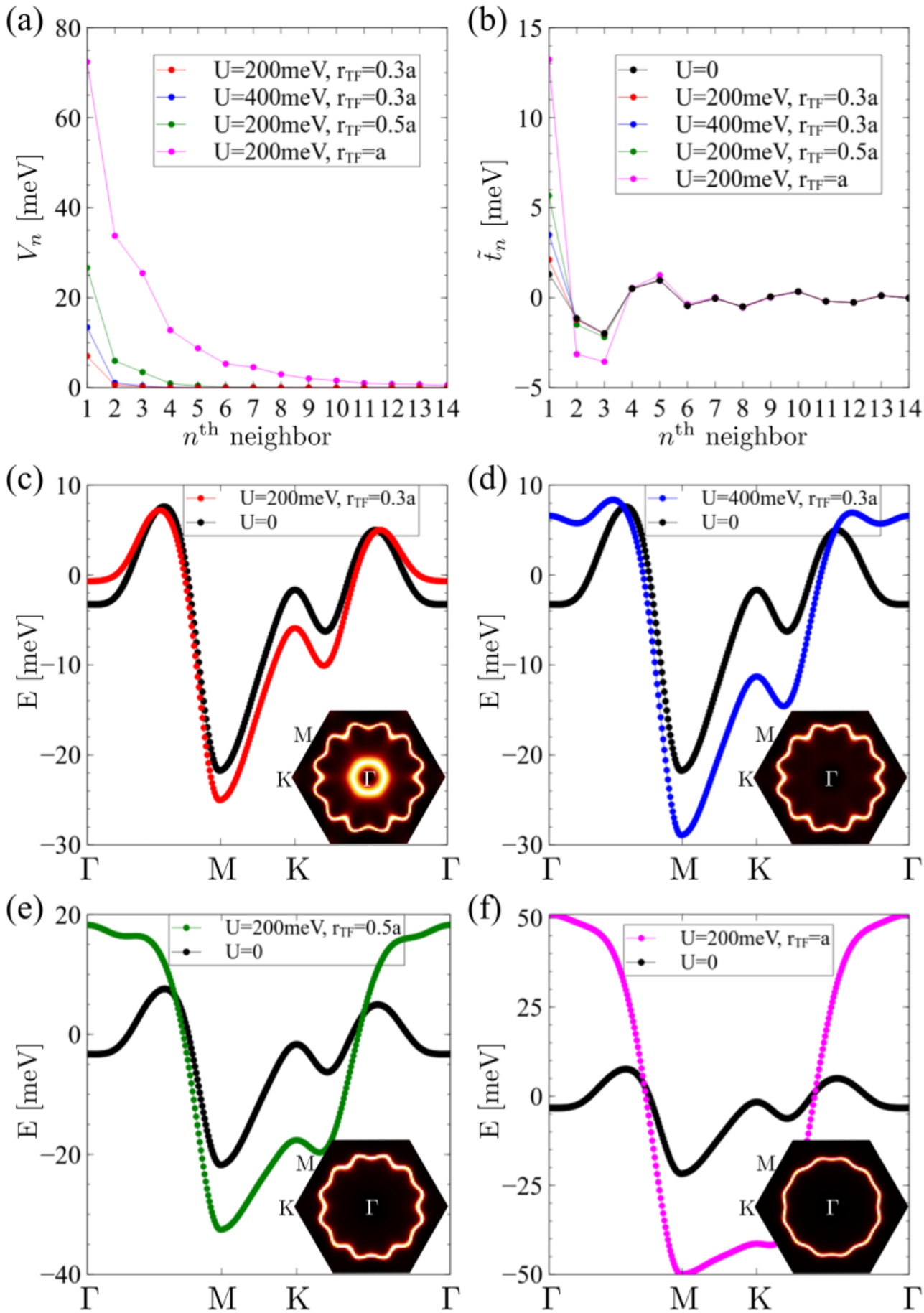


Figure 10.2: (a) Long-range Coulomb interactions $V_n$ and (b) the corresponding renormalized hoppings $\tilde{t}_n$ for different values of parameters $U$ and $r_{\mathrm{TF}}$. (c-f) band structure renormalization for different values of $U$ and $r_{\mathrm{TF}}$ in (a). The color matches with the color used in (a). The insets show the corresponding Fermi surfaces for the renormalized bands.

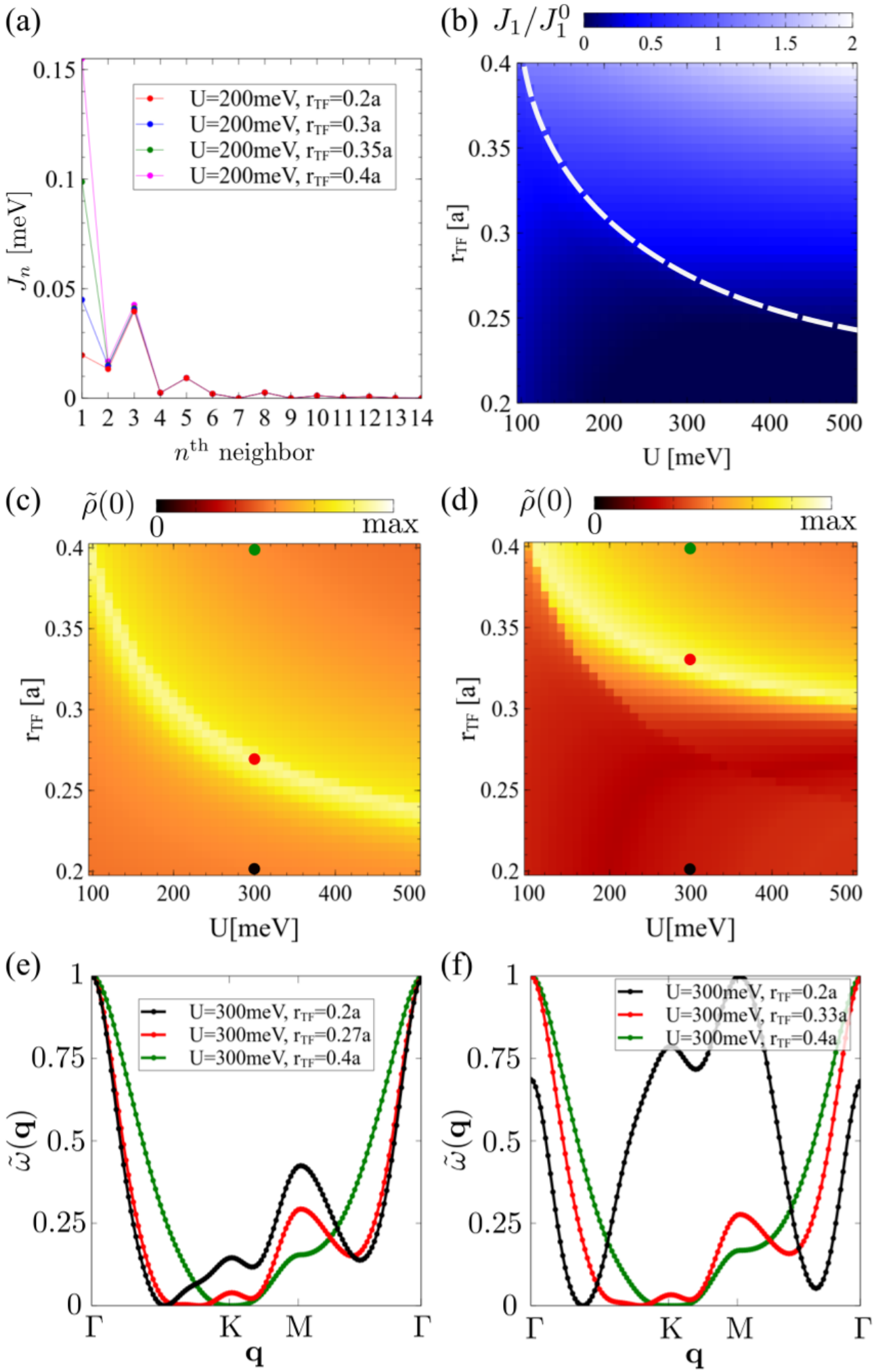


Figure 10.3: (a) Long-range spin superexchange couplings $J_n$ for different values of $U$ and $r_{\mathrm{TF}}$.

# 11 Ab initio theory of magnetism in two-dimensional $1T$-$TaS_2$ by Pasquier, Yazyev

## 11.1 Article

**Abstract**

We investigate, using a first-principles density-functional methodology, the nature of magnetism in monolayer $1T$-phase of tantalum disulfide ($1T$-$TaS_2$). Magnetism in the insulating phase of $TaS_2$ is a longstanding puzzle and has led to a variety of theoretical proposals including notably the realization of a two-dimensional quantum-spin-liquid phase. By means of non-collinear spin calculations, we derive *ab initio* spin Hamiltonians including two-spin bilinear Heisenberg exchange, as well as biquadratic and four-spin ring-exchange couplings. We find that both quadratic and quartic interactions are consistently ferromagnetic, for all the functionals considered. Relativistic calculations predict substantial magnetocrystalline anisotropy. Altogether, our results suggest that this material may realize an easy-plane XXZ quantum ferromagnet with large anisotropy.

**Introduction.**

Materials with flat bands near the Fermi level are an ideal platform to study correlated-electrons phenomena. There has recently been a renewal of interest in flat-band materials because of the discovery of correlated-insulating phases and superconductivty in twisted bilayer graphene near the so-called magic angle [1, 2]. Full characterization and understanding of magnetism in such systems remains a theoretical challenge. In certain transition metal dichalcogenides (TMDs), flat bands emerge near the Fermi level due to the occurence of a commensurate charge-density-wave (CDW) phase with star-of-David (SOD) reconstruction [3, 4, 5, 6]. Among those materials, the most studied one is undoubtedly octahedral tantalum disulfide, which will be the focus of the present work.

The polymorph of tantalum disulfide with distorted octahedral coordination of metal atoms ($1T$-$TaS_2$) is a special member of the family of transition metal dichalcogenides family of materials. Like many other metallic TMDs [7, 8, 9, 10, 11], it undergoes charge-density-wave (CDW) instabilities as the temperature is lowered. At low temperature, it crystallizes in the so-called SOD phase (illustrated in Fig.11.1), with $\sqrt{13}\times\sqrt{13}$ periodicity and 13 Ta atoms per supercell. In this SOD phase, insulating behaviour is observed, which has been commonly attributed to electron localization due to strong correlations [12, 3]. The reason is the following: in the SOD phase, the number of electrons per unit cell is odd, since each Ta atom contributes one conduction $t_{2g}$ electron [13], so conventional band theory would predict a metal. This argument is clear for the monolayer, but there is actually a caveat for the multi-layer and bulk cases: the stacking is not exactly known, so the three-dimensional character could become important and the exact role of interlayer interactions is unclear [14].

A longstanding question regarding $TaS_2$ concerns magnetism or, to be more precise, the apparent absence of it [14], as even the signature of local moment formation is not observed. Several scenarios have been proposed in the past decades. The peculiar properties of $TaS_2$ were part of the inspiring data behind Anderson's theory of resonating valence bonds [15]. Fazekas and Tosatti suggested that the strong spin-orbit coupling (SOC) of Ta atoms could suppress the magnetic moments [16]. A fluctuating Néel order was proposed in Ref. [17] and recently, the idea of a spin liquid in $TaS_2$ has gained momentum after Law and Lee proposed that $TaS_2$ might be a rare realization of a quasi-2D quantum-spin-liquid (QSL) phase [14]. In follow-up work [18], the theory was worked out, yielding the interesting proposal of the possible realization of a spinon Fermi surface in $TaS_2$. This interesting proposal has triggered experimental effort observe these unconventional states, not only in $TaS_2$ but also in similar materials such as $TaSe_2$

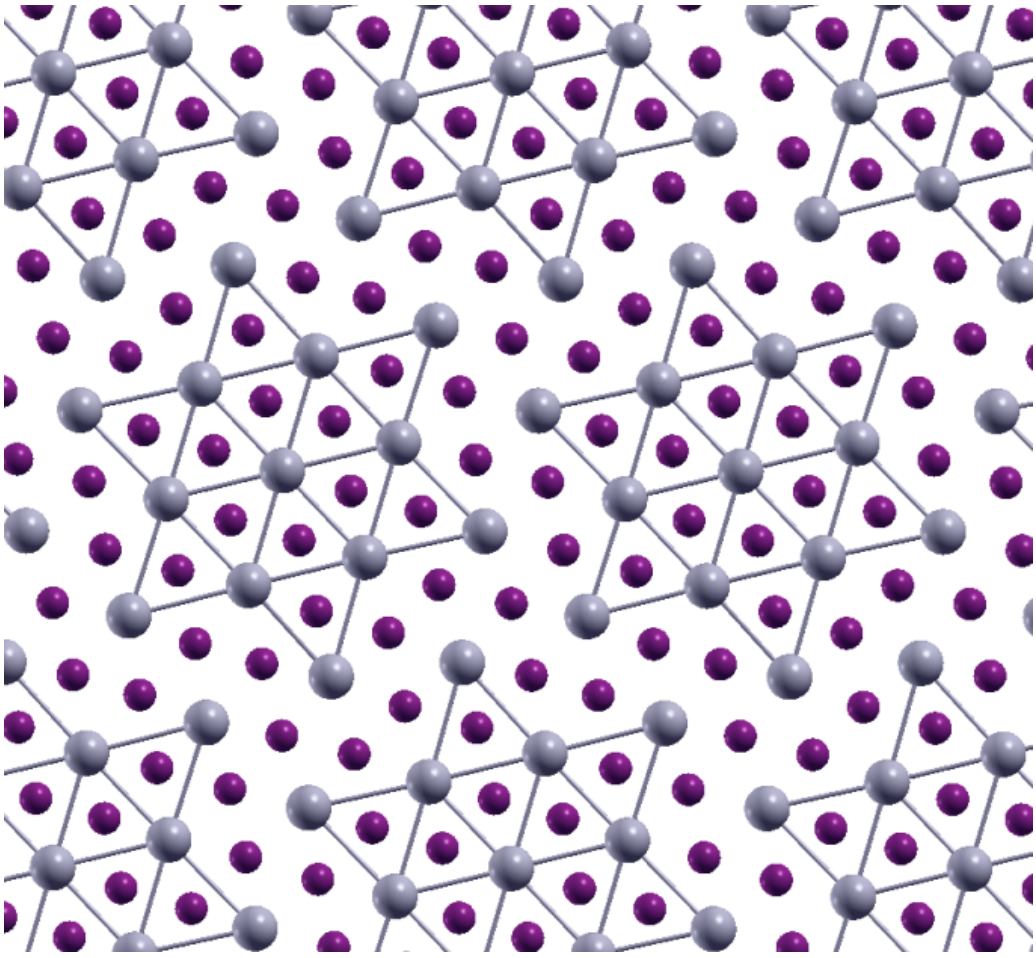

Figure 11.1: Ball-and-stick representation of $TaS_2$ in the commensurate CDW phase. Grey balls represent Ta atoms, while purple balls stand for S atoms. Only the shortest Ta-Ta bonds were drawn in order to facilitate visualization of the star-of-David pattern.

[19, 20]. A key ingredient in the theory is the presence, in the effective spin Hamiltonian, of a sizeable antiferromagnetic four-spin ring-exchange term beyond the conventional Heisenberg model.

The purpose of the present work is to propose a realistic picture of the nature of magnetism in 2D $1T$-$TaS_2$ derived from first principles, using a density-functional-theory (DFT) framework. Using non-collinear density-functional calculations, we aim to provide estimates for the magnetic interaction parameters. In particular, we address whether magnetism in this material is expected to deviate strongly from Heisenberg behavior indeed, as discussed above. While estimating Heisenberg exchange couplings using DFT is a relatively simple (although delicate) and well-established procedure, the calculation of quartic terms is less common and more challenging. The approach that we shall adopt here is that of non-collinear spin calculations (see e.g. Refs. [21, 22]). The method consists in calculating the total energy for a series of angles between the spins on different sites of the superlattice. While two-spin bilinear terms lead to a linear dependency on the angle cosine only, quartic terms lead to a quadratic dependency, allowing one to extract the biquadratic and ring-exchange couplings.

**Model Hamiltonian.**

Following He *et al.* [18] and neglecting anisotropy for the moment, we write $\mathcal{H}$, the low-energy Hamiltonian describing spin physics in the 2D Mott-insulating phase of $1T$-$TaS_2$:

$$\mathcal{H} = \mathcal{H}_{\text{Heis}} + \mathcal{H}_{\text{plaq}} + \mathcal{H}_{\text{b}} \ , \tag{11.1}$$

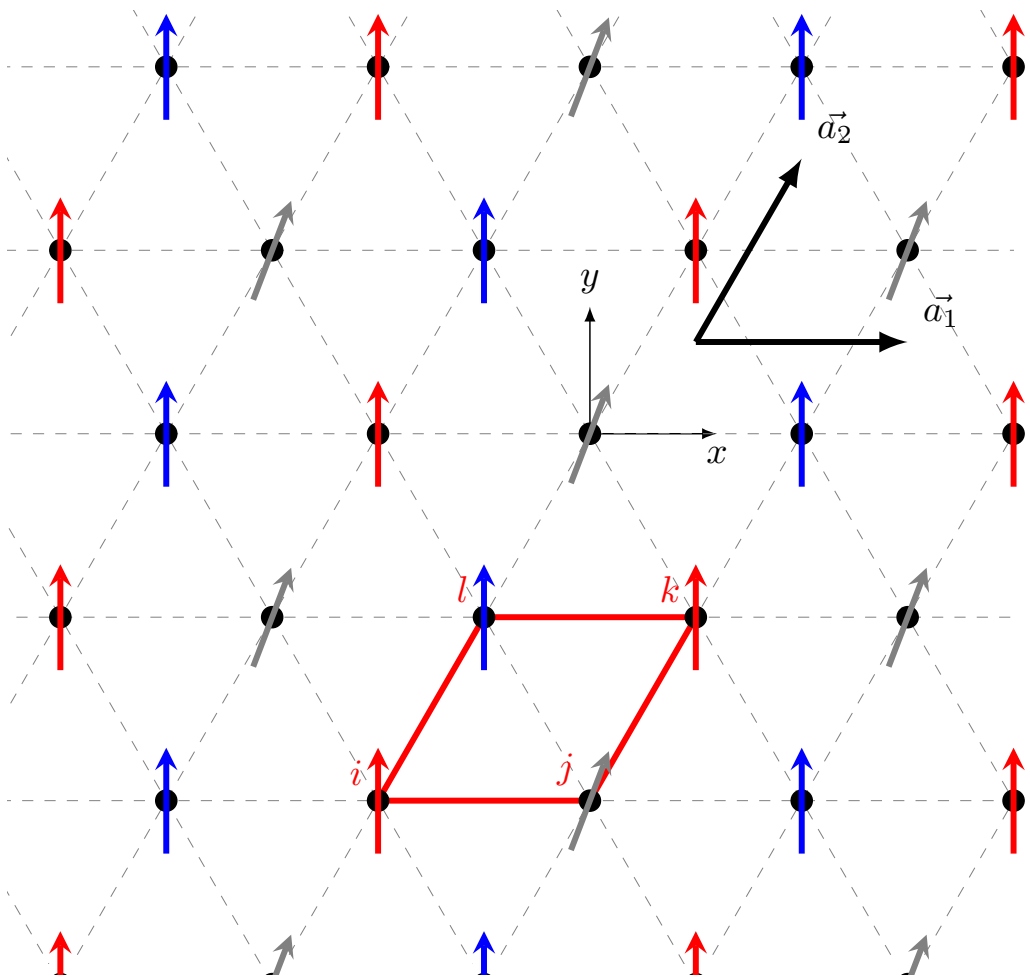


Figure 11.2: Schematic representation of the spin lattice employed for the spin-polarized calculations. Each black dot represents a David star with 39 atoms. The $\sqrt{3}\sqrt{13} \times \sqrt{3}\sqrt{13}$ supercell contains three spin sublattices (one of each color). The red diamond illustrates an example of plaquette on the triangular lattice.

where $\mathcal{H}_{\text{Heis}}$ is the usual Heisenberg Hamiltonian, describing bilinear spin interactions, and $\mathcal{H}_{\text{plaq}}$ describes quartic four-spin plaquette terms. In Eq. 11.1, we also explicitly include biquadratic interaction $\mathcal{H}_b$.

The Heisenberg Hamiltonian is given by

$$\mathcal{H}_{\text{Heis}} = J \sum_{<ij>} \vec{S}_i \cdot \vec{S}_j \ , \tag{11.2}$$

where $< ij >$ denotes nearest-neighbor (NN) sites of the triangular lattice, $J$ is the nearest-neighbor Heisenberg coupling, and $\vec{S}_i$ stands for the $S = 1/2$ spin operator at site $i$. Next-to-nearest-neighbor interactions can be safely neglected, because they are much smaller compared to NN ones. The biquadratic Hamiltonian is given by $\mathcal{H}_b = B \sum_{<ij>} (\vec{S}_i \cdot \vec{S}_j)^2$, and the four-spin Hamiltonian $\mathcal{H}_{\text{plaq}}$ describes higher-order spin-spin interactions and reads:

$$\begin{aligned} \mathcal{H}_{\text{plaq}} = K \sum_{<ijkl>} & (\vec{S}_i \cdot \vec{S}_j)(\vec{S}_k \cdot \vec{S}_l) + (\vec{S}_i \cdot \vec{S}_l)(\vec{S}_j \cdot \vec{S}_k) \\ & - (\vec{S}_i \cdot \vec{S}_k)(\vec{S}_j \cdot \vec{S}_l) \ , \end{aligned} \tag{11.3}$$

where $< ijkl >$ denotes a plaquette (see Fig. 11.2), and $K$ is the ring-exchange coupling.

**Methodology.**

All the first-principles calculations presented in this paper were carried out using the Quantum ESPRESSO package [23] . Lattice parameters and atomic positions were obtained by minimizing forces and stress in the $\sqrt{13} \times \sqrt{13}$ supercell, using the generalized-gradient approximation (GGA) [24, 25]. A grid of $8 \times 8$ k-points was used, with a Marzari-Vanderbilt (MV) [26] smearing of 0.01 Ry. Projector-augmented-wave (PAW) [27] pseudo-potentials from Ref. [28], including explicitly $s$ and $p$ semicore states for Ta atoms, were used to describe interaction between core and valence electrons. Plane-wave cutoffs were set to 60 Ry and 300 Ry for wave functions and charge density, respectively.

Heisenberg interactions were calculated by comparing total energies with different spin configurations in a $\sqrt{3}\sqrt{13} \times \sqrt{3}\sqrt{13}$ supercell ($2\sqrt{13} \times \sqrt{13}$ for the evaluation of the biquadratic term), using both the local-density approximation (LDA) and the GGA, with and without on-site Hubbard $U$ parameter for Ta $5d$ orbitals. For DFT+$U$ calculations, we have set $U = 2.5$ eV. For spin-polarized calculations, we have used a smaller MV smearing of 0.001 Ry, together with a grid of $3 \times 3$ $k$-points in the supercell. These parameters were chosen to ensure convergence of the exchange couplings.

**Structure.**

We begin by optimizing the lattice parameters and atomic positions, in a $\sqrt{13}\times\sqrt{13}$ supercell containing 13 Ta and 26 S atoms. The resulting structure minimizing forces and stress was found to be the well-known SOD phase, illustrated in Fig.11.1. The calculated superlattice parameter was 12.18 Å and the shortest Ta-Ta bonds inside the SOD was 3.18 Å (compared to 3.38 Å in the high-symmetry phase), in line with previous reports [4]. Fig. 11.3 shows the noninteracting DFT bands, exhibiting a half-filled narrow band with a bandwidth of $\sim 30$ meV. In accordance with the existing literature [4, 29, 30], we also find the corresponding electronic structure insulating when spin polarization is allowed. Parameters of an effective Hubbard model can be roughly estimated from the DFT results. Through a Wannier transformation we find a NN hopping of $t \approx 2.5$ meV, and the effective Hubbard interaction can be estimated by examining the correlation gap, which gives $U_{\text{eff}} \approx 125$ meV with DFT and $U_{\text{eff}} \approx 330$ meV with DFT+$U$, meaning the $U_{\text{eff}}/t \sim 132$ ratio sits well in the Mott-Hubbard regime.

**Ab initio parameters: isotropic case.**

Table 1: *Ab initio* Heisenberg, biquadratic, and ring-exchange parameters (in meV), calculated using different methods and approximations.

| Method | $J$ (collinear) | $J$ | $B$ | $K$ | $J'$ | $K'$ |
|---|---|---|---|---|---|---|
| LDA | $-1.11$ | $-1.15$ | $-0.22$ | $-0.02$ | $-1.12$ | $-0.24$ |
| LDA+$U$ | $-1.19$ | $-1.13$ | $-0.07$ | $-0.18$ | $-1.12$ | $-0.24$ |
| GGA | $-1.62$ | $-1.66$ | $-0.73$ | $-0.04$ | $-1.57$ | $-0.77$ |
| GGA+$U$ | $-1.11$ | $-1.11$ | $-0.55$ | $-0.03$ | $-1.04$ | $-0.57$ |

We turn to the investigation of magnetic properties and examine first the collinear case, neglecting SOC and higher-order interactions. This will allow us to compare with the values obtained from non-collinear calculations, in order to check the robustness and consistency of the methodology. We adopt a $\sqrt{3}\sqrt{13} \times \sqrt{3}\sqrt{13}$ supercell (see Fig. 11.2 ), containing three David stars. In the calculations, we can force the solution to converge to different spin configurations by appropriately choosing the initial spin orientation in the self-consistent cycle. The exchange

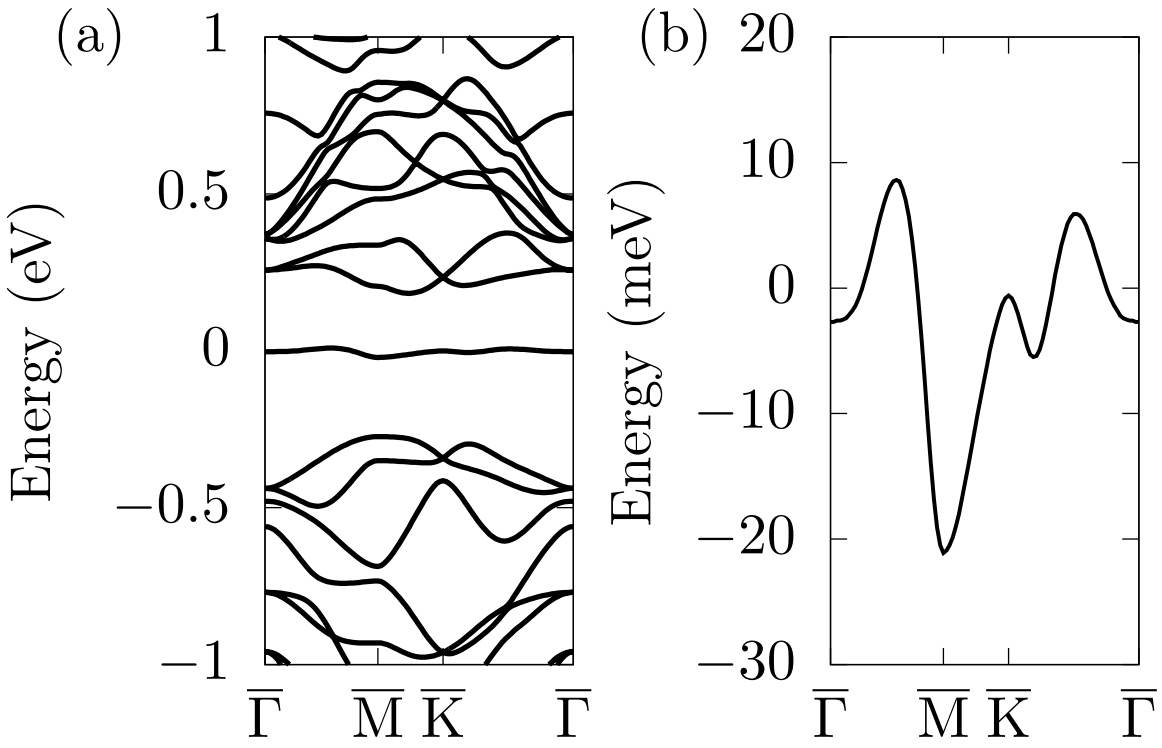


Figure 11.3: (a) DFT non-polarized band dispersion of single-layer $TaS_2$ in the star-of-David phase, along the high-symmetry directions of the mini-Brillouin zone. The Fermi energy is set to zero. (b) Dispersion of the half-filled flat band.

coupling is then given by:

$$J_{\text{collinear}} = \frac{E_{\uparrow\uparrow\uparrow} - E_{\downarrow\uparrow\uparrow}}{12S^2} \ , \tag{11.4}$$

with $S = 1/2$ for $TaS_2$. In Eq. 11.4, $E_{\uparrow\uparrow\uparrow}$ stands for the energy of the configuration with all the spin parallel to each other, while $E_{\downarrow\uparrow\uparrow}$ is the energy of the configuration in which the spin of one of the three stars points antiparallel to the other two. Results for different functionals are shown in Table 1. While the exact values of the parameter are somewhat sensitive to the choice of functional and Hubbard parameter, the qualitative picture remains robust, i.e. coupling is predicted to be ferromagnetic (with a rather small value of $\sim 1$ meV), in line with the cousin materials $NbSe_2$ and $NbS_2$ for which similar values of the parameters were reported [5, 31].

In a one-band Hubbard model, the antiferromagnetic exchange would be $J_{\text{AFM}} = 4t^2/U_{\text{eff}}$, which gives $\approx 0.08$ meV with our estimated DFT+$U$ parameters. This is an order of magnitude smaller than the estimated $J$, indicating that other mechanisms prevail. Multi-band Hubbard models can have ferromagnetic kinetic exchange (see Refs. [32, 33]) due to third-order (e.g. cyclic) processes, which tend to become dominant in the limit of a very flat band. Magic-angle twisted bilayer graphene was recently also proposed to be a ferromagnetic Mott insulator [34], driven by a large intersite direct Coulomb exchange that dominates the kinetic $J_{\text{AFM}}$, the latter being small due to the bands' flatness.

We then turn out attention the non-collinear case. Let us define $\alpha$ as the angle between the spin direction of different stars in the supercell, as shown in Fig. 11.2. We can write the total energy as a function of $\alpha$ in the following way:

$$E(\alpha) = E_0 + E_1 \cos(\alpha) + E_2 \cos^2\alpha \ . \tag{11.5}$$

The two-spin and four-spin exchange can then be extracted from the $E_1$ and $E_2$ parameters as:

$$J = \frac{2E_1 - E_2 + 6BS^4}{12S^2} \ , K = \frac{E_2 - 6BS^4}{6S^4} \ . \tag{11.6}$$

The system of equations 11.6 is underdetermined, so we need to first determine $B$ using a different supercell. This can be done by considering the $2\sqrt{13} \times \sqrt{13}$ supercell for which the quadratic term $E_2^{2\times1}$ depends only on $B$, with $B = E_2^{2\times1}/4S^4$.

Fig. 11.4 shows the calculated total energies in the GGA+$U$ case for a set of selected angles in both $\sqrt{3}\sqrt{13} \times \sqrt{3}\sqrt{13}$ and $2\sqrt{13} \times \sqrt{13}$ supercells. Fig. 11.4 also shows the least-square fits with linear and quadratic functions, showing that the quadratic form allows one to almost perfectly fit the DFT results, whilst the linear fit, which corresponds to a mapping to a simple Heisenberg model, shows deviations. However, it is evident from Fig. 11.4 that the deviations from the Heisenberg model are only modest. This is reflected by the ratio $E_2/E_1 \sim 0.1$ that shows that contributions beyond bilinear two-spin terms are subdominant. Using LDA, the ratio found is even smaller ($E_2/E_1 \sim 0.05$). Although GGA is in general an improvement compared to LDA, the formulation of non-collinear magnetism with gradient corrections is ambiguous, so we would expect the LDA results to be more rigorous. We have also checked that higher-order terms (i.e. higher power in the expansion) are negligible. This is one of the central results of the present work, that first-principles calculations predict no substantial deviations from Heisenberg physics, i.e. from a Hamiltonian truncated to quadratic terms in the spin operators. It was however not obvious *a priori* since it had been hypothesized otherwise in theoretical work, and was therefore worth checking. Our finding can be understood in light of the large $U_{\text{eff}}/t \gg 1$ ratio found, which is different than what was often taken in model Hamiltonians [17, 35, 18].

In Table 1, values for $J$ $B$, and $K$ obtained with different functionals are reported. We also show as a sensitivity analysis $J'$ and $K'$, which were obtained by mapping the DFT results to a model without biquadratic exchange. Bilinear Heisenberg terms obtained from collinear

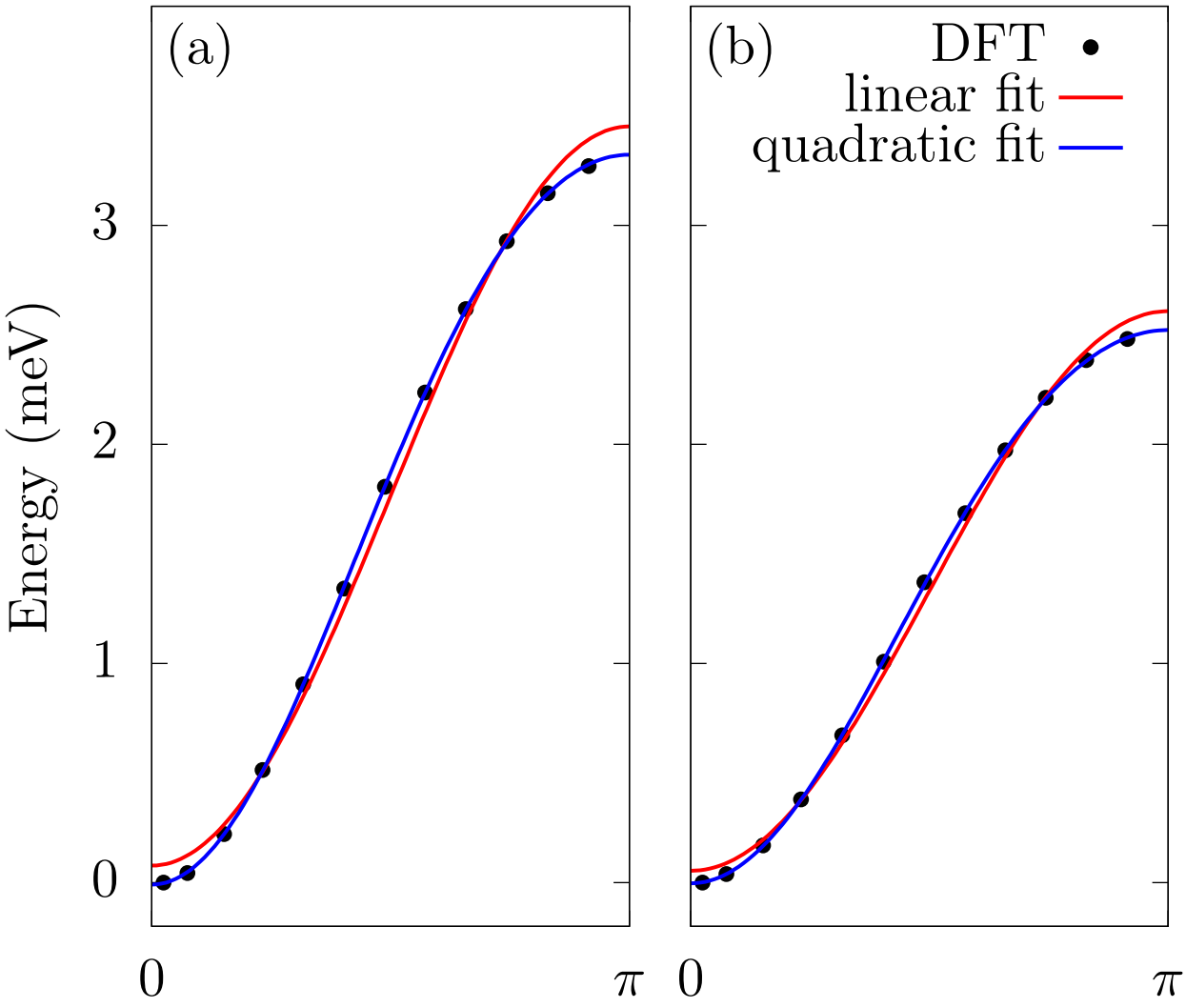


Figure 11.4: Total energy as a function of the angle between spins, calculated with GGA+$U$, in the (a) $\sqrt{3}\sqrt{13} \times \sqrt{3}\sqrt{13}$ and (b) $2\sqrt{13} \times \sqrt{13}$ supercells. Fits wit linear and quadratic functions are also presented.

and non-collinear calculations are consistent, demonstrating the soundness of our methodology. Biquadratic and ring exchange are also found to be ferromagnetic for both LDA and GGA, with or without the Hubbard correction $U$. Table 1 shows the extracted value of $K$ is very sensitive to the choice of model (i.e. with or without biquadratic coupling) and also quite sensitive to the choice of functional.. Nevertheless, the sign of the coupling is robust and indicates a QSL phase is not compatible with the DFT results because unlike other combinations [36], the scenario with both negative $J$ and $K$ is not predicted to host such state.

**Spin anisotropy.**

Our results suggest that a ferromagnetic state might be observed at low temperature in monolayer $TaS_2$. In two-dimensional systems, a finite Curie temperature requires spin anisotropy, driven by the SOC. We calculated, using the LDA(+$U$)+SOC functional, the in-plane and out-of-plane bilinear couplings denoted $J_x$ $J_y$ and $J_z$, with $z$ the out-of-plane direction. We consider here the quadratic Hamiltonian $\mathcal{H} = \sum_{<ij>}(J_x S_i^x S_j^x + J_y S_i^y S_j^y + J_z S_i^z S_j^z)$, neglecting possible anisotropy of the quartic terms. The methodology used is the same as for the evaluation of isotropic $J$ using collinear calculations, except that we consider three different spin orientations. For these non-collinear calculations including the SOC, we have not used the GGA because of possible convergence issues in that case.

Extracted parameters are shown in Table 2. In-plane couplings $J_x$ and $J_y$ are equal, indicating in-plane isotropy. We observe smaller couplings in the relativistic case compared to isotropic $J$, that we understand as due to the reduced magnetic moment induced by the SOC ($\approx 0.82\mu_{\mathrm{B}}$/SOD with LDA+$U$). The total energy difference between the ferromagnetic state with $x$ and $y$ polarization is negligibly small, $\mathcal{E}_x^{\mathrm{FM}} - \mathcal{E}_y^{\mathrm{FM}} < 0.1$ $\mu$eV/SOD, which we interpret as evidence for almost if not perfect isotropy. On the other hand, the out-of-plane coupling $J_z$ is significantly smaller, giving a negative anisotropy term $\gamma = J_z/J_x - 1 = -0.3$ in DFT+$U$. The exchange anistropy $\gamma$ was found to be insufficient to account for the calculated magnetocrystalline anistropy $\mathcal{E}_z^{\mathrm{FM}} - \mathcal{E}_x^{\mathrm{FM}} \approx 0.27$ meV/SOD in LDA+$U$. The simplest way to account for the remaining difference is through an on-site anisotropy term $D\sum_i (S_i^z)^2$ in the Hamiltonian. The corresponding extracted values for $D$ are shown in Table 2.

Our first-principles results thus indicate that, at the DFT(+$U$) level of theory, 2D $TaS_2$ in the SOD phase maps into an easy-plane quantum ferromagnet. For the XXZ model with easy-plane anisotropy, the Mermin-Wagner theorem applies meaning that no finite-temperature second-order phase transition is expected [37]. This is unlike the easy-axis case for which a finite Curie temperature is predicted due to the opening of a gap in the spin-wave dispersion (see e.g. Ref. [38] in the case of $CrI_3$). Classical Monte-Carlo simulations of the easy-axis XXZ model on a two-dimensional lattice show a Berenzinskii-Kosterlitz-Thouless transition with $T_{\mathrm{BKT}} \sim JS^2$ [39]. Results for the quantum model were less conclusive, since large fluctuation in the extreme quantum limit ($S = 1/2$) may reduce the effective anisotropy and exchange coupling magnitude [40]. We have found that the four-spin terms are also predicted to be ferromagnetic (and rather small), and in that case the expected effect of the ring-exchange term is to merely renormalize the spin wave dispersion [41].

Table 2: *Ab initio* relativistic Heisenberg and on-site anisotropy parameters (in meV), and the corresponding exchange anisotropy $\gamma$.

| Method | $J_x$ | $J_y$ | $J_z$ | $D$ | $\gamma$ |
|---|---|---|---|---|---|
| LDA+SOC | −0.94 | −0.94 | −0.75 | 0.19 | −0.20 |
| LDA+$U$+SOC | −0.78 | −0.78 | −0.54 | 0.37 | −0.30 |

**Discussion.**

Magnetism in the SOD phase of $TaS_2$ is a longstanding question, which as led to several interesting proposals. Theoretical understanding has been so far hindered by two factors. First, experimental work probing magnetism was only done on layered form of $TaS_2$. Uncertainty on the exact stacking remains and the approximation of a quasi-2D material is questionable. Secondly, an *ab initio* model Hamiltonian for spins was not known, and parameters were mostly derived from simplified one-band Hubbard models. Our results differ significantly from these models, as we have found opposite sign for both two-spin and four-spin couplings (i.e we have found both terms to be ferromagnetic). In theory, our results are derived from first principles so they should be more robust compared to a Hubbard model studied perturbatively to derive a spin Hamiltonian. However, in the presence of strong correlations, we cannot exlude that the approximations of the DFT+$U$ method break down and that it fails qualitatively, even though it usually performs well for magnetism in various correlated systems.

The present work suggests that single-layer $TaS_2$ could realize a 2D easy-plane ferromagnet. This could help interpret future experiments, not only on $TaS_2$ but also on similar materials such as $TaSe_2$, although the generalizability of the present results to other materials remains to be established. If confirmed, that would also have bearing on the understanding of bulk $TaS_2$, as it would mean that a quasi-2D spin-liquid cannot explain the absence of magnetic ordering observed. There is growing evidence that interlayer interactions are more important than initially thought and that this material might actually be quasi-one-dimensional rather than quasi-2D [4, 42, 43]. The origin of the observed insulating behaviour is still unclear and might therefore be explained from a different perspective than a Mott insulator [44]. Recently, it was proposed that bulk $TaS_2$ could actually be a simple band insulator, with gap formation driven by the stacking pattern [45, 46].

## 11.2 My Discussion

# Part X
# Other Explanations of Typical Theory

## 12 Theoretical Modeling of the Non-equilibrium Amorphous State in 1T-$TaS_2$ by Vodeb, Kabanov, Gerasimenko, Vaskivskyi, Ravnik, Mihailovic

**Abstract**

1T-$TaS_2$ is known for it's remarkably complex phase diagram and it's unique long-lived metastable hidden (H) state. Recently, a novel metastable state has been discovered using higher fluences for photoexcitation than in the case of the H state. The state has been dubbed as amorphous (A) due to it's similarity to glass. Expanding on the work of Brazovskii and Karpov, we show that the A state can be successfully modeled with classical interacting polarons on a two dimensional hexagonal lattice. We have found that the polaron configuration of the A state corresponds to a frustrated screened Coulomb system, where there is no order-disorder phase transition.

### 12.1 Introduction

The crystal of 1T-$TaS_2$ (TAS) exhibits a layered structure of S-Ta-S layers, where each of the atomic layers is arranged in a hexagonal lattice. Each Ta atom is surrounded by an octahedral arrangement of S atoms [1]. Due to this highly anisotropic character of the crystal we may neglect any kind of three dimensional behavior and only focus on a single layer of TAS.

The interplay of Coulomb interaction [16], spin-orbit coupling [3] and electron-phonon interaction [4] results in various competing phases of TAS, which emerge as external parameters such as temperature and pressure are varied. When subjected to high pressure TAS becomes superconducting [13]. At ambient pressure and high enough temperatures TAS is a homogeneous metal and upon lowering the temperature a series of charge density wave (CDW) transitions take place [6] as follows. At 540 K an incommensurate CDW is formed, where the CDW modulation is incommensurate with underlying atomic lattice. When the temperature is lowered even further, at 350 K, a nearly-commensurate CDW is formed, where a hexagonal structure of domains with a commensurate CDW is separated by domain walls, where the CDW is incommensurate with the atomic lattice. The phase below 190 $\sim$ 220 K has been interpreted as the commensurate CDW phase due to the perfect commensurability of the CDW with the underlying atomic lattice all throughout the crystal. The C phase also exhibits spin liquid like behavior [7]. Fig. 18.1 shows a schematic of the microscopic picture of the C phase. In this paper we adopt the interpretation of the C phase as a system of classical interacting polarons first proposed by Brazovskii [8]. Within this interpretation the ratio of the number of polarons and the number of atoms in the system or the *polaron concentration* is exactly 1/13. If polarons repel each other then they will arrange themselves in a hexagonal polaronic lattice, because this is the minimal energy configuration of such a system. The work of Stojchevska et al. [14] has shown that the C phase can be photoexcited via an ultra-short laser pulse into a long-lived metastable state. Due to the fact that the excited phase cannot be found on the equilibrium phase diagram of TAS it has been dubbed as the hidden (H) state. Karpov et al. [32] have subsequently shown by performing Monte Carlo simulations of a system of classical repulsive polarons that if the polaron concentration is perturbed slightly from 1/13, the H state can be obtained within the scope of this interpretation. The classical Monte Carlo calculations neglect the quantum aspects of polarons and instead focus on the large scale configurational ordering

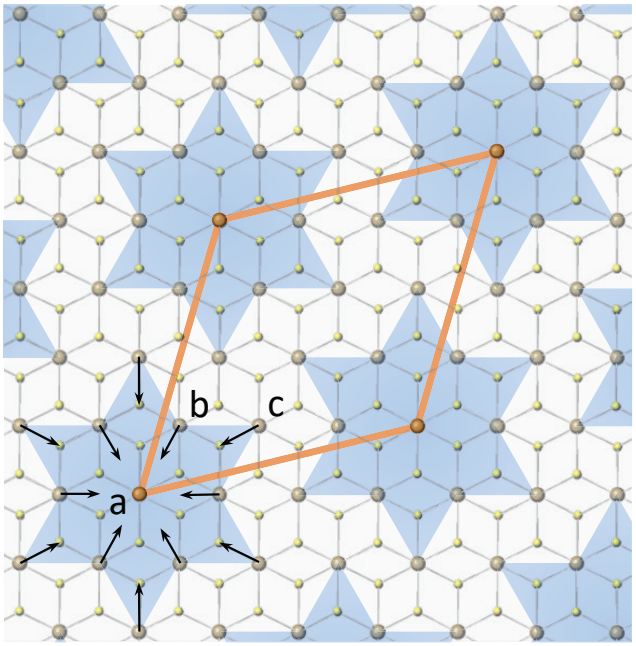


Figure 12.1: **A schematic of the microscopic picture in the C phase:** A new unit cell is formed, where 12 Ta atoms are pulled towards the 13th in the center (marked with the letter a) in the shape of a star of David. The two different types of atoms with respect to their deviation from a perfect atomic lattice are marked with the letters b and c. The electron wave function also becomes localized on top of the central Ta atom. We interpret this unit cell as the polaron quasiparticle. The orange colored rhombus shows the unit cell of the hexagonal polaron lattice

of polarons. Quantum mechanical methods cannot do so due to their computational intensity. Methods used for analyzing the quantum mechanical aspects of polarons in the ground state include exact diagonalization [11], variational exact diagonalization [12], quantum Monte Carlo [13], variational methods [14] and DMRG [15]. Other methods deal with the polaron dynamics and include Ehrenfest dynamics [16, 17], time-dependent density functional theory (TDDFT) [18], the multiconfiguration time-dependent Hartree method [19], its multilayer formulation [20] and the hierachical equations of motion [21, 22]. TDDFT has been proven particularly successful in studying phenomena involved in polaron formation and dynamics, such as transient vibration energy redistribution and spectroscopy [23] and defects in nanomaterials [24, 25].

A recent paper by Gerasimenko et al. [21] has reported the discovery of a novel long-lived metastable state, where polarons are arranged in a disordered pattern. It is formed via photoexcitation with an ultrafast laser pulse, which confirms the state's non-equilibrium nature. It exhibits remarkable stability (at least 10 hours), which excludes any transient nature typically present in excited states. Moreover, even though the polaronic pattern suggests localization of charge, the system exhibits metallic behavior. Therefore the nature of this state is highly non-trivial and physically interesting. The main purpose of this paper is to show that the configurational aspect of the localized charges of this amorphous (A) state can also be understood within the scope of the classical polaron picture and to try to elucidate the reason for the disordered pattern.

## 12.2 The Model

The final A state can be modeled in the classical polaron picture of correlated electrons on a hexagonal lattice. TAS is known for the strong presence of the electron-phonon interaction [9]. Therefore, we assume that equation 4.15 in chapter 4.2 in [28], where small interacting polarons form in a system of electrons and phonons, is applicable. We neglect polaron hopping

and spin, as we are only interested in the configurational aspect of the repulsive interaction between polarons. The Hamiltonian has the form

$$\mathcal{H} = \sum_{i,j} V(i,j)(n_i - \nu)(n_j - \nu), \tag{12.1}$$

where $V(i,j)$ is the potential energy of interacting polarons, $n_i$ is 1 if the site occupied by a polaron and 0 otherwise, and $\nu$ is the average polaron concentration. $\nu$ is defined as a ratio of the number of polarons in the system, which is fixed throughout the simulation, and the number of lattice sites in the finite lattice used in simulations. The interaction between polarons has two contributions. The attraction due to the overlap of phonon clouds and long range Coulomb repulsion. The first part may be short or long-range depending on the type of phonons involved in polaron formation. If we assume that only polar phonons are responsible for polaron formation, the resulting interaction will be reduced to

$$V(i,j) = \frac{e^2}{\epsilon_0 |\mathbf{r}_i - \mathbf{r}_j|} \tag{12.2}$$

where $\epsilon_0$ is the static dielectric constant of the material. Both the lattice and electrons contribute to it, however the lattice contribution is indeed dominant. The interaction with acoustic phonons as well as with nonpolar optical phonons leads to the short range attraction of polarons, but here we neglect the short range contribution to the potential. Since the system has finite conductivity the long range Coulomb repulsion is screened. Therefore, we approximate it by the Yukawa potential

$$V(i,j) = \frac{e^2}{\epsilon_0 |\mathbf{r}_i - \mathbf{r}_j|} exp(-|\mathbf{r}_i - \mathbf{r}_j|/r_s), \tag{12.3}$$

where $r_s$ is the screening radius.

## 12.3 Monte Carlo Method

Monte Carlo (MC) simulations of simulated annealing were performed using a standard Metropolis algorithm. A proposed successive state in the Markov chain consists of one polaron moving in a random direction and a finite distance away from its current position. Simulations were performed on a hexagonal lattice with the lattice constant $a$ and of the size of $84 \times 78$ sites, where periodic boundary conditions were imposed. The number of polarons in the system is constant throughout the simulation procedure. In order to simulate annealing, the system would always start off at a temperature of $10^{-2}$ measured in units of $e^2/\epsilon_0 a k_B$ , which corresponds to the high temperature phase of the model for the commensurate (C) state. Afterwards, the system is cooled slowly down to a temperature of $10^{-3}$ with a temperature step of $10^{-5}$. There were $14 \times 10^6$ MC steps performed at each temperature step. One of the main reasons for introducing the Yukawa form of the polaron interaction is in the substantial growth of the MC relaxation time with the growth of the range of interaction. The screening length $r_s$ has been chosen as $4.5a$ and the interaction has been manually set to 0 at distances greater than $24a$. At this value of $r_s$ the interaction range exceeds the radius of one polaron in C state ($\sqrt{13}a \approx 3.61a$). Furthermore, it is numerically feasible due to the manageable relaxation times, which follow from it. The code is available for reproducibility at [29].

## 12.4 Tiling

Tiling of a polaron configuration can serve as a good visual illustration of the effective charge density topography present in the system as well as all the different nearest neighbor

distances present between polarons. The way both tilings are achieved is with the help of the so called Voronoi diagram. When a set of coordinates on a plane is given, which are the polaron coordinates, the plane can be partitioned into regions. Each coordinate is assigned a region of points in the plane, which are closer to it than to any other coordinate. This is done for the experimental amorphous state and the theoretical model for it in Fig. 18.2. Every Voronoi cell has one polaron charge associated with it and if we divide the charge by the cell's area, we obtain the charge density of the cell. Since the charge of a polaron is fixed (at least in simulations), one can get a clearer perspective on the charge density present in the system just based on the coloring of all the different Voronoi cells. After the Voronoi diagram is complete, one can construct a different set of tiling polygons from the Voronoi diagram's polygons. Each new polygon has 4 vertices and represents a distance between two neighboring coordinates. The first two vertices are the two neighboring coordinates from which the distance that the polygon represents is calculated. The other two vertices are the two points, which are part of the Voronoi polygons containing the two coordinates and are also the closest to both coordinates. This can be done for any two coordinates, which share two vertices of their Voronoi polygons. Because the distances between polarons in the model are discrete due to the perfect underlying hexagonal lattice, one can specify a color for each tiling polygon based on the distance between the two coordinates it connects. The coloring scheme for the experimental polaron coordinates is extended in the sense that the color spectrum in between any two colors represents the spectrum of all the possible distances between the two discrete distances.

## 12.5 Results

Within the scope of the particular lattice gas model used in our simulations, the C phase can be understood as the ground state of a system of polarons, where the polaron concentration is exactly 1/13. Experimental measurements of the polaron density in the STM images of the C and amorphous (A) states indicate that the polaron density in A state is about 1.23 times higher than in C state [21]. Simulations were therefore performed at the corresponding polaron concentration and the result shows similarity with experimental data. Fig. 18.2 shows the comparison between experiment and theory. The takeaway from Fig. 18.2 is the fact that both the theoretical and experimental polaron pattern exhibit disorder. A clearer comparison may be achieved via the polaron pair correlation function $g^{(2)}_{pol}(r) = \langle n(r)n(0)\rangle$. Fig. 18.3 shows the comparison between the experimental data and theoretical modeling of A state within the scope of $g^{(2)}_{pol}(r)$. The behavior of the theoretical model's polaron pair correlation function is qualitatively very similar to the experimental behavior. Consider first Fig. 18.3a. The green dashed lines mark all the possible lattice constants of polaronic lattices which are commensurate with the hexagonal atomic lattice. From the orange curve it is obvious that the simulation exhibits peaks in these cases. In experiment however, there is a discrepancy in the position of the peaks from the theoretically expected green dashed lines. This can be explained if the underlying atomic lattice has moved slightly in order to accommodate the repulsion between polarons. The qualitative discrepancy in peak intensity is mostly present at the 1/7 polaron concentration peak, which is much more pronounced than in the experiment. Both of these discrepancies may vanish by incorporating also the movement of the atomic lattice in the model. This is the goal of future studies. In Fig. 18.3b we can also see a discrepancy between the experimental and simulated peak positions. This is expected already from Fig. 18.3a, because of the homogeneity of the sample. The behavior at close distances is reflected in long range behavior. Ergo, if there was a discrepancy in the peak positions at close range, it will also be present at long range. The main point of Fig. 18.3b is to show that despite the peak position discrepancies, both the experimental as well as the theoretical curve tend to the value 1 at large distances. This is a very important feature, as it shows that both exhibit no long range

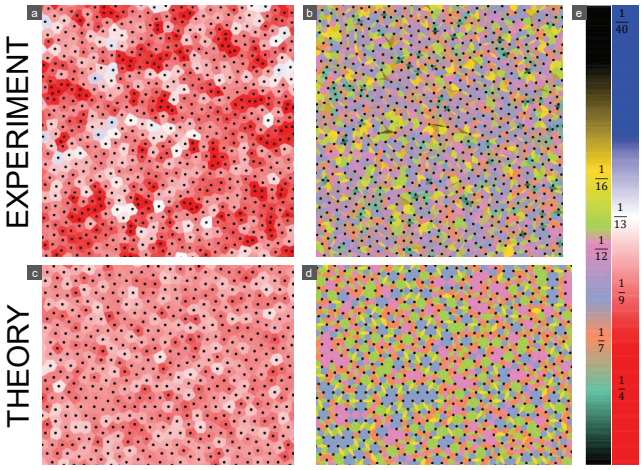


Figure 12.2: **Comparison between the two types of tiling of experimental and theoretical A states: a**, Voronoi diagram of the experimental STM image of A state. The color in each cell represents the area of the cell according to the right legend in e. **b**, Nearest neighbor distance tiling of the experimental STM image of A state. The color of each tile represents the distance between the two polarons it connects according to the left legend in e. **c**, Voronoi diagram of the model for A state. **d**, Nearest neighbor distance tiling of the model for A state. **e**, Color legend for the tiling images to its left. Each color represents a different area of a Voronoi cell (right legend) and a different distance between nearest neighbors (left legend). Colors labeled with different polaron concentrations for the right legend represent areas of Voronoi cells of a Voronoi diagram, which is constructed from an overlying polaronic hexagonal lattice structure, which emerges at the corresponding concentration. For the legend to the left, colors represent different distances between nearest neighbors in the overlying polaronic hexagonal lattice structure at the corresponding polaron concentration

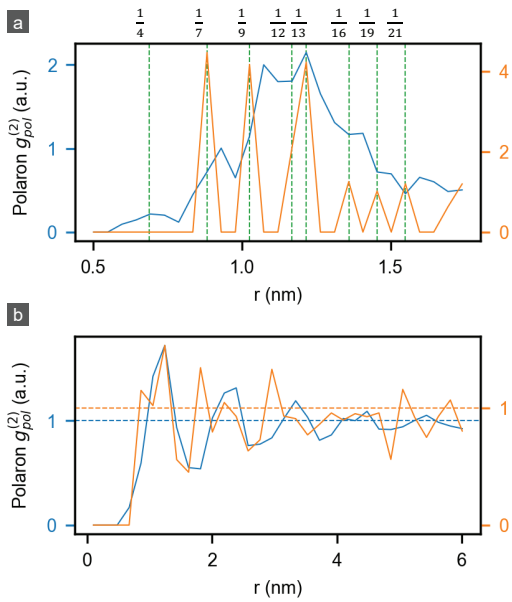


Figure 12.3: **Comparison between the experimental (blue) and theoretical (orange) polaron pair correlation function $g^{(2)}_{pol}(r)$: a**, Comparison between experiment and theory, plotted only at small distances, where both are referenced to the atomic lattice constant. The green lines represent nearest neighbor distances of different polaron lattices, which emerge at different polaron concentrations of the system (from left to right: 1/4, 1/7, 1/9, 1/12, 1/13, 1/16, 1/19, 1/21). The similarity between the theoretical model and experimental data can be observed from the qualitative matching of the polaron pair correlation peaks. The experimental peaks are almost all slightly shifted towards larger distances. However, the peaks of the theoretical model appear exactly at the expected positons and match the peaks of the experimental data. The quantitative comparison fails mostly at the 1/7 polaron concentration. **b**, Comparison between experiment and theory, plotted also at larger distances, where both are referenced to the atomic lattice constant. Both polaron pair correlations tend to the value 1 at large distances, which indicates a lack of ordering at large distances. The difference between them is in the oscillations around the value 1, where the theoretical model oscillates a lot more, which is due to the perfect underlying hexagonal lattice on which the polarons reside

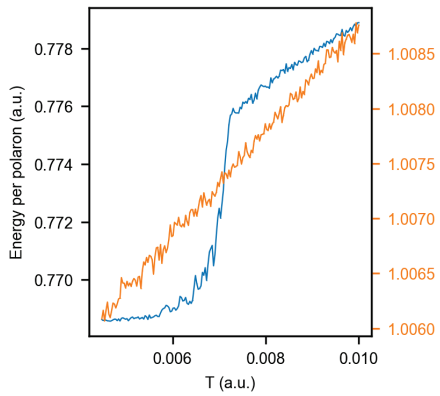


Figure 12.4: **Energy of the system per polaron versus temperature for the model for C state (Blue) and A state (Orange):** The plot clearly shows the difference between the two model systems of polarons. A first order phase transition from disorder to order occurs in the case of the model for C state and no such phenomenon is present in the case of the model for A state. Energy is measured in units of $e^2/\epsilon_0 a k_B$ and the error bars are smaller than the size of a single point

correlations. Within the scope of the theoretical model, the difference between C and A state can be understood by taking a look at a typical annealing process. Fig. 18.4 shows the energy of the system per polaron dependence on temperature for models of both states measured in units of $e^2/\epsilon_0 a k_B$. Fig. 18.5 shows typical configurations of both models at high and low temperatures. It points out a clear difference in the two low temperature phases of the model for C state (Fig. 18.5a,b) and A state (Fig. 18.5c,d). The high temperature configuration in both cases (Fig. 18.5b,d) is disordered, yet the C state shows a clear strong tendency towards crystallization at low temperatures evident by the dominance of the green color (Fig. 18.5a). The A state (Fig. 18.5c) is clearly still disordered even at low temperatures. In the case of the model for C state, there is a clear order-disorder phase transition, which is of the first order. Meanwhile, there is no phase transition present in the case of the model for A state. In the model for A state in Fig. 18.5c some aggregation of the same types of different nearest neighbor distances can be observed at low simulated temperatures, but no global lattice ever emerges like in the model for C state.

## 12.6 Discussion

We have clearly shown that the A state can be modeled successfully within the scope of the classical polaron picture. This result supports the model for the low temperature C state first proposed by Brazovskii [8]. This model was also successfully used by Karpov et al. [32] for simulating the H state. Our results imply that the A state's disordered characteristics are a consequence of commensurability frustration. The polaron hexagonal lattice at this polaron concentration cannot form due to the incommensurability with the underlying atomic lattice. One might argue that phase separation, where multiple commensurate lattices emerge in the system with domain walls in between them, might be energetically more favorable that the disordered phase seen in Fig. 18.5c. We have shown that this does not happen. Similar behavior has been observed before on a square lattice and it was also attributed to frustration with the underlying lattice [30, 31]. Minimization of the overlying hexagonal lattice energy on an underlying hexagonal lattice was done by Pokrovsky et al. [32]. They have shown that multiple minima very close in energy exist at integer polaron concentrations between 1/12 and 1/9 as well as between other concentrations. However, it is still not clear whether phase separation would result in further minimization of the energy of the system and whether unscreened interactions

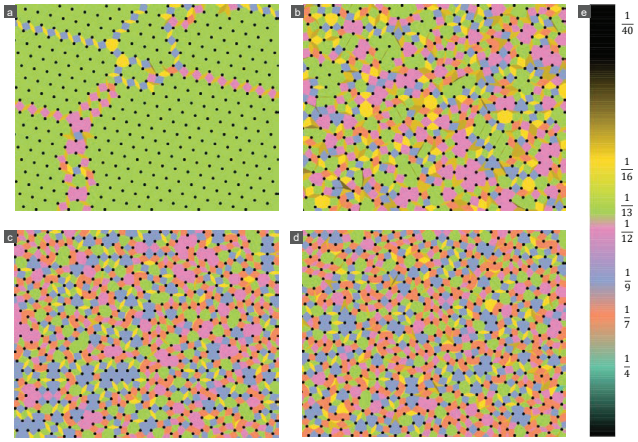


Figure 12.5: **An examination of the difference between the theoretical models for C and A states: a**, **b**, Tiling of typical low and high temperature polaron configurations, respectively, in the model for C state. Clearly, the high temperature phase is highly disordered, while only one nearest neighbor distance prevails globally at low temperatures. There are a few line defects present still, but this is only due to finite size effects. **c**, **d**, Tiling of typical low and high temperature polaron configurations, respectively, in the model for A state. The high temperature phase is again clearly disordered. The low temperature phase, unlike in the case of the model for C state is still highly disordered. There are some nucleation centers of different nearest neighbor distances, which are not present at high temperatures, but it is obvious that the emergence of a global polaron lattice is prohibited. This is due to the commensurability frustration mentioned in the main text. **e**, Color legend for the nearest neighbor distances tiling images to its left. Each color represents a different distance between nearest neighbors, which corresponds to a listed polaron concentration in the legend

would change the system's behavior. Therefore, the observed glassy behavior may merely be a consequence of the limitations of the Monte Carlo algorithm, or perhaps the glassy behavior is an actual thermodynamic property of the system at this polaron concentration.

## 12.7 Conclusion

In this paper the newly discovered meta-stable amorphous state in 1T-$TaS_2$ has been successfully modeled within the scope of a classical gas of polarons. The disordered structure has been found to be a consequence of frustration in the system. The hexagonal lattice of the polaron gas which seeks to emerge due to the repulsive interaction between them in not commensurate with the hexagonal underlying atomic lattice. According to our Monte Carlo simulations the result of this frustration is a remarkable stability of a disordered polaronic pattern, where there is no evidence of a first order crystallization phase transition. Our finding represent a new and important step in understanding photoexcitation in the complex system of 1T-$TaS_2$. The external laser pulse causes the system to form a greater number of polarons than in the thermodynamically stable commensurate state. Afterwards, polarons order in compliance with the screened interaction between them and the atomic lattice underneath into a stable disordered pattern.

# 13 Band insulator to Mott insulator transition in $1T-TaS_2$ (2020)

Y. D. Wang [1], W. L. Yao [1], Z. M. Xin [1], T. T. Han [1], Z. G. Wang [1], L. Chen® [1], C. Cai [1], Yuan Li [1,2] & Y. Zhang [1,2⊗]

(I added this article because GPT said that it can teach me about what is the band insulator? give some properties and formulas exactly about it)

**Abstract**

$1T-TaS_2$ undergoes successive phase transitions upon cooling and eventually enters an insulating state of mysterious origin. Some consider this state to be a band insulator with interlayer stacking order, yet others attribute it to Mott physics that support a quantum spin liquid state. Here, we determine the electronic and structural properties of $1T-TaS_2$ using angle-resolved photoemission spectroscopy and X-Ray diffraction. At low temperatures, the $2\pi/2c$-periodic band dispersion, along with half-integer-indexed diffraction peaks along the $c$ axis, unambiguously indicates that the ground state of $1T-TaS_2$ is a band insulator with interlayer dimerization. Upon heating, however, the system undergoes a transition into a Mott insulating state, which only exists in a narrow temperature window. Our results refute the idea of searching for quantum magnetism in $1T-TaS_2$ only at low temperatures, and highlight the competition between on-site Coulomb repulsion and interlayer hopping as a crucial aspect for understanding the material's electronic properties.

Transition-metal di-chalcogenides are layered quasi-twodimensional materials that not only show prominent potentials for making ultra-thin and flexible devices, but also exhibit rich electronic phases with unique properties [1–3]. 1T-$TaS_2$ is one prominent example. The crystal structure of $1T-TaS_2$ consists of S-Ta-S sandwiches, which in turn stack through van der Waals interactions. It is structurally undistorted and electronically metallic at high temperatures. With decreasing temperature, it undergoes successive first-order transitions, resulting in the formation of various charge density waves (CDWs) with increasing degree of commensurability [4–7]. As shown in Fig. 1a, with cooling, $1T-TaS_2$ sequentially enters an incommensurate CDW (I-CCDW) phase below 550 K, a nearly commensurate CDW (NC-CDW) phase below 350 K, and finally a commensurate CDW (C-CDW) phase below 180 K. Prominent hysteretic behavior can be observed when comparing the cooling and heating resistivities data. Upon heating, $1T-TaS_2$ enters triclinic CDW (T-CDW) phase at 220 K, and then the NC-CDW phase at 280 K. The space modulations of different CDW phases are illustrated in the inset of Fig. 1a. Every adjacent 13 Taatoms accumulate together, which is called star-of-David (SD) cluster [4–7]. Within one hexagonal SD, 12 Ta-atoms pair and form 6 occupied bands, leaving the center Ta atom localized and unpaired alone. As a result, the insulating ground state of $1T$ -$TaS_2$ has been proposed to be a Mott insulator [8–13]. In the C-CDW phase, the SD clusters cover entire lattice forming commensurate $p(\sqrt{13}\times\sqrt{13})R13.9^\circ$ phase. The localized electrons with $S=1/2$ spin arrange on a triangular lattice, making this system a promising candidate material for realizing quantum spin liquid [14–17].

Distinct from the possible Mott physics that occurs within one $TaS_2$ layer, interlayer coupling has recently been emphasized as a crucial aspect to understand the insulating property of $1T$ -$TaS_2$[18–20]. Through an interlayer Peierls CDW transition, interlayer staking order forms in the C-CDW phase. First, every two adjacent $TaS_2$ layers accumulate, forming dimerized bilayer structure. The dimerized $TaS_2$ bilayers then stack onto each other forming different types of

[1] International Center for Quantum Materials, School of Physics, Peking University, 100871 Beijing, China.
[2] Collaborative Innovation Center of Quantum Matter, 100871 Beijing, China. email: yzhang85@pku.edu.cn

staking order with different in-plane sliding configurations [19,20]. Recent scanning tunneling microscopy and transport measurements show possible existence of the stacking order in $1T-TaS_2$[21,22]. Band calculations show that without considering the strong electronic correlation the interlayer staking order itself can open a band gap at the Fermi energy ($E_F$), yielding an insulating property of $1T-TaS_2$. Under this scenario, the ground state of $1T-TaS_2$ is a band insulator rather than a Mott insulator.

The low-energy electronic structure of $1T-TaS_2$ consists of one half-filled nonbonding Ta $5d$ band. In the IC-CDW phase, angleresolved photoemission spectroscopy (ARPES) data shows that one Ta $5d$ band disperses crossing $E_F$, forming six oval-like circles around the Brillouin zone boundaries (M) (Fig. 1b). This is well consistent with the first-principle band calculations [11]. When entering the C-CDW phase, the CDW potential folds the Brillouin zone. The Fermi surface reconstructs into multiple disconnected spots, following the $p(\sqrt{13}\times\sqrt{13})R13.9°$ periodicity. Band folding and band gap opening split the Ta $5d$ band into a manifold of narrow subbands. One flat band emerges at ˜200 meV below $E_F$ (Fig. 1c). Under the Mott scenario, this flat band was attributed to the lower Hubbard band [8–13]. Previous timeresolved ARPES and inverse-photoemission spectroscopy also reported the observation of Mott gap between the flat band and upper Hubbard band [23–25], supporting the existence of Mott insulating ground state. However, recent ARPES studies show that the flat band is energy dispersive along the out-of-plane momentum ($k_z$) direction [19,26,27], which favors the existence of interlayer stacking order. It is then crucial to make a consensus on the detailed temperature evolution of electronic structure in $1T-TaS_2$. The results would help to understand how the on-site Coulomb repulsion and interlayer hopping play roles in $1T-TaS_2$.

In this work, we characterize the temperature dependence of electronic and lattice structures of $1T-TaS_2$ using ARPES and Xray diffraction (XRD). We find that, at low temperatures, the

band dispersion and diffraction peaks show $2\pi/2c$ and $2c$ periodicity, which indicates that the ground state of $1T-TaS_2$ is a band insulator with interlayer dimerization. More intriguingly, at high temperatures, the system undergoes an insulator-to-insulator transition and enters an intermediate Mott insulating state, which only exists in a narrow temperature region. Our results show that the energy scales of in-plane hopping, on-site Coulomb repulsion, and interlayer hopping are all comparable in $1T-TaS_2$. The competition between these interactions are responsible for the complex electronic properties of $1T-TaS_2$.

## Results

Temperature dependence of electronic structure. To characterize how the flat band forms in the C-CDW phase, we show the detailed temperature dependence of the energy distribution curves (EDCs) taken at the Brillouin zone center ( Γ ) (Fig. 2). Upon cooling, the spectral weight of the flat band shifts from $E_F$ to -200 meV at 193 K, indicating an energy gap opening at $E_F$. In contrast to the cooling process, the temperature evolution of EDCs during the heating process clearly identifies two-phase transitions (Fig. 2d-f). The first phase transition occurs at 217 K, where the peak width narrows and the peak position shifts from -210 to -170 meV. The second phase transition follows at 233 K , where the spectral weight of the flat band shifts to $E_F$.

In comparison with the resistivity data, the gap opening transition at 193 K can be attributed to the NC-CDW to C-CDW transition upon cooling, while the transition at 217 K coincides with the C-CDW to T-CDW transition upon heating. There is a small temperature deviation between the transition temperatures determined by different techniques. This can be explained by the standard deviation of transition temperatures among different samples due to a small sample inhomogeneity (Supplementary Figs. 1-3). However, the transition at 233 K does not show up in the transport measurements. It also cannot be explained by a sample in-

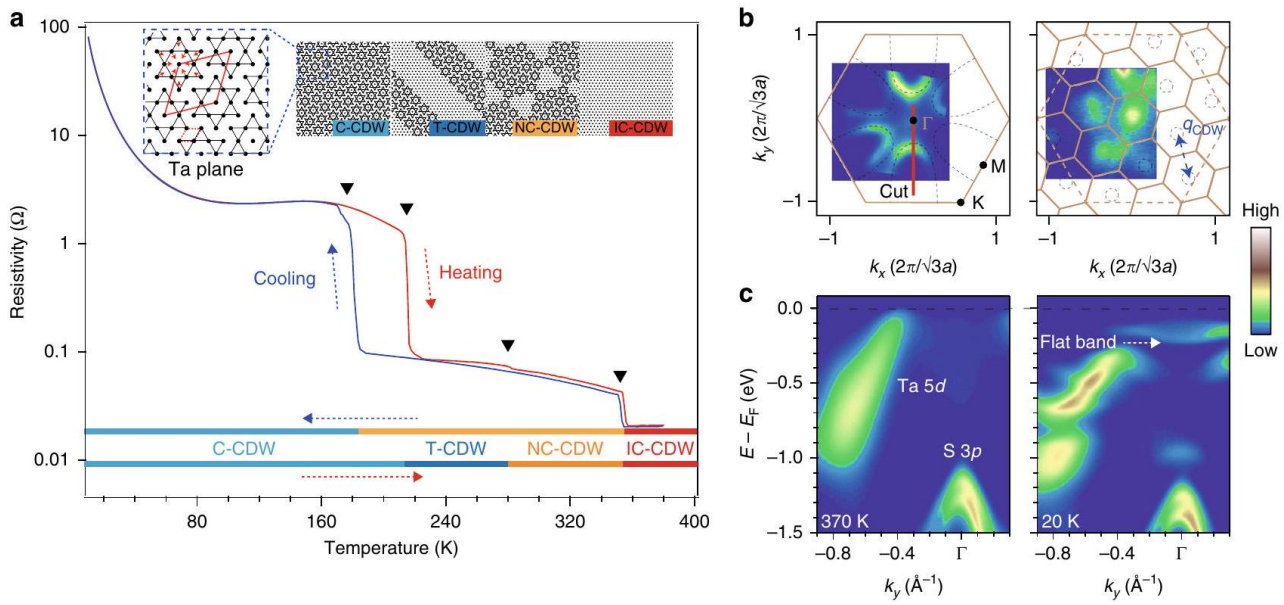


Fig. 1 Transport property and electronic structure of $\mathbf{1T-TaS_2}$. a Temperature dependence of in-plane resistivity taken upon heating and cooling. The black arrows mark the first-order transition points. The bars below the curves indicate temperature intervals corresponding to the different phases. Inset panels in a are schematic illustrations for the in-plane lattice modulations in the commensurate CDW (C-CDW) phase, nearly commensurate CDW (NC-CDW) phase, Triclinic CDW (T-CDW) phase, and In-commensurate CDW (IC-CDW) phase, respectively. The SD clusters are marked with the dark outlines. Black dots stand for the Ta atoms. b and c Fermi surface mappings and corresponding high symmetry cuts taken at 370 and 20 K, respectively. The cut momenta are illustrated as a red line in b.

homogeneity, because the temperature-dependent data are well reproducible in many different samples (Supplementary Fig. 1). Our results thereby identify an undiscovered intermediate (I) phase, which exists in a narrow temperature region (217-233 K) at the C-CDW to T-CDW phase transition. For the transition at 217 K, the spectra show insulating behavior on both sides of the transition (Fig. 2d), which is therefore an insulator-to-insulator transition. In the following, we present experimental evidence for distinct motives behind the two insulating states, which suggests that the I phase is, in fact, a Mott insulator.

The temperature evolution of flat band is shown in Fig. 3. The CDW band gap opens and the flat band forms at $E_F$ in the NC-CDW and T-CDW phases. Its bandwidth is narrow due to the large scale of the hexagonal SD structure. The flat band opens an energy gap and shifts from $E_F$ to -170 meV at 225 K in the I phase. In the C-CDW phase, the flat band shifts to around -200 meV and becomes more dispersive. Meanwhile, there is an energy spread of the flat band towards $E_F$, which is consistent with the peak broadening observed in Fig. 2d, e. Due to the surface sensitivity of ARPES technique, $k_z$ is not conserved during the photoemission process [28]. The ARPES spectra is thus a superposition of the bulk bands at different $k_z$ 's. If the band has moderate band dispersion along $k_z$ direction, its ARPES spectra is broadened. Such $k_z$ broadening effect explains the energy spread of the flat band, which also indicates that the $k_z$ band dispersion reconstructs significantly in the C-CDW phase.

To determine the band dispersion of the flat band along the $k_z$ direction, we measured the photon energy-dependent data in the

I and C-CDW phases. The results are compared in Fig. 4. The flat band is gapped at 225 K. The weak photon energy dependence indicates the two dimensionality of the flat band

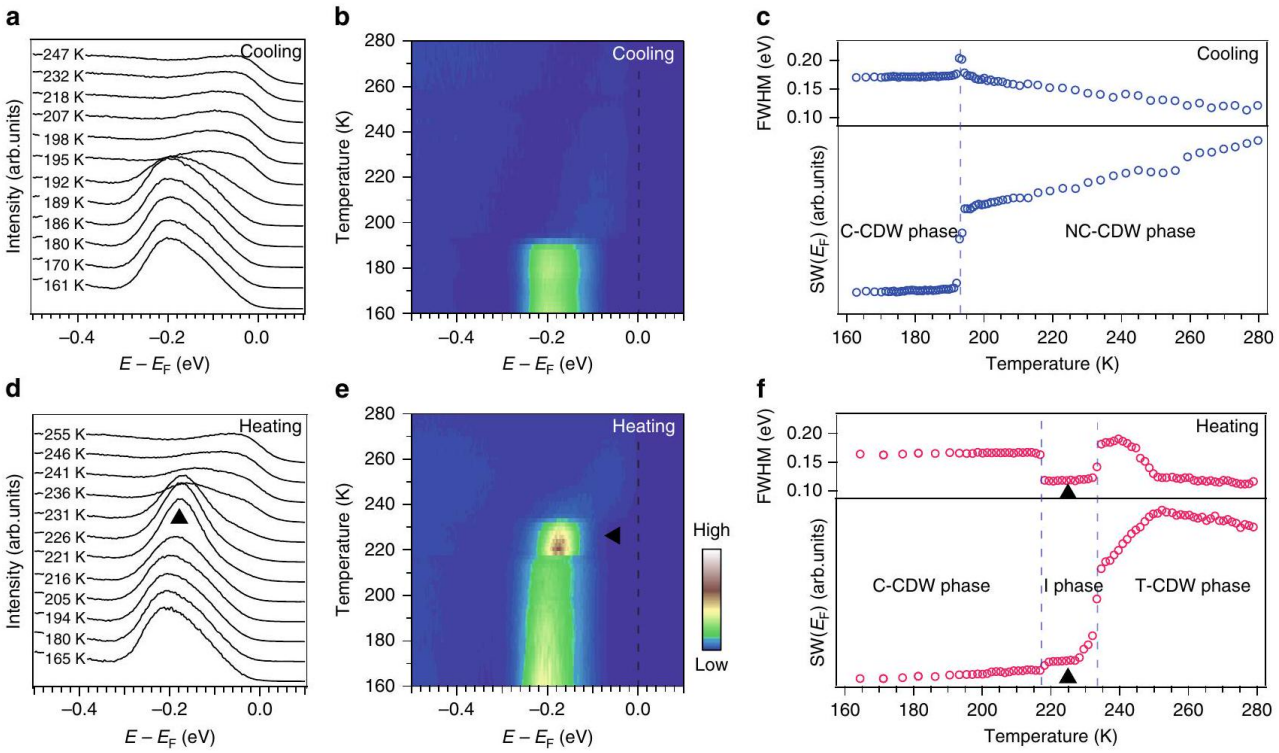


Fig. 2 Temperature-dependent ARPES study of $\mathbf{1}\boldsymbol{T}-\mathbf{TaS_2}$ upon cooling and heating. a Temperature dependence of energy distribution curves (EDCs) taken at the Γ point upon cooling. b The merged image of the data in a. c Corresponding temperature dependence of full width at half maximum (FWHM) for the data in a, and the spectral weight (SW) taken at where the Ta $5d$ band crosses $E_F$ $\left([-0.1, 0.1\text{eV}], \left[-0.4, -0.3\text{Å}^{-1}\right]\right)$. d-f are the same as a-c but for the heating process. Black arrows mark the intermediate (I) state.

in the I phase. However, when entering the C-CDW phase, the data become strongly photon energy dependent. The band positions shift from -230 to -90 meV periodically. This shows that the bandwidth along the $k_z$ direction is around 140 meV in the C-CDW phase, which is well consistent with the $k_z$ broadening effect observed in Fig. 3. The photon energy-dependent data confirm that the $k_z$ band dispersion reconstructs strongly at the I to C-CDW phase transition. More intriguingly, the periodicity of the $k_z$ dispersion is around $2\pi/2c$ in the C-CDW phase, which indicates the existence of an interlayer dimerization.

Temperature dependence of lattice structure. We then performed the single-crystal XRD measurement along the (0, 0, L) direction to confirm the existence of interlayer stacking order. Indeed, in addition to the regular integer-indexed Bragg peaks (Fig. 5a), a set of half-integer-indexed reflections are observed at 120 K. The fact that the (0, 0, 7/2) reflection is about twice more intense than the (0, 0, 5/2) reflection, i.e., with the intensity roughly proportional to $|\mathbf{Q}|^2$, suggests that these additional reflections are caused by $c$-axis displacive structural modulations that double the unit cell along $c$ (Fig. 5c). The appearance of halfinteger reflections in the C-CDW phase is a direct evidence for interlayer dimerization, which has to be caused by, and provide feedback to, interlayer coupling in the electronic structure. It is therefore no surprise that these half-integer reflections occur at 212 K which coincides with the enhancement of $k_z$ band dispersion observed by ARPES (Figs. 4 and 5b).

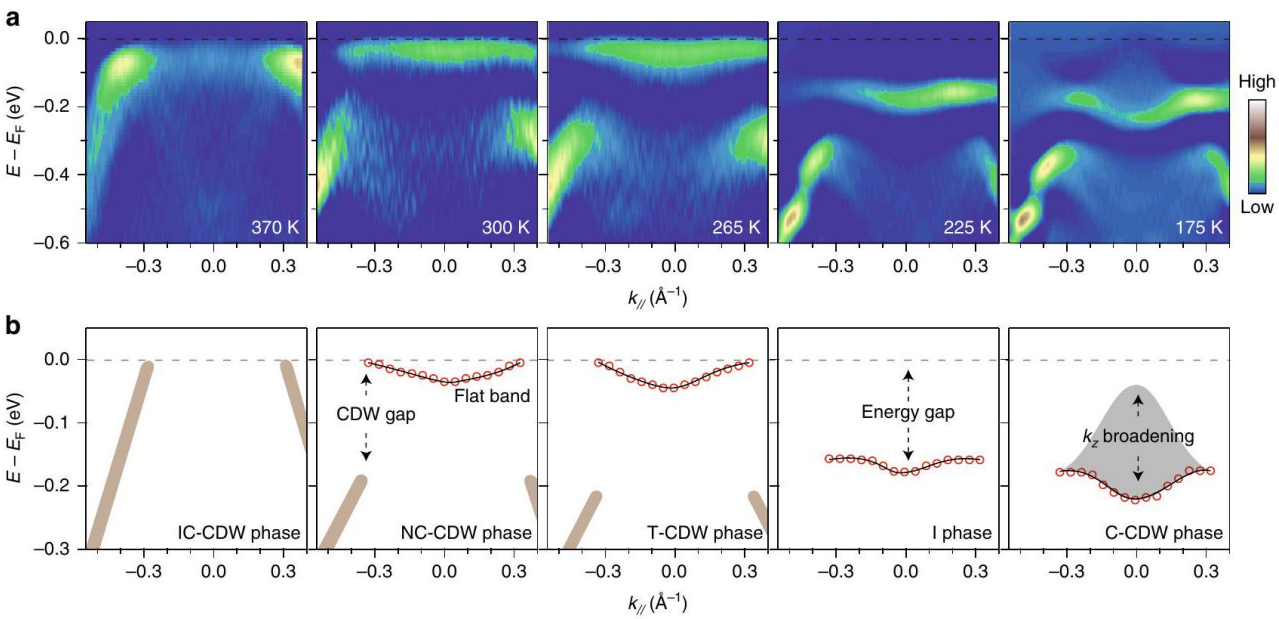


Fig. 3 Evolution of the flat band crossing different electronic phases. a The second derivative images of the energy-momentum cuts taken along the $\Gamma - \mathrm{M}$ direction in different electronic phases. b The schematic illustration of band evolution crossing different phases. Red circles show the fitted peak maxima from the data in a. Black lines guides the eyes to the flat band dispersions. Brown thick lines illustrate the bands at high binding energy.

## Discussion

For the C-CDW phase, its intra-layer CDW structure consists of SD clusters with the $p(\sqrt{13}\times\sqrt{13})R13.9^\circ$ periodicity. This has been well studied by previous diffraction experiments and also confirmed by the ARPES mapping in Fig. 1b. Here, our XRD and photon energy-dependent ARPES data show that, in addition to the intra-layer CDW, the system forms an interlayer stacking order along the $c$ direction. While the $2c$ periodicity could be attributed to an inter-layer dimerization, the stacking configuration between each bilayers remains unknown. Theoretical calculations show that the energy differences between different configurations are small [19,20]. Therefore, different stacking configurations could coexist, and the layers could stack randomly along the $c$ direction. This is consistent with our XRD data. The weak intensity of the half-integer diffraction peaks and the broadening of the CDW diffraction peak (Supplementary Fig. 5) suggest that the interlayer stacking shows certain randomness in the C-CDW phase. Therefore, to determine the stacking configuration experimentally, layer-resolved XRD studies are needed. Nevertheless, indirect evidences could be found by comparing the ARPES data with theoretical band calculations. Our result is more consistent with an alternating stacking configuration, where the predicted band structure is a small-gap band insulator [19,20].

Both ARPES and XRD data show the existence of interlayer stacking order in the C-CDW phase. This makes the low temperature ground state of $1T - \mathrm{TaS_2}$ a band insulator with two electrons fully occupied in the flat band near $E_\mathrm{F}$. The next question is then the origin of the I phase where the stacking order vanishes. Apparently, the I phase to C-CDW phase transition is an insulator-to insulator transition. Therefore, it cannot be explained by a simple interlayer Peierls CDW transition that is driven by the electronic instability at the Fermi surface. Electronic correlation need be considered. In a bilayer Hubbard band model, considering both the on-site Coulomb repulsion and interlayer hopping, theories show that the electronic system can transit from a Mott insulator to a band insulator when the interlayer hopping increase above a critical value [29,30]. The electronic states redistribute without closing

the energy gap, resulting in an insulator-to-insulator transition. This naturally explains the C-CDW phase to I phase transition observed here (Fig. 5d, e). The I phase is a two-dimensional Mott insulator originated from the on-site Coulomb repulsion ($U$). When entering the C-CDW phase, the interlayer hopping ($t_\perp$) as characterized by the $k_z$ bandwidth is strongly enhanced. As a result, the system transits from a Mott insulator into a band insulator. Consistently, the energy scale of the in-plane hopping $(t_{//})$is around 100 meV as determined by the in-plane bandwidth of the flat band (Fig. 3). The Mott gap between the lower and upper Hubbard band is around 400meV[13,18,25], representing the energy scale of $U$. The energy scale of $t_\perp$ is around 140 meV, which is the $k_z$ bandwidth of the flat band (Fig. 4). All these experimentally determined parameters are consistent with the theoretical parameters where the band-insulator to Mott-insulator transition could realize [29,30].

It is then intriguing to understand the enhancement of $t_\perp$ cross the I to C-CDW phase transition. In fact, the reconstruction of electronic structure along $c$ direction is so strong that upon entering the I phase from the C-CDW phase, the distance between adjacent $TaS_2$ layers undergoes an appreciable sudden decrease from 5.928 to 5.902Å as seen from the ( $0, 0, 4$ ) reflection (Fig. 5b). At first glance, the larger interlayer distance in the C-CDW phase compared to the I phase is at variance with the larger $t_\perp$ (hence stronger $k_z$ dispersion) in the C-CDW phase. This unexpected correlation between $t_\perp$ and interlayer distance requires further theoretical understanding. One possible explanation is that the complete in-plane commensurability of CDW in the C-CDW phase turns on additional hopping channels between nearby $TaS_2$ layers, which may further affect the average interlayer distance.

The phase transition at 233 K and the I phase have not been observed in both the resistivity and XRD data. Considering that APRES is more sensitive to the electronic state near the sample surface, we could explain this controversy using two different scenarios. On one hand, the I phase is a surface state that does not exist in the bulk layers. This resembles the Mott insulating phase that was observed at the surface of $1T - TaSe_2$[31,32]. However, this scenario contradicts with some of our observations. For example, the penetration depth of ARPES is normally around or over two layers. If the surface and bulk electronic states are different, we should observe two different sets of bands representing the surface and bulk, respectively. However, our data only show one set of bands, which suggests that the I phase extends along $c$ direction for at least two $TaS_2$ layers. Furthermore, the phase transition at 217 K observed by ARPES is well consistent with the C-CDW transition temperature determined by transport and XRD measurements. The photon energy-dependent data also clearly show the $k_z$ dispersion of bands, whose periodicity is well consistent with the bulk lattice parameter. All these results suggest that the ARPES data reflect the bulk electronic properties of $1T - TaS_2$. On the other hand, the I phase exists in bulk layers, but only emerges in certain layers which are phase separated from the other layers. Therefore, the I phase cannot be picked up by the resistivity and

XRD measurements. Under this scenario, the observation of I phase by ARPES should be highly dependent on the cleaved surface. However, this is not the case. The high reproducibility of our ARPES data seems to suggest that the I phase may have a high probability of occurrence near the sample surface.

To examine whether the I phase exists in the bulk or not, layerresolved transport and XRD measurements are required. The resistivity measurements on thin $1T - TaS_2$ films show that the transition becomes broad with the decreasing of sample thickness [33–35], which may suggest the existence of a phase separation. Moreover, the system remains insulating in an ultrathin film, while the C-CDW phase is fully suppressed [33–35]. This is consistent with our results that the interlayer hopping is important for the C-CDW phase. In an ultrathin film where the on-site Coulomb repulsion plays a more dominating role than the interlayer hopping, the insulating property may originate from the intermediate Mott insulating phase observed here.

In summary, we believe that the competition between $U$ (within SD) and $t_\perp$ (between neighboring $TaS_2$ layers) is responsible for the complex insulating phases in $1T - TaS_2$. While the C-CDW phase is a band insulator featuring strong interlayer hoping and dimerization, the I phase is likely a two-dimensional Mott insulator. Although we show that the low-temperature C-CDW phase is not a Mott insulator, the $S = 1/2$ degrees of freedom could still be realized in the I phase. Further experimental studies are required to characterize possible magnetism in the I phase and verify its occurrence in bulk layers. Meanwhile, if the stacking order in the C-CDW phase can be suppressed, such as by chemical doping or reducing dimensionality, quantum magnetism may still be realized down to the lowest temperature in $1T$ -$TaS_2$.

## Methods

Sample growth. High-quality single crystals of $1T - TaS_2$ were synthesized using chemical vapor transport (CVT) method. By mixing the appropriate ratio of Ta powder and S pieces (2% excess) well, the compound was sealed in a quartz tube with $ICl_3$ as transport agent. The quartz tube was put in the two-zone furnace with thermal gradient between 750 and 850 °C for 120 h, and then quenched in water. The refinement of power XRD data confirms the phase purity of our sample and the trigonal crystal structure of $1T - TaS_2$ with the $P - 3m1$ space group with the lattice parameters $a = b = 3.366$Å$, c = 5.898$Å (Supplementary Fig. 6).

Resistivity measurements. Resistivity data were measured in physical property measurement system (PPMS, Quantum Design, Inc.) utilizing standard four-probe method. The heating and cooling rates are 3 K $min^{-1}$.

ARPES measurements. ARPES measurements were performed at Peking University using a DA30L analyzer and a helium discharging lamp. The photon energy of helium lamp is 21.2 eV. Photon energy-dependent measurement was performed at the BL13U beamline in National Synchrotron Radiation Laboratory (NSRL). The overall energy resolution was ˜12 meV and the angular resolution was ˜0.3°. The crystals were cleaved in situ and measured in vacuum with a base pressure better than $6 \times 10^{-11}$mbar. The $E_F$ for the samples were referenced to that of a gold crystal attached onto the sample holder by Ag epoxy. For the measurements in a heating process, the samples were first cooled down from 300 to 80 K with a rapid fall of temperature (about 20 K $min^{-1}$ ). After adequate cooling for about 10 min at 80 K, the samples were cleaved and heated up to 190 K with a rate about 1.5 K $min^{-1}$; The samples were then heated up to 300 K slowly with a rate about 0.23 K $min^{-1}$. For the measurement in a cooling process, The sample was cleaved at 300 K directly and cooled down to 210 K with a rate about 2 K $min^{-1}$; The sample was then cooled down to 160 K slowly with a rate about 0.5 K $min^{-1}$. ARPES data were collected during the cooling and heating processes. More experimental details could be found in Supplementary Table 1.

XRD measurements. XRD data were recorded on a Bruker D8 diffractometer using CuK$\alpha$ radiation ($\lambda = 1.5418$Å). We mounted a high-quality single crystal of $1T - TaS_2$ in a liquid nitrogen cryostat sitting in an Euler cradle to measure the $c$ axis at different temperatures.

The sample was cooled down until 93 K with a rapid fall of temperature (about 10 K $min^{-1}$ ) from room temperature naturally. After adequate cooling for about 1 h at 120 K, we heated the sample from 120 to 170 K at 3 K $min^{-1}$. We then heated the sample to 370 K with a rate about 0.16 K $min^{-1}$. XRD data were collected during the heating process.

Experimental reproducibility. The ARPES and resistivity measurements were repeated on different samples. The observations are reproducible in all measured samples with a small variable of transition temperatures (Supplementary Figs. 1-3). The resistivity data in Fig. 1a were taken on sample #7. The ARPES data in Fig. 2a, b were taken on sample #6. The ARPES data in Figs. 2d, f and 3 were taken on sample #1. The XRD data were taken on sample #13. The ARPES data taken at 370 K in Figs. 1 and 3 were taken on sample #14. Photon energy-dependent data in Fig. 4 was taken on sample #15.

**References**


1. Novoselov, K. S. et al. Two-dimensional atomic crystals. Proc. Natl Acad. Sci. USA 102, 10451-10453 (2005).

2. Geim, A. K. & Grigorieva, I. V. Van der Waals heterostructures. Nature 499, 419-425 (2013).

3. Fiori, G. et al. Electronics based on two-dimensional materials. Nat. Nanotechnol. 9, 768-779 (2014).

4. Tosatti, E. & Fazekas, P. On the nature of the low temperature phase of 1T-$TaS_2$. J. Phys. Colloq. 37, C4-165-C164-168 (1976).

5. Thomson, R. E., Burk, B., Zettl, A. & Clarke, J. Scanning tunneling microscopy of the charge-density-wave structure in $1T-TaS_2$. Phys. Rev. B 49, 16899-16916 (1994).

6. Sipos, B. et al. From Mott state to superconductivity in $1T-TaS_2$. Nat. Mater. 7, 960-965 (2008).

7. Rossnagel, K. On the origin of charge-density waves in select layered transition-metal dichalcogenides. J. Phys. Condens. Matter 23, 213001 (2011).

8. Wilson, J. A., Di Salvo, F. J. & Mahajan, S. Charge-density waves and superlattices in the metallic layered transition metal dichalcogenides. Adv. Phys. 24, 117-201 (1975).

9. Fazekas, P. & Tosatti, E. Electrical, structural and magnetic properties of pure and doped $1T-TaS_2$. Philos. Mag. B 39, 229-244 (1979).

10. Manzke, R., Buslaps, T., Pfalzgraf, B., Skibowski, M. & Anderson, O. On the phase transitions in $1T-TaS_2$. Europhys. Lett. 8, 195 (1989).

11. Rossnagel, K. & Smith, N. V. Spin-orbit coupling in the band structure of reconstructed1T- $TaS_2$. Phys. Rev. B 73, 073106 (2006).

12. Perfetti, L., Gloor, T. A., Mila, F., Berger, H. & Grioni, M. Unexpected periodicity in the quasi-two-dimensional Mott insulator $1T-TaS_2$ revealed by angle-resolved photoemission. Phys. Rev. B 71, 153101 (2005).

13. Kim, J. J., Yamaguchi, W., Hasegawa, T. & Kitazawa, K. Observation of Mott localization gap using low temperature scanning tunnelling spectroscopy in commensurate $1T-TaS_2$. Phys. Rev. Lett. 73, 2103 (1994).

14. Klanjšek, M. et al. A high-temperature quantum spin liquid with polaron spins. Nat. Phys. 13, 1130-1134 (2017).

15. Law, K. T. & Lee, P. A. $1T-TaS_2$ as a quantum spin liquid. Proc. Natl Acad. Sci. USA 114, 6996-7000 (2017).

16. Ribak, A. et al. Gapless excitations in the ground state of $1T-TaS_2$. Phys. Rev. B 96, 195131 (2017).

17. He, W. Y., Xu, X. Y., Chen, G., Law, K. T. & Lee, P. A. Spinon Fermi surface in a cluster Mott insulator model on a triangular lattice and possible application to $1T-TaS_2$. Phys. Rev. Lett. 121, 046401 (2018).

18. Ritschel, T. et al. Orbital textures and charge density waves in transition metal dichalcogenides. Nat. Phys. 11, 328-331 (2015).

19. Ritschel, T., Berger, H. & Geck, J. Stacking-driven gap formation in layered 1 T- $TaS_2$. Phys. Rev. B 98, 195134 (2018).

20. Lee, S. H., Goh, J. S. & Cho, D. Origin of the insulating phase and first-order metal-insulator transition in $1T - TaS_2$. Phys. Rev. Lett. 122, 106404 (2019).

21. Butler, C. J., Yoshida, M., Hanaguri, T. & Iwasa, Y. Mottness versus unit-cell doubling as the driver of the insulating state in $1T - TaS_2$. Nat. Commun. 11, 2477 (2020).

22. Martino, E. et al. Preferential out-of-plane conduction and quasi-one-dimensional electronic states in layered van der Waals material $1T - TaS_2$.*npj* 2D Mater. Appl. 4, 7 (2020).

23. Ligges, M. et al. Ultrafast doublon dynamics in photoexcited $1T - TaS_2$. Phys. Rev. Lett. 120, 166401 (2018).

24. Perfetti, L. et al. Time evolution of the electronic structure of $1T - TaS_2$ through the insulator-metal transition. Phys. Rev. Lett. 97, 067402 (2006).

25. Sato, H. et al. Conduction-band electronic structure of $1T - TaS_2$ revealed by angle-resolved inverse-photoemission spectroscopy. Phys. Rev. B 89, 155137 (2014).

26. Ngankeu, A. S. et al. Quasi-one-dimensional metallic band dispersion in the commensurate charge density wave of $1T - TaS_2$. Phys. Rev. B 96, 195147 (2017).

27. Ma, L. et al. A metallic mosaic phase and the origin of Mott-insulating state in 1T- $TaS_2$. Nat. Commun. 7, 10956 (2016).

28. Himpsel, F. J. Angle-resolved measurements of the photoemission of electrons in the study of solids. Adv. Phys. 32, 1 (2006).

29. Fuhrmann, A., Heilmann, D. & Monien, H. From Mott insulator to band insulator: a dynamical mean-field theory study. Phys. Rev. B 73, 245118 (2006).

30. Kancharla, S. S. & Okamoto, S. Band insulator to Mott insulator transition in a bilayer Hubbard model. Phys. Rev. B 75, 193103 (2007).

31. Perfetti, L. et al. Spectroscopic signatures of a bandwidth-controlled Mott transition at the surface of $1T - TaSe_2$. Phys. Rev. Lett. 90, 166401 (2003).

32. Colonna, S. et al. Mott phase at the surface of $1T - TaSe_2$ observed by scanning tunneling microscopy. Phys. Rev. Lett. 94, 036405 (2005).

33. Yoshida, M. et al. Controlling charge-density-wave states in nano-thick crystals of $1T - TaS_2$. Sci. Rep. 4, 7302 (2014).

34. Tsen, A. W. et al. Structure and control of charge density waves in two-dimensional 1T-$TaS_2$. Proc. Natl Acad. Sci. USA 112, 15054-15059 (2015).

35. Yu, Y. Gate-tunable phase transitions in thin flakes of $1T - TaS_2$. Nat. Nanotechnol. 10, 270-276 (2015).

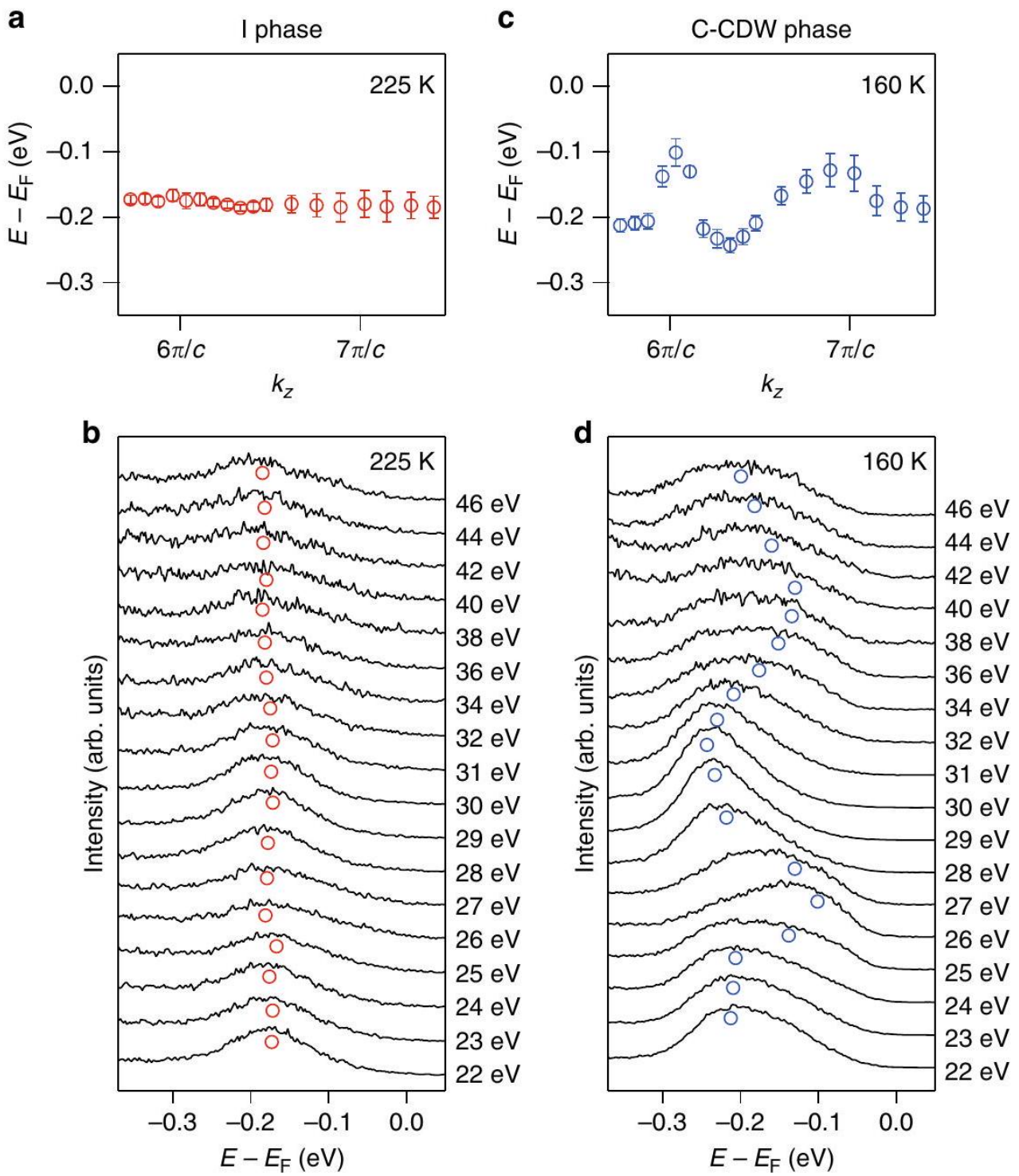


Fig. 4 Band dispersions along the $\boldsymbol{k_z}$ direction taken in the I and C-CDW phases. a $k_z$ dependence of the band positions in the I phase at 225 K. $k_z$ is calculated using the inner potential $V_0 = 17.5$eV. b Photon energy dependence of EDCs taken at Γ at 225 K.**c** and d are the same as a and b but taken in the C-CDW phase at 160 K. Red and blue circles are the fitted band positions. Error bars are estimated from peak fittings and defined as s.d.

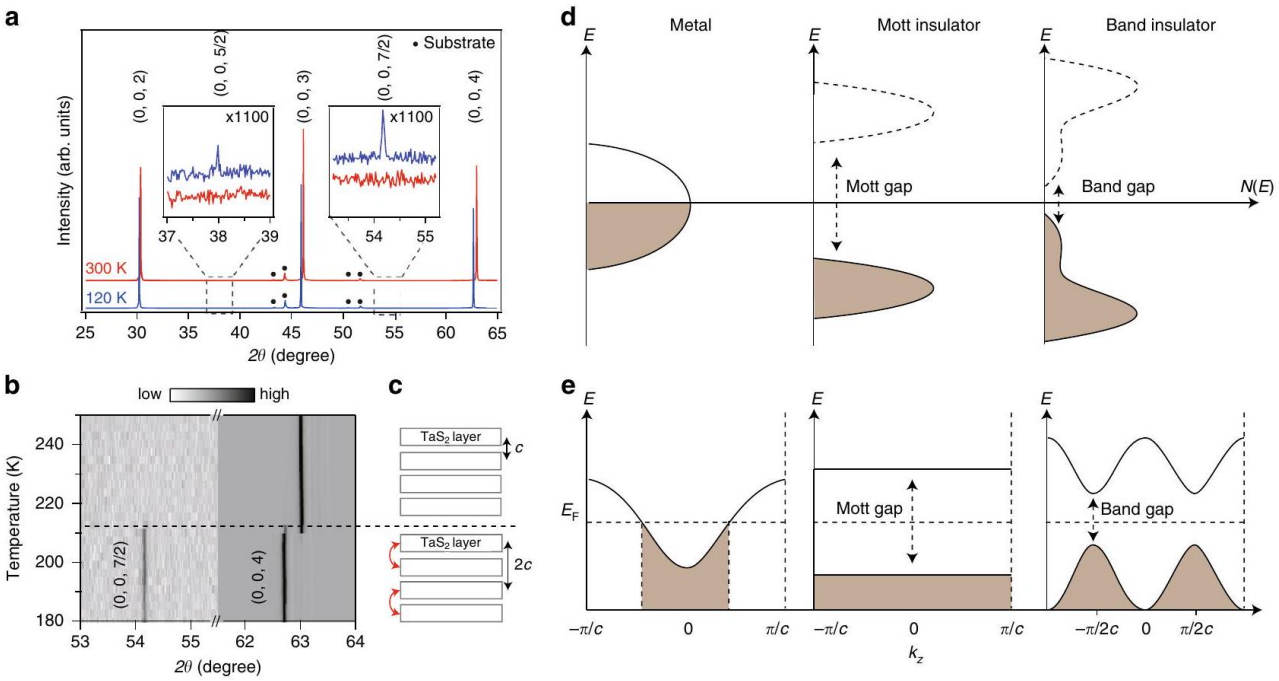


Fig. 5 Temperature-dependent XRD study and schematic depictions of band evolution. a XRD intensity of $1T-TaS_2$ measured along c axis at 120 and 300 K. Inset panels show the emergence of $(0, 0, 5/2)$ and $(0, 0, 7/2)$ peaks using 1100 times expanded scales. All the other peaks are from the polycrystalline substrate (Supplementary Fig. 4). b Temperature-dependence of the (0, 0, 7/2) and (0, 0, 4) peaks upon heating. c Schematic illustration of the interlayer dimerization. d Schematic illustration of the density of state distributions in different electronic phases. e Schematic illustration of the band dispersions along $k_z$ direction in different electronic phases.

# 14 Dynamical control of Coulomb interactions and Hubbard bands in monolayer 1T-$TaS_2$ by Notter, Aichhorn, Galler

**Abstract**

(there is CDW in monolayer TaS2) Monolayer 1T-$TaS_2$ hosts a star-of-David charge-density wave (CDW) that stabilizes(I don't think that word "stabilizes" is important) a low-temperature Mott-insulating state.

(some time-resolved results appear and something is not clear) Recent time-resolved spectroscopies indicate a coupling between the CDW amplitude mode (attention! CDW amplitude mode = model of a SOD, not of the total electron density modulation. this is how they want to call it, it is not strictly speaking correct) and the electronic correlation strength, yet the role of the screened Coulomb interaction remains unclear.

(we show how CDW changes Hubbars's U) Using the constrained random-phase approximation, we show that the CDW amplitude modifies the bare and screened on-site interactions, leading to sizable variations in the effective Hubbard $U$.

(we do DFT and DMFT, we show that if you decrease CDW amplitude, bands will shift and finally we'll get a metal) Our combined density-functional and dynamical mean-field theory calculations reveal that the Hubbard bands shift in concert with (=together with) the CDW amplitude, and that a reduced distortion drives a transition from a Mott insulator to a correlated metal. (it is purely mathematical setup, physically we can't vary CDW amplitude)

(abstract comment about coupling) These results demonstrate a direct link between lattice distortions and Coulomb interactions in transition-metal dichalcogenides, providing a microscopic mechanism for light-induced control of correlated phases in two-dimensional quantum materials.

## 14.1 Article

### 14.1.1 Introduction

(there are a lot of effects in 2D materials) Two-dimensional (2D) correlated materials exhibit a rich variety of quantum phases, including superconducting [1], charge- and spin-density wave [2] and quantum spin liquid states [3, 4].

(a lot of parameters influence them) The emergence of these phases is sensitive to external parameters such as pressure, strain, and static or dynamic electric and magnetic fields.

(there are a lot of exotic ideas also) Beyond this intrinsic tunability, 2D materials offer an additional degree of control through stacking and twisting, enabling emerging paradigms such as oxide electronics [5, 6], valleytronics [7, 8], and twistronics [9, 10, 11].

(abstract intro to TMDCs) Transition-metal dichalcogenides (TMDs) in the 1T polymorph [12, 13, 14, 15, 16, 17, 18, 19, 20, 21, 22] are van-der-Waals materials that allow us to explore strong correlation effects in 2D.

(TaS2 has SODs) Among them, 1T-$TaS_2$ exhibits a Star-of-David (SoD) charge density wave (CDW) phase below 180 K.

(SOD -> there is also insulation) The formation of this CDW phase, where clusters of 13 Ta atoms move closer in a star-shaped arrangement (Fig. 20.1b), is accompanied by a transition to an insulating state.

(bulk -> band insulator+ something, monolayer -> Mott insulator) While bulk 1T-$TaS_2$ is believed to consist of dimerized, band-insulating bilayers interspersed(=placing things at

different places) with AC-stacked monolayers (interspersed with AC-stacked monolayers??? so there are two types of layers in the bulk material?) [23, 24, 25], isolated monolayers are well established as Mott insulators [24, 17, 19].

(CDW in monolayer -> narrow band at FS) The CDW distortion in a monolayer generates a very narrow, half-filled (why half-filled?) band at the Fermi level.

(if we change el. correlation - band will change) This molecular orbital, with meV bandwidth and predominantly Ta $d_{3z^2-r^2}$ character (why $d_{3z^2-r^2}$ character? what does it mean?) , is highly susceptible to electronic correlations.

(Hubbard model describes 1T-TaS2 and can incorporate several factors) To first approximation, monolayer 1T-$TaS_2$ can be regarded as a prototypical realization of the Hubbard model on a triangular lattice, a system that recently attracted interest due to the interplay of strong correlations, geometric frustration, and unconventional ordering [26, 27, 28, 29, 30]. (is there a Hubbard model for 1H phase and others? maybe no..)

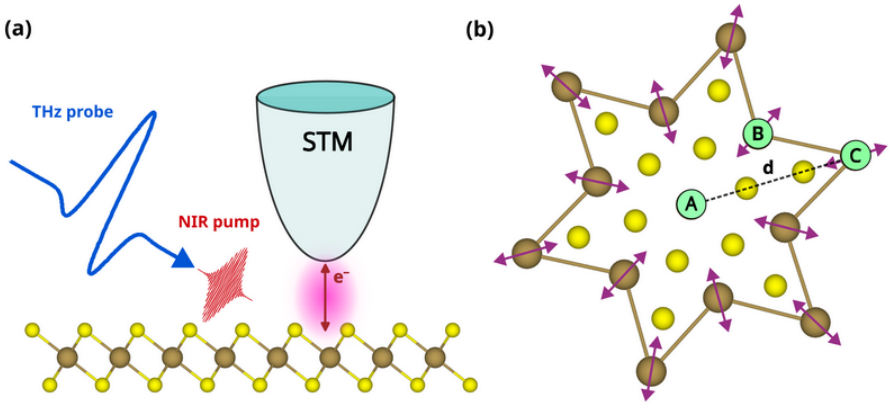


Figure 14.1: **(a)** (experiment: we shine two pulses and measure electrons) Illustration of a time-resolved STM experiment. A near-infrared (NIR) pulse indirectly excites the CDW amplitude mode in monolayer 1T-$TaS_2$, while a time-delayed THz probe pulse induces electron tunneling between the sample and STM tip to probe the local density of states.
**(b)** (SODs) Top view of the SoD supercell with Ta (brown) and S (yellow) atoms. $d$ denotes the distance between the central (site A) and the outer (site C) Ta atoms. Violet arrows indicate the CDW amplitude mode oscillation.

(this is an abstract and unclear sentence, basically it is meant "we'll be changing CDW and see how other properties will change") The CDW distortion clearly plays a central role in stabilizing the correlated state, suggesting that it could serve as a control knob (=small, rounded handle or control device) to manipulate the electronic properties.

(external strain somehow influences transition) Initial experiments indicated that external strain, which modifies the amplitude of the SoD CDW, can influence the Mott transition (how it can influence the transition?) [31].

(some experiments show something that makes the authors think that maybe it is possible do control dynamically densities of electrons. It is not written here, what exactly they mean by results from experiments and "correlation strength") More recent studies using terahertz (THz) scanning tunneling microscopy (STM) [32] and time- and angle-resolved photoemission spectroscopy (tr-ARPES) [33, 34, 35, 36], which excite a coherent 2.4 THz CDW amplitude mode [37] in 1T-$TaS_2$, point toward the possibility of dynamically controlling the correlation strength.

(there were some calculations, but still Coulomb interaction after shining light is not understood) However, despite recent density-functional theory (DFT) and non-equilibrium dynamical mean-field theory (DMFT) calculations [33] (I downloaded this article, it is experimental

one, but there are also some calculation) , the role of the screened Coulomb interaction in the photoinduced dynamics remains insufficiently understood. (It is not clear from this sentence what is the problem?)

(some screening is hard to calculate. again, it is not clear, what they mean. see cited papers) This limitation primarily stems from the difficulty of quantitatively evaluating the screened interaction within the large SoD supercell.

(they do cRPA) Using first-principles calculations within the constrained random-phase approximation (cRPA) [41, 42, 43] (reminder: learn cRPA) , we show that the screened Coulomb interaction in 1T-$TaS_2$ is highly sensitive to the amplitude of the SoD CDW (it is not clear here what they want to show, but later it should be written) .

(Big CDW -> smaller Coulomb interaction. more screening from somewhere -> smaller on-site interaction) Increasing the CDW amplitude reduces the localization of the Ta $d_{3z^2-r^2}$ molecular orbital, lowering the bare Coulomb interaction (Coulomb interaction between neighboring electrons, I guess) , while enhanced electronic screening (I guess screening also comes from CDW) further decreases the equilibrium on-site interaction of $U$=0.4 eV by up to 0.1 eV for a 1% amplitude change (see below). (it is not explain here, why is it so????)

(even 3% increase in CDW destroys insulating properties) Consequently, the Hubbard bands shift and the Mott gap shrinks, and strikingly, a 3% increase in the CDW amplitude drives a transition from a Mott insulator to a correlated metal(correlated metal? how is it?) .

(we'll show how lattice distortion is connected with el. spectrum, so you'll be able to control if with light or interpret some experiments) These results establish a direct, quantitative link between structural distortions and electronic correlations in TMDs, providing a route toward optical control of correlated phases and guiding the interpretation of ultrafast spectroscopic experiments in 2D CDW materials.

### 14.1.2 Results

(intro to pump probe setup) We start by describing the idealized pump–probe setup underlying our simulations, illustrated in Fig. 20.1.

(description of fig. 1a, typical STM) The configuration resembles a THz-lightwave–driven STM experiment [32], where a near-infrared (NIR) laser pulse excites coherent phonon dynamics in a monolayer of 1T-$TaS_2$ through photoinduced charge redistribution.

(we shine the light into SOD) In particular, the pulse drives the 2.4 THz CDW amplitude mode [37] (they mean the periodic lattice distortion, not the CDW mode) , schematically depicted in Fig. 20.1b.

(we excite some atoms in SOD) This breathing phonon mode(breathing phonon mode is some artistic expression) corresponds to oscillations of the outer Ta atoms (sites B and C) around their equilibrium positions within the SoD CDW structure.

(def. of oscillation amplitude $a$) Throughout this work, we express the oscillation amplitude $a$ as a percentage of the distance $d$ between the central (site A) and outer (site C) Ta atoms in the SoD cluster, i.e. $a = (d - d_{\mathrm{eq}})/d_{\mathrm{eq}}$, where $d_{\mathrm{eq}}$ is the distance in the equilibrium CDW distortion.

(meaning of positive, negative $a$) A positive $a$ thus indicates an expanded star, corresponding to a configuration closer to the undistorted phase (which corresponds to $a = 6.5\%$(why 6.5? was it measured somewhere?) ), while a negative $a$ denotes a contracted star with enhanced CDW distortion.

(repetition of abstract, that we'll see spectrum as function of $a$) The resulting lattice vibration modulates the electronic states — a key effect we aim to quantify in this study.

(intro to experiment that measures bands) The time-dependent electronic spectral function(=experimentally observable version of the band structure) can be probed by a THz pulse,

which induces electron tunneling between the STM tip and the sample, as depicted in Fig. 20.1a.

(they can measure time-dependent dynamics) By varying the time delay between the NIR and THz pulses, one can track the evolution of the electronic structure over an entire CDW amplitude-mode oscillation. (did they measure this time dependence?)

(they will model oscillation of SOD somehow) In our simulations, we model the coherent amplitude-mode oscillation of the SoD CDW in 1T-$TaS_2$ using a frozen-phonon approach(frozen-phonon approach??) that decouples electronic and ionic degrees of freedom.

(they'll find spectrum for different SOD amplitudes) The amplitude $a$ is modulated, and the corresponding electronic structure is evaluated separately for each frozen ionic configuration.

(electrons adapt immediately to the lattice) This treatment assumes that the electronic response, which occurs on femtosecond timescales, rapidly adapts to each lattice configuration. (is there a justification of such fast adaptation of el. spectrum?)

(some tiny effects will be neglected) While not accounting for electron-phonon or phonon-phonon interactions, we expect this approach captures the essential changes of the electronic structure over the THz CDW amplitude mode oscillations, where one period lasts approximately 0.4 ps. (why 0.4 ps?)

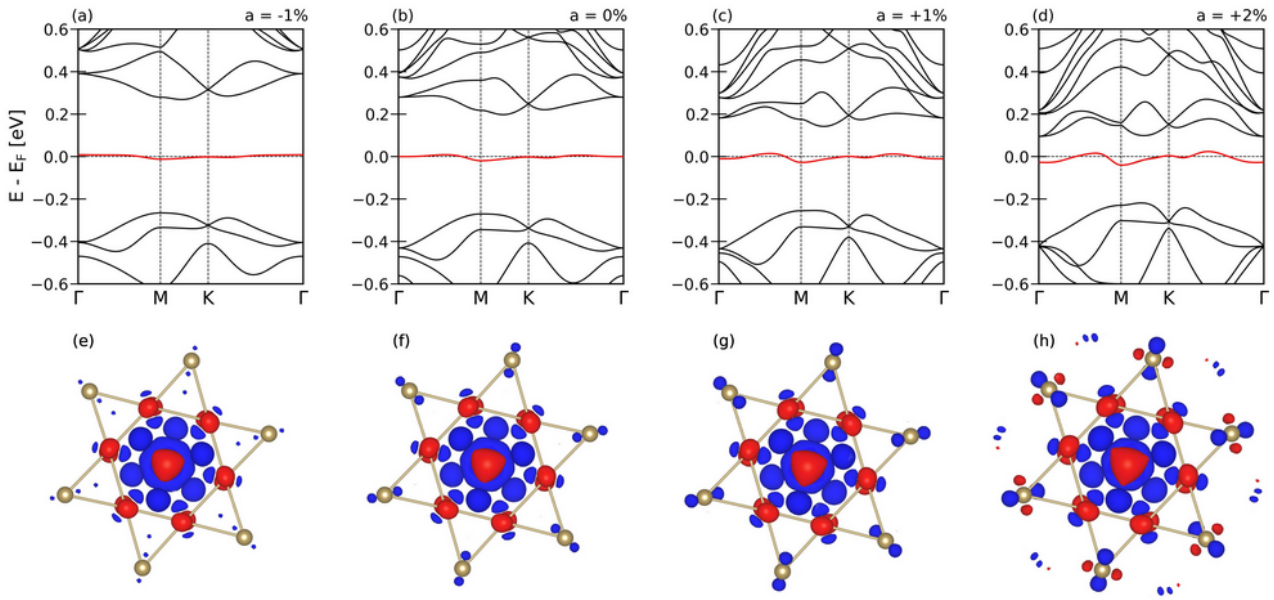


Figure 14.2: (we see that nothing is changed much in the bands) ( The surrounding black DFT bands are additional bands of the material. They should not be identified with the Hubbard bands. The lower and upper Hubbard bands appear only after the narrow red band is treated with $U_a$ in DMFT: one red DFT band $\xrightarrow{\text{DMFT } +U_a}$ LHB + UHB. .) **DFT band structure and Wannier projection for varying CDW distortion. (a–d)** Electronic band structure of monolayer 1T-$TaS_2$ for CDW amplitudes $a = -1\%$ to $a = +2\%$ around equilibrium, computed with PBE [39] in VASP [39](they are alreay in my todo list for dft learning) .
The half-filled band at the Fermi level (red) is projected(projected? how is it???) onto a maximally localized Wannier function [40].
**(e–h)** Wannier isosurfaces (Wannier isosurfaces= wave function of a free electron in atom, I assume) centered on the central Ta atom with smaller weight on surrounding atoms. Red/blue denote positive/negative values.
(there are new spots at the sides =) The orbital becomes increasingly delocalized with larger CDW amplitude.

(descript. of fig. 2) In Fig. 20.2, we present the DFT band structure of monolayer 1T-

$TaS_2$, computed for different amplitudes $a$ of the CDW distortion, ranging from $a = -1\%$ to $a = +2\%$. The reference case $a = 0\%$ (Fig. 20.2b) corresponds to the equilibrium SoD CDW.

(there is a flat band) A prominent feature in all cases is the emergence of a very narrow, half-filled band at the Fermi level (highlighted in red) with a bandwidth of just a few tens of meV.

(they get the wave function from the band using special code. it is impossible to understand better what is going on, since I don't know wannier90) Using WANNIER90 [40, 44, 39] (learn this method!) , we project this band onto a maximally localized Wannier orbital, which turns out to be a molecular-like state with predominant Ta $d_{3z^2-r^2}$ character.

(description of orbitals) As shown in Fig. 20.2e–h, the Wannier orbital is centered on the central Ta atom (site A) but extends significantly onto the surrounding Ta atoms of the SoD cluster.

(bigger a -> wider orbitals) Upon increasing the CDW amplitude from $a = -1\%$ (Fig. 20.2e) to $a = +2\%$ (Fig. 20.2h), the Wannier orbital becomes progressively more delocalized, with its spread increasing from 24 $\text{Å}^2$ to 95 $\text{Å}^2$.

(bigger a -> bigger bandwidth) This enhanced delocalization directly correlates with an increase in bandwidth of the half-filled band, which grows from 20 meV (Fig. 20.2a) to 70 meV (Fig. 20.2d). (I guess their clever code knows how the bandwidth and orbitals are connected)

(we need a screened V for calculation of bandwidth) The narrow, half-filled band is highly susceptible to electronic correlations, making it essential to evaluate the screened Coulomb interaction within this correlated subspace.

(formula for screened potential from RPA) In the random-phase approximation (RPA), the fully screened interaction is given by $W = (1 - V\chi_0)^{-1}V$, with the bare interaction $V$ and the independent-particle polarization $\chi_0$. (check this in the theory of RPA!!!)

(we for some reason use cRPA and here is a key formula for the potential) In constrained RPA (cRPA) [41, 42, 43](learn cRPA!) (why do we need cRPA?) , $\chi_0$ is decomposed into contributions from the correlated target subspace ($\chi_0^t$) and the remainder $\chi_0^r$, yielding the partially screened interaction [45, 46]

$$U = W(1 + \chi_0^t W)^{-1}, \tag{14.1}$$

where $\chi_0^t$ is the static, independent-particle polarization in the target space

$$\chi_0^t(\mathbf{r}, \mathbf{r}') = 2 \sum_{nn' \in t} \sum_{\mathbf{qk}} \frac{f_{n'\mathbf{k}+\mathbf{q}} - f_{n\mathbf{k}}}{\epsilon_{n'\mathbf{k}+\mathbf{q}} - \epsilon_{n\mathbf{k}}} \psi^*_{n\mathbf{k}}(\mathbf{r}) \psi_{n'\mathbf{k}+\mathbf{q}}(\mathbf{r}) \psi^*_{n'\mathbf{k}+\mathbf{q}}(\mathbf{r}') \psi_{n\mathbf{k}}(\mathbf{r}'), \tag{14.2}$$

with $\{\psi_{n\mathbf{k}}, \epsilon_{n\mathbf{k}}\}$ denoting single-particle wave functions and energies, and $f$ the Fermi functions.

(all this in the code VASP) We employ the projector cRPA method as implemented in VASP, defining the target space via the Wannier projection.

(some useless computational details) Calculations are performed in the SoD supercell, using 1024 bands(what if they took 10 bands?s) and $8\times8\times1$ $\mathbf{k}$-points to achieve convergence (further computational details are provided in the Supplementary Information).

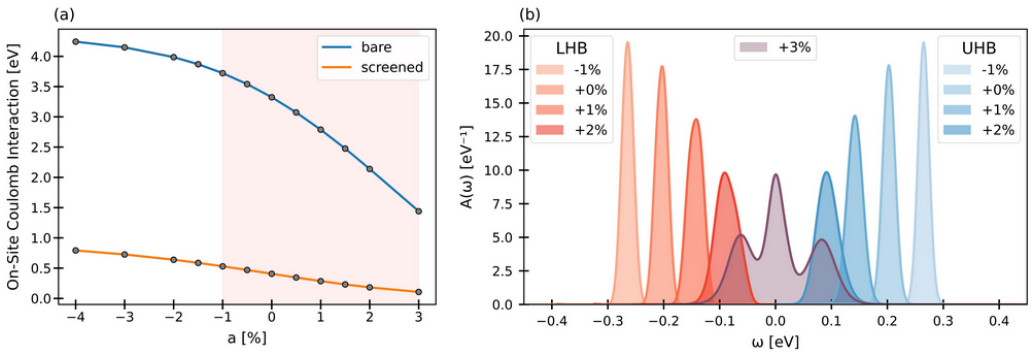


Figure 14.3: **Tuning the screened Coulomb interaction and Mott gap via CDW amplitude modulation. (a)** (how stronger electrons interact as function of SOD closeness) Bare and screened on-site Coulomb interaction as a function of CDW amplitude $a$.
The shaded region highlights the parameter range for which the electronic spectral functions $A(\omega)$ are shown in **(b)**.
(sp. function for different SODs) Increasing the CDW amplitude from -1% to +2% shifts the lower (LHB) and upper Hubbard bands (UHB) and reduces the Mott gap.
(with small SOD -> metallicity) At $a = 3\%$, the system undergoes a transition to a correlated metallic state.
In (b) the chemical potential was set to the center of the gap.

(see fig. 3) Fig. 20.3 presents the central result of this work.

(V(a) is in fig. 3) Panel (a) shows the bare and screened on-site Coulomb interactions in the molecular Ta $d_{3z^2-r^2}$ Wannier orbital for CDW amplitudes $a$ ranging from -4% to +3% around the equilibrium value ($a = 0\%$).

(they repeat the idea that V is decreased because electrons become delocalized) The bare interaction $V$ decreases markedly from 4.2 eV to 1.4eV as $a$ increases from –4% to +3%, reflecting the progressive delocalization of the Wannier orbital: as the orbital spreads out, the Coulomb repulsion is reduced.

(also, screening increases) In parallel, electronic screening becomes stronger due to global changes in the band structure. (which formula is assumed by "electronic screening depends on band structure"?)

(they assume some knowledge about screening and connect more screening with the fact that bands become closer. the question about this was already written before) This trend is evident in the DFT band structures shown in Fig. 20.2a-d, where larger CDW amplitudes bring the valence-band maximum and conduction-band minimum closer together, enhancing screening in the narrow correlated band.

(there is also a screened potential in fig. 3a, here is a description of it) The resulting screened interaction $U$ is plotted in orange in Fig. 20.3a. At the equilibrium distortion ($a = 0\%$), we obtain $U = 0.4$eV. Around this point, $U$ varies approximately linearly, changing by about 0.1 eV for $a = \pm 1\%$.

(next, sp function from U) Next, we employ the screened Coulomb interaction $U$ obtained from cRPA to compute the electronic spectral function of monolayer 1T-$TaS_2$ as a function of the CDW distortion.

(this is the Hubbard model that is there for a SOD. the derivation is written in my discussion section) For each CDW distortion with amplitude $a$, we derive a single-band Hubbard model,

$$\hat{H}_a = \sum_{ij,\sigma} H_a^{(\mathbf{R}_i - \mathbf{R}_j)} \hat{c}_{i\sigma}^\dagger \hat{c}_{j\sigma} + U_a \sum_i \hat{n}_{i\uparrow} \hat{n}_{i\downarrow}, \tag{14.3}$$

where $H_a^{(\mathbf{R}_i-\mathbf{R}_j)}$ represents the single-particle Hamiltonian in the Wannier basis, and $U_a$ denotes the screened on-site interaction in the correlated Ta $d_{3z^2-r^2}$ orbital.

(typical notation) The operators $\hat{c}_{i\sigma}^\dagger$ and $\hat{c}_{i\sigma}$ create and annihilate an electron with spin $\sigma$ at lattice site $\mathbf{R}_i$, respectively, and $\hat{n}_{i\sigma} = \hat{c}_{i\sigma}^\dagger \hat{c}_{i\sigma}$.

(name of a code and method) The resulting model is solved within DMFT using the continuous-time quantum Monte Carlo (CT-HYB) impurity solver implemented in w2dynamics [47](look at this article) .

(value of low temperature) All computations are performed at an inverse temperature $\beta = 1200\text{eV}^{-1}$, corresponding to approximately 10K. ($T = \frac{1}{k_\text{B}\beta} = \frac{1}{(8.6173\times10^{-5}\text{eVK}^{-1})(1200\text{eV}^{-1})} \approx$ 9.67 K)

(another code for the second step) Analytical continuation to real frequencies is carried out using the maximum entropy method (learn the maximum entropy method) as implemented in the ana_cont package [48]. (The imaginary-frequency Green's function calculated by CT-HYB is related to $A(\omega)$ through $G(i\omega_n) = \int_{-\infty}^{\infty} d\omega \frac{A(\omega)}{i\omega_n - \omega}$. Obtaining $A(\omega)$ requires inverting this integral relation. This inversion is called analytical continuation.)

(some extra statements in SM) Further technical details of the DFT+DMFT calculations are provided in the Supplementary Information.

(look at fig. 3b) In equilibrium ($a = 0\%$), the electronic spectral function $A(\omega)$ of monolayer 1T-$TaS_2$ is split into lower (LHB) and upper Hubbard bands (UHB), as shown in Fig. 20.3b.

(distance btw gap) These bands are separated by a Mott gap of approximately 0.4 eV.

(oscillations: bigger positive a -> LHB, UHB come close, bigger negative a -> they go apart) Upon excitation of the CDW amplitude mode, i.e., when $a$ is varied, the Hubbard bands exhibit a pronounced oscillatory behavior: for negative $a$ (enhanced distortion), the bands move further apart, while for positive $a$ (reduced distortion), the Mott gap narrows.

(Ua gives the bands) The evolution of the Mott gap closely follows the variation of the screened interaction $U_a$ obtained from cRPA. (I think that this is the comment about how their code works, they just calculate bands from Ua)

(big distortion -> phase transition) At $a = +3\%$, a transition to a correlated metallic state occurs, as evidenced by the emergence of a pronounced quasiparticle peak at the Fermi level, coexisting with reminiscent LHB and UHB features.

(distribution of electrons influence bands) These results demonstrate that the screened Coulomb interaction, Mott physics, and metal-to–insulator transition in monolayer 1T-$TaS_2$ can be effectively tuned by the CDW amplitude (they mean by $a$) .

(so we can shine light, make orbitals oscillate and electronic bands will be oscillating.) Furthermore, since the Hubbard band positions oscillate in phase with the CDW amplitude mode, this mechanism opens a route to dynamically control electronic correlations through lightwave-driven lattice vibrations. (actually, I don't think that it is so straightforward, because light will also influence electrons, there is a back action of electrons to a lattice, which is not taken into account here. So, it might not work)

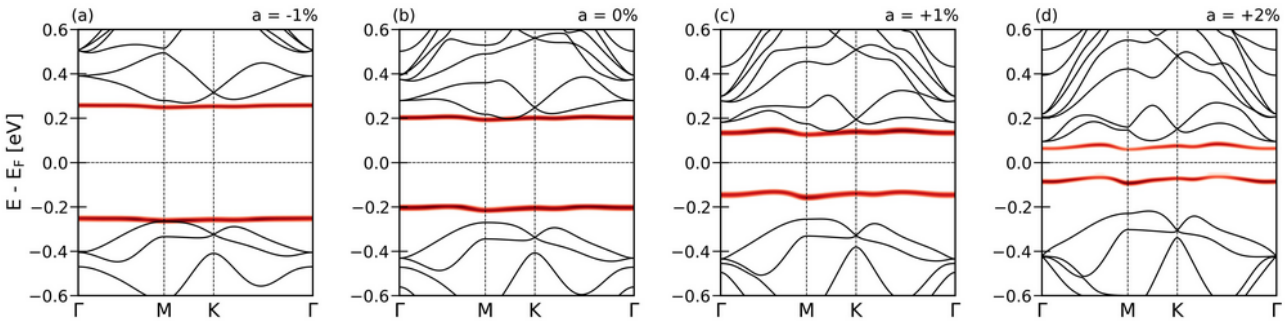


Figure 14.4: (finally, real bands. below is an obvious description of them) **Momentum-resolved spectral function as a function of CDW amplitude.**
The electronic spectral function of the Ta $d_{3z^2-r^2}$ orbital (red) obtained from DFT+DMFT is shown together with the DFT band structure (black).
As the CDW amplitude $a$ is varied from **(a)** -1% to **(d)** +2%, the Mott gap—defined as the spectral gap between the occupied LHB and the unoccupied UHB—gradually decreases from 0.5 to 0.1 eV.

(final bands on fig. 4) Finally, Fig. 20.4 presents the **k**-resolved electronic spectral function (in red), obtained from DMFT and overlaid with the DFT band structure.

(somehow they put new bands correctly near previous bands) The alignment between the correlated Ta $d_{3z^2-r^2}$ band and the remaining states was set using a fully localized limit double-counting correction (double-counting correction???) [49], $E_{\mathrm{DC}} = U_a/2$.

(description of fig. 4) The panels (a-d) show spectra for CDW amplitudes from $a = -1\%$ to $a = +2\%$.

(description of fig. 4) As in the **k**-integrated spectra of Fig. 20.3b, the Ta $d_{3z^2-r^2}$ orbital splits into LHB and UHB, and the Mott gap narrows as the CDW amplitude increases.

(again, repetition about general idea of the proposed experiment) The predicted **k**-resolved spectral signatures can be probed by tr-ARPES experiments, where coherent excitation of the CDW amplitude mode can dynamically tune the Mott state.

### 14.1.3 Discussion

(maybe we need to know how to influence matter dynamically) Discovering effective ways to tune correlated phases in quantum materials remains a central challenge in condensed matter physics, with significant implications for future technologies.

(distortion of SOD -> change of interactions of electrons) Here, we demonstrate a direct and quantitative link between structural distortions and electronic correlations in monolayer 1T-$TaS_2$.

(somehow we calculate distortion of SOD -> change of interactions of electrons) Using a combination of ab-initio and many-body simulations, we show that the CDW amplitude $a$ acts as an efficient tuning parameter for the screened Coulomb interaction and thus for the overall correlation strength.

(repetition of the results) A variation of $a = 1\%$ leads to substantial shifts of the Hubbard bands and a change of the Mott gap up to 0.1 eV, highlighting a strong coupling between lattice and electronic degrees of freedom.

(experiments do not confirm their calculations and they have ideas why) These predicted changes exceed those observed experimentally (what was observed?) [32, 34, 36], which we attribute to

(influence of other layers) (i) enhanced screening effects in bulk samples, where adjacent layers reduce the effective Coulomb interaction, and

(nearly no distortion of SODs) (ii) smaller amplitude-mode oscillations achieved in pump–probe experiments. (what is the dist. ampl in experiment??????)

(but these results still show the connection $a$ -> spectrum ) Importantly, our simulations provide a quantitative link between Hubbard-band shifts and CDW amplitude, offering experimentalists a direct route to extract CDW amplitudes from spectroscopic data.

(we calculated U, it might be useful somehow) Our first-principles evaluation of the screened Coulomb interaction $U$ provides essential microscopic input for interpreting time-resolved spectroscopies of 1T-$TaS_2$ and related materials.

(again, this unjustified promise for dyn. controlling el. properties) It establishes a direct pathway for manipulating Mott insulating states in 2D CDW systems via coherent lattice dynamics.

(we don't know how electrons change in time, but on some timescales the result might make sense) While our equilibrium simulations isolate the impact of structural modulations and do not capture the ultrafast nonequilibrium regime immediately following photoexcitation, they describe the relevant electronic states on longer (100 fs–1 ps) (why these timescales??) timescales, where electrons have thermalized and respond adiabatically to the lattice's 2.4 THz amplitude mode oscillation.

(ideas of more realistic model) Future extensions including coupled electron-phonon dynamics (or make U as dynamical parameter, or use another model, where electrons are dynamically coupled somehow) and nonlocal Coulomb interactions may further refine this picture (this is the extended Hubbard model, which was already analyzed) .

(again repetition of what they did and promise that it is important) Overall, our work uncovers how CDW lattice distortions can govern electronic correlations, offering both a conceptual framework and a practical guide for engineering correlated phases in low-dimensional quantum materials.

### 14.1.4 SM

#### IV. CRPA CALCULATIONS AND CONVERGENCE TESTS

The cRPA [9–11] calculations were performed in VASP using the following 3 step procedure: (i) a self-consistent DFT ground state calculation, followed by (ii) a one-shot exact-diagonalization step to obtain the unoccupied orbitals and the long-wavelength limit of the polarizability, and (iii) the evaluation of the screened interaction using VASP's internal cRPA implementation. To exclude screening processes within the correlated subspace, we employed the projector method [12].

All three steps of the cRPA procedure in VASP were carried out using a Γ-centered $8\times8\times1$k-mesh, a plane-wave energy cutoff of 300 eV, and Gaussian smearing with a width of 0.05 eV. The electronic self-consistency criterion was set to an energy tolerance of $10^{-8}$eV. GW-optimized PAW pseudopotentials were employed to include semicore states relevant for screening.

In the exact-diagonalization and cRPA steps, 1024 bands were included to account for a sufficient number of virtual states. The frequency-dependent dielectric matrix was computed (LOPTICS =.TRUE.) to accurately capture the long-wavelength limit of the polarizability. To improve convergence for the Ta $d$-states, higher angular components in the charge-density mixing were included up to $l = 4$. The energy cutoff for the Coulomb matrix elements in the cRPA step was set to the converged value of 400 eV.

The screened on-site interaction $U$ and the bare on-site interaction $V$ were systematically converged with respect to the plane-wave cutoff (ENCUT), the number of bands (NBANDS), and the k-mesh. The convergence of $U$ and $V$ with ENCUT is shown in Fig. S3, where 512 bands and a coarse $3 \times 3 \times 1$k-mesh were used. A final ENCUT value of 300 eV was chosen.

Convergence with respect to the k -mesh is presented in Fig. S2, keeping ENCUT = 300eV and NBANDS = 512. Computational cost reached 44000 core-hours at a $10 \times 10 \times 1$ mesh; therefore, an $8 \times 8 \times 1$ mesh was adopted for the final calculations as a compromise between accuracy and efficiency.

The number of Kohn-Sham orbitals was determined from the convergence of $U; V$ is insensitive to NBANDS, as its value is determined by the bare Coulomb matrix elements. A coarse $3 \times 3 \times 1$k-grid with ENCUT = 300eV was used to test NBANDS convergence, as shown in Fig. S4(a). NBANDS = 1024 was chosen for all subsequent calculations. The bare on-site interaction $V$ was further converged with respect to the cutoff for the bare Coulomb matrix elements (VCUTOFF), using an $8 \times 8 \times 1$k-mesh, ENCUT = 300eV, and NBANDS = 1024. Convergence is illustrated in Fig. S4(b), and VCUTOFF = 400eV was adopted as the final value.

## V. DMFT CALCULATIONS

The single-band DMFT impurity model was solved using the continuous-time hybridization-expansion quantum Monte Carlo (CT-HYB) impurity solver implemented in w2dynamics. [13] All calculations were performed at an inverse temperature of $\beta = 1200\text{eV}^{-1}$. For the CT-HYB solver, we employed $2 \times 10^7$ measurement sweeps with $10^7$ warmup steps and a decorrelation interval of $N$ Corr = 50. Convergence of the DMFT calculations was verified by monitoring the Green's functions and self-energies at each DMFT iteration.

We measured $G(\tau)$ in the Legendre basis to reduce statistical noise and obtain smooth high-frequency behavior. [14] Including more Legendre orders retains more $\tau$-structure and improves the high-frequency tail. But once the noise floor is reached, higher orders mainly introduce statistical noise. Too small orders on the other hand, bias the tail. To determine a suited order for the Legendre polynomials, test runs with different orders were conducted for each CDW amplitude $a$. The final orders were selected based on visual inspection of the Green's function and self-energy, yielding NLegMax and NLegOrder values between 40 and 70. Stronger CDW distortions (smaller $a$ ) typically benefit from higher orders, while weaker distortions (larger $a$ ) are adequately captured with $40-50$ polynomials. In the case of $a = +2\%$, the Legendre order could be increased beyond 80 without introducing visible noise, consistent with the particularly smooth $G(\tau)$ observed for this CDW amplitude.

## VI. ANALYTICAL CONTINUATION

We used the ana_cont package [15] to perform analytical continuations using the maximum entropy method [16,17] with singular value decomposition. The hyperparameter $\alpha$ was determined using the "chi2kink" method [18,19]. Continuations were carried out in two ways: (i) direct analytical continuation of the Green's function $G(i\omega_n)$, and (ii) analytic continuation of the cumulant

$$M(i\omega_n) = \frac{1}{i\omega_n - \mu - \Sigma(i\omega_n)}, \tag{S3}$$

from which the self-energy $\Sigma(\omega)$ on the real-frequency axis is reconstructed as

$$\Sigma(\omega) = \omega + \mu - \frac{1}{M(\omega)}. \tag{S4}$$

The self-energy obtained from the cumulant-based continuation was used to compute the momentum-resolved spectral function $A(k, \omega)$ shown in Fig. 3 of the main text. The momentum-integrated spectral function, $A(\omega) = \sum_{\mathbf{k}} A(\mathbf{k}, \omega)$, can then be directly compared to the result obtained from the continuation of $G(i\omega_n)$.

To mitigate unphysical artifacts around the Fermi energy, a slight preblur was applied, with the blur width ranging from 0.0 to 0.0125 depending on the CDW amplitude $a$. For the computation of the spectral function, a small imaginary $i\eta$ (ranging from 0.008 to 0.012) was added to the denominator of the real-frequency Green's function.

## 14.2 My Discussion

### 14.2.1 My Conclusion and Analysis of the article

**My conclusion**

Interesting idea, good advanced calculations, but the real usefulness is very unclear.

**Connection with experiments is missing?**

Did they do a calculation which is confirmed or not with experiment?
It is not clear.

**Absence of electronic back-action on the Star-of-David dynamics.**

(GPT:)
A central limitation of the frozen-phonon approach used in the article is that it treats the influence between the lattice and the electrons only in one direction. For each imposed Star-of-David structural coordinate $Q$, the ionic positions determine the electronic Hamiltonian,

$$Q \longrightarrow \hat{H}_{\mathrm{e}}(Q), \tag{14.4}$$

from which the electronic density, Wannier orbitals, screened interaction, and spectral function are calculated,

$$\hat{H}_{\mathrm{e}}(Q) \longrightarrow n_Q(\mathbf{r}) \longrightarrow \{w_Q(\mathbf{r}), U_Q, A(\mathbf{k}, \omega; Q)\}\,. \tag{14.5}$$

The electronic density is therefore allowed to adjust self-consistently to each fixed ionic configuration. However, the reverse influence of the resulting electronic state on the subsequent motion of the Star-of-David structure is not included. In particular, the electronic contribution to the force,

$$F_{\mathrm{e}}(Q) = -\frac{\partial E_{\mathrm{e}}(Q)}{\partial Q}, \tag{14.6}$$

is not used to determine the evolution of $Q$. A self-consistent description would require the ionic coordinate to satisfy an equation such as

$$M_{\mathrm{eff}}\ddot{Q}(t) = -\frac{\partial E_{\mathrm{ion}}(Q)}{\partial Q} - \frac{\partial E_{\mathrm{e}}(Q)}{\partial Q} + F_{\mathrm{ext}}(t), \tag{14.7}$$

or, more generally,

$$M_{\mathrm{eff}}\ddot{Q}(t) = -\left\langle \Psi_{\mathrm{e}}(t) \left| \frac{\partial \hat{H}_{\mathrm{e}}[Q(t)]}{\partial Q} \right| \Psi_{\mathrm{e}}(t) \right\rangle - \frac{\partial E_{\mathrm{ion}}}{\partial Q} + F_{\mathrm{ext}}(t). \tag{14.8}$$

The calculation in the article instead stops after obtaining

$$Q \longrightarrow A(\mathbf{k}, \omega; Q), \tag{14.9}$$

without completing the feedback loop

$$Q(t) \longrightarrow |\Psi_{\mathrm{e}}(t)\rangle \longrightarrow F_{\mathrm{e}}(t) \longrightarrow Q(t + \Delta t). \tag{14.10}$$

Consequently, the calculation does not determine whether a chosen non-equilibrium Star-of-David configuration is dynamically accessible, how long it persists, or whether the electronically induced forces drive it back toward equilibrium, enhance the displacement, or stabilize another configuration. It also does not predict the actual oscillation amplitude or damping. The results should therefore be interpreted as the conditional electronic spectra of externally imposed frozen structures, rather than as a self-consistent prediction of the coupled electron–lattice dynamics. Strictly speaking, electronic effects are not absent from the calculation, since the electrons are solved self-consistently at every fixed $Q$; what is absent is their dynamical back-action on the Star-of-David motion.

**Justification and limitations of adjusting the electronic state to the instantaneous Star-of-David structure.**

(GPT:)

The electronic structure and the Star-of-David lattice distortion mutually influence each other: the ionic positions determine the electronic Hamiltonian, while the electronic state determines the forces acting on the ions. Nevertheless, calculating the electronic spectrum for a sequence of fixed ionic configurations can be justified within the Born–Oppenheimer, or adiabatic, approximation. The essential assumption is a separation of electronic and ionic timescales,

$$\tau_{\mathrm{e}} \ll \tau_{\mathrm{ion}}, \tag{14.11}$$

such that the electrons adapt approximately instantaneously to the slowly evolving ionic configuration. If $Q(t)$ denotes the structural coordinate describing the Star-of-David distortion, the electronic state is approximated by

$$|\Psi_{\mathrm{e}}(t)\rangle \approx |\Psi_{\mathrm{e}}^{\mathrm{eq}}[Q(t)]\rangle, \tag{14.12}$$

and the time-dependent electronic spectrum may be estimated as

$$A(\mathbf{k}, \omega, t) \approx A_{\mathrm{eq}}(\mathbf{k}, \omega; Q(t))\,. \tag{14.13}$$

For the 2.4 THz structural mode considered in the article, the oscillation period is

$$T_{\mathrm{ion}} = \frac{1}{2.4\,\mathrm{THz}} \approx 417\,\mathrm{fs}, \tag{14.14}$$

which is considerably longer than typical electronic adjustment times. This makes the adiabatic approximation plausible after the initial strongly nonequilibrium stage following photoexcitation.

The mutual influence of the electronic and ionic subsystems is not absent within the complete Born–Oppenheimer description. For every fixed $Q$, the electrons determine an electronic energy $E_{\mathrm{e}}(Q)$, which contributes to the effective ionic potential,

$$E_{\mathrm{BO}}(Q) = E_{\mathrm{ion}}(Q) + E_{\mathrm{e}}(Q). \tag{14.15}$$

The electronic state consequently affects the structural motion through the force

$$F_Q = -\frac{dE_{\mathrm{BO}}(Q)}{dQ}. \tag{14.16}$$

A fully self-consistent adiabatic calculation would therefore involve the sequence

$$Q(t) \longrightarrow |\Psi_{\mathrm{e}}^{\mathrm{eq}}[Q(t)]\rangle \longrightarrow E_{\mathrm{BO}}(Q) \longrightarrow F_Q \longrightarrow Q(t + \Delta t). \tag{14.17}$$

The article, however, performs only the first part of this procedure,

$$Q \longrightarrow A_{\mathrm{eq}}(\mathbf{k}, \omega; Q). \tag{14.18}$$

The Star-of-David geometries are imposed as frozen configurations, and the resulting electronic forces are not used to propagate the ions. Consequently, the calculation determines how the equilibrium electronic spectrum depends parametrically on an assumed instantaneous lattice geometry, but it does not predict the actual structural trajectory $Q(t)$, the oscillation amplitude, or the electronic back-reaction on the lattice dynamics.

The frozen-phonon treatment is therefore justified as a conditional adiabatic calculation if the structural motion is independently known or assumed. It becomes unreliable immediately after strong photoexcitation, when the electronic distribution is nonthermal, or whenever electronic and ionic dynamics occur on comparable timescales. In such regimes, the coupled equations

$$i\hbar \frac{\partial}{\partial t} |\Psi_{\mathrm{e}}(t)\rangle = \hat{H}_{\mathrm{e}}[Q(t), t] |\Psi_{\mathrm{e}}(t)\rangle \tag{14.19}$$

and

$$M_{\mathrm{eff}} \ddot{Q}(t) = -\left\langle \Psi_{\mathrm{e}}(t) \left| \frac{\partial \hat{H}_{\mathrm{e}}}{\partial Q} \right| \Psi_{\mathrm{e}}(t) \right\rangle - \frac{\partial E_{\mathrm{ion}}}{\partial Q} \tag{14.20}$$

would need to be solved self-consistently. Thus, the article establishes the conditional relation between a frozen Star-of-David distortion and its electronic spectrum, but does not provide a complete theory of the coupled light-induced electron–lattice dynamics.

### Neglect of nonlocal interactions between Star-of-David clusters

Another limitation of the model is that it includes electron hopping between different Star-of-David clusters but retains only the local Coulomb interaction within a single cluster,

$$\hat{H}_a = \sum_{ij,\sigma} H_a^{(\mathbf{R}_i - \mathbf{R}_j)} \hat{c}_{i\sigma}^{\dagger} \hat{c}_{j\sigma} + U_a \sum_i \hat{n}_{i\uparrow} \hat{n}_{i\downarrow}. \tag{14.21}$$

The hopping matrix elements $H_a^{(\mathbf{R}_i - \mathbf{R}_j)}$ allow electrons to propagate between clusters and therefore generate the dispersion of the correlated band. However, the model neglects the direct Coulomb interaction between electrons occupying neighbouring Star-of-David Wannier orbitals. A more complete description is provided by the extended Hubbard model,

$$\hat{H}_a^{\mathrm{ext}} = \sum_{ij,\sigma} H_a^{(\mathbf{R}_i - \mathbf{R}_j)} \hat{c}_{i\sigma}^{\dagger} \hat{c}_{j\sigma} + U_a \sum_i \hat{n}_{i\uparrow} \hat{n}_{i\downarrow} + \frac{1}{2} \sum_{i \neq j} V_{ij,a} \hat{n}_i \hat{n}_j, \tag{14.22}$$

where $V_{ij,a}$ is the screened inter-cluster Coulomb interaction. Previous first-principles calculations for monolayer commensurate $1T$-$TaS_2$ have found a sizable nearest-neighbour interaction $V$ and have therefore calculated the correlated spectrum using an extended Hubbard model treated within GW+EDMFT [? ]. Those calculations found that the equilibrium insulating state is primarily driven by the local interaction $U$, while the effect of $V$ on the spectrum is comparatively small in the deep Mott regime because charge fluctuations are strongly suppressed. Nevertheless, this does not justify neglecting $V_{ij,a}$ for every distortion. As the Star-of-David Wannier orbital becomes more delocalized and the system approaches the correlated metallic state, inter-cluster interactions, nonlocal screening, and charge fluctuations may become more important. Moreover, single-site DMFT assumes a purely local self-energy,

$$\Sigma_{ij}(\omega) = \delta_{ij} \Sigma(\omega), \tag{14.23}$$

and therefore neglects nonlocal correlation effects between neighbouring clusters. Consequently, the single-band local Hubbard model used in the article provides a simplified description of the distortion-dependent spectrum, but the robustness of its predicted Hubbard-band shifts and metal–insulator transition should be verified using an extended Hubbard model with distortion-dependent $V_{ij,a}$ and, ideally, a method capable of treating nonlocal correlations.

### 14.2.2 Questions about Assumed Knowledge

**Derivation of the effective Hubbard Hamiltonian**

(GPT:)

The single-band Hubbard Hamiltonian is obtained by projecting the electronic problem onto the isolated narrow band at the Fermi level. For each fixed CDW amplitude $a$, the ionic positions are treated within the frozen-phonon approximation, and the corresponding single-particle Hamiltonian $\hat{h}_a$ is calculated using DFT. The resulting narrow, half-filled band is then represented by maximally localized Wannier functions $w_{ia}(\mathbf{r})$, where $i$ labels a Star-of-David cluster centered at $\mathbf{R}_i$. Thus, each Star-of-David cluster constitutes one effective site of the Hubbard model.

Restricting the electronic field operator to this low-energy subspace gives

$$\hat{\psi}_\sigma(\mathbf{r}) \approx \sum_i w_{ia}(\mathbf{r})\hat{c}_{i\sigma}. \tag{14.24}$$

Substitution into the single-particle part of the electronic Hamiltonian yields

$$\hat{H}_{0,a} = \sum_{ij,\sigma} \langle w_{ia}|\hat{h}_a|w_{ja}\rangle \hat{c}^\dagger_{i\sigma}\hat{c}_{j\sigma}. \tag{14.25}$$

The Wannier-basis matrix elements are defined as

$$H_a^{(\mathbf{R}_i-\mathbf{R}_j)} = \langle w_{ia}|\hat{h}_a|w_{ja}\rangle. \tag{14.26}$$

For $i \neq j$, these matrix elements describe electron hopping between different Star-of-David clusters, while the diagonal elements contain the on-site orbital energy. Equivalently, they can be obtained by Fourier transforming the Wannier-interpolated band dispersion,

$$H_a^{(\mathbf{R})} = \frac{1}{N_\mathbf{k}} \sum_\mathbf{k} e^{-i\mathbf{k}\cdot\mathbf{R}} \varepsilon_{\mathbf{k}a}. \tag{14.27}$$

Projecting the screened electron–electron interaction $W_a(\mathbf{r},\mathbf{r}')$ onto the same Wannier subspace produces the general interaction matrix elements

$$U^a_{ijkl} = \int d\mathbf{r}\, d\mathbf{r}'\, w^*_{ia}(\mathbf{r}) w^*_{ja}(\mathbf{r}') W_a(\mathbf{r},\mathbf{r}') w_{ka}(\mathbf{r}) w_{la}(\mathbf{r}'). \tag{14.28}$$

The single-band Hubbard approximation retains only the local density–density matrix element

$$U_a = \int d\mathbf{r}\, d\mathbf{r}'\, |w_{ia}(\mathbf{r})|^2 W_a(\mathbf{r},\mathbf{r}') |w_{ia}(\mathbf{r}')|^2, \tag{14.29}$$

which represents the energy cost of placing two electrons with opposite spins in the same molecular-like Wannier orbital. In the article, $W_a$, and hence $U_a$, is evaluated using the constrained random-phase approximation.

Combining the projected single-particle and interaction terms gives

$$\hat{H}_a = \sum_{ij,\sigma} H_a^{(\mathbf{R}_i-\mathbf{R}_j)} \hat{c}_{i\sigma}^\dagger \hat{c}_{j\sigma} + U_a \sum_i \hat{n}_{i\uparrow}\hat{n}_{i\downarrow}. \tag{14.30}$$

This Hamiltonian is therefore a low-energy effective model rather than the complete microscopic Hamiltonian of $1T$-$TaS_2$. Its construction assumes that the isolated half-filled band dominates the low-energy physics and that nonlocal Coulomb interactions, exchange terms, and correlated hopping can be neglected. The CDW amplitude enters parametrically through both the Wannier Hamiltonian $H_a^{(\mathbf{R}_i-\mathbf{R}_j)}$ and the screened interaction $U_a$, since the lattice distortion modifies the band dispersion, Wannier-orbital localization, and electronic screening.

**How to calculate the electronic structure for a new Star-of-David distortion.**

(GPT:)

The calculation begins by choosing a new ionic configuration of the Star-of-David cluster. The procedure then consists of a DFT calculation, construction of the low-energy Wannier Hamiltonian, evaluation of the screened interaction using cRPA, and solution of the resulting Hubbard model using DMFT. The DFT calculation produces the noninteracting band shown in Fig. 2, whereas the final interacting spectral structure, including the lower and upper Hubbard bands, is obtained only after the DMFT calculation.

**Step 1: Define the distorted ionic structure.**

Let $\mathbf{R}_\alpha^{\mathrm{eq}}$ denote the equilibrium position of atom $\alpha$, and let $\mathbf{e}_\alpha$ describe the displacement pattern associated with the Star-of-David breathing distortion. A structure with amplitude $a$ may be written as

$$\mathbf{R}_\alpha(a) = \mathbf{R}_\alpha^{\mathrm{eq}} + a\,\mathbf{e}_\alpha. \tag{14.31}$$

In the article, the structural parameter is defined more specifically as

$$a = \frac{d - d_{\mathrm{eq}}}{d_{\mathrm{eq}}}, \tag{14.32}$$

where $d$ is the distance between the central Ta atom and an outer Ta atom of the Star-of-David cluster. Therefore,

$$d(a) = (1 + a)d_{\mathrm{eq}}. \tag{14.33}$$

The parameter $a$ is thus a structural coordinate and not the electronic CDW order-parameter amplitude.

**Step 2: Construct the ionic potential.**

The new atomic positions determine the external potential acting on the electrons,

$$V_{\mathrm{ion}}^a(\mathbf{r}) = \sum_\alpha V_\alpha\big(\mathbf{r} - \mathbf{R}_\alpha(a)\big), \tag{14.34}$$

where $V_\alpha$ is the ionic or pseudopotential associated with atom $\alpha$. Changing the Star-of-David distortion therefore changes the potential entering the electronic Hamiltonian.

**Step 3: Solve the Kohn–Sham equations self-consistently.**

For the new ionic configuration, one solves

$$\hat{h}_{\mathrm{KS},a}[n_a]\psi_{n\mathbf{k}a}(\mathbf{r}) = \varepsilon^{\mathrm{KS}}_{n\mathbf{k}a}\psi_{n\mathbf{k}a}(\mathbf{r}), \tag{14.35}$$

with

$$\hat{h}_{\mathrm{KS},a}[n_a] = -\frac{\nabla^2}{2m} + V^a_{\mathrm{ion}}(\mathbf{r}) + V_{\mathrm{H}}[n_a](\mathbf{r}) + V_{\mathrm{xc}}[n_a](\mathbf{r}). \tag{14.36}$$

The density is recalculated from the occupied Kohn–Sham states,

$$n_a(\mathbf{r}) = \sum_{n\mathbf{k}\sigma} f\left(\varepsilon^{\mathrm{KS}}_{n\mathbf{k}a}\right) \left|\psi_{n\mathbf{k}a\sigma}(\mathbf{r})\right|^2, \tag{14.37}$$

where $f$ is the Fermi–Dirac distribution. Because the Hamiltonian depends on $n_a(\mathbf{r})$, these equations must be iterated until self-consistency,

$$n_a^{(m+1)}(\mathbf{r}) \simeq n_a^{(m)}(\mathbf{r}). \tag{14.38}$$

The resulting eigenvalues

$$\varepsilon^{\mathrm{KS}}_{n\mathbf{k}a} \tag{14.39}$$

form the DFT band structure for the chosen distortion. This is the type of band structure shown in Fig. 2.

**Step 4: Select the narrow low-energy band.**

The Star-of-David reconstruction produces a narrow, approximately half-filled band near the Fermi level. Denoting this band by

$$\varepsilon_{\mathbf{k}a} \equiv \varepsilon^{\mathrm{KS}}_{n_0\mathbf{k}a}, \tag{14.40}$$

the low-energy subspace is defined as

$$\mathcal{H}^a_{\mathrm{low}} = \mathrm{span}\left\{|\psi_{n_0\mathbf{k}a}\rangle\right\}_{\mathbf{k}}. \tag{14.41}$$

This band has predominantly Ta $d_{3z^2-r^2}$ character and provides the correlated target subspace used in the subsequent calculation.

**Step 5: Construct the Wannier orbital.**

A localized Wannier orbital centered on Star-of-David cluster $i$ is obtained from the selected Bloch states,

$$|w_{ia}\rangle = \frac{1}{\sqrt{N_{\mathbf{k}}}} \sum_{\mathbf{k}} e^{-i\mathbf{k}\cdot\mathbf{R}_i} e^{i\phi_{\mathbf{k}a}} |\psi_{n_0\mathbf{k}a}\rangle, \tag{14.42}$$

where the phases $\phi_{\mathbf{k}a}$ are chosen to localize the Wannier function. More generally, if several bands are involved in the disentanglement procedure,

$$|w_{ia}\rangle = \frac{1}{\sqrt{N_{\mathbf{k}}}} \sum_{\mathbf{k},n} e^{-i\mathbf{k}\cdot\mathbf{R}_i} U^{(\mathbf{k})}_{na} |\psi_{n\mathbf{k}a}\rangle. \tag{14.43}$$

The new distortion changes both the spatial form and the localization of $w_{ia}(\mathbf{r})$.

**Step 6: Calculate the effective hopping parameters.**

The single-particle Hamiltonian is projected onto the Wannier basis,

$$H_a^{(\mathbf{R}_i-\mathbf{R}_j)} = \left\langle w_{ia} \middle| \hat{h}_{\mathrm{KS},a} \middle| w_{ja} \right\rangle . \tag{14.44}$$

For $i \neq j$, these matrix elements describe hopping between Star-of-David clusters, while for $i = j$ they give the local orbital energy. In the isolated single-band case, they can equivalently be calculated as

$$H_a^{(\mathbf{R})} = \frac{1}{N_{\mathbf{k}}} \sum_{\mathbf{k}} e^{-i\mathbf{k}\cdot\mathbf{R}} \varepsilon_{\mathbf{k}a}. \tag{14.45}$$

The reverse Fourier transformation reconstructs the Wannier-interpolated DFT band,

$$\varepsilon_{\mathbf{k}a} = \sum_{\mathbf{R}} e^{i\mathbf{k}\cdot\mathbf{R}} H_a^{(\mathbf{R})}. \tag{14.46}$$

Its bandwidth is

$$W_a = \max_{\mathbf{k}} \varepsilon_{\mathbf{k}a} - \min_{\mathbf{k}} \varepsilon_{\mathbf{k}a}. \tag{14.47}$$

**Step 7: Calculate the partially screened Coulomb interaction.**

The bare Coulomb interaction in the Wannier orbital is

$$V_a = \int d\mathbf{r}\, d\mathbf{r}'\, |w_{ia}(\mathbf{r})|^2 \frac{e^2}{|\mathbf{r}-\mathbf{r}'|} |w_{ia}(\mathbf{r}')|^2. \tag{14.48}$$

Screening processes outside the correlated target band are described by the constrained polarization

$$\chi_a^r = \chi_a^0 - \chi_a^t, \tag{14.49}$$

where $\chi_a^0$ is the full independent-particle polarization and $\chi_a^t$ contains transitions entirely within the selected target subspace. The partially screened interaction is

$$W_a^r(\omega) = \left[1 - v\chi_a^r(\omega)\right]^{-1} v, \tag{14.50}$$

where $v(\mathbf{r},\mathbf{r}') = e^2/|\mathbf{r}-\mathbf{r}'|$. The static on-site Hubbard interaction is then obtained by projecting $W_a^r(\omega = 0)$ onto the Wannier orbital,

$$U_a = \int d\mathbf{r}\, d\mathbf{r}'\, |w_{ia}(\mathbf{r})|^2 W_a^r(\mathbf{r},\mathbf{r}';0) |w_{ia}(\mathbf{r}')|^2. \tag{14.51}$$

The distortion changes $U_a$ through both the localization of the Wannier orbital and the screening generated by the remaining bands.

**Step 8: Construct the distortion-dependent Hubbard model.**

The DFT-derived single-particle Hamiltonian and the cRPA interaction are combined into

$$\hat{H}_a = \sum_{ij,\sigma} H_a^{(\mathbf{R}_i-\mathbf{R}_j)} \hat{c}_{i\sigma}^\dagger \hat{c}_{j\sigma} + U_a \sum_i \hat{n}_{i\uparrow}\hat{n}_{i\downarrow}. \tag{14.52}$$

Thus, every structural configuration $a$ generates a different effective model,

$$a \longrightarrow \left\{ H_a^{(\mathbf{R})}, U_a \right\}. \tag{14.53}$$

The important correlation scale is approximately determined by

$$\frac{U_a}{W_a}. \tag{14.54}$$

**Step 9: Solve the interacting model using DMFT.**

In single-site DMFT, the lattice self-energy is approximated as local,

$$\Sigma_a(\mathbf{k}, i\omega_n) \approx \Sigma_a(i\omega_n). \tag{14.55}$$

The interacting lattice Green's function is

$$G_a(\mathbf{k}, i\omega_n) = \frac{1}{i\omega_n + \mu - \varepsilon_{\mathbf{k}a} - \Sigma_a(i\omega_n)}. \tag{14.56}$$

The local Green's function is obtained by summing over momentum,

$$G_{\mathrm{loc},a}(i\omega_n) = \frac{1}{N_{\mathbf{k}}} \sum_{\mathbf{k}} G_a(\mathbf{k}, i\omega_n). \tag{14.57}$$

It defines the effective impurity Weiss field through

$$\mathcal{G}_{0,a}^{-1}(i\omega_n) = G_{\mathrm{loc},a}^{-1}(i\omega_n) + \Sigma_a(i\omega_n). \tag{14.58}$$

The corresponding impurity problem is solved, in the article using CT-HYB, to obtain a new impurity Green's function and self-energy,

$$\Sigma_a(i\omega_n) = \mathcal{G}_{0,a}^{-1}(i\omega_n) - G_{\mathrm{imp},a}^{-1}(i\omega_n). \tag{14.59}$$

These equations are iterated until DMFT self-consistency is reached,

$$G_{\mathrm{imp},a}(i\omega_n) = G_{\mathrm{loc},a}(i\omega_n). \tag{14.60}$$

**Step 10: Continue the Green's function to real frequencies.**

The CT-HYB calculation provides the Green's function at imaginary Matsubara frequencies,

$$i\omega_n = i(2n+1)\frac{\pi}{\beta}. \tag{14.61}$$

To obtain the experimentally relevant real-frequency spectrum, one uses the relation

$$G_{\mathrm{loc},a}(i\omega_n) = \int_{-\infty}^{\infty} d\omega \, \frac{A_a(\omega)}{i\omega_n - \omega}. \tag{14.62}$$

The inversion of this equation is an ill-conditioned problem and is regularized in the article using the maximum entropy method. This gives the local spectral function

$$A_a(\omega) = -\frac{1}{\pi} \operatorname{Im} G_{\mathrm{loc},a}^R(\omega). \tag{14.63}$$

**Step 11: Calculate the momentum-resolved interacting spectrum.**

After obtaining the real-frequency self-energy, the retarded Green's function is

$$G_a^R(\mathbf{k}, \omega) = \frac{1}{\omega + \mu - \varepsilon_{\mathbf{k}a} - \Sigma_a^R(\omega)}. \tag{14.64}$$

The momentum-resolved spectral function is therefore

$$A_a(\mathbf{k}, \omega) = -\frac{1}{\pi} \operatorname{Im} \left[ \frac{1}{\omega + \mu - \varepsilon_{\mathbf{k}a} - \Sigma_a^R(\omega)} \right]. \tag{14.65}$$

This is the interacting analogue of the band structure and can contain a lower Hubbard band, an upper Hubbard band, a Mott gap, and, in the metallic regime, a quasiparticle peak. Unlike the DFT bands, these features are not simply eigenvalues of a static single-particle Hamiltonian; they represent electron-removal and electron-addition excitations of the interacting system.

**Complete calculation chain.**

The complete procedure can be summarized as

$$\mathbf{R}_\alpha(a) \longrightarrow V^a_{\text{ion}} \longrightarrow \left\{\varepsilon^{\text{KS}}_{n\mathbf{k}a}, \psi_{n\mathbf{k}a}\right\} \longrightarrow w_{ia} \longrightarrow \left\{H^{(\mathbf{R})}_a, U_a\right\} \longrightarrow \Sigma_a(\omega) \longrightarrow A_a(\mathbf{k}, \omega). \tag{14.66}$$

The DFT part determines how the structural distortion changes the noninteracting electronic states, whereas cRPA and DMFT determine how the same distortion modifies the screened interaction and the final correlated electronic spectrum.

**Why the Hubbard interaction is not explicitly present in DFT?**

In other words, why wouldn't we get the right bands from just DFT?
(GPT:)

**Coulomb interaction in the microscopic Hamiltonian.**

The microscopic electronic Hamiltonian contains an explicit two-particle Coulomb interaction,

$$\hat{H} = \sum_\sigma \int d\mathbf{r}\, \hat{\psi}^\dagger_\sigma(\mathbf{r}) \hat{h}_0 \hat{\psi}_\sigma(\mathbf{r}) + \frac{1}{2} \sum_{\sigma\sigma'} \int d\mathbf{r}\, d\mathbf{r}'\, \hat{\psi}^\dagger_\sigma(\mathbf{r}) \hat{\psi}^\dagger_{\sigma'}(\mathbf{r}') \frac{e^2}{|\mathbf{r} - \mathbf{r}'|} \hat{\psi}_{\sigma'}(\mathbf{r}') \hat{\psi}_\sigma(\mathbf{r}). \tag{14.67}$$

Projection of the second term onto a localized Star-of-David Wannier orbital produces, among other interaction matrix elements, the on-site Hubbard interaction

$$U = \int d\mathbf{r}\, d\mathbf{r}'\, |w_i(\mathbf{r})|^2 \frac{e^2}{|\mathbf{r} - \mathbf{r}'|} |w_i(\mathbf{r}')|^2, \tag{14.68}$$

and the corresponding operator $U \hat{n}_{i\uparrow} \hat{n}_{i\downarrow}$.

**Replacement of the interaction in Kohn–Sham DFT.**

Kohn–Sham DFT maps the interacting many-electron problem onto an auxiliary noninteracting problem,

$$\hat{H}_{\text{KS}} = \sum_\sigma \int d\mathbf{r}\, \hat{\psi}^\dagger_\sigma(\mathbf{r}) \left[\hat{h}_0 + V_{\text{H}}[n](\mathbf{r}) + V_{\text{xc}}[n](\mathbf{r})\right] \hat{\psi}_\sigma(\mathbf{r}). \tag{14.69}$$

The explicit two-particle Coulomb operator is therefore replaced by the Hartree and exchange–correlation potentials, which depend on the average electron density. Consequently, the Kohn–Sham Hamiltonian is quadratic in the fermionic operators,

$$\hat{H}_{\text{KS}} = \sum_{mn,\sigma} h^{\text{KS}}_{mn} \hat{c}^\dagger_{m\sigma} \hat{c}_{n\sigma}, \tag{14.70}$$

and does not contain an explicit quartic operator of the form

$$U \hat{n}_{i\uparrow} \hat{n}_{i\downarrow} = U \hat{c}^\dagger_{i\uparrow} \hat{c}^\dagger_{i\downarrow} \hat{c}_{i\downarrow} \hat{c}_{i\uparrow}. \tag{14.71}$$

**Projection onto the low-energy Wannier subspace.**

Projecting the quadratic Kohn–Sham Hamiltonian onto the narrow half-filled band gives

$$\hat{H}_{\text{DFT},a} = \sum_{ij,\sigma} H^{(\mathbf{R}_i - \mathbf{R}_j)}_a \hat{c}^\dagger_{i\sigma} \hat{c}_{j\sigma}. \tag{14.72}$$

A change of basis cannot transform a quadratic operator into a quartic interaction. Therefore, the Wannier projection of the DFT Hamiltonian provides the hopping matrix elements and on-site energies, but cannot generate an explicit Hubbard interaction.

**Addition of the residual local interaction.**

The missing local interaction must be calculated separately by projecting an appropriately screened two-electron interaction onto the correlated Wannier orbital. In the article, this is performed using the constrained random-phase approximation,

$$U_a = \int d\mathbf{r}\, d\mathbf{r}'\, |w_{ia}(\mathbf{r})|^2 W_a^r(\mathbf{r}, \mathbf{r}') |w_{ia}(\mathbf{r}')|^2, \tag{14.73}$$

where $W_a^r$ is the partially screened interaction obtained after excluding screening processes internal to the correlated target band. The resulting effective low-energy model is

$$\hat{H}_a = \sum_{ij,\sigma} H_a^{(\mathbf{R}_i - \mathbf{R}_j)} \hat{c}_{i\sigma}^\dagger \hat{c}_{j\sigma} + U_a \sum_i \hat{n}_{i\uparrow} \hat{n}_{i\downarrow}. \tag{14.74}$$

**Double-counting correction.**

Because approximate interaction effects are already included in the DFT Hartree and exchange–correlation potentials, adding the explicit Hubbard term introduces a double-counting problem. DFT+DMFT therefore subtracts an approximate double-counting contribution,

$$\hat{H}_{\text{DFT+DMFT}} = \hat{H}_{\text{DFT}} + \hat{H}_U - \hat{H}_{\text{DC}}. \tag{14.75}$$

In the article, the correlated states are aligned with the remaining DFT bands using the fully localized limit correction $E_{\text{DC}} = U_a/2$. Thus, DFT provides the effective single-particle band structure, while cRPA and DMFT restore and treat the explicit local interaction required to describe the Mott gap and Hubbard bands.

### 14.2.3 Questions about Reproduction of Results

**Calculate the V and U. Reproduce at least 1 point on the fig. 3.**

(????? how to do it???)

**Write all these derivation as a one self-consistent derivation**

We basically have jumps from different models and methods. The task is to write all this as a one method, one formalism, without many labels. It will make much more clear understanding.

I asked GPT, but it gave a summary, but not a one derivation. One needs to think about it to do this.

**why do we have SODs, but not insulator? We were told that SODs correspond always to an insulting state?**

(GPT:)

The formation of Star-of-David clusters does not, by itself, necessarily make the system insulating. The structural reconstruction produces a narrow, approximately half-filled electronic band near the Fermi level. Within ordinary DFT, this band crosses the Fermi level and therefore corresponds to a metallic state,

$$\varepsilon_{\mathbf{k}} = E_{\text{F}} \qquad \text{for some } \mathbf{k}. \tag{14.76}$$

An insulating state appears only when an additional mechanism opens a gap in this narrow band. In the model adopted in the article, this mechanism is the strong local Coulomb interaction,

$$U \sum_i \hat{n}_{i\uparrow}\hat{n}_{i\downarrow}. \tag{14.77}$$

When the interaction is sufficiently strong relative to the bandwidth,

$$\frac{U}{W} > \left(\frac{U}{W}\right)_{\mathrm{c}}, \tag{14.78}$$

the half-filled band splits into lower and upper Hubbard bands and a Mott gap appears. A Star-of-David structure therefore creates the narrow band that makes Mott localization possible, but it does not guarantee an insulating state. The final state also depends on $U$, the bandwidth, screening, dimensionality, stacking, doping, and temperature. In the calculations, increasing the structural parameter $a$ broadens the narrow band and reduces the screened $U$, eventually producing a correlated metal despite the continued presence of the Star-of-David pattern.

**So, did they correctly or not correctly calculated the influence of Coulomb interaction?**

(maybe no, there should be another model that should be more precise, but I'll think later about it)

(GPT:)

The calculation reproduces a physically plausible qualitative mechanism: changing the imposed Star-of-David distortion modifies the Wannier-orbital localization and electronic screening, which changes $U_a$, the Hubbard-band positions, and the Mott gap. However, the authors explicitly state that the predicted spectral changes exceed those observed experimentally. Therefore, the model is not quantitatively accurate for the experimental systems and excitation conditions with which it is compared.

This disagreement does not necessarily mean that the cRPA calculation of $U_a$ is mathematically incorrect. The theoretical calculation considers an ideal isolated monolayer and assumes specific frozen structural amplitudes, whereas the experiments may involve bulk or multilayer samples with stronger interlayer screening and smaller actual atomic displacements. Consequently, the comparison depends on both the calculated response,

$$\frac{\partial A(\mathbf{k}, \omega; a)}{\partial a}, \tag{14.79}$$

and the experimentally realized trajectory $a(t)$. A smaller experimental displacement produces a smaller spectral shift even if the calculated dependence on $a$ is correct,

$$\delta E_{\mathrm{exp}} \approx \frac{\partial E}{\partial a} \delta a_{\mathrm{exp}}. \tag{14.80}$$

The article does not calculate $\delta a_{\mathrm{exp}}$ self-consistently and therefore does not provide a complete quantitative prediction of the measured signal.

Nevertheless, the disagreement may also indicate limitations of the electronic model itself. The calculation uses a single correlated band, a static local interaction $U_a$, single-site DMFT, and equilibrium frozen structures. It neglects nonlocal Coulomb interactions, interlayer effects, explicit electron–phonon dynamics, nonthermal electronic occupations, and electronic back-action on the structural motion. Any of these approximations may affect the predicted sensitivity of sensitivity of the Hubbard bands to the distortion.

The appropriate conclusion is therefore that the calculation is qualitatively successful but not experimentally validated at the quantitative level. It identifies a possible mechanism by which structural motion changes electronic correlations, but it does not accurately reproduce the magnitude of the observed spectral shifts. Additional calculations using the actual experimental geometry, independently measured structural amplitudes, and a more complete interaction model would be required to determine whether the discrepancy originates from experimental conditions or from an overestimation of the Coulomb-interaction effect.

**can we say that the band for the whole material is the same as for 1 SOD?**

(GPT:)

No. A single isolated Star-of-David cluster has discrete molecular energy levels rather than a continuous electronic band. The narrow band of the material is formed when equivalent molecular-like orbitals on different Star-of-David clusters hybridize throughout the periodic lattice. If $|w_i\rangle$ denotes one Wannier orbital centered on cluster $i$, the hopping matrix elements are

$$t_{ij} = \langle w_i|\hat{h}|w_j\rangle. \tag{14.81}$$

The band dispersion of the complete periodic material is then obtained by Fourier transforming these inter-cluster matrix elements,

$$\varepsilon_{\mathbf{k}} = \sum_{\mathbf{R}} t(\mathbf{R})e^{i\mathbf{k}\cdot\mathbf{R}}. \tag{14.82}$$

Thus, one Star of David provides one effective orbital, or one effective site, while the periodic lattice of interacting Star-of-David clusters produces the band. If all inter-cluster hopping were neglected,

$$t_{ij} = 0 \qquad \text{for } i \neq j, \tag{14.83}$$

the band would become a dispersionless molecular level. The band of the entire material is therefore derived from the orbital associated with one Star of David, but it is not identical to the spectrum of an isolated Star-of-David cluster.

**connect this theoretical prediction with experimental results**

(GPT:)

The calculations are motivated by time-resolved STM and photoemission experiments in which a pump pulse excites a coherent structural oscillation associated with the Star-of-David pattern. The reported frequency is approximately

$$f = 2.4\,\text{THz}, \tag{14.84}$$

corresponding to a period

$$T = \frac{1}{f} \approx 0.42\,\text{ps}. \tag{14.85}$$

The theoretical calculation provides a relation between an imposed instantaneous structural coordinate $a$ and the electronic spectral function,

$$a \longrightarrow A(\mathbf{k}, \omega; a). \tag{14.86}$$

If the experimentally excited structural trajectory is $a(t)$, the frozen-phonon approximation gives

$$A(\mathbf{k}, \omega, t) \approx A(\mathbf{k}, \omega; a(t))\,. \tag{14.87}$$

The theory therefore predicts that the lower and upper Hubbard bands should oscillate as the Star-of-David structure moves, with the Mott gap decreasing when the system approaches the less distorted structure. Such changes may be probed through time-resolved STM, which measures the local spectral function, or through time-resolved ARPES, which probes the momentum-resolved occupied spectral function.

The predicted spectral changes are larger than those reported experimentally. The authors attribute this quantitative disagreement mainly to stronger screening in bulk or multilayer samples and to smaller experimentally achieved structural oscillation amplitudes. Furthermore, the calculation does not simulate the initial photoexcitation or calculate the actual structural trajectory. It therefore provides an interpretation of the measured spectral oscillations rather than a complete first-principles prediction of the pump–probe experiment.

**how to take into account other effects beyond this model?**

(GPT:)

Several extensions are required for a more complete description. First, nonlocal Coulomb interactions between electrons on different Star-of-David clusters can be included through an extended Hubbard model,

$$\hat{H}_{\text{ext}} = \sum_{ij,\sigma} t_{ij}(Q)\hat{c}^{\dagger}_{i\sigma}\hat{c}_{j\sigma} + U(Q)\sum_{i}\hat{n}_{i\uparrow}\hat{n}_{i\downarrow} + \frac{1}{2}\sum_{i\neq j} V_{ij}(Q)\hat{n}_i\hat{n}_j. \tag{14.88}$$

Such a model could be treated using GW+EDMFT or related methods that include both local and nonlocal screening effects.

Second, the structural coordinate should be treated dynamically rather than imposed as a frozen parameter. A semiclassical description would couple the electronic state to the ionic equation of motion,

$$i\hbar\frac{\partial}{\partial t}|\Psi_{\text{e}}(t)\rangle = \hat{H}_{\text{e}}[Q(t),t]|\Psi_{\text{e}}(t)\rangle, \tag{14.89}$$

$$M_{\text{eff}}\ddot{Q}(t) = -\left\langle \Psi_{\text{e}}(t)\left|\frac{\partial \hat{H}_{\text{e}}}{\partial Q}\right|\Psi_{\text{e}}(t)\right\rangle - \frac{\partial E_{\text{ion}}}{\partial Q} + F_{\text{pump}}(t). \tag{14.90}$$

This would include the electronic back-action on the Star-of-David motion and determine the structural trajectory self-consistently.

Third, electron–phonon coupling can be introduced explicitly, for example,

$$\hat{H}_{\text{e-ph}} = \sum_{ij,\sigma,\nu} g^{\nu}_{ij}\left(\hat{b}_{\nu} + \hat{b}^{\dagger}_{\nu}\right)\hat{c}^{\dagger}_{i\sigma}\hat{c}_{j\sigma}, \tag{14.91}$$

or through a phonon-dependent interaction,

$$U(Q) \simeq U_0 + \frac{\partial U}{\partial Q}Q. \tag{14.92}$$

These terms would permit the investigation of phonon-assisted processes, polaronic effects, and the dynamical modulation of both the hopping and Coulomb interaction.

Finally, multiband models, cluster DMFT, nonequilibrium DMFT, and spatially inhomogeneous calculations could be used to include other orbitals, short-range inter-cluster correlations, nonthermal electronic distributions, domain walls, stacking effects, and differently distorted neighbouring Star-of-David clusters. These extensions would make the model more realistic, but would also considerably increase its computational complexity.

### 14.2.4 Things That I Maybe Understood Wrongly

**Treating the Star-of-David clusters as isolated groups of attracted atoms.**

**What I said (approximately 00:06:39–00:07:08 and 00:27:43–00:28:00):** *"Atoms are attracted to the central atom, and near this star there is another star. The other atoms do not form a Star of David; they just remain there without being distorted."* This description incorrectly suggests that the crystal consists of isolated thirteen-atom objects separated by unaffected Ta atoms. In the commensurate CDW structure, the Star of David is the repeated $\sqrt{13} \times \sqrt{13}$ supercell of the Ta lattice. The central Ta atom and the two surrounding rings are inequivalent sites within this periodic distortion, and the neighbouring stars form a triangular superlattice. Thus, the calculation is not about a collection of isolated clusters embedded among undistorted atoms; it is about a periodically reconstructed monolayer. The word "attracted" is also too literal: the atoms undergo a collective displacement pattern determined by the lattice energetics, rather than being bound to the central atom as an isolated molecule would be.

**Calling the CDW amplitude merely an atomic displacement and a misleading name.**

**What I said (approximately 00:14:29–00:15:17):** *"By charge-density-wave amplitude they mean just the displacement of the atoms of a lattice. Strictly speaking, it is a very confusing label because a charge-density wave is about charge, not about the lattice."* This separates the electronic and structural parts of a CDW too sharply. In $1T$-$TaS_2$, the periodic charge modulation and the periodic lattice distortion are coupled components of the same CDW order. The 2.4 THz amplitude mode is a collective mode in which the magnitude of this coupled order changes; experimentally and computationally, its structural component is represented by the breathing displacement of the Ta atoms. In this paper, $a = (d - d_{\mathrm{eq}})/d_{\mathrm{eq}}$ is specifically a structural coordinate used as a proxy for the CDW amplitude. It is fair to note that $a$ is not by itself a direct measurement of the electronic charge modulation, but it is not correct to imply that calling it a CDW amplitude mode is physically inappropriate.

**Reversing the meaning of increasing distortion amplitude.**

**What I said (approximately 00:36:59–00:37:17 and 00:59:16–00:59:49):** *"If you have a bigger distortion, then you have a smaller gap; if you have a smaller distortion, you have a bigger gap. If we increase the distortion, the bare and screened interactions decay."* This reverses the sign convention used in the article. A positive $a$ means that the outer Ta atoms move farther from the central Ta atom: the star expands and the structure approaches the undistorted phase. Hence increasing $a$ means a *reduction* of the equilibrium CDW distortion. With increasing $a$, the Wannier orbital becomes more delocalized, the bandwidth grows, the bare matrix element $V$ and screened on-site interaction $U$ decrease, and the Mott gap narrows. Negative $a$ contracts the star, enhances the CDW distortion, localizes the orbital more strongly, and increases the gap. Thus the correct trend is

$$a \uparrow \quad \Longrightarrow \quad \text{weaker CDW distortion}, \quad W_{\mathrm{band}} \uparrow, \quad U \downarrow, \quad \Delta_{\mathrm{Mott}} \downarrow . \tag{14.93}$$

**Interpreting the metallic state as the disappearance of the Hubbard bands.**

**What I said (approximately 00:09:56–00:10:23):** *"At three percent there is no gap and no two Hubbard bands, but one metallic state where the bands have collapsed into one conducting region."* Gap closure does not mean that the lower and upper Hubbard-band features disappear or merge into a single ordinary band. At $a = +3\%$, the DMFT spectrum develops a quasiparticle peak at the Fermi level while remnants of the lower and upper Hubbard bands remain at higher binding energies. This three-feature structure is characteristic of a correlated metal close to

a Mott transition. The correct statement is therefore that the Mott gap closes and coherent low-energy spectral weight appears, coexisting with incoherent Hubbard-band features.

**Treating a remaining lattice distortion and a closed Mott gap as contradictory.**

**What I said (approximately 00:21:03–00:21:35):** *"Usually a lattice deformation gives a gap, but here a special deformation gives no gap, so this is contradictory to the well-known theory."* There is no contradiction because the insulating gap discussed here is a correlation-driven Mott gap, not a gap determined solely by whether a lattice distortion is present. The CDW reconstruction creates a narrow half-filled band, but whether this band is Mott insulating depends mainly on the competition between interaction and kinetic energy, commonly characterized by $U/W_{\text{band}}$. As $a$ increases, both $U$ decreases and $W_{\text{band}}$ increases, so $U/W_{\text{band}}$ can cross the metal–insulator boundary even while a nonzero structural distortion remains.

**Reducing the bulk–monolayer distinction to two universally separate mechanisms.**

**What I said (approximately 00:22:25–00:23:07):** *"If you have bulk, then you have a band insulator and not the Mott mechanism; in a monolayer you have a Mott insulator. There are two mechanisms, and both approaches are correct."* This is too categorical. The article describes a current microscopic picture in which parts of bulk $1T$-$TaS_2$ form dimerized, band-insulating bilayers, while AC-stacked monolayer-like units may also occur. Stacking, interlayer hybridization, correlations, and the detailed stacking sequence all matter, and the character of the bulk insulating state remains an active topic. The safer statement is that the isolated monolayer is well described as a Mott insulator, whereas interlayer dimerization can generate an important band-insulating contribution in bulk material; it is not a universal rule that correlations are absent in the bulk.

**Saying that the CDW distortion itself produces the two Hubbard bands.**

**What I said (approximately 00:23:38–00:24:14 and 00:26:09–00:26:48):** *"Finally this distortion gives us two bands. They could have written that the charge-density wave gives these two bands and not shown the intermediate band without correlations."* The two computational stages represent different physics and should not be conflated. The structural CDW reconstruction produces the isolated, narrow, half-filled Kohn–Sham band shown in red in Fig. 2. When the effective Coulomb interaction is subsequently treated using DMFT, the spectral weight associated with that band separates into a lower and an upper Hubbard band, producing the Mott gap. Therefore,

$$\text{CDW reconstruction} \longrightarrow \text{narrow half-filled band}, \qquad \text{strong correlations} \longrightarrow \text{LHB and UHB}. \tag{14.94}$$

The DFT result is not a disposable intermediate picture; it supplies the hopping Hamiltonian, Wannier orbital, bandwidth, and polarization processes needed to construct the effective interacting model.

**Describing the THz probe as photoemission into the STM tip.**

**What I said (approximately 00:28:31–00:29:24):** *"The second pulse kicks electrons from the material, they go to the microscope tip, and the tip measures the current."* This description mixes THz-driven STM with photoemission. In the proposed THz-STM experiment, the delayed THz electric-field transient changes the instantaneous voltage across the tip–sample junction and thereby drives tunnelling current. The electrons tunnel through the junction; they are not photoemitted into vacuum and then collected by the tip. By scanning the delay relative

to the NIR pump, the experiment samples the time-dependent local tunnelling response and hence the evolving local density of states.

**Assuming that a band is calculated from one isolated Star of David.**

**What I said (approximately 00:41:05–00:42:06):** *"Here we mean the band corresponding to one cluster. Let us assume that we can calculate the band from just one cluster and not bother much about interactions between clusters."* A single isolated cluster has discrete molecular levels, not a Bloch band. The DFT calculation uses a periodically repeated Star-of-David supercell, so the result is already the band structure of an extended crystal. In the Wannier representation, one low-energy orbital is associated with each Star-of-David cell, and the matrix elements $H_a^{(\mathbf{R}_i-\mathbf{R}_j)}$ explicitly describe hopping between different cells. This inter-cluster hopping produces the dispersion and bandwidth of the narrow band. What the simplified model neglects is not hopping, but nonlocal Coulomb terms such as $V_{ij}n_in_j$ and nonlocal components of the self-energy.

**Interpreting the frozen-phonon approach as the absence of a phonon.**

**What I said (approximately 00:44:58–00:45:19):** *"Maybe frozen phonon means that nothing is breathing; they just assume that the electron states adjust to the lattice deformation."* The frozen-phonon method represents a phonon by a series of static snapshots along its normal-mode displacement pattern. The ions are frozen only while the electronic problem is solved for a particular value of $a$; the collection of configurations samples the breathing-mode coordinate. The method therefore retains the structural geometry of the phonon but does not dynamically propagate the mode, predict its amplitude or damping, or include scattering among phonons. Assuming that the electrons adjust to each snapshot is the additional adiabatic approximation.

**Concluding that the paper contains no electron–phonon connection.**

**What I said (approximately 00:46:17–00:47:04 and 01:29:31–01:30:30):** *"The whole cluster is formed because of electron–phonon interaction, so it is hard to understand how they can say that electron–phonon interactions are not included. Here we do not see any connection between electrons and phonons."* The article includes a *parametric, static* electron–lattice coupling: changing the phonon coordinate $a$ changes the Kohn–Sham Hamiltonian, the Wannier orbital, the hopping amplitudes, screening, $U_a$, and the electronic spectrum. What it neglects is an *explicit dynamical* electron–phonon Hamiltonian, electronic scattering by phonons, phonon self-energies, energy transfer, and the feedback of the electronic state on the subsequent ionic trajectory. Thus it is correct to criticize the absence of coupled nonequilibrium electron–phonon dynamics, but not to say that the calculation contains no electron–phonon connection at all.

**Identifying a Wannier isosurface with the wavefunction of one particular electron.**

**What I said (approximately 00:48:36–00:50:21):** *"These are just wavefunctions of one electron. There are thirteen electrons in the cluster, twelve create the cluster, and one hops from one star to another; this is the wavefunction of that one electron."* A Wannier function is a localized single-particle basis orbital constructed from Bloch states of the selected band. It is not the many-body wavefunction of a labelled electron, and an electron is not permanently assigned to that orbital. In the usual low-energy electron-counting picture, thirteen Ta $5d$ electrons per Star-of-David cell form reconstructed molecular bands: twelve electrons fill lower-lying states and one electron per cell remains in the narrow half-filled band. The plotted Wannier orbital represents the local basis state spanning that band; its occupation fluctuates and it can

host spin-up and spin-down electrons. Moreover, the displayed red and blue isosurfaces show opposite signs (phases) of the orbital amplitude, not positive and negative charge densities.

**Confusing the screened kernel with the local Hubbard interaction.**

**What I said (approximately 00:54:21–00:55:19):** *"Maybe the formula is for an electron in one cluster interacting with an electron in another cluster, or for two electrons in the same cluster; perhaps it is valid for both."* The RPA quantity $W(\mathbf{r}, \mathbf{r}')$ is indeed a general screened interaction kernel, but the $U$ used in this paper is a specific matrix element of the *partially* screened cRPA interaction projected onto the same local Wannier orbital. It is the energy cost for opposite-spin occupation of one effective Star-of-David site. Intersite matrix elements $V_{ij}$ could be obtained by projecting the same kernel onto Wannier orbitals on different cells, but those nonlocal terms are omitted from the single-band Hubbard Hamiltonian used here. Therefore the plotted $U$ should not be interpreted simultaneously as both the on-site and inter-cluster interaction.

**Calling $f$ in the polarization formula the Fermi energy.**

**What I said (approximately 00:56:58–00:57:08):** *"$f$ is the Fermi energy, and the epsilons are the energies."* Here $f_{n\mathbf{k}}$ is the Fermi–Dirac *occupation function*, not the Fermi energy. The numerator

$$f_{n'\mathbf{k}+\mathbf{q}} - f_{n\mathbf{k}} \tag{14.95}$$

selects transitions between states with different occupations, while the denominator contains their energy difference. The target-space label $t$ means that the band indices are restricted to the correlated low-energy subspace—here, the narrow band represented by the Star-of-David Wannier orbital.

**Interpreting $V$ and $U$ as total energies of a cluster.**

**What I said (approximately 00:58:27–00:59:16):** *"Maybe it is the total energy of one cluster; if we increase distortion, this energy decreases."* Neither curve in Fig. 3(a) is the total energy of a Star-of-David cluster. The curve labelled $V$ is the bare on-site Coulomb matrix element evaluated in the distortion-dependent Wannier orbital, while $U$ is its partially screened cRPA counterpart and is the parameter used in the Hubbard Hamiltonian. They quantify the repulsive energy cost of double occupation of that effective orbital. A structural total-energy curve would instead be required to determine the equilibrium position, restoring force, and phonon frequency; such a curve is not what Fig. 3(a) shows.

**Reducing the spectral function to a broadened delta function.**

**What I said (approximately 01:00:17–01:00:41):** *"The spectral function should generally be a delta function for a band, and in reality we have an approximation to a delta function; the band is where the spectral function has a peak."* This is true only for a noninteracting quasiparticle with infinite lifetime at a fixed momentum, for which $A(\mathbf{k}, \omega)$ contains a delta peak at the one-particle energy. In the interacting DMFT solution, the spectral function contains finite-width coherent and incoherent features determined by the frequency-dependent self-energy. The Hubbard bands are not merely numerically broadened delta functions. In addition, Fig. 3(b) shows the momentum-integrated $A(\omega)$, so its peaks collect spectral weight over all momenta rather than tracing a single dispersion. Fig. 4 shows $A(\mathbf{k}, \omega)$ and therefore contains the momentum-resolved dispersion.

**Saying that the Mott gap follows from $U_a$ alone.**

**What I said (approximately 01:11:35–01:11:57 and 01:03:59–01:04:26):** *"The gap is present because of the parameter $U_a$; the next step is simply to get the spectral function from $U$."* The spectral function is not determined by $U_a$ alone. For each distortion, the DMFT input contains both the full Wannier hopping Hamiltonian $H_a^{(\mathbf{R}_i-\mathbf{R}_j)}$, which fixes the dispersion and bandwidth, and the screened interaction $U_a$. The chemical potential and temperature also enter. The closing of the gap with increasing $a$ is especially strong because $U_a$ decreases while the bandwidth simultaneously grows. A more accurate schematic dependence is

$$A_a(\mathbf{k},\omega) = \mathcal{F}_{\mathrm{DMFT}}\left[H_a^{(\mathbf{R})}, U_a, T, \mu\right], \tag{14.96}$$

not $A = \mathcal{F}(U)$.

**Calling the DFT band unreal and only the momentum-resolved DMFT plot the "true bands."**

**What I said (approximately 00:47:19–00:47:58 and 01:11:53–01:13:33):** *"In reality they do not have this red band; they have the gapped plot. Figure 2 is distracting, and now in Figure 4 we see the true bands."* Figures 2–4 display different, complementary quantities. Figure 2 gives the Kohn–Sham band structure and the Wannier representation used to construct the low-energy Hamiltonian. Figure 3(b) gives the momentum-integrated interacting spectral function, which is useful for seeing the Mott gap and Hubbard-band spectral weight. Figure 4 gives the momentum-resolved interacting spectral function overlaid with the DFT bands. The DFT band is not an experimental interacting excitation spectrum, but it is a well-defined and essential theoretical starting point; likewise, the momentum-integrated spectrum is not less real than the momentum-resolved one. They answer different questions.

**Reading a quantitative discrepancy as a failure of experimental confirmation.**

**What I said (approximately 01:16:29–01:17:24):** *"The predicted changes exceed the experimental ones, so they say that the theory is not confirmed by experiment and perhaps should not be taken seriously."* "Exceed" describes a mismatch in magnitude, not necessarily a disagreement in the sign or qualitative mechanism. The authors argue that their idealized monolayer calculation predicts larger Hubbard-band shifts than those measured in bulk pump–probe experiments because bulk layers provide additional screening and the experimental mode amplitude is smaller than the amplitudes sampled in some calculations. This comparison limits direct quantitative application, but it does not by itself falsify the predicted coupling between the structural coordinate and the spectrum. A fair conclusion is that the qualitative relation is physically motivated, whereas quantitative comparison requires the actual experimental $a(t)$ and a model appropriate to the measured sample.

**Concluding that electronic back-action makes the frozen configurations meaningless.**

**What I said (approximately 01:24:48–01:29:11):** *"We will never have this configuration, because the electronic distribution will immediately influence it and everything will return to equilibrium. Therefore it may make no sense to calculate the spectrum for different distortions."* The criticism correctly identifies what the calculation does not provide: it does not determine the driven trajectory $a(t)$, damping, or electronic force on the phonon. However, it is incorrect to conclude that the displaced configurations cannot exist or that the conditional spectra are meaningless. A coherently excited phonon has inertia and oscillates about equilibrium, and the pump can maintain a finite displacement for part of the cycle. If electronic

relaxation is faster than the approximately 417 fs period of the 2.4 THz mode, the electronic state can approximately follow the instantaneous ionic configuration. Then

$$A(\mathbf{k}, \omega, t) \simeq A_{\mathrm{eq}}(\mathbf{k}, \omega; a(t)) \tag{14.97}$$

is a useful adiabatic mapping. What remains unpredicted is $a(t)$ itself. Thus the proper limitation is that the work is a conditional frozen-structure calculation, not a self-consistent theory of the complete pump-driven dynamics.

**Saying that hopping between Star-of-David cells is neglected.**

**What I said (approximately 01:32:21–01:33:16):** *"How useful can it be to neglect the Star-of-David hopping? Here they neglect the interaction between different polarons or blobs of electron density."* The Hamiltonian explicitly retains inter-cell hopping through $H_a^{(\mathbf{R}_i - \mathbf{R}_j)}$ for $i \neq j$; without it, the narrow band would have no dispersion. The omitted terms are the direct nonlocal Coulomb interactions $V_{ij}$ between occupations of different Wannier orbitals and the nonlocal spatial dependence of the self-energy in single-site DMFT. Therefore the valid question is whether neglecting intersite *Coulomb correlations* is accurate, especially near the metallic transition—not whether hopping was neglected.

**Treating a prescribed $U(t)$ as a complete electron–phonon dynamics model.**

**What I said (approximately 01:21:16–01:21:41):** *"If we make the Hubbard U dynamically changeable, that can already capture the electron–phonon dynamics."* A time-dependent $U(t) = U[a(t)]$ may capture one important consequence of the driven lattice coordinate, namely the modulation of screening and local repulsion. It is not by itself a complete electron–phonon theory. The hopping amplitudes and orbital basis also change with $a(t)$, and a self-consistent model must specify the phonon coordinate, its equation of motion, the electronic force, dissipation, and possibly nonthermal electronic occupations. At minimum, the effective electronic Hamiltonian would contain both $H_{a(t)}^{(\mathbf{R})}$ and $U_{a(t)}$, coupled to an equation for $a(t)$.

**Concluding that the calculation most likely has no practical use.**

**What I said (approximately 01:40:47–01:41:08):** *"Can it be used? Most likely no; most likely it cannot be used. It mainly teaches us that an efficient code can do the calculation."* This conclusion is stronger than the limitations justify. The paper supplies a microscopic, distortion-dependent mapping from structure to the bare interaction, screened $U$, bandwidth, Hubbard-band positions, and metal–insulator crossover. Even without predicting the pump-driven trajectory, that mapping can be combined with a measured or independently calculated $a(t)$ to interpret time-resolved STM or ARPES spectra, and it identifies mechanisms that simpler calculations with a fixed empirical $U$ miss. The appropriate conclusion is therefore that the work is not a complete predictive simulation of a pump–probe experiment, but it provides a quantitatively useful electronic-structure component for such a description.

### 14.2.5 Potential Future Research Directions

**Derive such results using polaronic theory**

(??? I don't know how to do it)

# 15 Orbital-driven Mottness collapse in 1T-$TaS_{2-x}Se_x$ transition metal dichalcogenide by Qiao et al. (2016)

**Abstract**

The layered transition metal dichalcogenide 1T-$TaS_2$ has been recently found to undergo a Mott-insulator-to-superconductor transition induced by high pressure, charge doping, or isovalent substitution. By combining scanning tunneling microscopy (STM) measurements and first-principles calculations, we investigate the atomic scale electronic structure of 1T-$TaS_2$ Mott insulator and its evolution to the metallic state upon isovalent substitution of S with Se. We identify two distinct types of orbital textures - one localized and the other extended - and demonstrate that the interplay between them is the key factor that determines the electronic structure. Especially, we show that the continuous evolution of the charge gap visualized by STM is due to the immersion of the localized-orbital-induced Hubbard bands into the extended-orbital-spanned Fermi sea, featuring a unique evolution from a Mott gap to a charge-transfer gap. This new mechanism of orbital-driven Mottness collapse revealed here suggests an interesting route for creating novel electronic states and designing future electronic devices.

## 15.1 INTRODUCTION

The vicinity of a Mott insulating phase has constantly been a fertile ground for finding exotic quantum states, most notably the high $T_c$ cuprates and colossal magnetoresistance manganites. The layered transition metal dichalcogenide 1T-$TaS_2$ represents another intriguing example. More interestingly, it has been recently found that 1T-$TaS_2$ undergoes a Mott-insulator-to-superconductor transition induced by high pressure [1], charge doping [2, 3, 4, 5], or isovalent substitution [6, 7, 8].

The nature of the Mott insulator phase and transition mechanism to the conducting state is still under heated debate. Much of the challenge originates from a series of complicated charge density wave (CDW) orders entwined with the electronics phases [9, 10, 11]. The Mott insulator phase is believed to be a consequence of the commensurate CDW order [11, 12, 13, 14, 15]. Superconductivity emerges as the Mott insulator state is suppressed, and the electronic phase diagram [1, 4, 7, 5] displays many similarities to that of the cuprates.

Different scenarios were proposed to account for the Mott-insulator-to-superconductor transition. For the pressurization case, it was assumed that the superconductivity formed within the metallic interdomain spaces of the nearly commensurate CDW (NCCDW) phase [1]. This scenario is consistent with the phase separation picture of the NCCDW phase [16]. It also naturally explains the continuous extension of superconductivity into the incommensurate CDW (ICDW) phase, where the interdomain spaces grow to the whole sample and the CCDW domains completely disappear. On the other hand, for the chemical doping cases, angle-resolved photoemission measurements did not reveal any signature of phase separation [3], suggesting instead strong electronic hybridization across domains. The electrons were found to form a global melted Mott state with a single electron pocket around the $\Gamma$ point, from which superconductivity could emerged. Another perspective on the melted Mott state was recently developed by viewing doped 1T-$TaS_2$ as a disordered Mott insulator [17], in which the interplay of strong interaction and disorder generates a novel pseudogap metallic state.

Most of the previous explanations were essentially based on a one-band Hubbard model [17, 18, 19], and the efforts were made to reproduce the phase transition by tuning some parameters. The problems, however, are that the microscopic meaning of the one band basis is ambiguous, and the dependence of the associated parameters on the material details is unclear. Consequently, it heavily relies on the researcher's perspective to select the key parameters and

the tuning range. This leads to rather controversial interpretations emphasizing on different aspects of the material [1, 3, 6, 8, 20, 21, 22, 23, 17, 24, 25], such as spin-orbit coupling, interlayer coupling, p-d hybridization and disorder.

The aim of the present Article is to establish a concrete foundation that describes the low-energy physics in 1T-$TaS_2$. By combining STM measurements and *ab initio* Wannier function analysis, we single out two distinct types of orbital textures, and formulate a multi-orbital effective Hamiltonian based on these two orbital textures. This construction reveals an orbital-driven origin of the Mott-insulator-to-superconductivity transition in 1T-$TaS_2$. We map out the complete transition process by inhomogeneous Se substitution, and demonstrate an excellent agreement between experiment and theory. The remainder of the Article is organized as follows. Section II describes the experiment and calculation methods. Section III presents the STM and first-principles data on pristine $TaS_2$, based on which the two types of most relevant orbital textures are identified. Section IV discusses results on Se-substituted samples. By taking advantage of the chemical inhomogeneity in these samples, we map out the complete collapsing process of the Mott phase. Section V discusses the theoretical formalism of the orbital-driven transition in details. Section VI concludes this Article.

## 15.2 EXPERIMENT AND CALCULATION METHODS

The high-quality single crystals of 1T-$TaS_{2-x}Se_x$ ($0 < x < 2$) are synthesized by chemical vapor transport method with iodine as the transport agent. The powder of Ta, S, and Se is weighted stoichiometrically and thoroughly grounded. Then the mixture together with 150 mg $I_2$ is sealed into an evacuated quartz tube and placed into a two-zone furnace with the temperature gradient of 1253 K-1153 K for 1 week. The products are washed with ethanol to remove the iodine at the surface.

The STM experiments are performed with a cryogenic variable temperature ultrahigh vacuum STM system. The 1T-$TaS_{2-x}Se_x$ crystal is cleaved in situ at $T = 77$ K, and the measurement is taken at 5 K with an electrochemically etched tungsten tip calibrated on a clean Au (111) surface [26]. The STM topography is taken in the constant current mode, and the $dI/dV$ spectra are obtained with a standard lock-in technique with modulation frequency $f = 423$ Hz.

The first-principles calculation based on the density functional theory is performed using the Vienna *Ab initio* Simulation Package [27, 28, 29, 30] with a 280 eV plane-wave basis cutoff. The Perdew-Burke-Ernzerh generalized gradient approximation [31] and the projector augmented wave method [32] are employed. The Wannier function analysis is performed using the WANNIER90 code [33, 34, 35] on the plain DFT level in order to quantify the single-electron properties, such as p-d hybridization and interatomic hopping. The $+U$ correction is employed to compare with the STM $dI/dV$ spectra, which captures the Coulomb interaction of Ta 5d orbitals on the mean-field level, following the simplified (rotational invariant) approach introduced by Dudarev [36, 37]. We employ the lattice parameters determined by experiment [38], and relax the atomic coordination self-consistently until the forces are less than 0.002 eV/Å. To simulate the CCDW order, we employ a $\sqrt{13} \times \sqrt{13}$ supercell consisting of 13 Ta atoms forming a Star-of-David (SD) structure. The integration over the Brillouin zone is obtained on a $\Gamma$-centered $6 \times 6 \times 1$ k mesh. The electronic self-consistent iterations are converged to $10^{-5}$ eV precision of the total energy.

It has been shown by earlier studies that at least for band structure effects alone, 1T-$TaS_2$ should always be describable as a quasi-two-dimensional system [11, 39]. Indeed, recent calculations [25] emphasizing the inter-layer orbital texture showed that the Mott-insulating ground state cannot be correctly reproduced once an artificial c-axis stacking sequence is imposed. On the other hand, in 1T-$TaSe_2$ inter-layer coupling plays a more important role [40]. Therefore, we will restrict our discussion within the S-riched regime, and focus on the *intralayer* CCDW

order and orbital textures. All our calculations are based on a 2D structural configuration with a 15 Å-thick vacuum space to eliminate coupling between different layers.

## 15.3 ORBITAL TEXTURES IN PRISTINE $TaS_2$

### 15.3.1 Structural and electronic properties

1T-$TaS_2$ has a layered structure as shown in Fig. 21.1(a), in which the Ta atoms form a planar triangular lattice sandwiched by two S-atom planes. STM is an ideal experimental technique for probing the atomic scale electronic structure of such a quasi-2D material. Figure 21.1(b) displays the STM topographic image of pristine 1T-$TaS_2$, which clearly reveals the CCDW order with a $\sqrt{13} \times \sqrt{13}$ superlattice where 13 Ta atoms form a Star-of-David (SD) structure. Note that the bright spots correspond to the S atoms lying in the uppermost layer, and the position of the Ta atoms can be determined according to the octahedral coordination. In Fig. 21.1(c) we show the spatially averaged differential conductance $dI/dV$, which is approximately proportional to the electron density of states (DOS), of pristine 1T-$TaS_2$. An energy gap around the Fermi level ($E_F$) can be clearly observed, which is attributed to the Mott-Hubbard gap of the insulating CCDW phase.

These spectroscopic features can be captured by density functional theory (DFT) calculations including the onsite Hubbard $U$ correction in a Hartree-Fock manner [41]. As shown in Fig. 21.1(d), there is a full charge gap around the ($E_F$), which is bounded by two narrow bands, corresponding to the upper and lower Hubbard bands (UHB/LHB), respectively. The gap size is found to depend on the Hubbard repulsion $U$ and a choice of $U = 2.27$ eV as previously derived from the linear-response calculation is used to reproduce the experimental value [41]. There is another energy gap below the LHB isolating it from the underneath dispersive valence band continuum [VB shaded in blue in Fig. 21.1(d)], which is commonly referred to as the CDW gap ($\Delta_{CDW}$) [42, 43, 44]. This gap is manifested in the $dI/dV$ spectrum as a dip below the LHB [Fig. 21.1(c)].

### 15.3.2 Low-energy orbital textures and their origin

Besides the CCDW superstructure and energy spectrum, equally important is the local DOS (LDOS) mapping at selected energies, which contains the spatial characteristics of electronic wavefunctions, i.e., the orbital texture. Figure 21.2(a) displays the $dI/dV$, or LDOS, mapping measured at two representative energies. At $V_b$ = -207 mV (upper panel), which corresponds to the LHB, the LDOS map shows a periodic pattern that is commensurate with the CCDW superlattice. By comparing the LDOS map with the topographic image of the same area [Fig. 21.1(b)], the bright spots are identified to be the center of SDs. Moving to lower energy with bias $V_b$ = -422 mV (lower panel), a distinctly different orbital texture is revealed for the VB: the LDOS map exhibits a kagome-like superstructure. Its bright/dark spots are inverse of the previous texture, indicating contributions mainly from the surrounding Ta orbitals. LDOS maps at positive biases give a nearly symmetric picture, demonstrating the same two types of orbital textures: the UHB $V_b = 199$ mV [Fig. 21.2(c) upper panel] corresponds to an orbital texture concentrated on the center of SDs, whereas at higher energy $V_b = 484$ mV [Fig. 21.2(c) lower panel] for the conduction bands (CB), the bright spots shift to the surrounding Ta orbitals.

To determine the nature of these two orbital textures discussed above, we proceed by performing *ab initio* Wannier function analysis. Consider that the oxidation state of Ta atom is +4, there is one unpaired 5d electron left per Ta that plays the most important role around the Fermi level. For a SD consisting of 13 Ta atoms, we need seven Wannier functions (without the spin degree of freedom) to fully accommodate these 13 unpaired 5d electrons. Accordingly, the

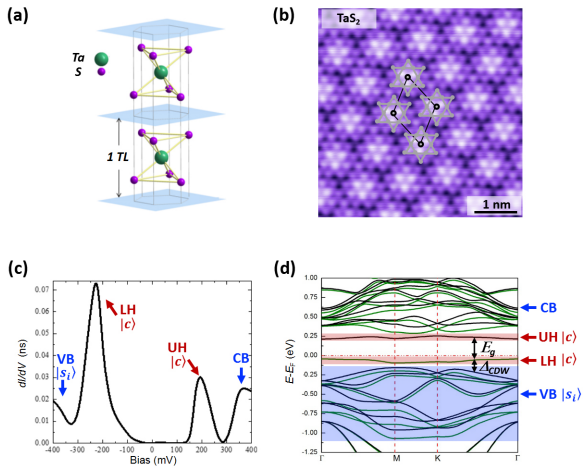


Figure 15.1: Structural and electronic properties of 1T-$TaS_2$. (a) Crystal structure of 1T-$TaS_2$. (b) Atomic resolved topographic image of 1T-$TaS_2$ with bias voltage $V_b = 1$ V and tunneling current $I_t = 20$ pA. Each bright site on the surface corresponds to a S-atom in the topmost layer. The gray dots and the black lines mark the SD structure and the CCDW superlattice, respectively. The crystal cleaves easily between two adjacent S layers, as indicated by the blue planes in (a), exposing the triangular lattice of S atoms. (c) Spatial averaged STM $dI/dV$ spectrum acquired at 5 K. (d) DFT+$U$ band structure of 1T-$TaS_2$. The black/green colored curves represent the two spin components. The shaded regions indicate the energy range belonging to the different orbitals.

Bloch states of the seven highest occupied energy bands are chosen to construct the Wannier functions. The spatial distributions of the resulting maximally localized Wannier functions are plotted in Fig. 21.2(b), which automatically separate into two groups. The one denoted by $|c\rangle$ concentrates at the central Ta atom with a typical $d_{z^2}$ geometry. The remaining six Wannier functions distribute dominantly along the edge of the SD ($|s_{\alpha=1...6}\rangle$), which can be viewed as the bonding orbitals of the surrounding Ta atoms. This Wannier function analysis gives a natural explanation for the two types of orbital textures observed by STM. In particular, it clarifies that the kagome-like texture arises from a set of linear-shaped molecular orbitals.

We note that previous STM mapping indicated additional center-surrounding variation of the orbital texture for the deeper occupied states [24]. This feature is also observed in our experiment and calculation. These deep occupied states are associated with a different set of Wannier functions orthogonal to $|c\rangle$ and $|s_{\alpha=1...6}\rangle$, which can be clarified using the same technique. However, those Wannier functions are irrelevant to the low-energy physics. By mapping out the low-energy orbitals, we also note that the previously employed one-band Hubbard model is implicitly based on the $|c\rangle$ orbital alone. Since this orbital is largely localized, it is susceptible to a Mott transition, giving rise to the UHB and LHB. However, it is important to notice that the validity of the one-band Hubbard model is guaranteed only by a large $\Delta_{CDW}$. When $\Delta_{CDW}$ is reduced, a one-band-to-multi-band transition has to be considered, which in turn plays an important role in the collapse of the Mott phase.

## 15.4 MOTTNESS COLLAPSE UPON *Se* SUBSTITUTION

To test the validity of the two-orbital-texture model, we further investigate the electronic structure of 1T-$TaS_2$ under external influence. A rather gentle perturbation to the 1T-$TaS_2$ structure is to modify the buckling of the S atoms around the central Ta, which is expected to affect the CCDW order. Experimentally this can be effectively realized through isovalent substitution of S by Se [6, 7], which has a larger ionic size and is expected to increase the

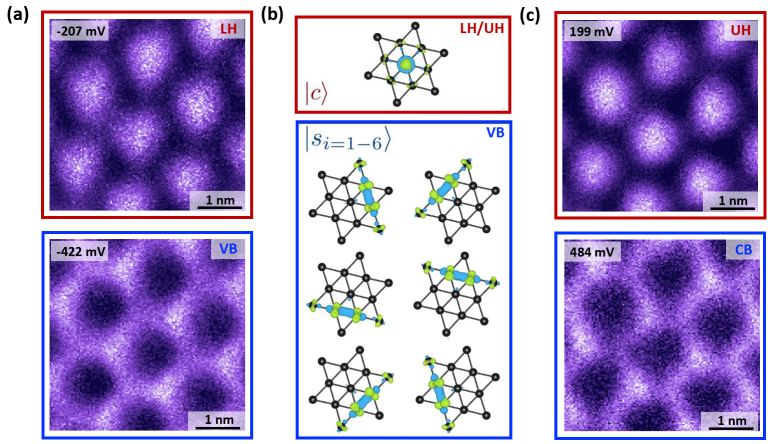


Figure 15.2: Two types of orbital textures in 1T-$TaS_2$. (a)/(c) Differential conductance ($dI/dV$) maps (42×42 Å$^2$) measured at $V_b$ = -207/199 mV (up) and $V_b$ = -422/484 mV (bottom) with tunneling current $I_t$ = 20 pA. The center of each CDW cluster is brighter at -0.2/0.2 V while the edges brighter at -0.4/0.4 V. (b) Isovalue surface of the two types of Wannier functions.

buckling of the surrounding S atoms. We have synthesized a series of Se-doped 1T-$TaS_2$ single crystals, and use these samples to map out the collapse of the Mott phase.

### 15.4.1 Phase transitions

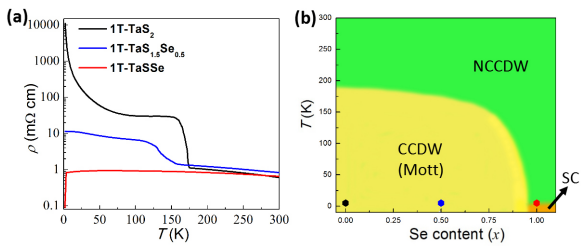


Figure 15.3: (a) Temperature dependence of the in-plane resistivity of three typical 1T-$TaS_{2-x}Se_x$ samples. (b) Schematic electronic phase diagram of 1T-$TaS_{2-x}Se_x$ and the location of the three samples under STM measurements.

Substituting S with Se is known to suppress the Mott-insulating phase in 1T-$TaS_2$ [6, 7], which can be seen from the transport data. Figure 21.3(a) shows the in-plane resistance data of three 1T-$TaS_{2-x}Se_x$ samples that are used for discussion in this work. For the pristine 1T-$TaS_2$, there is a well-defined CCDW ordering around 180 K. Below this transition temperature, the resistance exhibits a typical insulating behavior. Clearly, Se substitution strongly suppresses this phase transition. For the $x = 0.5$ sample, the resistance jump around the phase transition point is weakened. For the $x = 1$ sample, it completely vanishes, and a flat resistance curve stays unperturbed until about 3 K, at which a sudden drop occurs. This is known to be a superconducting transition. Figure 21.3(b) displays the schematic phase diagram [7], and the location of the three samples under discussion.

We note that for Se-substitution, due to its chemical similarity to S, the disorder effect is expected to be weak. This can be observed from the transport data: above the CCDW transition temperature, the resistance curves of the three samples almost coincide; the difference only becomes evidence after the CCDW order kicks in.

### 15.4.2 Topographic change

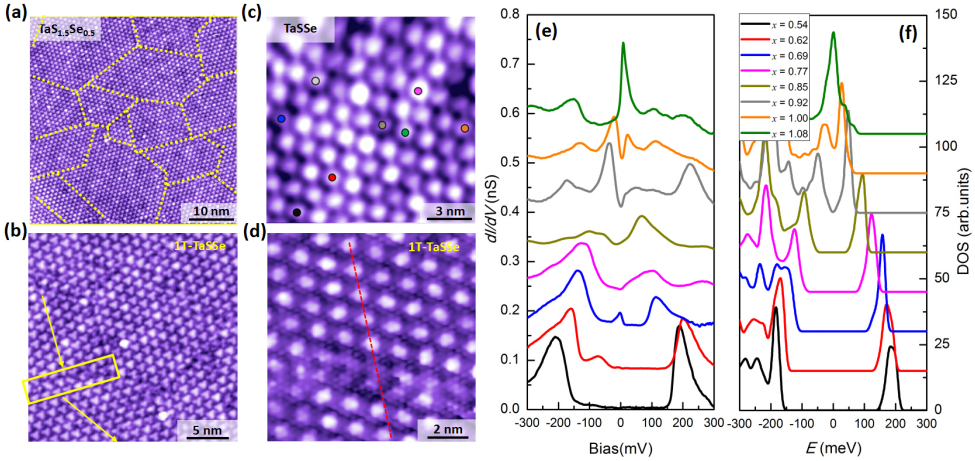


Figure 15.4: Structural and electronic properties evolution of Se substituted 1T-$TaS_2$. Topographic images acquired with $V_b$ = -500 mV and $I_t$ = 20 pA on the 1T-$TaS_{2-x}Se_x$ samples with the averaged Se concentration (a) $x = 0.5$ and (b)−(d) $x = 1$. (e) Local STM $dI/dV$ spectroscopy measured at various locations on the surface as marked in (c). (f) DFT+$U$ density of states of Se-substituted SDs in comparison with (e). In (a), the yellow dot lines indicate the sharp domain boundaries. In (b) and (d), the marks guide for eyes the rotational and translational mismatch in different domains.

How does Se-substitution modify the CCDW order? Figure 21.4(a) displays a large area STM image on the surface of the $x = 0.5$ sample. Unlike the pristine sample, the surface structure now splits into domains with varied domain size and sharp boundaries in between [Fig. 21.4(a)], which resembles the so-called "mosaic"phase in 1T-$TaS_2$ induced by voltage pulse in STM experiments [45, 46]. Increasing the Se concentration from $x = 0.5$ to $x = 1$ creates more domain walls and defects, but the general topographic properties remain the same. A closer examination around the domain walls reveals both 30°degree rotational and translational mismatch between different domains [Figs. 21.4(b) and (d)]. According to the transport data, this domained phase in the $x = 1$ sample should adiabatically extend to the high-$T$ NCCDW regime, in which the domains might shrink in size and the sharp domain boundaries melt into finite-width interdomain channels free of CCDW order [16]. However, close to the superconducting transition temperature, our STM image shows that the CCDW domains fill the whole space. Within a single domain, the CCDW superlattice retains the SD patterns as that in the undoped $TaS_2$ sample.

### 15.4.3 Electronic inhomogeneity

STM $dI/dV$ spectra are measured at various locations on the surface of the $x = 1$ sample [Fig. 21.4(c)], which are found to be surprisingly random. By ordering them with respect to the gap size, we observe a complete evolution [Fig. 21.4(e)]. There are still areas (small in size) showing a spectrum similar to that in pristine 1T-$TaS_2$ with a nearly unperturbed Mott gap (black curve). Moving upwards, the Mottness gap shrinks continuously. With further shrinking of the Mott gap, a broad V-shaped gap forms near $E_F$, which looks reminiscent of the pseudogap in underdoped cuprates. The V-shaped gap also shrinks gradually, and a finite DOS appears at $E_F$, indicating the transition into a metallic state. Eventually the gap vanishes completely and a sharp peak emerges near $E_F$, which looks similar to the Van Hove singularity (VHS) in overdoped cuprates.

A natural speculation on the origin of the inhomogeneous spectra is that the Se concentration in different SDs varies. We have calculated a series of SD structures by progressively replacing the S atoms with Se atoms. For a given Se concentration, the lowest-energy substitution configuration is determined, and the DFT structural relaxation confirms that the main effect of Se substitution is to increase the local buckling of the Ta-Se-Ta bonding geometry. We plot the DOS evolution as a function of Se concentration in Fig. 21.4(f), rendering a direct comparison with the STM $dI/dV$ spectra. The overall evolution of the gap can be nicely reproduced in the theoretical simulation. Besides, several distinct features, e.g. the U-shaped Mottness gap, the V-shaped pseudogap, and the sharp VHS-type peak, are also in good agreement.

Before explaining the underlying orbital-driven physics, it is worth addressing two possible concerns. Firstly, it is technically difficult to exclude the existence of other sources of inhomogeneity. However, given that our pristine sample is of very high quality, we believe that the predominant effect of Se substitution is to generate chemical inhomogeneity. The degree of inhomogeneity may rely on the sample preparation condition, cf. a previous experiment has reported complete ordering of S/Se atoms in the TaSSe sample [8]. Secondly, our calculation only considers doping one single SD with a 2D periodic boundary condition. We assume that the local electronic properties are primarily governed by the intra-cluster coupling within the SD, and the chemical variation in the nearby SDs do not qualitatively change the local spectrum evolution. However, for the global or spatially averaged properties, such as transport behaviors and photoemission spectrum, the situation is beyond this local approximation, which could be an interesting question for further investigation.

### 15.4.4 Orbital shifts

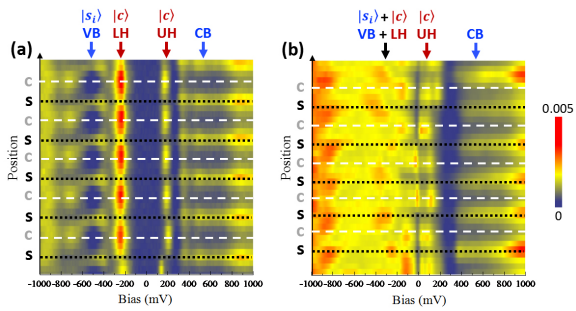


Figure 15.5: STM line map. The $dI/dV$ data for (a) $x = 0$ and (b) $x = 1$ case in an extensive two-dimensional parameter space. The horizontal axis is the STM bias and the vertical axis is the position. The white dash (black dot) lines mark the center (surrounding) of the SDs.

Due to the spatial inhomogeneity, a 2D periodic pattern as shown in Fig. 21.2 no longer exists. To uncover the changes of the relevant orbitals, we perform a comparative analysis on the spectra linecut crossing multiple SDs before and after Se-substitution.

In Fig. 21.5(a), we first present the linecut map of pristine 1T-$TaS_2$. The horizontal axis is the STM bias, ranging from -1000 meV to 1000 meV. The vertical axis is the position, measured along the line crossing five SDs. The LHB and UHB are evident at the bias of -200 and +200 meV. Along the position axis, they exhibit a periodic intensity variation, which peaks at the center of each SD (c) and weakens at the surrounding (s). The peak of the $dI/dV$ shifts by half the period when moving the bias below (above) the LHB (UHB), indicating that the orbital component changes from $|c\rangle$ to $|s\rangle$.

For the doped sample [Fig. 21.5(b)], the orbital textures vary from one SD to another, and their spatial distributions become complicated. We first note that the deep CB/VB states, e.g. states around $\pm 1000$ meV, remain largely periodic in space, exhibiting the similar textures as

in the pristine sample, which again suggests that these states are not involved in the electronic phase transition. Around the Fermi level, the UHB can still be identified, which is bound by two clear gaps in most SDs. Despite a spatially varied magnitude, the UHB in general shifts to the lower energy, leaving a large gap between the CB, and almost touching the VB in some SDs. The strong narrow LHB peak now merges with the top of the VB. For some SDs, a narrow peak around the SD center appears as a remnant of the original LHB. In general, the surrounding orbitals play an equally important role in the low-energy physics. Because of these orbital shifts, the Mott-insulator-to-metal transition occurs.

These orbital shifts can be further compared with the DFT+U band structures. Figure. 21.6(a) traces the band evolution as the Se concentration increases. The results indicate progressive downward shift of UHB and LHB, in agreement with the STM line map. At low-doping concentration, despite a reduction of $\Delta_{CDW}$, $E_g$ stays unchanged as it is dictated by the effective Hubbard $U$ of the $|c\rangle$-orbital alone. After the LHB touches the $|s_\alpha\rangle$-orbital bands, the Mott gap transforms into the charge-transfer type gap because now the lowest energy excitation is from the continuum band formed by the $|s_\alpha\rangle$-orbitals to the UHB formed by the $|c\rangle$-orbital. The gap size shrinks continuously upon further doping. According to the calculation, the critical point is reached at $x \approx 0.92$, where the charge-transfer gap becomes zero. Beyond this critical doping concentration, the UHB also sinks into the $|s_\alpha\rangle$-orbital bands, driving the system into the metallic regime. For the high-doping case, the $|c\rangle$-orbital and $|s_\alpha\rangle$-orbitals are strongly hybridized so that we can barely see the remnants of the narrow UHB around the $\Gamma$ point at $E_F$. The excellent agreement between theory and experiment confirms the validity of the orbital-driven Mott insulator to metal transition, in which the orbital sequence determines the electronic property. We note that in the calculation no additional complexities, such as spin-orbit coupling, interlayer coupling and disorder, are introduced. In addition, after Se substitution, Wannier function analysis shows that the geometry of the $|c\rangle$ and $|s_\alpha\rangle$ orbitals remain nearly unchanged. Therefore, we believe that the interplay between the $|c\rangle$-orbital and $|s_\alpha\rangle$-orbitals represents a universal origin of Mottness collapse in 1T-$TaS_2$.

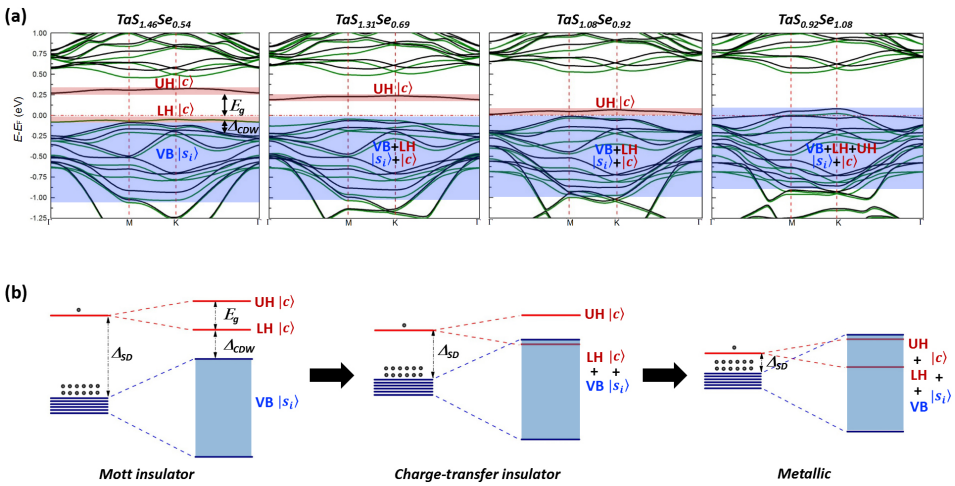


Figure 15.6: (a) DFT+U band structures of Se substituted 1T-$TaS_2$. The meaning of the colors is the same as in Fig. 21.1(d). (b) Schematic energy level diagrams of the Mott insulating phase, the charge-transfer insulator phase and the metallic phase.

## 15.5 THEORETICAL FORMALISM

To capture the essential physics, we propose a multi-orbital Hubbard model as formulated below:

| Unit (eV) | Pristine | Se-doped | Struct. mod. |
|---|---|---|---|
| $\Delta_{SD}$ | 0.212 | 0.146 | 0.143 |
| $t_{sc}$ | 0.162 | 0.099 | 0.105 |
| $t_{ss1}$ | 0.150 | 0.175 | 0.171 |
| $t_{ss2}$ | 0.091 | 0.089 | 0.087 |
| $t_{ss3}$ | 0.072 | 0.021 | 0.013 |
| $t_{ss4}$ | 0.050 | 0.047 | 0.043 |
| $t_{ss5}$ | 0.042 | 0.043 | 0.036 |

Table 3: Single-electron parameters from Wannier function analysis. The three columns correspond to the pristine 1T-$TaS_2$, 1T-$TaS_{2-x}Se_x$ ($x = 0.92$) and an artificial 1T-$TaS_2$ that retains the same structure of 1T-$TaS_{2-x}Se_x$,respectively.

$$\begin{aligned} H &= \Delta_{SD}\sum_{I} c_I^\dagger c_I + t_{cs}\sum_{I\alpha}(c_I^\dagger s_{I\alpha} + H.c.) \\ &+ \sum_{(I\alpha,J\beta)} t_{ss}^{I\alpha,J\beta} s_{I\alpha}^\dagger s_{J\beta} + U_c\sum_{I} c_{I\uparrow}^\dagger c_{I\downarrow}^\dagger c_{I\downarrow} c_{I\uparrow}, \end{aligned} \tag{15.1}$$

where $\Delta_{SD}$ is the onsite energy difference between $|c\rangle$ and $|s_{\alpha=1...6}\rangle$ generated by the formation of SD [Fig. 21.6(b)], and $I$,$J$ indexes the SDs. The central orbital $|c\rangle$ experiences an effective onsite Coulomb repulsion $U_c$ of the magnitude of LHB/UHB splitting ∼0.25 eV, whereas the interaction terms of $|s_{\alpha=1...6}\rangle$ are neglected considering they are less localized. Note that the Wannier function $|c\rangle$ is also a molecular orbital [Fig. 21.2(b)], and the associated Coulomb repulsion $U_c$ is much smaller than its original 5d atomic-orbital counterpart as used in the DFT+U calculation. The values of $\Delta_{SD}$ and the dominant hopping parameter ($t$) can be extracted by exploiting the same Fourier transformation as used in the Wannier function analysis (Tab. I).

For pristine 1T-$TaS_2$, the onsite energy of $|c\rangle$ is 0.21 eV higher than $|s_{\alpha=1...6}\rangle$. The largest hopping amplitude is $t_{sc}$ that is between $|c\rangle$ and $|s_{\alpha=1...6}\rangle$, followed by several hopping processes among $|s_{\alpha=1...6}\rangle$ (Fig. 21.7). Intercluster hopping is possible via $t_{ss2}$ and $t_{ss4}$. The set of obtained parameters for pristine 1T-$TaS_2$ is susceptible to a Mott transition owing to a relatively large positive $\Delta_{SD}$. For the Se-substituted sample, we present in Tab. I the parameters obtained from calculations on the ($x = 0.92$) supercell. Transition from the Mott phase to a metal is in principle described by Eq. (1) when the parameters vary, but solving Eq. (1) including the Hubbard term requires the hard-core many-body calculation that is beyond the scope of the current work. Nevertheless, a quick test can be made by only keeping the largest $t_{ss}$ and $t_{sc}$ terms and then diagonalizing the 7-by-7 Hamiltonian matrix. It shows that the highest eigenstate transforms from a dominant $|c\rangle$ character to a $|s_{\alpha=1...6}\rangle$ character, which reflects the concept of the orbital-driven transition.

According to this effective model, we schematically summarize the overall physics of the orbital-driven electronic structure evolution in Se doped 1T-$TaS_2$ [Fig. 21.6(b)]. The key ingredient is the organization of the two types of orbital textures $|c\rangle$ and $|s_{\alpha=1...6}\rangle$ accompanied by the formation of the SD structures. The central orbital is isolated by the surrounding ones, making inter-cluster hopping of central-orbital electrons possible only via high-order process. It is thus susceptible to a Mott transition when $|c\rangle$ is separated from $|s_\alpha\rangle$ in energy. On the other hand, the $|s_\alpha\rangle$ orbitals are extended with sizable hopping amplitude, naturally giving rise to a metallic phase when $|c\rangle$ and $|s_\alpha\rangle$ mix.

Previous DMFT calculations on the effective one-band Hubbard model [47, 48, 49], manually tuned the $U$ value, or equivalently, the $t/U$ ratio over a very wide range in order to trace

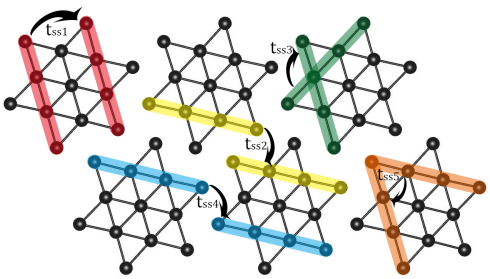


Figure 15.7: Physical meaning of the hopping parameters between the surrounding orbitals listed in Tab. I

the Mott-insulator-to-metal transition. As discussed above, the one-band Hubbard model is a downfolded version of our multi-orbital model by integrating out the $|s_{\alpha=1...6}\rangle$-orbitals. The downfolded $U$ is affected not only by $U_c$ associated with the $|c\rangle$-orbital, but also the energy separation between $|c\rangle$ and $|s_{\alpha=1...6}\rangle$. In this sense, our work complements the previous speculation on a change of effective $t/U$ ratio that induces the transition, and presents an explicit formalism to explain why the effective $t/U$ ratio varies so greatly.

Finally, it is worth mentioning several points that bridges Se substitution with mechanical modulation. As noted in Sec. IVC, the main effect of Se substitution is to increase the local buckling of the Ta-Se-Ta bonding geometry. In calculation, we have tested to retain this buckled geometry, but change Se back to S. It is found that very similar band structure and single-electron parameters can be obtained (c.f. the last two columns of Tab. I). In this sense, the possible structural modification as demonstrated by STM pulsing [45, 46] may share the same orbital-driven physics as discussed above.

## 15.6 CONCLUSION

Our experimental observations and first-principle calculations in 1T-$TaS_2$ reveal a new mechanism of Mottness collapse, which is fundamentally different from previously known examples such as charge-doping-induced collapse in cuprates and pressure-induced collapse in weak Mott insulators. In the layered 1T-$TaS_2$, the isovalent substitution of S with Se does not induce additional charge carriers. Instead, it tunes the CDW order, and in turn drives the direct Mott gap into an effective "charge-transfer"gap. To the best of our knowledge, it is the first time that such a novel evolution between Mott gap and charge-transfer gap can be adiabatically accessed in the same material. Upon further substitution, after the charge gap fully collapses, the low energy degrees of freedom include the Fermi-surface-forming itinerant carriers and fluctuating local magnetic moments, just like in heavy-fermion systems and iron pnictides/chalcogenides. It is thus interesting to ask whether this parent state for superconductivity is a heavy fermion liquid or a magnetic metal. A even more unique feature of 1T-$TaS_2$ is that the Mott physics is built upon a triangular lattice, in which spin frustrating is intrinsically coded. Therefore, the magnetic ground state of 1T-$TaS_2$ might be highly nontrivial. We believe that the richness of the orbital-tunable electronic structure in Se-doped $TaS_2$ will shed important insights into several important topics of condensed matter physics.

# Part XI
# Other Experiments and Simulations

## 16 Possible origin of nonlinear conductivity and large dielectric constant in the commensurate charge-density-wave phase of $1T - TaS_2$ by Ma, Hou, Lu, Li, Petrovic (2017)

DOI: 10.1103/PhysRevB.97.195117

(Jaka said that he took constant $\varepsilon_\infty$ from this paper. It is not clear if there are confirmation of these results from other articles and that indeed it is a correct constant, since it changes with frequency. I'll think about it later)

**Abstract**

The electric field dependence of the dielectric properties and the nonlinear conductance of $1T - \mathrm{TaS_2}$ below 50 K has been investigated. A large dielectric constant of about $10^4$ is obtained up to $10^7$ Hz, which cannot be attributed to hopping of the localized carriers alone, the collective excitations of the commensurate charge-density-wave must be another contributor. The dielectric spectra disperse slightly in our measured temperature and frequency range. At a moderate dc bias field, the real part of the dielectric constant $\epsilon_1(\omega)$ decreases. We propose that the separation of bound soliton-antisoliton pairs may be a contributor to the reduction of $\epsilon_1(\omega)$ and the accompanying nonlinear conductivity with increasing dc bias.

### 16.0.1 I. INTRODUCTION

Nonlinear conductivity and large polarization effects are the well-known phenomena in charge-density-wave (CDW) systems [1-3]. Though researchers have made considerable progress in understanding the associated transport properties in quasi-one-dimensional CDW compounds [4-12], less discussions for two-dimensional (2D) CDW crystals have been carried out, especially the polarization properties [13-17]. In recent years, the investigation of 2D CDW compounds has been revitalized, because they would be helpful in understanding the mechanisms of the high- $T_c$ superconductors [18-20] and the origin of ultrafast switching to a stable hidden quantum state [21,22]. Hence, it is of interest to investigate the charge transport behavior in 2D CDW systems.

A 2D CDW often reveals itself in layered transition-metal dichalcogenides and rare-earth tritellurides [13,14,23-26]. Researchers began to study the charge transport properties of 2D CDW systems ( $1T-\mathrm{TaS_2}$ ) about 40 years ago. References [14,27,28] suggested that the carriers localization induced by disorder may be responsible for the unique low-temperature transport properties, whereas Uchida et al. [16] proposed that the nonlinear conduction in the presence of a moderate electric field at low temperatures might be explained by the collective excitations in pinned CDWs-the creation of a soliton in a pair with an antisoliton. In the subsequent experiments, though the electronic nature was probed by various powerful spectroscopies [29-33], until recent years the mechanisms for the charge dynamics of the commensurate CDW (CCDW) phase in $1T-\mathrm{TaS_2}$ had not been disclosed yet. The discrepancy in understanding the transport properties at low temperatures has prompted us to study the fundamental question of whether the collective excitations of CCDW exist in $1T-\mathrm{TaS_2}$. As proposed by Rajaraman [34], for a system described by the equation of motion with soliton solutions, the soliton-antisoliton

"doublet" also exists, in which the equally but oppositely charged solitons are in confinement and lead to a large static dielectric constant [35]. Since localized electrons have a distinct role in the dispersion of the dielectric spectrum, $\epsilon_{r1}(\omega) \propto \omega^s$( s $< 0$) [36,37], investigations of the dielectric properties of $1T - \mathrm{TaS_2}$ would be helpful to demonstrate whether the doublets have an essential contribution. On the other hand, by applying a dc electric field, the bound charges in the soliton-antisoliton doublets may obtain a larger probability to decouple into carriers with long mean-free-paths and accordingly drive a nonlinear conductivity superposing on the Ohmic behavior.

A temperature- and field-dependent complex dielectric or conductivity spectrum is a powerful probe for investigating the charge transport and polarization behavior of various systems $[9, 10, 38 - 41]$. At a fixed temperature $T_0$, the complex dielectric or conductivity spectrum is ultimately defined by the polarization or conductance of the total contributing charged microscopic particles. In quasi-1D CDW systems, exceptionally large dielectric constants with strong dispersion and novel conducting behavior in radio and audio frequencies were observed $[1, 10, 42]$. Further, the dc-biased charge dynamics would be of great interest, since nonclassical characteristics often reveal, e.g., the well-known current oscillations and mode-locking [1]. Clearly, these novel properties should not be attributed to normal carriers but to the newborn currentcarrying mechanisms associated with CDWs by applying an electric field. For $1T - \mathrm{TaS_2}$, the non-ohmic behavior manifests in a current-voltage characteristic (CVC), naturally it is expected to be relevant to individual particles or collective
excitations of CDW condensates [16,17]. To the best of our knowledge, the discussions on dielectric or ac conductance behavior in 2D CDW systems are limited, possibly due to strong screening effects from normal carriers thermally excited over the nonuniform CDW gap opening at the Fermi level [29,31]. Usually, normal carriers respond extremely fast ($< 10^{-12}$ s), and if their density is large enough, the features of the conductivity in radio and audio frequencies relevant to the excitations of CDW condensates will become too weak to be identified well. However, below $T = 50$ K, the number of normal electrons excited by thermal energy remarkably decreases [14,21], providing good opportunities to clarify the mechanisms of carriers' motion in the CCDW phase of $1T - \mathrm{TaS_2}$.

In this article we systematically study the polarization properties of $1T - \mathrm{TaS_2}$ flakes below 50 K . To clarify the origin of the nonlinear conductance in a CVC, the dielectric properties under various dc biases, $E_B$, are also probed. The Joule-heating effects on ac conductivity under a constant bias field of $E_B \leqslant 20.0$ V/cm are analyzed by comparing them with the pulsed approach. We propose that the large relative dielectric constant ( $\epsilon_r \sim 10^4$ ) up to frequency $10^7$ Hz cannot originate mainly from the hopping process of the localized states, but is possibly driven by the existence of bound solitonantisoliton pairs (BSPs). Besides the hopping of localized carriers, the separation of BSPs may also be the driving force for the reduction of $\epsilon_1(\omega)$ and the nonlinear conductivity with increasing of dc bias.

## 16.0.2 II. EXPERIMENT

The $1T - \mathrm{TaS_2}$ single crystals were successfully grown by the conventional chemical vapor transport method in a gradient furnace. The stoichiometric tantalum and sulfur pieces were put into an alumina crucible before being sealed in a quartz tube and prereacted at 900°C for 50 h and then cooled to 760°C within 12 h followed by natural cooling. For single crystals' growth, the temperature of the hot (cold) end was 900°C (800°C). After 1 week of growth time, the quartz tube was quickly pulled out and then quenched into cold water. Consistent with the earlier reports [24], the as-grown single crystals show thin flakelike shapes and gold-shining color, with typical sizes in the range $(3 \sim 10) \times (2 \sim 3) \times (0.02 \sim 0.08)\mathrm{mm}^3$. Reference [28] shows $\rho_\perp/\rho_\parallel \sim 500$ over the range $1.3 < T < 240$ K , where $\rho_\parallel$and $\rho_\perp$ are the resistivity

perpendicular and parallel to the layers of the $1T - TaS_2$ crystal, respectively, indicating an essential 2D system. In the experiments, we focused on the in-plane polarization and transport properties of the sample with a surface area of $3.0 \times 0.4$ mm$^2$ and a thickness (along the $c$ axis) of about $25\mu$ m, and the distance between two potential contacts was about 1.0 mm .

Temperature-dependent resistivity was measured with the current $I = 10\mu$ A before probing the dielectric spectra. The CVCs showed linear behavior in a weak electric field, confirming good ohmic contacts by silver paste. We also compared the contact resistance of the four-contact and two-contact probes and found the difference was negligible compared to the sample resistance from 300 to 12 K . The Hall coefficients were probed under a magnetic field $H = 10.0$kG parallel to the $c$ axis of the sample. In addition, we confirmed that the
impedance spectra were unaffected by the difference between substrates by comparing data obtained with sapphire and the ultrathin mica sheets. The complex impedance properties under various dc biases up to 40 V/cm$\hat{z}(\omega) = |\hat{z}(\omega)| \cos\theta(\omega) + i|\hat{z}(\omega)| \sin\theta(\omega)$ were probed on an Agilent 4294A precision impedance analyzer through four-coaxial cables in two pairs (corresponding to two electrodes on the sample), where $\theta(\omega)$ was the phase difference between the ac driving potential and the response current at frequency $\omega$. The sample was mounted on a cryostat of a closed-cycle refrigerator (JANIS) with the experimental temperature range from 12 to 300 K monitored by a Cryo•con 32 temperature controller. All the impedance spectra were measured with a driving voltage of 30 mV (rms), where the nonlinear conductance does not appear in $I - V$ measurements. In analysis, the sample was seen as a leakage capacitor, both the dielectric constant $\hat{\epsilon}(\omega) = \epsilon_1(\omega) + i\epsilon_2(\omega)$ and the complex conductivity spectrum $\hat{\sigma}(\omega) = \sigma_1(\omega) + i\sigma_2(\omega)$ could be deduced from the raw data $\hat{z}(\omega)$ based on the universal relations $\hat{\epsilon}(\omega) = \frac{\hat{\sigma}(\omega) - \sigma_{dc}}{i\omega}$ and $\hat{\sigma}(\omega) = 1/\hat{z}(\omega)$; thus $\epsilon_1(\omega) = \frac{-\sin\theta(\omega)}{\omega|\hat{z}(\omega)|}\frac{d}{S}$, where $\epsilon_i(\omega) = \epsilon_0\epsilon_{ri}(\omega)(i = 1$ and 2), and $d$ and $S$ are the length and the cross-sectional area of the sample, respectively.

### 16.0.3 III. RESULTS AND DISCUSSION

The temperature-dependent resistivity $\rho_{dc}(T)$, the CCDW transition temperature $T_{\mathrm{CCDW}} = 180$ K, and the hysteresis feature upon warming are all consistent with previous reports [17,21,23], indicating good quality of the $1T - TaS_2$ singlecrystal samples. The existence of nonlinear conductivity in the CCDW phase was confirmed, as shown in Fig. 1. In our experiments, the electric field is limited within a moderate range, no more than 20 V/cm. The previous data have already shown that the carriers in the CCDW phase of $1T - TaS_2$ are positively charged and the density is larger than $10^{19}$/cm$^3$; hence the interface or the contact effects induced by the Schottky barrier can be neglected. In the following, the experimental data were obtained upon decreasing temperature in the CCDW phase. We

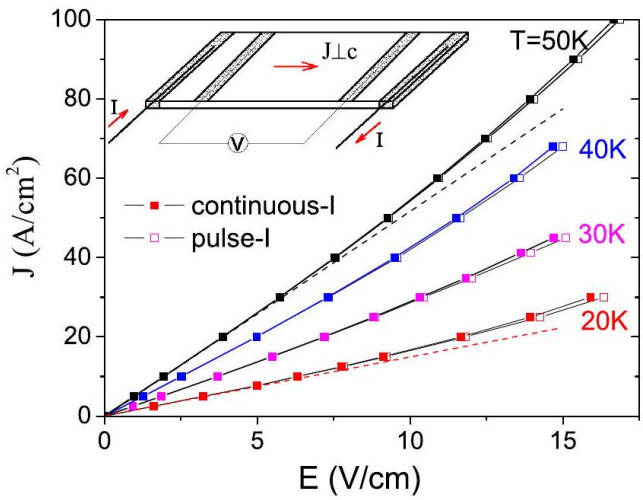


FIG. 1. The current voltage characteristics of the $1T-\mathrm{TaS_2}$ crystal at various temperatures below 50 K . The inset is a drawing of the experimental measurement geometry.

focus on the polarization behavior of $1T-\mathrm{TaS_2}$ in the presence of the nonlinear conductance below $T = 50$ K.

To obtain the intrinsic CVCs, a narrow-width pulsed-current method is often required [4,16,17]. However, to investigate the polarization properties of the $1T-\mathrm{TaS_2}$ single crystals in the presence of the nonlinear conductivity, a continuous dc bias would inevitably heat the sample (the Joule-heating effects). The only question is how much does it change the temperature of the sample. Considering that the nonlinear conductance was present in a moderate field, we compared the difference between the pulsed approach with a pulse duration of 0.1 ms and the continous method below $T = 50$ K (see Fig. 1). At different temperatures, the data are similar except the initial slopes of the CVCs. Below $E = 5.0$ V/cm at a fixed temperature, the CVCs differ only slightly, indicating a trivial Joule heating, whereas above $E = 8.0$ V/cm, a deviation starts to appear. Generally, it is shown that self-heating has strong effects on dc transport properties in all systems with a negative temperature coefficient of resistance [43,44].

### A. The self-heating effects to conductivity spectrum under dc bias

The self-heating in an external dc field and its influence on transport properties is important. To clarify this effect, the CVC at $T = 30$ K in a wide electric field range was obtained [see Fig. 2(a)]. For the current in continuous mode, an extra conductivity is superimposed on the pulsed results, indicating the effect of local Joule heating (the self-heating effect), not the intrinsic properties of the $1T-\mathrm{TaS_2}$ system.

For the conductivity and dielectric spectra measured at constant dc bias using small ac voltage with changing $\omega$, at low frequency, $\sigma_1\,(\omega \ll 1/\tau_{SH})$ is proportional to the differential conductivity ( $dI/dV$ ), where $\tau_{SH}$ is the relaxation time from self-heating, at high frequency, $\sigma_1\,(\omega \gg 1/\tau_{SH})$ is proportional to the chordal conductivity $(I/V)$.$\tau_{SH}$ is related to the specific heat by the expression $\left[\tau_{SH} = \frac{N_M c}{\kappa}\frac{d}{S}\right]$, where $N_M$ is the number of moles of material with specific heat $c$ and thermal conductance $\kappa$ [45]. In our experiments, $N_M \simeq 2.8 \times 10^{-7}$ mol, $c = 5.0$ J/molK at 30 K [46], and $\tau_{SH}$ is estimated to be approximately milliseconds for heat flow parallel to the $ab$ plane, larger than the perpendicular direction [47-49].

Nevertheless, above 10 kHz the thermal relaxation effect under $E_B$ nearly disappears [Fig. 2(b)], being consistent with the measurement in the pulsed approach with a duration of 0.1 ms . However, an increase of frequency does not remove the local Joule heating. Specifically, the total conductivity $\sigma_T = \sigma_{NM} + \sigma_{NL} + \sigma_{SH}$, where the subscripts NM, NL, and SH represent

the contribution of normal carriers, the nonlinear conductance, and the self-heating effect. These three components behave differently with increases in frequency. $\sigma_{NM}$ should reveal the well-known Drude free-electron properties and has no dispersion below GHz . $\sigma_{NL}$ remains unresolved at present, whereas for $\sigma_{SH}$, because the averaged temperature of the sample elevates under dc bias, thus an increase of the frequency-independent conductivity is expected, since $1T-\mathrm{TaS}_2$ is a system with a negative temperature coefficient of resistance.

In order to study the charged dynamics in the presence of the nonlinear conductance in $1T-\mathrm{TaS}_2$, the evaluation of the

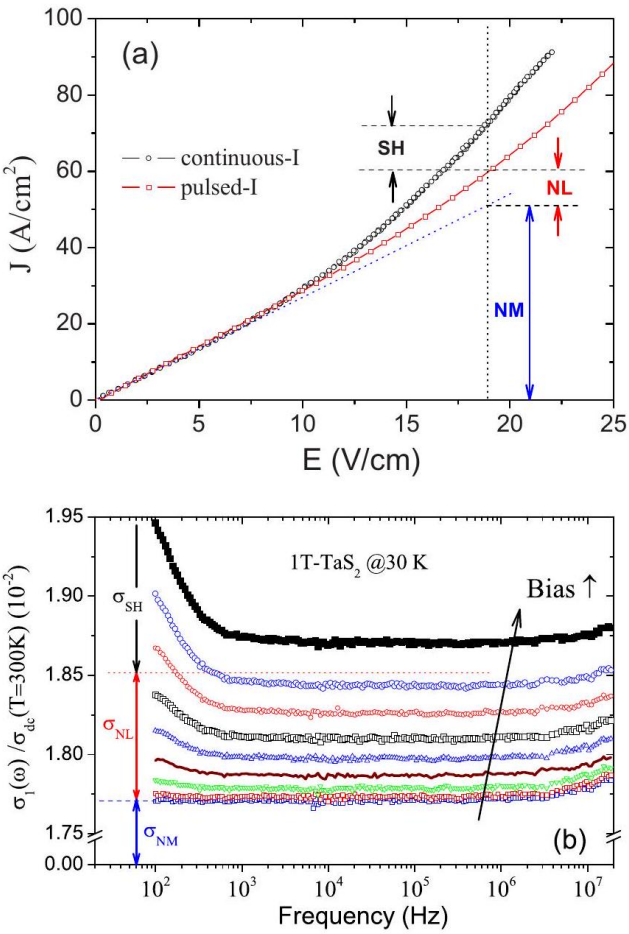


FIG. 2. (a) The current-voltage characteristics up to 25 V/cm of the $1T-\mathrm{TaS}_2$ crystal at 30 K . (b) The conductivity spectra of the 1 $\mathrm{T}-\mathrm{TaS}_2$ crystal at 30 K normalized to the dc conductivity at 300 K under various dc biases (from bottom to top, $0, 1, 2, 3, 4$, $5, 6, 8$, and 10 V/cm ). The notations SH, NL, and NM are the conductivity from self-heating, nonlinear conductance, and normal carriers, respectively. The dotted-line in panel (b) presents $\sigma_{NL}$, which is obtained from the CVC results where the self-heating effect could be neglected in the pulsed approach with a duration of 0.1 ms and a magnitude of 10 V/cm (solid square).

temperature elevation under dc bias is necessary. We compare $\sigma_1(\omega)$ in Fig. 2(b) at 10 kHz with the CVC results measured in the pulsed approach and find that the enhancement of the averaged temperature at bias 10 V/cm is no more than 0.5 K in our experimental configuration. Above several MHz , $\sigma_1\left(\omega, E_B=0\right)$ increases with increasing frequency. Clearly, this behavior should not originate from normal carriers or a thermal effect, but rather should be associated with a large dielectric constant.

### B. The large dielectric constant in the MHz region

In 1D CDW systems, the exceptionally large dielectric constants and strong dispersion in the audio frequency range have been extensively investigated [9,10,42,50]. However, the investigations of dielectric behavior are rarely reported for

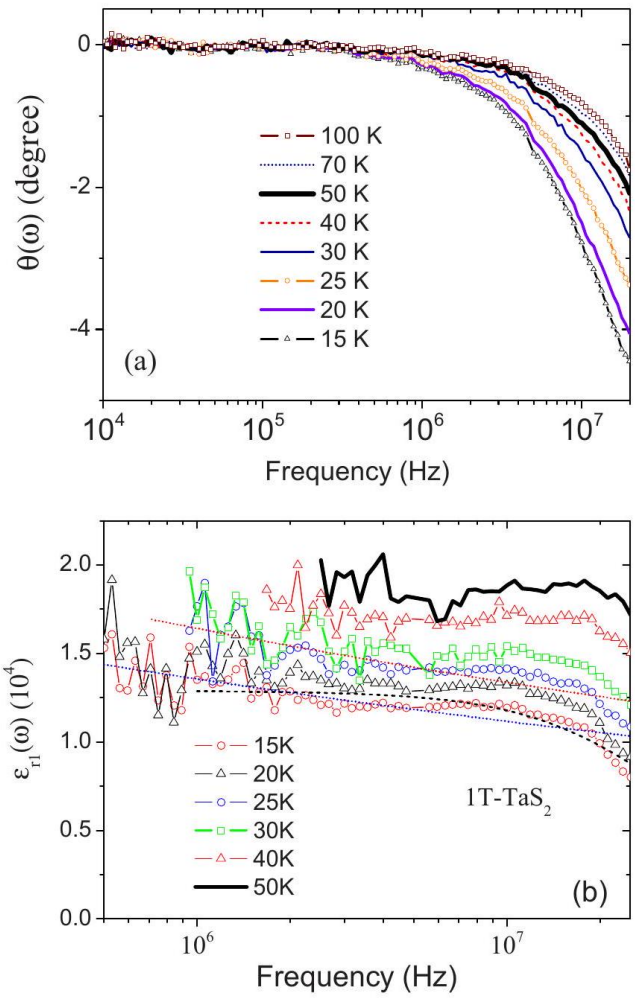


FIG. 3. (a) The spectra $\theta(\omega)$ of $1T-\mathrm{TaS}_2$ in the CCDW phase at various temperatures below 100 K . (b) The temperature-dependent dielectric constant of $1T-\mathrm{TaS}_2$ in the MHz region below 50 K . Note that the dotted lines using the hopping model alone cannot fit the data well at $T=15$ and 25 K , while the dashed lines (hopping + Debye) provide good-fitting results.

2D CDW compounds, possibly due to the large screening effects from the normal carriers excited over the nonuniform CDW gap opening at the Fermi surface. Nevertheless, for the polarization properties of the 2D CDW system $1T-\mathrm{TaS}_2$, a large static dielectric constant is expected for its highly polarizable structure, as suggested by Vaskivskyi et al. [17]. In our experiments, relatively small minus $\theta(\omega)$ could be identified below $T=100$ K, revealing capacitive responses, as shown in Fig. 3(a). For dielectric spectra $\epsilon_{r1}(\omega)$, there is much noise below 2.0 MHz , whereas a distinct decrease could be identified above $10^7$ Hz [see Fig. 3(b)]. At present, we cannot obtain complete relaxation behavior of the corresponding polarization process for the limited measuring frequency range. With decreasing temperature below 50 K , the dielectric spectra are suppressed, whereas the line shapes remain unchanged.

The large dielectric constant $\epsilon_{r1}$ of the order of $10^4$ in the MHz region is of interest. In the incommensurate CDW

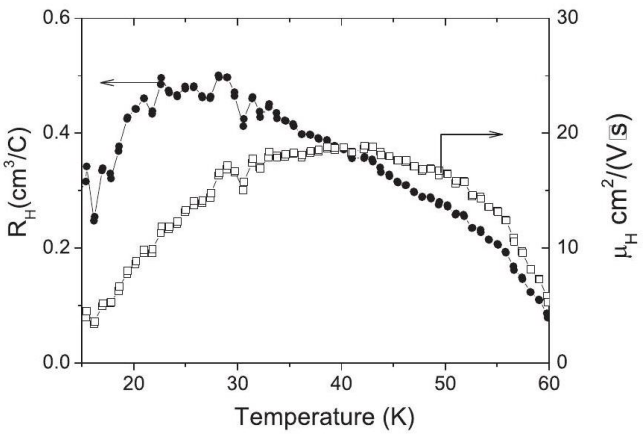


FIG. 4. The temperature-dependent Hall coefficient and the carriers' mobility of the $1T-TaS_2$ crystal below 60 K .

system, extremely large polarization effects are expected due to weak pinning from impurities or defects [51]. For the CCDW state in $1T-TaS_2$, unlike the incommensurate 2D system $TbTe_3$ where Sinchenko et al. observed CDW sliding [25], it would be difficult to slide in a moderate electric field due to the strong pinning by the underlying lattice and hence the contribution to the static dielectric constant would be much smaller [51]. Here one may argue that the mechanism in establishing the colossal dielectric constant in $(NbSe_4)_3I$ (due to the slight shift of the single chains against each other) can be a potential substitute for $1T-TaS_2$; however, such similar features of the lattice structure have not been identified yet [10].

As discussed by Lunkenheimer et al. [36], the hopping process of localized states can also give rise to large values of the dielectric constant. In Ref. [28] Hambourger and Di Salvo suggested that the disorder-induced localization may explain the transport properties in the $1T-TaS_{2-x}Se_x$ system, as supported by Dardel et al. [29] and Kim et al. [30]. Indeed, our data of the temperature-dependent Hall coefficient (Fig. 4) is consistent with Ref. [28], indicating the occurrence of carriers' localization in the single-band approximation. However, we note that the dielectric spectrum cannot be fitted well by the hopping process alone [36, 37, 52] : $\epsilon_{r1}(\omega) \propto \omega^s (s < 0)$. In Fig. 3(b), the dotted-curve fittings with $s = -0.08$ show a slightly upward curvature, which is inconsistent with the experimental data exhibiting a downward curvature above 10 MHz . Clearly, the cases at other temperatures behave similarly. Hence it seems that a relaxation process must exist besides the hopping of localized electrons based on the dielectric properties. On the other hand, the interfacial effects, such as a grain boundary or a surface depletion layer, also contribute to colossal dielectric constants. However, the positively charged carriers with density larger than $10^{19}/cm^3$ in the CCDW phase exclude the Schottky-barrier effects. As for the polaron contribution to the dielectric constant, we note that in the infrared conductivity spectrum, no such characteristic could be identified without photoexcitations [53].

We propose that the polarization properties of $1T-TaS_2$ could be described by the well-known soliton model used in 1D CDWs. To the best of our knowledge, the complete theoretical model for the phase solitons in 2D CDW materials
is not available at the moment. The existence of CDW phase solitons-topological phase defects-is a particular form of collective excitation in the CDW condensate and has been confirmed in quasi-1D systems [54-57]. Recently, there are suggestions that soliton contribution must be rather important for the unconventional transport properties associated with CDW systems [58-60]. Rojo-Bravo et al. [61] indicated that the transport mechanism of traveling soliton lattice may open new perspectives in controlling correlated charges over long distances, explaining the main features of sliding CDW systems.

In Ref. [35], Krive and Rozhavsky proposed that the phase solitons significantly contribute the dielectric susceptibility. As shown in Fig. 5(a), the localized compressions or rarefaction in the local condensed electron density (or deformations of the CDW phase $\varphi$ ) correspond to the soliton-antisoliton pair. A sketch of the charge density and the lattice arrangement is shown in Fig. 5(b) [36,62]. It is plausible that the central Ta atoms attract more electronic cloud which favors the commensurate CDW. In the equation of motion relevant to the CDW phase, $d^2\varphi/dt^2 - c_0^2\nabla_x^2\varphi + \omega_F^2 dV(\varphi)/d\varphi = 0$, where $c_0$ is a characteristic velocity of the undeformed condensate and $\omega_F$ is the pinning frequency, and the realistic pinning potential of the phase $V(\varphi)$ has a periodic form as expected [56,57]. The exact solutions of the equation should consist of several forms characteristic of solitons, including the solitonantisoliton doublet [34], whose excitation energy is relatively lower due to the existence of coupling, compared with the case of the discreet soliton and antisoltion [see Fig. 5(c)]. Instead of separating into the discrete soliton and antisoliton which are infinitely far apart from each other in infinite time, the relative separation for the members of the doublets oscillates periodically [34]. This doublet solution is also a "breathing" one and can be thought of as a BSP.

As the equally but inversely charged phase excitations are confined in BSPs, they would contribute to the dielectric constant of the system. This can be estimated using a simple expression for the dipole oscilliator [35]: $\epsilon_\varphi \sim \epsilon_\Delta\,(E_s/\omega_0)\ln(E_s/\omega_0)$, where $E_s/\omega_0 = \Delta/M\omega_Q, \Delta$ is the energy gap in the electronic spectrum, $M$ is the commensurability index, and $\omega_Q$ is the bare frequency of phonons with momentum $Q = 2k_F$ (Fermi wave vector). As suggested by Krive and Rozhavsky [35], $\epsilon_\varphi \sim 10^{1\sim 2}\epsilon_\Delta$, where $\epsilon_\Delta$ is about $10^3$, hence a dielectric constant of $\sim 10^4$ would be reasonable. In Ref. [16], Uchida et al. considered the collective excitation of a soliton in pair with an "antisoliton" under a moderate field to explain the field-independent Hall coefficient at $T = 4.2$ K. However, solitons in CDW systems are always excited in pairs; whenever a soliton ( $\varphi$ compression) is created, an antisoliton ( $\varphi$ rarefaction) appears. Though the explanation of Uchida et al. [16] demonstrates that mobile solitons and antisolitons are excited by applying an electric field, they can not identify whether the excitation is ground state $\rightarrow$ II or BSP $\rightarrow$ II, where II presents the state of free solitons and antisoltions [Fig. 5(c)]. Reference [16] and the associated research work [21,27,28] on the dc transport did not provide the dielectric properties of the CCDW state of $1T-\mathrm{TaS_2}$. As bound charged microscopic states contribute to large electric polarizations, the BSPs are expected to exist.

Though the polarization properties of the BSPs are far from being understood, a Debye relaxation or Cole-Cole empirical

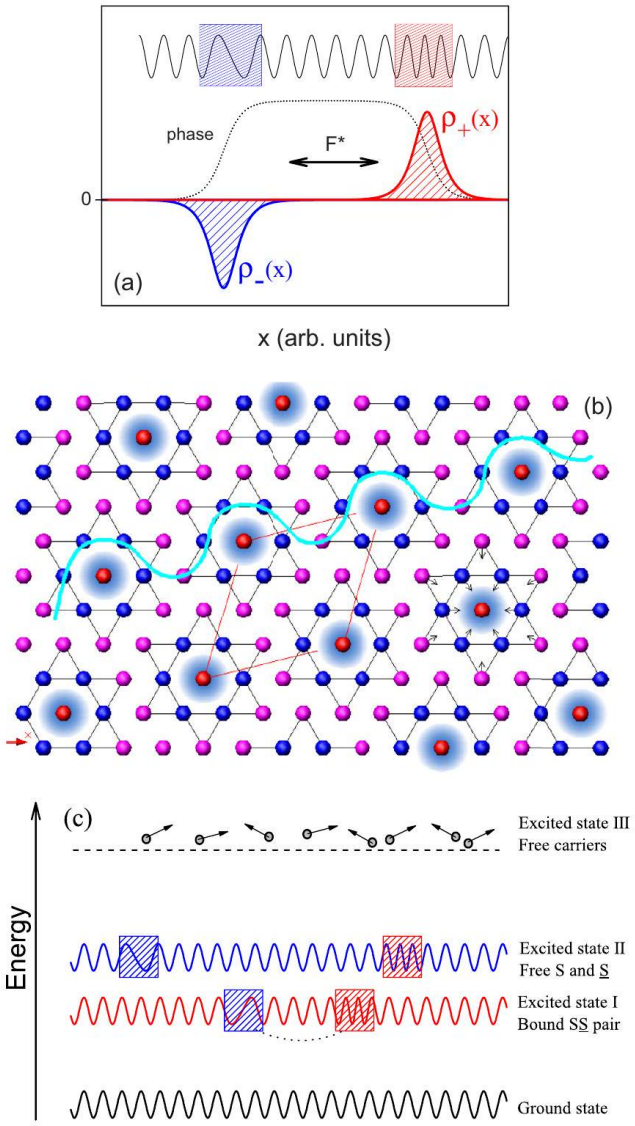


FIG. 5. (a) Real-space picture of a materialized solitonantisoliton pair, showing the qualitatively position-dependent phase $\varphi(x,t)$ at a fixed time, excess charge density $\rho(x) \propto \partial\varphi/\partial x$ [34]. (b) The schematic pattern of the charge arrangement of $1T-\mathrm{TaS_2}$ in real space. Note the charge ordering of the star of David cluster. The wave form stands for the commensurate charge density relative to the lattice. (c) The schematic illustration for the various excitations of the CDW condensate. Note that S represents soliton, whereas $\underline{S}$ represents antisoliton.

equation may be plausible. In Fig. 3(b), good fittings to the dielectric spectra were provided by the sum of the hopping process and the Debye relaxation model: $\epsilon_0\epsilon_{r1} = \epsilon_{HF} + (\epsilon_s - \epsilon_{HF}) / [1 + (i\omega\tau_0)] + A_{hp}\omega^s$, where $\tau_0$ is a characteristic relaxation time; $\epsilon_s$ and $\epsilon_{HF}$ are the dielectric constant in static and at a higher frequency limit of the Debye relaxation model, respectively; $A_{hp}$ is the coefficient of the hopping term; and $s$ is assumed to be $-0.2$[37, 52]. The resultant parameters are shown in Table I. It is remarkable that the feature above 10 MHz is associated with the Debye relaxation, whereas the hopping

TABLE I. The resultant parameters for fitting the dielectric spectra of $1T-\mathrm{TaS_2}$ at $T = 15$ K and 25 K.$\epsilon_{HF}$ is not a dominant parameter and has been determined empirically.

| $T$( K) | $\epsilon_s\,(10^3\epsilon_0)$ | $\epsilon_{HF}\,(10^3\epsilon_0)$ | $\tau_0\,(10^{-8}$ s) | $A_{hp}\,(10^3\epsilon_0)$ |
|---|---|---|---|---|
| 15 | 10.6 | 1.0 | 2.7 | 40 |
| 25 | 12.2 | 1.0 | 2.2 | 56 |

process would be responsible for the slight dispersion in the low-frequency region.

Other promising explanations for the observation of large dielectric constants are connected with the spontaneously arising interfaces. These are induced by the electronic phase separation or charge order as commonly observed in many transition-metal oxides. Though the true reason for the colossal polarization has not been completely clarified yet, it is possible that at least in some cases internal interfaces between the different phase-separated regions may play a role [36]. It is suggested that the dielectric behavior of these spontaneously forming heterogeneous regions represents a type of the long-known Maxwell-Wagner polarization effects, with the heterogeneity arising on a much finer scale close to the crystal unit cell. Here we suggest that this interpretation is associated with the following two aspects: (i) the density of charges arranges periodically in real space [see Fig. 5(b)]; however, whether such CCDW states of $1T-\mathrm{TaS_2}$ can be considered as a particular form of heterogeneity and drive large polarizations is not clear at present; (ii) the domain wall configurations are on a scale of the unit cell and accordingly they would remarkably contribute to the dielectric properties of the system [17,33]. Therefore further investigations are necessary to clarify this issue.

### C. The suppression of the dielectric constant by de bias

The dielectric behavior we discussed here is attributed to BSPs that could be locally polarized, rather than to the free solitons that can transfer in long distances. In a weak applied dc electric field $E$, the bound soliton-antisoliton pair does not contribute to the dc transport due to its charge neutrality, but it does contribute to polarization [35,59].

The increase in the field strength suppresses the dielectric constant distinctly in the MHz frequency region; the relative dielectric constant $\epsilon_{r1}$ decreases from about $1.25\times10^4$ to $1.05\times10^4$ in the field of 10 V/cm at 2.0 MHz , as shown in Fig. 6(a). One may argue that under dc bias, the true temperature of the "heated" sample must be higher than the apparent temperature. Here we would clarify that $E_B$ is moderate, and in contrast, stronger polarization is observed at higher temperatures [Fig. 6(b)]. Thus it is confirmed that the dielectric constant $\epsilon_{r1}$ decreases with the increasing of dc bias. Qualitatively, $\epsilon_{r1} \propto N\alpha$, where $N$ is the number of dipoles per unit volume and $\alpha$ is the polarization coefficient. If $N$ remains unchanged in the electric field, then $\alpha$ should decrease. Since $\alpha$ describes the local polarization, its decrease will not change the dc conductivity, in contrast with the experimental data.

Hence, $N$ would decrease in an external dc bias field, consistent with the soliton tunneling model (Fig. 7). As the applied dc field increases, the potential barrier for the BSP activation decreases. For the solitons having positive charges,

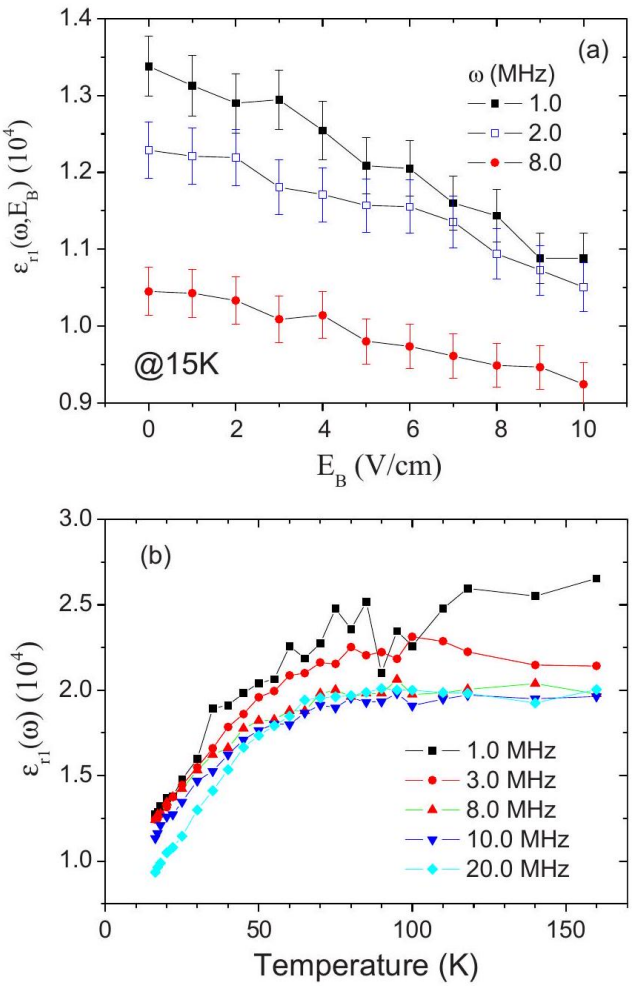


FIG. 6. (a) The dc-bias-dependent dielectric constant of $1T - TaS_2$ in the MHz region at $T = 15$ K. (b) The temperature-dependent $\epsilon_{r1}(\omega)$ at various MHz of $1T - TaS_2$ single-crystal samples.

the preferred direction of tunnelling would be along the external electric field, whereas the inverse applies for the negatively charged solitons, as shown in Fig. 7. Consequently, the probability of soliton tunneling is enhanced, inducing the suppression of polarization by dc bias.

The "grain and grain boundary" model should also be discussed in connection with the suppression of the dielectric constant in dc bias [63]. The model describes a reduction of the dielectric constant with increasing dc bias in ceramic systems. In such materials, double back-to-back Schottky potential barriers in micrometer scales are created at interfaces between grains due to charge trapping. Under a dc bias, the total width of the depletion region increases and then the dielectric constant should be suppressed [63]. However, in our experiment below $T = 50$ K, such polarization (often found at higher temperatures) should be frozen out and thus can be excluded.

### D. The mechanisms of nonlinear conductance in the CCDW phase

Intrinsic nonlinearity unrelated to the CCDW ground state of $1T - TaS_2$ should be discussed. The two most common

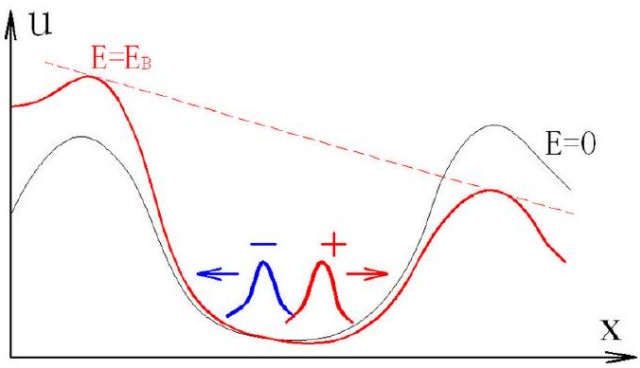


FIG. 7. The schematic pattern of a doublet, or a bound solitonantisoliton pair (shown by bell-like curves, red for positively charged solitons and blue for negatively charged solitons), tunneling under dc bias. The label of the horizontal axis $x$ presents the position of the real space, whereas for the vertical axis, $u$ presents the potential energy. Note that the arrows represent the preference directions of the tunneling.

single-particle mechanisms are field ionization and impact ionization of charged impurities. To ionize impurity electrons with a binding energy of about 20 K by applying an electric field of about 10 V/cm would require that the impurity wave function extend over lengths of an order of $1.0\mu$ m. It is possible, however, to generate extra carriers in weak electric fields if free carriers can be accelerated to sufficient kinetic energies to ionize bound electrons upon collision. This would require the mobility of carriers to be about $10^5$ cm$^2$/(V $\cdot$ s). However, $\sigma_{dc}$ at $T = 20$ K is about $2.5(\Omega \cdot$ cm$)^{-1}$ and the density of carriers is of the order of $10^{19}$/cm$^3$ [16], thus the mobility is estimated to be only several cm$^2$/(V$\cdot$s). Further, the experimental results from Ref. [28] also support a mobility of less than 20 cm$^2$/(V$\cdot$s). Hence it is plausible to believe that the nonlinear conductivity is associated with the electrons' localization or the CCDW condensate.

The previous studies of $1T-\mathrm{TaS_2}$ reported that in the presence of the nonlinear conductance the changes of the Hall coefficient could be neglected at $T = 4.2$ K [16]. Uchida et al. [16] proposed that the nonlinear conduction in $1T-\mathrm{TaS_2}$ might be explained in terms of the collective excitations in pinned CDWs, if the creation of a soliton in pair with an antisoliton occurs in 2D CDW systems. Such excitations are expected to occur in the current temperature range as Rice et al. [56] proposed that the average number of $\varphi$-particle pairs $N(T) \propto \exp(-E_0/k_BT)$, where $E_0$ is the activation energy of solitons inside the Peierls gap. Therefore, the existence of BSPs' bearing with relatively small excitation energies would be more plausible as Rajaraman discussed [34] and the associated contribution to nonlinear conductivity may be understood. They cannot move freely without external excitations, as the applied dc field increases, and the potential barrier for both of the positively charged and negatively charged solitons would decrease [Fig. 5(b)], driving a nonlinear dc conductivity accompanied by the suppressed dielectric constant.

Vaskivskyi et al. [17] also observed the nonlinear CVCs and suggested that the unusual exponential curves can be understood within the model in terms of trapped carrier tunneling through barriers resulting from the transient domain wall structure. Nevertheless, as it becomes easier for the localized or trapped electrons to form delocalized charges in the presence of a dc field, the conductivity of the system is enhanced. However, we note that the CVCs in the CCDW state of $1T-\mathrm{TaS_2}$ could not be fitted well by an exponential relation in the weak field range [17]. Thus the transport properties of $1T-\mathrm{TaS_2}$ at low temperatures may be a complex issue. In combination with our experimental results on dielectric properties, a process which cannot be attributed to the hopping charge transport has been identified; thus we suggest that the collective excitations in the CCDW state of $1T-\mathrm{TaS_2}$ cannot be neglected. In a recent

report, Cho et al. [33] did observe two well-confined and nonmetallic in-gap states, located on the domain wall center and edges of neighboring domains. Further experiments are necessary to clarify whether the two in-gap states correspond to the two contributors: the localization states and the collective excitations (BSPs).

In Ref. [64], Rozhavsky et al. proposed a dynamic mechanism of topological charge creation in a commensurate 1D CDW near the contact with a normal metal and also predicted the presence of nonlinear conductivity. However, the associated feature of the CVC has a downward curvature in their model, which is inconsistent with our experimental data. To disclose the mechanisms of the nonlinear conductivity in 2D CDW systems is a complex issue; it is always a problem to distinguish the motion of solitons from other forms of nonuniform CDW excitations (e.g., creep), and thus more efforts are needed in future research work.

### 16.0.4 IV. SUMMARY

In summary, we have studied the in-plane electric-fielddependent charge dynamics in the in-plane of $1T - TaS_2$ single crystals in the CCDW phase. A large dielectric constant of $\sim 10^4$ exhibits up to $10^7$ Hz, which is possibly due to the occurrence of bound soliton pairs or charge ordering of the system. The dielectric spectra disperse only slightly in our measured temperature and frequency range. We propose that besides the hopping carriers, the delocalization of BSPs may be another contributor to suppress $\epsilon_1(\omega)$ and the nonlinear conductivity with increasing of dc bias.

## 16.1 My Discussion

### 16.1.1 My Conclusion

### 16.1.2 My Left Questions

### 16.1.3 Things That I Maybe Understood Wrongly

### 16.1.4 Potential Future Research Directions

# 17 Real-time imaging of quasiparticle dynamics at a topological defect in an electronic crystal by Vaskivskyi, Vodeb, Vaskivskyi, Mihailovic

Defects formed during nonequilibrium self-assembly of quantum matter can dominate its emergent properties. Their macroscopic manifestations are typically characterised as noise, but their internal dynamics remain largely experimentally inaccessible. Making significant advances into the investigation of the microscopic degrees of freedom of such defects, we use fast scanning tunnelling microscopy to resolve, in real time, both internal and global dynamics of a mesoscopic Y-junction defect in an electronic crystal created through self-assembly after a local electromagnetic perturbation. We directly track individual electron rearrangements on millisecond timescales and map spatially localised telegraph noise characteristic of a two-level system. The phase and amplitude of these fluctuations are correlated with the observed charged particle trajectories, revealing a direct connection between collective order-parameter dynamics and microscopic charge motion. We model the dynamics as arising from the interplay of local Coulomb correlations, non-local configurational constraints and hybridised amplitude-phase collective modes bound to the junction. These constraints, together with the non-trivial broken symmetries of the defect, protect long-lived local quasiparticle configurations against

external perturbations. Our results establish fast scanning tunnelling microscopy as a means of probing the internal dynamics of metastable quantum defects and reveal how microscopic correlations and collective modes are intertwined within topologically non-trivial structures in electronic crystals.

## 17.1 Article

### 17.1.1 Introduction

The choreography of self-assembly in nonequilibrium systems is governed by symmetry, topology and causality constraints [1]. Systems emerging through a phase transition may form metastable spatially localised states that break long-range order, effectively forming defects. When such defects are topologically non-trivial, they are robust against external influence and consequently can be very difficult to manipulate or remove. Such situations arise anywhere from rapid crystal growth to molecular self-assembly in biological systems and in quantum many-body systems in the process of formation of emergent orders after a phase transition [2,3]. This problem extends to processes of practical importance, such as thin film deposition and crystal growth on substrates, where such defects play an important role in limiting the performance of devices. In quantum devices such as superconducting qubits, they may trap quasiparticles, forming two-level systems with internal degrees of freedom that effectively generate noise. Being able to identify and characterise such defects in detail is thus of both fundamental and practical importance.

Beyond defects formed by chance, we may engineer the formation of topologically and symmetry-protected mesoscopic metastable states with new and desired emergent properties by guiding the trajectory of the nonequilibrium system with appropriate perturbations, such as ambient temperature gradients or local charge currents. The resulting states are of interest when they show robustness against external perturbations, and particularly if they harbour dynamics on an energy scale which is below the thermal energy scale [4,5]. Electronic crystals are an excellent playground for experimentally investigating such behaviour. They controllably form metastable domains and topological defects associated with domain wall junctions in the electronic superlattice after rapid self-assembly [6–11]. Robust topological defects -solitons have previously been statically imaged by scanning-tunnelling microscopy (STM) in quasi-1D systems [12]. In 2D, the topological structure of such states is more complex, but it was shown that it can be controlled and manipulated by external perturbation [13], while domain walls have been shown to contain low-energy states [10,11,14–16] and as yet unidentified sources of noise [17,18].

Here we first create mesoscopic defects in an electronic crystal superlattice using a localised transient electrical perturbation with an STM tip. We then choose a particularly interesting metastable topologically non-trivial (Y-junction) defect at the intersection of three different domain walls in the hexagonal electronic superlattice. Using a fast-scanning tunnelling microscope (FSTM) [19–21], we record movies of density of states fluctuations in real time that correspond to motion of individual polarons -electrons surrounded by a local lattice deformation - localised within the Y-junction defect. 2D maps of tunnelling current temporal fluctuations reveal localised emergent two-level system (TLS) 'telegraph' noise whose analysis leads to a very detailed picture of the mesoscopic emergent quasiparticle states and poses fundamental questions on the origin of its slow dynamics and unprecedented robustness to external perturbations.

The electronic crystal chosen for this investigation is 1 $T-TaS_2$, a layered transition-metal dichalcogenide (Fig. 1a) which exhibits multiple charge ordered phases, including a 'hidden' metastable state with intricate mesoscopic structure created by external perturbation [7,11,15,22]. Its ordered equilibrium phases have traditionally been described in terms of classical field theory with a complex charge-density-wave (CDW) order parameter. This framework captures the

amplitude, phase, commensurability and discommensuration structure of the electronic modulation [23,24]. The ground state is a commensurate superlattice with two possible orientations $\chi_L$ and $\chi_R$ relative to the crystal lattice, related by mirror symmetry $\sigma$[25,26]. Microscopically, however, 1T-TaS $_2$ exhibits a propensity for electron localisation and the formation of polarons with well-defined lattice distortions, as shown in Fig. 1a(ii). A particularly relevant recent experiment has revealed the existence of individual polarons at temperatures well above any charge ordering temperature ($>$ 600 K), and elucidated their local structural distortions [27]. The charge ordering of the system through different symmetry-breaking transitions can thus also be understood in terms of crystallisation of polarons subject to lattice strain and Coulomb repulsion [27–31], which was verified by X-ray local structure analysis [27]. The importance of the crystallisation approach is that it can help understand phenomena which traditional approaches cannot explain, such as the existence of the polaron jamming into an amorphous polaronic state [32] and metastable states exhibiting topologically arrested defect annihilation dynamics [13]. This motivates a microscopic description in which the localised polarons self-organise to form a correlated electronic crystal [31–33]. A basic Mott state description [29,34–36] may be useful for describing single layers of $1\ \mathrm{T}-\mathrm{TaS}_2$[35,37], but is not suitable for addressing the amorphous polaronic state [32] or the structure and dynamics of vertex-antivertex annihilation in its metastable domain state [8,13]. However, the related charged Coulomb lattice gas (CLG) model of correlated polarons [31] leads to useful predictions of a variety of nonequilibrium states that have since been experimentally observed [38].

This complexity of the system makes it particularly interesting from the point of view of defect formation, and here we will find it necessary to discuss both a correlated-polaron approach for the microscopic configurations and rearrangements within the defect, and a conventional order parameter analysis to describe the slow coarse-grained collective dynamics of three intersecting long-range ordered domains.

To create a topologically non-trivial embedded defect in the surface layer, we apply an electrical pulse through a sharp STM tip, which locally destroys the C order [13–15] and typically forms quite diverse domain structures [8,11,13–15] with a variety of domain walls and junctions. The rapid self-assembly of polarons results in a mesoscopic network of topologically non-trivial domain walls and vertices [9,11,13] that can be manipulated by a metal tip or externally sourced current [13] (Fig. 1a iv). A Y-junction at the intersection of a particularly interesting set of domain walls sets the stage for this detailed study. Importantly for obtaining consistent results, the structure was found to be stable at low temperatures, and for tip currents below ˜2 nA, allowing a detailed investigation. Fig. 1b shows a time-averaged topographic FSTM image of a Y-junction vertex forming at the intersection of three domains (labelled A, B and C) within such a structure. A schematic construction of the Y-junction is shown in Fig. 1c, showing the polaron positions (denoted as idealised hexagrams) at the domain boundary. Domains A and B both have the same chirality ($\chi_L$), while domain C has $\chi_R$ chirality. Choosing a clockwise path, A and B are related to each other via a translation vector $\boldsymbol{T}_{A\to B} = (3\boldsymbol{a} - \boldsymbol{b})$, where $\boldsymbol{a}$ and $\boldsymbol{b}$ are crystal lattice constants (Fig. 1c). B and C are related by a mirror operation $\boldsymbol{\sigma}_{\boldsymbol{a}-\boldsymbol{b}}$ about the $\boldsymbol{a} - \boldsymbol{b}$ axis followed by a translation $-\boldsymbol{b}$, while A and C are related by a combination of a mirror operation $\boldsymbol{\sigma}_{\boldsymbol{a}}$ about the $\boldsymbol{a}$ axis, followed by a translation $-\boldsymbol{a}$. A schematic image of the CDW order at the vertex corresponding to the FSTM image in Fig. 1b is shown in Fig. 1d.

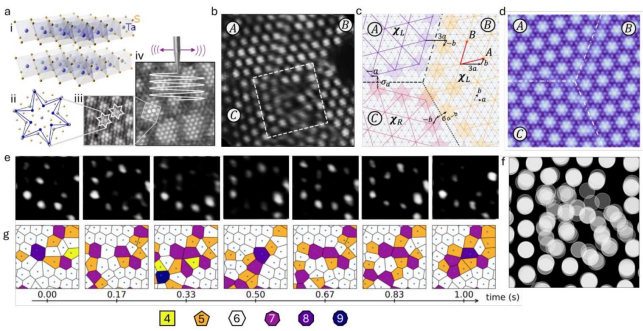


Fig. 1. Real-time dynamics of semi-localised electrons in a vertex trap. a. (i) The crystal structure of 1 T $-$ $TaS_2$, (ii) the polaronic lattice distortion at different temperatures [27] and (iii) high-resolution STM topography of the C CDW state. (iv) the domain state created by external perturbation with a schematic description of the fast-scanning STM measurement. b. The 7-minute time-average of an STM movie (videos S1 and S2) recorded with the STM tip at a constant height above the surface (V = 0.4 V, i = 1.5 nA) shows continuity of QP motion. c. The vertex structure showing broken mirror and translational symmetries, indicated by the vector constructions at the domain walls. d. The order parameter $\Psi_{\mathrm{CDW}}$ (x) at the vertex corresponding to (B) and (C) (the Ta atoms in the crystal lattice are also visible). e. A set of extracted frames measured 0.17 seconds apart, extracted from the full frame showing quasi-periodic individual polaron motion (see Video S3 for full sequence). f. A time-averaged image emphasising polaron motion. The trajectories are analysed in Fig. 3. g. A W-S tessellation of (E) showing 5-gon-7-gon and 4-gon-8-gon dislocations as well as single n-gon disclinations. A full movie is available in the supplement (S4).

The temporal and spatial current fluctuations $i(\boldsymbol{r}, t)$ in the vertex recorded by an FSTM reveal real-time motion of individual polarons. A movie recorded with constant tip height (voltage) over an area of $15 \times 15nm^2$ at a frame rate of $R_F \sim 6fps$ (25 MHz sampling rate, T = 77 K ) is shown in videos S 1 and S2. Fig. 1e shows a short sequence of frames extracted from Video S3 showing polaron movements in time on the millisecond timescale ( $\tau \sim 10ms$ ). The time-integrated polaron positions (depicted by circles) are shown in Fig. 1f, emphasising their trajectories. The observed strongly sub-thermal fluctuations ($kT \gg hv$) are persistent on the timescale of the experiment (7 minutes). Dislocations (DL) and disclinations (DC) associated with moving polarons are revealed by a Wigner-Seitz (W-S) tessellation (Fig. 1g) and appear as pentagon/heptagon pairs or individual $N$-gons ( $N = 4, 5, 7, 8$ ). Such defects are important, as they are topologically protected, which can lead to arrested electron dynamics [39,40]. The full Video S4 of defect dynamics shows that DCs occur primarily at the intersection of the $\chi_L/\chi_R$ domains and along B-C domain walls (DWs). DLs are present at the $\boldsymbol{T}$-symmetry-breaking DW boundary and show quite lively dynamics on the millisecond timescale (see Video S4).

Time-series plots of the temporal and spatial fluctuations of the tip current $i(\boldsymbol{r}, t)$ for a few chosen positions $\boldsymbol{r}$ identified by coloured dots in Fig. 2d are shown in Fig. 2a. (A larger data set is presented in the SI). We clearly identify two types of behaviour: (i) TLS telegraph noise in regions where particle motion is observed, and (ii) 'single-level' noise far from these regions. The corresponding current distribution $\theta(i(\boldsymbol{r}, t))$ is shown in Fig. 2b. Further, we observe in Fig. 2a that the telegraph noise of trace 3 has opposite phase compared with traces 1, 2 and 4. Thus, we note that the overall TLS behaviour is spatially correlated and phase-locked: the effective phase relation between the pixels $\phi(t)$ is maintained throughout the duration of the measurement even for pixels that are far apart (see SI). A map of $\phi(\boldsymbol{r})$ in Fig. 2f shows phase modulations across the entire image, with reference to the phase of the centre of the vertex.

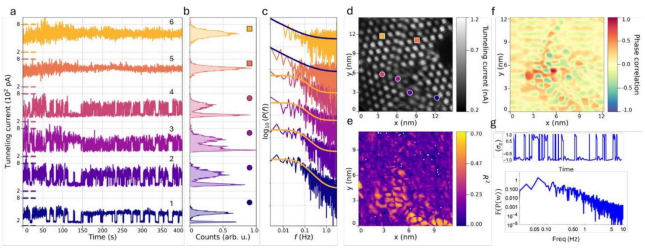


Fig. 2. Noise analysis of charge fluctuations. a. Time-traces of tunnelling current i(r, t) recorded at constant tip height at a few selected points shown in (d). They show temporally correlated 'telegraph noise' traces (1-4) with 0 or $\pi$ phase shift $\phi$, or featureless noise (traces 5 and 6). b. The dwell time distributions for the traces shown in (A) showing either single level or TLS behaviour. c. Fits to the power spectra of i($\mathbf{r}$, t) at points shown in (A) give either flat-top Lorentz spectra with $1/f^2$ tails or 1/f noise with frequency-independent tails at high f. e. A pixel map of the amplitude of TLS noise expressed as the fit confidence factor $r^2$ of Lorentz fits to F(i($\mathbf{r}$, t)) shown in (d). f. A map of the variation of phase $\phi(\mathbf{r})$ across the vertex space. g. Level occupancy $\langle\sigma^z\rangle$ and power spectrum F(P(w)) for an external noise-driven model TLS system.

Fourier power spectra $F_t(i(\boldsymbol{r},t))$ corresponding to the temporal current fluctuations $i(\boldsymbol{r},t)$ are shown in Fig. 2c. In the regions that show telegraph noise $F_t(i(\boldsymbol{r},t))$ clearly show characteristic 'flat-top'

Lorentzian curves $L(f)$ (Fig. 2c) with a $1/f^2$ high-frequency tail. Elsewhere, we ubiquitously see $1/f$ power spectra - attributed to current originating from many TLSs with different level spacings [17,41–43]. These areas show no saturation at low frequencies and exhibit frequency-independent 'white' noise at high frequencies, presumed to be of thermal origin. Separating the three different noise contributions $S = L(f) + \beta/f + \gamma$ for each pixel, we can spatially separate TLS noise from $1/f$ noise and obtain high-resolution maps of the amplitude of the TLS noise source (Fig. 2f). It is relevant to note here that the FSTM tip frame rate (6 Hz) is much faster than the observed polaron TLS dynamics shown in Fig. 2. We also note that there is no external source of noise in the observed TLS frequency range, that could drive the dynamics directly.

In addition to the amplitude and phase fluctuations of $i(\boldsymbol{r},t)$ above, plotting the polaron centre positions in the $x-y$ plane as a function of time (Fig. 3a and Video S5), we see that some particles appear to show dumbbell-like oscillating motion (Fig. 3b). The polaron motion patterns are also clearly discernible in the FSTM movies (S1 and S2). To examine if and how these displacements are correlated, in Fig. 3c and 3d we present an analysis of the positional correlations of pairs of polarons. The coloured dots depict the correlations between pairs of adjacent polarons along the $x$ and y coordinates (see SI for details). We observe particularly non-trivial polaron motion at the vertex core. For example, an abrupt change from symmetric (red dots) to antisymmetric polaron-pair displacements (blue dots) is visible at the centre of the vertex. Further away from the vertex, the displacements along the $\boldsymbol{T}$-symmetry-breaking A-B DW boundary show antisymmetric motion, seen as a line of pale blue dots along the A-B domain wall.

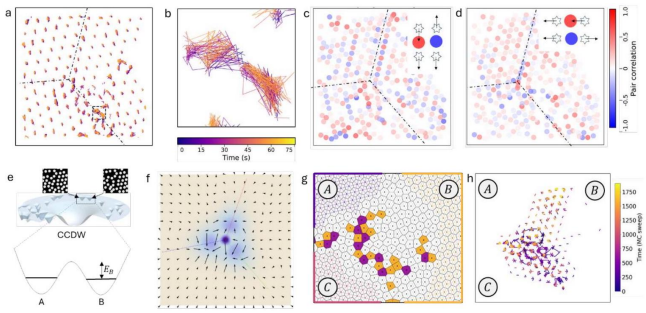


Fig. 3. Inter-particle motion correlations and modelling of Y-junction dynamics. a. and b. the measured spatial trajectory of polarons. The timeline is indicated by the colour bar. c. The polaron-pair displacement correlation coefficient $\xi$ (indicated by colour) along the x direction and d. The y direction. The displacements are defined by the legend. Note the cross-over from symmetric to antisymmetric motion at the vertex core. e. An energy landscape describing the domain configurational space. Neighbouring configurational states described by a double-well potential giving rise to TLS behaviour shown in Fig. 2g. f. A model simulation showing $\Delta^2(\boldsymbol{r}, t)$ (blue colour) and vector field proportional to the gradient $\nabla\phi(\boldsymbol{r}, t)$ for the low-energy branch of the hybridised Higgs-Goldstone mode. (See Video S6 for the temporal fluctuations. g. An MC simulation of defect time evolution. See Video S8 for the full sequence. h. Local MC polaron trajectories (See also Video S9).

Turning to a theoretical understanding of the dynamics, it is clear that neither a macroscopic CDW theory nor a microscopic, correlated electron model on their own can account for the rich set of observations described above. In particular, the microscopic motion of individual polarons at the core
of the defect is difficult to model in terms of CDW theory but can be faithfully reproduced using correlated polaron dynamics. In contrast, an order parameter approach is useful in understanding the overall slow dynamics at the Y junction in terms of a low-frequency Goldstone collective mode. Since collective modes are supported both by correlated polaronic crystals as well as CDWs, we don't run into contradictions. We thus proceed with a theoretical discussion on two levels. A correlated-polaron model is used to describe the microscopic re-configuration dynamics subject to Coulomb interactions between individual polarons, which are also subject to constraints imposed by the surrounding domain topology.
The collective order parameter, understood here as either the coarse-grained order parameter of the polaron crystal or directly describing a CDW, describes the amplitude and phase fluctuations that drive transitions between these re-configurations.

We first consider the microscopic polaron dynamics. The polarons are described by the Hamiltonian (19):

$$H = -\sum_{i,j} t_{ij} c_i^+ c_j + \sum_{i<j} V_{i,j} n_i n_j \tag{1}$$

where $t_{i,j}$ is the polaron tunnelling amplitude between sites $i$ and $j, c_i^+, c_i, n_i$ are the spinless fermion creation, annihilation, and occupation number operators at site $i, V_{i,j} = \frac{V_0}{r_{ij}} \exp\left(-\frac{r_{ij}}{r_s}\right)$ is the Coulomb screening potential, $r_{ij}$ is the real space distance between sites $i$ and $j, r_s = 4.5a \sim 1.5nm$ is the screening radius, $V_0 = \frac{e^2}{\epsilon_0 a} \sim 1eV$, and $a$ is the lattice constant we can calculate the polaron dynamics at the Y junction. Previous work has shown that domain-wall networks can host fractionalised charge and topologically entangled configurations that strongly constrain local polaron motion (12). For the Monte Carlo calculation, we consider the classical interaction-dominated limit $t_{ij} = 0$ and impose the experimentally observed domains

as fixed boundary conditions around the model space. These non-local constraints restrict the allowed polaron rearrangements at the Y-junction. The simulated defect evolution, shown as a Wigner-Seitz tessellation in Fig. 3g and Video S8, tends to form dislocation chains along the two mirror-symmetry-breaking domain walls. The corresponding trajectories in Fig. 3h and Video S9 qualitatively reproduce the confined and directionally correlated polaron motion observed experimentally in Fig. 3a, demonstrating the role of non-local boundary constraints in the microscopic dynamics.

We next consider the collective fluctuations that drive transitions between the allowed polaron configurations. At larger length scales, the system is described by the conventional complex order parameter commonly written as $\Psi(\boldsymbol{r},t) = \Delta(\boldsymbol{r},t)e^{i\phi(\boldsymbol{r},t)}$, where $\Delta(\boldsymbol{r},t)$ is the "Higgs" amplitude and $\phi$ describes the phason or "Goldstone mode". In commensurate systems such as 1 T $-$ $TaS_2$, the bulk Goldstone mode is gapped with an energy scale corresponding to the pinning energy [41]. Approaching the Y junction, $\Psi(\boldsymbol{r},t)$ is suppressed as $\Delta(\boldsymbol{r},t) \to 0$ and the local fluctuations of the phase stiffness $K(\boldsymbol{r},t) \propto \Delta(\boldsymbol{r},t)^2$ slow down and diverge in relative magnitude as $\frac{\delta K(\boldsymbol{r},t)}{K} \sim \frac{\delta\Delta(\boldsymbol{r},t)}{\Delta}$. Near the Y-junction, the spatially varying order parameter and broken translational and mirror symmetries couple the amplitude and phase fluctuations, giving rise to hybridised collective modes. To describe these dynamics we use a phenomenological Ginzburg-Landau Lagrangian for the two collective fields, $\Delta(\boldsymbol{r},t)$ and $\phi(\boldsymbol{r},t)$,

$$\mathcal{L} = \frac{\chi}{2}\left(\partial_t\phi\right)^2 + \frac{1}{2v^2}\left(\partial_t\Delta\right)^2 - \frac{\rho_s}{2}(\nabla\phi)^2 - \frac{\kappa}{2}(\nabla\Delta)^2 - \frac{\mu^2}{2}\left(\Delta - \Delta_0\right)^2 - \frac{\rho_0}{2}\Delta^2(\nabla\phi)^2. \tag{2}$$

The first two terms describe the inertial dynamics of the phase and amplitude fields, respectively. The terms proportional to $\rho_s$ and $\kappa$ penalise spatial variations of the phase and amplitude, while the term proportional to $\mu^2$ restores the amplitude towards its equilibrium value $\Delta_0$. The final term makes the phase stiffness dependent on the local amplitude and therefore couples the Higgs and phase degrees of freedom. In a uniform system the two modes are approximately distinct, whereas the strongly
inhomogeneous order parameter near the Y-junction leads to their hybridisation. The corresponding equations of motion are obtained from the Euler-Lagrange equations for $\Delta$ and $\phi$. (See SI for calculation details). We are particularly interested in the low-frequency hybrid branch localised at the Y vertex core to describe the observed dynamics. The predicted fluctuations of the phase for this mode are primarily longitudinal along the DWs, but also include skew motion, arising from the non-trivial broken symmetries at the Y junction, as shown in Fig. 3f. The phase currents, which are proportional to the charge currents - and drive polaron motion, are given by $\boldsymbol{j}_\phi(\boldsymbol{r},t) = -K(\boldsymbol{r},t)\nabla\phi(\boldsymbol{r},t)$, depicted by the arrows in Fig. 3f. (Videos S6 and S7 show the temporal fluctuations of $\boldsymbol{j}_\phi(\boldsymbol{r},t)$.) The observed TLS behaviour can be thought to arise from transitions between neighbouring minima of the constrained polaron configurational landscape (Fig. 3e). Each minimum represents a locally stable polaron arrangement compatible with the Y-junction boundary conditions. Collective amplitude-phase fluctuations modulate the barriers between these configurations, producing telegraph switching and the corresponding flat-top Lorentzian noise spectrum shown in Fig. 2g. Thus, the microscopic model determines which polaron rearrangements are allowed, while the collective mode drives transitions between them. A calculated noise spectrum $S_k(\boldsymbol{r},\omega) = \int dt e^{i\omega t}\langle\delta K(\boldsymbol{r},t)\delta K(\boldsymbol{r},0)\rangle$, calculated using Langevin dynamics is enhanced and shifted to low frequencies, with the appearance of telegraph-like noise and a flat-top spectrum (Fig. 2g), like the experimental spectra in Fig. 2c (See SI for calculation details).

### 17.1.2 Discussion

The observed polaron dynamics at the Y-junction defect are consistent with transitions between discrete, correlated configurations, rather than the free motion of isolated electrons (or polarons). These transitions are governed by local Coulomb interactions and constrained by the non-local topology of the surrounding domains, while the slow time scale of dynamics is consistent with collective amplitudephase fluctuations. The persistence of this motion under continuous STM measurement underscores the robustness of this topologically constrained degree of freedom against local perturbations. While electrical noise of unidentified origin has been observed in diverse systems - such as 1 T $-$ $TaS_2$[17,41], Al-Si superconducting circuits [45], and strongly correlated materials [46,47], where it is even associated with local pairing [48] - our FSTM mapping pioneers the identification, characterisation, and potential control of such two-level systems (TLSs) in metastable quantum states. This approach could be extended to other systems, including glasses, other quantum materials with fabrication-induced defects, or purposefully engineered defects for quantum circuits.

The domain structures and junctions observed here are not unique to 1 T- $TaS_2$ but are ubiquitous in transition metal chalcogenides [31,49,50] and other systems with similar phase diagrams. For instance, discommensurations in the correlated-polaron phase diagram suggest that deviations from magicnumber filling fractions ($f = 1/13, 1/9, 1/7$)[31] lead to domains and junctions of varying sizes and shapes. This has direct relevance to doped pseudogap phases [50], where incompletely ordered phases may host various defects. Furthermore, hexagonal lattices are not a prerequisite: square lattices of misfit dislocations also exhibit arrested dynamics at domain wall crossings [51], hosting local excitations. A particularly striking parallel is the ultraslow-frequency noise spectrum observed in transmon qubits [52], suggesting that the mechanisms uncovered here may contribute to understanding and mitigating noise in quantum computing devices.

### 17.1.3 Methods

#### Materials

Single-crystal 1 T- $TaS_2$ samples used in the research were in-house grown using the chemical vapour deposition method, as described previously [7,26].

#### Fast STM

The fast-scanning electronics module (Elettra-Sincrotrone Trieste S.C.p.A.) is implemented on top of an LT Nanoprobe STM system (Scienta Omicron AB). The system records the tunnelling current $i_t(V)$ from the Pt/Ir tip to the surface of the 1T-TaS $_2$ crystal with a tip that controllably oscillates laterally across the sample surface (Fig. 1a). The measured STM tunnelling current at time $t$ and position $\boldsymbol{r}$ is $i(\boldsymbol{r}, t) \propto |M_{\text{tip-sample}}|^2 D_s(\boldsymbol{r}, t)$, where $M_{\text{tip-sample}}$ is the usual matrix element for the tunnelling transition between the tip states and the sample, $D_s(\boldsymbol{r}, t)$ is the density of states at the surface of the sample at any given time $t$. The total current $i(\boldsymbol{r}, t)$ is an incoherent integration over time of the individual electron tunnelling currents as the tip moves across the sample. The $V-i$ curves in conventional scanning mode are consistent with those reported previously [9,11,14,15]. The $V$ and $i$ parameters are shown in the figure captions for each case. In the C state, the bright 'blobs' approximately correspond to individual polarons. In the vertex region and in the domain walls, the CDW acquires non-trivial time-dependent phase fluctuations $\boldsymbol{\delta}(\boldsymbol{r}, t)$, so this approximation is no longer valid, and $D_s(\boldsymbol{r}, t)$ is determined by the structure of microscopic electronic wavefunctions [9,11,14,15]. The Fast STM typically records $100 \times 100$ pixel image sequences with a tunnelling current sampling rate of $25 \sim 100$MHz, averaged typically for $10 \sim 20\mu s$ per pixel limited by the amplifier bandwidth (400 kHz), recorded line-wise (Fig. 1b), resulting in frame rates $R_F = 5\tilde{}100$ Hz. Note that all dynamics

that is slower than the individual frame recording time $t > \tau_{\text{frame}}$ ($\sim 0.1s$) is visible as real-time motion. Dynamics that occurs on timescales $\tau_{\text{frame}} > t > \tau_{\text{pixel}}$ ($\sim 10^{-8}s$) leads to temporal and spatial distortions of the images. Faster dynamics with $t \ll \tau_{\text{pixel}}$ averages out and the structure appears static. If there is no motion blur, the FTSM gives atomicresolution images.

### Monte Carlo simulations of the defect dynamics at a T-junction

Monte Carlo simulations of the Markov chain dynamics for the Hamiltonian on a triangular lattice were performed using the standard Metropolis algorithm. The proposed successive state in the chain consists of setting $n_i = 0$ at an occupied site and $n_j = 1$ at a randomly selected neighbouring unoccupied site. The simulations were performed with a fixed number of charged particles on a lattice of the size of $80 \times 80$ atomic sites with lattice period $a$. The boundary conditions were fixed in the sense that for approximately 2 rows of polarons from the edge, polarons cannot move. This imposes the ordering of polarons towards the middle of the system, resulting in a highly frustrated topologically imposed structure in the exact same way as in the experiment. The number of polarons was chosen to be 492, closely resembling the experiment. The interaction potential $V(i,j)$ in the simulations shown in the paper has a Yukawa form $V_{i,j} = \frac{V_0}{r_{ij}} \exp\left(-\frac{r_{ij}}{r_s}\right)$ with the screening radius $r_s = 4.5a$ and was cut at distances larger than $24a$. Note that the screening length is larger than the polaron radius in the C state. The annealing simulations were performed by decreasing the temperature from $0.005V_0$ to $0.003V_0$, which is deep within the ordered phase, with 2000 temperature steps with equal increments, where 70 Monte Carlo sweeps ( $70 \times 80 \times 80$ steps) were performed at each temperature point. The initial configuration was chosen by setting all the polarons that are able to move next to each other in the centre of the system.

### References


1. Self-Assembly at All Scales | Science. https://www.science.org/doi/full/10.1126/science.1070821.

2. Zurek, W. H. Cosmological experiments in superfluid helium? Nature 317, 505-508 (1985).

3. Kibble, T. W. B. Topology of cosmic domains and strings. J. Phys. A: Math. Gen. 9, 1387 (1976).

4. Schreiber, M. et al. Observation of many-body localization of interacting fermions in a quasirandom optical lattice. Science 349, 842-845 (2015).

5. Wei, K. X., Ramanathan, C. & Cappellaro, P. Exploring Localization in Nuclear Spin Chains. Phys. Rev. Lett. 120, 070501 (2018).

6. Yusupov, R. et al. Coherent dynamics of macroscopic electronic order through a symmetry breaking transition. Nature Phys 6, 681-684 (2010).

7. Stojchevska, L. et al. Ultrafast Switching to a Stable Hidden Quantum State in an Electronic Crystal. Science 344, 177-180 (2014).

8. Kranjec, A. et al. Electronic Dislocation Dynamics in Metastable Wigner Crystal States. Symmetry 14, 926 (2022).

9. Gerasimenko, Y. A., Karpov, P., Vaskivskyi, I., Brazovskii, S. & Mihailovic, D. Intertwined chiral charge orders and topological stabilization of the light-induced state of a prototypical transition metal dichalcogenide. npj Quantum Mater. 4, 1-9 (2019).

10. Cho, D. et al. Nanoscale manipulation of the Mott insulating state coupled to charge order in 1T-TaS2. Nat Commun 7, 10453 (2016).

11. Ma, L. et al. A metallic mosaic phase and the origin of Mott-insulating state in 1T-TaS2. Nat Commun 7, 10956 (2016).

12. Brazovskii, S., Brun, C., Wang, Z.-Z. & Monceau, P. Scanning-Tunneling Microscope Imaging of Single-Electron Solitons in a Material with Incommensurate Charge-Density Waves. Phys. Rev. Lett. 108, 096801 (2012).

13. Mraz, A. et al. Manipulation of fractionalized charge in the metastable topologically entangled state of a doped Wigner crystal. Nat Commun 14, 8214 (2023).

14. Park, J. W., Cho, G. Y., Lee, J. & Yeom, H. W. Emergent honeycomb network of topological excitations in correlated charge density wave. Nat Commun 10, 4038 (2019).

15. Park, J. W., Lee, J. & Yeom, H. W. Zoology of domain walls in quasi-2D correlated charge density wave of 1T-TaS2. npj Quantum Mater. 6, 1-6 (2021).

16. Skolimowski, J., Gerasimenko, Y. & Žitko, R. Mottness collapse without metallization in the domain wall of the triangular-lattice Mott insulator $1T\ensuremath{-} { mathrm {TaS} }_{2} $. Phys. Rev. Lett. 122, 036802 (2019).

17. Salgado, R. et al. Low-frequency noise spectroscopy of charge-density-wave phase transitions in vertical quasi-2D 1T-TaS2 devices. Appl. Phys. Express 12, 037001 (2019).

18. Geremew, A. K., Rumyantsev, S., Debnath, B., Lake, R. K. & Balandin, A. A. High-frequency current oscillations in charge-density-wave 1T-TaS2 devices: Revisiting the "narrow band noise" concept. Appl. Phys. Lett. 116, 163101 (2020).

19. Magnussen, O. M., Polewska, W., Zitzler, L. & Behm, R. J. In situ video-STM studies of dynamic processes at electrochemical interfaces. Faraday Discuss. 121, 43-52 (2002).

20. Schitter, G. & Rost, M. J. Scanning probe microscopy at video-rate. Materials Today 11, 40-48 (2008).

21. Dri, C. et al. The new FAST module: A portable and transparent add-on module for time-resolved investigations with commercial scanning probe microscopes. Ultramicroscopy 205, 49-56 (2019).

22. Vaskivskyi, I. et al. Controlling the metal-to-insulator relaxation of the metastable hidden quantum state in 1T-TaS2. Science Advances 1, e1500168 (2015).

23. Nakanishi, K. & Shiba, H. Domain-like Incommensurate Charge-Density-Wave States and the First-Order Incommensurate-Commensurate Transitions in Layered Tantalum Dichalcogenides. I. 1T-Polytype. Journal of the Physical Society of Japan 43, 1839-1847 (1977).

24. Rossnagel, K. On the origin of charge-density waves in select layered transition-metal dichalcogenides. J. Phys.: Condens. Matter 23, 213001 (2011).

25. Zong, A. et al. Ultrafast manipulation of mirror domain walls in a charge density wave. Science Advances 4, eaau5501 (2018).

26. Ravnik, J. et al. Chiral domain dynamics and transient interferences of mirrored superlattices in nonequilibrium electronic crystals. Sci Rep 13, 19622 (2023).

27. Bozin, E. S. et al. Crystallization of polarons through charge and spin ordering transitions in 1T-TaS2. Nat Commun 14, 7055 (2023).

28. Wilson, J. A., Di Salvo, F. J. & Mahajan, S. Charge-density waves and superlattices in the metallic layered transition metal dichalcogenides. Advances in Physics 24, 117-201 (1975).

29. Sipos, B. et al. From Mott state to superconductivity in 1T-TaS2. Nature Mater 7, 960-965 (2008).

30. Rossnagel, K. Suppression and emergence of charge-density waves at the surfaces of layered 1T-TiSe2 and 1T-TaS2 by in situ Rb deposition. New J. Phys. 12, 125018 (2010).

31. Vodeb, J. et al. Configurational electronic states in layered transition metal dichalcogenides. New J. Phys. 21, 083001 (2019).

32. Gerasimenko, Y. A. et al. Quantum jamming transition to a correlated electron glass in 1T-TaS2. Nat. Mater. 18, 1078-1083 (2019).

33. Vodeb, J. et al. Non-equilibrium quantum domain reconfiguration dynamics in a two-dimensional electronic crystal and a quantum annealer. Nat Commun 15, 4836 (2024).

34. Tosatti, E. & Fazekas, P. ON THE NATURE OF THE LOW-TEMPERATURE PHASE OF 1T-TaS2. J. Phys. Colloques 37, C4-168 (1976).

35. Petocchi, F. et al. Mott versus Hybridization Gap in the Low-Temperature Phase of $1T\text{\ensuremath{-}}{\mathrm{TaS}}_{2}$. Phys. Rev. Lett. 129, 016402 (2022).

36. Butler, C. J., Yoshida, M., Hanaguri, T. & Iwasa, Y. Mottness versus unit-cell doubling as the driver of the insulating state in 1T-TaS2. Nat Commun 11, 2477 (2020).

37. Law, K. T. & Lee, P. A. 1T-TaS2 as a quantum spin liquid. Proceedings of the National Academy of Sciences 114, 6996-7000 (2017).

38. Ravnik, J. et al. A time-domain phase diagram of metastable states in a charge ordered quantum material. Nat Commun 12, 2323 (2021).

39. Pretko, M. & Radzihovsky, L. Fracton-Elasticity Duality. Phys. Rev. Lett. 120, 195301 (2018).

40. Pretko, M. Emergent gravity of fractons: Mach's principle revisited. Phys. Rev. D 96, 024051 (2017).

41. Liu, G., Rumyantsev, S., Bloodgood, M. A., Salguero, T. T. & Balandin, A. A. Low-Frequency Current Fluctuations and Sliding of the Charge Density Waves in Two-Dimensional Materials. Nano Lett. 18, 3630-3636 (2018).

42. Weissman, M. B. $ frac{1} {f}$ noise and other slow, nonexponential kinetics in condensed matter. Rev. Mod. Phys. 60, 537-571 (1988).

43. Noise in Nanoscale Semiconductor Devices. (Springer International Publishing, Cham, 2020). doi:10.1007/978-3-030-37500-3.

44. Ma, Y., Hou, Y., Lu, C., Li, L. & Petrovic, C. Possible origin of nonlinear conductivity and large dielectric constant in the commensurate charge-density-wave phase of 1T-$TaS_2$. Phys. Rev. B 97, 195117 (2018).

45. Kristen, M., Voss, J. N., Wildermuth, M., Rotzinger, H. & Ustinov, A. V. Random telegraph fluctuations in granular microwave resonators. Appl. Phys. Lett. 122, 202602 (2023).

46. Pokharel, B. K., Wang, Y., Jaroszynski, J., Sasagawa, T. & Popović, D. Charge-order dynamics in underdoped La1.6-xNd0.4SrxCuO4 revealed by electric pulses. Appl. Phys. Lett. 118, 244104 (2021).

47. Caplan, D. S. et al. Anomalous Noise in the Pseudogap Regime of $YBa_2Cu_3O_{7-\delta}$. Phys. Rev. Lett. 104, 177001 (2010).

48. Zhou, P. et al. Electron pairing in the pseudogap state revealed by shot noise in copper oxide junctions. Nature 572, 493-496 (2019).

49. Yan, S. et al. Influence of Domain Walls in the Incommensurate Charge Density Wave State of Cu Intercalated $1T\text{\ensuremath{-}} {\mathrm{TiSe}}_{2}$. Phys. Rev. Lett. 118, 106405 (2017).

50. Joe, Y. I. et al. Emergence of charge density wave domain walls above the superconducting dome in 1T-TiSe2. Nature Phys 10, 421-425 (2014).

51. Liu, Y. et al. Strain relaxation from annealing of SiGe heterostructures for qubits. J. Appl. Phys. 134, 035302 (2023).

52. Schlör, S. et al. Correlating Decoherence in Transmon Qubits: Low Frequency Noise by Single Fluctuators. Phys. Rev. Lett. 123, 190502 (2019).

### 17.1.4 SM

**Experimental data acquisition**

The STM data is measured using a combination of "LT Nanoprobe" (Scienta Omicron AB, Sweden) multi-tip scanning tunnelling microscope and a "FAST SPM" (Elettra Sincrotrone Trieste S.C.p.A., Italy) module. The experiments discussed in the main text were performed at 77 K with liquid nitrogen as a coolant in the bath cryostat of the STM.

The image rasterisation is performed by applying a sine wave along one axis (X', fast axis) and a triangular wave along the second axis (Y', slow axis) as shown in Fig. S1. The image size and framerate are chosen to be compatible with the mechanical properties of the piezo drives controlling the tunnelling tip at this temperature, as well as their physical arrangement in the instrument (as shown in the Figure).

The Fast STM is performed in the quasi-constant-height mode, with the feedback loop being much slower than the tip modulation along the fast axis. To compensate for the sample orientation relative to the scanning axes (tilt), additional modulation is performed in the Z' axis synchronously to the X' and Y' axes. The experiment's feedback setpoint (stabilised tunnelling current) is kept at the level of 1.0 to 1.5 nA to ensure both a good signal-to-noise ratio and low electrical disturbance to the sample in case of the conventional STM measurement.

The scanning parameters for the movie presented in the main text are: $100 \times 100$px with a pixel frequency of 119990 Hz, which corresponds to a 6 frames per second output movie (refer to the next section for the pixel data conversion details).

### Experimental data conversion

The tunnelling current is recorded as a 1D array of values with a 16 -bit ADC. To reconstruct the fast movie, the following steps are performed:

1. The current time trace is cut into frames.
   A fast scan of a size $X_{px} \times Y_{px}$ and length $N_f$ frames is represented by an array of size $2 \times \mathrm{x_{px}} \times \mathrm{y_{px}} \times N_f$ due to the "subframes" representing the "forward" and "backward" directions (half-periods of the harmonic driving signal, shown in Fig. S1b-c).

2. The fast grid of a corresponding size is triangulated onto the regular square grid using the standard Delaunay triangulation method.
   The fast grid represents equally spaced points in time. Due to the shape of the harmonic signal, this would correspond to the spatial distribution as shown in Fig. S1. The current values are interpolated linearly for the regular grid. The resolution used in the experiment ensures an average of 8 pixels per CDW unit cell to coincide with the resolution usually used for such studies.

3. The drift correction is done on the frames (Fig. S2).
   The drift between each pair of frames is found independently in $X_r$ and $Y_r$ (orthogonal) directions using standard methods. The overall drift of the scanning tip relative to the sample is found as a square function for each direction (Fig. S2a).
   The found drift is used to redo Step 2. The perfect fast grid is offset by the corresponding drift value before the triangulation to the regular square grid is performed. This allows us to avoid double interpolation to obtain the drift-corrected images (Fig. S2b).

These three steps ensure as little data processing as possible before it is used in further analysis. At the same time, for plotting and visualising purposes in the Main text and the Supplementary Information, additional contrast adjustment or data filtering can be performed on the images to highlight features or parts of interest (Fig. S2c).

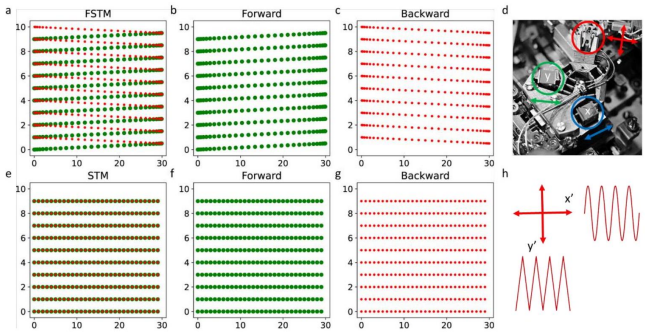


Fig. S1. Fast STM raster compared to the conventional STM. a. Fast STM raster of a single "frame" and its components (b, c). e. Conventional STM raster and its components (f, g). d. STM scanner photo with the tip (red) and two piezo elements (green and blue) marked. Note that the relative arrangement of the actual device X and Y piezo drives is not orthogonal. h. Temporal shape of the voltage signal applied to x' and y' piezo.

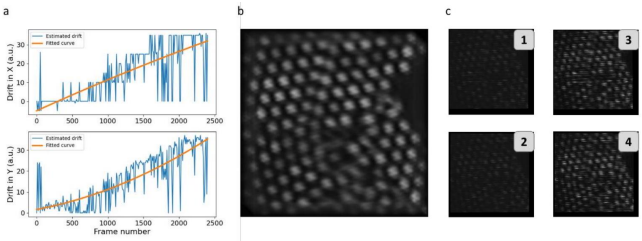

Fig. S2. Drift compensation for the fast STM movie. a. Example of the drift between the frames for a time sequence. b. The sum of all the frames showing the "average" frame over the movie. This panel shows the different domains of the CDW in 1T-TaS $_2$, which stay static for all the frames and the dynamic part in between, which is getting blurred when taking the sum. c. Example of raw frames after the drift compensation $(1, 2)$ and after the visualisation adjustment $(3, 4-$ same frames as 1,2$)-$ in this case, only outliers by the current value are masked (0.01 and 99.99 percentiles).

### Single- and multi-level current signals

If we consider time traces of the measured tunnelling current at some positions on the surface, we can clearly see two types of behaviour: single-level-like and two-level-like (telegraph noise) as shown in Fig. S3a. All the positions for this analysis are defined from the polaron positions defined for the reference (time-averaged) image of the surface (Fig. 1b of the main text). The first case is observed for the positions inside the domains (curve 1 in the figure), while the second is characteristic of the area of "dynamic" polaron behaviour (curves 2-6). Points with the telegraph noise show different ratios between the "high" and "low" states, with only a single one (curve 7) showing a clear preferential level. At the same time, for several positions (curves 8-10), three different levels can be defined. Most of the dynamic points show some kind of temporal synchronisation, which can clearly be seen at times 110-145 s, 360-370 s and others. At the same time, they can have opposite phases as shown in the section "Signal phase analysis".

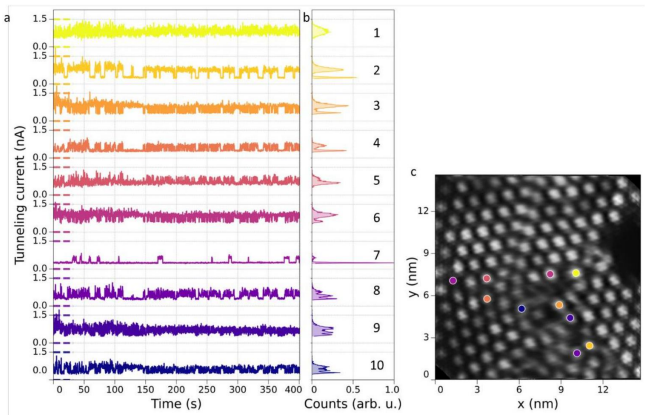


Fig. S3. Examples of the single- and multi-level behaviour of the current signal measured for the selected polaron positions. a. Time traces of the current value measured at the selected positions centred on the "polaron positions". b. Current values distribution for the traces from (a). c. Reference frame with the positions marked and colour-coded in the same way as in (a) and (b).

### Current level noise

As can be seen in the previous section and from the main text, the observed "width" of the current measured seems to depend on its absolute value, which is most prominent in the case of two-level behaviour (dynamic polarons), where the "low" level looks sharper than the "high" level. To check
whether this is a signature of the energetic levels' properties on the material surface or an instrumental limitation, we performed the following analysis:

1. We took all the points with the single-level behaviour of the current:

a) The first case corresponded to the regular square grid over the entire surface (Fig. S4c).

b) The second case corresponded only to the polaron positions as defined before (Fig. S4d).

2. We fitted a standard Gaussian function to the noise (current) distribution for each spatial point, considering and analysing the distribution of the peak FWHM from the peak centre position.

3. We fitted a linear function to the distribution from (2).

As can be seen from Fig. S4, except for some outliers, most of the extracted data points fit well to the linear dependence between the measured current and the noise distribution in the measurement. This implies that the observed effect of the level width distribution is mostly instrumental.

While the analysis was performed only on the "static" points, we consider this data as representative of the whole dataset since the measured current values cover a wide range of current values. The multi-level points were excluded due to the additional uncertainty added by the multi-peak Gaussian fitting.

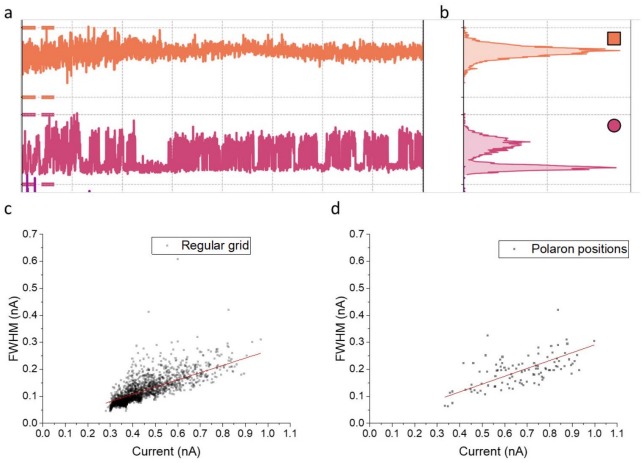


Fig. S4. Dependence of the noise on the absolute current level measured for a single sample position. a. Time trace of the tunnelling current measured for single static (one level) and dynamic (two levels) points (cut from Fig. 2 or the main text) and b. The corresponding current distribution. c, d. Dependence of the FWHM of a Gaussian peak fitted to the current level (only single-level cases) from its centre position for the regular grid over the whole scanned area (c) and only on the polarons positions (d) as defined in the main text and Fig. 1.

### Frequency-domain analysis

The frequency-domain (noise) analysis is performed on the drift-corrected raw data as discussed in Section “Experimental Data Conversion”. The analysis of each spatial point is done in the following way:

1. The time trace of a single point is found as $I_{(x,y,r_s)}$, where $x, y$ are the coordinates and $r_s$ - is the size of the window in which the mean intensity value is calculated for each point in time. The window size for analysis is constant for analysis of all the points of a single movie and allows for compensating for single-pixel noise in the data, if any. For computational ease and to avoid extra conversion operations, the window is taken as a square of size $(2r_s+ 1) \times (2r_s + 1)$, centred on the position $(x, y)$.

2. The frequency-domain behaviour of the point data is calculated using a standard Fast Fourier Transform (FFT).

3. The frequency data fitting.
   The power spectrum ( $P(f)$ ) is fitted with the following functions to find the type of signal present at the point:

   a. Lorentzian function corresponding to the single oscillator behaviour:
   $$F(f) \approx a\frac{1}{f^2+\gamma^2} + c$$
   For this fitting, the Lorentzian is considered centred at $x_0 = 0$.

   b. $1/f$ function corresponding to the average of many oscillators:
   $$F(f) \approx b\frac{1}{f} + c$$
   After the fits are found, they are compared in terms of the following characteristic values:

   i. Coefficient of Determination (how well a model explains the variance in the data)
   $$R^2 = 1 - \frac{\sum\left(f_i - \hat{f}_i\right)^2}{\sum\left(f_i - \bar{f}_i\right)^2}$$
   Higher value $R^2$ is better;

   ii. Root Mean Square Error
   $$RMSE = \sqrt{\frac{1}{n}\sum\left(f_i - \hat{f}_i\right)^2}$$
   Lower value is better.

4. The best model is found as the one with higher $R^2$ and lower $RMSE$.

5. Movie map reconstruction.

For the full movie, the frame is split into a regular "downsampled" grid, and for each point, Steps 3 and 4 are performed, resulting in a spatial map of the frequency features (Fig. S5).

To ensure that the statistics (and as a result, the fitting) is the same, the edges of the movie frame obtained during the drift correction process are not considered in the map.

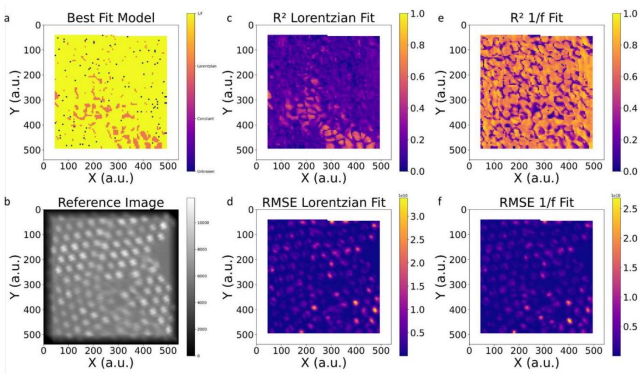


Fig. S5. Spatial map of the sample features. a. Best fit model distribution obtained as the highest $R^2$ and the lowest RMSE for the selected spatial point on the surface as referenced in panel (b). Spatial maps of $R^2$ and $RMSE$ are shown for the Lorentzian fit $(\mathbf{c}, \mathbf{d})$ and $1/f$ fit $(\mathbf{e}, \mathbf{f})$ correspondingly.

Signal phase analysis

Since the sample shows two-level-like behaviour as seen from Fig. 2 of the main text, we can analyse the phase component of such a signal across the surface of the sample. For this, we can take a single pre-defined point and calculate the relative phase of the rest of the movie in the following way.

1. As a reference, we take a time-dependent signal of a single position on the sample (e.g., corresponding to a defined polaron position). The time trace is calculated for a square window of pixels, as discussed in Section "Frequency-domain Analysis". This signal is taken as $I_{\text{ref}}$ .

2. For a point with coordinates $(x, y)$, we calculate its time trace $I_{(x,y)}$ in a similar fashion.

3. We calculate a sliding-window Pearson correlation coefficient $r_{k_{(x,y)}}$ :

$$r_{k_{(x,y)}} = \frac{\sum \left(I_{(x,y)_i} - \bar{I}_{(x,y)_i}\right)\left(I_{\text{ref}\ i} - \bar{I}_{\text{ref}\ i}\right)}{\sqrt{\sum \left(I_{(x,y)_i} - \bar{I}_{(x,y)_i}\right)^2 \sum \left(I_{\text{ref}\ i} - \bar{I}_{\text{ref}\ i}\right)^2}}$$

   Two examples of such correlation traces are shown in Fig. S6d.

4. A single point value of the phase is defined as a mean value of the correlation trace:

$$\mathrm{r}_{(x,y)} = \overline{r_{k_{(x,y)}}}$$

5. The map is reconstructed for a regular grid.

Several examples of the signal phase calculation are shown in Fig. S6a-c. As can be seen, the features of the map do not depend on the selected reference within the same phase. When a point of the opposite phase is selected as the reference, the map inverts (Fig. S6e). For a static position on the sample with no two-level-like behaviour, no features are observed in the phase map (Fig. S6f).

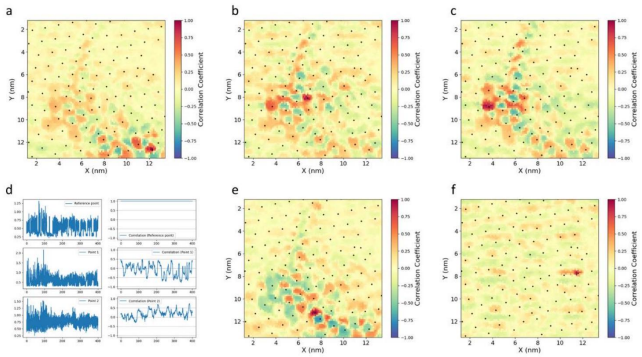


Fig. S6. Signal phase analysis. a. The phase map clearly demonstrates areas with a two-level-like signal. Positive and negative values correspond to the in-sync and anti-sync signals. The maximum value of 1 (red) corresponds to the reference point. b, c. Same as panel (a) for different reference points of the same phase. d. Examples of the single-point correlation traces $\left(r_{k_{(x,y)}}\right)$ for the reference point, a two-level-like point of the opposite phase, and a static position on the sample (right) and the corresponding time traces (left). e. The anti-sync to (a-c) point taken as a reference inverts the map. f) The signal phase map calculated by taking a static point as a reference shows no features.

Pair correlation for polaron positions

The pair correlation analysis shown in Fig. 3c of the main text is done in the following way:

1. A dataset is taken in the form of polarons' positions on the surface across the movie.
2. A global (common for all polarons) quadratic drift trend is removed to avoid offset in the correlation calculation in the later steps.
3. For all the known polarons, a Voronoi reconstruction is done to find nearest neighbours (NNs).
4. For each pair of NNs, a Pearson correlation coefficient is calculated using the formula from the previous section for the full time trace of X and Y coordinates independently.
5. The corresponding coefficient from (4) is plotted as a point centred at the mid-point between the two Voronoi sites.

The corresponding results for X and Y coordinates are shown in Fig. S7. The same results for X are also presented in Fig. 3c of the main text. It can be seen in the figure that the Y coordinate results show a periodic (every second) change in the sign of the correlation coefficient for the top of the movie. This can be attributed to the experimental noise in the movie, where frames scanned "up" and "down" have different Y intensity distributions for the top and bottom of the polarons observed.

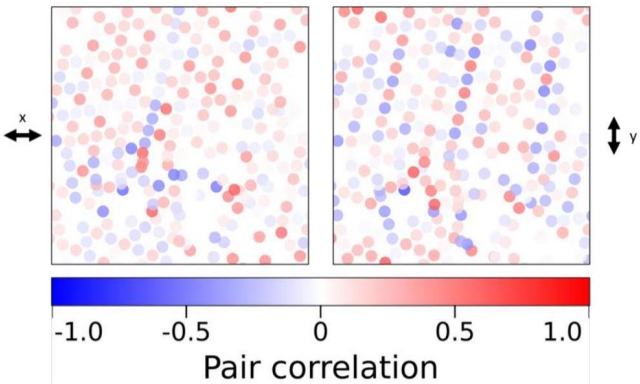


Fig. S7. Pair correlations for the positions of the nearest neighbour polarons in X and Y directions.

Properties of the $\boldsymbol{\sigma} - \boldsymbol{T}$ vertex in 1T-TaS2

The structure of the vertex shown in the movie and Fig. 1 of the main text is shown in Fig. S8. The figure corresponds to the experimentally observed structure. The three superlattice domains A, B and C are individually fit to the time-averaged topographic movie image, taking into account drift and motional averaging. The crystal lattice (fine triangular mesh) is superimposed without further adjustment of the domain positions. The orientation of the David stars remains the same, as it is fixed by the crystal lattice.

Because the $\boldsymbol{Q}_i$ are restricted by the lattice commensurability condition, the net phase circulating around the vertex $\oint_l \nabla\phi.d\boldsymbol{l}$, where $\phi = \sum_{i=1}^{3}(\boldsymbol{Q}_i.\boldsymbol{r} + \varphi)$, does not in general result in a winding number of 0 or $2\pi n$, where $n$ is an integer. In particular, the combination of mirror and translation operation at the AB wall, as well as additional translations at BC and AC domain walls, introduces non-trivial phase jumps. The phase jump across the mirror wall $\psi_B(r) = \psi_A(\sigma\boldsymbol{r})^*$, ($^*$ is complex conjugation caused by M) is not simply additive, as it reverses the sign of the imaginary part of the order parameter $\psi_i = A_i e^{i\phi} \rightarrow \psi_i^m = A_i e^{-i\phi}$.

The transformation operators representing the domain walls AB, BC and CA, respectively, are described below.

(i) Domains A and B are related by a translation vector $\boldsymbol{T}_{A\to B} = (3\boldsymbol{a} - \boldsymbol{b})$, such that $\boldsymbol{T}_{A\to B}\chi_L^B = \chi_R^A$. Thus, the order parameter $\psi_B(\boldsymbol{r}) = \psi_A(\boldsymbol{r} + \boldsymbol{T}_{A\to B})$, etc.

(ii) For clockwise winding domains B and C are related by a mirror operation $\sigma_{\boldsymbol{a}-\boldsymbol{b}}$ about the $\boldsymbol{a} - \boldsymbol{b}$ axis, followed by a translation $-\boldsymbol{b}$ along the $\boldsymbol{a}$ axis $M_{B\to C}(\sigma_{a-b}, -\boldsymbol{b})\,\chi_L^B = \chi_R^C$. For anticlockwise winding $M_{C\to B}(\sigma_{a-b}, -\boldsymbol{a})\,\chi_R^C = \chi_L^B$. The order parameter change is $\psi_C(\boldsymbol{r}) = \psi_B(\sigma\boldsymbol{r} + \boldsymbol{a})^*$ for clockwise winding, and $\psi_C(\boldsymbol{r}) = \psi_B(\sigma\boldsymbol{r} - \boldsymbol{a})^*$ for anticlockwise winding.

(iii) Domains A and C are related by a combination of a mirror operation $\sigma_{\boldsymbol{a}}$ about the $\boldsymbol{a}$ axis, followed by translation $-\boldsymbol{a}$ axis, written as: $M_{A\to B}(\sigma_a, -\boldsymbol{a})\,\chi_L^A = \chi_R^C$ for clockwise, and $M_{B\to A}(\sigma_a, \boldsymbol{a})\,\chi_R^C = \chi_L^A$ for anticlockwise winding. The order parameter change is $\psi_B(\boldsymbol{r}) = \psi_A(\sigma\boldsymbol{r} - \boldsymbol{a})^*$ for clockwise winding, and $\psi_C(\boldsymbol{r}) = \psi_B(\sigma\boldsymbol{r} + \boldsymbol{a})^*$ for anticlockwise winding.

In summary, global chirality is broken by the mirror walls. The net winding is non-zero due to the phase and chirality mismatch, resulting in a vortex-like defect which may attract charge and give rise to localised in-gap states as well as pinning of collective excitations (e.g. phase modes of the CDW). Under non-equilibrium conditions, chiral CDW currents are possible around such a defect.

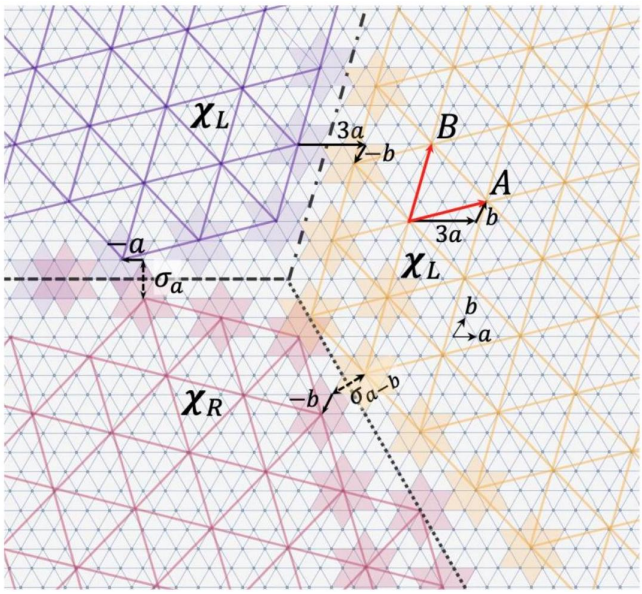


Fig. S8. Symmetry-breaking properties of the M-T vertex. The legend shows the crystal lattice and superlattice vectors, respectively. Domains A and B have the same chirality with respect to the crystal axes ($\chi_L$). They are related to each other through a translation $T_{A-B}$. Domain C is of opposite chirality ($\chi_R$). In addition to the mirror symmetry breaking at the A-B and B-C domain walls, there is an additional translation in both cases. The legends show lattice vectors $\boldsymbol{a}, \boldsymbol{b}$, the superlattice vectors $\boldsymbol{A}, \boldsymbol{B}$, and the mirror ($\sigma$) and translation ($\boldsymbol{T}$) operations shown by dashed and solid arrows, respectively.

Hybrid Goldstone-Higgs modes in the 1/13 commensurate CDW superlattice

Coupled amplitude-phase dynamics

The complex CDW order parameter is written as

$$\Psi(\mathbf{r}, t) = \Delta(\mathbf{r}, t)e^{i\phi(\mathbf{r},t)},$$

with amplitude $\Delta$ and phase $\phi$ describing, respectively, the "Higgs" and "Goldstone" sectors of the condensate.

At the DW, and particularly at the Y junction $\Delta(\mathbf{r}, t) \to 0$. Furthermore, due to breaking of symmetry at the DW and Y-junction, the two components of the order parameter can mix, leading to hybridisation. In the commensurate 1/13 charge-density-wave (CDW) phase of $1T - \mathrm{TaS}_2$, the electronic density modulation forms a $\sqrt{13} \times \sqrt{13}$ superstructure. The underlying lattice vectors a and **b** of the hexagonal layer define the real-space basis, while the commensurate superlattice is generated by

$$\mathbf{A} = 3\mathbf{a} + \mathbf{b}, \quad \mathbf{B} = -4\mathbf{b} + 3\mathbf{a}.$$

The corresponding reciprocal vectors $\mathbf{G}_A$ and $\mathbf{G}_B$ are defined by $\mathbf{G}_A \cdot \mathbf{A} = 2\pi, \mathbf{G}_B \cdot \mathbf{B} = 2\pi$, and $\mathbf{G}_A.\ \mathbf{B} = \mathbf{G}_B \cdot \mathbf{A} = 0$.

A translation of a CDW domain by a lattice vector T induces a discrete phase slip

$$\Delta\phi(\mathbf{T}) = \frac{1}{13}\left(\mathbf{G}_A \cdot \mathbf{T} + \mathbf{G}_B \cdot \mathbf{T}\right),$$

reflecting the 1/13 commensurability.
The general time-dependent Ginzburg-Landau functional can be written as

$$\mathcal{L}_0 = \frac{1}{2}M_\Delta \dot{A}^2 + \frac{1}{2}M_\phi \dot{\varphi}^2 - \frac{1}{2}K_\Delta A^2 - \frac{1}{2}K_\phi \varphi^2 - GA\varphi.$$

where $M_\Delta, M_\phi$ are effective inertial parameters, $K_\Delta, K_\phi$ are stiffnesses setting the bare Higgs- and (Goldstone-) phason-like frequencies, $G$ describes Higgs-phason hybridization arising from spatial overlap of amplitude and phase gradients at the junction.

The undamped equations of motion follow from the Euler-Lagrange equations:

$$\begin{aligned} M_\Delta \ddot{A} + K_\Delta A + G\varphi &= 0 \\ M_\phi \ddot{\varphi} + K_\phi \varphi + GA &= 0 \end{aligned}$$

In both the Y-junction and circular geometries, the term $(\nabla\phi)^2$ couples the phase rotation (Goldstone sector) to the amplitude oscillation (Higgs sector), creating a mixed collective mode. Dissipation can be included phenomenologically in the equations of motion via a Rayleigh dissipation function

$$\mathcal{R} = \frac{1}{2}\gamma_\Delta \dot{A}^2 + \frac{1}{2}\gamma_\phi \dot{\phi}^2$$

where $\gamma_\Delta$ and $\gamma_\phi$ are damping coefficients for the amplitude-like and phase-like components, respectively, which yields to damped equations of motion:

$$\begin{aligned} M_\Delta \ddot{A} + \gamma_\Delta \dot{A} + K_\Delta A + G\varphi &= 0 \\ M_\phi \ddot{\varphi} + \gamma_\phi \dot{\varphi} + K_\phi \varphi + GA &= 0. \end{aligned}$$

The role of the damping is to reduce amplitude and slow down the motion.

### Y-junction of domain walls

At a trijunction of three CDW domains, domain walls meeting at ˜ 120° carry distinct microscopic translations:

$$\mathbf{T}_{\mathrm{DW}} = 3\mathbf{a} - \mathbf{b}, \quad \mathbf{T}_{\mathrm{C1}} = -\mathbf{b}, \quad \mathbf{T}_{\mathrm{C2}} = -\mathbf{a}.$$

The first, $\mathbf{T}_{\mathrm{DW}}$ , preserves mirror symmetry and mainly breaks translational invariance, whereas $\mathbf{T}_{\mathrm{C1}}$ and $\mathbf{T}_{\mathrm{C2}}$ break both mirror and translational symmetry in opposite chiral senses.

The corresponding phase gradients along each arm are proportional to $\Delta\phi\left(\mathbf{T}_i\right)$ and define local longitudinal wavevectors $k_i = \Delta\phi\left(\mathbf{T}_i\right)/\ell_\phi$, where $\ell_\phi$ sets the relaxation length of the phase ramp.

Within each domain arm, the static phase profile is modeled as

$$\phi_i(\mathbf{r}) = k_i s_i w\left(s_i\right) g_i\left(n_i\right) + \chi_i \frac{n_i}{\ell_\phi} w\left(s_i\right) g_i\left(n_i\right),$$

where $s_i$ and $n_i$ are the longitudinal and transverse coordinates with respect to the $i$ th arm, $w\left(s_i\right)$ is a logistic envelope confining the arm to one side of the vertex, $g_i\left(n_i\right) = e^{-n_i^2/2\sigma_i^2}$ represents transverse confinement, and $\chi_i$ encodes mirror-symmetry breaking ( $\chi_{\mathrm{C1}} = -\chi_{\mathrm{C2}}$ for opposite handedness).

The full dynamic phase field is a time-dependent superposition of these arm components:

$$\phi(\mathbf{r}, t) = c_T(t)\phi_{\mathrm{DW}}(\mathbf{r}) + c_{C1}(t)\phi_{\mathrm{C1}}(\mathbf{r}) + c_{C2}(t)\phi_{\mathrm{C2}}(\mathbf{r}) + \phi_{\mathrm{tw}}(\mathbf{r}, t),$$

with slowly varying weights

$$c_i(t) = 1 + \delta_i \sin\left(\omega_G t + \varphi_i\right),$$

and a small vertex-localized "twist" field $\phi_{\mathrm{tw}}(\mathbf{r}, t) \propto \left(n_{\mathrm{C1}} - n_{\mathrm{C2}}\right) e^{-r^2/2}$ that breaks the residual threefold symmetry. The amplitude field $\Delta(\mathbf{r}, t)$ has a similar envelope structure but oscillates in time as

$$\Delta(\mathbf{r}, t) = \Delta_0(\mathbf{r})\left[1 + a_0 \cos\left(\omega_H t\right)\right].$$

The coupled oscillations at the Goldstone frequency $\omega_G$ and Higgs frequency $\omega_H$ produce a local hybrid mode at the vertex in which the phase currents $\mathbf{v}_\phi = \nabla\phi$ periodically shear and rotate between the three arms. The simulation of Sec. 3 visualizes $\rho(\mathbf{r}, t) = |\Psi|^2 = \Delta^2$ as a density map and $\mathbf{v}_\phi$ as arrows (Fig. 3f of main text and Supplementary Video S6).

### Circular (vortex-like) hybrid mode

A second class of collective excitation occurs when the phase field forms a continuous circulation around a topological core. The order parameter is written in polar coordinates $(r, \theta)$ as

$$\Psi(r, \theta, t) = \left[\Delta_0(r) + \delta\Delta(r, t)\right] \exp\left\{i\left[m\theta + \eta_2(t)\cos(2\theta) f_2(r) + \eta_3(t)\sin(3\theta) f_3(r)\right]\right\},$$

where: $m = \pm 1$ is the vortex charge (direction of circulation); $f_{2,3}(r)$ are Gaussian radial envelopes confining higher angular harmonics near the core; $\eta_{2,3}(t)$ are slowly varying harmonic amplitudes, modulated at the Goldstone frequency $\omega_G$; $\delta\Delta(r, t) = \Delta_0(r) a_0 \cos\left(\omega_H t\right)$ describes the breathing of the amplitude (Higgs) mode.

The functions

$$\eta_2(t) = A_2 \sin\left(\omega_G t + \varphi_2\right), \quad \eta_3(t) = A_3 \cos\left(\omega_G t + \varphi_3\right),$$

introduce an angular wobble or twist of the phase fronts, causing the direction of $\mathbf{v}_\phi = \nabla\phi$ to evolve continuously in time. The simultaneous amplitude breathing and phase wobble constitute a localised Goldstone-Higgs hybridised mode (Supplementary Video S7).

**Energy Comparison Between the Y-Junction and Circular Hybrid Modes**

In the commensurate 1/13 charge-density-wave (CDW) phase of $1T - \mathrm{TaS}_2$, the phase of the order parameter is strongly locked to the lattice through the commensurability potential. The energy cost of collective excitations can therefore be understood in terms of the elastic stiffness $\rho_S$, the amplitude stiffness $\kappa$, and the commensurate

**(a) Y-junction hybridised mode.**

The Y-junction consists of three domain walls meeting at a vertex, each wall characterised by a local phase slip $\Delta\phi_i = \mathbf{G} \cdot \mathbf{T}_i/13$. Because the phase variations are confined along three narrow arms, the total energy is localised and finite:

$$E_{\mathrm{Y}} \simeq 3\tau\ell + E_{\mathrm{vertex}} \ ,$$

where $\tau$ is the line tension (energy per unit length) of a domain wall and $\ell$ is the local relaxation length of the phase ramp along the arm. There is no net $2\pi$ phase winding around the vertex, so the Y-junction hybrid does not incur global topological cost. The mode energy therefore saturates at the vertex and typically lies at low frequency. At the intersection of three domain walls, the phase
currents periodically shear between the arms, producing a hybrid mode localised at the vertex. The dynamic mixing of translational and chiral arms represents a "three-pronged" collective excitation.

**(b) Circular (vortex-like) hybridised mode.**

In contrast, the circular hybrid mode carries an azimuthal phase winding $\phi(\mathbf{r}) \sim m\theta$ with integer vorticity $m = \pm 1$. Such a configuration produces a circulating phase gradient and hence a finite supercurrent density $\mathbf{j}_\phi = \rho_s \nabla\phi$ throughout the region. Its energy in a continuous medium is approximately

$$E_{\mathrm{vortex}} \approx \pi\rho_s m^2 \ln\frac{R}{\xi} + E_{\mathrm{core}}$$

where $\xi$ is the core (Higgs) healing length and $R$ is the system size. In the commensurate CDW, the lock-in potential further converts the logarithmic divergence into a linear confinement: $E_{\mathrm{vortex}} \propto \kappa R + E_{\mathrm{core}}$ , since the phase winding must be sustained by a closed loop of discommensurations.

Around a topological defect or discommensuration loop, the CDW phase can circulate continuously. Higher harmonic terms ( $\cos 2\theta, \sin 3\theta$ ) modulate this flow in time, creating a breathing, twisting vortex. The resulting mode interpolates between pure rotational Goldstone motion and isotropic amplitude breathing.

**(c) Relative ordering.**

Because the Y-junction mode involves only localised shears and amplitude modulations along three arms, while the circular mode requires a global phase rotation, we have the hierarchy

$$E_{\mathrm{Y}} < E_{\mathrm{vortex}} \ ,$$

with the Y-junction hybrid mode being the lower-energy collective mode.
Simulation of telegraph noise
Telegraph noise typically refers to a two-level fluctuating signal that randomly switches between two discrete states over time. It is often associated with stochastic processes such as trapping/de-trapping of charges in semiconductors or fluctuations in quantum systems. Here, we aim to describe the current fluctuations arising from fluctuations of the CDW phase $\phi$ of the order parameter in the $TM$ intersection.

Assuming a potential energy landscape shown in Fig. S9 (also in Fig. 3 of the main text), we can model the TLS system as either quantum or classical dynamics, which are applicable in different temperature regimes. Presently, due to the relatively high temperature (77 K), below we present a calculation of the Langevin dynamics. We note that the results of a quantum Lindblad calculation are qualitatively similar.

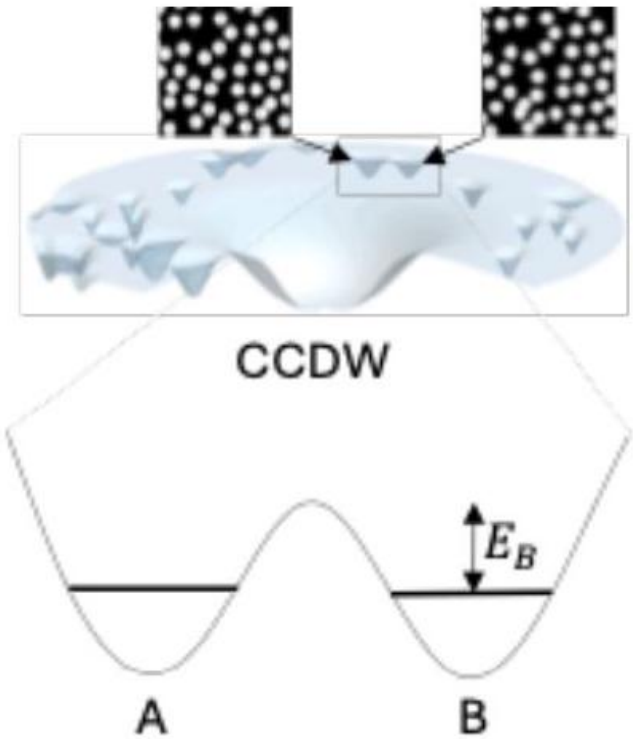


Fig. S9. A schematic energy landscape depicting multiple near-degenerate configurational domain states and the C ground state as the global minimum. Thermally driven and noise-driven tunnelling processes are indicated.

**Langevin TLS dynamics**

The simplest case to consider is a double-well particle potential $V(x) = ax^4 - bx^2$, (Fig. S9) where $x$ is the configurational coordinate, and a and b are constants. The appropriate equation of motion depicting dynamics driven by Brownian motion (overdamped Langevin equation) is given by:

$$\gamma \frac{dx}{dt} = -\frac{dV}{dx} + \sqrt{2\gamma k_B T}\eta(t) + D(t)$$

where $\gamma$ is the damping, $\eta(t)$ is the noise source and $D(t)-$ is an external drive, which is here the hybridised low-frequency collective mode.

The trajectory of the system is calculated using the Euler-Maruyama method and is shown in Fig. S10 (and Fig. 2g of the main text) for the case of a sinusoidal drive $D(t)$ that simulates

the STM tip scan across the sample.

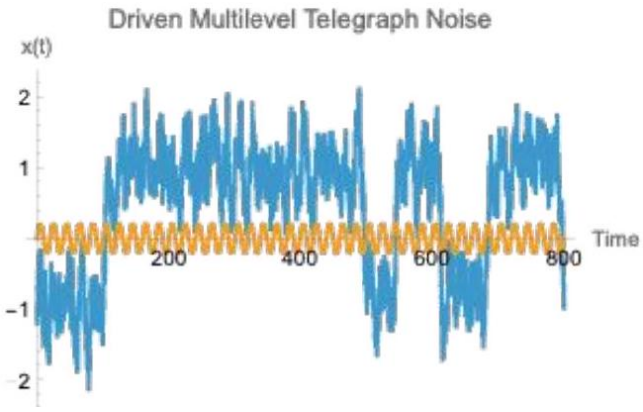


Fig. S10. The noise trajectory for a Langevin oscillator using a non-linear double-well potential and a sinusoidal external perturbation (orange).

The corresponding state occupancy histogram shown in Fig. S11 shows an asymmetric two-peak structure that appears if we introduce a slight asymmetry of the potential, but the peak widths are similar. Note that in the experiment, the peak widths are significantly different, which cannot be simulated by the present model, even by introducing different state lifetimes, multiple levels or modest changes to the potential. The power spectrum that corresponds to the trajectory in Fig. S10 is shown in Fig. S12 and Fig. 2g of the main text.

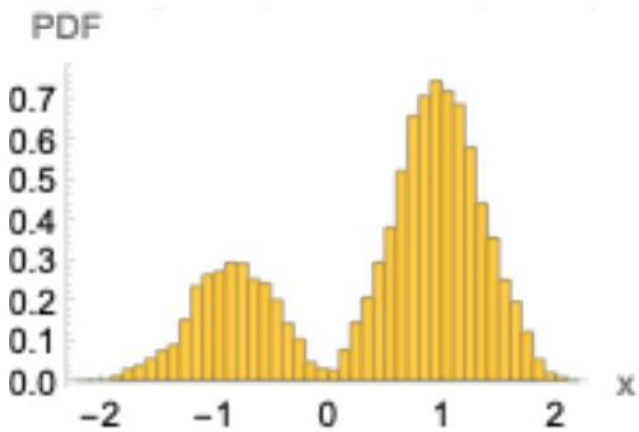


Fig. S11. The state occupation histogram corresponding to the calculation shown in Fig. S10. Note the asymmetric shape of the distribution.

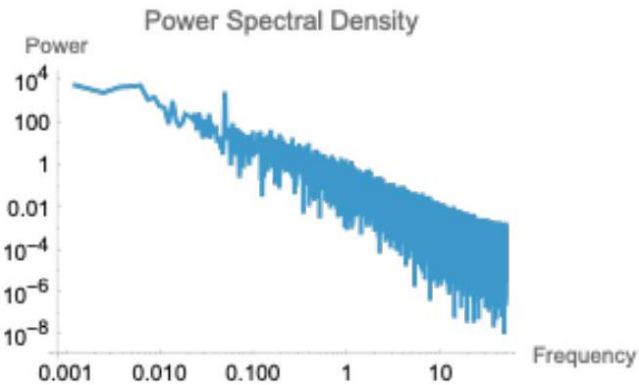


Fig. S12. Shows the power spectral density that corresponds to the trajectory in Fig. S10. Note the flat top response at low frequencies and $1/f^2$ behaviour at higher frequencies. The sharp peak corresponds to the sinusoidal drive frequency used in this simulation. Its presence has no significant effect on the general behaviour unless it exceeds the stochastic term $\eta(t)$.

**Supplementary Videos for Real-time imaging of quasiparticle dynamics at a topological defect in an electronic crystal**

Video S1.
https://www.youtube.com/watch?v=khGoK60tQn0&list=PLBvdEMM5_r8s&index=1
Sequence of Fast STM frames on the surface of 1T- $TaS_2$ at 77 K (6 FPS). The raw data measured with the Fast STM is shown in real time. The data is drift-corrected with no additional processing except for the outlier filter (0.05 and 99.95 percentiles), and the colour scale is adjusted for the best visualisation. The time counter represents the data time.

Video S2.
https://www.youtube.com/watch?v=O190yB-rM1w&list=PLBvdEMM5_r8s&index=2
Filtered sequence of Fast STM frames on the surface of 1 $T - TaS_2$ at 77 K. The Fast STM movie is shown at 5x speed, highlighting the circular motion. The data is drift corrected. Additional directional blur (vertical) and Gaussian blur (both directions) per frame is applied. The colour scale is adjusted for the best visualisation. The time counter represents the data time.

Video S3.
https://www.youtube.com/watch?v=RlVYd8l6VlQ&list=PLBvdEMM5_r8s&index=3
Circular individual polaron motion on the surface of 1 $T - TaS_2$ at 77 K . Quasi-periodic individual polaron motion next to the vertex in the domain structure. The data processing and visualisation correspond to Supplementary Video S2, with additional colour scale adjustment. The time counter represents the data time.

Video S4.
https://www.youtube.com/watch?v=NnLMxC-J0k4&list=PLBvdEMM5_r8s&index=4
Sequence of Wigner-Seitz tessellations of the CDW on the surface of 1 $T - TaS_2$ at 77 K . The Voronoi reconstruction is performed using standard methods for individual frames of the raw data (Supplementary Video S1). The colour scale is chosen to highlight non-hexagonal elements in the structure, and is shown in the video. The time counter represents the data time.

Video S5.
https://www.youtube.com/watch?v=V6aMH6inCIs&list=PLBvdEMM5_r8s&index=5
Trajectories of polarons on the surface of 1 T − $TaS_2$ at 77 K. Each element trajectory segment represents the shift between the current polaron position and the position of this polaron in the previous frame. The time counter represents the data time.

Video S6.
https://www.youtube.com/watch?v=iUPI0FQTCb8&list=PLBvdEMM5_r8s&index=6
Temporal fluctuations for the Y-junction mode. A model simulation showing $\Delta 2(\boldsymbol{r}, t)$ (blue) and a vector field proportional to the gradient $\nabla\phi(\boldsymbol{r}, t)$ for the low-energy branch of the hybridised Higgs-Goldstone mode for the Y-junction mode.

Video S7.
https://www.youtube.com/watch?v=5Neafefmvnw&list=PLBvdEMM5_r8s&index=7
Temporal fluctuations for circular (vortex-like) mode. A model simulation showing $\Delta 2(\boldsymbol{r}, t)$ (blue) and a vector field proportional to the gradient $\nabla\phi(\boldsymbol{r}, t)$ for the low-energy branch of the hybridised Higgs-Goldstone mode for the circular (vertex-like) mode.

Video S8.
https://www.youtube.com/watch?v=4eQdD9BVlZ4&list=PLBvdEMM5_r8s&index=8
Simulation of spontaneous polaron self-organisation at 1/13 filling with non-trivial boundary conditions. The Monte Carlo simulations are performed as described in the main text. The data is represented in terms of the Wigner-Seitz tessellation for polarons. The black solid dots represent positions of the polarons, and the grey dots represent the atomic lattice. The colour scale is chosen to highlight non-hexagonal elements in the structure, and is shown in the video. The counter represents different "frames" in calculations.

Video S9.
https://www.youtube.com/watch?v=GBw5AnIU36Y&list=PLBvdEMM5_r8s&index=9
Trajectories of polarons during self-organisation at 1/13 filling with non-trivial boundary conditions. The Monte Carlo simulations are performed as described in the main text. Each segment represents a single motion step of a single polaron. The counter represents frames in the calculations.

# Part XII
# Other Explanations of a Typical Theories

## 18 Theoretical Modeling of the Non-equilibrium Amorphous State in 1T-$TaS_2$ by Vodeb, Kabanov, Gerasimenko, Vaskivskyi, Ravnik, Mihailovic

**Abstract**

1T-$TaS_2$ is known for it's remarkably complex phase diagram and it's unique long-lived metastable hidden (H) state. Recently, a novel metastable state has been discovered using higher fluences for photoexcitation than in the case of the H state. The state has been dubbed as amorphous (A) due to it's similarity to glass. Expanding on the work of Brazovskii and Karpov, we show that the A state can be successfully modeled with classical interacting polarons on a two dimensional hexagonal lattice. We have found that the polaron configuration of the A state corresponds to a frustrated screened Coulomb system, where there is no order-disorder phase transition.

### 18.1 Introduction

The crystal of 1T-$TaS_2$ (TAS) exhibits a layered structure of S-Ta-S layers, where each of the atomic layers is arranged in a hexagonal lattice. Each Ta atom is surrounded by an octahedral arrangement of S atoms [1]. Due to this highly anisotropic character of the crystal we may neglect any kind of three dimensional behavior and only focus on a single layer of TAS.

The interplay of Coulomb interaction [16], spin-orbit coupling [3] and electron-phonon interaction [4] results in various competing phases of TAS, which emerge as external parameters such as temperature and pressure are varied. When subjected to high pressure TAS becomes superconducting [13]. At ambient pressure and high enough temperatures TAS is a homogeneous metal and upon lowering the temperature a series of charge density wave (CDW) transitions take place [6] as follows. At 540 K an incommensurate CDW is formed, where the CDW modulation is incommensurate with underlying atomic lattice. When the temperature is lowered even further, at 350 K, a nearly-commensurate CDW is formed, where a hexagonal structure of domains with a commensurate CDW is separated by domain walls, where the CDW is incommensurate with the atomic lattice. The phase below 190 $\sim$ 220 K has been interpreted as the commensurate CDW phase due to the perfect commensurability of the CDW with the underlying atomic lattice all throughout the crystal. The C phase also exhibits spin liquid like behavior [7]. Fig. 18.1 shows a schematic of the microscopic picture of the C phase. In this paper we adopt the interpretation of the C phase as a system of classical interacting polarons first proposed by Brazovskii [8]. Within this interpretation the ratio of the number of polarons and the number of atoms in the system or the *polaron concentration* is exactly 1/13. If polarons repel each other then they will arrange themselves in a hexagonal polaronic lattice, because this is the minimal energy configuration of such a system. The work of Stojchevska et al. [14] has shown that the C phase can be photoexcited via an ultra-short laser pulse into a long-lived metastable state. Due to the fact that the excited phase cannot be found on the equilibrium phase diagram of TAS it has been dubbed as the hidden (H) state. Karpov et al. [32] have subsequently shown by performing Monte Carlo simulations of a system of classical repulsive polarons that if the polaron concentration is perturbed slightly from 1/13, the H state can be obtained within the scope of this interpretation. The classical Monte Carlo calculations neglect the quantum aspects of polarons and instead focus on the large scale configurational ordering

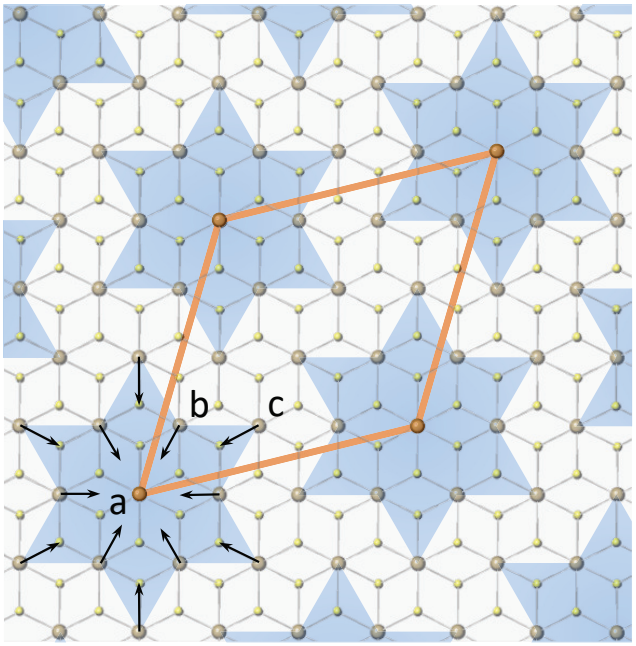


Figure 18.1: **A schematic of the microscopic picture in the C phase:** A new unit cell is formed, where 12 Ta atoms are pulled towards the 13th in the center (marked with the letter a) in the shape of a star of David. The two different types of atoms with respect to their deviation from a perfect atomic lattice are marked with the letters b and c. The electron wave function also becomes localized on top of the central Ta atom. We interpret this unit cell as the polaron quasiparticle. The orange colored rhombus shows the unit cell of the hexagonal polaron lattice

of polarons. Quantum mechanical methods cannot do so due to their computational intensity. Methods used for analyzing the quantum mechanical aspects of polarons in the ground state include exact diagonalization [11], variational exact diagonalization [12], quantum Monte Carlo [13], variational methods [14] and DMRG [15]. Other methods deal with the polaron dynamics and include Ehrenfest dynamics [16, 17], time-dependent density functional theory (TDDFT) [18], the multiconfiguration time-dependent Hartree method [19], its multilayer formulation [20] and the hierachical equations of motion [21, 22]. TDDFT has been proven particularly successful in studying phenomena involved in polaron formation and dynamics, such as transient vibration energy redistribution and spectroscopy [23] and defects in nanomaterials [24, 25].

A recent paper by Gerasimenko et al. [21] has reported the discovery of a novel long-lived metastable state, where polarons are arranged in a disordered pattern. It is formed via photoexcitation with an ultrafast laser pulse, which confirms the state's non-equilibrium nature. It exhibits remarkable stability (at least 10 hours), which excludes any transient nature typically present in excited states. Moreover, even though the polaronic pattern suggests localization of charge, the system exhibits metallic behavior. Therefore the nature of this state is highly non-trivial and physically interesting. The main purpose of this paper is to show that the configurational aspect of the localized charges of this amorphous (A) state can also be understood within the scope of the classical polaron picture and to try to elucidate the reason for the disordered pattern.

## 18.2 The Model

The final A state can be modeled in the classical polaron picture of correlated electrons on a hexagonal lattice. TAS is known for the strong presence of the electron-phonon interaction [9]. Therefore, we assume that equation 4.15 in chapter 4.2 in [28], where small interacting polarons form in a system of electrons and phonons, is applicable. We neglect polaron hopping

and spin, as we are only interested in the configurational aspect of the repulsive interaction between polarons. The Hamiltonian has the form

$$\mathcal{H} = \sum_{i,j} V(i,j)(n_i - \nu)(n_j - \nu), \tag{18.1}$$

where $V(i,j)$ is the potential energy of interacting polarons, $n_i$ is 1 if the site occupied by a polaron and 0 otherwise, and $\nu$ is the average polaron concentration. $\nu$ is defined as a ratio of the number of polarons in the system, which is fixed throughout the simulation, and the number of lattice sites in the finite lattice used in simulations. The interaction between polarons has two contributions. The attraction due to the overlap of phonon clouds and long range Coulomb repulsion. The first part may be short or long-range depending on the type of phonons involved in polaron formation. If we assume that only polar phonons are responsible for polaron formation, the resulting interaction will be reduced to

$$V(i,j) = \frac{e^2}{\epsilon_0 |\mathbf{r}_i - \mathbf{r}_j|} \tag{18.2}$$

where $\epsilon_0$ is the static dielectric constant of the material. Both the lattice and electrons contribute to it, however the lattice contribution is indeed dominant. The interaction with acoustic phonons as well as with nonpolar optical phonons leads to the short range attraction of polarons, but here we neglect the short range contribution to the potential. Since the system has finite conductivity the long range Coulomb repulsion is screened. Therefore, we approximate it by the Yukawa potential

$$V(i,j) = \frac{e^2}{\epsilon_0 |\mathbf{r}_i - \mathbf{r}_j|} exp(-|\mathbf{r}_i - \mathbf{r}_j|/r_s), \tag{18.3}$$

where $r_s$ is the screening radius.

## 18.3 Monte Carlo Method

Monte Carlo (MC) simulations of simulated annealing were performed using a standard Metropolis algorithm. A proposed successive state in the Markov chain consists of one polaron moving in a random direction and a finite distance away from its current position. Simulations were performed on a hexagonal lattice with the lattice constant $a$ and of the size of $84 \times 78$ sites, where periodic boundary conditions were imposed. The number of polarons in the system is constant throughout the simulation procedure. In order to simulate annealing, the system would always start off at a temperature of $10^{-2}$ measured in units of $e^2/\epsilon_0 a k_B$ , which corresponds to the high temperature phase of the model for the commensurate (C) state. Afterwards, the system is cooled slowly down to a temperature of $10^{-3}$ with a temperature step of $10^{-5}$. There were $14 \times 10^6$ MC steps performed at each temperature step. One of the main reasons for introducing the Yukawa form of the polaron interaction is in the substantial growth of the MC relaxation time with the growth of the range of interaction. The screening length $r_s$ has been chosen as $4.5a$ and the interaction has been manually set to 0 at distances greater than $24a$. At this value of $r_s$ the interaction range exceeds the radius of one polaron in C state ($\sqrt{13}a \approx 3.61a$). Furthermore, it is numerically feasible due to the manageable relaxation times, which follow from it. The code is available for reproducibility at [29].

## 18.4 Tiling

Tiling of a polaron configuration can serve as a good visual illustration of the effective charge density topography present in the system as well as all the different nearest neighbor

distances present between polarons. The way both tilings are achieved is with the help of the so called Voronoi diagram. When a set of coordinates on a plane is given, which are the polaron coordinates, the plane can be partitioned into regions. Each coordinate is assigned a region of points in the plane, which are closer to it than to any other coordinate. This is done for the experimental amorphous state and the theoretical model for it in Fig. 18.2. Every Voronoi cell has one polaron charge associated with it and if we divide the charge by the cell's area, we obtain the charge density of the cell. Since the charge of a polaron is fixed (at least in simulations), one can get a clearer perspective on the charge density present in the system just based on the coloring of all the different Voronoi cells. After the Voronoi diagram is complete, one can construct a different set of tiling polygons from the Voronoi diagram's polygons. Each new polygon has 4 vertices and represents a distance between two neighboring coordinates. The first two vertices are the two neighboring coordinates from which the distance that the polygon represents is calculated. The other two vertices are the two points, which are part of the Voronoi polygons containing the two coordinates and are also the closest to both coordinates. This can be done for any two coordinates, which share two vertices of their Voronoi polygons. Because the distances between polarons in the model are discrete due to the perfect underlying hexagonal lattice, one can specify a color for each tiling polygon based on the distance between the two coordinates it connects. The coloring scheme for the experimental polaron coordinates is extended in the sense that the color spectrum in between any two colors represents the spectrum of all the possible distances between the two discrete distances.

## 18.5 Results

Within the scope of the particular lattice gas model used in our simulations, the C phase can be understood as the ground state of a system of polarons, where the polaron concentration is exactly 1/13. Experimental measurements of the polaron density in the STM images of the C and amorphous (A) states indicate that the polaron density in A state is about 1.23 times higher than in C state [21]. Simulations were therefore performed at the corresponding polaron concentration and the result shows similarity with experimental data. Fig. 18.2 shows the comparison between experiment and theory. The takeaway from Fig. 18.2 is the fact that both the theoretical and experimental polaron pattern exhibit disorder. A clearer comparison may be achieved via the polaron pair correlation function $g^{(2)}_{pol}(r) = \langle n(r)n(0)\rangle$. Fig. 18.3 shows the comparison between the experimental data and theoretical modeling of A state within the scope of $g^{(2)}_{pol}(r)$. The behavior of the theoretical model's polaron pair correlation function is qualitatively very similar to the experimental behavior. Consider first Fig. 18.3a. The green dashed lines mark all the possible lattice constants of polaronic lattices which are commensurate with the hexagonal atomic lattice. From the orange curve it is obvious that the simulation exhibits peaks in these cases. In experiment however, there is a discrepancy in the position of the peaks from the theoretically expected green dashed lines. This can be explained if the underlying atomic lattice has moved slightly in order to accommodate the repulsion between polarons. The qualitative discrepancy in peak intensity is mostly present at the 1/7 polaron concentration peak, which is much more pronounced than in the experiment. Both of these discrepancies may vanish by incorporating also the movement of the atomic lattice in the model. This is the goal of future studies. In Fig. 18.3b we can also see a discrepancy between the experimental and simulated peak positions. This is expected already from Fig. 18.3a, because of the homogeneity of the sample. The behavior at close distances is reflected in long range behavior. Ergo, if there was a discrepancy in the peak positions at close range, it will also be present at long range. The main point of Fig. 18.3b is to show that despite the peak position discrepancies, both the experimental as well as the theoretical curve tend to the value 1 at large distances. This is a very important feature, as it shows that both exhibit no long range

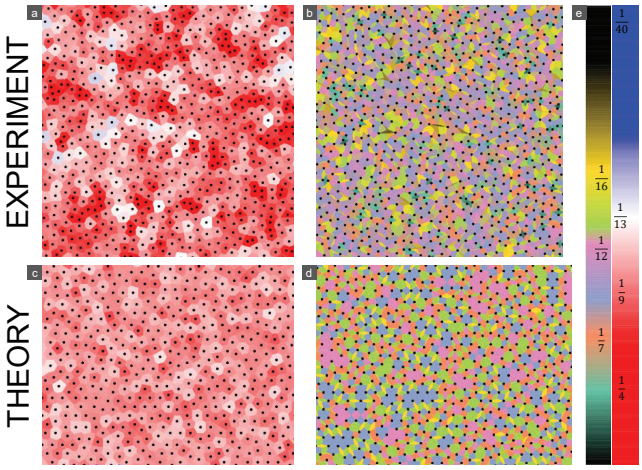


Figure 18.2: **Comparison between the two types of tiling of experimental and theoretical A states: a**, Voronoi diagram of the experimental STM image of A state. The color in each cell represents the area of the cell according to the right legend in e. **b**, Nearest neighbor distance tiling of the experimental STM image of A state. The color of each tile represents the distance between the two polarons it connects according to the left legend in e. **c**, Voronoi diagram of the model for A state. **d**, Nearest neighbor distance tiling of the model for A state. **e**, Color legend for the tiling images to its left. Each color represents a different area of a Voronoi cell (right legend) and a different distance between nearest neighbors (left legend). Colors labeled with different polaron concentrations for the right legend represent areas of Voronoi cells of a Voronoi diagram, which is constructed from an overlying polaronic hexagonal lattice structure, which emerges at the corresponding concentration. For the legend to the left, colors represent different distances between nearest neighbors in the overlying polaronic hexagonal lattice structure at the corresponding polaron concentration

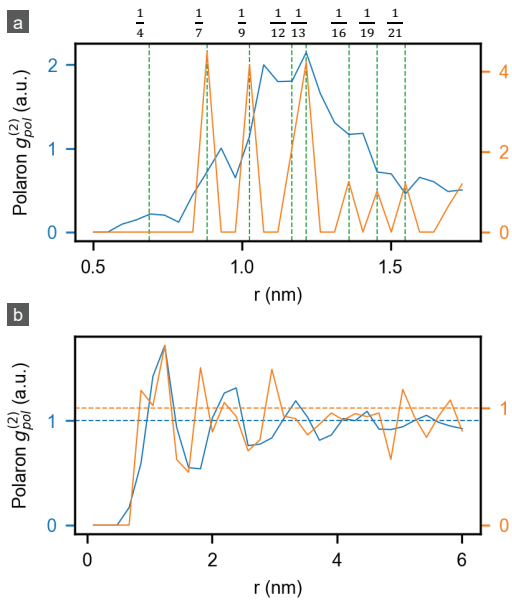


Figure 18.3: **Comparison between the experimental (blue) and theoretical (orange) polaron pair correlation function $g^{(2)}_{pol}(r)$: a**, Comparison between experiment and theory, plotted only at small distances, where both are referenced to the atomic lattice constant. The green lines represent nearest neighbor distances of different polaron lattices, which emerge at different polaron concentrations of the system (from left to right: 1/4, 1/7, 1/9, 1/12, 1/13, 1/16, 1/19, 1/21). The similarity between the theoretical model and experimental data can be observed from the qualitative matching of the polaron pair correlation peaks. The experimental peaks are almost all slightly shifted towards larger distances. However, the peaks of the theoretical model appear exactly at the expected positons and match the peaks of the experimental data. The quantitative comparison fails mostly at the 1/7 polaron concentration. **b**, Comparison between experiment and theory, plotted also at larger distances, where both are referenced to the atomic lattice constant. Both polaron pair correlations tend to the value 1 at large distances, which indicates a lack of ordering at large distances. The difference between them is in the oscillations around the value 1, where the theoretical model oscillates a lot more, which is due to the perfect underlying hexagonal lattice on which the polarons reside

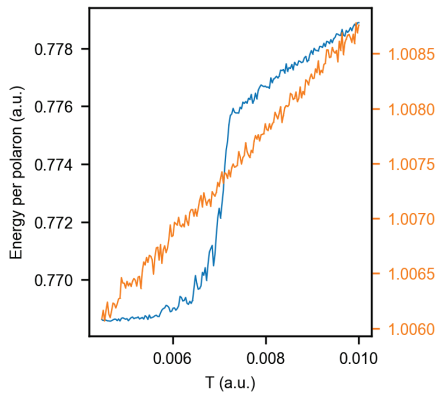


Figure 18.4: **Energy of the system per polaron versus temperature for the model for C state (Blue) and A state (Orange):** The plot clearly shows the difference between the two model systems of polarons. A first order phase transition from disorder to order occurs in the case of the model for C state and no such phenomenon is present in the case of the model for A state. Energy is measured in units of $e^2/\epsilon_0 a k_B$ and the error bars are smaller than the size of a single point

correlations. Within the scope of the theoretical model, the difference between C and A state can be understood by taking a look at a typical annealing process. Fig. 18.4 shows the energy of the system per polaron dependence on temperature for models of both states measured in units of $e^2/\epsilon_0 a k_B$. Fig. 18.5 shows typical configurations of both models at high and low temperatures. It points out a clear difference in the two low temperature phases of the model for C state (Fig. 18.5a,b) and A state (Fig. 18.5c,d). The high temperature configuration in both cases (Fig. 18.5b,d) is disordered, yet the C state shows a clear strong tendency towards crystallization at low temperatures evident by the dominance of the green color (Fig. 18.5a). The A state (Fig. 18.5c) is clearly still disordered even at low temperatures. In the case of the model for C state, there is a clear order-disorder phase transition, which is of the first order. Meanwhile, there is no phase transition present in the case of the model for A state. In the model for A state in Fig. 18.5c some aggregation of the same types of different nearest neighbor distances can be observed at low simulated temperatures, but no global lattice ever emerges like in the model for C state.

## 18.6 Discussion

We have clearly shown that the A state can be modeled successfully within the scope of the classical polaron picture. This result supports the model for the low temperature C state first proposed by Brazovskii [8]. This model was also successfully used by Karpov et al. [32] for simulating the H state. Our results imply that the A state's disordered characteristics are a consequence of commensurability frustration. The polaron hexagonal lattice at this polaron concentration cannot form due to the incommensurability with the underlying atomic lattice. One might argue that phase separation, where multiple commensurate lattices emerge in the system with domain walls in between them, might be energetically more favorable that the disordered phase seen in Fig. 18.5c. We have shown that this does not happen. Similar behavior has been observed before on a square lattice and it was also attributed to frustration with the underlying lattice [30, 31]. Minimization of the overlying hexagonal lattice energy on an underlying hexagonal lattice was done by Pokrovsky et al. [32]. They have shown that multiple minima very close in energy exist at integer polaron concentrations between 1/12 and 1/9 as well as between other concentrations. However, it is still not clear whether phase separation would result in further minimization of the energy of the system and whether unscreened interactions

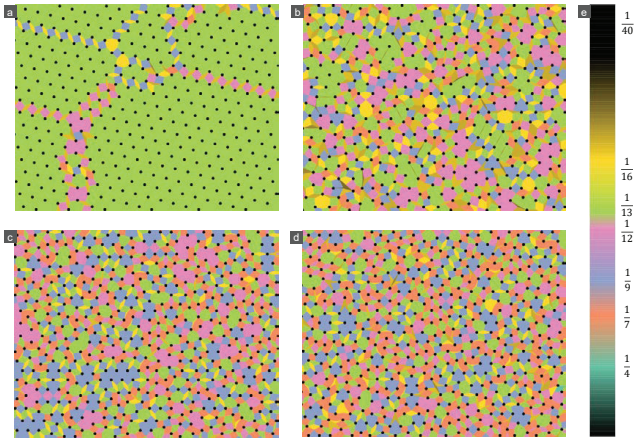


Figure 18.5: **An examination of the difference between the theoretical models for C and A states: a**, **b**, Tiling of typical low and high temperature polaron configurations, respectively, in the model for C state. Clearly, the high temperature phase is highly disordered, while only one nearest neighbor distance prevails globally at low temperatures. There are a few line defects present still, but this is only due to finite size effects. **c**, **d**, Tiling of typical low and high temperature polaron configurations, respectively, in the model for A state. The high temperature phase is again clearly disordered. The low temperature phase, unlike in the case of the model for C state is still highly disordered. There are some nucleation centers of different nearest neighbor distances, which are not present at high temperatures, but it is obvious that the emergence of a global polaron lattice is prohibited. This is due to the commensurability frustration mentioned in the main text. **e**, Color legend for the nearest neighbor distances tiling images to its left. Each color represents a different distance between nearest neighbors, which corresponds to a listed polaron concentration in the legend

would change the system's behavior. Therefore, the observed glassy behavior may merely be a consequence of the limitations of the Monte Carlo algorithm, or perhaps the glassy behavior is an actual thermodynamic property of the system at this polaron concentration.

## 18.7 Conclusion

In this paper the newly discovered meta-stable amorphous state in 1T-$TaS_2$ has been successfully modeled within the scope of a classical gas of polarons. The disordered structure has been found to be a consequence of frustration in the system. The hexagonal lattice of the polaron gas which seeks to emerge due to the repulsive interaction between them in not commensurate with the hexagonal underlying atomic lattice. According to our Monte Carlo simulations the result of this frustration is a remarkable stability of a disordered polaronic pattern, where there is no evidence of a first order crystallization phase transition. Our finding represent a new and important step in understanding photoexcitation in the complex system of 1T-$TaS_2$. The external laser pulse causes the system to form a greater number of polarons than in the thermodynamically stable commensurate state. Afterwards, polarons order in compliance with the screened interaction between them and the atomic lattice underneath into a stable disordered pattern.

# 19 Band insulator to Mott insulator transition in $1T-TaS_2$ (2020)

Y. D. Wang [1], W. L. Yao [1], Z. M. Xin [1], T. T. Han [1], Z. G. Wang [1], L. Chen® [1], C. Cai [1], Yuan Li [1,2] & Y. Zhang [1,2⊗]

(I added this article because GPT said that it can teach me about what is the band insulator? give some properties and formulas exactly about it)

**Abstract**

$1T-TaS_2$ undergoes successive phase transitions upon cooling and eventually enters an insulating state of mysterious origin. Some consider this state to be a band insulator with interlayer stacking order, yet others attribute it to Mott physics that support a quantum spin liquid state. Here, we determine the electronic and structural properties of $1T-TaS_2$ using angle-resolved photoemission spectroscopy and X-Ray diffraction. At low temperatures, the $2\pi/2c$-periodic band dispersion, along with half-integer-indexed diffraction peaks along the $c$ axis, unambiguously indicates that the ground state of $1T-TaS_2$ is a band insulator with interlayer dimerization. Upon heating, however, the system undergoes a transition into a Mott insulating state, which only exists in a narrow temperature window. Our results refute the idea of searching for quantum magnetism in $1T-TaS_2$ only at low temperatures, and highlight the competition between on-site Coulomb repulsion and interlayer hopping as a crucial aspect for understanding the material's electronic properties.

Transition-metal di-chalcogenides are layered quasi-twodimensional materials that not only show prominent potentials for making ultra-thin and flexible devices, but also exhibit rich electronic phases with unique properties [1–3]. 1T-$TaS_2$ is one prominent example. The crystal structure of $1T-TaS_2$ consists of S-Ta-S sandwiches, which in turn stack through van der Waals interactions. It is structurally undistorted and electronically metallic at high temperatures. With decreasing temperature, it undergoes successive first-order transitions, resulting in the formation of various charge density waves (CDWs) with increasing degree of commensurability [4–7]. As shown in Fig. 1a, with cooling, $1T-TaS_2$ sequentially enters an incommensurate CDW (I-CCDW) phase below 550 K, a nearly commensurate CDW (NC-CDW) phase below 350 K, and finally a commensurate CDW (C-CDW) phase below 180 K. Prominent hysteretic behavior can be observed when comparing the cooling and heating resistivities data. Upon heating, $1T-TaS_2$ enters triclinic CDW (T-CDW) phase at 220 K, and then the NC-CDW phase at 280 K. The space modulations of different CDW phases are illustrated in the inset of Fig. 1a. Every adjacent 13 Taatoms accumulate together, which is called star-of-David (SD) cluster [4–7]. Within one hexagonal SD, 12 Ta-atoms pair and form 6 occupied bands, leaving the center Ta atom localized and unpaired alone. As a result, the insulating ground state of $1T$ -$TaS_2$ has been proposed to be a Mott insulator [8–13]. In the C-CDW phase, the SD clusters cover entire lattice forming commensurate $p(\sqrt{13}\times\sqrt{13})R13.9^\circ$ phase. The localized electrons with $S=1/2$ spin arrange on a triangular lattice, making this system a promising candidate material for realizing quantum spin liquid [14–17].

Distinct from the possible Mott physics that occurs within one $TaS_2$ layer, interlayer coupling has recently been emphasized as a crucial aspect to understand the insulating property of $1T$ -$TaS_2$[18–20]. Through an interlayer Peierls CDW transition, interlayer staking order forms in the C-CDW phase. First, every two adjacent $TaS_2$ layers accumulate, forming dimerized bilayer structure. The dimerized $TaS_2$ bilayers then stack onto each other forming different types of

[1] International Center for Quantum Materials, School of Physics, Peking University, 100871 Beijing, China.
[2] Collaborative Innovation Center of Quantum Matter, 100871 Beijing, China. email: yzhang85@pku.edu.cn

staking order with different in-plane sliding configurations [19,20]. Recent scanning tunneling microscopy and transport measurements show possible existence of the stacking order in $1T-TaS_2$[21,22]. Band calculations show that without considering the strong electronic correlation the interlayer staking order itself can open a band gap at the Fermi energy ($E_F$), yielding an insulating property of $1T-TaS_2$. Under this scenario, the ground state of $1T-TaS_2$ is a band insulator rather than a Mott insulator.

The low-energy electronic structure of $1T-TaS_2$ consists of one half-filled nonbonding Ta $5d$ band. In the IC-CDW phase, angleresolved photoemission spectroscopy (ARPES) data shows that one Ta $5d$ band disperses crossing $E_F$, forming six oval-like circles around the Brillouin zone boundaries (M) (Fig. 1b). This is well consistent with the first-principle band calculations [11]. When entering the C-CDW phase, the CDW potential folds the Brillouin zone. The Fermi surface reconstructs into multiple disconnected spots, following the $p(\sqrt{13}\times\sqrt{13})R13.9°$ periodicity. Band folding and band gap opening split the Ta $5d$ band into a manifold of narrow subbands. One flat band emerges at ˜200 meV below $E_F$ (Fig. 1c). Under the Mott scenario, this flat band was attributed to the lower Hubbard band [8–13]. Previous timeresolved ARPES and inverse-photoemission spectroscopy also reported the observation of Mott gap between the flat band and upper Hubbard band [23–25], supporting the existence of Mott insulating ground state. However, recent ARPES studies show that the flat band is energy dispersive along the out-of-plane momentum ($k_z$) direction [19,26,27], which favors the existence of interlayer stacking order. It is then crucial to make a consensus on the detailed temperature evolution of electronic structure in $1T-TaS_2$. The results would help to understand how the on-site Coulomb repulsion and interlayer hopping play roles in $1T-TaS_2$.

In this work, we characterize the temperature dependence of electronic and lattice structures of $1T-TaS_2$ using ARPES and Xray diffraction (XRD). We find that, at low temperatures, the

band dispersion and diffraction peaks show $2\pi/2c$ and $2c$ periodicity, which indicates that the ground state of $1T-TaS_2$ is a band insulator with interlayer dimerization. More intriguingly, at high temperatures, the system undergoes an insulator-to-insulator transition and enters an intermediate Mott insulating state, which only exists in a narrow temperature region. Our results show that the energy scales of in-plane hopping, on-site Coulomb repulsion, and interlayer hopping are all comparable in $1T-TaS_2$. The competition between these interactions are responsible for the complex electronic properties of $1T-TaS_2$.

## Results

Temperature dependence of electronic structure. To characterize how the flat band forms in the C-CDW phase, we show the detailed temperature dependence of the energy distribution curves (EDCs) taken at the Brillouin zone center ( Γ ) (Fig. 2). Upon cooling, the spectral weight of the flat band shifts from $E_F$ to -200 meV at 193 K, indicating an energy gap opening at $E_F$. In contrast to the cooling process, the temperature evolution of EDCs during the heating process clearly identifies two-phase transitions (Fig. 2d-f). The first phase transition occurs at 217 K, where the peak width narrows and the peak position shifts from -210 to -170 meV. The second phase transition follows at 233 K , where the spectral weight of the flat band shifts to $E_F$.

In comparison with the resistivity data, the gap opening transition at 193 K can be attributed to the NC-CDW to C-CDW transition upon cooling, while the transition at 217 K coincides with the C-CDW to T-CDW transition upon heating. There is a small temperature deviation between the transition temperatures determined by different techniques. This can be explained by the standard deviation of transition temperatures among different samples due to a small sample inhomogeneity (Supplementary Figs. 1-3). However, the transition at 233 K does not show up in the transport measurements. It also cannot be explained by a sample in-

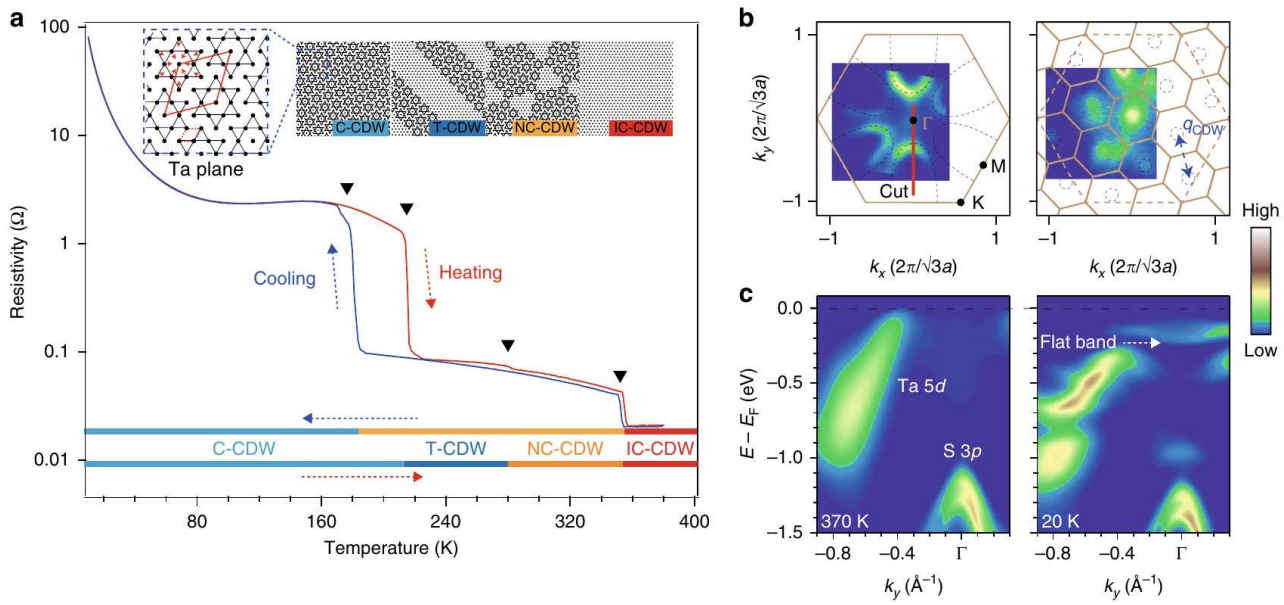


Fig. 1 Transport property and electronic structure of $\mathbf{1T-TaS_2}$. a Temperature dependence of in-plane resistivity taken upon heating and cooling. The black arrows mark the first-order transition points. The bars below the curves indicate temperature intervals corresponding to the different phases. Inset panels in a are schematic illustrations for the in-plane lattice modulations in the commensurate CDW (C-CDW) phase, nearly commensurate CDW (NC-CDW) phase, Triclinic CDW (T-CDW) phase, and In-commensurate CDW (IC-CDW) phase, respectively. The SD clusters are marked with the dark outlines. Black dots stand for the Ta atoms. b and c Fermi surface mappings and corresponding high symmetry cuts taken at 370 and 20 K, respectively. The cut momenta are illustrated as a red line in b.

homogeneity, because the temperature-dependent data are well reproducible in many different samples (Supplementary Fig. 1). Our results thereby identify an undiscovered intermediate (I) phase, which exists in a narrow temperature region (217-233 K) at the C-CDW to T-CDW phase transition. For the transition at 217 K, the spectra show insulating behavior on both sides of the transition (Fig. 2d), which is therefore an insulator-to-insulator transition. In the following, we present experimental evidence for distinct motives behind the two insulating states, which suggests that the I phase is, in fact, a Mott insulator.

The temperature evolution of flat band is shown in Fig. 3. The CDW band gap opens and the flat band forms at $E_{\mathrm{F}}$ in the NC-CDW and T-CDW phases. Its bandwidth is narrow due to the large scale of the hexagonal SD structure. The flat band opens an energy gap and shifts from $E_{\mathrm{F}}$ to -170 meV at 225 K in the I phase. In the C-CDW phase, the flat band shifts to around -200 meV and becomes more dispersive. Meanwhile, there is an energy spread of the flat band towards $E_{\mathrm{F}}$, which is consistent with the peak broadening observed in Fig. 2d, e. Due to the surface sensitivity of ARPES technique, $k_z$ is not conserved during the photoemission process [28]. The ARPES spectra is thus a superposition of the bulk bands at different $k_z$ 's. If the band has moderate band dispersion along $k_z$ direction, its ARPES spectra is broadened. Such $k_z$ broadening effect explains the energy spread of the flat band, which also indicates that the $k_z$ band dispersion reconstructs significantly in the C-CDW phase.

To determine the band dispersion of the flat band along the $k_z$ direction, we measured the photon energy-dependent data in the

I and C-CDW phases. The results are compared in Fig. 4. The flat band is gapped at 225 K. The weak photon energy dependence indicates the two dimensionality of the flat band

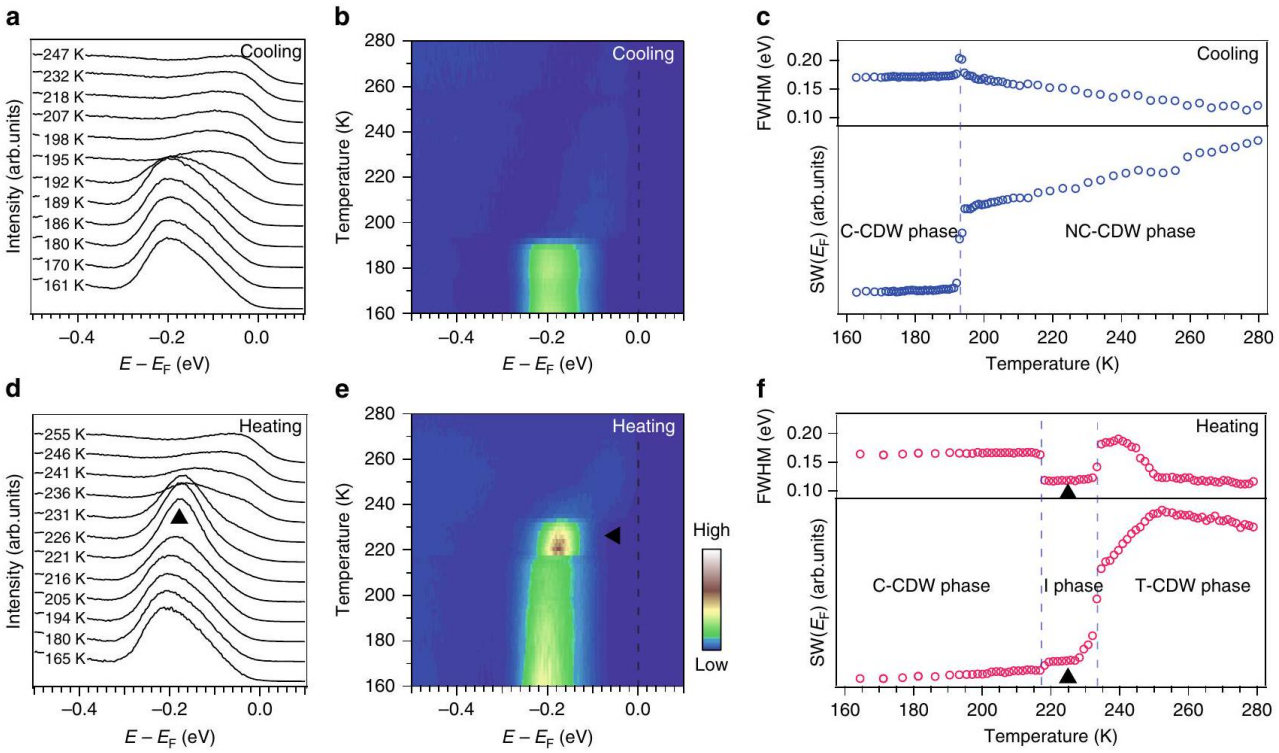


Fig. 2 Temperature-dependent ARPES study of $\mathbf{1}\boldsymbol{T}-\mathbf{TaS_2}$ upon cooling and heating. a Temperature dependence of energy distribution curves (EDCs) taken at the Γ point upon cooling. b The merged image of the data in a. c Corresponding temperature dependence of full width at half maximum (FWHM) for the data in a, and the spectral weight (SW) taken at where the Ta $5d$ band crosses $E_F$ $\left([-0.1, 0.1\text{eV}], \left[-0.4, -0.3\text{Å}^{-1}\right]\right)$. d-f are the same as a-c but for the heating process. Black arrows mark the intermediate (I) state.

in the I phase. However, when entering the C-CDW phase, the data become strongly photon energy dependent. The band positions shift from -230 to -90 meV periodically. This shows that the bandwidth along the $k_z$ direction is around 140 meV in the C-CDW phase, which is well consistent with the $k_z$ broadening effect observed in Fig. 3. The photon energy-dependent data confirm that the $k_z$ band dispersion reconstructs strongly at the I to C-CDW phase transition. More intriguingly, the periodicity of the $k_z$ dispersion is around $2\pi/2c$ in the C-CDW phase, which indicates the existence of an interlayer dimerization.

Temperature dependence of lattice structure. We then performed the single-crystal XRD measurement along the (0, 0, L) direction to confirm the existence of interlayer stacking order. Indeed, in addition to the regular integer-indexed Bragg peaks (Fig. 5a), a set of half-integer-indexed reflections are observed at 120 K. The fact that the (0, 0, 7/2) reflection is about twice more intense than the (0, 0, 5/2) reflection, i.e., with the intensity roughly proportional to $|\mathbf{Q}|^2$, suggests that these additional reflections are caused by $c$-axis displacive structural modulations that double the unit cell along $c$ (Fig. 5c). The appearance of halfinteger reflections in the C-CDW phase is a direct evidence for interlayer dimerization, which has to be caused by, and provide feedback to, interlayer coupling in the electronic structure. It is therefore no surprise that these half-integer reflections occur at 212 K which coincides with the enhancement of $k_z$ band dispersion observed by ARPES (Figs. 4 and 5b).

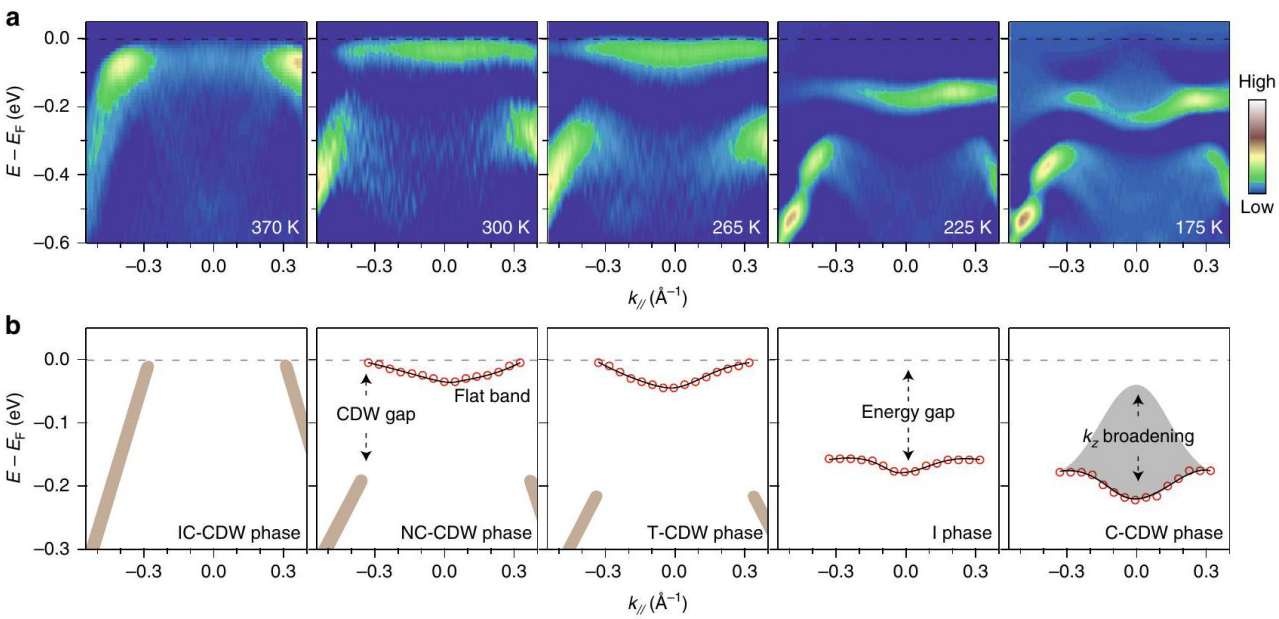


Fig. 3 Evolution of the flat band crossing different electronic phases. a The second derivative images of the energy-momentum cuts taken along the $\Gamma - \mathrm{M}$ direction in different electronic phases. b The schematic illustration of band evolution crossing different phases. Red circles show the fitted peak maxima from the data in a. Black lines guides the eyes to the flat band dispersions. Brown thick lines illustrate the bands at high binding energy.

## Discussion

For the C-CDW phase, its intra-layer CDW structure consists of SD clusters with the $p(\sqrt{13}\times\sqrt{13})R13.9^\circ$ periodicity. This has been well studied by previous diffraction experiments and also confirmed by the ARPES mapping in Fig. 1b. Here, our XRD and photon energy-dependent ARPES data show that, in addition to the intra-layer CDW, the system forms an interlayer stacking order along the $c$ direction. While the $2c$ periodicity could be attributed to an inter-layer dimerization, the stacking configuration between each bilayers remains unknown. Theoretical calculations show that the energy differences between different configurations are small [19,20]. Therefore, different stacking configurations could coexist, and the layers could stack randomly along the $c$ direction. This is consistent with our XRD data. The weak intensity of the half-integer diffraction peaks and the broadening of the CDW diffraction peak (Supplementary Fig. 5) suggest that the interlayer stacking shows certain randomness in the C-CDW phase. Therefore, to determine the stacking configuration experimentally, layer-resolved XRD studies are needed. Nevertheless, indirect evidences could be found by comparing the ARPES data with theoretical band calculations. Our result is more consistent with an alternating stacking configuration, where the predicted band structure is a small-gap band insulator [19,20].

Both ARPES and XRD data show the existence of interlayer stacking order in the C-CDW phase. This makes the low temperature ground state of $1T - \mathrm{TaS_2}$ a band insulator with two electrons fully occupied in the flat band near $E_\mathrm{F}$. The next question is then the origin of the I phase where the stacking order vanishes. Apparently, the I phase to C-CDW phase transition is an insulator-to insulator transition. Therefore, it cannot be explained by a simple interlayer Peierls CDW transition that is driven by the electronic instability at the Fermi surface. Electronic correlation need be considered. In a bilayer Hubbard band model, considering both the on-site Coulomb repulsion and interlayer hopping, theories show that the electronic system can transit from a Mott insulator to a band insulator when the interlayer hopping increase above a critical value [29,30]. The electronic states redistribute without closing

the energy gap, resulting in an insulator-to-insulator transition. This naturally explains the C-CDW phase to I phase transition observed here (Fig. 5d, e). The I phase is a two-dimensional Mott insulator originated from the on-site Coulomb repulsion ($U$). When entering the C-CDW phase, the interlayer hopping ($t_\perp$) as characterized by the $k_z$ bandwidth is strongly enhanced. As a result, the system transits from a Mott insulator into a band insulator. Consistently, the energy scale of the in-plane hopping $(t_{//})$is around 100 meV as determined by the in-plane bandwidth of the flat band (Fig. 3). The Mott gap between the lower and upper Hubbard band is around 400meV[13,18,25], representing the energy scale of $U$. The energy scale of $t_\perp$ is around 140 meV, which is the $k_z$ bandwidth of the flat band (Fig. 4). All these experimentally determined parameters are consistent with the theoretical parameters where the band-insulator to Mott-insulator transition could realize [29,30].

It is then intriguing to understand the enhancement of $t_\perp$ cross the I to C-CDW phase transition. In fact, the reconstruction of electronic structure along $c$ direction is so strong that upon entering the I phase from the C-CDW phase, the distance between adjacent $TaS_2$ layers undergoes an appreciable sudden decrease from 5.928 to 5.902Å as seen from the ( $0, 0, 4$ ) reflection (Fig. 5b). At first glance, the larger interlayer distance in the C-CDW phase compared to the I phase is at variance with the larger $t_\perp$ (hence stronger $k_z$ dispersion) in the C-CDW phase. This unexpected correlation between $t_\perp$ and interlayer distance requires further theoretical understanding. One possible explanation is that the complete in-plane commensurability of CDW in the C-CDW phase turns on additional hopping channels between nearby $TaS_2$ layers, which may further affect the average interlayer distance.

The phase transition at 233 K and the I phase have not been observed in both the resistivity and XRD data. Considering that APRES is more sensitive to the electronic state near the sample surface, we could explain this controversy using two different scenarios. On one hand, the I phase is a surface state that does not exist in the bulk layers. This resembles the Mott insulating phase that was observed at the surface of $1T - TaSe_2$[31,32]. However, this scenario contradicts with some of our observations. For example, the penetration depth of ARPES is normally around or over two layers. If the surface and bulk electronic states are different, we should observe two different sets of bands representing the surface and bulk, respectively. However, our data only show one set of bands, which suggests that the I phase extends along $c$ direction for at least two $TaS_2$ layers. Furthermore, the phase transition at 217 K observed by ARPES is well consistent with the C-CDW transition temperature determined by transport and XRD measurements. The photon energy-dependent data also clearly show the $k_z$ dispersion of bands, whose periodicity is well consistent with the bulk lattice parameter. All these results suggest that the ARPES data reflect the bulk electronic properties of $1T - TaS_2$. On the other hand, the I phase exists in bulk layers, but only emerges in certain layers which are phase separated from the other layers. Therefore, the I phase cannot be picked up by the resistivity and

XRD measurements. Under this scenario, the observation of I phase by ARPES should be highly dependent on the cleaved surface. However, this is not the case. The high reproducibility of our ARPES data seems to suggest that the I phase may have a high probability of occurrence near the sample surface.

To examine whether the I phase exists in the bulk or not, layerresolved transport and XRD measurements are required. The resistivity measurements on thin $1T - TaS_2$ films show that the transition becomes broad with the decreasing of sample thickness [33−35], which may suggest the existence of a phase separation. Moreover, the system remains insulating in an ultrathin film, while the C-CDW phase is fully suppressed [33−35]. This is consistent with our results that the interlayer hopping is important for the C-CDW phase. In an ultrathin film where the on-site Coulomb repulsion plays a more dominating role than the interlayer hopping, the insulating property may originate from the intermediate Mott insulating phase observed here.

In summary, we believe that the competition between $U$ (within SD) and $t_\perp$ (between neighboring $TaS_2$ layers) is responsible for the complex insulating phases in $1T - TaS_2$. While the C-CDW phase is a band insulator featuring strong interlayer hoping and dimerization, the I phase is likely a two-dimensional Mott insulator. Although we show that the low-temperature C-CDW phase is not a Mott insulator, the $S = 1/2$ degrees of freedom could still be realized in the I phase. Further experimental studies are required to characterize possible magnetism in the I phase and verify its occurrence in bulk layers. Meanwhile, if the stacking order in the C-CDW phase can be suppressed, such as by chemical doping or reducing dimensionality, quantum magnetism may still be realized down to the lowest temperature in $1T$ -$TaS_2$.

## Methods

Sample growth. High-quality single crystals of $1T - TaS_2$ were synthesized using chemical vapor transport (CVT) method. By mixing the appropriate ratio of Ta powder and S pieces (2% excess) well, the compound was sealed in a quartz tube with $ICl_3$ as transport agent. The quartz tube was put in the two-zone furnace with thermal gradient between 750 and 850 °C for 120 h, and then quenched in water. The refinement of power XRD data confirms the phase purity of our sample and the trigonal crystal structure of $1T - TaS_2$ with the $P - 3m1$ space group with the lattice parameters $a = b = 3.366$Å, $c = 5.898$Å (Supplementary Fig. 6).

Resistivity measurements. Resistivity data were measured in physical property measurement system (PPMS, Quantum Design, Inc.) utilizing standard four-probe method. The heating and cooling rates are 3 K $min^{-1}$.

ARPES measurements. ARPES measurements were performed at Peking University using a DA30L analyzer and a helium discharging lamp. The photon energy of helium lamp is 21.2 eV. Photon energy-dependent measurement was performed at the BL13U beamline in National Synchrotron Radiation Laboratory (NSRL). The overall energy resolution was ˜12 meV and the angular resolution was ˜0.3°. The crystals were cleaved in situ and measured in vacuum with a base pressure better than $6 \times 10^{-11}$mbar. The $E_F$ for the samples were referenced to that of a gold crystal attached onto the sample holder by Ag epoxy. For the measurements in a heating process, the samples were first cooled down from 300 to 80 K with a rapid fall of temperature (about 20 K $min^{-1}$ ). After adequate cooling for about 10 min at 80 K, the samples were cleaved and heated up to 190 K with a rate about 1.5 K $min^{-1}$; The samples were then heated up to 300 K slowly with a rate about 0.23 K $min^{-1}$. For the measurement in a cooling process, The sample was cleaved at 300 K directly and cooled down to 210 K with a rate about 2 K $min^{-1}$; The sample was then cooled down to 160 K slowly with a rate about 0.5 K $min^{-1}$. ARPES data were collected during the cooling and heating processes. More experimental details could be found in Supplementary Table 1.

XRD measurements. XRD data were recorded on a Bruker D8 diffractometer using CuK$\alpha$ radiation ($\lambda = 1.5418$Å). We mounted a high-quality single crystal of $1T - TaS_2$ in a liquid nitrogen cryostat sitting in an Euler cradle to measure the $c$ axis at different temperatures.

The sample was cooled down until 93 K with a rapid fall of temperature (about 10 K $min^{-1}$ ) from room temperature naturally. After adequate cooling for about 1 h at 120 K, we heated the sample from 120 to 170 K at 3 K $min^{-1}$. We then heated the sample to 370 K with a rate about 0.16 K $min^{-1}$. XRD data were collected during the heating process.

Experimental reproducibility. The ARPES and resistivity measurements were repeated on different samples. The observations are reproducible in all measured samples with a small variable of transition temperatures (Supplementary Figs. 1-3). The resistivity data in Fig. 1a were taken on sample #7. The ARPES data in Fig. 2a, b were taken on sample #6. The ARPES data in Figs. 2d, f and 3 were taken on sample #1. The XRD data were taken on sample #13. The ARPES data taken at 370 K in Figs. 1 and 3 were taken on sample #14. Photon energy-dependent data in Fig. 4 was taken on sample #15.

**References**


1. Novoselov, K. S. et al. Two-dimensional atomic crystals. Proc. Natl Acad. Sci. USA 102, 10451-10453 (2005).

2. Geim, A. K. & Grigorieva, I. V. Van der Waals heterostructures. Nature 499, 419-425 (2013).

3. Fiori, G. et al. Electronics based on two-dimensional materials. Nat. Nanotechnol. 9, 768-779 (2014).

4. Tosatti, E. & Fazekas, P. On the nature of the low temperature phase of 1T-$TaS_2$. J. Phys. Colloq. 37, C4-165-C164-168 (1976).

5. Thomson, R. E., Burk, B., Zettl, A. & Clarke, J. Scanning tunneling microscopy of the charge-density-wave structure in $1T - TaS_2$. Phys. Rev. B 49, 16899-16916 (1994).

6. Sipos, B. et al. From Mott state to superconductivity in $1T - TaS_2$. Nat. Mater. 7, 960-965 (2008).

7. Rossnagel, K. On the origin of charge-density waves in select layered transition-metal dichalcogenides. J. Phys. Condens. Matter 23, 213001 (2011).

8. Wilson, J. A., Di Salvo, F. J. & Mahajan, S. Charge-density waves and superlattices in the metallic layered transition metal dichalcogenides. Adv. Phys. 24, 117-201 (1975).

9. Fazekas, P. & Tosatti, E. Electrical, structural and magnetic properties of pure and doped $1T - TaS_2$. Philos. Mag. B 39, 229-244 (1979).

10. Manzke, R., Buslaps, T., Pfalzgraf, B., Skibowski, M. & Anderson, O. On the phase transitions in $1T - TaS_2$. Europhys. Lett. 8, 195 (1989).

11. Rossnagel, K. & Smith, N. V. Spin-orbit coupling in the band structure of reconstructed1T- $TaS_2$. Phys. Rev. B 73, 073106 (2006).

12. Perfetti, L., Gloor, T. A., Mila, F., Berger, H. & Grioni, M. Unexpected periodicity in the quasi-two-dimensional Mott insulator $1T - TaS_2$ revealed by angle-resolved photoemission. Phys. Rev. B 71, 153101 (2005).

13. Kim, J. J., Yamaguchi, W., Hasegawa, T. & Kitazawa, K. Observation of Mott localization gap using low temperature scanning tunnelling spectroscopy in commensurate $1T - TaS_2$. Phys. Rev. Lett. 73, 2103 (1994).

14. Klanjšek, M. et al. A high-temperature quantum spin liquid with polaron spins. Nat. Phys. 13, 1130-1134 (2017).

15. Law, K. T. & Lee, P. A. $1T - TaS_2$ as a quantum spin liquid. Proc. Natl Acad. Sci. USA 114, 6996-7000 (2017).

16. Ribak, A. et al. Gapless excitations in the ground state of $1T - TaS_2$. Phys. Rev. B 96, 195131 (2017).

17. He, W. Y., Xu, X. Y., Chen, G., Law, K. T. & Lee, P. A. Spinon Fermi surface in a cluster Mott insulator model on a triangular lattice and possible application to $1T - TaS_2$. Phys. Rev. Lett. 121, 046401 (2018).

18. Ritschel, T. et al. Orbital textures and charge density waves in transition metal dichalcogenides. Nat. Phys. 11, 328-331 (2015).

19. Ritschel, T., Berger, H. & Geck, J. Stacking-driven gap formation in layered 1 T- $TaS_2$. Phys. Rev. B 98, 195134 (2018).

20. Lee, S. H., Goh, J. S. & Cho, D. Origin of the insulating phase and first-order metal-insulator transition in $1T - TaS_2$. Phys. Rev. Lett. 122, 106404 (2019).

21. Butler, C. J., Yoshida, M., Hanaguri, T. & Iwasa, Y. Mottness versus unit-cell doubling as the driver of the insulating state in $1T - TaS_2$. Nat. Commun. 11, 2477 (2020).

22. Martino, E. et al. Preferential out-of-plane conduction and quasi-one-dimensional electronic states in layered van der Waals material $1T - TaS_2$.*npj* 2D Mater. Appl. 4, 7 (2020).

23. Ligges, M. et al. Ultrafast doublon dynamics in photoexcited $1T - TaS_2$. Phys. Rev. Lett. 120, 166401 (2018).

24. Perfetti, L. et al. Time evolution of the electronic structure of $1T - TaS_2$ through the insulator-metal transition. Phys. Rev. Lett. 97, 067402 (2006).

25. Sato, H. et al. Conduction-band electronic structure of $1T - TaS_2$ revealed by angle-resolved inverse-photoemission spectroscopy. Phys. Rev. B 89, 155137 (2014).

26. Ngankeu, A. S. et al. Quasi-one-dimensional metallic band dispersion in the commensurate charge density wave of $1T - TaS_2$. Phys. Rev. B 96, 195147 (2017).

27. Ma, L. et al. A metallic mosaic phase and the origin of Mott-insulating state in 1T- $TaS_2$. Nat. Commun. 7, 10956 (2016).

28. Himpsel, F. J. Angle-resolved measurements of the photoemission of electrons in the study of solids. Adv. Phys. 32, 1 (2006).

29. Fuhrmann, A., Heilmann, D. & Monien, H. From Mott insulator to band insulator: a dynamical mean-field theory study. Phys. Rev. B 73, 245118 (2006).

30. Kancharla, S. S. & Okamoto, S. Band insulator to Mott insulator transition in a bilayer Hubbard model. Phys. Rev. B 75, 193103 (2007).

31. Perfetti, L. et al. Spectroscopic signatures of a bandwidth-controlled Mott transition at the surface of $1T - TaSe_2$. Phys. Rev. Lett. 90, 166401 (2003).

32. Colonna, S. et al. Mott phase at the surface of $1T - TaSe_2$ observed by scanning tunneling microscopy. Phys. Rev. Lett. 94, 036405 (2005).

33. Yoshida, M. et al. Controlling charge-density-wave states in nano-thick crystals of $1T - TaS_2$. Sci. Rep. 4, 7302 (2014).

34. Tsen, A. W. et al. Structure and control of charge density waves in two-dimensional 1T-TaS $_2$. Proc. Natl Acad. Sci. USA 112, 15054-15059 (2015).

35. Yu, Y. Gate-tunable phase transitions in thin flakes of $1T - TaS_2$. Nat. Nanotechnol. 10, 270-276 (2015).

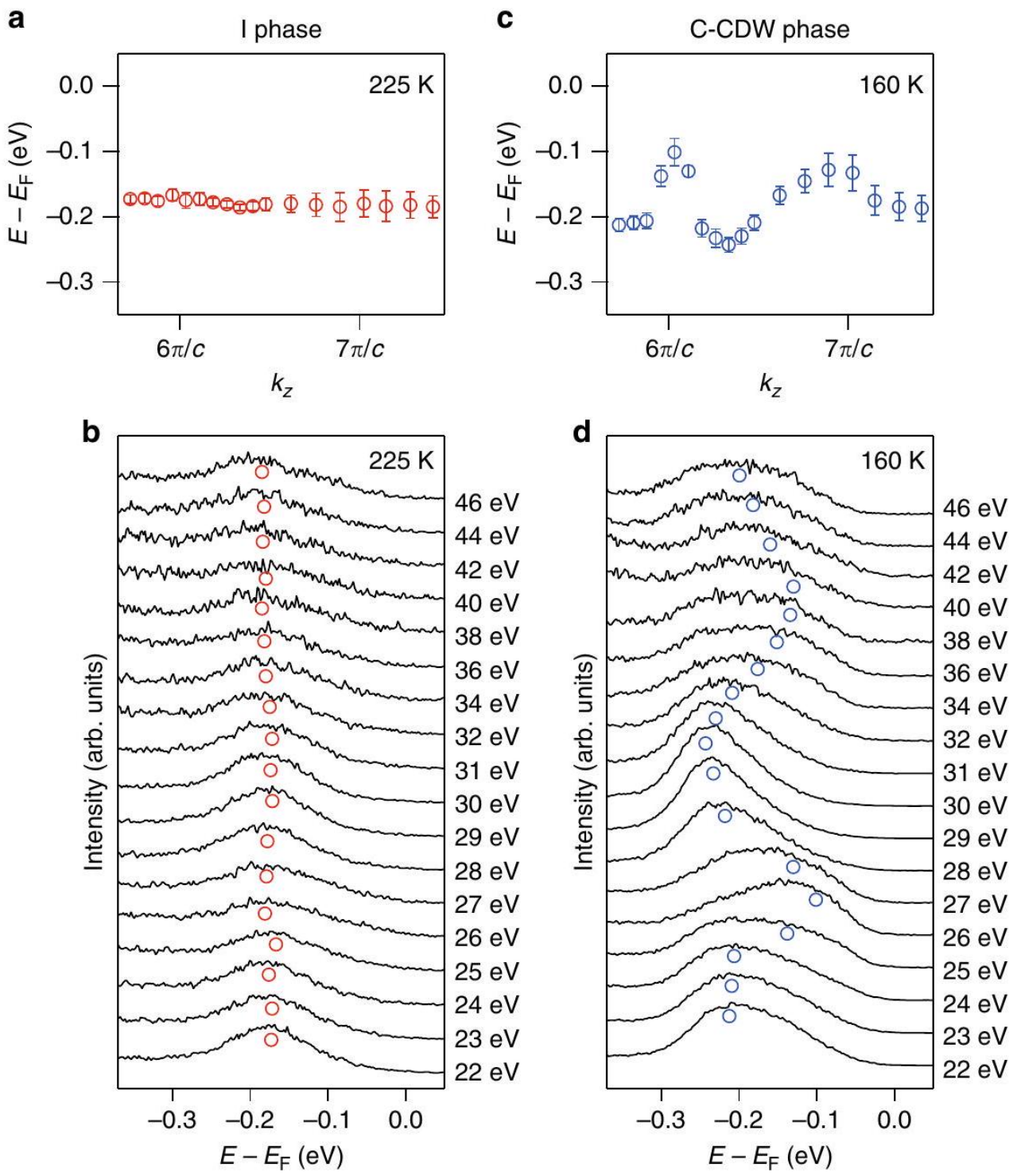


Fig. 4 Band dispersions along the $\boldsymbol{k_z}$ direction taken in the I and C-CDW phases. a $k_z$ dependence of the band positions in the I phase at 225 K. $k_z$ is calculated using the inner potential $V_0 = 17.5$eV. b Photon energy dependence of EDCs taken at Γ at 225 K.**c** and d are the same as a and b but taken in the C-CDW phase at 160 K. Red and blue circles are the fitted band positions. Error bars are estimated from peak fittings and defined as s.d.

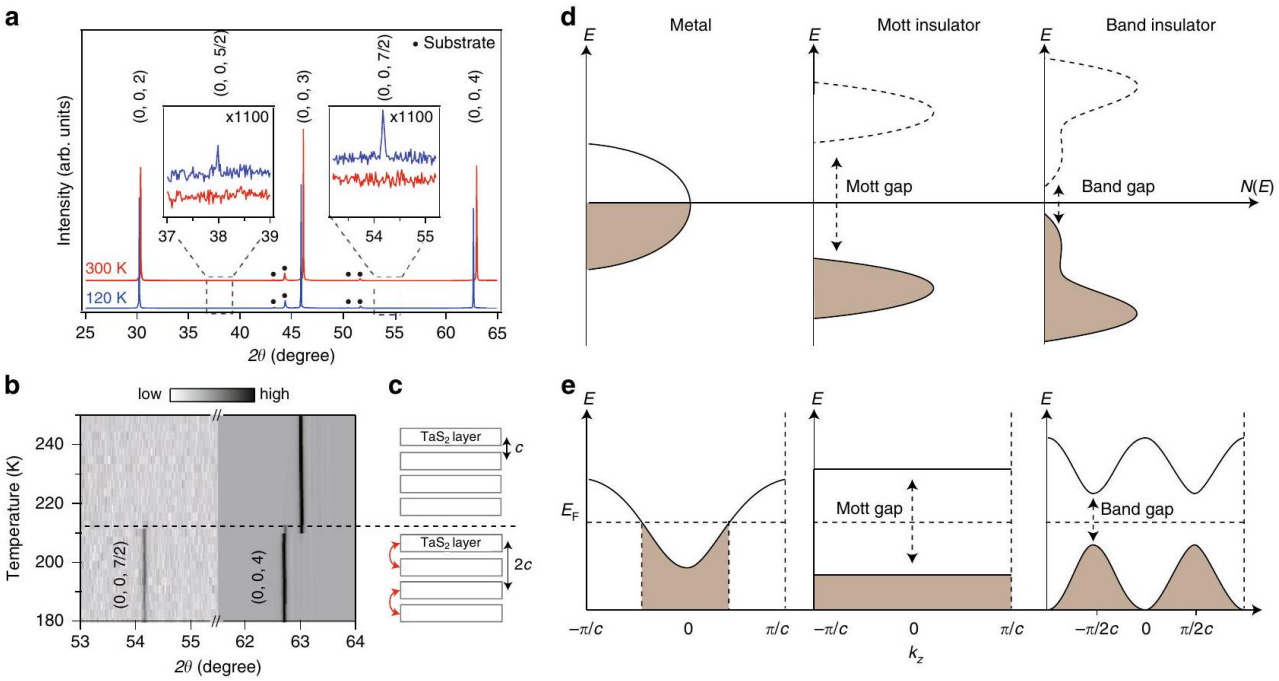


Fig. 5 Temperature-dependent XRD study and schematic depictions of band evolution. a XRD intensity of $1T-TaS_2$ measured along c axis at 120 and 300 K. Inset panels show the emergence of $(0, 0, 5/2)$ and $(0, 0, 7/2)$ peaks using 1100 times expanded scales. All the other peaks are from the polycrystalline substrate (Supplementary Fig. 4). b Temperature-dependence of the (0, 0, 7/2) and (0, 0, 4) peaks upon heating. c Schematic illustration of the interlayer dimerization. d Schematic illustration of the density of state distributions in different electronic phases. e Schematic illustration of the band dispersions along $k_z$ direction in different electronic phases.

# 20 Dynamical control of Coulomb interactions and Hubbard bands in monolayer 1T-$TaS_2$ by Notter, Aichhorn, Galler

**Abstract**

(there is CDW in monolayer TaS2) Monolayer 1T-$TaS_2$ hosts a star-of-David charge-density wave (CDW) that stabilizes(I don't think that word "stabilizes" is important) a low-temperature Mott-insulating state.

(some time-resolved results appear and something is not clear) Recent time-resolved spectroscopies indicate a coupling between the CDW amplitude mode (attention! CDW amplitude mode = model of a SOD, not of the total electron density modulation. this is how they want to call it, it is not strictly speaking correct) and the electronic correlation strength, yet the role of the screened Coulomb interaction remains unclear.

(we show how CDW changes Hubbars's U) Using the constrained random-phase approximation, we show that the CDW amplitude modifies the bare and screened on-site interactions, leading to sizable variations in the effective Hubbard $U$.

(we do DFT and DMFT, we show that if you decrease CDW amplitude, bands will shift and finally we'll get a metal) Our combined density-functional and dynamical mean-field theory calculations reveal that the Hubbard bands shift in concert with (=together with) the CDW amplitude, and that a reduced distortion drives a transition from a Mott insulator to a correlated metal. (it is purely mathematical setup, physically we can't vary CDW amplitude)

(abstract comment about coupling) These results demonstrate a direct link between lattice distortions and Coulomb interactions in transition-metal dichalcogenides, providing a microscopic mechanism for light-induced control of correlated phases in two-dimensional quantum materials.

## 20.1 Article

### 20.1.1 Introduction

(there are a lot of effects in 2D materials) Two-dimensional (2D) correlated materials exhibit a rich variety of quantum phases, including superconducting [1], charge- and spin-density wave [2] and quantum spin liquid states [3, 4].

(a lot of parameters influence them) The emergence of these phases is sensitive to external parameters such as pressure, strain, and static or dynamic electric and magnetic fields.

(there are a lot of exotic ideas also) Beyond this intrinsic tunability, 2D materials offer an additional degree of control through stacking and twisting, enabling emerging paradigms such as oxide electronics [5, 6], valleytronics [7, 8], and twistronics [9, 10, 11].

(abstract intro to TMDCs) Transition-metal dichalcogenides (TMDs) in the 1T polymorph [12, 13, 14, 15, 16, 17, 18, 19, 20, 21, 22] are van-der-Waals materials that allow us to explore strong correlation effects in 2D.

(TaS2 has SODs) Among them, 1T-$TaS_2$ exhibits a Star-of-David (SoD) charge density wave (CDW) phase below 180 K.

(SOD -> there is also insulation) The formation of this CDW phase, where clusters of 13 Ta atoms move closer in a star-shaped arrangement (Fig. 20.1b), is accompanied by a transition to an insulating state.

(bulk -> band insulator+ something, monolayer -> Mott insulator) While bulk 1T-$TaS_2$ is believed to consist of dimerized, band-insulating bilayers interspersed(=placing things at

different places) with AC-stacked monolayers (interspersed with AC-stacked monolayers??? so there are two types of layers in the bulk material?) [23, 24, 25], isolated monolayers are well established as Mott insulators [24, 17, 19].

(CDW in monolayer -> narrow band at FS) The CDW distortion in a monolayer generates a very narrow, half-filled (why half-filled?) band at the Fermi level.

(if we change el. correlation - band will change) This molecular orbital, with meV bandwidth and predominantly Ta $d_{3z^2-r^2}$ character (why $d_{3z^2-r^2}$ character? what does it mean?) , is highly susceptible to electronic correlations.

(Hubbard model describes 1T-TaS2 and can incorporate several factors) To first approximation, monolayer 1T-$TaS_2$ can be regarded as a prototypical realization of the Hubbard model on a triangular lattice, a system that recently attracted interest due to the interplay of strong correlations, geometric frustration, and unconventional ordering [26, 27, 28, 29, 30]. (is there a Hubbard model for 1H phase and others? maybe no..)

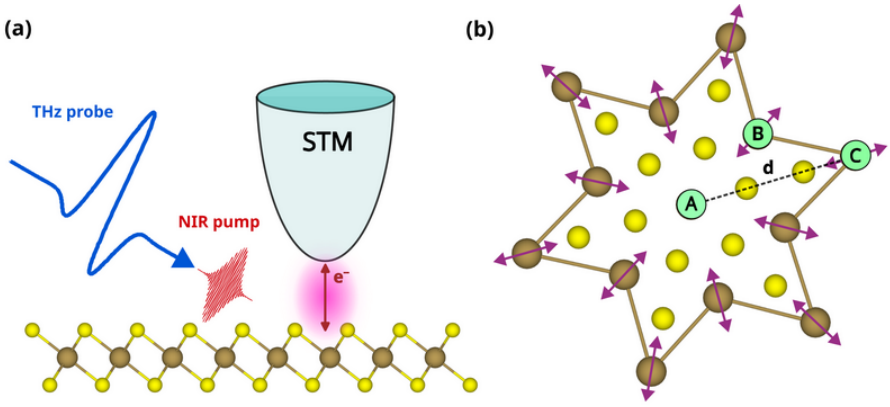


Figure 20.1: **(a)** (experiment: we shine two pulses and measure electrons) Illustration of a time-resolved STM experiment. A near-infrared (NIR) pulse indirectly excites the CDW amplitude mode in monolayer 1T-$TaS_2$, while a time-delayed THz probe pulse induces electron tunneling between the sample and STM tip to probe the local density of states.
**(b)** (SODs) Top view of the SoD supercell with Ta (brown) and S (yellow) atoms. $d$ denotes the distance between the central (site A) and the outer (site C) Ta atoms. Violet arrows indicate the CDW amplitude mode oscillation.

(this is an abstract and unclear sentence, basically it is meant "we'll be changing CDW and see how other properties will change") The CDW distortion clearly plays a central role in stabilizing the correlated state, suggesting that it could serve as a control knob (=small, rounded handle or control device) to manipulate the electronic properties.

(external strain somehow influences transition) Initial experiments indicated that external strain, which modifies the amplitude of the SoD CDW, can influence the Mott transition (how it can influence the transition?) [31].

(some experiments show something that makes the authors think that maybe it is possible do control dynamically densities of electrons. It is not written here, what exactly they mean by results from experiments and "correlation strength") More recent studies using terahertz (THz) scanning tunneling microscopy (STM) [32] and time- and angle-resolved photoemission spectroscopy (tr-ARPES) [33, 34, 35, 36], which excite a coherent 2.4 THz CDW amplitude mode [37] in 1T-$TaS_2$, point toward the possibility of dynamically controlling the correlation strength.

(there were some calculations, but still Coulomb interaction after shining light is not understood) However, despite recent density-functional theory (DFT) and non-equilibrium dynamical mean-field theory (DMFT) calculations [33] (I downloaded this article, it is experimental

one, but there are also some calculation) , the role of the screened Coulomb interaction in the photoinduced dynamics remains insufficiently understood. (It is not clear from this sentence what is the problem?)

(some screening is hard to calculate. again, it is not clear, what they mean. see cited papers) This limitation primarily stems from the difficulty of quantitatively evaluating the screened interaction within the large SoD supercell.

(they do cRPA) Using first-principles calculations within the constrained random-phase approximation (cRPA) [41, 42, 43] (reminder: learn cRPA) , we show that the screened Coulomb interaction in 1T-$TaS_2$ is highly sensitive to the amplitude of the SoD CDW (it is not clear here what they want to show, but later it should be written) .

(Big CDW -> smaller Coulomb interaction. more screening from somewhere -> smaller on-site interaction) Increasing the CDW amplitude reduces the localization of the Ta $d_{3z^2-r^2}$ molecular orbital, lowering the bare Coulomb interaction (Coulomb interaction between neighboring electrons, I guess) , while enhanced electronic screening (I guess screening also comes from CDW) further decreases the equilibrium on-site interaction of $U$=0.4 eV by up to 0.1 eV for a 1% amplitude change (see below). (it is not explain here, why is it so????)

(even 3% increase in CDW destroys insulating properties) Consequently, the Hubbard bands shift and the Mott gap shrinks, and strikingly, a 3% increase in the CDW amplitude drives a transition from a Mott insulator to a correlated metal(correlated metal? how is it?) .

(we'll show how lattice distortion is connected with el. spectrum, so you'll be able to control if with light or interpret some experiments) These results establish a direct, quantitative link between structural distortions and electronic correlations in TMDs, providing a route toward optical control of correlated phases and guiding the interpretation of ultrafast spectroscopic experiments in 2D CDW materials.

### 20.1.2 Results

(intro to pump probe setup) We start by describing the idealized pump–probe setup underlying our simulations, illustrated in Fig. 20.1.

(description of fig. 1a, typical STM) The configuration resembles a THz-lightwave–driven STM experiment [32], where a near-infrared (NIR) laser pulse excites coherent phonon dynamics in a monolayer of 1T-$TaS_2$ through photoinduced charge redistribution.

(we shine the light into SOD) In particular, the pulse drives the 2.4 THz CDW amplitude mode [37] (they mean the periodic lattice distortion, not the CDW mode) , schematically depicted in Fig. 20.1b.

(we excite some atoms in SOD) This breathing phonon mode(breathing phonon mode is some artistic expression) corresponds to oscillations of the outer Ta atoms (sites B and C) around their equilibrium positions within the SoD CDW structure.

(def. of oscillation amplitude $a$) Throughout this work, we express the oscillation amplitude $a$ as a percentage of the distance $d$ between the central (site A) and outer (site C) Ta atoms in the SoD cluster, i.e. $a = (d - d_{\mathrm{eq}})/d_{\mathrm{eq}}$, where $d_{\mathrm{eq}}$ is the distance in the equilibrium CDW distortion.

(meaning of positive, negative $a$) A positive $a$ thus indicates an expanded star, corresponding to a configuration closer to the undistorted phase (which corresponds to $a = 6.5\%$(why 6.5? was it measured somewhere?) ), while a negative $a$ denotes a contracted star with enhanced CDW distortion.

(repetition of abstract, that we'll see spectrum as function of $a$) The resulting lattice vibration modulates the electronic states — a key effect we aim to quantify in this study.

(intro to experiment that measures bands) The time-dependent electronic spectral function(=experimentally observable version of the band structure) can be probed by a THz pulse,

which induces electron tunneling between the STM tip and the sample, as depicted in Fig. 20.1a.

(they can measure time-dependent dynamics) By varying the time delay between the NIR and THz pulses, one can track the evolution of the electronic structure over an entire CDW amplitude-mode oscillation. (did they measure this time dependence?)

(they will model oscillation of SOD somehow) In our simulations, we model the coherent amplitude-mode oscillation of the SoD CDW in 1T-$TaS_2$ using a frozen-phonon approach(frozen-phonon approach??) that decouples electronic and ionic degrees of freedom.

(they'll find spectrum for different SOD amplitudes) The amplitude $a$ is modulated, and the corresponding electronic structure is evaluated separately for each frozen ionic configuration.

(electrons adapt immediately to the lattice) This treatment assumes that the electronic response, which occurs on femtosecond timescales, rapidly adapts to each lattice configuration. (is there a justification of such fast adaptation of el. spectrum?)

(some tiny effects will be neglected) While not accounting for electron-phonon or phonon-phonon interactions, we expect this approach captures the essential changes of the electronic structure over the THz CDW amplitude mode oscillations, where one period lasts approximately 0.4 ps. (why 0.4 ps?)

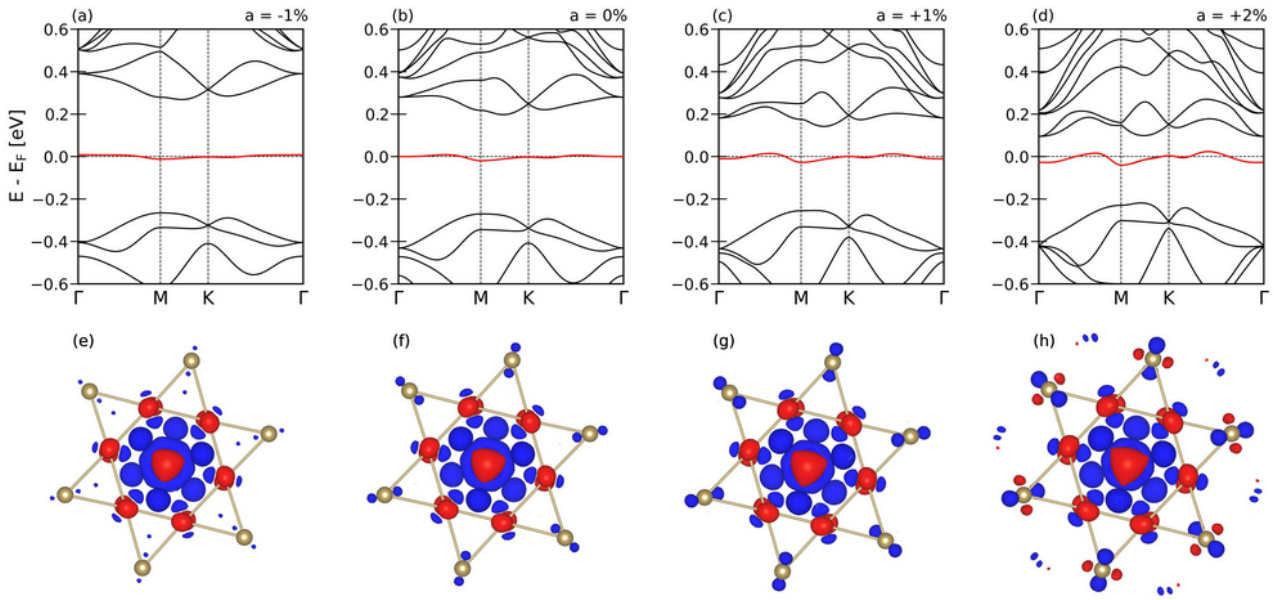


Figure 20.2: (we see that nothing is changed much in the bands) ( The surrounding black DFT bands are additional bands of the material. They should not be identified with the Hubbard bands. The lower and upper Hubbard bands appear only after the narrow red band is treated with $U_a$ in DMFT: one red DFT band $\xrightarrow{\text{DMFT } +U_a}$ LHB + UHB. .) **DFT band structure and Wannier projection for varying CDW distortion. (a–d)** Electronic band structure of monolayer 1T-$TaS_2$ for CDW amplitudes $a = -1\%$ to $a = +2\%$ around equilibrium, computed with PBE [39] in VASP [39](they are alreay in my todo list for dft learning) .
The half-filled band at the Fermi level (red) is projected(projected? how is it???) onto a maximally localized Wannier function [40].
**(e–h)** Wannier isosurfaces (Wannier isosurfaces= wave function of a free electron in atom, I assume) centered on the central Ta atom with smaller weight on surrounding atoms. Red/blue denote positive/negative values.
(there are new spots at the sides =) The orbital becomes increasingly delocalized with larger CDW amplitude.

(descript. of fig. 2) In Fig. 20.2, we present the DFT band structure of monolayer 1T-

$TaS_2$, computed for different amplitudes $a$ of the CDW distortion, ranging from $a = -1\%$ to $a = +2\%$. The reference case $a = 0\%$ (Fig. 20.2b) corresponds to the equilibrium SoD CDW.

(there is a flat band) A prominent feature in all cases is the emergence of a very narrow, half-filled band at the Fermi level (highlighted in red) with a bandwidth of just a few tens of meV.

(they get the wave function from the band using special code. it is impossible to understand better what is going on, since I don't know wannier90) Using WANNIER90 [40, 44, 39] (learn this method!) , we project this band onto a maximally localized Wannier orbital, which turns out to be a molecular-like state with predominant Ta $d_{3z^2-r^2}$ character.

(description of orbitals) As shown in Fig. 20.2e–h, the Wannier orbital is centered on the central Ta atom (site A) but extends significantly onto the surrounding Ta atoms of the SoD cluster.

(bigger a -> wider orbitals) Upon increasing the CDW amplitude from $a = -1\%$ (Fig. 20.2e) to $a = +2\%$ (Fig. 20.2h), the Wannier orbital becomes progressively more delocalized, with its spread increasing from 24 $Å^2$ to 95 $Å^2$.

(bigger a -> bigger bandwidth) This enhanced delocalization directly correlates with an increase in bandwidth of the half-filled band, which grows from 20 meV (Fig. 20.2a) to 70 meV (Fig. 20.2d). (I guess their clever code knows how the bandwidth and orbitals are connected)

(we need a screened V for calculation of bandwidth) The narrow, half-filled band is highly susceptible to electronic correlations, making it essential to evaluate the screened Coulomb interaction within this correlated subspace.

(formula for screened potential from RPA) In the random-phase approximation (RPA), the fully screened interaction is given by $W = (1 - V\chi_0)^{-1}V$, with the bare interaction $V$ and the independent-particle polarization $\chi_0$. (check this in the theory of RPA!!!)

(we for some reason use cRPA and here is a key formula for the potential) In constrained RPA (cRPA) [41, 42, 43](learn cRPA!) (why do we need cRPA?) , $\chi_0$ is decomposed into contributions from the correlated target subspace ($\chi_0^t$) and the remainder $\chi_0^r$, yielding the partially screened interaction [45, 46]

$$U = W(1 + \chi_0^t W)^{-1}, \tag{20.1}$$

where $\chi_0^t$ is the static, independent-particle polarization in the target space

$$\chi_0^t(\mathbf{r}, \mathbf{r}') = 2 \sum_{nn' \in t} \sum_{\mathbf{qk}} \frac{f_{n'\mathbf{k}+\mathbf{q}} - f_{n\mathbf{k}}}{\epsilon_{n'\mathbf{k}+\mathbf{q}} - \epsilon_{n\mathbf{k}}} \psi^*_{n\mathbf{k}}(\mathbf{r})\psi_{n'\mathbf{k}+\mathbf{q}}(\mathbf{r})\psi^*_{n'\mathbf{k}+\mathbf{q}}(\mathbf{r}')\psi_{n\mathbf{k}}(\mathbf{r}'), \tag{20.2}$$

with $\{\psi_{n\mathbf{k}}, \epsilon_{n\mathbf{k}}\}$ denoting single-particle wave functions and energies, and $f$ the Fermi functions.

(all this in the code VASP) We employ the projector cRPA method as implemented in VASP, defining the target space via the Wannier projection.

(some useless computational details) Calculations are performed in the SoD supercell, using 1024 bands(what if they took 10 bands?s) and 8×8×1 **k**-points to achieve convergence (further computational details are provided in the Supplementary Information).

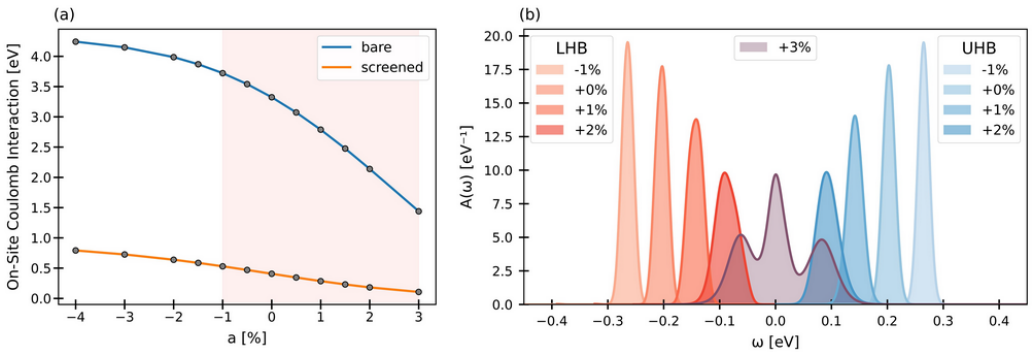


Figure 20.3: **Tuning the screened Coulomb interaction and Mott gap via CDW amplitude modulation. (a)** (how stronger electrons interact as function of SOD closeness) Bare and screened on-site Coulomb interaction as a function of CDW amplitude $a$.
The shaded region highlights the parameter range for which the electronic spectral functions $A(\omega)$ are shown in **(b)**.
(sp. function for different SODs) Increasing the CDW amplitude from -1% to +2% shifts the lower (LHB) and upper Hubbard bands (UHB) and reduces the Mott gap.
(with small SOD -> metallicity) At $a = 3\%$, the system undergoes a transition to a correlated metallic state.
In (b) the chemical potential was set to the center of the gap.

(see fig. 3) Fig. 20.3 presents the central result of this work.

(V(a) is in fig. 3) Panel (a) shows the bare and screened on-site Coulomb interactions in the molecular Ta $d_{3z^2-r^2}$ Wannier orbital for CDW amplitudes $a$ ranging from -4% to +3% around the equilibrium value ($a = 0\%$).

(they repeat the idea that V is decreased because electrons become delocalized) The bare interaction $V$ decreases markedly from 4.2 eV to 1.4eV as $a$ increases from –4% to +3%, reflecting the progressive delocalization of the Wannier orbital: as the orbital spreads out, the Coulomb repulsion is reduced.

(also, screening increases) In parallel, electronic screening becomes stronger due to global changes in the band structure. (which formula is assumed by "electronic screening depends on band structure"?)

(they assume some knowledge about screening and connect more screening with the fact that bands become closer. the question about this was already written before) This trend is evident in the DFT band structures shown in Fig. 20.2a-d, where larger CDW amplitudes bring the valence-band maximum and conduction-band minimum closer together, enhancing screening in the narrow correlated band.

(there is also a screened potential in fig. 3a, here is a description of it) The resulting screened interaction $U$ is plotted in orange in Fig. 20.3a. At the equilibrium distortion ($a = 0\%$), we obtain $U = 0.4$eV. Around this point, $U$ varies approximately linearly, changing by about 0.1 eV for $a = \pm 1\%$.

(next, sp function from U) Next, we employ the screened Coulomb interaction $U$ obtained from cRPA to compute the electronic spectral function of monolayer 1T-$TaS_2$ as a function of the CDW distortion.

(this is the Hubbard model that is there for a SOD. the derivation is written in my discussion section) For each CDW distortion with amplitude $a$, we derive a single-band Hubbard model,

$$\hat{H}_a = \sum_{ij,\sigma} H_a^{(\mathbf{R}_i - \mathbf{R}_j)} \hat{c}_{i\sigma}^\dagger \hat{c}_{j\sigma} + U_a \sum_i \hat{n}_{i\uparrow} \hat{n}_{i\downarrow}, \tag{20.3}$$

where $H_a^{(\mathbf{R}_i-\mathbf{R}_j)}$ represents the single-particle Hamiltonian in the Wannier basis, and $U_a$ denotes the screened on-site interaction in the correlated Ta $d_{3z^2-r^2}$ orbital.

(typical notation) The operators $\hat{c}_{i\sigma}^\dagger$ and $\hat{c}_{i\sigma}$ create and annihilate an electron with spin $\sigma$ at lattice site $\mathbf{R}_i$, respectively, and $\hat{n}_{i\sigma} = \hat{c}_{i\sigma}^\dagger \hat{c}_{i\sigma}$.

(name of a code and method) The resulting model is solved within DMFT using the continuous-time quantum Monte Carlo (CT-HYB) impurity solver implemented in w2dynamics [47](look at this article) .

(value of low temperature) All computations are performed at an inverse temperature $\beta = 1200\text{eV}^{-1}$, corresponding to approximately 10K. ($T = \frac{1}{k_\text{B}\beta} = \frac{1}{(8.6173\times10^{-5}\text{eVK}^{-1})(1200\text{eV}^{-1})} \approx$ 9.67 K)

(another code for the second step) Analytical continuation to real frequencies is carried out using the maximum entropy method (learn the maximum entropy method) as implemented in the ana_cont package [48]. (The imaginary-frequency Green's function calculated by CT-HYB is related to $A(\omega)$ through $G(i\omega_n) = \int_{-\infty}^{\infty} d\omega \frac{A(\omega)}{i\omega_n - \omega}$. Obtaining $A(\omega)$ requires inverting this integral relation. This inversion is called analytical continuation.)

(some extra statements in SM) Further technical details of the DFT+DMFT calculations are provided in the Supplementary Information.

(look at fig. 3b) In equilibrium ($a = 0\%$), the electronic spectral function $A(\omega)$ of monolayer 1T-$TaS_2$ is split into lower (LHB) and upper Hubbard bands (UHB), as shown in Fig. 20.3b.

(distance btw gap) These bands are separated by a Mott gap of approximately 0.4 eV.

(oscillations: bigger positive a -> LHB, UHB come close, bigger negative a -> they go apart) Upon excitation of the CDW amplitude mode, i.e., when $a$ is varied, the Hubbard bands exhibit a pronounced oscillatory behavior: for negative $a$ (enhanced distortion), the bands move further apart, while for positive $a$ (reduced distortion), the Mott gap narrows.

(Ua gives the bands) The evolution of the Mott gap closely follows the variation of the screened interaction $U_a$ obtained from cRPA. (I think that this is the comment about how their code works, they just calculate bands from Ua)

(big distortion -> phase transition) At $a = +3\%$, a transition to a correlated metallic state occurs, as evidenced by the emergence of a pronounced quasiparticle peak at the Fermi level, coexisting with reminiscent LHB and UHB features.

(distribution of electrons influence bands) These results demonstrate that the screened Coulomb interaction, Mott physics, and metal-to–insulator transition in monolayer 1T-$TaS_2$ can be effectively tuned by the CDW amplitude (they mean by $a$) .

(so we can shine light, make orbitals oscillate and electronic bands will be oscillating.) Furthermore, since the Hubbard band positions oscillate in phase with the CDW amplitude mode, this mechanism opens a route to dynamically control electronic correlations through lightwave-driven lattice vibrations. (actually, I don't think that it is so straightforward, because light will also influence electrons, there is a back action of electrons to a lattice, which is not taken into account here. So, it might not work)

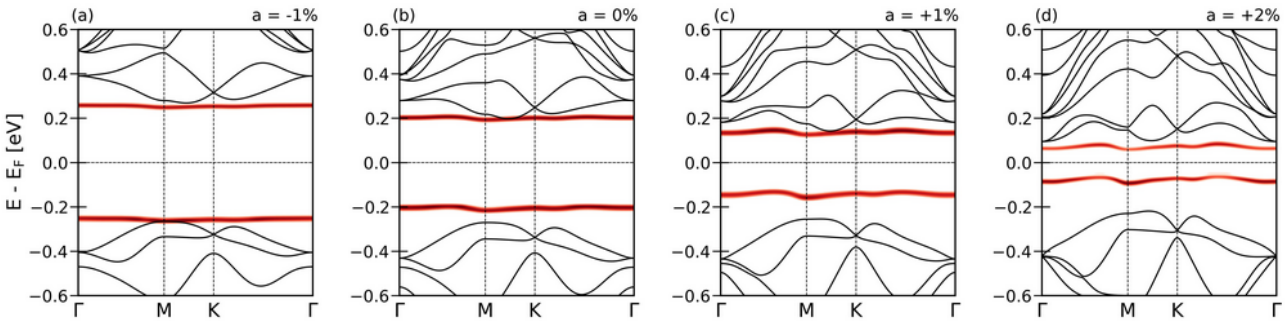


Figure 20.4: (finally, real bands. below is an obvious description of them) **Momentum-resolved spectral function as a function of CDW amplitude.**
The electronic spectral function of the Ta $d_{3z^2-r^2}$ orbital (red) obtained from DFT+DMFT is shown together with the DFT band structure (black).
As the CDW amplitude $a$ is varied from **(a)** -1% to **(d)** +2%, the Mott gap—defined as the spectral gap between the occupied LHB and the unoccupied UHB—gradually decreases from 0.5 to 0.1 eV.

(final bands on fig. 4) Finally, Fig. 20.4 presents the **k**-resolved electronic spectral function (in red), obtained from DMFT and overlaid with the DFT band structure.

(somehow they put new bands correctly near previous bands) The alignment between the correlated Ta $d_{3z^2-r^2}$ band and the remaining states was set using a fully localized limit double-counting correction (double-counting correction???) [49], $E_{\mathrm{DC}} = U_a/2$.

(description of fig. 4) The panels (a-d) show spectra for CDW amplitudes from $a = -1\%$ to $a = +2\%$.

(description of fig. 4) As in the **k**-integrated spectra of Fig. 20.3b, the Ta $d_{3z^2-r^2}$ orbital splits into LHB and UHB, and the Mott gap narrows as the CDW amplitude increases.

(again, repetition about general idea of the proposed experiment) The predicted **k**-resolved spectral signatures can be probed by tr-ARPES experiments, where coherent excitation of the CDW amplitude mode can dynamically tune the Mott state.

### 20.1.3 Discussion

(maybe we need to know how to influence matter dynamically) Discovering effective ways to tune correlated phases in quantum materials remains a central challenge in condensed matter physics, with significant implications for future technologies.

(distortion of SOD -> change of interactions of electrons) Here, we demonstrate a direct and quantitative link between structural distortions and electronic correlations in monolayer 1T-$TaS_2$.

(somehow we calculate distortion of SOD -> change of interactions of electrons) Using a combination of ab-initio and many-body simulations, we show that the CDW amplitude $a$ acts as an efficient tuning parameter for the screened Coulomb interaction and thus for the overall correlation strength.

(repetition of the results) A variation of $a = 1\%$ leads to substantial shifts of the Hubbard bands and a change of the Mott gap up to 0.1 eV, highlighting a strong coupling between lattice and electronic degrees of freedom.

(experiments do not confirm their calculations and they have ideas why) These predicted changes exceed those observed experimentally (what was observed?) [32, 34, 36], which we attribute to

(influence of other layers) (i) enhanced screening effects in bulk samples, where adjacent layers reduce the effective Coulomb interaction, and

(nearly no distortion of SODs) (ii) smaller amplitude-mode oscillations achieved in pump–probe experiments. (what is the dist. ampl in experiment??????)

(but these results still show the connection $a$ -> spectrum ) Importantly, our simulations provide a quantitative link between Hubbard-band shifts and CDW amplitude, offering experimentalists a direct route to extract CDW amplitudes from spectroscopic data.

(we calculated U, it might be useful somehow) Our first-principles evaluation of the screened Coulomb interaction $U$ provides essential microscopic input for interpreting time-resolved spectroscopies of 1T-$TaS_2$ and related materials.

(again, this unjustified promise for dyn. controlling el. properties) It establishes a direct pathway for manipulating Mott insulating states in 2D CDW systems via coherent lattice dynamics.

(we don't know how electrons change in time, but on some timescales the result might make sense) While our equilibrium simulations isolate the impact of structural modulations and do not capture the ultrafast nonequilibrium regime immediately following photoexcitation, they describe the relevant electronic states on longer (100 fs–1 ps) (why these timescales??) timescales, where electrons have thermalized and respond adiabatically to the lattice's 2.4 THz amplitude mode oscillation.

(ideas of more realistic model) Future extensions including coupled electron-phonon dynamics (or make U as dynamical parameter, or use another model, where electrons are dynamically coupled somehow) and nonlocal Coulomb interactions may further refine this picture (this is the extended Hubbard model, which was already analyzed) .

(again repetition of what they did and promise that it is important) Overall, our work uncovers how CDW lattice distortions can govern electronic correlations, offering both a conceptual framework and a practical guide for engineering correlated phases in low-dimensional quantum materials.

### 20.1.4 SM

#### IV. CRPA CALCULATIONS AND CONVERGENCE TESTS

The cRPA [9–11] calculations were performed in VASP using the following 3 step procedure: (i) a self-consistent DFT ground state calculation, followed by (ii) a one-shot exact-diagonalization step to obtain the unoccupied orbitals and the long-wavelength limit of the polarizability, and (iii) the evaluation of the screened interaction using VASP's internal cRPA implementation. To exclude screening processes within the correlated subspace, we employed the projector method [12].

All three steps of the cRPA procedure in VASP were carried out using a Γ-centered $8\times8\times1$k-mesh, a plane-wave energy cutoff of 300 eV, and Gaussian smearing with a width of 0.05 eV. The electronic self-consistency criterion was set to an energy tolerance of $10^{-8}$eV. GW-optimized PAW pseudopotentials were employed to include semicore states relevant for screening.

In the exact-diagonalization and cRPA steps, 1024 bands were included to account for a sufficient number of virtual states. The frequency-dependent dielectric matrix was computed (LOPTICS =.TRUE.) to accurately capture the long-wavelength limit of the polarizability. To improve convergence for the Ta $d$-states, higher angular components in the charge-density mixing were included up to $l = 4$. The energy cutoff for the Coulomb matrix elements in the cRPA step was set to the converged value of 400 eV.

The screened on-site interaction $U$ and the bare on-site interaction $V$ were systematically converged with respect to the plane-wave cutoff (ENCUT), the number of bands (NBANDS), and the k-mesh. The convergence of $U$ and $V$ with ENCUT is shown in Fig. S3, where 512 bands and a coarse $3 \times 3 \times 1$k-mesh were used. A final ENCUT value of 300 eV was chosen.

Convergence with respect to the k -mesh is presented in Fig. S2, keeping ENCUT = 300eV and NBANDS = 512. Computational cost reached 44000 core-hours at a $10 \times 10 \times 1$ mesh; therefore, an $8 \times 8 \times 1$ mesh was adopted for the final calculations as a compromise between accuracy and efficiency.

The number of Kohn-Sham orbitals was determined from the convergence of $U; V$ is insensitive to NBANDS, as its value is determined by the bare Coulomb matrix elements. A coarse $3 \times 3 \times 1$k-grid with ENCUT = 300eV was used to test NBANDS convergence, as shown in Fig. S4(a). NBANDS = 1024 was chosen for all subsequent calculations. The bare on-site interaction $V$ was further converged with respect to the cutoff for the bare Coulomb matrix elements (VCUTOFF), using an $8 \times 8 \times 1$k-mesh, ENCUT = 300eV, and NBANDS = 1024. Convergence is illustrated in Fig. S4(b), and VCUTOFF = 400eV was adopted as the final value.

## V. DMFT CALCULATIONS

The single-band DMFT impurity model was solved using the continuous-time hybridization-expansion quantum Monte Carlo (CT-HYB) impurity solver implemented in w2dynamics. [13] All calculations were performed at an inverse temperature of $\beta = 1200\text{eV}^{-1}$. For the CT-HYB solver, we employed $2 \times 10^7$ measurement sweeps with $10^7$ warmup steps and a decorrelation interval of $N$ Corr = 50. Convergence of the DMFT calculations was verified by monitoring the Green's functions and self-energies at each DMFT iteration.

We measured $G(\tau)$ in the Legendre basis to reduce statistical noise and obtain smooth high-frequency behavior. [14] Including more Legendre orders retains more $\tau$-structure and improves the high-frequency tail. But once the noise floor is reached, higher orders mainly introduce statistical noise. Too small orders on the other hand, bias the tail. To determine a suited order for the Legendre polynomials, test runs with different orders were conducted for each CDW amplitude $a$. The final orders were selected based on visual inspection of the Green's function and self-energy, yielding NLegMax and NLegOrder values between 40 and 70. Stronger CDW distortions (smaller $a$ ) typically benefit from higher orders, while weaker distortions (larger $a$ ) are adequately captured with $40-50$ polynomials. In the case of $a = +2\%$, the Legendre order could be increased beyond 80 without introducing visible noise, consistent with the particularly smooth $G(\tau)$ observed for this CDW amplitude.

## VI. ANALYTICAL CONTINUATION

We used the ana_cont package [15] to perform analytical continuations using the maximum entropy method [16,17] with singular value decomposition. The hyperparameter $\alpha$ was determined using the "chi2kink" method [18,19]. Continuations were carried out in two ways: (i) direct analytical continuation of the Green's function $G(i\omega_n)$, and (ii) analytic continuation of the cumulant

$$M(i\omega_n) = \frac{1}{i\omega_n - \mu - \Sigma(i\omega_n)}, \tag{S3}$$

from which the self-energy $\Sigma(\omega)$ on the real-frequency axis is reconstructed as

$$\Sigma(\omega) = \omega + \mu - \frac{1}{M(\omega)}. \tag{S4}$$

The self-energy obtained from the cumulant-based continuation was used to compute the momentum-resolved spectral function $A(k, \omega)$ shown in Fig. 3 of the main text. The momentum-integrated spectral function, $A(\omega) = \sum_{\mathbf{k}} A(\mathbf{k}, \omega)$, can then be directly compared to the result obtained from the continuation of $G(i\omega_n)$.

To mitigate unphysical artifacts around the Fermi energy, a slight preblur was applied, with the blur width ranging from 0.0 to 0.0125 depending on the CDW amplitude $a$. For the computation of the spectral function, a small imaginary $i\eta$ (ranging from 0.008 to 0.012) was added to the denominator of the real-frequency Green's function.

## 20.2 My Discussion

### 20.2.1 My Conclusion and Analysis of the article

#### My conclusion

Interesting idea, good advanced calculations, but the real usefulness is very unclear.

#### Connection with experiments is missing?

Did they do a calculation which is confirmed or not with experiment?
It is not clear.

#### Absence of electronic back-action on the Star-of-David dynamics.

(GPT:)
A central limitation of the frozen-phonon approach used in the article is that it treats the influence between the lattice and the electrons only in one direction. For each imposed Star-of-David structural coordinate $Q$, the ionic positions determine the electronic Hamiltonian,

$$Q \longrightarrow \hat{H}_{\mathrm{e}}(Q), \tag{20.4}$$

from which the electronic density, Wannier orbitals, screened interaction, and spectral function are calculated,

$$\hat{H}_{\mathrm{e}}(Q) \longrightarrow n_Q(\mathbf{r}) \longrightarrow \{w_Q(\mathbf{r}), U_Q, A(\mathbf{k}, \omega; Q)\}\,. \tag{20.5}$$

The electronic density is therefore allowed to adjust self-consistently to each fixed ionic configuration. However, the reverse influence of the resulting electronic state on the subsequent motion of the Star-of-David structure is not included. In particular, the electronic contribution to the force,

$$F_{\mathrm{e}}(Q) = -\frac{\partial E_{\mathrm{e}}(Q)}{\partial Q}, \tag{20.6}$$

is not used to determine the evolution of $Q$. A self-consistent description would require the ionic coordinate to satisfy an equation such as

$$M_{\mathrm{eff}}\ddot{Q}(t) = -\frac{\partial E_{\mathrm{ion}}(Q)}{\partial Q} - \frac{\partial E_{\mathrm{e}}(Q)}{\partial Q} + F_{\mathrm{ext}}(t), \tag{20.7}$$

or, more generally,

$$M_{\mathrm{eff}}\ddot{Q}(t) = -\left\langle \Psi_{\mathrm{e}}(t) \left| \frac{\partial \hat{H}_{\mathrm{e}}[Q(t)]}{\partial Q} \right| \Psi_{\mathrm{e}}(t) \right\rangle - \frac{\partial E_{\mathrm{ion}}}{\partial Q} + F_{\mathrm{ext}}(t). \tag{20.8}$$

The calculation in the article instead stops after obtaining

$$Q \longrightarrow A(\mathbf{k}, \omega; Q), \tag{20.9}$$

without completing the feedback loop

$$Q(t) \longrightarrow |\Psi_{\mathrm{e}}(t)\rangle \longrightarrow F_{\mathrm{e}}(t) \longrightarrow Q(t + \Delta t). \tag{20.10}$$

Consequently, the calculation does not determine whether a chosen non-equilibrium Star-of-David configuration is dynamically accessible, how long it persists, or whether the electronically induced forces drive it back toward equilibrium, enhance the displacement, or stabilize another configuration. It also does not predict the actual oscillation amplitude or damping. The results should therefore be interpreted as the conditional electronic spectra of externally imposed frozen structures, rather than as a self-consistent prediction of the coupled electron–lattice dynamics. Strictly speaking, electronic effects are not absent from the calculation, since the electrons are solved self-consistently at every fixed $Q$; what is absent is their dynamical back-action on the Star-of-David motion.

**Justification and limitations of adjusting the electronic state to the instantaneous Star-of-David structure.**

(GPT:)

The electronic structure and the Star-of-David lattice distortion mutually influence each other: the ionic positions determine the electronic Hamiltonian, while the electronic state determines the forces acting on the ions. Nevertheless, calculating the electronic spectrum for a sequence of fixed ionic configurations can be justified within the Born–Oppenheimer, or adiabatic, approximation. The essential assumption is a separation of electronic and ionic timescales,

$$\tau_{\mathrm{e}} \ll \tau_{\mathrm{ion}}, \tag{20.11}$$

such that the electrons adapt approximately instantaneously to the slowly evolving ionic configuration. If $Q(t)$ denotes the structural coordinate describing the Star-of-David distortion, the electronic state is approximated by

$$|\Psi_{\mathrm{e}}(t)\rangle \approx |\Psi_{\mathrm{e}}^{\mathrm{eq}}[Q(t)]\rangle, \tag{20.12}$$

and the time-dependent electronic spectrum may be estimated as

$$A(\mathbf{k}, \omega, t) \approx A_{\mathrm{eq}}(\mathbf{k}, \omega; Q(t))\,. \tag{20.13}$$

For the 2.4 THz structural mode considered in the article, the oscillation period is

$$T_{\mathrm{ion}} = \frac{1}{2.4\,\mathrm{THz}} \approx 417\,\mathrm{fs}, \tag{20.14}$$

which is considerably longer than typical electronic adjustment times. This makes the adiabatic approximation plausible after the initial strongly nonequilibrium stage following photoexcitation.

The mutual influence of the electronic and ionic subsystems is not absent within the complete Born–Oppenheimer description. For every fixed $Q$, the electrons determine an electronic energy $E_{\mathrm{e}}(Q)$, which contributes to the effective ionic potential,

$$E_{\mathrm{BO}}(Q) = E_{\mathrm{ion}}(Q) + E_{\mathrm{e}}(Q). \tag{20.15}$$

The electronic state consequently affects the structural motion through the force

$$F_Q = -\frac{dE_{\mathrm{BO}}(Q)}{dQ}. \tag{20.16}$$

A fully self-consistent adiabatic calculation would therefore involve the sequence

$$Q(t) \longrightarrow |\Psi_{\mathrm{e}}^{\mathrm{eq}}[Q(t)]\rangle \longrightarrow E_{\mathrm{BO}}(Q) \longrightarrow F_Q \longrightarrow Q(t + \Delta t). \tag{20.17}$$

The article, however, performs only the first part of this procedure,

$$Q \longrightarrow A_{\mathrm{eq}}(\mathbf{k}, \omega; Q). \tag{20.18}$$

The Star-of-David geometries are imposed as frozen configurations, and the resulting electronic forces are not used to propagate the ions. Consequently, the calculation determines how the equilibrium electronic spectrum depends parametrically on an assumed instantaneous lattice geometry, but it does not predict the actual structural trajectory $Q(t)$, the oscillation amplitude, or the electronic back-reaction on the lattice dynamics.

The frozen-phonon treatment is therefore justified as a conditional adiabatic calculation if the structural motion is independently known or assumed. It becomes unreliable immediately after strong photoexcitation, when the electronic distribution is nonthermal, or whenever electronic and ionic dynamics occur on comparable timescales. In such regimes, the coupled equations

$$i\hbar \frac{\partial}{\partial t} |\Psi_{\mathrm{e}}(t)\rangle = \hat{H}_{\mathrm{e}}[Q(t), t] |\Psi_{\mathrm{e}}(t)\rangle \tag{20.19}$$

and

$$M_{\mathrm{eff}} \ddot{Q}(t) = -\left\langle \Psi_{\mathrm{e}}(t) \left| \frac{\partial \hat{H}_{\mathrm{e}}}{\partial Q} \right| \Psi_{\mathrm{e}}(t) \right\rangle - \frac{\partial E_{\mathrm{ion}}}{\partial Q} \tag{20.20}$$

would need to be solved self-consistently. Thus, the article establishes the conditional relation between a frozen Star-of-David distortion and its electronic spectrum, but does not provide a complete theory of the coupled light-induced electron–lattice dynamics.

### Neglect of nonlocal interactions between Star-of-David clusters

Another limitation of the model is that it includes electron hopping between different Star-of-David clusters but retains only the local Coulomb interaction within a single cluster,

$$\hat{H}_a = \sum_{ij,\sigma} H_a^{(\mathbf{R}_i - \mathbf{R}_j)} \hat{c}_{i\sigma}^{\dagger} \hat{c}_{j\sigma} + U_a \sum_i \hat{n}_{i\uparrow} \hat{n}_{i\downarrow}. \tag{20.21}$$

The hopping matrix elements $H_a^{(\mathbf{R}_i - \mathbf{R}_j)}$ allow electrons to propagate between clusters and therefore generate the dispersion of the correlated band. However, the model neglects the direct Coulomb interaction between electrons occupying neighbouring Star-of-David Wannier orbitals. A more complete description is provided by the extended Hubbard model,

$$\hat{H}_a^{\mathrm{ext}} = \sum_{ij,\sigma} H_a^{(\mathbf{R}_i - \mathbf{R}_j)} \hat{c}_{i\sigma}^{\dagger} \hat{c}_{j\sigma} + U_a \sum_i \hat{n}_{i\uparrow} \hat{n}_{i\downarrow} + \frac{1}{2} \sum_{i \neq j} V_{ij,a} \hat{n}_i \hat{n}_j, \tag{20.22}$$

where $V_{ij,a}$ is the screened inter-cluster Coulomb interaction. Previous first-principles calculations for monolayer commensurate $1T$-$TaS_2$ have found a sizable nearest-neighbour interaction $V$ and have therefore calculated the correlated spectrum using an extended Hubbard model treated within GW+EDMFT [? ]. Those calculations found that the equilibrium insulating state is primarily driven by the local interaction $U$, while the effect of $V$ on the spectrum is comparatively small in the deep Mott regime because charge fluctuations are strongly suppressed. Nevertheless, this does not justify neglecting $V_{ij,a}$ for every distortion. As the Star-of-David Wannier orbital becomes more delocalized and the system approaches the correlated metallic state, inter-cluster interactions, nonlocal screening, and charge fluctuations may become more important. Moreover, single-site DMFT assumes a purely local self-energy,

$$\Sigma_{ij}(\omega) = \delta_{ij} \Sigma(\omega), \tag{20.23}$$

and therefore neglects nonlocal correlation effects between neighbouring clusters. Consequently, the single-band local Hubbard model used in the article provides a simplified description of the distortion-dependent spectrum, but the robustness of its predicted Hubbard-band shifts and metal–insulator transition should be verified using an extended Hubbard model with distortion-dependent $V_{ij,a}$ and, ideally, a method capable of treating nonlocal correlations.

### 20.2.2 Questions about Assumed Knowledge

**Derivation of the effective Hubbard Hamiltonian**

(GPT:)

The single-band Hubbard Hamiltonian is obtained by projecting the electronic problem onto the isolated narrow band at the Fermi level. For each fixed CDW amplitude $a$, the ionic positions are treated within the frozen-phonon approximation, and the corresponding single-particle Hamiltonian $\hat{h}_a$ is calculated using DFT. The resulting narrow, half-filled band is then represented by maximally localized Wannier functions $w_{ia}(\mathbf{r})$, where $i$ labels a Star-of-David cluster centered at $\mathbf{R}_i$. Thus, each Star-of-David cluster constitutes one effective site of the Hubbard model.

Restricting the electronic field operator to this low-energy subspace gives

$$\hat{\psi}_\sigma(\mathbf{r}) \approx \sum_i w_{ia}(\mathbf{r})\hat{c}_{i\sigma}. \tag{20.24}$$

Substitution into the single-particle part of the electronic Hamiltonian yields

$$\hat{H}_{0,a} = \sum_{ij,\sigma} \langle w_{ia}|\hat{h}_a|w_{ja}\rangle \hat{c}^\dagger_{i\sigma}\hat{c}_{j\sigma}. \tag{20.25}$$

The Wannier-basis matrix elements are defined as

$$H_a^{(\mathbf{R}_i-\mathbf{R}_j)} = \langle w_{ia}|\hat{h}_a|w_{ja}\rangle. \tag{20.26}$$

For $i \neq j$, these matrix elements describe electron hopping between different Star-of-David clusters, while the diagonal elements contain the on-site orbital energy. Equivalently, they can be obtained by Fourier transforming the Wannier-interpolated band dispersion,

$$H_a^{(\mathbf{R})} = \frac{1}{N_\mathbf{k}} \sum_\mathbf{k} e^{-i\mathbf{k}\cdot\mathbf{R}} \varepsilon_{\mathbf{k}a}. \tag{20.27}$$

Projecting the screened electron–electron interaction $W_a(\mathbf{r},\mathbf{r}')$ onto the same Wannier subspace produces the general interaction matrix elements

$$U^a_{ijkl} = \int d\mathbf{r}\, d\mathbf{r}'\, w^*_{ia}(\mathbf{r}) w^*_{ja}(\mathbf{r}') W_a(\mathbf{r},\mathbf{r}') w_{ka}(\mathbf{r}) w_{la}(\mathbf{r}'). \tag{20.28}$$

The single-band Hubbard approximation retains only the local density–density matrix element

$$U_a = \int d\mathbf{r}\, d\mathbf{r}'\, |w_{ia}(\mathbf{r})|^2 W_a(\mathbf{r},\mathbf{r}') |w_{ia}(\mathbf{r}')|^2, \tag{20.29}$$

which represents the energy cost of placing two electrons with opposite spins in the same molecular-like Wannier orbital. In the article, $W_a$, and hence $U_a$, is evaluated using the constrained random-phase approximation.

Combining the projected single-particle and interaction terms gives

$$\hat{H}_a = \sum_{ij,\sigma} H_a^{(\mathbf{R}_i-\mathbf{R}_j)} \hat{c}_{i\sigma}^\dagger \hat{c}_{j\sigma} + U_a \sum_i \hat{n}_{i\uparrow}\hat{n}_{i\downarrow}. \tag{20.30}$$

This Hamiltonian is therefore a low-energy effective model rather than the complete microscopic Hamiltonian of $1T$-$TaS_2$. Its construction assumes that the isolated half-filled band dominates the low-energy physics and that nonlocal Coulomb interactions, exchange terms, and correlated hopping can be neglected. The CDW amplitude enters parametrically through both the Wannier Hamiltonian $H_a^{(\mathbf{R}_i-\mathbf{R}_j)}$ and the screened interaction $U_a$, since the lattice distortion modifies the band dispersion, Wannier-orbital localization, and electronic screening.

**How to calculate the electronic structure for a new Star-of-David distortion.**

(GPT:)

The calculation begins by choosing a new ionic configuration of the Star-of-David cluster. The procedure then consists of a DFT calculation, construction of the low-energy Wannier Hamiltonian, evaluation of the screened interaction using cRPA, and solution of the resulting Hubbard model using DMFT. The DFT calculation produces the noninteracting band shown in Fig. 2, whereas the final interacting spectral structure, including the lower and upper Hubbard bands, is obtained only after the DMFT calculation.

**Step 1: Define the distorted ionic structure.**

Let $\mathbf{R}_\alpha^{\mathrm{eq}}$ denote the equilibrium position of atom $\alpha$, and let $\mathbf{e}_\alpha$ describe the displacement pattern associated with the Star-of-David breathing distortion. A structure with amplitude $a$ may be written as

$$\mathbf{R}_\alpha(a) = \mathbf{R}_\alpha^{\mathrm{eq}} + a\,\mathbf{e}_\alpha. \tag{20.31}$$

In the article, the structural parameter is defined more specifically as

$$a = \frac{d - d_{\mathrm{eq}}}{d_{\mathrm{eq}}}, \tag{20.32}$$

where $d$ is the distance between the central Ta atom and an outer Ta atom of the Star-of-David cluster. Therefore,

$$d(a) = (1 + a)d_{\mathrm{eq}}. \tag{20.33}$$

The parameter $a$ is thus a structural coordinate and not the electronic CDW order-parameter amplitude.

**Step 2: Construct the ionic potential.**

The new atomic positions determine the external potential acting on the electrons,

$$V_{\mathrm{ion}}^a(\mathbf{r}) = \sum_\alpha V_\alpha\big(\mathbf{r} - \mathbf{R}_\alpha(a)\big), \tag{20.34}$$

where $V_\alpha$ is the ionic or pseudopotential associated with atom $\alpha$. Changing the Star-of-David distortion therefore changes the potential entering the electronic Hamiltonian.

**Step 3: Solve the Kohn–Sham equations self-consistently.**

For the new ionic configuration, one solves

$$\hat{h}_{\mathrm{KS},a}[n_a]\psi_{n\mathbf{k}a}(\mathbf{r}) = \varepsilon^{\mathrm{KS}}_{n\mathbf{k}a}\psi_{n\mathbf{k}a}(\mathbf{r}), \tag{20.35}$$

with

$$\hat{h}_{\mathrm{KS},a}[n_a] = -\frac{\nabla^2}{2m} + V^a_{\mathrm{ion}}(\mathbf{r}) + V_{\mathrm{H}}[n_a](\mathbf{r}) + V_{\mathrm{xc}}[n_a](\mathbf{r}). \tag{20.36}$$

The density is recalculated from the occupied Kohn–Sham states,

$$n_a(\mathbf{r}) = \sum_{n\mathbf{k}\sigma} f\left(\varepsilon^{\mathrm{KS}}_{n\mathbf{k}a}\right) \left|\psi_{n\mathbf{k}a\sigma}(\mathbf{r})\right|^2, \tag{20.37}$$

where $f$ is the Fermi–Dirac distribution. Because the Hamiltonian depends on $n_a(\mathbf{r})$, these equations must be iterated until self-consistency,

$$n_a^{(m+1)}(\mathbf{r}) \simeq n_a^{(m)}(\mathbf{r}). \tag{20.38}$$

The resulting eigenvalues

$$\varepsilon^{\mathrm{KS}}_{n\mathbf{k}a} \tag{20.39}$$

form the DFT band structure for the chosen distortion. This is the type of band structure shown in Fig. 2.

**Step 4: Select the narrow low-energy band.**

The Star-of-David reconstruction produces a narrow, approximately half-filled band near the Fermi level. Denoting this band by

$$\varepsilon_{\mathbf{k}a} \equiv \varepsilon^{\mathrm{KS}}_{n_0\mathbf{k}a}, \tag{20.40}$$

the low-energy subspace is defined as

$$\mathcal{H}^a_{\mathrm{low}} = \mathrm{span}\left\{|\psi_{n_0\mathbf{k}a}\rangle\right\}_{\mathbf{k}}. \tag{20.41}$$

This band has predominantly Ta $d_{3z^2-r^2}$ character and provides the correlated target subspace used in the subsequent calculation.

**Step 5: Construct the Wannier orbital.**

A localized Wannier orbital centered on Star-of-David cluster $i$ is obtained from the selected Bloch states,

$$|w_{ia}\rangle = \frac{1}{\sqrt{N_{\mathbf{k}}}} \sum_{\mathbf{k}} e^{-i\mathbf{k}\cdot\mathbf{R}_i} e^{i\phi_{\mathbf{k}a}} |\psi_{n_0\mathbf{k}a}\rangle, \tag{20.42}$$

where the phases $\phi_{\mathbf{k}a}$ are chosen to localize the Wannier function. More generally, if several bands are involved in the disentanglement procedure,

$$|w_{ia}\rangle = \frac{1}{\sqrt{N_{\mathbf{k}}}} \sum_{\mathbf{k},n} e^{-i\mathbf{k}\cdot\mathbf{R}_i} U^{(\mathbf{k})}_{na} |\psi_{n\mathbf{k}a}\rangle. \tag{20.43}$$

The new distortion changes both the spatial form and the localization of $w_{ia}(\mathbf{r})$.

**Step 6: Calculate the effective hopping parameters.**

The single-particle Hamiltonian is projected onto the Wannier basis,

$$H_a^{(\mathbf{R}_i-\mathbf{R}_j)} = \left\langle w_{ia} \middle| \hat{h}_{\mathrm{KS},a} \middle| w_{ja} \right\rangle . \tag{20.44}$$

For $i \neq j$, these matrix elements describe hopping between Star-of-David clusters, while for $i = j$ they give the local orbital energy. In the isolated single-band case, they can equivalently be calculated as

$$H_a^{(\mathbf{R})} = \frac{1}{N_{\mathbf{k}}} \sum_{\mathbf{k}} e^{-i\mathbf{k}\cdot\mathbf{R}} \varepsilon_{\mathbf{k}a}. \tag{20.45}$$

The reverse Fourier transformation reconstructs the Wannier-interpolated DFT band,

$$\varepsilon_{\mathbf{k}a} = \sum_{\mathbf{R}} e^{i\mathbf{k}\cdot\mathbf{R}} H_a^{(\mathbf{R})}. \tag{20.46}$$

Its bandwidth is

$$W_a = \max_{\mathbf{k}} \varepsilon_{\mathbf{k}a} - \min_{\mathbf{k}} \varepsilon_{\mathbf{k}a}. \tag{20.47}$$

**Step 7: Calculate the partially screened Coulomb interaction.**

The bare Coulomb interaction in the Wannier orbital is

$$V_a = \int d\mathbf{r}\, d\mathbf{r}'\, |w_{ia}(\mathbf{r})|^2 \frac{e^2}{|\mathbf{r}-\mathbf{r}'|} |w_{ia}(\mathbf{r}')|^2. \tag{20.48}$$

Screening processes outside the correlated target band are described by the constrained polarization

$$\chi_a^r = \chi_a^0 - \chi_a^t, \tag{20.49}$$

where $\chi_a^0$ is the full independent-particle polarization and $\chi_a^t$ contains transitions entirely within the selected target subspace. The partially screened interaction is

$$W_a^r(\omega) = \left[1 - v\chi_a^r(\omega)\right]^{-1} v, \tag{20.50}$$

where $v(\mathbf{r},\mathbf{r}') = e^2/|\mathbf{r}-\mathbf{r}'|$. The static on-site Hubbard interaction is then obtained by projecting $W_a^r(\omega = 0)$ onto the Wannier orbital,

$$U_a = \int d\mathbf{r}\, d\mathbf{r}'\, |w_{ia}(\mathbf{r})|^2 W_a^r(\mathbf{r},\mathbf{r}';0) |w_{ia}(\mathbf{r}')|^2. \tag{20.51}$$

The distortion changes $U_a$ through both the localization of the Wannier orbital and the screening generated by the remaining bands.

**Step 8: Construct the distortion-dependent Hubbard model.**

The DFT-derived single-particle Hamiltonian and the cRPA interaction are combined into

$$\hat{H}_a = \sum_{ij,\sigma} H_a^{(\mathbf{R}_i-\mathbf{R}_j)} \hat{c}_{i\sigma}^\dagger \hat{c}_{j\sigma} + U_a \sum_i \hat{n}_{i\uparrow}\hat{n}_{i\downarrow}. \tag{20.52}$$

Thus, every structural configuration $a$ generates a different effective model,

$$a \longrightarrow \left\{ H_a^{(\mathbf{R})}, U_a \right\}. \tag{20.53}$$

The important correlation scale is approximately determined by

$$\frac{U_a}{W_a}. \tag{20.54}$$

**Step 9: Solve the interacting model using DMFT.**

In single-site DMFT, the lattice self-energy is approximated as local,

$$\Sigma_a(\mathbf{k}, i\omega_n) \approx \Sigma_a(i\omega_n). \tag{20.55}$$

The interacting lattice Green's function is

$$G_a(\mathbf{k}, i\omega_n) = \frac{1}{i\omega_n + \mu - \varepsilon_{\mathbf{k}a} - \Sigma_a(i\omega_n)}. \tag{20.56}$$

The local Green's function is obtained by summing over momentum,

$$G_{\mathrm{loc},a}(i\omega_n) = \frac{1}{N_{\mathbf{k}}} \sum_{\mathbf{k}} G_a(\mathbf{k}, i\omega_n). \tag{20.57}$$

It defines the effective impurity Weiss field through

$$\mathcal{G}_{0,a}^{-1}(i\omega_n) = G_{\mathrm{loc},a}^{-1}(i\omega_n) + \Sigma_a(i\omega_n). \tag{20.58}$$

The corresponding impurity problem is solved, in the article using CT-HYB, to obtain a new impurity Green's function and self-energy,

$$\Sigma_a(i\omega_n) = \mathcal{G}_{0,a}^{-1}(i\omega_n) - G_{\mathrm{imp},a}^{-1}(i\omega_n). \tag{20.59}$$

These equations are iterated until DMFT self-consistency is reached,

$$G_{\mathrm{imp},a}(i\omega_n) = G_{\mathrm{loc},a}(i\omega_n). \tag{20.60}$$

**Step 10: Continue the Green's function to real frequencies.**

The CT-HYB calculation provides the Green's function at imaginary Matsubara frequencies,

$$i\omega_n = i(2n+1)\frac{\pi}{\beta}. \tag{20.61}$$

To obtain the experimentally relevant real-frequency spectrum, one uses the relation

$$G_{\mathrm{loc},a}(i\omega_n) = \int_{-\infty}^{\infty} d\omega \, \frac{A_a(\omega)}{i\omega_n - \omega}. \tag{20.62}$$

The inversion of this equation is an ill-conditioned problem and is regularized in the article using the maximum entropy method. This gives the local spectral function

$$A_a(\omega) = -\frac{1}{\pi} \operatorname{Im} G_{\mathrm{loc},a}^R(\omega). \tag{20.63}$$

**Step 11: Calculate the momentum-resolved interacting spectrum.**

After obtaining the real-frequency self-energy, the retarded Green's function is

$$G_a^R(\mathbf{k}, \omega) = \frac{1}{\omega + \mu - \varepsilon_{\mathbf{k}a} - \Sigma_a^R(\omega)}. \tag{20.64}$$

The momentum-resolved spectral function is therefore

$$A_a(\mathbf{k}, \omega) = -\frac{1}{\pi} \operatorname{Im} \left[ \frac{1}{\omega + \mu - \varepsilon_{\mathbf{k}a} - \Sigma_a^R(\omega)} \right]. \tag{20.65}$$

This is the interacting analogue of the band structure and can contain a lower Hubbard band, an upper Hubbard band, a Mott gap, and, in the metallic regime, a quasiparticle peak. Unlike the DFT bands, these features are not simply eigenvalues of a static single-particle Hamiltonian; they represent electron-removal and electron-addition excitations of the interacting system.

**Complete calculation chain.**

The complete procedure can be summarized as

$$\mathbf{R}_\alpha(a) \longrightarrow V^a_{\text{ion}} \longrightarrow \left\{\varepsilon^{\text{KS}}_{n\mathbf{k}a}, \psi_{n\mathbf{k}a}\right\} \longrightarrow w_{ia} \longrightarrow \left\{H^{(\mathbf{R})}_a, U_a\right\} \longrightarrow \Sigma_a(\omega) \longrightarrow A_a(\mathbf{k},\omega). \tag{20.66}$$

The DFT part determines how the structural distortion changes the noninteracting electronic states, whereas cRPA and DMFT determine how the same distortion modifies the screened interaction and the final correlated electronic spectrum.

**Why the Hubbard interaction is not explicitly present in DFT?**

In other words, why wouldn't we get the right bands from just DFT?
(GPT:)

**Coulomb interaction in the microscopic Hamiltonian.**

The microscopic electronic Hamiltonian contains an explicit two-particle Coulomb interaction,

$$\hat{H} = \sum_\sigma \int d\mathbf{r}\, \hat{\psi}^\dagger_\sigma(\mathbf{r})\hat{h}_0\hat{\psi}_\sigma(\mathbf{r}) + \frac{1}{2}\sum_{\sigma\sigma'} \int d\mathbf{r}\, d\mathbf{r}'\, \hat{\psi}^\dagger_\sigma(\mathbf{r})\hat{\psi}^\dagger_{\sigma'}(\mathbf{r}')\frac{e^2}{|\mathbf{r}-\mathbf{r}'|}\hat{\psi}_{\sigma'}(\mathbf{r}')\hat{\psi}_\sigma(\mathbf{r}). \tag{20.67}$$

Projection of the second term onto a localized Star-of-David Wannier orbital produces, among other interaction matrix elements, the on-site Hubbard interaction

$$U = \int d\mathbf{r}\, d\mathbf{r}'\, |w_i(\mathbf{r})|^2 \frac{e^2}{|\mathbf{r}-\mathbf{r}'|}|w_i(\mathbf{r}')|^2, \tag{20.68}$$

and the corresponding operator $U\hat{n}_{i\uparrow}\hat{n}_{i\downarrow}$.

**Replacement of the interaction in Kohn–Sham DFT.**

Kohn–Sham DFT maps the interacting many-electron problem onto an auxiliary noninteracting problem,

$$\hat{H}_{\text{KS}} = \sum_\sigma \int d\mathbf{r}\, \hat{\psi}^\dagger_\sigma(\mathbf{r}) \left[\hat{h}_0 + V_{\text{H}}[n](\mathbf{r}) + V_{\text{xc}}[n](\mathbf{r})\right] \hat{\psi}_\sigma(\mathbf{r}). \tag{20.69}$$

The explicit two-particle Coulomb operator is therefore replaced by the Hartree and exchange–correlation potentials, which depend on the average electron density. Consequently, the Kohn–Sham Hamiltonian is quadratic in the fermionic operators,

$$\hat{H}_{\text{KS}} = \sum_{mn,\sigma} h^{\text{KS}}_{mn}\hat{c}^\dagger_{m\sigma}\hat{c}_{n\sigma}, \tag{20.70}$$

and does not contain an explicit quartic operator of the form

$$U\hat{n}_{i\uparrow}\hat{n}_{i\downarrow} = U\hat{c}^\dagger_{i\uparrow}\hat{c}^\dagger_{i\downarrow}\hat{c}_{i\downarrow}\hat{c}_{i\uparrow}. \tag{20.71}$$

**Projection onto the low-energy Wannier subspace.**

Projecting the quadratic Kohn–Sham Hamiltonian onto the narrow half-filled band gives

$$\hat{H}_{\text{DFT},a} = \sum_{ij,\sigma} H^{(\mathbf{R}_i-\mathbf{R}_j)}_a \hat{c}^\dagger_{i\sigma}\hat{c}_{j\sigma}. \tag{20.72}$$

A change of basis cannot transform a quadratic operator into a quartic interaction. Therefore, the Wannier projection of the DFT Hamiltonian provides the hopping matrix elements and on-site energies, but cannot generate an explicit Hubbard interaction.

**Addition of the residual local interaction.**

The missing local interaction must be calculated separately by projecting an appropriately screened two-electron interaction onto the correlated Wannier orbital. In the article, this is performed using the constrained random-phase approximation,

$$U_a = \int d\mathbf{r}\, d\mathbf{r}'\, |w_{ia}(\mathbf{r})|^2 W_a^r(\mathbf{r}, \mathbf{r}') |w_{ia}(\mathbf{r}')|^2, \tag{20.73}$$

where $W_a^r$ is the partially screened interaction obtained after excluding screening processes internal to the correlated target band. The resulting effective low-energy model is

$$\hat{H}_a = \sum_{ij,\sigma} H_a^{(\mathbf{R}_i - \mathbf{R}_j)} \hat{c}_{i\sigma}^\dagger \hat{c}_{j\sigma} + U_a \sum_i \hat{n}_{i\uparrow} \hat{n}_{i\downarrow}. \tag{20.74}$$

**Double-counting correction.**

Because approximate interaction effects are already included in the DFT Hartree and exchange–correlation potentials, adding the explicit Hubbard term introduces a double-counting problem. DFT+DMFT therefore subtracts an approximate double-counting contribution,

$$\hat{H}_{\text{DFT+DMFT}} = \hat{H}_{\text{DFT}} + \hat{H}_U - \hat{H}_{\text{DC}}. \tag{20.75}$$

In the article, the correlated states are aligned with the remaining DFT bands using the fully localized limit correction $E_{\text{DC}} = U_a/2$. Thus, DFT provides the effective single-particle band structure, while cRPA and DMFT restore and treat the explicit local interaction required to describe the Mott gap and Hubbard bands.

### 20.2.3 Questions about Reproduction of Results

**Calculate the V and U. Reproduce at least 1 point on the fig. 3.**

(????? how to do it???)

**Write all these derivation as a one self-consistent derivation**

We basically have jumps from different models and methods. The task is to write all this as a one method, one formalism, without many labels. It will make much more clear understanding.

I asked GPT, but it gave a summary, but not a one derivation. One needs to think about it to do this.

**why do we have SODs, but not insulator? We were told that SODs correspond always to an insulting state?**

(GPT:)

The formation of Star-of-David clusters does not, by itself, necessarily make the system insulating. The structural reconstruction produces a narrow, approximately half-filled electronic band near the Fermi level. Within ordinary DFT, this band crosses the Fermi level and therefore corresponds to a metallic state,

$$\varepsilon_{\mathbf{k}} = E_{\text{F}} \qquad \text{for some } \mathbf{k}. \tag{20.76}$$

An insulating state appears only when an additional mechanism opens a gap in this narrow band. In the model adopted in the article, this mechanism is the strong local Coulomb interaction,

$$U \sum_i \hat{n}_{i\uparrow}\hat{n}_{i\downarrow}. \tag{20.77}$$

When the interaction is sufficiently strong relative to the bandwidth,

$$\frac{U}{W} > \left(\frac{U}{W}\right)_{\mathrm{c}}, \tag{20.78}$$

the half-filled band splits into lower and upper Hubbard bands and a Mott gap appears. A Star-of-David structure therefore creates the narrow band that makes Mott localization possible, but it does not guarantee an insulating state. The final state also depends on $U$, the bandwidth, screening, dimensionality, stacking, doping, and temperature. In the calculations, increasing the structural parameter $a$ broadens the narrow band and reduces the screened $U$, eventually producing a correlated metal despite the continued presence of the Star-of-David pattern.

**So, did they correctly or not correctly calculated the influence of Coulomb interaction?**

(maybe no, there should be another model that should be more precise, but I'll think later about it)

(GPT:)

The calculation reproduces a physically plausible qualitative mechanism: changing the imposed Star-of-David distortion modifies the Wannier-orbital localization and electronic screening, which changes $U_a$, the Hubbard-band positions, and the Mott gap. However, the authors explicitly state that the predicted spectral changes exceed those observed experimentally. Therefore, the model is not quantitatively accurate for the experimental systems and excitation conditions with which it is compared.

This disagreement does not necessarily mean that the cRPA calculation of $U_a$ is mathematically incorrect. The theoretical calculation considers an ideal isolated monolayer and assumes specific frozen structural amplitudes, whereas the experiments may involve bulk or multilayer samples with stronger interlayer screening and smaller actual atomic displacements. Consequently, the comparison depends on both the calculated response,

$$\frac{\partial A(\mathbf{k}, \omega; a)}{\partial a}, \tag{20.79}$$

and the experimentally realized trajectory $a(t)$. A smaller experimental displacement produces a smaller spectral shift even if the calculated dependence on $a$ is correct,

$$\delta E_{\mathrm{exp}} \approx \frac{\partial E}{\partial a}\delta a_{\mathrm{exp}}. \tag{20.80}$$

The article does not calculate $\delta a_{\mathrm{exp}}$ self-consistently and therefore does not provide a complete quantitative prediction of the measured signal.

Nevertheless, the disagreement may also indicate limitations of the electronic model itself. The calculation uses a single correlated band, a static local interaction $U_a$, single-site DMFT, and equilibrium frozen structures. It neglects nonlocal Coulomb interactions, interlayer effects, explicit electron–phonon dynamics, nonthermal electronic occupations, and electronic back-action on the structural motion. Any of these approximations may affect the predicted sensitivity of sensitivity of the Hubbard bands to the distortion.

The appropriate conclusion is therefore that the calculation is qualitatively successful but not experimentally validated at the quantitative level. It identifies a possible mechanism by which structural motion changes electronic correlations, but it does not accurately reproduce the magnitude of the observed spectral shifts. Additional calculations using the actual experimental geometry, independently measured structural amplitudes, and a more complete interaction model would be required to determine whether the discrepancy originates from experimental conditions or from an overestimation of the Coulomb-interaction effect.

**can we say that the band for the whole material is the same as for 1 SOD?**

(GPT:)

No. A single isolated Star-of-David cluster has discrete molecular energy levels rather than a continuous electronic band. The narrow band of the material is formed when equivalent molecular-like orbitals on different Star-of-David clusters hybridize throughout the periodic lattice. If $|w_i\rangle$ denotes one Wannier orbital centered on cluster $i$, the hopping matrix elements are

$$t_{ij} = \langle w_i|\hat{h}|w_j\rangle. \tag{20.81}$$

The band dispersion of the complete periodic material is then obtained by Fourier transforming these inter-cluster matrix elements,

$$\varepsilon_{\mathbf{k}} = \sum_{\mathbf{R}} t(\mathbf{R})e^{i\mathbf{k}\cdot\mathbf{R}}. \tag{20.82}$$

Thus, one Star of David provides one effective orbital, or one effective site, while the periodic lattice of interacting Star-of-David clusters produces the band. If all inter-cluster hopping were neglected,

$$t_{ij} = 0 \qquad \text{for } i \neq j, \tag{20.83}$$

the band would become a dispersionless molecular level. The band of the entire material is therefore derived from the orbital associated with one Star of David, but it is not identical to the spectrum of an isolated Star-of-David cluster.

**connect this theoretical prediction with experimental results**

(GPT:)

The calculations are motivated by time-resolved STM and photoemission experiments in which a pump pulse excites a coherent structural oscillation associated with the Star-of-David pattern. The reported frequency is approximately

$$f = 2.4\,\text{THz}, \tag{20.84}$$

corresponding to a period

$$T = \frac{1}{f} \approx 0.42\,\text{ps}. \tag{20.85}$$

The theoretical calculation provides a relation between an imposed instantaneous structural coordinate $a$ and the electronic spectral function,

$$a \longrightarrow A(\mathbf{k}, \omega; a). \tag{20.86}$$

If the experimentally excited structural trajectory is $a(t)$, the frozen-phonon approximation gives

$$A(\mathbf{k}, \omega, t) \approx A(\mathbf{k}, \omega; a(t))\,. \tag{20.87}$$

The theory therefore predicts that the lower and upper Hubbard bands should oscillate as the Star-of-David structure moves, with the Mott gap decreasing when the system approaches the less distorted structure. Such changes may be probed through time-resolved STM, which measures the local spectral function, or through time-resolved ARPES, which probes the momentum-resolved occupied spectral function.

The predicted spectral changes are larger than those reported experimentally. The authors attribute this quantitative disagreement mainly to stronger screening in bulk or multilayer samples and to smaller experimentally achieved structural oscillation amplitudes. Furthermore, the calculation does not simulate the initial photoexcitation or calculate the actual structural trajectory. It therefore provides an interpretation of the measured spectral oscillations rather than a complete first-principles prediction of the pump–probe experiment.

**how to take into account other effects beyond this model?**

(GPT:)

Several extensions are required for a more complete description. First, nonlocal Coulomb interactions between electrons on different Star-of-David clusters can be included through an extended Hubbard model,

$$\hat{H}_{\text{ext}} = \sum_{ij,\sigma} t_{ij}(Q)\hat{c}^{\dagger}_{i\sigma}\hat{c}_{j\sigma} + U(Q)\sum_{i}\hat{n}_{i\uparrow}\hat{n}_{i\downarrow} + \frac{1}{2}\sum_{i\neq j} V_{ij}(Q)\hat{n}_i\hat{n}_j. \tag{20.88}$$

Such a model could be treated using GW+EDMFT or related methods that include both local and nonlocal screening effects.

Second, the structural coordinate should be treated dynamically rather than imposed as a frozen parameter. A semiclassical description would couple the electronic state to the ionic equation of motion,

$$i\hbar\frac{\partial}{\partial t}|\Psi_{\text{e}}(t)\rangle = \hat{H}_{\text{e}}[Q(t),t]|\Psi_{\text{e}}(t)\rangle, \tag{20.89}$$

$$M_{\text{eff}}\ddot{Q}(t) = -\left\langle \Psi_{\text{e}}(t)\left|\frac{\partial \hat{H}_{\text{e}}}{\partial Q}\right|\Psi_{\text{e}}(t)\right\rangle - \frac{\partial E_{\text{ion}}}{\partial Q} + F_{\text{pump}}(t). \tag{20.90}$$

This would include the electronic back-action on the Star-of-David motion and determine the structural trajectory self-consistently.

Third, electron–phonon coupling can be introduced explicitly, for example,

$$\hat{H}_{\text{e-ph}} = \sum_{ij,\sigma,\nu} g^{\nu}_{ij}\left(\hat{b}_{\nu} + \hat{b}^{\dagger}_{\nu}\right)\hat{c}^{\dagger}_{i\sigma}\hat{c}_{j\sigma}, \tag{20.91}$$

or through a phonon-dependent interaction,

$$U(Q) \simeq U_0 + \frac{\partial U}{\partial Q}Q. \tag{20.92}$$

These terms would permit the investigation of phonon-assisted processes, polaronic effects, and the dynamical modulation of both the hopping and Coulomb interaction.

Finally, multiband models, cluster DMFT, nonequilibrium DMFT, and spatially inhomogeneous calculations could be used to include other orbitals, short-range inter-cluster correlations, nonthermal electronic distributions, domain walls, stacking effects, and differently distorted neighbouring Star-of-David clusters. These extensions would make the model more realistic, but would also considerably increase its computational complexity.

### 20.2.4 Things That I Maybe Understood Wrongly

**Treating the Star-of-David clusters as isolated groups of attracted atoms.**

**What I said (approximately 00:06:39–00:07:08 and 00:27:43–00:28:00):** *"Atoms are attracted to the central atom, and near this star there is another star. The other atoms do not form a Star of David; they just remain there without being distorted."* This description incorrectly suggests that the crystal consists of isolated thirteen-atom objects separated by unaffected Ta atoms. In the commensurate CDW structure, the Star of David is the repeated $\sqrt{13} \times \sqrt{13}$ supercell of the Ta lattice. The central Ta atom and the two surrounding rings are inequivalent sites within this periodic distortion, and the neighbouring stars form a triangular superlattice. Thus, the calculation is not about a collection of isolated clusters embedded among undistorted atoms; it is about a periodically reconstructed monolayer. The word "attracted" is also too literal: the atoms undergo a collective displacement pattern determined by the lattice energetics, rather than being bound to the central atom as an isolated molecule would be.

**Calling the CDW amplitude merely an atomic displacement and a misleading name.**

**What I said (approximately 00:14:29–00:15:17):** *"By charge-density-wave amplitude they mean just the displacement of the atoms of a lattice. Strictly speaking, it is a very confusing label because a charge-density wave is about charge, not about the lattice."* This separates the electronic and structural parts of a CDW too sharply. In $1T$-$TaS_2$, the periodic charge modulation and the periodic lattice distortion are coupled components of the same CDW order. The 2.4 THz amplitude mode is a collective mode in which the magnitude of this coupled order changes; experimentally and computationally, its structural component is represented by the breathing displacement of the Ta atoms. In this paper, $a = (d - d_{\mathrm{eq}})/d_{\mathrm{eq}}$ is specifically a structural coordinate used as a proxy for the CDW amplitude. It is fair to note that $a$ is not by itself a direct measurement of the electronic charge modulation, but it is not correct to imply that calling it a CDW amplitude mode is physically inappropriate.

**Reversing the meaning of increasing distortion amplitude.**

**What I said (approximately 00:36:59–00:37:17 and 00:59:16–00:59:49):** *"If you have a bigger distortion, then you have a smaller gap; if you have a smaller distortion, you have a bigger gap. If we increase the distortion, the bare and screened interactions decay."* This reverses the sign convention used in the article. A positive $a$ means that the outer Ta atoms move farther from the central Ta atom: the star expands and the structure approaches the undistorted phase. Hence increasing $a$ means a *reduction* of the equilibrium CDW distortion. With increasing $a$, the Wannier orbital becomes more delocalized, the bandwidth grows, the bare matrix element $V$ and screened on-site interaction $U$ decrease, and the Mott gap narrows. Negative $a$ contracts the star, enhances the CDW distortion, localizes the orbital more strongly, and increases the gap. Thus the correct trend is

$$a \uparrow \quad \Longrightarrow \quad \text{weaker CDW distortion}, \quad W_{\mathrm{band}} \uparrow, \quad U \downarrow, \quad \Delta_{\mathrm{Mott}} \downarrow . \tag{20.93}$$

**Interpreting the metallic state as the disappearance of the Hubbard bands.**

**What I said (approximately 00:09:56–00:10:23):** *"At three percent there is no gap and no two Hubbard bands, but one metallic state where the bands have collapsed into one conducting region."* Gap closure does not mean that the lower and upper Hubbard-band features disappear or merge into a single ordinary band. At $a = +3\%$, the DMFT spectrum develops a quasiparticle peak at the Fermi level while remnants of the lower and upper Hubbard bands remain at higher binding energies. This three-feature structure is characteristic of a correlated metal close to

a Mott transition. The correct statement is therefore that the Mott gap closes and coherent low-energy spectral weight appears, coexisting with incoherent Hubbard-band features.

**Treating a remaining lattice distortion and a closed Mott gap as contradictory.**

**What I said (approximately 00:21:03–00:21:35):** *"Usually a lattice deformation gives a gap, but here a special deformation gives no gap, so this is contradictory to the well-known theory."* There is no contradiction because the insulating gap discussed here is a correlation-driven Mott gap, not a gap determined solely by whether a lattice distortion is present. The CDW reconstruction creates a narrow half-filled band, but whether this band is Mott insulating depends mainly on the competition between interaction and kinetic energy, commonly characterized by $U/W_{\text{band}}$. As $a$ increases, both $U$ decreases and $W_{\text{band}}$ increases, so $U/W_{\text{band}}$ can cross the metal–insulator boundary even while a nonzero structural distortion remains.

**Reducing the bulk–monolayer distinction to two universally separate mechanisms.**

**What I said (approximately 00:22:25–00:23:07):** *"If you have bulk, then you have a band insulator and not the Mott mechanism; in a monolayer you have a Mott insulator. There are two mechanisms, and both approaches are correct."* This is too categorical. The article describes a current microscopic picture in which parts of bulk $1T$-$TaS_2$ form dimerized, band-insulating bilayers, while AC-stacked monolayer-like units may also occur. Stacking, interlayer hybridization, correlations, and the detailed stacking sequence all matter, and the character of the bulk insulating state remains an active topic. The safer statement is that the isolated monolayer is well described as a Mott insulator, whereas interlayer dimerization can generate an important band-insulating contribution in bulk material; it is not a universal rule that correlations are absent in the bulk.

**Saying that the CDW distortion itself produces the two Hubbard bands.**

**What I said (approximately 00:23:38–00:24:14 and 00:26:09–00:26:48):** *"Finally this distortion gives us two bands. They could have written that the charge-density wave gives these two bands and not shown the intermediate band without correlations."* The two computational stages represent different physics and should not be conflated. The structural CDW reconstruction produces the isolated, narrow, half-filled Kohn–Sham band shown in red in Fig. 2. When the effective Coulomb interaction is subsequently treated using DMFT, the spectral weight associated with that band separates into a lower and an upper Hubbard band, producing the Mott gap. Therefore,

$$\text{CDW reconstruction} \longrightarrow \text{narrow half-filled band}, \qquad \text{strong correlations} \longrightarrow \text{LHB and UHB}. \tag{20.94}$$

The DFT result is not a disposable intermediate picture; it supplies the hopping Hamiltonian, Wannier orbital, bandwidth, and polarization processes needed to construct the effective interacting model.

**Describing the THz probe as photoemission into the STM tip.**

**What I said (approximately 00:28:31–00:29:24):** *"The second pulse kicks electrons from the material, they go to the microscope tip, and the tip measures the current."* This description mixes THz-driven STM with photoemission. In the proposed THz-STM experiment, the delayed THz electric-field transient changes the instantaneous voltage across the tip–sample junction and thereby drives tunnelling current. The electrons tunnel through the junction; they are not photoemitted into vacuum and then collected by the tip. By scanning the delay relative

to the NIR pump, the experiment samples the time-dependent local tunnelling response and hence the evolving local density of states.

**Assuming that a band is calculated from one isolated Star of David.**

**What I said (approximately 00:41:05–00:42:06):** *"Here we mean the band corresponding to one cluster. Let us assume that we can calculate the band from just one cluster and not bother much about interactions between clusters."* A single isolated cluster has discrete molecular levels, not a Bloch band. The DFT calculation uses a periodically repeated Star-of-David supercell, so the result is already the band structure of an extended crystal. In the Wannier representation, one low-energy orbital is associated with each Star-of-David cell, and the matrix elements $H_a^{(\mathbf{R}_i-\mathbf{R}_j)}$ explicitly describe hopping between different cells. This inter-cluster hopping produces the dispersion and bandwidth of the narrow band. What the simplified model neglects is not hopping, but nonlocal Coulomb terms such as $V_{ij}n_in_j$ and nonlocal components of the self-energy.

**Interpreting the frozen-phonon approach as the absence of a phonon.**

**What I said (approximately 00:44:58–00:45:19):** *"Maybe frozen phonon means that nothing is breathing; they just assume that the electron states adjust to the lattice deformation."* The frozen-phonon method represents a phonon by a series of static snapshots along its normal-mode displacement pattern. The ions are frozen only while the electronic problem is solved for a particular value of $a$; the collection of configurations samples the breathing-mode coordinate. The method therefore retains the structural geometry of the phonon but does not dynamically propagate the mode, predict its amplitude or damping, or include scattering among phonons. Assuming that the electrons adjust to each snapshot is the additional adiabatic approximation.

**Concluding that the paper contains no electron–phonon connection.**

**What I said (approximately 00:46:17–00:47:04 and 01:29:31–01:30:30):** *"The whole cluster is formed because of electron–phonon interaction, so it is hard to understand how they can say that electron–phonon interactions are not included. Here we do not see any connection between electrons and phonons."* The article includes a *parametric, static* electron–lattice coupling: changing the phonon coordinate $a$ changes the Kohn–Sham Hamiltonian, the Wannier orbital, the hopping amplitudes, screening, $U_a$, and the electronic spectrum. What it neglects is an *explicit dynamical* electron–phonon Hamiltonian, electronic scattering by phonons, phonon self-energies, energy transfer, and the feedback of the electronic state on the subsequent ionic trajectory. Thus it is correct to criticize the absence of coupled nonequilibrium electron–phonon dynamics, but not to say that the calculation contains no electron–phonon connection at all.

**Identifying a Wannier isosurface with the wavefunction of one particular electron.**

**What I said (approximately 00:48:36–00:50:21):** *"These are just wavefunctions of one electron. There are thirteen electrons in the cluster, twelve create the cluster, and one hops from one star to another; this is the wavefunction of that one electron."* A Wannier function is a localized single-particle basis orbital constructed from Bloch states of the selected band. It is not the many-body wavefunction of a labelled electron, and an electron is not permanently assigned to that orbital. In the usual low-energy electron-counting picture, thirteen Ta $5d$ electrons per Star-of-David cell form reconstructed molecular bands: twelve electrons fill lower-lying states and one electron per cell remains in the narrow half-filled band. The plotted Wannier orbital represents the local basis state spanning that band; its occupation fluctuates and it can

host spin-up and spin-down electrons. Moreover, the displayed red and blue isosurfaces show opposite signs (phases) of the orbital amplitude, not positive and negative charge densities.

**Confusing the screened kernel with the local Hubbard interaction.**

**What I said (approximately 00:54:21–00:55:19):** *"Maybe the formula is for an electron in one cluster interacting with an electron in another cluster, or for two electrons in the same cluster; perhaps it is valid for both."* The RPA quantity $W(\mathbf{r}, \mathbf{r}')$ is indeed a general screened interaction kernel, but the $U$ used in this paper is a specific matrix element of the *partially* screened cRPA interaction projected onto the same local Wannier orbital. It is the energy cost for opposite-spin occupation of one effective Star-of-David site. Intersite matrix elements $V_{ij}$ could be obtained by projecting the same kernel onto Wannier orbitals on different cells, but those nonlocal terms are omitted from the single-band Hubbard Hamiltonian used here. Therefore the plotted $U$ should not be interpreted simultaneously as both the on-site and inter-cluster interaction.

**Calling $f$ in the polarization formula the Fermi energy.**

**What I said (approximately 00:56:58–00:57:08):** *"$f$ is the Fermi energy, and the epsilons are the energies."* Here $f_{n\mathbf{k}}$ is the Fermi–Dirac *occupation function*, not the Fermi energy. The numerator

$$f_{n'\mathbf{k}+\mathbf{q}} - f_{n\mathbf{k}} \tag{20.95}$$

selects transitions between states with different occupations, while the denominator contains their energy difference. The target-space label $t$ means that the band indices are restricted to the correlated low-energy subspace—here, the narrow band represented by the Star-of-David Wannier orbital.

**Interpreting $V$ and $U$ as total energies of a cluster.**

**What I said (approximately 00:58:27–00:59:16):** *"Maybe it is the total energy of one cluster; if we increase distortion, this energy decreases."* Neither curve in Fig. 3(a) is the total energy of a Star-of-David cluster. The curve labelled $V$ is the bare on-site Coulomb matrix element evaluated in the distortion-dependent Wannier orbital, while $U$ is its partially screened cRPA counterpart and is the parameter used in the Hubbard Hamiltonian. They quantify the repulsive energy cost of double occupation of that effective orbital. A structural total-energy curve would instead be required to determine the equilibrium position, restoring force, and phonon frequency; such a curve is not what Fig. 3(a) shows.

**Reducing the spectral function to a broadened delta function.**

**What I said (approximately 01:00:17–01:00:41):** *"The spectral function should generally be a delta function for a band, and in reality we have an approximation to a delta function; the band is where the spectral function has a peak."* This is true only for a noninteracting quasiparticle with infinite lifetime at a fixed momentum, for which $A(\mathbf{k}, \omega)$ contains a delta peak at the one-particle energy. In the interacting DMFT solution, the spectral function contains finite-width coherent and incoherent features determined by the frequency-dependent self-energy. The Hubbard bands are not merely numerically broadened delta functions. In addition, Fig. 3(b) shows the momentum-integrated $A(\omega)$, so its peaks collect spectral weight over all momenta rather than tracing a single dispersion. Fig. 4 shows $A(\mathbf{k}, \omega)$ and therefore contains the momentum-resolved dispersion.

**Saying that the Mott gap follows from $U_a$ alone.**

**What I said (approximately 01:11:35–01:11:57 and 01:03:59–01:04:26):** *"The gap is present because of the parameter $U_a$; the next step is simply to get the spectral function from $U$."* The spectral function is not determined by $U_a$ alone. For each distortion, the DMFT input contains both the full Wannier hopping Hamiltonian $H_a^{(\mathbf{R}_i-\mathbf{R}_j)}$, which fixes the dispersion and bandwidth, and the screened interaction $U_a$. The chemical potential and temperature also enter. The closing of the gap with increasing $a$ is especially strong because $U_a$ decreases while the bandwidth simultaneously grows. A more accurate schematic dependence is

$$A_a(\mathbf{k},\omega) = \mathcal{F}_{\mathrm{DMFT}}\left[H_a^{(\mathbf{R})}, U_a, T, \mu\right], \tag{20.96}$$

not $A = \mathcal{F}(U)$.

**Calling the DFT band unreal and only the momentum-resolved DMFT plot the "true bands."**

**What I said (approximately 00:47:19–00:47:58 and 01:11:53–01:13:33):** *"In reality they do not have this red band; they have the gapped plot. Figure 2 is distracting, and now in Figure 4 we see the true bands."* Figures 2–4 display different, complementary quantities. Figure 2 gives the Kohn–Sham band structure and the Wannier representation used to construct the low-energy Hamiltonian. Figure 3(b) gives the momentum-integrated interacting spectral function, which is useful for seeing the Mott gap and Hubbard-band spectral weight. Figure 4 gives the momentum-resolved interacting spectral function overlaid with the DFT bands. The DFT band is not an experimental interacting excitation spectrum, but it is a well-defined and essential theoretical starting point; likewise, the momentum-integrated spectrum is not less real than the momentum-resolved one. They answer different questions.

**Reading a quantitative discrepancy as a failure of experimental confirmation.**

**What I said (approximately 01:16:29–01:17:24):** *"The predicted changes exceed the experimental ones, so they say that the theory is not confirmed by experiment and perhaps should not be taken seriously."* "Exceed" describes a mismatch in magnitude, not necessarily a disagreement in the sign or qualitative mechanism. The authors argue that their idealized monolayer calculation predicts larger Hubbard-band shifts than those measured in bulk pump–probe experiments because bulk layers provide additional screening and the experimental mode amplitude is smaller than the amplitudes sampled in some calculations. This comparison limits direct quantitative application, but it does not by itself falsify the predicted coupling between the structural coordinate and the spectrum. A fair conclusion is that the qualitative relation is physically motivated, whereas quantitative comparison requires the actual experimental $a(t)$ and a model appropriate to the measured sample.

**Concluding that electronic back-action makes the frozen configurations meaningless.**

**What I said (approximately 01:24:48–01:29:11):** *"We will never have this configuration, because the electronic distribution will immediately influence it and everything will return to equilibrium. Therefore it may make no sense to calculate the spectrum for different distortions."* The criticism correctly identifies what the calculation does not provide: it does not determine the driven trajectory $a(t)$, damping, or electronic force on the phonon. However, it is incorrect to conclude that the displaced configurations cannot exist or that the conditional spectra are meaningless. A coherently excited phonon has inertia and oscillates about equilibrium, and the pump can maintain a finite displacement for part of the cycle. If electronic

relaxation is faster than the approximately 417 fs period of the 2.4 THz mode, the electronic state can approximately follow the instantaneous ionic configuration. Then

$$A(\mathbf{k}, \omega, t) \simeq A_{\mathrm{eq}}(\mathbf{k}, \omega; a(t)) \tag{20.97}$$

is a useful adiabatic mapping. What remains unpredicted is $a(t)$ itself. Thus the proper limitation is that the work is a conditional frozen-structure calculation, not a self-consistent theory of the complete pump-driven dynamics.

**Saying that hopping between Star-of-David cells is neglected.**

**What I said (approximately 01:32:21–01:33:16):** *"How useful can it be to neglect the Star-of-David hopping? Here they neglect the interaction between different polarons or blobs of electron density."* The Hamiltonian explicitly retains inter-cell hopping through $H_a^{(\mathbf{R}_i - \mathbf{R}_j)}$ for $i \neq j$; without it, the narrow band would have no dispersion. The omitted terms are the direct nonlocal Coulomb interactions $V_{ij}$ between occupations of different Wannier orbitals and the nonlocal spatial dependence of the self-energy in single-site DMFT. Therefore the valid question is whether neglecting intersite *Coulomb correlations* is accurate, especially near the metallic transition—not whether hopping was neglected.

**Treating a prescribed $U(t)$ as a complete electron–phonon dynamics model.**

**What I said (approximately 01:21:16–01:21:41):** *"If we make the Hubbard U dynamically changeable, that can already capture the electron–phonon dynamics."* A time-dependent $U(t) = U[a(t)]$ may capture one important consequence of the driven lattice coordinate, namely the modulation of screening and local repulsion. It is not by itself a complete electron–phonon theory. The hopping amplitudes and orbital basis also change with $a(t)$, and a self-consistent model must specify the phonon coordinate, its equation of motion, the electronic force, dissipation, and possibly nonthermal electronic occupations. At minimum, the effective electronic Hamiltonian would contain both $H_{a(t)}^{(\mathbf{R})}$ and $U_{a(t)}$, coupled to an equation for $a(t)$.

**Concluding that the calculation most likely has no practical use.**

**What I said (approximately 01:40:47–01:41:08):** *"Can it be used? Most likely no; most likely it cannot be used. It mainly teaches us that an efficient code can do the calculation."* This conclusion is stronger than the limitations justify. The paper supplies a microscopic, distortion-dependent mapping from structure to the bare interaction, screened $U$, bandwidth, Hubbard-band positions, and metal–insulator crossover. Even without predicting the pump-driven trajectory, that mapping can be combined with a measured or independently calculated $a(t)$ to interpret time-resolved STM or ARPES spectra, and it identifies mechanisms that simpler calculations with a fixed empirical $U$ miss. The appropriate conclusion is therefore that the work is not a complete predictive simulation of a pump–probe experiment, but it provides a quantitatively useful electronic-structure component for such a description.

### 20.2.5 Potential Future Research Directions

**Derive such results using polaronic theory**

(??? I don't know how to do it)

# 21 Orbital-driven Mottness collapse in 1T-$TaS_{2-x}Se_x$ transition metal dichalcogenide by Qiao et al. (2016)

**Abstract**

The layered transition metal dichalcogenide 1T-$TaS_2$ has been recently found to undergo a Mott-insulator-to-superconductor transition induced by high pressure, charge doping, or isovalent substitution. By combining scanning tunneling microscopy (STM) measurements and first-principles calculations, we investigate the atomic scale electronic structure of 1T-$TaS_2$ Mott insulator and its evolution to the metallic state upon isovalent substitution of S with Se. We identify two distinct types of orbital textures - one localized and the other extended - and demonstrate that the interplay between them is the key factor that determines the electronic structure. Especially, we show that the continuous evolution of the charge gap visualized by STM is due to the immersion of the localized-orbital-induced Hubbard bands into the extended-orbital-spanned Fermi sea, featuring a unique evolution from a Mott gap to a charge-transfer gap. This new mechanism of orbital-driven Mottness collapse revealed here suggests an interesting route for creating novel electronic states and designing future electronic devices.

## 21.1 INTRODUCTION

The vicinity of a Mott insulating phase has constantly been a fertile ground for finding exotic quantum states, most notably the high $T_c$ cuprates and colossal magnetoresistance manganites. The layered transition metal dichalcogenide 1T-$TaS_2$ represents another intriguing example. More interestingly, it has been recently found that 1T-$TaS_2$ undergoes a Mott-insulator-to-superconductor transition induced by high pressure [1], charge doping [2, 3, 4, 5], or isovalent substitution [6, 7, 8].

The nature of the Mott insulator phase and transition mechanism to the conducting state is still under heated debate. Much of the challenge originates from a series of complicated charge density wave (CDW) orders entwined with the electronics phases [9, 10, 11]. The Mott insulator phase is believed to be a consequence of the commensurate CDW order [11, 12, 13, 14, 15]. Superconductivity emerges as the Mott insulator state is suppressed, and the electronic phase diagram [1, 4, 7, 5] displays many similarities to that of the cuprates.

Different scenarios were proposed to account for the Mott-insulator-to-superconductor transition. For the pressurization case, it was assumed that the superconductivity formed within the metallic interdomain spaces of the nearly commensurate CDW (NCCDW) phase [1]. This scenario is consistent with the phase separation picture of the NCCDW phase [16]. It also naturally explains the continuous extension of superconductivity into the incommensurate CDW (ICDW) phase, where the interdomain spaces grow to the whole sample and the CCDW domains completely disappear. On the other hand, for the chemical doping cases, angle-resolved photoemission measurements did not reveal any signature of phase separation [3], suggesting instead strong electronic hybridization across domains. The electrons were found to form a global melted Mott state with a single electron pocket around the $\Gamma$ point, from which superconductivity could emerged. Another perspective on the melted Mott state was recently developed by viewing doped 1T-$TaS_2$ as a disordered Mott insulator [17], in which the interplay of strong interaction and disorder generates a novel pseudogap metallic state.

Most of the previous explanations were essentially based on a one-band Hubbard model [17, 18, 19], and the efforts were made to reproduce the phase transition by tuning some parameters. The problems, however, are that the microscopic meaning of the one band basis is ambiguous, and the dependence of the associated parameters on the material details is unclear. Consequently, it heavily relies on the researcher's perspective to select the key parameters and

the tuning range. This leads to rather controversial interpretations emphasizing on different aspects of the material [1, 3, 6, 8, 20, 21, 22, 23, 17, 24, 25], such as spin-orbit coupling, interlayer coupling, p-d hybridization and disorder.

The aim of the present Article is to establish a concrete foundation that describes the low-energy physics in 1T-$TaS_2$. By combining STM measurements and *ab initio* Wannier function analysis, we single out two distinct types of orbital textures, and formulate a multi-orbital effective Hamiltonian based on these two orbital textures. This construction reveals an orbital-driven origin of the Mott-insulator-to-superconductivity transition in 1T-$TaS_2$. We map out the complete transition process by inhomogeneous Se substitution, and demonstrate an excellent agreement between experiment and theory. The remainder of the Article is organized as follows. Section II describes the experiment and calculation methods. Section III presents the STM and first-principles data on pristine $TaS_2$, based on which the two types of most relevant orbital textures are identified. Section IV discusses results on Se-substituted samples. By taking advantage of the chemical inhomogeneity in these samples, we map out the complete collapsing process of the Mott phase. Section V discusses the theoretical formalism of the orbital-driven transition in details. Section VI concludes this Article.

## 21.2 EXPERIMENT AND CALCULATION METHODS

The high-quality single crystals of 1T-$TaS_{2-x}Se_x$ ($0 < x < 2$) are synthesized by chemical vapor transport method with iodine as the transport agent. The powder of Ta, S, and Se is weighted stoichiometrically and thoroughly grounded. Then the mixture together with 150 mg $I_2$ is sealed into an evacuated quartz tube and placed into a two-zone furnace with the temperature gradient of 1253 K-1153 K for 1 week. The products are washed with ethanol to remove the iodine at the surface.

The STM experiments are performed with a cryogenic variable temperature ultrahigh vacuum STM system. The 1T-$TaS_{2-x}Se_x$ crystal is cleaved in situ at $T = 77$ K, and the measurement is taken at 5 K with an electrochemically etched tungsten tip calibrated on a clean Au (111) surface [26]. The STM topography is taken in the constant current mode, and the $dI/dV$ spectra are obtained with a standard lock-in technique with modulation frequency $f = 423$ Hz.

The first-principles calculation based on the density functional theory is performed using the Vienna *Ab initio* Simulation Package [27, 28, 29, 30] with a 280 eV plane-wave basis cutoff. The Perdew-Burke-Ernzerh generalized gradient approximation [31] and the projector augmented wave method [32] are employed. The Wannier function analysis is performed using the WANNIER90 code [33, 34, 35] on the plain DFT level in order to quantify the single-electron properties, such as p-d hybridization and interatomic hopping. The $+U$ correction is employed to compare with the STM $dI/dV$ spectra, which captures the Coulomb interaction of Ta 5d orbitals on the mean-field level, following the simplified (rotational invariant) approach introduced by Dudarev [36, 37]. We employ the lattice parameters determined by experiment [38], and relax the atomic coordination self-consistently until the forces are less than 0.002 eV/Å. To simulate the CCDW order, we employ a $\sqrt{13} \times \sqrt{13}$ supercell consisting of 13 Ta atoms forming a Star-of-David (SD) structure. The integration over the Brillouin zone is obtained on a $\Gamma$-centered $6 \times 6 \times 1$ k mesh. The electronic self-consistent iterations are converged to $10^{-5}$ eV precision of the total energy.

It has been shown by earlier studies that at least for band structure effects alone, 1T-$TaS_2$ should always be describable as a quasi-two-dimensional system [11, 39]. Indeed, recent calculations [25] emphasizing the inter-layer orbital texture showed that the Mott-insulating ground state cannot be correctly reproduced once an artificial c-axis stacking sequence is imposed. On the other hand, in 1T-$TaSe_2$ inter-layer coupling plays a more important role [40]. Therefore, we will restrict our discussion within the S-riched regime, and focus on the *intralayer* CCDW

order and orbital textures. All our calculations are based on a 2D structural configuration with a 15 Å-thick vacuum space to eliminate coupling between different layers.

## 21.3 ORBITAL TEXTURES IN PRISTINE $TaS_2$

### 21.3.1 Structural and electronic properties

1T-$TaS_2$ has a layered structure as shown in Fig. 21.1(a), in which the Ta atoms form a planar triangular lattice sandwiched by two S-atom planes. STM is an ideal experimental technique for probing the atomic scale electronic structure of such a quasi-2D material. Figure 21.1(b) displays the STM topographic image of pristine 1T-$TaS_2$, which clearly reveals the CCDW order with a $\sqrt{13} \times \sqrt{13}$ superlattice where 13 Ta atoms form a Star-of-David (SD) structure. Note that the bright spots correspond to the S atoms lying in the uppermost layer, and the position of the Ta atoms can be determined according to the octahedral coordination. In Fig. 21.1(c) we show the spatially averaged differential conductance $dI/dV$, which is approximately proportional to the electron density of states (DOS), of pristine 1T-$TaS_2$. An energy gap around the Fermi level ($E_F$) can be clearly observed, which is attributed to the Mott-Hubbard gap of the insulating CCDW phase.

These spectroscopic features can be captured by density functional theory (DFT) calculations including the onsite Hubbard $U$ correction in a Hartree-Fock manner [41]. As shown in Fig. 21.1(d), there is a full charge gap around the ($E_F$), which is bounded by two narrow bands, corresponding to the upper and lower Hubbard bands (UHB/LHB), respectively. The gap size is found to depend on the Hubbard repulsion $U$ and a choice of $U = 2.27$ eV as previously derived from the linear-response calculation is used to reproduce the experimental value [41]. There is another energy gap below the LHB isolating it from the underneath dispersive valence band continuum [VB shaded in blue in Fig. 21.1(d)], which is commonly referred to as the CDW gap ($\Delta_{CDW}$) [42, 43, 44]. This gap is manifested in the $dI/dV$ spectrum as a dip below the LHB [Fig. 21.1(c)].

### 21.3.2 Low-energy orbital textures and their origin

Besides the CCDW superstructure and energy spectrum, equally important is the local DOS (LDOS) mapping at selected energies, which contains the spatial characteristics of electronic wavefunctions, i.e., the orbital texture. Figure 21.2(a) displays the $dI/dV$, or LDOS, mapping measured at two representative energies. At $V_b$ = -207 mV (upper panel), which corresponds to the LHB, the LDOS map shows a periodic pattern that is commensurate with the CCDW superlattice. By comparing the LDOS map with the topographic image of the same area [Fig. 21.1(b)], the bright spots are identified to be the center of SDs. Moving to lower energy with bias $V_b$ = -422 mV (lower panel), a distinctly different orbital texture is revealed for the VB: the LDOS map exhibits a kagome-like superstructure. Its bright/dark spots are inverse of the previous texture, indicating contributions mainly from the surrounding Ta orbitals. LDOS maps at positive biases give a nearly symmetric picture, demonstrating the same two types of orbital textures: the UHB $V_b = 199$ mV [Fig. 21.2(c) upper panel] corresponds to an orbital texture concentrated on the center of SDs, whereas at higher energy $V_b = 484$ mV [Fig. 21.2(c) lower panel] for the conduction bands (CB), the bright spots shift to the surrounding Ta orbitals.

To determine the nature of these two orbital textures discussed above, we proceed by performing *ab initio* Wannier function analysis. Consider that the oxidation state of Ta atom is +4, there is one unpaired 5d electron left per Ta that plays the most important role around the Fermi level. For a SD consisting of 13 Ta atoms, we need seven Wannier functions (without the spin degree of freedom) to fully accommodate these 13 unpaired 5d electrons. Accordingly, the

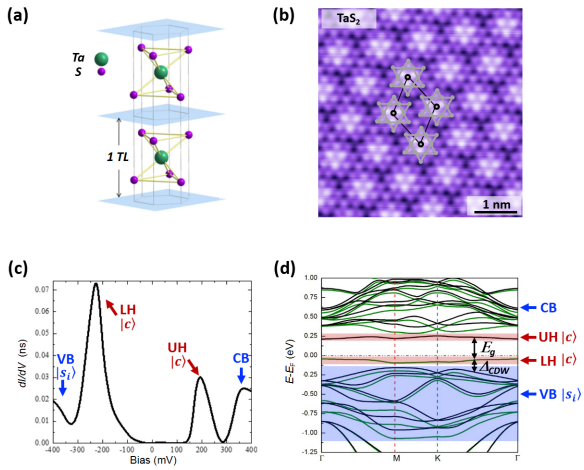


Figure 21.1: Structural and electronic properties of 1T-$TaS_2$. (a) Crystal structure of 1T-$TaS_2$. (b) Atomic resolved topographic image of 1T-$TaS_2$ with bias voltage $V_b = 1$ V and tunneling current $I_t = 20$ pA. Each bright site on the surface corresponds to a S-atom in the topmost layer. The gray dots and the black lines mark the SD structure and the CCDW superlattice, respectively. The crystal cleaves easily between two adjacent S layers, as indicated by the blue planes in (a), exposing the triangular lattice of S atoms. (c) Spatial averaged STM $dI/dV$ spectrum acquired at 5 K. (d) DFT+$U$ band structure of 1T-$TaS_2$. The black/green colored curves represent the two spin components. The shaded regions indicate the energy range belonging to the different orbitals.

Bloch states of the seven highest occupied energy bands are chosen to construct the Wannier functions. The spatial distributions of the resulting maximally localized Wannier functions are plotted in Fig. 21.2(b), which automatically separate into two groups. The one denoted by $|c\rangle$ concentrates at the central Ta atom with a typical $d_{z^2}$ geometry. The remaining six Wannier functions distribute dominantly along the edge of the SD ($|s_{\alpha=1...6}\rangle$), which can be viewed as the bonding orbitals of the surrounding Ta atoms. This Wannier function analysis gives a natural explanation for the two types of orbital textures observed by STM. In particular, it clarifies that the kagome-like texture arises from a set of linear-shaped molecular orbitals.

We note that previous STM mapping indicated additional center-surrounding variation of the orbital texture for the deeper occupied states [24]. This feature is also observed in our experiment and calculation. These deep occupied states are associated with a different set of Wannier functions orthogonal to $|c\rangle$ and $|s_{\alpha=1...6}\rangle$, which can be clarified using the same technique. However, those Wannier functions are irrelevant to the low-energy physics. By mapping out the low-energy orbitals, we also note that the previously employed one-band Hubbard model is implicitly based on the $|c\rangle$ orbital alone. Since this orbital is largely localized, it is susceptible to a Mott transition, giving rise to the UHB and LHB. However, it is important to notice that the validity of the one-band Hubbard model is guaranteed only by a large $\Delta_{CDW}$. When $\Delta_{CDW}$ is reduced, a one-band-to-multi-band transition has to be considered, which in turn plays an important role in the collapse of the Mott phase.

## 21.4 MOTTNESS COLLAPSE UPON *Se* SUBSTITUTION

To test the validity of the two-orbital-texture model, we further investigate the electronic structure of 1T-$TaS_2$ under external influence. A rather gentle perturbation to the 1T-$TaS_2$ structure is to modify the buckling of the S atoms around the central Ta, which is expected to affect the CCDW order. Experimentally this can be effectively realized through isovalent substitution of S by Se [6, 7], which has a larger ionic size and is expected to increase the

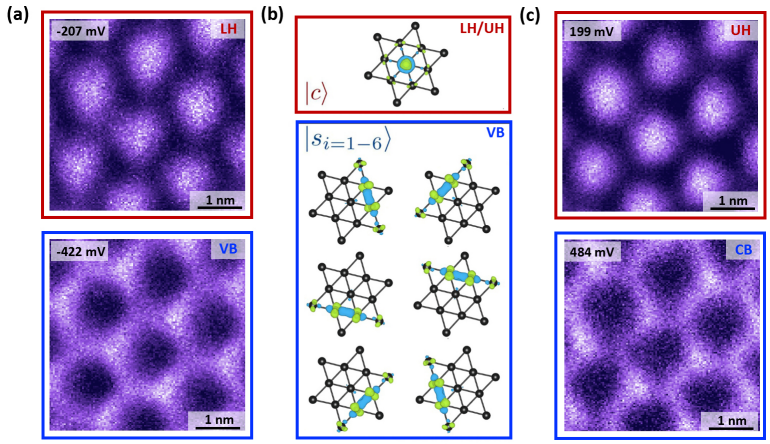


Figure 21.2: Two types of orbital textures in 1T-$TaS_2$. (a)/(c) Differential conductance ($dI/dV$) maps (42×42 Å$^2$) measured at $V_b$ = -207/199 mV (up) and $V_b$ = -422/484 mV (bottom) with tunneling current $I_t$ = 20 pA. The center of each CDW cluster is brighter at -0.2/0.2 V while the edges brighter at -0.4/0.4 V. (b) Isovalue surface of the two types of Wannier functions.

buckling of the surrounding S atoms. We have synthesized a series of Se-doped 1T-$TaS_2$ single crystals, and use these samples to map out the collapse of the Mott phase.

### 21.4.1 Phase transitions

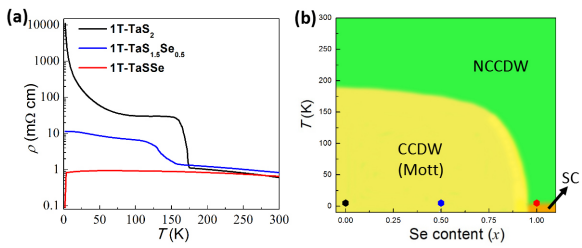


Figure 21.3: (a) Temperature dependence of the in-plane resistivity of three typical 1T-$TaS_{2-x}Se_x$ samples. (b) Schematic electronic phase diagram of 1T-$TaS_{2-x}Se_x$ and the location of the three samples under STM measurements.

Substituting S with Se is known to suppress the Mott-insulating phase in 1T-$TaS_2$ [6, 7], which can be seen from the transport data. Figure 21.3(a) shows the in-plane resistance data of three 1T-$TaS_{2-x}Se_x$ samples that are used for discussion in this work. For the pristine 1T-$TaS_2$, there is a well-defined CCDW ordering around 180 K. Below this transition temperature, the resistance exhibits a typical insulating behavior. Clearly, Se substitution strongly suppresses this phase transition. For the $x = 0.5$ sample, the resistance jump around the phase transition point is weakened. For the $x = 1$ sample, it completely vanishes, and a flat resistance curve stays unperturbed until about 3 K, at which a sudden drop occurs. This is known to be a superconducting transition. Figure 21.3(b) displays the schematic phase diagram [7], and the location of the three samples under discussion.

We note that for Se-substitution, due to its chemical similarity to S, the disorder effect is expected to be weak. This can be observed from the transport data: above the CCDW transition temperature, the resistance curves of the three samples almost coincide; the difference only becomes evidence after the CCDW order kicks in.

### 21.4.2 Topographic change

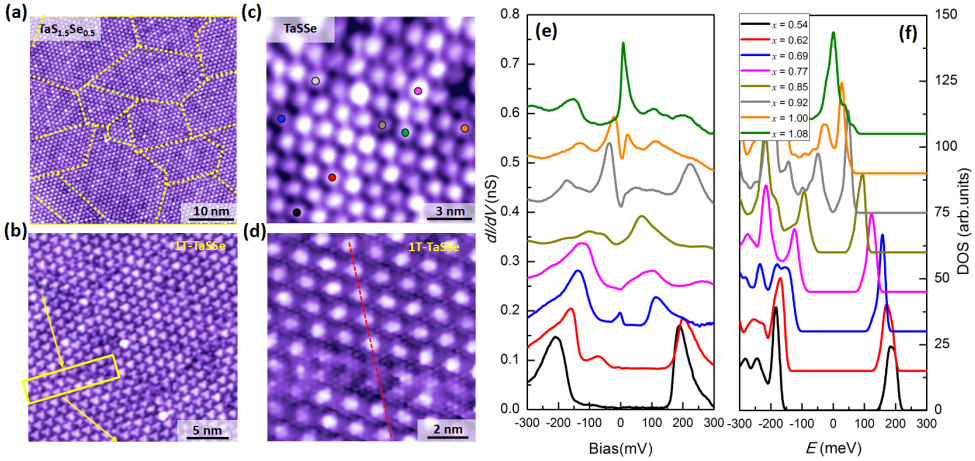


Figure 21.4: Structural and electronic properties evolution of Se substituted 1T-$TaS_2$. Topographic images acquired with $V_b$ = -500 mV and $I_t$ = 20 pA on the 1T-$TaS_{2-x}Se_x$ samples with the averaged Se concentration (a) $x = 0.5$ and (b)−(d) $x = 1$. (e) Local STM $dI/dV$ spectroscopy measured at various locations on the surface as marked in (c). (f) DFT+$U$ density of states of Se-substituted SDs in comparison with (e). In (a), the yellow dot lines indicate the sharp domain boundaries. In (b) and (d), the marks guide for eyes the rotational and translational mismatch in different domains.

How does Se-substitution modify the CCDW order? Figure 21.4(a) displays a large area STM image on the surface of the $x = 0.5$ sample. Unlike the pristine sample, the surface structure now splits into domains with varied domain size and sharp boundaries in between [Fig. 21.4(a)], which resembles the so-called "mosaic"phase in 1T-$TaS_2$ induced by voltage pulse in STM experiments [45, 46]. Increasing the Se concentration from $x = 0.5$ to $x = 1$ creates more domain walls and defects, but the general topographic properties remain the same. A closer examination around the domain walls reveals both 30°degree rotational and translational mismatch between different domains [Figs. 21.4(b) and (d)]. According to the transport data, this domained phase in the $x = 1$ sample should adiabatically extend to the high-$T$ NCCDW regime, in which the domains might shrink in size and the sharp domain boundaries melt into finite-width interdomain channels free of CCDW order [16]. However, close to the superconducting transition temperature, our STM image shows that the CCDW domains fill the whole space. Within a single domain, the CCDW superlattice retains the SD patterns as that in the undoped $TaS_2$ sample.

### 21.4.3 Electronic inhomogeneity

STM $dI/dV$ spectra are measured at various locations on the surface of the $x = 1$ sample [Fig. 21.4(c)], which are found to be surprisingly random. By ordering them with respect to the gap size, we observe a complete evolution [Fig. 21.4(e)]. There are still areas (small in size) showing a spectrum similar to that in pristine 1T-$TaS_2$ with a nearly unperturbed Mott gap (black curve). Moving upwards, the Mottness gap shrinks continuously. With further shrinking of the Mott gap, a broad V-shaped gap forms near $E_F$, which looks reminiscent of the pseudogap in underdoped cuprates. The V-shaped gap also shrinks gradually, and a finite DOS appears at $E_F$, indicating the transition into a metallic state. Eventually the gap vanishes completely and a sharp peak emerges near $E_F$, which looks similar to the Van Hove singularity (VHS) in overdoped cuprates.

A natural speculation on the origin of the inhomogeneous spectra is that the Se concentration in different SDs varies. We have calculated a series of SD structures by progressively replacing the S atoms with Se atoms. For a given Se concentration, the lowest-energy substitution configuration is determined, and the DFT structural relaxation confirms that the main effect of Se substitution is to increase the local buckling of the Ta-Se-Ta bonding geometry. We plot the DOS evolution as a function of Se concentration in Fig. 21.4(f), rendering a direct comparison with the STM $dI/dV$ spectra. The overall evolution of the gap can be nicely reproduced in the theoretical simulation. Besides, several distinct features, e.g. the U-shaped Mottness gap, the V-shaped pseudogap, and the sharp VHS-type peak, are also in good agreement.

Before explaining the underlying orbital-driven physics, it is worth addressing two possible concerns. Firstly, it is technically difficult to exclude the existence of other sources of inhomogeneity. However, given that our pristine sample is of very high quality, we believe that the predominant effect of Se substitution is to generate chemical inhomogeneity. The degree of inhomogeneity may rely on the sample preparation condition, cf. a previous experiment has reported complete ordering of S/Se atoms in the TaSSe sample [8]. Secondly, our calculation only considers doping one single SD with a 2D periodic boundary condition. We assume that the local electronic properties are primarily governed by the intra-cluster coupling within the SD, and the chemical variation in the nearby SDs do not qualitatively change the local spectrum evolution. However, for the global or spatially averaged properties, such as transport behaviors and photoemission spectrum, the situation is beyond this local approximation, which could be an interesting question for further investigation.

### 21.4.4 Orbital shifts

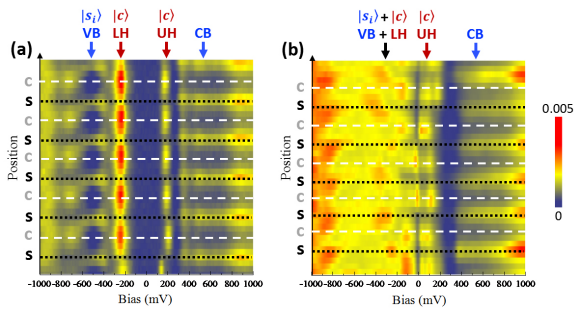


Figure 21.5: STM line map. The $dI/dV$ data for (a) $x = 0$ and (b) $x = 1$ case in an extensive two-dimensional parameter space. The horizontal axis is the STM bias and the vertical axis is the position. The white dash (black dot) lines mark the center (surrounding) of the SDs.

Due to the spatial inhomogeneity, a 2D periodic pattern as shown in Fig. 21.2 no longer exists. To uncover the changes of the relevant orbitals, we perform a comparative analysis on the spectra linecut crossing multiple SDs before and after Se-substitution.

In Fig. 21.5(a), we first present the linecut map of pristine 1T-$TaS_2$. The horizontal axis is the STM bias, ranging from -1000 meV to 1000 meV. The vertical axis is the position, measured along the line crossing five SDs. The LHB and UHB are evident at the bias of -200 and +200 meV. Along the position axis, they exhibit a periodic intensity variation, which peaks at the center of each SD (c) and weakens at the surrounding (s). The peak of the $dI/dV$ shifts by half the period when moving the bias below (above) the LHB (UHB), indicating that the orbital component changes from $|c\rangle$ to $|s\rangle$.

For the doped sample [Fig. 21.5(b)], the orbital textures vary from one SD to another, and their spatial distributions become complicated. We first note that the deep CB/VB states, e.g. states around $\pm 1000$ meV, remain largely periodic in space, exhibiting the similar textures as

in the pristine sample, which again suggests that these states are not involved in the electronic phase transition. Around the Fermi level, the UHB can still be identified, which is bound by two clear gaps in most SDs. Despite a spatially varied magnitude, the UHB in general shifts to the lower energy, leaving a large gap between the CB, and almost touching the VB in some SDs. The strong narrow LHB peak now merges with the top of the VB. For some SDs, a narrow peak around the SD center appears as a remnant of the original LHB. In general, the surrounding orbitals play an equally important role in the low-energy physics. Because of these orbital shifts, the Mott-insulator-to-metal transition occurs.

These orbital shifts can be further compared with the DFT+U band structures. Figure. 21.6(a) traces the band evolution as the Se concentration increases. The results indicate progressive downward shift of UHB and LHB, in agreement with the STM line map. At low-doping concentration, despite a reduction of $\Delta_{CDW}$, $E_g$ stays unchanged as it is dictated by the effective Hubbard $U$ of the $|c\rangle$-orbital alone. After the LHB touches the $|s_\alpha\rangle$-orbital bands, the Mott gap transforms into the charge-transfer type gap because now the lowest energy excitation is from the continuum band formed by the $|s_\alpha\rangle$-orbitals to the UHB formed by the $|c\rangle$-orbital. The gap size shrinks continuously upon further doping. According to the calculation, the critical point is reached at $x \approx 0.92$, where the charge-transfer gap becomes zero. Beyond this critical doping concentration, the UHB also sinks into the $|s_\alpha\rangle$-orbital bands, driving the system into the metallic regime. For the high-doping case, the $|c\rangle$-orbital and $|s_\alpha\rangle$-orbitals are strongly hybridized so that we can barely see the remnants of the narrow UHB around the $\Gamma$ point at $E_F$. The excellent agreement between theory and experiment confirms the validity of the orbital-driven Mott insulator to metal transition, in which the orbital sequence determines the electronic property. We note that in the calculation no additional complexities, such as spin-orbit coupling, interlayer coupling and disorder, are introduced. In addition, after Se substitution, Wannier function analysis shows that the geometry of the $|c\rangle$ and $|s_\alpha\rangle$ orbitals remain nearly unchanged. Therefore, we believe that the interplay between the $|c\rangle$-orbital and $|s_\alpha\rangle$-orbitals represents a universal origin of Mottness collapse in 1T-$TaS_2$.

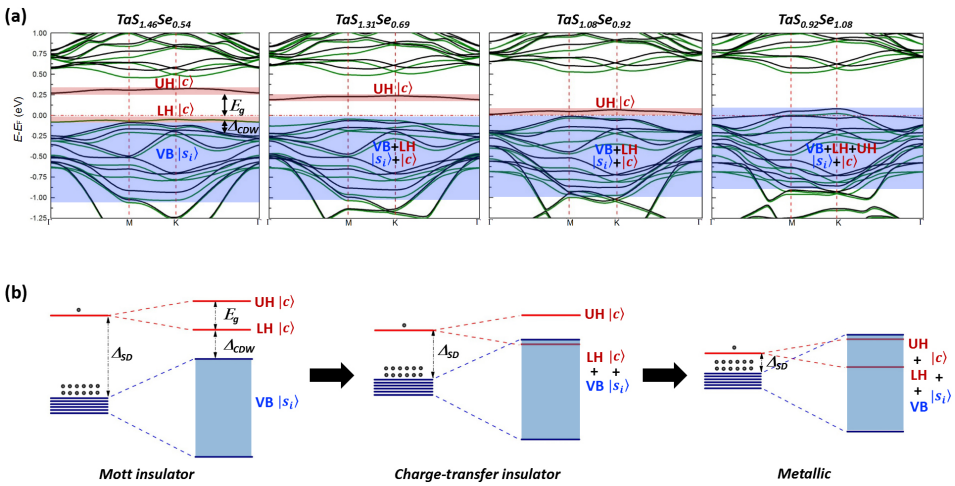


Figure 21.6: (a) DFT+U band structures of Se substituted 1T-$TaS_2$. The meaning of the colors is the same as in Fig. 21.1(d). (b) Schematic energy level diagrams of the Mott insulating phase, the charge-transfer insulator phase and the metallic phase.

## 21.5 THEORETICAL FORMALISM

To capture the essential physics, we propose a multi-orbital Hubbard model as formulated below:

| Unit (eV) | Pristine | Se-doped | Struct. mod. |
|---|---|---|---|
| $\Delta_{SD}$ | 0.212 | 0.146 | 0.143 |
| $t_{sc}$ | 0.162 | 0.099 | 0.105 |
| $t_{ss1}$ | 0.150 | 0.175 | 0.171 |
| $t_{ss2}$ | 0.091 | 0.089 | 0.087 |
| $t_{ss3}$ | 0.072 | 0.021 | 0.013 |
| $t_{ss4}$ | 0.050 | 0.047 | 0.043 |
| $t_{ss5}$ | 0.042 | 0.043 | 0.036 |

Table 5: Single-electron parameters from Wannier function analysis. The three columns correspond to the pristine 1T-$TaS_2$, 1T-$TaS_{2-x}Se_x$ ($x = 0.92$) and an artificial 1T-$TaS_2$ that retains the same structure of 1T-$TaS_{2-x}Se_x$,respectively.

$$\begin{aligned} H &= \Delta_{SD}\sum_{I} c_I^\dagger c_I + t_{cs}\sum_{I\alpha}(c_I^\dagger s_{I\alpha} + H.c.) \\ &+ \sum_{(I\alpha,J\beta)} t_{ss}^{I\alpha,J\beta} s_{I\alpha}^\dagger s_{J\beta} + U_c\sum_{I} c_{I\uparrow}^\dagger c_{I\downarrow}^\dagger c_{I\downarrow} c_{I\uparrow}, \end{aligned} \tag{21.1}$$

where $\Delta_{SD}$ is the onsite energy difference between $|c\rangle$ and $|s_{\alpha=1...6}\rangle$ generated by the formation of SD [Fig. 21.6(b)], and $I$,$J$ indexes the SDs. The central orbital $|c\rangle$ experiences an effective onsite Coulomb repulsion $U_c$ of the magnitude of LHB/UHB splitting ∼0.25 eV, whereas the interaction terms of $|s_{\alpha=1...6}\rangle$ are neglected considering they are less localized. Note that the Wannier function $|c\rangle$ is also a molecular orbital [Fig. 21.2(b)], and the associated Coulomb repulsion $U_c$ is much smaller than its original 5d atomic-orbital counterpart as used in the DFT+U calculation. The values of $\Delta_{SD}$ and the dominant hopping parameter ($t$) can be extracted by exploiting the same Fourier transformation as used in the Wannier function analysis (Tab. I).

For pristine 1T-$TaS_2$, the onsite energy of $|c\rangle$ is 0.21 eV higher than $|s_{\alpha=1...6}\rangle$. The largest hopping amplitude is $t_{sc}$ that is between $|c\rangle$ and $|s_{\alpha=1...6}\rangle$, followed by several hopping processes among $|s_{\alpha=1...6}\rangle$ (Fig. 21.7). Intercluster hopping is possible via $t_{ss2}$ and $t_{ss4}$. The set of obtained parameters for pristine 1T-$TaS_2$ is susceptible to a Mott transition owing to a relatively large positive $\Delta_{SD}$. For the Se-substituted sample, we present in Tab. I the parameters obtained from calculations on the ($x = 0.92$) supercell. Transition from the Mott phase to a metal is in principle described by Eq. (1) when the parameters vary, but solving Eq. (1) including the Hubbard term requires the hard-core many-body calculation that is beyond the scope of the current work. Nevertheless, a quick test can be made by only keeping the largest $t_{ss}$ and $t_{sc}$ terms and then diagonalizing the 7-by-7 Hamiltonian matrix. It shows that the highest eigenstate transforms from a dominant $|c\rangle$ character to a $|s_{\alpha=1...6}\rangle$ character, which reflects the concept of the orbital-driven transition.

According to this effective model, we schematically summarize the overall physics of the orbital-driven electronic structure evolution in Se doped 1T-$TaS_2$ [Fig. 21.6(b)]. The key ingredient is the organization of the two types of orbital textures $|c\rangle$ and $|s_{\alpha=1...6}\rangle$ accompanied by the formation of the SD structures. The central orbital is isolated by the surrounding ones, making inter-cluster hopping of central-orbital electrons possible only via high-order process. It is thus susceptible to a Mott transition when $|c\rangle$ is separated from $|s_\alpha\rangle$ in energy. On the other hand, the $|s_\alpha\rangle$ orbitals are extended with sizable hopping amplitude, naturally giving rise to a metallic phase when $|c\rangle$ and $|s_\alpha\rangle$ mix.

Previous DMFT calculations on the effective one-band Hubbard model [47, 48, 49], manually tuned the $U$ value, or equivalently, the $t/U$ ratio over a very wide range in order to trace

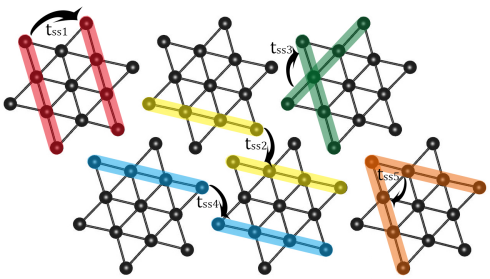


Figure 21.7: Physical meaning of the hopping parameters between the surrounding orbitals listed in Tab. I

the Mott-insulator-to-metal transition. As discussed above, the one-band Hubbard model is a downfolded version of our multi-orbital model by integrating out the $|s_{\alpha=1...6}\rangle$-orbitals. The downfolded $U$ is affected not only by $U_c$ associated with the $|c\rangle$-orbital, but also the energy separation between $|c\rangle$ and $|s_{\alpha=1...6}\rangle$. In this sense, our work complements the previous speculation on a change of effective $t/U$ ratio that induces the transition, and presents an explicit formalism to explain why the effective $t/U$ ratio varies so greatly.

Finally, it is worth mentioning several points that bridges Se substitution with mechanical modulation. As noted in Sec. IVC, the main effect of Se substitution is to increase the local buckling of the Ta-Se-Ta bonding geometry. In calculation, we have tested to retain this buckled geometry, but change Se back to S. It is found that very similar band structure and single-electron parameters can be obtained (c.f. the last two columns of Tab. I). In this sense, the possible structural modification as demonstrated by STM pulsing [45, 46] may share the same orbital-driven physics as discussed above.

## 21.6 CONCLUSION

Our experimental observations and first-principle calculations in 1T-$TaS_2$ reveal a new mechanism of Mottness collapse, which is fundamentally different from previously known examples such as charge-doping-induced collapse in cuprates and pressure-induced collapse in weak Mott insulators. In the layered 1T-$TaS_2$, the isovalent substitution of S with Se does not induce additional charge carriers. Instead, it tunes the CDW order, and in turn drives the direct Mott gap into an effective "charge-transfer"gap. To the best of our knowledge, it is the first time that such a novel evolution between Mott gap and charge-transfer gap can be adiabatically accessed in the same material. Upon further substitution, after the charge gap fully collapses, the low energy degrees of freedom include the Fermi-surface-forming itinerant carriers and fluctuating local magnetic moments, just like in heavy-fermion systems and iron pnictides/chalcogenides. It is thus interesting to ask whether this parent state for superconductivity is a heavy fermion liquid or a magnetic metal. A even more unique feature of 1T-$TaS_2$ is that the Mott physics is built upon a triangular lattice, in which spin frustrating is intrinsically coded. Therefore, the magnetic ground state of 1T-$TaS_2$ might be highly nontrivial. We believe that the richness of the orbital-tunable electronic structure in Se-doped $TaS_2$ will shed important insights into several important topics of condensed matter physics.

# Part XIII
# Potential Applications

## 22 Charge Configuration Memory Devices: Energy Efficiency and Switching Speed by Mraz et al. (2022)

**Abstract**

Current trends in data processing have given impetus for an intense search of new concepts of memory devices with emphasis on efficiency, speed, and scalability. A promising new approach to memory storage is based on resistance switching between charge-ordered domain states in the layered dichalcogenide 1T-$TaS_2$. Here we investigate the energy efficiency scaling of such charge configuration memory (CCM) devices as a function of device size and data write time $\tau_W$ as well as other parameters that have bearing on efficient device operation. We find that switching energy efficiency scales approximately linearly with both quantities over multiple decades, departing from linearity only when $\tau_W$ approaches the $\sim 0.5$ps intrinsic switching limit. Compared to current state of the art memory devices, CCM devices are found to be much faster and significantly more energy efficient, demonstrated here with two-terminal switching using $2.2\text{fJ}, 16\text{ps}$ electrical pulses.

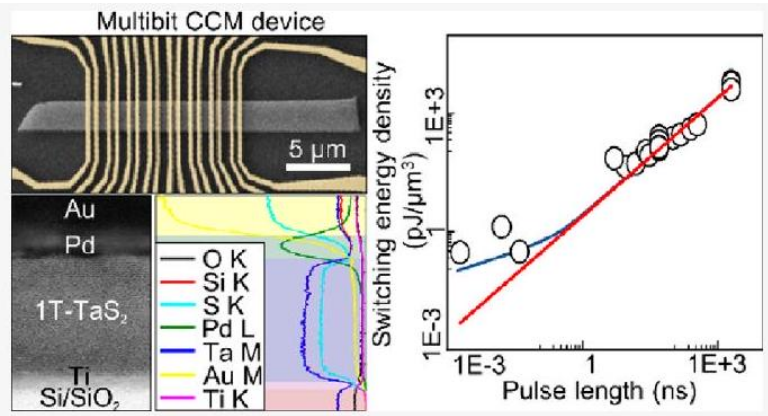


KEYWORDS: charge configuration memory, $TaS_2$, ultrafast, energy-efficient, cryogenic, nonvolatile

Research in the area of novel memory devices has been intense in the recent decades, but there have been few breakthroughs that have led to implementation. [1–3] As a result, technologies such as cryocomputing that promise large improvements in energy consumption have been seriously hindered by the absence of a suitable fast and energy-efficient memory for more than two decades. [4,5] As an alternative to modern magnetic devices, manipulating charge, rather than spins, for data storage could be more efficient because it can be directly driven by electrical charge injection that promises to be extremely fast and efficient. Unfortunately, the direct coupling of an electronic two-level system to lattice degrees of freedom causes rapid state decoherence and dissipation, which fundamentally limits charge-storage based memory concepts. As an apparent solution to this problem, it was shown recently that topological protection that stabilizes different charge density wave (CDW) domain states in the quasi-2D layered transition metal chalcogenide $1\text{ T} - \text{TaS}_2$ can be used for memory devices. [6,7] The basic mechanism for such a charge configuration memory (CCM) was shown to be unique to this material, [7–9] involving reversible charge reconfiguration from an insulating, spatially uniform CDW state to a metallic domain state [10] with accompanying restacking of the CDW along the direction perpendicular to the layers. [11] To develop the CCM concept into viable practical devices, a better understanding of the device characteristics is required, particularly the operational limitations,

such as write speed, energy efficiency, and endurance, as well as size scaling limitations and contact material compatibility. For low temperature operation, minimization of dissipation is essential, so investigation of how the switching energy scales with device size is particularly important. The write ( W ) cycle of the CCM device was shown to be nonthermal, while the erase (E) cycle is at least partially thermal. [7] Intrinsic nonohmic behavior and dissipation at the contacts, [12] especially if energy barriers are formed as a result of interface chemistry, may limit the energy efficiency in small devices. [13] In this paper we investigate CCM scaling properties in the nonvolatile resistance switching region, which is particularly relevant for incorporation into cryocomputing environments where the device has potential applications. We investigate the electrical contact structure with high resolution electron microscopy, searching for possible interfacial layers that may limit device performance. We conclude by comparing the measured characteristics of CCM with other current and emerging memory devices.

The devices were nanofabricated by evaporating metal contacts on 1 $T-TaS_2$ single crystal flakes as can be seen on a scanning electron microscope (SEM) image in Figure 1a (see

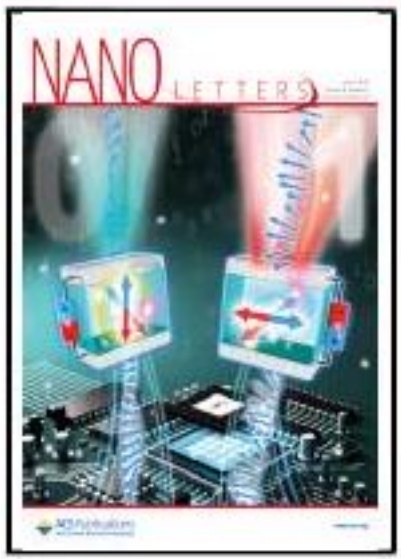

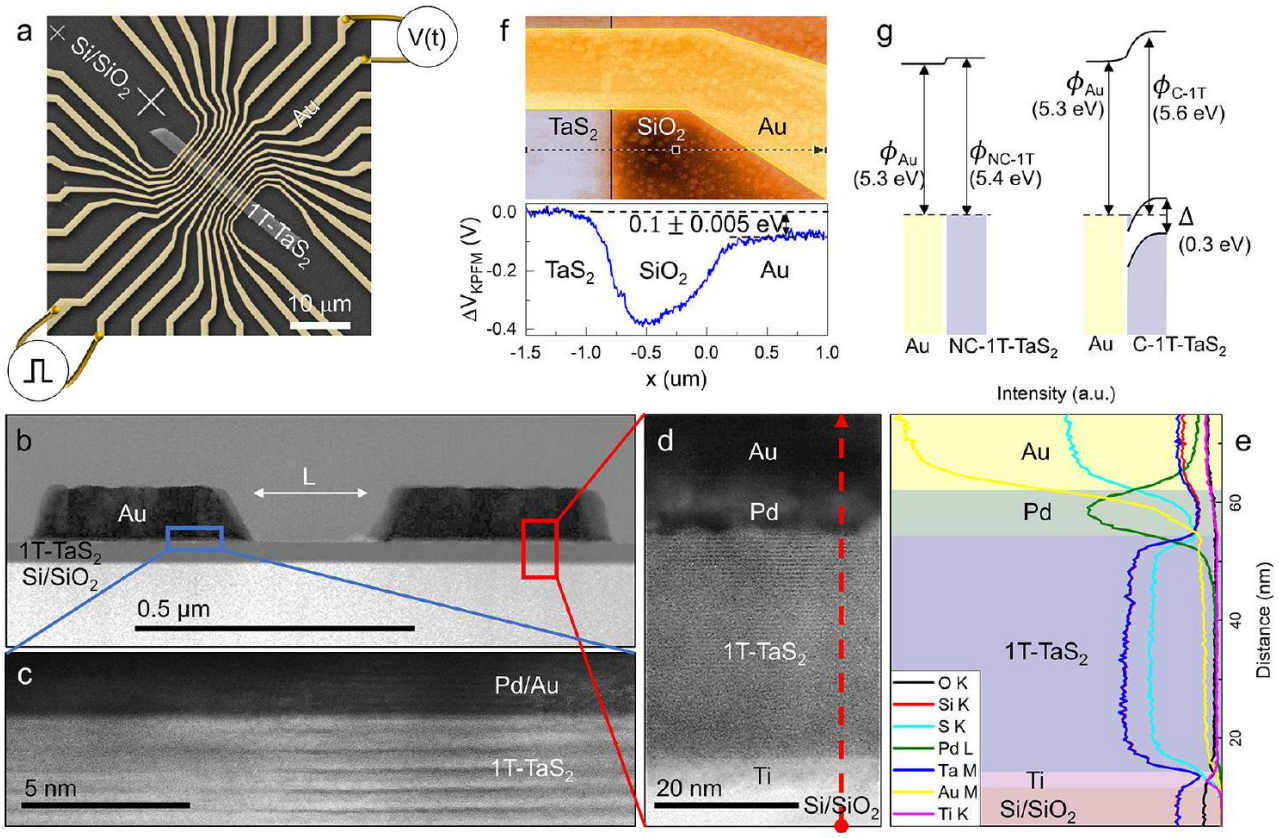


Figure 1. CCM device, EDS, and work function analysis. (a) SEM image of a typical CCM device used for measurements with transmission line contacts. (b) BF-STEM image of a cross-section of a fabricated CCM device (one memory bit). (c) Zoom-in to the interface between the metal electrode and $1 \mathrm{~T -\mathrm{TaS}_{2}$ crystal. (d) Zoom-in to a part of the cross-section with the EDS line scan marked. (e) EDS analysis of the zoomed-in section, where individual layers are identified: Au (yellow), Pd (green), Ta (dark blue), S (light blue), Si (red), O (black), Ti (pink). (f) Top panel shows an AFM image of a part of the CCM device with the line scan for the KPFM measurement marked. Bottom panel shows KPFM measurement of the work functions for $1\ \mathrm{T}-\mathrm{TaS}_2, \mathrm{SiO}_2$, and Au electrodes along the line scan. (g) Schematic band diagram of the device based on the KPFM measurements. On the left is a band diagram of an interface between the Au electrode and the nearly commensurate (NC) metallic state at room temperature, and on the right is an interface between the Au electrode and the commensurate (C) charge density wave state at cryogenic temperature.}

Methods in Suppporting Information). Switching characteristics were measured on many devices with very different gap sizes $L$ (Figure 1b) between the Au electrodes, using a large range of "write" pulse lengths $\tau_{\mathrm{W}}$, from 16 ps to 600 ms. For short pulse switching, low-attenuation transmission line circuits were used in combination with picosecond digital electronics (see Methods in Supporting Information). We first present an analysis of the contact structure in $\mathrm{Au}/1\ \mathrm{T}-\mathrm{TaS}_2$ devices on $\mathrm{Si}/\mathrm{SiO}_2$ substrates. A bright-field scanning transmission electron microscope (BF-STEM) image of a crosssection of two electrodes (one memory bit) and a zoom-in on the interface between the metal electrodes and $1\ \mathrm{T}-\mathrm{TaS}_2$ can be seen in Figure 1b and Figure 1c, respectively. The layered structure of the $1\ \mathrm{T}-\mathrm{TaS}_2$ crystal is clearly visible in Figure 1c. Part of the cross-section showing the entire structure of the device can be seen in Figure 1d. An energy-dispersive X-ray spectroscopy (EDS) analysis of the device's interfaces is presented in Figure 1e, along the line scan marked with the red line in Figure 1d. Considering

the overlap in the EDS spectrum for certain characteristic lines of elements ( Ta M and Si K, Au $M$ and $SK$ ), the individual layers of the fabricated CCM device can be identified (Figure 1e). Importantly, multiple EDS analyses (at $\sim$ 1 nm resolution) on different devices do not show any evidence of an oxide layer at the interface between the 1 T $-$ $TaS_2$ crystal and the metal electrode, consistent with a previous report [13] and the voltage-current characteristics discussed below.

To further ascertain the possible role of contacts in device functionality we measured the relative difference in work functions $\phi$ of the 1T- $TaS_2$ and Au in a CCM device using a Kelvin probe force microscopy (KPFM). The upper panel in Figure 1f shows an atomic force microscope (AFM) image of a part of the CCM device, while the bottom panel in Figure 1f shows the KPFM potential difference $\Delta V_{\mathrm{KPFM}}$ as a function of the scanning position on the device. The scanning is performed across the 1 T $-$ $TaS_2$ crystal, the $Si/SiO_2$ substrate and the Au electrode, as indicated with the dashed line in Figure 1f, top panel. While the absolute value of $\phi$ was not calibrated, the relative difference of work functions is accurately determined,

$$\phi_{1\ \mathrm{T-TaS2}} - \phi_{\mathrm{Au}} = 0.1 \pm 0.005\mathrm{eV}$$

in agreement with published values for $\phi_{1\ \mathrm{T-TaS2}} = 5.5 \pm 0.01$ eV (single crystal) [14] and $\phi_{\mathrm{Au}} = 5.1 - 5.47\mathrm{eV}$.[15] Judging from the KPFM measurement and the values from ref 15, it looks like our gold layer has facets with predominantly (100) or (110) orientation. The corresponding band diagrams for the room-temperature nearly commensurate (NC) metallic state and the low-temperature commensurate charge density wave (C-CDW) are shown in Figure 1g. Ideally electron injection from Au metal into the 1 T $-$ $TaS_2$ CDW-gapped semiconductor with a gap $\Delta = 0.3\mathrm{eV}$[16] takes place (Figure 1 g ), and the junction is expected to be ohmic. 1 T $-$ $TaS_2$ reacts to charge injection by forming a conducting interface layer parallel to the interface. We thus do not expect a barrier to form at the

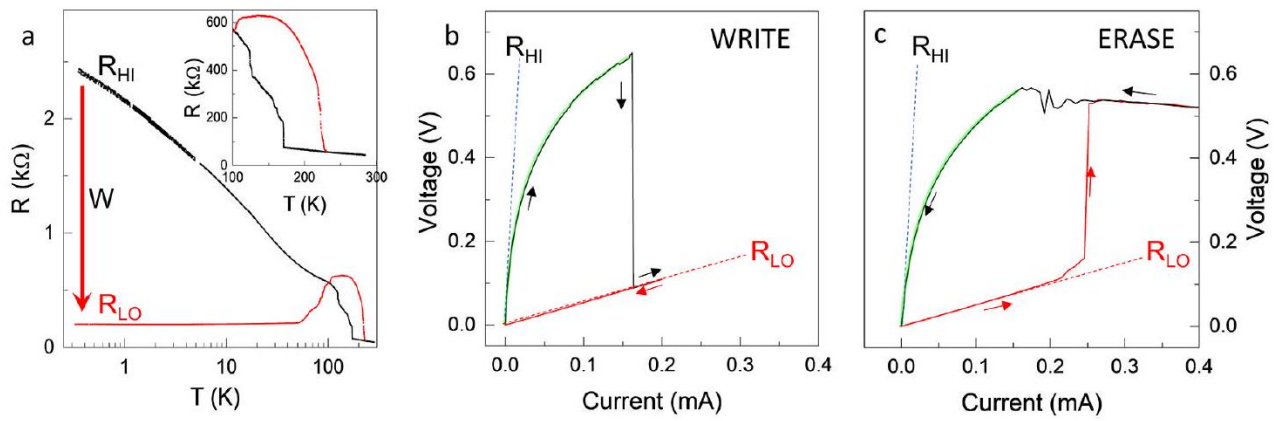


Figure 2. Resistance switching and voltage-current characteristics of CCM devices. (a) Temperature dependence of the four-contact resistance $R$. Switching from $R_{\mathrm{HI}}$ to $R_{\mathrm{LO}}$ at 350 mK is caused by an electrical W pulse as indicated by the arrow. Heating above 90 K (red line) reverts the system to the $R_{\mathrm{HI}}$ state. Inset to (a) shows the expanded scale of the $R - T$ curve. (b, c) Pulsed measurements of the $V - I$ curve for the W and E operations, respectively.}

interface with Au contacts due to carrier diffusion, which is consistent with the observed linear voltage-current curves [6] and the scaling behavior with device size and $\tau_{\mathrm{W}}$ described in the following section.

While basic memristive switching of the CCM device at higher temperatures was discussed elsewhere, [6] a measurement that demonstrates millikelvin operation and switching from the

high resistance ( HI ) state $R_{\mathrm{HI}}$ to low ( LO ) resistance state $R_{\mathrm{LO}}$ is illustrated by the $R-T$ curve in Figure 2a, for a device with intercontact distance $L \sim 300$ nm. The entire measurement cycle is shown starting from 280 K, cooling and switching at 350 mK by a single write (W) pulse, and heating back to 280 K, where the system reverts to its original state. Upon heating we observe characteristic steps, previously attributed to relaxation of domains. [7,17] The insert to Figure 2a shows the $R-T$ curves on an expanded scale, showing a commonly observed hysteresis associated with the presence of additional phases [18,19] above 100 K.

A typical voltage-current ($V-I$) curve for a W cycle at 20 K is shown in Figure 2b for incrementally increasing current pulses $I_{\mathrm{W}}$ through the CCM device with an intercontact distance $L = 145$ nm (see insert to Figure 3b). In this measurement, the pulses were very long ( $\tau_{\mathrm{W}} = 600$ ms ), illustrating the versatility of the device (fast measurements are shown later). The $V-I$ measurement allows us to accurately determine the switching threshold for both the write and erase processes. We observe a nonlinear $V-I$ curve with an initial slope $R_{\mathrm{HI}}$ (dashed $R_{\mathrm{HI}}$ line) up to the $I_{\mathrm{W}}^{T} \simeq 0.165$ mA. Above this current the voltage drops from 0.65 to 0.08 V and the device switches to a linear $V-I$ relation with resistance $R_{\mathrm{LO}}$ (dashed $R_{\mathrm{LO}}$ line), remaining in this state indefinitely at this temperature. The $V-I$ curve for W can be fit with

$$V = V_0 \ln\left(I/I_0 + 1\right)$$

for $I < I_{\mathrm{W}}^{T}$ (green line) and $V = R_{\mathrm{LO}} I$ for $I > I_{\mathrm{W}}^{T}$ (dashed $R_{\mathrm{LO}}$ line) in agreement with ref 6. To switch back to the pristine state, the erase (E) sequence is illustrated in Figure 2c where the current is ramped from $I = 0$ to 0.4 mA. Initially we follow the $R_{\mathrm{LO}}$ curve. Above a threshold $I_{\mathrm{E}}^{T} \simeq 0.25$ mA the device switches to a high resistance state. As current is lowered to zero, the device remains in $R_{\mathrm{HI}}$ at low currents. The behavior is consistent with the previous $V-I$ measurements with $10\mu$ s pulses, [6] implying that it is not dependent on the pulse length over the range $\tau_{\mathrm{W}} = 10^{-5} - 1$ s.

Using 60 GHz Au transmission line contacts, fabricated on $\sim 50$ nm thick 1 T $-$ $TaS_2$ flakes on $Si/SiO_2$ substrates (see Figure 1a, Methods in Supporting Information), we systematically study the W sequence of multiple CCM devices for different W pulse lengths $\tau_{\mathrm{W}}$ ranging from 16 ps to $20\mu$ s generated by electronic pulse generators in a single-pulse mode. For each pulse length, the pulse voltage was incrementally increased until the switching threshold $V_{\mathrm{W}}$ was reached and recorded. Since the $V_{\mathrm{W}}$ depends on sample geometry, in Figure 3a, we plot the switching energy density instead: $\varepsilon_{\mathrm{W}} = E_{\mathrm{W}}/\mathcal{V}$($\mathcal{V}$ is the crystal volume between electrodes, and $E_{\mathrm{W}} = V_{\mathrm{W}}^2/R_{\mathrm{HI}}$ is defined as the switching energy). The error bars include the systematic error of measurements and the estimated variation between different devices. The red line shows a linear relation $\varepsilon\left(\tau_{\mathrm{W}}\right) = \gamma\tau_{\mathrm{W}}$, with $\gamma \simeq 2.5\frac{\mathrm{pJ}}{\mathrm{ns}\mu^3}$. At shorter pulse lengths $\tau_{\mathrm{W}}$ there is a departure from linearity denoted with the blue line, which most likely occurs due to an increase in transmission line losses in the GHz range. For the fastest device measured here ( $\tau_{\mathrm{W}} = 16$ps fwhm), the distance between contacts is $L = 75$ nm and threshold W voltage $V_{\mathrm{W}} = 1 \pm 0.1$ V, which gives a switching energy per bit of $E_{\mathrm{W}} = 2.2$fJ at 20 K. The resistance measured before and after switching is $R_{\mathrm{HI}} = 8200\Omega$ and $R_{\mathrm{LO}} = 1800\Omega$, respectively. The resistance ratio is lower than the value observed with longer W pulses at low temperatures such as that shown in Figure 2a, which may be attributed to incomplete switching. However, both $R_{\mathrm{HI}}$ and $R_{\mathrm{LO}}$ resistance states have long-term stability at this temperature ( 20 K ). To explore the switching capabilities of the CCM device in the ultrafast limit, an electro-optical setup that allows for ps pulse generation and detection was reported in ref 21, from which we include a data point $\tau_{\mathrm{W}} = 1.9$ps in Figure 3a.

The scaling of the switching threshold voltage $V_{\mathrm{W}}$ with intercontact distance $L$ is shown in Figure 3b. (A device with multiple $L$ is shown in the inset.) Approximately linear scaling of $V_{\mathrm{W}}$ is observed over nearly 2 orders of magnitude, 60 nm $< L < 4\mu$ m, that extrapolates to the

origin, with a slight departure from linearity at the smallest $L$. Considering the fact that the EDS analyses do not show any intermediate layer between Au and 1T- $TaS_2$ and that the work function mismatch suggests ohmic contact behavior, we cannot directly attribute the observed small deviation from linearity to electrical contacts. One possible reason for the departure at small sizes may be related to the fact that the device size approaches the

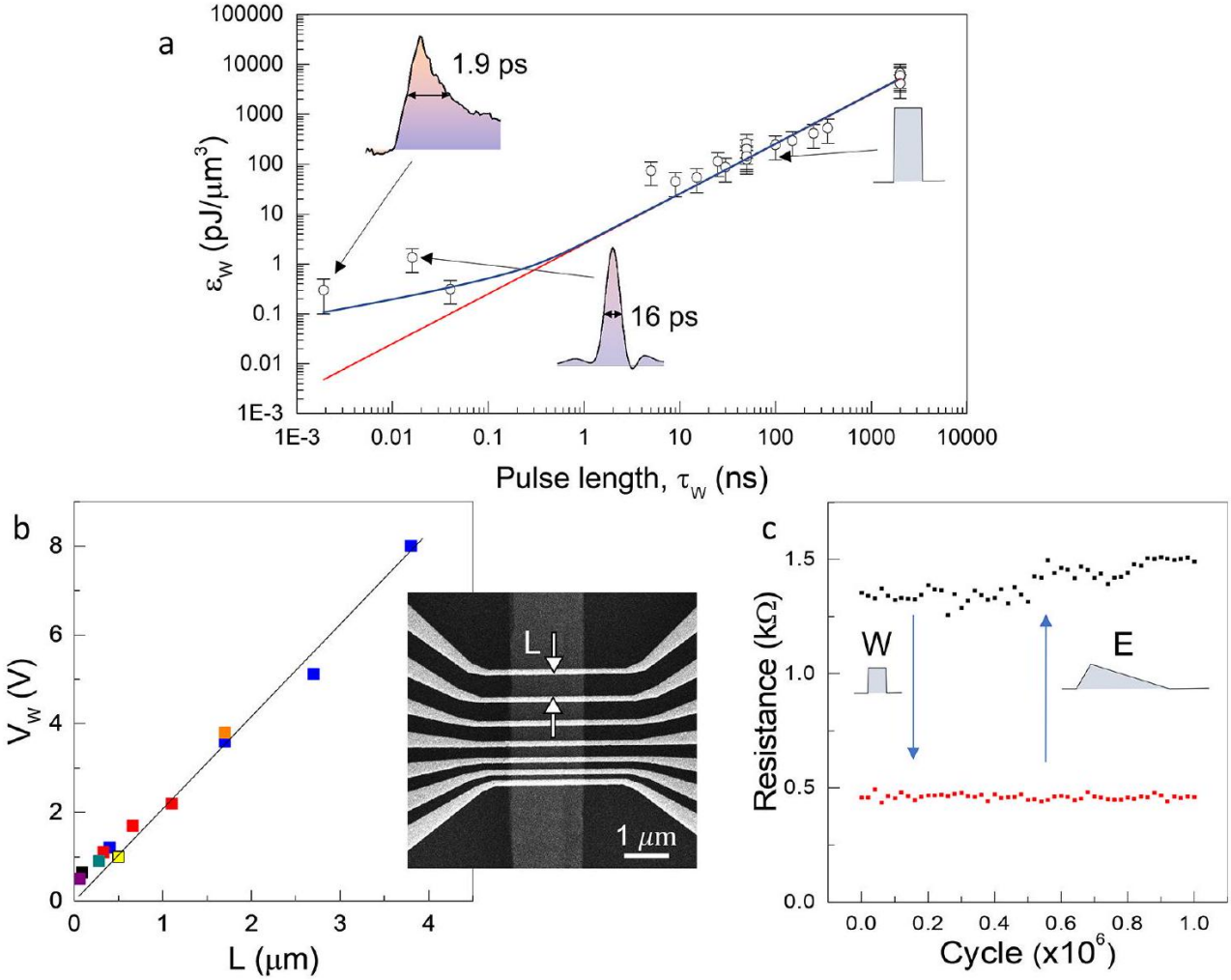


Figure 3. Speed and energy efficiency scaling at 20 K. (a) Switching energy density $\varepsilon_{\mathrm{W}}$ as a function of pulse length $\tau_{\mathrm{W}}$. The inset shows the actual pulse shapes. Red line shows linear scaling, and blue line shows departure from linearity at short $\tau_{\mathrm{W}}$. The data point at 1.9 ps was taken from ref 21. (b) Switching threshold voltage $V_{\mathrm{W}}$ as a function of distance between the electrodes $L$. The inset shows a device with variable $L$ used in the measurement. Different symbol colors are for different physical devices. (c) Endurance measurement showing cycling between $R_{\mathrm{LO}}$ and $R_{\mathrm{HI}}$ for $10^6$ cycles. Each pair of points represents $2 \times 10^4$ W/E cycles.}

intrinsic $10 - 20$ nm domain size measured in the lowresistance state of single crystals. [9,20] The efficiency of devices with feature sizes comparable to the domain size may be expected to decrease due to charge configuration pinning at the contacts.

In Figure 3c we show a typical endurance measurement at 20 K for a device with $L = 300$ nm. Square pulses with $\tau_{\mathrm{W}} = 2.7\mu$ s and amplitude $V_{\mathrm{W}} = 0.45$ V are used for W, and asymmetric triangular E pulses with peak amplitude $V_{\mathrm{E}} = 0.43$ V and $\tau_{\mathrm{E}} = 20$ ms are used for

erase (shown in the inset to Figure 3c). Each pair of corresponding $R_{\mathrm{HI}}$ and $R_{\mathrm{LO}}$ values shown by black and red dots, respectively, represents a measurement after 20000 W/E cycles. We see that $R_{\mathrm{LO}}$ is remarkably stable over $10^6$ cycles, while $R_{\mathrm{HI}}$ initially increases slightly and later stabilizes after $8 \times 10^5$ cycles when the measurement was terminated.

An immediate application of the device could be in cryocomputing, which has been heralded as an obvious solution to the overall challenge of reducing dissipation of computer systems. [5,22] In spite of huge research efforts and availability of superconducting circuits performing both single flux quantum (SFQ) and quantum information processing, [22] the absence of a fast low-energy cryogenic memory has prevented significant upscaling, [4,5] so CCM devices may offer a possible breakthrough. Considering the scaling limits of CCM devices, we find that while the measured value of $E_{\mathrm{W}}^{\mathrm{CCM}} = 2.2\mathrm{fJ}$ is small compared with other current memory devices, the observed scaling laws suggest that $E_{\mathrm{W}}^{\mathrm{CCM}}$ can be reduced further by reducing $L$ and/or $\tau_{\mathrm{W}}$. Optimization of microwave electrical contacts seems to be essential in reducing the $E_{\mathrm{W}}^{\mathrm{CCM}}$ as well, since the losses in the transmission of GHz pulses are likely to be the cause for the departure from linear scaling in Figure 3a. Deviations from linearity might still be expected when $\tau_{\mathrm{W}}$ approaches the intrinsic switching time $\tau_{\mathrm{s}} = 0.45\mathrm{ps}$.[23] These effects are likely to be important for device optimization, particulary for erase protocols. [7] Fundamentally, the measured $E_{\mathrm{W}}^{\mathrm{CCM}}$ is still significantly larger than the measured microscopic barrier $E_{\mathrm{B}} = 15-21\mathrm{meV}((2.4-3.4)\times 10^{-6}\mathrm{fJ})$ obtained from thermal activation measurements. [17] This implies that in principle devices with much smaller $E_{\mathrm{W}}^{\mathrm{CCM}}$ can be built before reaching fundamental limits. It is also instructive to compare $E_{\mathrm{W}}^{\mathrm{CCM}}$ and $E_{\mathrm{B}}$ with the lowest possible energy difference between two states that can be discerned thermodynamically on the basis of their entropy difference $\Delta E_{\mathrm{B-L}} = k_{\mathrm{B}} T \ln 2$ (the Brillouin-Landauer (BL) thermodynamic limit [24] ). At $T = 4\ \mathrm{K}, \Delta E_{\mathrm{B-L}} \simeq 3.8 \times 10^{-8}\mathrm{fJ}$, so the presented CCM devices in Figure 3 are still far from this limit. For cryogenic memory applications, it is important that the CCM device could be driven by single flux quantum (SFQ)

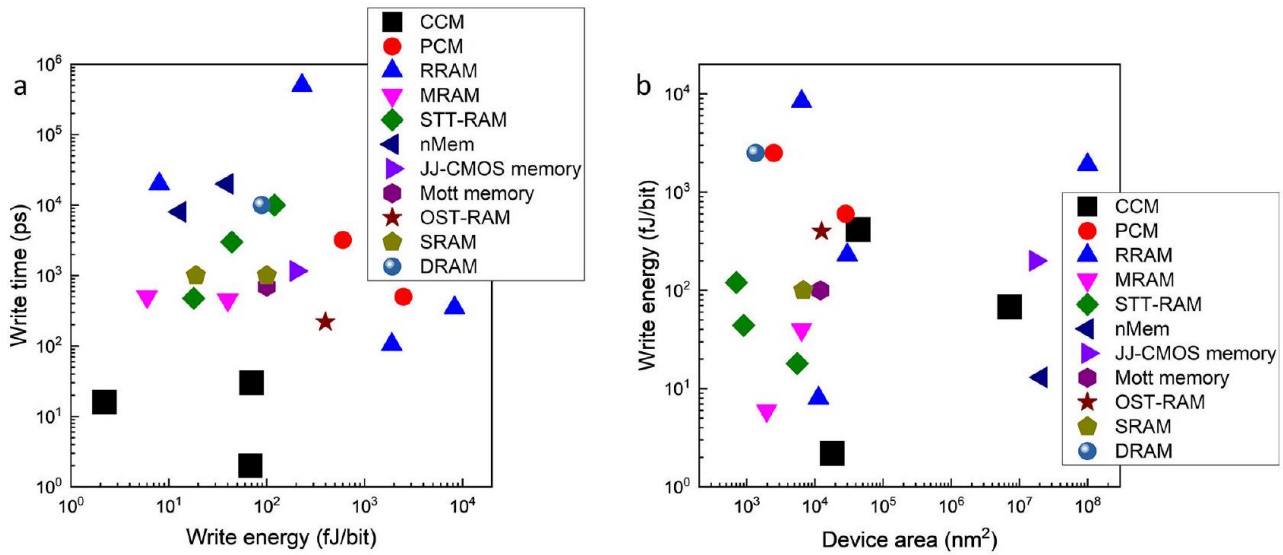


Figure 4. Measured switching energy $E_{\mathrm{W}}$ and speed of leading memory devices: (a) switching energy in correlation with device area; (b) switching times $\tau_{\mathrm{W}}$ plotted against switching energy. References: PCM, [28,29] RRAM, [26,33−35] STT-RAM, [36−38] MRAM, [25,39] nMem, [40,41] JJ-CMOS memory, [42] OST-RAM, [43] Mott memory, [44] SRAM, [45−47] and DRAM. [47]

pulses. For a single SFQ pulse, the pulse energy may be estimated to $E_{\phi_0} = \phi_0 J_{\mathrm{c}} \simeq 0.2 \times 10^{-3}\mathrm{fJ}$, where we have assumed a typical critical current $J_{\mathrm{c}} \sim 100\mu$ A in the SFQ driver

circuit. For a realistic CCM device with $100 \times 20$ nm$^2$ device area and a crystal thickness of 20 nm, the estimation from the linear fit in Figure 3a for switching with 2ps[21] pulses gives $E_{\mathrm{W}}^{\mathrm{CCM}} \sim 0.2 \times 10^{-3}$fJ. Thus, on the basis of the presented scaling laws, CCM devices constructed using current fabrication techniques could be driven with single SFQ pulses, provided the coupling between the SFQ driver and the CCM microwave circuit is optimized.

In Figure 4 we compare operating parameters of the CCM with leading alternative technologies, including magnetic random-access memory (MRAM), phase change memory (PCM), and others. The smallest energy/bit values of 6fJ/ bit [25] and 8fJ/bit[26] were reported for voltage-controlled magnetic anisotropy switching (MRAM) in Ta/CoFeB/MgO magnetic tunnel junctions (MTJ) and resistive switching in Ni/GeO$_x$/HfON/TaN resistive random access memory (RRAM) devices, respectively (Figure 4 b ). The lowest theoretically predicted value for MTJs of a few fJ/ bit [27] is comparable to the 2.2 fJ, which was already experimentally achieved in CCM. This value is still much higher than the theoretical limit of $10^{-6}$fJ predicted for CCM. PCMs have both significantly higher switching energies ( $>$ 600fJ[28] ) and switching voltages ( $>$ 1 V[29,30] ) than CCM, and even the smallest memristors such as 6 nm crossbar memristor arrays have a write power of $P_{\mathrm{W}} = 0.23\mu$ W, [31] which is higher than the predicted $\sim 0.1\mu$ W for a much bigger CCM device ( $100 \times 20 \times 20$ nm$^3$ ), estimated from the linear fit in Figure 3a. We note that our demonstration of a man-made nonvolatile electronic memory device uses less energy per bit ( 2.2fJ/bit ) than a human brain ( $\sim$ 10fJ/ synapse ) and potentially much less than artificial synapses. [32] The CCM's advantage is that it is $>$9 orders of magnitude faster.

Picosecond switching speeds of CCMs are similar to those reported by photomagnetic recording. [48] However, the switching energy density per bit is significantly smaller for CCM: ( 0.3 J/cm$^3$ for CCM[21] vs 6 J/cm$^3$ for photomagnetic recording), with the added advantage of two-contact electrical W/E and read (R) operations and the possibility of a very high packing density. For CCMs the current size limit is $10 - 20$ nm, but for photomagnetic recording the size is limited by optical wavelengths used for W/E/R (hundreds of nm ). Nanowire memory (nMem)[40,41] based on superconductive loops and nanowire cryotrons, Josephson magnetic random access memory (JMRAM), [49] superconducting quantum interference device (SQUID) memory, [50] and hybrid Josephson complementary metal oxide semiconductor (JJ-CMOS) memory [42,51,52] are all very promising solutions for a cryogenic memory. However, they are hard to scale down to the 10-20 nm regime and require additional driving periphery [4,53] (nMem, JMRAM and SQUID memory) or require voltage amplification for proper operation [4] (JJ-CMOS memory), which introduces additional dissipation into the circuits.

Thus, with presently demonstrated scalability (feature size, 60 nm to $4\mu$ m; pulse length, 16 ps to 600 ms ; voltage, $0.3 - 10$V) and with a wide operating temperature range ( 350 mK to 190 K ), the CCM devices appear to be very versatile in comparison. The operating temperature range could be extended to higher $T$ by appropriate choice of substrate. [17] So far, no other electronically ordered material has been found to exhibit significant metastability and thus 1 T $-$ TaS$_2$ currently is the only material for CCM application. The device variability is small, as seen from the data on multiple devices shown in the scaling plots. Importantly for applications, thin films of 1TTaS$_2$ can be grown by various means [54–56] promising technological flexibility. For interfacing present CCM devices with single flux quantum devices, which is an obvious target application, nanocryotrons (nTrons) have been demonstrated to be a match in terms of output voltage, speed, and impedance. [57,58] However, nTrons could introduce additional design complexity and dissipation due to higher bias currents, [51] so direct driving by SFQ pulses might be preferable.

In comparison to complementary metal oxide semiconductor (CMOS) devices [42,51,52,59] and nanowire memories, [40,41] the CCM concept potentially offers advantages in terms of scaling, size, speed, energy efficiency, and operational simplicity. Compared with

other fast memory, such as photomagnetic storage, [48] CCMs are more energy efficient and offer much higher data packing densities. The disadvantage is low-temperature operation, but considering its primary virtues are speed and energy efficiency, the target applications are in the cryocomputing environment. The presently measured energy efficiency ( 2.2fJ/ bit ) is a consequence of very short write pulses needed, allowed by the inherent switching mechanism. Thus, the values shown here are limited by device size and transmission characteristics of the highspeed microwave circuit, not the intrinsic mechanism.

We conclude that while 1 $T-TaS_2$ appears to be unique in exhibiting combined set of properties useful for CCM operation, multilayer structures may introduce additional functionality that may result in improved performance and extended temperature range of operation. The additional degrees of freedom arising from interlayer interactions and proximity coupling [60] in 2D heterostructures may be expected to offer new possibilities for new CCM devices beyond the currently available materials.

# Part XIV
# Exotic Effects

## 23 Quantum billiards with correlated electrons confined in triangular transition metal dichalcogenide monolayer nanostructures (2021) by Ravnik et al.

authors: Ravnik, Vaskivskyi, Vodeb, Aupič, Vaskivskyi, Golež, Gerasimenko, Kabanov, Mihailovic.

**Abstract**

Forcing systems through fast non-equilibrium phase transitions offers the opportunity to study new states of quantum matter that self-assemble in their wake. Here we study the quantum interference effects of correlated electrons confined in monolayer quantum nanostructures, created by femtosecond laser-induced quench through a first-order polytype structural transition in a layered transition-metal dichalcogenide material. Scanning tunnelling microscopy of the electrons confined within equilateral triangles, whose dimensions are a few crystal unit cells on the side, reveals that the trajectories are strongly modified from freeelectron states both by electronic correlations and confinement. Comparison of experiments with theoretical predictions of strongly correlated electron behaviour reveals that the confining geometry destabilizes the Wigner/Mott crystal ground state, resulting in mixed itinerant and correlation-localized states intertwined on a length scale of 1 nm. The work opens the path toward understanding the quantum transport of electrons confined in atomic-scale monolayer structures based on correlated-electron-materials.

Alaser-induced quench through a first-order structural transition can create small domain structures with atomically precise shapes that are beyond the reach of current nanofabrication technologies. Viewed from a quantum physics perspective, such structures represent a fruitful playground for investigating the quantum behavior of particles in geometrically confined systems. Regular shapes, and equilateral triangles (ETs) in particular, are of special interest because they allow the study of the crossover from periodic limit cycles to chaotic trajectories [1–3]. Quantum scars-quantum interference (QI) patterns that follow traces of the paths of classical particles [4–7]-were investigated until now in fabricated mesoscopic semiconductor heterostructures and graphene by scanning gate microscopy [8,9]. However, with strongly interacting electrons such patterns are not expected due to their tendency for localization, and more elaborate structures are expected that require new theoretical approaches beyond the noninteracting electron approach. Recently, oscillating patterns were observed in interacting Rydberg atom arrays and theoretically motivated by the existence of many-body scars-manifold of low entangled excited states [10,11]. Correlation effects may be expected to give rise to perturbed trajectories in which the entanglement dynamics show a dependence on the nature of the perturbation. The observation of QI in confined correlated electron systems would be of both fundamental interest, and also of practical importance for designing coherent electron devices with correlated materials.

[11] Dept. of Complex Matter, Jožef Stefan Institute, Ljubljana, Slovenia. [2] Laboratory for Micro and Nanotechnology, Paul Scherrer Institut, Villigen, PSI, Switzerland. [3] Dept. of Physics, Faculty of Mathematics and Physics, University of Ljubljana, Ljubljana, Slovenia. [4] CENN Nanocenter, Ljubljana, Slovenia. [5] Dept. of Theoretical Physics, Jožef Stefan Institute, Ljubljana, Slovenia. [6] Flatiron Institute, New York, NY, USA. email: jan.ravnik@psi.ch; dragan. mihailovic@ijs.si

Here we use scanning tunneling microscopy to investigate QI in ET-shaped monolayer nanostructures of $TaS_2$ as small as ˜2.6 to ˜12.5 nm wide (8-38 unit cells) (Fig. 1). $TaS_2$ is a prototypical electronically correlated quasi-2D material, which is prone to carrier localization and the formation of different charge orders at different temperatures that become commensurate at 'magic' filling fractions [12].

The orthorhombic 1T polytype of 1T- $TaS_2$ below ˜180 K, has a commensurate charge-density-wave (CCDW) with a large modulation amplitude of ˜ 1 electron per 13 Ta sites, localized in a $\sqrt{13} \times \sqrt{13}$ superlattice structure, which can exhibit either left (L) or right (R) chirality with respect to the crystal lattice [13] (Fig. 1a). The lattice surrounding each 13th Ta atom is distorted by the extra charge [14] resulting in the formation of a polaron. Due to Coulomb interactions between such polarons, the system is correlated and thought to be susceptible to the formation of a Mott state [14,15], whence it is often discussed in terms of a polaronic Wigner crystal [12,16,17]. The 2H (trigonal) polytype is metallic above 75 K, but forms a commensurate CCDW below this temperature, which-in contrast to the 1T polytype-is metallic down to 1 K, below which it becomes superconducting [18].

The ET nanostructures are created by a laser pulse-induced quench through an inversion-symmetry-breaking polytype transformation of the surface atomic monolayer of a 1T polytype $TaS_2$ single crystal. The resulting ET domains are embedded laterally by a $1H-TaS_2$ crystalline layer (the 1H signifies it is a monolayer). The entire structure is epitaxial on a $1\ T-TaS_2$ single crystal (Fig. 1a, b)).

Understanding the behavior of correlated electrons confined in such small ETs theoretically represents a substantial challenge.

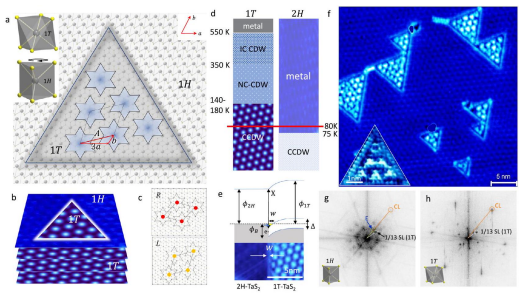


Fig. 1 Monolayer $\mathbf{1T-TaS_2}$ structure in the shape of an ET bounded by a $\mathbf{1H-TaS_2}$ monolayer. a A schematic picture of the left-handed packing of polarons in a C superlattice within an ET of outer dimensions 16a (inner dimensions I = 11a ), where a = 0.33Å is the lattice constant. The CCDW superlattice vector A is shown in terms of the lattice vectors a and b. The unit cells of the 1T and 1H crystal structures are shown in the insert. b The schematic structure of ETs on top of a $1\ T-TaS_2$ substrate. c Ideal polaron packing in L and R-handed CCDW superlattices. d A phase diagram showing the charge density wave ordering transitions of the 1T- and 2H- polytypes as a function of temperature. The measurement temperature and phase transition temperatures are indicated. e A band diagram of the 1T-1H boundary. An edge state of width w forms within the 1T phase as a result of band bending (see Supplementary information). f An STM image of different sized a $1\ T-TaS_2$ETs embedded laterally within a $1H-TaS_2$ monolayer on the surface of a $1\ T-TaS_2$ single crystal. Note the ubiquitous presence of the edge state. The insert (bottom-left) shows a high-resolution image of a small ET with 6 polarons. More images are shown in the Supplementary information. g, h Fourier transforms of the 1H and 1T regions respectively. The $\sqrt{13} \times \sqrt{13}$CCDW SL and CL peaks are indicated. A peak attributed to the polarons ordered parallel to the edge of the ETs is also indicated (E).

Considering CDWs as standing wave interferences formed by counter-propagating Fermi electrons [19−21] suggests an investigation using the quantum billiards (QB) approach with Fermi

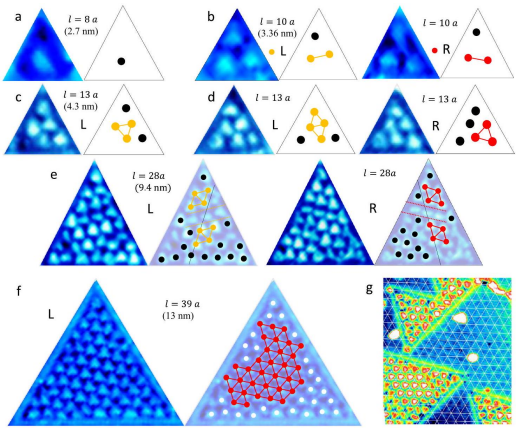


Fig. 2 STM images of different sized ETs with **I = 8 . . . 38a** at **80 K** with a bias voltage of **0.8 V**. Each STM image is accompanied by a schematic figure indicating the appearance of L or R chirality of the C order (yellow and red respectively). Multiple localized QI features do not conform to the C order (black dots). a A single dot is observed for I = 8a. b For I = 10a, L and R chiralities of C order appear. **cl** = 13 a with 5 polarons, **dl** = 13 a with 6 polarons of L and R chiralities. **el** = 28 a with L and R chiralities created nearby with the same laser pulse exposure. Similar domain wall patterns (dashed lines) are observed in both cases, as schematically shown. f An ET with I = 38a showing a single C domain at the center, surrounded by QPI at the edges (white dots). g The registry of the CCDW orders in the ETs and the 1 $T - TaS_2$ layer below. The grid pattern is centered on the CCDW in the 1T layer below the 1H layer. All ETs show phase shifts of the polaron order with respect to the substrate, and to each other.

electrons. On the other hand, the 2D polaronic Wigner crystal picture, where the polarons are subject to Mott localization [14] suggests a correlated electron picture. Here we compare conventional QB calculations, a (classical) charged lattice gas strongly correlated electron model, and a fully quantum many-body correlated electron model using exact diagonalization methods with the aim to understand the rich variety of QI textures in both classical and quantum regimes observed by STM.

### 23.0.1 Results

The ET structures (Fig. 1f) are created by a controlled exposure of a freshly exfoliated 1 $T - TaS_2$ single crystal to laser pulses in ultrahigh vacuum at 80 K[22], where the majority of the top surface is transformed to the 1H polytype, but ET structures of 1T polytype remain structurally unchanged [23,24]. The domains have atomically defined sides parallel to the crystal axes of the 1T layer, matching the lattice structure of the surrounding 1H layer, forming a perfect ET shape with edges at 60° to each other (Fig. 1a, b). The work functions for the 1 $T - TaS_2$ and $2H - TaS_2$ polytypes are $\phi = 5.6$ and 5.2 eV respectively, so the H phase acts as a barrier for electrons in the 1T ET nanostructure [25]. At 80 K, where the measurements are preformed, the 1H polytype is metallic, while the 1T polytype is nominally in the insulating CCDW phase [14]. (For reference, low-temperature scans showing the appearance of the 3 × 3 CDW of the 1T layer are shown in the Supplementary information). The H-polytype layer thus defines a confining potential barrier $\phi_B$ to the electrons inside the ET (Fig. 1e). As a result of self-organization of charges at the $1T-$ $1H$ interface, an edge state is formed which is clearly visible in ETs of all sizes (Fig. 1f). An interfacial band diagram based on a conventional metal-semiconductor junction is shown in Fig. 1e (see Supplementary information for details).

The width $w$ of the edge state (ES) is approximately equal to the screening length in 1T-$TaS_2$, $\zeta = 1 \sim 2$ nm[26,27].

The presented STM images in Figs. 1f and 2 are measurements of the local density of states (LDOS), which may be considered either in the local state approximation as $\rho_{\text{local}}(E, \mathbf{r})$ at the tip position r, for states without long-range translation invariance, $\rho_{\text{local}}(E, \mathbf{r}) \propto \Sigma_{i=1,N} |\psi_i(E_i, \mathbf{r})|^2 \delta(E - E_i)$; or in the quasiparticle approximation $\rho_{QP}(E, \mathbf{r}) \propto \Sigma_k |\psi_k(\mathbf{r})|^2 \delta(E - \varepsilon(\mathbf{k}))$, where $\varepsilon(\mathbf{k})$ is the energy of all the electrons with different wavevector k that interfere locally at position r. The latter case is relevant when we discuss the electrons in the unconfined 1H layer. It applies also to the interfering itinerant ET-confined electron eigenstates with different $\mathbf{k}_i$ but the same energy $E(\mathbf{k})$. In either case, the resulting

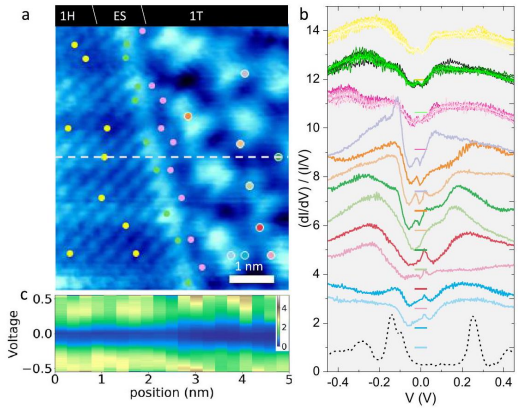


Fig. 3 NDC curves of the 1H layer outside, the 1T layer inside, and the ES of an ET. a An STM image at $V = -0.8$ V with indicated positions where STS curves are recorded, using color coded dots. b The STS curves (in corresponding color) for the 1H layer, the edge state (ES) inside, and outside the ET boundary, and the 1T phase inside the ET. The zero level is indicated in each case by a line in the same color code. The STS of the CCDW state of a 1 T $-$ $TaS_2$ monocrystal at 4 K is shown for comparison (dotted). c An STS line scan showing the LDOS (color scale) across the ET boundary. The opening of a pseudogap in the 1H polytype is clearly observed, which increases in the 1T layer inside the ET.

LDOS patterns inside the ET can be observed by STM topography at constant current. The QI is superimposed on the fine sub-nm structure of the atomic orbitals (see, for example, the highresolution image in the insert to Fig. 1f). This detailed orbital structure of surface atoms is related to structural effects and is not of present concern, so we shall focus primarily on the mesoscopic QI patterns.

Large-area Fourier transforms of the inside and outside of the ETs, shown in Fig. 1g, h respectively, reveal both crystal lattice (CL) peaks and CCDW superlattice (SL) peaks. The areas outside the ETs give sharp FFT peaks corresponding to the 1H CL and weak SL peaks from the 1T- $TaS_2$ CCDW layer underneath (Fig. 1h). Inside the ETs, we see an additional intensity that is almost uniformly distributed between the CCDW FFT peaks. This is attributed to QI features, and the periodic ordering along the inside edges of the ETs (labeled E).

In Fig. 2 we show a representative set of STM images of the inside of ETs, with inner ET dimensions ranging from $l = 8a$ (2.64 nm) to 38a (12.35 nm), where $a$ is the CL constant of 1T-$TaS_2$. Universally, we observe that the electrons try to form commensurate order at the center. The CCDW superlattice structure is significantly distorted, however, particularly in small ETs. For the smallest ETs such as the one with $l = 8a$ (Fig. 2a), a single, deformed dot

is visible at the center of the ET. Already with $l = 10a$ (Fig. 2b), the pattern with 3 maxima adjusts to the preferred CCDW order of either L or R chirality. In Fig. 2c, d, we clearly see very different QI textures in ETs with the same $l$, which is likely caused by small geometrical imperfections and/or initial conditions that results in different electron trajectories within ETs of equal size. In the same vein, two ETs with $l = 28a$ (Fig. 2e) created simultaneously nearby to each other show quite complicated but closely matching, mirror images of opposite chirality [28]. A remarkable feature of these ETs, particularly well visible in the R structure in Fig. 2e is the nontrivial QI pattern in the corner which does not fit the CCDW order. As the size of the ETs further increases, the polaron pattern approaches the CCDW superstructure. Thus, for $l = 38a$ the CCDW fills almost the entire ET, with QI distortions visible only at the edges.

Remarkably, the CCDW charge order within the ETs is not in register with respect to the CCDW order of the layer below. (The latter is visible through the surrounding 1H monolayer, and is emphasized by the mesh in Fig. 2h.) Moreover, neighboring ETs also have different register (Fig. 2f). This implies that the effect of the underlying CCDW and lattice potential is not sufficiently strong to force the CCDW order in the top layer. The QI patterns appear to be determined by the ET boundary, not by the interlayer coupling as has been suggested in bulk crystals [29].

The tunneling spectra inside, outside and across the edge of an ET at 80 K are presented as the normalized differential conductance (NDC), (dI/dV)/(I/V) in Fig. 3. The recorded positions are color coded. For comparison, we also show a 1T- $TaS_2$ CCDW bulk crystal spectrum at 4 K showing the characteristic upper and lower Hubbard bands (UHB and LHB) at -0.15 and +0.25 V, and CCDW-derived bands at -0.28 and +0.42 V [30].

Overall, the states within ±0.32eV of the Fermi level correspond to Ta-5 $d$ zone-folded sub-bands of the 1T- $TaS_2$ CCDW phase [31], and pristine Ta-5d bands of the 1H monolayer which give rise to the observed NDC. A line scan across the ES (Fig. 3c) shows the spatial variation of LDOS across the ET boundary, which can be compared with the naive band diagram in Fig. 1e. As the STM tip moves across the ES, the screening length 1-2 nm limits the sharpness of the features. Concurrent with the band alignment between 1T and 1H phases, charges will self-organize at the boundary, resulting in the observed ES. On the 1H side, we observe a uniform pseudogap, which we associate with the CDW state nearby (below 75 K).

A most striking feature of the data is the high degree of spatial homogeneity of the NDC curves outside the ET (the 1T layer) and

of the edge state itself. This is contrasted by the huge spatial spectral variations inside the ET occurring on a scale of 1 nm. Outside the ETs, beside the broad bands, a small, asymmetric gap-like feature is visible around ±20mV with peaks at ±50mV. This feature is similar to the one reported in single layer 1H-$TaSe_2$ on epitaxial bi-layer graphene substrates at 5 K[32] and monolayer $2H - TaS_2$ on graphene [18], where it is was attributed to the CDW gap of the 1H monolayer. Considering that the data were recorded at 80 K, this would suggest that in the monolayer, the CDW gap is already present above the $T_c = 75$ K of the bulk material. However, no modulation is visible in the FFTs corre-sponding to the $3 \times 3$ period of the $1H - TaS_2$CCDW (Fig. 1g), implying that there is no long-range CDW order in the 1H layer at 80 K. In some positions we also observe signatures of the characteristic peak at +0.25 V that corresponds to the UHB of bulk $1\ T - TaS_2$, which are attributed to the CCDW in the layer below. On the 1T side of the ES, inside the ET, the pseudogap size increases significantly.

Analysing the STS map in more detail at selected points, we note that the ES shows remarkable homogeneity along both sides of the boundary (green and pink dots respectively). The NDCs on the outside edge (the bright border, green) are very similar to the 1H monolayer (yellow). However, the broad peak at -0.21 V (yellow) splits into two, at -0.15 and -0.25 V (green). Inside the ET, the ES peak at -0.25 V shifts further to -0.28 V (pink), but no other significant differences are observed.

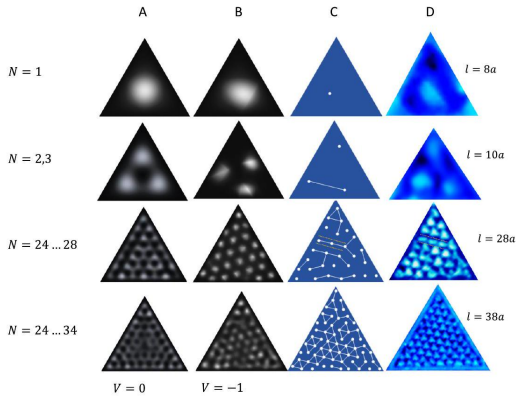


Fig. 4 A comparison of QB, QB + V and CLG model predictions for integrated LDOS with experiment for ETs of different sizes with different sides I. a Column A represents the QB solution (V = 0) for different summed states ($N$), corresponding to $V_B \simeq 0.8$ V. b Column B shows the QB + V model eigenstates with $= -1$, and c column C is the CLG MC calculation result at 1/13 filling. d Column D shows experimental images for $I = 8a, 10a, 28a$ and $38a$. Note the domain wall predicted for $I = 28a$ (col. C), and corresponding STM image (col. D) shown by dashed lines.

Inside the ET, the NDC curves vary significantly from spot to spot. A number of sharp peaks are observed that have no parallel in bulk 1T or $2H-TaS_2$. Such large spatial variations of LDOS are indeed expected for a confined system with no long-range order. For example, the observation of nodal domains in space is one of the expected features for a QB[33] that modify the CCDW pattern. The sharp features on the energy scale ±0.1 V are thus attributed to eigenstates of the confined nanostructure.

Investigating the effect of different bias voltages, a set of images at the ET boundary are shown in the Supplementary information. The detailed pattern and contrast change with V, but the correlation-localized polarons remain in place, in accordance with modeling of the correlated electron state. The contrast changes most when the scanning bias voltage is close to zero, as the contribution of the occupied polaronic states to the LDOS is small and we only see the states very close to the Fermi level.

## Discussion

Within a noninteracting picture, electrons confined within ETs are expected to exhibit canonical QB behavior. On the other hand, the presence of strong correlations localizes electrons in a commensurate structure [12], filling all available space. The noninteracting and strongly interacting pictures are at odds with each other. To investigate the dichotomy, we will compare the observed LDOS patterns with theoretical modeling ranging from noninteracting quantum billiard description to strongly interacting classical gas. We find that the strongly correlated approach is more appropriate but fails to fully describe the QI patterns. Finally, in an attempt to combine the itinerant electron picture with correlations, we calculate electron density patterns that show spatial localization textures using full quantum correlated electron calculation using exact diagonalization methods, finding a remarkable propensity for localization as commensurate filling is approached.

The quantum billiard with inter-layer interactions [12]. For an ideal ET with multiple noninteracting electrons, the levels are filled subject to the Pauli principle. The calculated integrated LDOS based on solutions of the Schrödinger equation are compared with the STM images for different ETs in Fig. 4, column A). The integrated LDOS is given by $\Sigma_{N=n..m} |\psi_N|^2$, where the

integers $n$ and $m$ indicate the range of eigenstates for the summation. By choosing appropriate $n$ and $m$ (by inspection), the predicted integrated LDOS patterns show the correct number of maxima within the ET, but the pattern is always symmetric with respect to the ET shape, and parallel with the edges, which the experimental patterns are not. While qualitatively describing

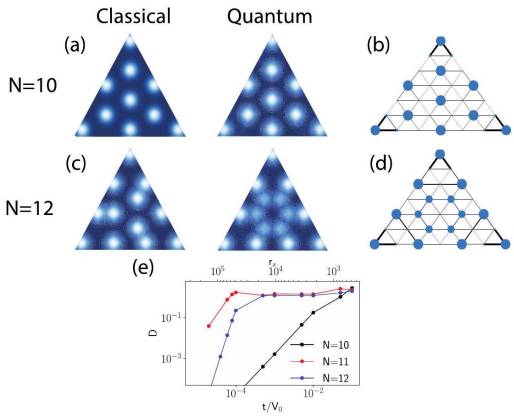


Fig. 5 Density plot of the charge distribution for spin-less particles on a triangle with $\boldsymbol{L} = \mathbf{7}$. The first row shows the commensurate case with $N = 10$ electrons. The second row shows the incommensurate case with $N = 12$ electrons. The first column represents the classical case with $t/V = 0$. The second column (a, c) shows the quantum case with $t/V = 0.01$. The size of the dot is a measure of the electron density. The last column (b, d) represents the quantum $t/V = 0.01$ solution in a graph representation where the thickness of the bond represents a relative contribution to the total kinetic energy and a size of the dot the electronic density. e The norm of the density difference distribution D (see the main text) for various number of electrons N versus the ratio between the hopping integral and the interaction $t/V$ or the Wigner-Seitz radius $r_s = 1.92e^2/\hbar v_F$, and $v_F$ is the Fermi velocity.

the integrated LDOS patterns, the QB approach fails to describe the unusual features of the experimentally observed integrated LDOS (column D of Fig. 4).

The energy scale of the states is given by the confinement energy $E \sim \frac{N^2\hbar^2\pi^2}{2m^*l^2}$. Assuming $m^* \sim m_e$, for the smallest ET with side $l = 2.15$ nm$(8a)$, the first four levels $N = 1\ldots4$ have energies ranging from $E \approx 0.08 - 1.26$eV, while in the largest ET shown here, with $l = 12.8$ nm$(38a)$, for $N = 1\ldots21$, $E \approx 0.0022 - 0.97$eV. A more realistic effective mass $\sim 3m_e$ would compress the energy scale, increasing the number of experimentally observed levels in the STS range $\pm0.5$ V. The temperature broadening at 80 K is ˜7 meV, so the levels are likely too closely spaced to be experimentally resolved. Nevertheless, the energy scale of the observed spectral features (Fig. 3b) is in qualitative agreement with the experiment.

Next, we introduce a periodic potential $V(x, y)$ with magnitude $\mathrm{V_B}$ in the QB calculation, $-\frac{\hbar^2}{2m}\left[\Delta_{\mathrm{x,y}} + V(x, y)\right]\psi(x, y) = E\psi(x, y)$, to account for the periodic lattice distortion created by interaction of the top layer with the CCDW in the layer below. The results are shown in Column B of Fig. 4. Now the 2D pattern corresponding to the CCDW is tilted at 13° with respect to the ET edges, and the crystal axes. As expected, for a significantly large $V(\mathbf{r})$, the calculated integrated LDOS pattern follows the CCDW ordering at the center of the ETs quite well. The periodic potential also introduces a gap in the integrated LDOS which bears resemblance to the observed STS gap (Fig. 3). However, the calculation fails to reproduce the complex features and malleable nature of the integrated LDOS patterns at the edges. It also completely fails to reproduce the observed domain walls. (The predicted integrated LDOS patterns and spectra for the QB, and QB + V models are described in the Supplementary information).

Classical correlated electrons confined within an ET. A correlated electron model is needed to account for the malleable features in the electronic order within ETs. Within a chargelattice gas (CLG) Monte-Carlo (MC) calculation, classical point charges, subject to screened Coulomb repulsion can move via thermal hopping on an atomic lattice shaped in the form of an ET (Fig. 4c). A crucial parameter in the presented modeling is the filling, defined as the number of electrons divided by the number of lattice sites $f$. At various magic fillings, such as $f = \frac{1}{13}$ for the case of bulk 1T- $TaS_2$, the model predicts an electronic superlattice which is perfectly commensurate with the underlying atomic lattice [12]. Confining the system size to a small triangle inevitably introduces edge effects and distortions into the configurational ordering of electrons. This is simply due to the fact that a $\frac{1}{13}$ electronic lattice does not match the edges of the triangle as shown in Fig. 4c, requiring the particles to accommodate. (For more details concerning the model refer to the Supplementary information.) Here we outline the similarities between experimental observations and the simulated electronic configurations (Fig. 4, column C): (1) The model predicts the spontaneous formation of two chiralities of the 1/13 electronic lattice at angles ±13,9° with respect to the ET edges, which are both experimentally observed. In contrast to previous calculations where the external potential fixed the angle of the QI pattern, here it emerges as a nontrivial consequence of many-body correlations. (2) Smaller triangles induce stronger edge effects into the electron configuration, to the point of entirely breaking up the expected 1/13 electronic lattice. Electrons at the triangle's edge align with the edge and since the edges are close one to another, there is no room for a proper 1/13 lattice to emerge. The resulting configuration is still largely influenced by strong correlations, as electrons on average are $\sqrt{13}$ atomic lattice spacings apart. This is shown by the connecting lines in Fig. 4 (column C). (3) Edge effects in larger triangles are diminished towards the center, as shown for $l = 38a$ in Fig. 4 (column D), and the 1/13 Wigner
crystal lattice emerges. However, near the edges the electrons still align with the edge of the ET.

In the simple classical calculation above, all charges are equivalent and should ideally have the same LDOS and thus appear identical under a tunneling microscope. However, the experimental STM images show various irregular, elongated and triangular shapes within the triangles that are sometimes aligned in rows (e.g. Fig. 4) which such modeling cannot describe.

Quantum correlated electrons confined within an ET. For an understanding of the departures from the simple CLG model, we need to consider the itinerant correlated electrons which follow quantum billiard trajectories inside the triangle. To account for the interplay of the strong electronic repulsions and their itinerant nature we perform a quantum many-body calculation on small ET using the exact diagonalization of the spin-less fermions with the long-range interaction:

$$H = -t \sum_{\langle i,j \rangle} c_i^\dagger c_j + \sum_{i \neq j} V(|i-j|) \left[n_i - \bar{n}\right] \left[n_j - \bar{n}\right], \tag{1}$$

where $c_i\,(n_i)$ is the annihilation (density) operator at site $i, t$ is the hopping parameter, $(V(|i-j|))$ is the Yukawa interaction. To ensure charge neutrality, we have subtracted the uniform background charge density n (see Methods for details). While in the classical limit the relevant parameter is filling $N$, the quantum extension introduces another dimensionless parameter $t/V$ that governs the transition between the localized $(t/V = 0)$ and the delocalized regime $(t/V \gg 1)$. In agreement with the classical simulation, there exist special fillings where the electrons form commensurate fillings of the ET. Due to the size restrictions in the many-body simulation, we consider an ET with the lattice size $L = 8$ and the number of electrons $N = 10$ corresponding to the special filling f = 1/3, see Fig. 5a). In this commensurate situation, the state is extremely robust against the delocalization which can be observed by comparing the density distribution in the quantum $t/V = 0$ and the classical case $t/V = 0.01$,

see Fig. 5a). The analogous comparison of the density distribution for the incommensurate filling exhibits a strong redistribution of charges forming nontrivial QPI and their delocalization tendency is driven by lowering the kinetic energy via the closed loops QPI, see Fig. 5c, d.

As a more quantitative measure of the electron delocalization with respect to the classical limit we introduce the parameter $D = \sqrt{\Sigma_i \left[\langle n_i \rangle - \langle n_i \rangle^{t=0}\right]^2}$. A comparison for different fillings shows that incommensurate states ( $N \neq 10$ ) are orders of magnitude more susceptible to delocalization than commensurate ones (Fig. 5e). The geometrical constrains of ET can therefore dramatically shift the delocalization transitions and this resolves the apparent contradiction how we can observe delocalized QPI patterns in small structures while the corresponding bulk situation would be localized.

In larger ETs, electron trajectories are modified by correlations within the center, and boundary conditions at the barriers which cannot be understood solely on the basis of semi-classical correlated polaron packing, or free-electron QB. However, correlated electron modeling quite successfully predicts the appearance of domain walls in the CCDW structure forced by the confinement, which cannot be explained by any free-electron QB model. The observation of mirrored, but slightly different QPI patterns within ETs of the same size reveals that the QPI patterns are emergent, self-organized many-body electronic states. The fact that very small changes in geometry and/or barely perceptible imperfections on the atomic level give rise to dramatic changes of the QPI patterns is consistent with chaotic behavior. However, the imperfections in the ET construction (Fig. 1) are expected to change the detailed QI patterns, but not the observed generic features. We showed that for special fillings the system is robust toward these small imperfections, and it would be interesting to understand the implications of these correlations on the many-body spectrum and the time-evolution in light of recently observed many-body scars in quantum simulators [11,34]. The understanding of behavior and interaction of itinerant electrons with correlation-localized polarons in intertwined textures opens the way to microscopic electronics devices with correlated quantum materials. Moreover, the intertwined orders visible in the ET QPI patterns may help in understanding quantum materials in which a coexistence of itinerant and polaronic correlation-localized carriers is observed, reconciling the seeming dichotomy of different experiments that observe itinerant states (e.g. ARPES, quantum oscillations [35] ) and localized states (e.g. optics [36,37], STM [38] ) within the same material under seemingly identical conditions.

## 23.1 SM

### SM 1. Experimental details

The transformation was performed directly within the UHV chamber of an Omicron Nanoprobe LT STM as shown schematically in Supplementary Figure 1. We use an amplified 800 nm Ti:sapphire laser at a repetition rate of 100kHz to induce the single-layer transformation in the sample. The Gaussian laser pulses have a duration of 40 fs and peak fluence of up to 12 mJ/cm2. An optical microscope and a vertical SEM microscope are used for alignment and wide area search on the sample respectively.

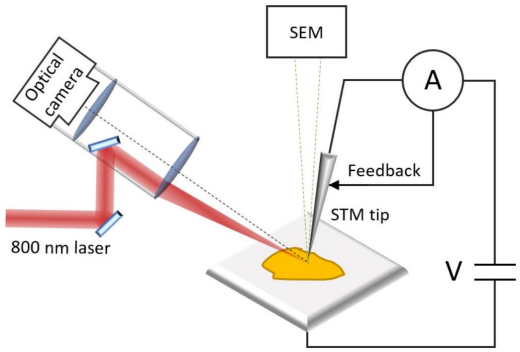


Supplementary Figure 1. Schematic representation of the experimental apparatus. Above the scanning tunneling microscope (STM) we have a scanning electron microscope (SEM) which enables us precise tip positioning on the sample. At the side of the STM there is a quartz window, through which we introduce the laser pulses. In case of imaging, we use the constant current mode, with the feedback controlling the height of the tip. For the I-V curves, the feedback is turned off.

Unlike with UHV in-situ thermal conversion [1], the laser transformation process results in triangular domain formation required for this study. The properties of single polytype transformed layers of $1H - TaS_2$ on $1\ T - TaS_2$ were reported previously [2]. The conditions for creating triangles are found to be very delicate. The transformed areas vary between the experiments. In some cases, we observe the transformation of the full layer, leading to the temperature-dependent interference patterns between the top two layers [2]. In other cases, the surface is only partially transformed, with the ratio of the transformed area with respect to the observed area of the sample ranging anywhere between 0 and 1 . This ratio not only varies between the experiments, but also between different areas of the laser exposure. We succeeded in producing the desired ETs of different sizes only 3 times out of about 20 attempts, in each case the transformed spot was scanned in multiple positions.

## SM 2. Raw STM images and ET dimensions.

Here we show the full images from which the triangles in the main text are taken. Among the large number of observed triangles, we have specifically chosen a few to show in the main text, paying attention to show the most representative examples. The triangles in the main paper thus cover various sizes of the triangles, which show different ordering patterns. In the main text we only discuss the perfect equilateral triangles, even though the 1T/1H areas that are created using the laser pulse cover many more possible shapes, which are discussed in the Supplementary Note 3.

The dimensions of the triangles are presented in Table 1 in terms of nanometers and the number of unit cells ( $l$ is given both in terms of 1T and 2H polytype unit cell dimensions for comparison.).

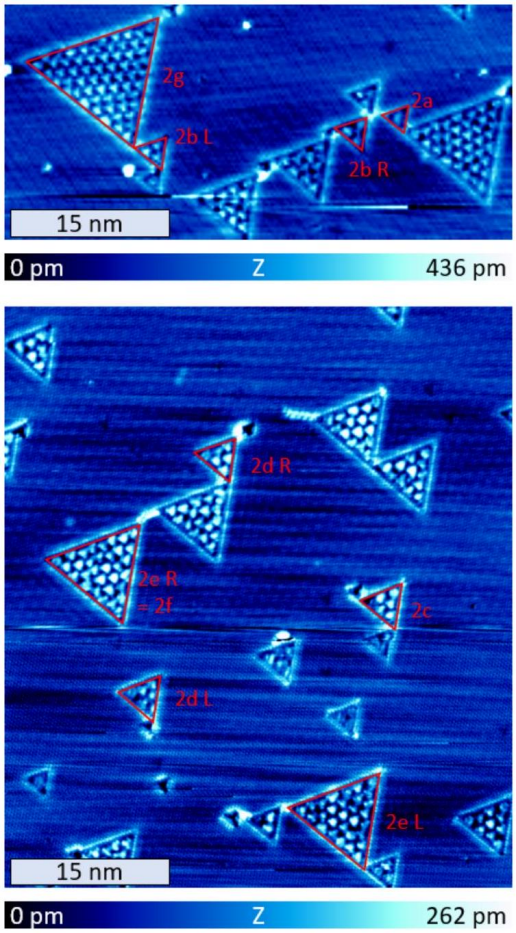


Supplementary Figure 2: Raw STM data. STM scans of the small triangular 1T areas embedded within a large 1H area. Red triangles mark the triangles that are presented in the main text.

| | $l$( nm) | No. of 1T unit cells | No. of 2H unit cells |
|---|---|---|---|
| 2a | 2.69 | 8.02 | 8.09 |
| 2b R | 3.36 | 9.99 | 10.08 |
| 2b L | 3.36 | 9.99 | 10.08 |
| 2c | 4.32 | 12.86 | 12.98 |
| 2d R | 4.37 | 13.01 | 13.13 |
| 2d L | 4.37 | 13.01 | 13.13 |
| 2e R | 9.46 | 28.15 | 28.40 |
| 2e L | 9.36 | 27.85 | 28.10 |
| 2f | 13.02 | 38.74 | 39.09 |

Supplementary Table 1. ET size measurements $l$ of the triangles presented in Figure 2 of the main text.

**SM 3. Areas of different shapes and larger 1T areas.**

Both 1 T and 1 H polytypes have a triangular lattice symmetry and it is only natural that the borders between the polytypes within a single layer will take on 60 and 120 degree angles. This, however does not limit the structures only to triangles, which are extensively discussed in the main text, but allows also for countless possibilities of zig-zag borders and shapes that

are seemingly composed of many triangles. The 1T regions can be very small (triangles of only a few atoms on the side), to very large, covering most of the surface with only an occasional 1H triangle. In the very large 1T regions, where the borders do not anymore have a significant effect, we see that the electron ordering mostly resembles that of the top surface in a bulk material (C state or photoinduced H state). We have focused our modelling only on the perfect equilateral triangles for two main reasons. Firstly, the more complex shapes are usually larger and the borders do not have a significant effect and are thus less interesting for a theoretical analysis. Secondly, the borders of arbitrary shapes are increasingly difficult to model with each additional considered shape, while the triangles represent a clean toy model.

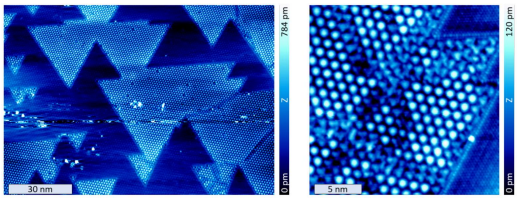


Supplementary Figure 3. STM scans of the large 1T areas intermixed with large 1H areas. Left image shows the 1T polytype in the commensurate state at 80 K, while the right image shows it in the photoinduced hidden state at 4 K. In both cases we can see the disordered polarons appearing especially in the corners.

## SM 4. STM measurements below 75K.

The bulk $2H-TaS_2$ has a CDW transition temperature at 75 K[3], but the transition temperature to the CDW state in the single layer $1H$ phase is not completely clear. In a previous STM tip switching report, the CDW in single transformed $1H$ layer was not seen at temperatures as low as 6.5 K[4]. This could either be due to the poor tip resolution or inappropriate scanning conditions (the $3 \times 3$CDW is weak and the authors have likely optimized the tip conditions to have the best signal from the investigated 1T polytype, rather than from 1H, which in their case was just a byproduct). Another very likely possibility is that the $3 \times 3$ CDW does not appear in the small confined areas. This is however not discussed in their paper, as the transformed part was only found as a byproduct of electronic switching to the hidden state. We have performed the top layer 1T->1H transformation also at 4 K, where we were able to observe the $3 \times 3$ CDW modulation in the top 1H layer, however it was much weaker than the modulation in the 1T polytype and not easily observed everywhere. In either case the appearance (or absence) of the CDW in the 1H layer does not seem to influence the electronic ordering within the triangles.

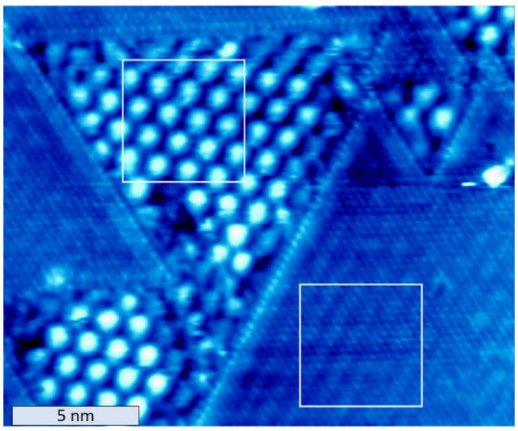


86 pm

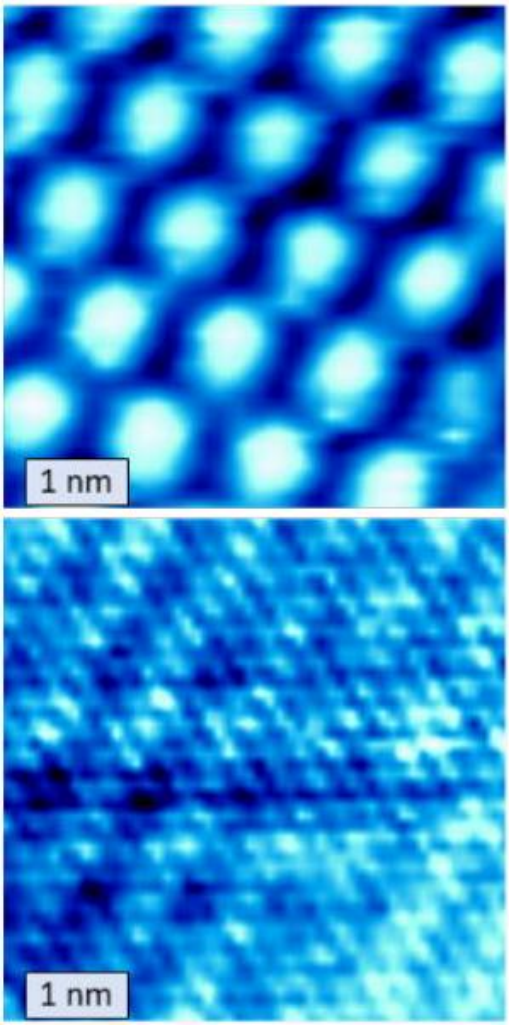


EQGIN NNATICA

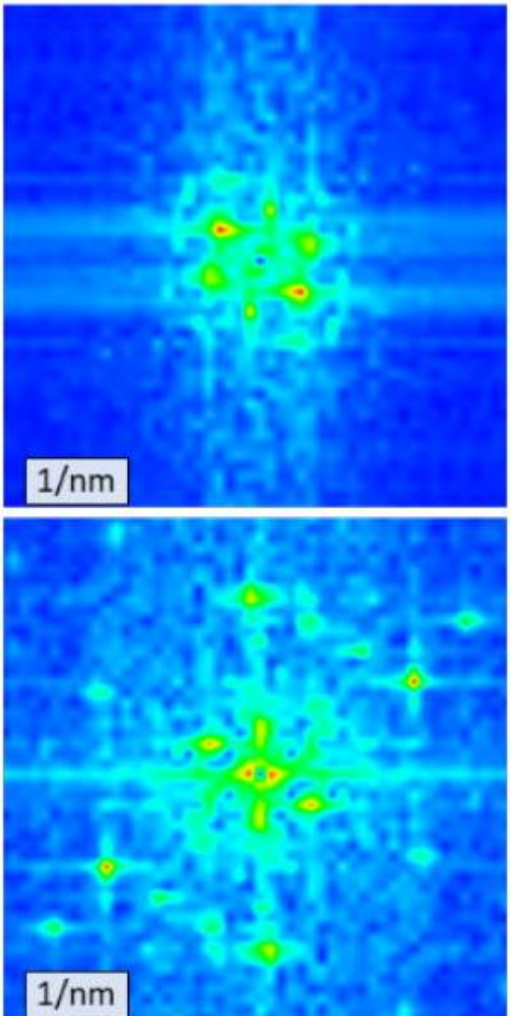


0 Z, Vnm 0.0290 Z, Vnm 0.067

Supplementary Figure 4. Mixture of **1T** and **1H** polytypes at **4 K**. (left) We can see both the $\sqrt{\mathbf{13}} \times \sqrt{\mathbf{13}}$CDW in the 1T polytype and the $\mathbf{3} \times \mathbf{3}$CDW in the 1H polytype. The images in the middle show the zoomed in region of the 1T (top) and 1H (bottom) polytype. The images on the left show their respective FFTs.

## SM 5. STM imaging at different bias voltages

With changing the bias voltage for STM imaging, we can make different features in the material better visible. Here we show a few different cases of STM imaging on the border between the 1T and 1H polytype. In the 1H regions (bottom right in all three images in Supplementary Figure 5 and top left in all 4 images in Supplementary Figure 6) we see that the CDW in the C state from the bottom 1T layers is in general the best visible at slightly positive voltages. More precisely, we see that the commensurate CDW from the bottom 1T layers is best seen at +0.1 V. In the 1T region (top left in all three images in Supplementary Figure 5 and bottom right in all 4 images in Supplementary Figure 6), the best way to observe individual polarons is to scan at voltages below -0.5 V. For the best contrast when scanning the 1T polytype, we use the bias voltage of -0.8 V (most of the figures in this paper were indeed taken at -0.8 V ). When changing the voltage towards zero, the relative contribution of the bands in the polarons gets lower and certain features become more pronounced. This shows as the shapes of polarons slightly change and sometimes other modulations become visible. In Supplementary Figure 5. we can see that some polarons become brighter and that there

are additional states between the polarons that get much better visible at voltages close to zero. In Supplementary Figure 6, we see that only certain regions of the 1T polytype become highlighted at very low voltages.

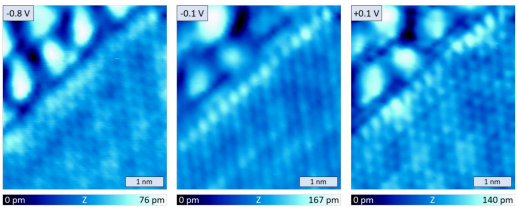


Supplementary Figure 5. Constant current STM scans of the border between the **1*T*** and **1*H*** polytypes at different voltages. We can see that in the 1T polytype, different polarons are brighter at different voltages. In 1H polytype, we can see that the CDW from the bottom 1T layer is best visible at +0.1V.

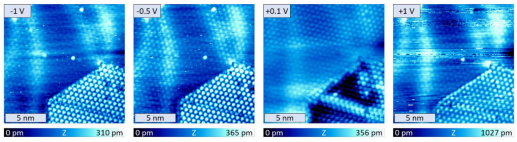


Supplementary Figure 6. Border between 1H and 1T polytype. In this case the surface was fully transformed to 1H polytype and only a small 1T part was later reversely transformed by the STM tip [2]. The stripes on the 1H polytype appear in very large transformed regions due to the mismatch between the lattice unit cells. Same as in Supplementary Figure 5, we can see that the bottom layer CDW is the best seen through the 1H layer at 0.1 V. In the 1T region, we can see that slightly positive voltages make domain walls stand out.

## SM 6. Interlayer stacking

At certain bias voltages (typically within 0.1 V around zero or slightly above that) we can very clearly see the CDW modulation from the untransformed 1T polytype bottom layers, (Supplementary Figure 5 and 6). Due to the fact that we can "see through" one single 1H layer, we directly uncover the interlayer stacking of the CDW in the z-direction, by comparing the positions of the polarons in the bottom layer with the positions of polarons in the top layer. The stacking is found to be both indirect (with the polarons not directly above each other in the neighboring layers, shown in Supplementary Figure 7a) and direct (with the polarons directly above each other, shown in Supplementary Figure 7b). We attribute the stacking to the parameters such as pinning impurities, which depend on the sample growth conditions and we cannot directly and controllably repeat. It is worth mentioning that when transforming one (or more) of the layers to the textured hidden state, the stacking varies if the domain walls are not directly above each other, which was found to be the case. We clearly see this from Figure 5c in the paper by Ma et. al [4], where they induced a single triangle within a larger area of the metallic textured hidden state of the 1T polytype. In the image, we see the top two layers of the hidden state with variable vertical stacking of polarons. Furthermore, when we observe various domains of different chirality, this necessarily leads to the misalignment of the polarons between the layers, except for the special case, where the domain in the bottom layer is exactly the same as the one in the top layer, which is extremely unlikely.

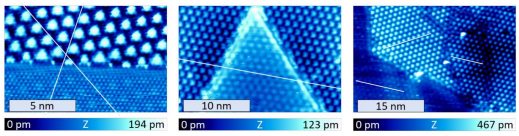


Supplementary Figure 7. The polaronic modulation of the bottom $1T$ C phase. a) The polarons are not vertically above each other and b) the polarons are vertically stacked above each other. In c) we show domains of different chirality in the top layer, while the bottom layer likely has only one ordering. The white lines are aligned with the polarons and serve as a guide to the eye.

## SM 7. Band structure of the 1T/1H monolayer junction.

The band alignment diagram of the 1T/1H junction at T = 77 K, assuming on spatially homogeneous metal-semiconductor junction, is shown in Supplementary Figure 8a. (For the sake of argument, we assume that the initial band structure of $1\mathrm{H}-\mathrm{TaS}_2$ is the same as $2\mathrm{H}-\mathrm{TaS}_2$.) At this temperature, the $1\mathrm{H}-\mathrm{TaS}_2$ is above its ordering temperature, and is assumed to be metallic like its parent 2H compound, while the 1T phase supports a charge density wave (since $T_{\mathrm{CCDW}\downarrow} = 140K$ ). Accordingly, the STM image (Supplementary Figure 8b) shows a uniform density on the 1H side, and a characteristic $\sqrt{13}\times\sqrt{13}$ charge modulation on the 1T side.

The edge state. The work function $\phi$ for 1 $\mathrm{T}-\mathrm{TaS}_2$ is larger than for $2\mathrm{H}-\mathrm{TaS}_2$, $\phi_{2H-TaS_2} < \phi_{1T-TaS_2}$, so electron injection from the 1H-TaS $_2$ metal into the 1T semiconductor can take place, and the junction is expected to be ohmic. Due to the fact that $\phi_{1T-TaS2} - \phi_{2H-TaS_2} < \Delta/2$, where $\Delta$ is the gap in 1T- $\mathrm{TaS}_2$, upon the alignment of the Fermi levels, the charge carriers in the conduction band of the 1T-TaS $_2$ form a 'pocket' of width $w$ (orange), which implies the formation of a charged edge state along the boundary. The width of the resulting metallic wire $w$ is related to the screening length. Note that the edge state is susceptible to self-organization of charge. On a phenomenological level, the boundary presents an effective confining potential barrier $\Phi_B \simeq \Delta/2$ for electrons on the $1\ \mathrm{T}-\mathrm{TaS}_2$ side.

The STM image shown in Supplementary Figure 8b clearly reveals the presence of the edge state along the 1T/1H boundary, with a width $w = 0.5 \sim 1$ nm, consistent with previous observations by STM at the boundary of the gapped C phase and the metallic phase of 1T-$\mathrm{TaS}_2$ (see for example paper by Ma et al. [4] ). The charge density wave order in the 1T state appears to be unperturbed beyond ˜ 1.5 nm from the interface. At the edge, on the 1T side, the $\sqrt{13}\times\sqrt{13}$ commensurate CDW pattern appears distorted by the presence of the boundary, which is at an angle of 13.5 degrees with respect to the CCDW charge ordering vector.

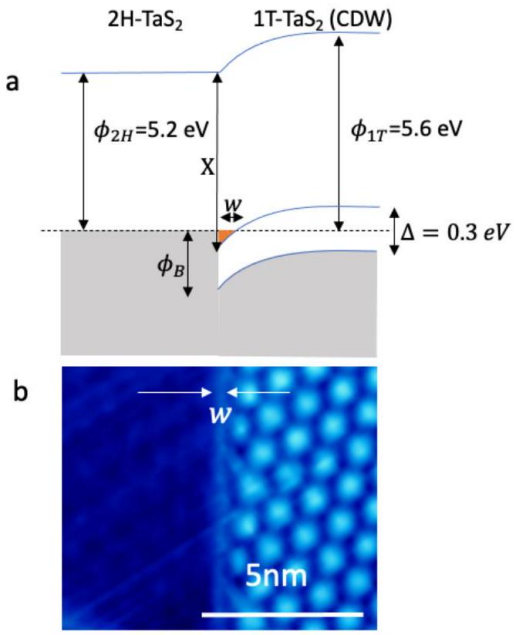


Supplementary Figure 8. The in-plane line boundary between semiconducting 1T-TaS $_2$ and metallic 1H-$\mathbf{TaS_2}$ at 77 K. a) Schematic diagram of a metal-semiconductor ohmic contact. b) An STM image showing the edge state of width $\boldsymbol{w}$ on the boundary of the 1T and 1H monolayers.

Supplementary note 8. A quantum billiard with a CDW potential (QB+V model): model prediction of the observed salient features.

The QB calculation entails the solving of the Schrödinger equation $-\frac{\hbar^2}{2m}[\Delta_{\mathrm{x,y}}+V(x,y)]\psi(x,y)=E\psi(x,y)$ with Dirichlet boundary conditions in the shape of an ET either for free particles (noninteracting single-electron billiards, V = 0 ), or with an underlying 2D potential $V(\boldsymbol{r})$, imposed by interaction with the CDW in the layer below of the form: $\rho(\boldsymbol{r})=e^{i\boldsymbol{q}_1\cdot\boldsymbol{r}}+e^{i\boldsymbol{q}_2\cdot\boldsymbol{r}}+e^{i\boldsymbol{q}_1\cdot\boldsymbol{r}}$, where $\boldsymbol{q_i}$ are the CDW wavevectors, at an angle of $\pi/3$ to each other. The CDW is rotated with respect to the crystal lattice (and edges of the ET) by $\phi=13°$, corresponding to the $\sqrt{13}\times\sqrt{13}$CCDW, where $\frac{2\pi}{\boldsymbol{q}_1}=3\boldsymbol{a}+\boldsymbol{b}$, as shown in Figure 1 of the main text. Thus $V(x,y)=-V_0 Re\left[\rho\left(\boldsymbol{r}'\right)\right]$, where $\boldsymbol{r}'=\begin{pmatrix}\cos\phi & -\sin\phi\\ \sin\phi & \cos\phi\end{pmatrix}\binom{x}{y}$, to take into account the rotation of the CDW.

The solutions of the QB + V model are shown in Figure 4 of the main paper and in the Supplementary Figures 8 and 9.

The dependence on the potential. The dependence on $|V_0|$ in units of $t\left(\frac{\hbar^2}{2m}=1\right)$ is shown in Supplementary Figure 9, ranging from $|V_0|=0$ to 5t. Note the appearance of a 13 degree twist of the QI pattern at $|V_0|=t$ which becomes more pronounced with increasing $V_0$.

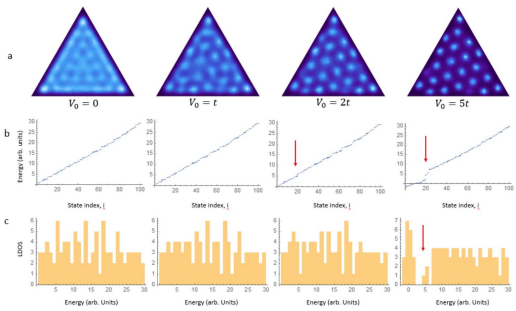


Supplementary Figure 9. Model calculations of spatial probability density, energy as a function of state index and LDOS spectrum showing a gap. A calculation of the QB+V model for different values of $|\boldsymbol{V_0}| = \mathbf{0} \ldots \mathbf{5}\boldsymbol{t}$. a) a plot of the eigenfunctions $\boldsymbol{\Sigma_i} \left|\boldsymbol{\psi_i}\right|^{\mathbf{2}}$ within the ET where $\boldsymbol{N} = \mathbf{1} \ldots \mathbf{32}$, and $\boldsymbol{N} = \mathbf{32}$. The twist in the pattern is clearly visible with increasing $\boldsymbol{V_0}$. b) The eigenstate energy $\boldsymbol{E_i}$ as a function of $\boldsymbol{i}$ for different values of $|\boldsymbol{V_0}|$. The gap for t/V>0.5 is indicated by the arrow. c) the LDOS as a function of energy $\boldsymbol{E}$ for different values of $|\boldsymbol{V_0}|$.

In Supplementary Figure 9b we plot the state energies $E_i$ as a function of state index $i$, and in Supplementary Figure 9c we plot the local density of states (LDOS), presented with states binned together in the form of a histogram. With increasing $V_0$, as expected, the periodic potential creates a gap in the spectrum (shown by the arrow). It is perhaps surprising that a rotation of the QPI pattern is seen already for $V_0 = t$, while a clear gap in the LDOS appears only for much larger values of $V_0 = 5$ (arrow). A jump in the state energy as a function of $i$ is visible already at $2t$, but there are other jumps at higher energies which are hard to distinguish from the fundamental gap.

QI pattern of states below the gap. In Supplementary Figure 10 we plot the LDOS spatial pattern $\Sigma_{i=1\ldots N} \left|\psi_i\right|^2$ summing up to different values of $N$ to show the QI pattern for states that appear below and above the external CDW-induced gap. The LDOS is plotted in the insert, indicating the centre of the gap at state index $i = 5$. Thus summing up the eigenstates up to $N = 5$, we can plot the states below the gap that contribute to the QI pattern. Clearly the dominant pattern is already visible, but some spots are missing around the edges, which clearly have higher energy. Understandably, higher energy (shorter wavelength) states are necessary to fill in the space around the boundary. For $N = 32$, the LDOS spatial pattern fills all available space. With $N = 49$, no additional features are observed.

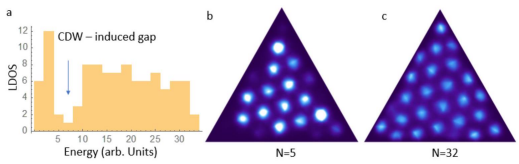


Supplementary Figure 10. Gap in the LDOS and associated probability density plots. A plot of the LDOS $\sim \boldsymbol{\Sigma_{i=1\ldots N}} \mid \boldsymbol{\psi_i}|^{\mathbf{2}}$ for different values of N, as indicated in the plots, and $V = -10$. The insert shows the LDOS as a function of energy with a clearly visible gap in the spectrum.

The QI patterns for different levels, and effective mass. The presented STM images in the main text are measured at $V = 0.8V$. Let us roughly estimate the relevant range of eigenvalue index for a voltage range up to 0.8 eV . Using $N = \sqrt{\frac{2m^* El^2}{\hbar^2 \pi^2}}$, and assuming $m^* = m_e$, for the smallest triangle ($l = 8a = 2.64nm$), we obtain $N \approx 4$. For larger triangles, $l = 10a, N \approx 5$; for $l = 27a, N \approx 13$; and for $l = 38a, N \approx 18$. Taking into account electron-phonon coupling and polaronic effects, the effective mass may be increased. Using $m^* \simeq 4m_e$, this compresses

the energy scale a factor of ˜2. At low temperature, and in the absence of scattering and interactions of the tunneling interactions with phonons, a single eigenstate is expected to be observed in the smallest triangles (in agreement with QI pattern shown in Figure 2a of the main text).

### SM 9. Confined correlated electrons in the classical limit

To simulate charges on a discrete lattice in the shape of an equilateral triangle, we assume a sceened Coulomb repulsion between charges as well as open boundary conditions at the edges of a triangle. In order to satisfy electroneutrality, the following Hamiltonian is employed (Vodeb et al, 2019, Karpov and Brazovskii, 2018):

$$\mathcal{H} = \frac{1}{2}\sum_{i,j}^{N} V'(i,j)\left(n_i - \bar{n}\right)\left(n_j - \bar{n}\right), \tag{1}$$

where $V'(i,j) = \exp\left(-r_{i,j}/r_s\right)/r_{i,j}, r_s$ is the screening radius (4,5 lattice spacings) $r_{i,j} = r_i - r_j, r_i$ is the $i$-th out of $N$ lattice sites, $n_i$ is the occupation number of lattice site $i$, the sum runs over all lattice sites and $\bar{n} = \sum_i^N n_i/N.\bar{n}$ represents the interaction of each charge with underlying uniformly and oppositely charged plate. Only here the plate is represented by uniformly charged lattice sites on which the charges can reside. The lattice sites form a triangular lattice in the shape of an equilateral triangle. $\mathcal{H}$ can be simplified to:

$$\mathcal{H} = \sum_{i,j}^{N} V(i,j) n_i n_j, \tag{2}$$

where $V(i,j) = \frac{1}{2}V'(i,j) - \frac{1}{2N}\sum_k^N \left(V'(i,k) + V'(k,j)\right) + \frac{1}{2N^2}\sum_{k,l}^N V'(k,l)$. With this simplified version we simulated a fixed number of charges on differently sized triangles. The classical Monte Carlo method used has been described previously [5]. Since we were interested in what happens in the vicinity of the $f$ = number of charges $/N = 1/13$ state, we initialized all the simulations in the $1/13$ state. The main features predicted by the model are shown in the main text.

# 24 Band insulator to Mott insulator transition in a bilayer Hubbard model by Kancharla, Okamoto

(one paper about shifting of layers was telling me that this is the best paper for this transition from band model to Mott's model)

**Abstract**

The ground state phase diagram of the half-filled repulsive Hubbard model in a bilayer is investigated using cluster dynamical mean field theory. For weak to intermediate values of Coulomb repulsion $U$, the system undergoes a transition from a Mott insulating phase to a metallic phase and then onto a band insulating phase as the interlayer hopping is increased. In the strong coupling case, the model exhibits a direct crossover from a Mott insulating phase to a band insulating phase. These results are robust with respect to the presence or absence of magnetic order.

## 24.1 Article

Strong Coulomb interaction can localize electrons even in the absence of disorder to give rise to a gapped electronic state known as the Mott insulator. This state is of tremendous interest because upon addition of carriers it produces high temperature superconductivity and intriguing features such as a pseudogap in the normal state of the cuprates. Band insulators, on the other hand, lack the ability to conduct because they have either a filled or an empty band. The topic of transitions between band and Mott insulators has received considerable attention recently[7, 6, 5, 3, 1, 2, 4], because it provides a useful tool to understand the fundamental differences between the two states. Recent progress in the control of Fermionic atoms trapped in optical lattices adds to the experimental interest as it would be feasible to investigate the evolution of correlated ground states in a many body system. In a recent study, it was shown that the ground state of a Mott-insulating Haldane phase in a generalized Hubbard ladder can be connected *adiabatically* to a band insulating phase[8]. On the other hand, studies of the two dimensional ionic Hubbard model (IHM), which contains an alternating local potential $\pm\Delta$ on the A or B sublattice, find an intervening phase between the band and Mott insulating phases rather than a continuous evolution when the Coulomb repulsion is varied. Cluster dynamical mean field theory (CDMFT) calculations for the IHM at zero temperature suggest that the intervening phase is a bond-ordered insulator[7] whereas finite temperature Quantum Monte Carlo techniques propose it to be a metal[6].

Another theoretical model for the study of the band to Mott insulator crossover is the bilayer Hubbard model (BHM). The presence of copper-oxide bilayers, well described by doped Hubbard planes, in many of the high-$T_c$ materials adds to the practical importance of studying the bilayer Mott system theoretically. The BHM was studied recently using Dynamical mean field theory (DMFT),[5] and a smooth crossover between band and Mott insulators was observed. Since this study dealt with the infinite dimensional lattice, intralayer spatial correlations are absent. As a two-dimensional Hubbard model exhibits fundamentally different behavior from the infinite-dimensional Hubbard model, such as a pseudogap[9] and $d$-wave superconductivity[10] upon doping, a study incorporating the two-dimensional nature of the Hubbard planes in the BHM is expected to show richer physics.

In this work, we study the evolution of an antiferromagnetic (AF) Mott insulator into a band insulator as the interlayer hopping is varied in a bilayer Hubbard model at half-filling using cluster dynamical mean field theory[11]. With interplane hopping set to $t_\perp$, the Hamiltonian for the bilayer Hubbard model can be written as

$$\begin{aligned} H &= -t \sum_{\langle ij\rangle\sigma\alpha} \left( c^\dagger_{i\sigma\alpha} c_{j\sigma\alpha} + H.c. \right) + U \sum_{i\alpha} n_{i\downarrow\alpha} n_{i\uparrow\alpha} \\ &\quad -t_\perp \sum_{i\sigma\alpha} c^\dagger_{i\sigma\alpha} c_{i\sigma(1-\alpha)}. \end{aligned} \tag{24.1}$$

Here $\alpha = 0, 1$ labels the two Hubbard planes and $U$ represents the onsite Coulomb repulsion. $c_{i\sigma\alpha}$ denotes the destruction operator at site $i$, with spin $\sigma$ and on plane $\alpha$. Chemical potential is chosen as $\mu = U/2$ so that the density is fixed to unity. In the limit $U \to 0$, it can be seen that the system goes from an uncorrelated metal to a band insulator at $t_\perp = 4t$ when the splitting between the bonding and antibonding bands produced by the two layers results in a finite gap. At large $U$ and $t_\perp \to 0$, the system decouples into two Hubbard systems with a finite Mott gap and AF long range order in each layer.

In the recent study on the infinite-dimensional BHM, the two-plane system was reduced to two impurities embedded in a self-consistently determined bath[5]. For $t_\perp = 0$ the authors found a phase transition at $U = U_c$ from a metallic phase to a Mott insulating phase. As $t_\perp$ is switched on, the Mott insulator (MI) evolves continuously into a band insulator (BI) with no sign of a

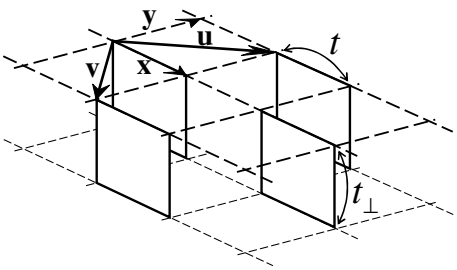


Figure 24.1: Tiling the infinite bilayer with a $2 \times 2$ cluster

phase transition. In what follows, we shall argue that in-plane spatial correlations provide a competing energy scale that is missing in the infinite dimension. Taking both intraplane and interplane spatial correlations into account within CDMFT we find that for $U < 8t$ as $t_\perp$ is increased from zero the MI goes through a metallic phase before entering a band insulating phase. For larger values of $U$, the system undergoes a direct crossover from a MI to a BI without an intervening metallic phase.

CDMFT is a non-perturbative technique where the full many-body problem is mapped onto local degrees of freedom treated exactly within a finite cluster that is embedded in a self-consistent bath[11, 12]. It is a natural generalization of single-site DMFT[13] to incorporate spatial correlations. The method has passed rigorous tests for the 1D Hubbard model where it compares well to exact solutions[14] and has been applied to a variety of problems[9, 10]. The first step in the CDMFT method involves a tiling of the infinite lattice by a finite cluster. As seen in Fig. 24.1, we consider a $2 \times 2$ tiling cluster which includes both the in-plane and interplane hopping processes with a unit cell defined by the vectors $\mathbf{u} = \mathbf{x} + \mathbf{y}$ and $\mathbf{v} = \mathbf{x} - \mathbf{y}$. Using CDMFT, the BHM on the infinite lattice reduces to the cluster-bath Hamiltonian below, that is subject to a self-consistency condition:

$$\begin{aligned} H_c &= \sum_{\langle\mu\nu\rangle\sigma} t_{\mu\nu}\left(c^\dagger_{\mu\sigma}c_{\nu\sigma} + H.c.\right) + U\sum_{\mu} n_{\mu\uparrow}n_{\mu\downarrow} \\ &+ \sum_{m\sigma}\epsilon_{m\sigma}a^\dagger_{m\sigma}a_{m\sigma} + \sum_{m\mu\sigma} V_{m\mu\sigma}(a^\dagger_{m\sigma}c_{\mu\sigma} + H.c). \end{aligned} \tag{24.2}$$

Here, $\mu, \nu = 1, \cdots, N_c$ denote indices labeling the cluster sites and $m = 1, \cdots, N_b$ represent those in the bath. The self-consistent calculation proceeds by an initial guess for the cluster-bath hybridization $V_{m\mu\sigma}$ and the bath site energies $\epsilon_{m\sigma}$ to obtain the cluster Green's function $G_c^{\mu\nu}$. Applying the Dyson's equation, $\mathbf{\Sigma}_c = \mathbf{G}_0^{-1} - \mathbf{G}_c^{-1}$, where $\mathbf{G}_0$ denotes the non-interacting Green's function for the Hamiltonian in Eq. (24.2), the cluster self-energy is obtained. $\mathbf{\Sigma}_c$ is then used in the self-consistency condition below to determine the local Green's function for the lattice:

$$\mathbf{G}_{loc}(z) = \frac{N_c}{2\pi^2}\int d\mathbf{P_u}d\mathbf{P_v}\frac{1}{z + \mu - t(\mathbf{P_u}, \mathbf{P_v}) - \mathbf{\Sigma}_c(z)} \tag{24.3}$$

Here, $\mathbf{P_u}$ and $\mathbf{P_v}$ denote reciprocal lattice vectors conjugate to the spatial unit vectors $\mathbf{u}$ and $\mathbf{v}$ respectively, while $z = i\omega_n$ is the Fermionic Mastubara frequency. $\mathbf{G}_{loc}$ can be used to obtain a new Weiss field, $\mathbf{G}_0$, and consequently, a new set of $V_{m\mu\sigma}$ and $\epsilon_{m\sigma}$'s by means of a conjugate gradient minimization program to close the iterative loop. In this work, the Lanczos method is used to solve the cluster-bath Hamiltonian and we fix the bath size to $N_b = 8$. The Lanczos method can access both the strong and weak coupling regimes with equal ease and it is well suited to compute dynamical quantities directly in real frequency. Rotational symmetries of the cluster on a square lattice, together with particle-hole symmetry at half-filling, reduce the number of bath parameters significantly. These bath parameters can depend on spin, allowing for symmetry breaking solutions. For details of the method, we refer to earlier work[11, 14].

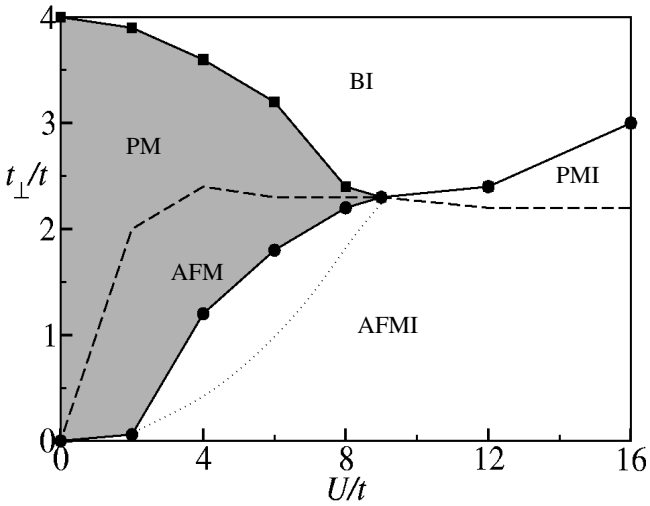


Figure 24.2: Phase diagram for bilayer Hubbard model. Shaded portion shows the extent of the metallic region (paramagnetic metal (PM) and antiferromagnetic metal (AFM)) in the presence of magnetic order. Dashed line showing the magnetic phase boundary extends into the insulating region separating the paramagnetic Mott insulator (PMI) from the antiferromagnetic Mott insulator (AFMI). Suppression of magnetic order extends the metallic phase down to lower $t_\perp$ shown by the dotted curve.

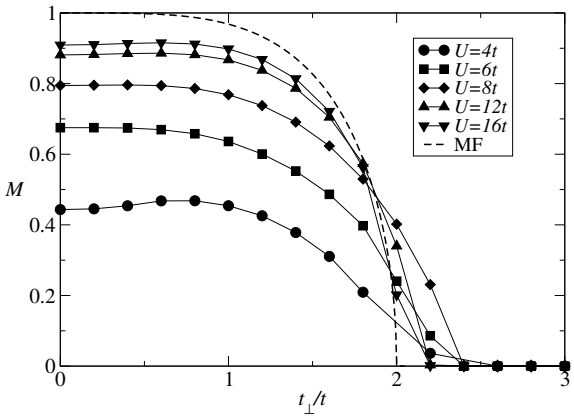


Figure 24.3: Staggered magnetization a function of $t_\perp$ for $U = 4t, 6t, 8t, 12t, 16t$

Let us start from the phase diagram with suppression of the magnetic order. Numerical results are shown in Fig. 24.2. We observe three states; a Mott insulating state at large $U$, a band insulating state at large $t_\perp$, and a metallic state in between. At $U = 0$, the BI and the metallic states are separated at $t_\perp = 4$ where the bonding and antibonding bands are separated. Critical $t_\perp$ decreases with increasing $U$ because the width of bonding and antibonding bands broaden due to correlation. Above $U = 12$, the BI and the MI states are adiabatically connected, but by close inspection of the charge gap, two regions are distinguishable; in the MI (BI) phase, $\Delta_c$ decreases (increases) with increasing $t_\perp$. Those features are consistent with the DMFT result on the infinite-dimensional BHM. In contrast to the infinite-dimensional case, the MI state extends down to small $U$ and $t_\perp$ in the two-dimensional case because of the intralayer spatial correlation, and the system passes through two phase transitions when increasing $t_\perp$ at $0 < U < 12$. Thus, the two-dimensional BHM provides topologically distinct behavior as compared to the infinite-dimensional one. As will be discussed in detail below, this essential feature is not altered even by including the magnetic ordering.

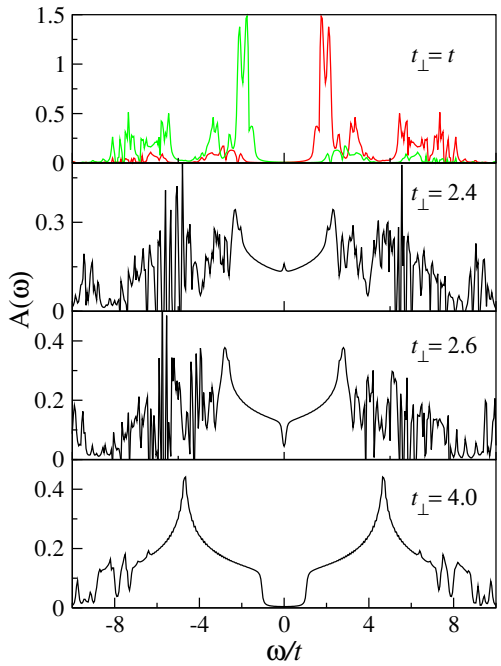


Figure 24.4: Local density of states as $t_\perp$ is varied at $U = 8t$. Spin-resolved density of states shown for $t_\perp = 1.0$ where magnetic order exists. Note the metallic state at $t_\perp = 2.4t$.

We next investigate the magnetic properties of the bilayer Hubbard model in detail. The staggered magnetization $M = n_\uparrow - n_\downarrow$ is plotted as the interplane hopping is varied in Fig. 24.3 for different values of $U$. At $t_\perp = 0$, the two planes are decoupled and the value of the staggered magnetization increases as $U$ is increased, but quickly saturates to a value below unity because of quantum fluctuations. With increasing $t_\perp$, $M$ stays fairly constant until $t_\perp = t$ and then drops rapidly to zero at about $t_\perp = 2t$. This value of $t_\perp = 2t$ is universal and does not depend on $U$ for all $U > 8t$. The vanishing of the staggered magnetization at small $U$ is caused by an increase in the effective bandwidth and a consequent reduction in the exchange coupling. In contrast, critical value $t_\perp \approx 2t$ at large $U$ is due to the instability toward the formation of a local singlet. In this limit, the BHM is reduced to the $S = 1/2$ Heisenberg model with the intralayer exchange $J = 4t^2/U$ and the interlayer exchange $J_\perp = 4t_\perp^2/U$. By taking a dimer on the interlayer bond as a unit and introducing a mean-field decoupling on the intralayer bonds, critical exchange coupling for the transition from a Néel ordered state to an interlayer dimerized state is obtained as $J_\perp = 4J$ at $T = 0$, thus, $t_\perp = 2t$. Staggered magnetization $M = 2\langle S_z \rangle$ at $t_\perp < 2t$ is also computed. As shown with a dashed line in Fig. 24.3, this mean-field approximation to the bilayer Heisenberg model gives reasonable agreement with CDMFT at large $U$.

Next, we look at the local density of states for the BHM as a function of $t_\perp$ at $U = 8t$ as shown in Fig. 24.4. As $t_\perp$ is increased the Mott gap reduces till it closes completely at $t_\perp = 2t$ to give rise to a metallic state. The LDOS shows a clear quasiparticle peak along with the lower and upper Hubbard bands characteristic of Mott physics at $t_\perp = 2.4t$. Upon further increase of $t_\perp$ we see that a gap opens abruptly to reveal a band insulating state. Increasing $t_\perp$ in the band insulating phase causes the charge gap to grow monotonously unlike the Mott insulating phase where it reduces to zero. In Fig. 24.5 we plot the double occupancy and the charge gap as a function of $t_\perp$ for different values of $U$. For $U < 8t$, as $t_\perp$ is increased in the Mott phase, the double occupancy rises and then shows a sharp kink as the system enters a metallic phase and also upon going into a band insulating phase. For larger values of $U$, as expected, the crossover from a Mott insulator to a band insulator is smooth with the double occupancy showing no

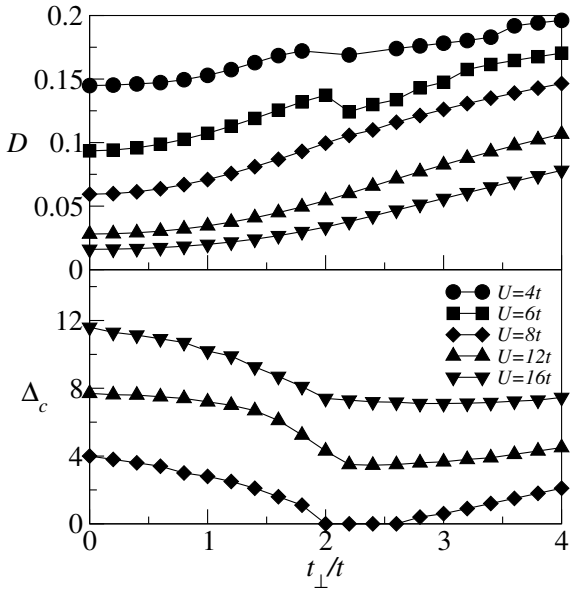


Figure 24.5: Double occupancy (top panel) and charge excitation gap (bottom) as functions of $t_\perp$ for various $U$ indicated.

signs of a kink. The charge gap for large $U$ shows a continuous decrease in the Mott phase but never goes to zero. The crossover to a band insulator around $t_\perp = 2t$ is easily identified by the increase in the charge gap with $t_\perp$.

The phase diagram for the bilayer Hubbard model that emerges for our calculation is shown in Fig. 24.2. We identify a region in the phase diagram which shows an intermediate metallic region, depicted by the shaded portion, which separates the band and Mott insulating phases. The width of the metallic region narrows with increasing $U$ and eventually for $U > 8t$ there is a direct crossover from a band insulator to a Mott insulator. The magnetic phase boundaries are depicted by the dashed line which separates a antiferromagnetic metal from a paramagnetic metal. In the insulating portion of the phase diagram the magnetic phase boundary separates the antiferromagnetic Mott insulator (AFMI) from a paramagnetic Mott insulator (PMI). As we discussed earlier, emergence of intermediate metallic region separating BI and MI is a generic behavior in two-dimensional BHM independent of magnetic ordering.

In summary, we have obtained the zero temperature phase diagram of the bilayer Hubbard model at half-filling using cluster dynamical mean field theory. We computed the double occupancy and the local density of states as a function of the interlayer coupling $t_\perp$ and the Coulomb repulsion $U$ to identify a clear demarcation between a Mott insulating phase and a band insulating phase as the interlayer coupling is varied. For weak to intermediate values of interaction ($U < 12t$), the Mott insulator at small $t_\perp$ is separated from the band insulator at large $t_\perp$ by an intermediate metallic phase. For $U > 12t$, there is a direct crossover from a Mott insulator to a band insulator as $t_\perp$ is increased. This crossover is most clearly manifest in the behavior of the charge gap which first reduces in the Mott phase with increasing $t_\perp$ and then increases in the band insulating phase. These results should be contrasted with the DMFT results for the infinite-dimensional model which always find a smooth crossover between the BI and MI states.[5] These differences arise due to the presence of in-plane spatial correlations in the two-dimensional model stabilizing a Mott phase for all $U$ at half-filling which is accessible by cluster DMFT. We completed the phase diagram by further allowing for magnetic order. The phase diagram is essentially unchanged, except that the onset of the metallic phase occurs at a larger value of $t_\perp$ for a fixed value of $U$.

S.S.K acknowledges discussions with Achim Rosch. S.S.K. is supported by the LDRD pro-

gram at Oak Ridge National Laboratory. This work is supported by the Division of Materials Sciences and Engineering, Office of Basic Energy Sciences, U.S. Department of Energy, under contract DE-AC05-00OR22725 with Oak Ridge National Laboratory, managed and operated by UT-Battelle, LLC.

## References

[1] A. P. Kampf, M. Sekania, G. I. Japaridze and P. Brune, J. Phys. Cond. Matter **15** 5895 (2003).

[2] S. R. Manmana, V. Meden, R. M. Noack and K. Schonhammer, Phys. Rev. B **70**, 155115 (2004).

[3] C. D. Batista and A. A. Aligia, Phys. Rev. Lett., **92**, 246405 (2004).

[4] A. Garg, H. R. Krishnamurthy and M. Randeria, Phys. Rev. Lett. 97, 046403 (2006).

[5] A. Fuhrmann, D. Heilmann, H. Monien, Phys. Rev. B **73**, 245118 (2006).

[6] N. Paris, K. Bouadim, F. Hebert, G.G. Batrouni and R.T. Scalettar, Phys. Rev. Lett. **98**, 046403 (2007).

[7] S. S. Kancharla and E. Dagotto, Phys. Rev. Lett. **98**, 016402 (2007).

[8] F. Anfuso and A. Rosch, arXiv:cond-mat/0609051 (2006)

[9] B. Kyung, S. S. Kancharla, D. Senechal, A.-M. S. Tremblay, M. Civelli and G. Kotliar, Phys. Rev. B **73**, 165114 (2006).

[10] S. S. Kancharla, M. Civelli, M. Capone, B. Kyung, D. Senechal, G. Kotliar and A.-M. S. Tremblay, arXiv:cond-mat/0508205 (2005).

[11] G. Kotliar, S. Y. Savrasov, G. Palsson and G. Biroli, Phys. Rev. Lett. **87**, 186401 (2001).

[12] T. Maier, M. Jarrell, T. Prushcke and M. H. Hettler, Rev. Mod. Phys., **77**, (2005).

[13] A. Georges, G. Kotliar, W. Krauth and M. Rozenberg, Rev. Mod. Phys., **13**, (1996).

[14] C. J. Bolech, S. S. Kancharla, and G. Kotliar, Phys. Rev. B **67**, 075110 (2003); M. Capone, M. Civelli, S. S. Kancharla, C. Castellani, and G. Kotliar, Phys. Rev. B **69**, 195105 (2004).

# 25 Ultrafast Electronic Structure Engineering in $1T$-$TaS_2$: Role of Doping and Amplitude Mode Dynamics by Jayabalan et al.

Authors: J. Jayabalan, Jiyu Chen, Laura Pätzold, Francesco Petocchi, Florian K. Diekmann, Negar Najafianpour, Ping Zhou, Walter Schnelle, Gesa-R. Siemann, Philip Hofmann, Kai Roßnagel, Tim Wehling, Martin Eckstein, Philipp Werner, Uwe Bovensiepen

(one paper wrote that there are DFT and DMFT calculations of some UF dynamics, for me it is interesting in general to understand what are the measurements and effects?)

**Abstract**

In strongly correlated transition metal dichalcogenides, an intricate interplay of polaronic distortions, stacking arrangement, and electronic correlations determines the nature of the insulating state. Here, we study the response of the electronic structure to optical excitations to reveal the effect of chemical electron doping on this complex interplay. Transient changes in pristine and electron-doped $1T$-$TaS_2$ are measured by femtosecond time-resolved photoelectron spectroscopy and compared to theoretical modeling based on non-equilibrium dynamical mean-field theory and density functional theory. The fine changes in the oscillatory signal of the charge density wave amplitude mode indicate phase-dependent modifications in the Coulomb interaction and the hopping. Furthermore, we find indications for an enhanced fraction of monolayers in the doped system. Our work demonstrates how the combination of time-resolved spectroscopy and advanced theoretical modeling provides insights into the physics of correlated transition metal dichalcogenides.

## Article

The properties of correlated materials are governed by many-body effects, which give rise to density waves, superconductivity, Mott-insulating ground states, and interesting nonequilibrium phenomena [1, 7, 3, 4, 5]. Among those compounds, the group 5 transition metal dichalcogenides (TMDC) are of particular interest due to their structural instabilities, charge density wave (CDW) formation, and Mott insulating character [2, 7, 7]. A much-studied member of this family is $1T$-$TaS_2$, which is metallic at temperatures $T$ above 540 K. As $T$ is lowered, a CDW is formed with increasing long range order. The CDW consists of individual Star-of-David shaped entities formed out of 13 Ta atoms each [7]. At $T < 350$ K these stars form clusters and a nearly commensurate CDW (NCCDW). Below 200 K a long range ordered, commensurate CDW develops into a $(\sqrt{13} \times \sqrt{13})R13.9°$ superstructure of the Ta atoms. In recent years, the early proposal of a Mott insulating ground state for $1T$-$TaS_2$ by Fazekas and Tosatti [2] has been challenged. The stacking of individual layers was shown to be essential to understand the insulating character [56, 9, 10]. Surface and bulk contributions were considered [11, 12], bilayer formation and Mott localization were disentangled, and it was shown that Mott insulating monolayers make up only about 20% of the bulk [25, 14]. Substitutional [15, 24] and hole doping [17] have been investigated and coexisting metallic and insulating domains were reported. On this basis, $1T$-$TaS_2$ has become an interesting material platform to study intertwined electronic and vibrational excitations [37, 7, 19, 20, 21, 35, 23, 34]. Remarkably, the electronic structure changes associated with the CDW amplitude mode [7, 35, 25, 12] are, so far, not understood microscopically.

In this work, we model the transient electronic structure change of the amplitude mode in $1T$-$TaS_2$ in real time and distinguish the response of mono- and bilayers in the parent and the electron-doped compound. Time-resolved photoemission spectra compare well with the developed theory. We establish, thereby, a phase-sensitive real-time observable of the dynamic electronic structure in strongly correlated 2D materials that provides additional insights into the stacking of mono- and bilayers.

The temperature-dependent electric resistivity was measured for single crystals of $1T$-$Ta_{(1-x)}Mo_xS_2$. The results are shown in Fig. 25.1(a). The transition to the NCCDW phase prevails for all $x$ while the long-range order below $T = 200$ K is strongly suppressed upon doping. The satellite features observed in LEED, see Fig. 25.1(b-d) indicate that locally the Star-of-David (SOD) superstructure prevails, although at reduced intensity. Thus, Mo doping reduces the fraction containing the superstructure. For $x = 0.06$ we identify more complex satellite features indicating two domains rotated with respect to each other by $30° \pm 4°$. From these findings we conclude that electric conductivity channels persist in the presence of Mo doping at all temperatures. For further characterization, µ-ARPES studies were conducted.

We found homogeneous crystal surfaces and no indication of dopant agglomeration, see the appendix 25.

Femtosecond laser pulses with a fundamental photon energy of $h\nu$ =1.51 eV and 50 fs pulse duration were used for pumping, combined with probing by photoemission spectroscopy using the 4th harmonic at 6.04 eV and delay time $t$. The incident pump fluence was 0.2 mJcm$^{-2}$. The crystals were cleaved at 300 K. All measurements were performed at 30 K using $p$-polarized pulses. The kinetic energy of the photoelectrons emitted within an angle of $\pm 3°$ to the normal surface was measured by electron time-of-flight spectroscopy [26]. The Fermi energy $E_{\mathrm{F}}$ is determined by the high energy spectral cutoff without pumping at 300 K [7].

Time-dependent photoelectron emission spectra were taken for $1T$-$\mathrm{Ta}_{(1-x)}\mathrm{Mo}_x\mathrm{S}_2$ with $x = 0; 0.02; 0.04; 0.06$. Fig. 25.2(a) shows the intensity for $x = 0.02$ as a function of energy $E - E_{\mathrm{F}}$ and $t$. The spectrum at $t < 0$ before excitation is 0.6 eV wide. At $t = 0$ a slight intensity reduction below $E_{\mathrm{F}}$ and a clear increase above $E_{\mathrm{F}}$ represents the electronic response of the optical excitation. At delays $t < 5$ ps, oscillations in the vicinity of $E_{\mathrm{F}}$ are observed. Their frequency is $\Omega = 2.4$ THz and the oscillations dephase during 5 ps. This frequency represents the breathing of the Star-of-David and the CDW amplitude mode [37, 7, 27]. Subtraction of the spectrum at $t < 0$ provides the dynamic spectral changes plotted for $x = 0.02; 0$ in Fig. 25.2(b,c). Very similar results were obtained for $x = 0.06$.

We find pronounced transient spectral changes with characteristic differences for the parent and the electron doped compound. For $x = 0$ they cover a wide range of 0.5 eV and exhibit a rich fine structure. For $x = 0.02$ the transient changes are confined to 100 meV around $E_{\mathrm{F}}$ for $t > 0.6$ ps. At earlier $t$, during the presence of hot holes, they reach to $E - E_{\mathrm{F}} = -0.5$ eV. Comparing $x = 0$ and $x = 0.02$ establishes that chemical doping by Mo confines the transient spectral changes, upon relaxation of hot charge carriers, to a narrow range around $E_{\mathrm{F}}$. We attribute this behavior to a larger scattering phase space and enhanced screening induced by the increased electron density that originates from the additional valence electron in Mo compared to Ta.

To describe the changes in the electronic structure induced by the photoexcitation we combine density functional theory (DFT) calculations with nonequilibrium dynamical meanfield theory (DMFT) simulations. The results of the DFT calculations, which are summarized in the appendix 25, illustrate how the breathing mode of the SOD cluster changes the electronic structure at the well-known amplitude mode frequency of 2.4 THz [37, 7, 8]. We compare modulations of the electronic structure for a monolayer and a bilayer of $1T$-$\mathrm{TaS}_2$, see Fig. 25.6 (d-f) and (g-i) in the appendix. For monolayers (bilayers), the emergence of one (two) flat bands near $E_{\mathrm{F}}$ is found upon approaching the relaxed CDW structure characterized by a distortion $\alpha = 1$. $\alpha$ represents the scaled CDW distortion with the relaxed CDW structure corresponding to $\alpha = 1$ and the high-temperature structure without CDW to $\alpha = 0$. In the case of the bilayer, the two flat bands near $E_{\mathrm{F}}$ are split by a bonding-antibonding splitting due to interlayer hopping, which dominates over the in-plane kinetic energy contributions of the flat band. Upon reducing the CDW displacement amplitude by 40%, corresponding to $\alpha = 0.6$, the flat bands become more dispersive in both cases and most strikingly, the bonding-antibonding splitting in the bilayer case is reduced. As visualized in Fig. 25.3(a), the change in bonding-antibonding splitting is one order of magnitude larger than the effects on the in-plane kinetic energy contributions. This motivates the modulation of the interlayer hopping terms in the subsequent many-body treatment to mimic the dynamic effect of the Ta ion core vibration on the electronic structure. At the same time, the oscillation of the cluster orbital associated with the flat band should lead to a modulation in the effective Coulomb repulsion.

To model the transient electronic structure we use a previously developed single-orbital multi-layer description of $1T$-$\mathrm{TaS}_2$ in the CDW phase [13, 30]. The tight-binding Hamiltonian $\mathcal{H}_{\mathrm{SOD}}$ describing a single layer was obtained with DFT and maximally localized Wannier orbitals

[31]. The resulting single-orbital model is supplemented with a local Hubbard repulsion to incorporate electronic correlations. To describe the stacking order, the neighboring layers are connected via two hopping amplitudes: $h^{\mathrm{A}} = 0.2$ eV for the intra-bilayer hybridization and $h^{\mathrm{L}} = 0.045$ eV for the hopping between two van-der-Waals bonded layers [13, 30], see Fig. 25.3(b). The kinetic part of the Hamiltonian is

$$\mathcal{H}_{ab}\left(\mathbf{R}\right) = \mathcal{H}_{\mathrm{SOD}}\left(\mathbf{R}\right)\delta_{ab} - h^{A}_{ab}\delta_{\mathbf{R},\mathbf{0}} - h^{L}_{ab}\left(\mathbf{R}\right), \tag{25.1}$$

where $\{a, b\}$ is a layer index and $\mathbf{R}$ is the unit cell vector. To study the time evolution after a photo-excitation pulse, we use the nonequilibrium generalization of DMFT [32] in combination with a non-crossing approximation (NCA) [33, 34] impurity solver. A simplified Bethe-lattice type self-consistency allows us to capture the essential correlation and hybridization effects by constructing an approximate real-space hybridization function [40, 36, 37, 38], at the cost of losing the information on the dispersion relation. This approximation significantly reduces the computational effort and memory requirement, thus enabling multi-layer real-time simulations.

To fully capture the strong bilayer hybridization resulting from the intra-bilayer hopping $h^{\mathrm{A}}$, we employ a two-site cluster DMFT [39], where the two sites of a cluster represent the two planes of a bilayer (red box in Fig. 25.3(b)). The local Hamiltonian for this cluster DMFT description of the bilayer has the form

$$\begin{aligned}\mathcal{H}_i\left(t\right) = &-\mu\left(n_{i1} + n_{i2}\right) + U\left(n_{i1\uparrow}n_{i1\downarrow} + n_{i2\uparrow}n_{i2\downarrow}\right)\\ &-\sum_{\sigma}\left[h^{i}_{12}\left(t\right)c^{\dagger}_{i1\sigma}c_{i2\sigma} + h.c.\right],\end{aligned} \tag{25.2}$$

where $U$ is the local Hubbard interaction and $\mu$ is the chemical potential, which can be adjusted to realize the desired doping.

In the presence of the laser pulse, the hopping matrices become complex, $h_{mn}(t) = h_{mn}(0)e^{i\phi_{mn}(t)}$, where the Peierls phase $\phi_{mn}(t) = -\int_0^t dt'\boldsymbol{E}(t')\cdot\boldsymbol{r}_{mn}$ is determined by the time integral of the vector product between the electric field of the laser $\boldsymbol{E}(t)$ and the real space displacement $\boldsymbol{r}_{mn}$ between the centers of orbitals $m$ and $n$ [32]. The DMFT loop starts from the atomic Green's functions $G_i$ of the different bilayers $i$ as initial guess. To construct the time-dependent hybridization function for bilayer $i$, we consider 18 DFT-derived in-plane hoppings $\mathcal{H}_{i,\mathrm{SOD}}(\mathbf{R})$ within bilayer $i$, and 3 weak inter-bilayer hoppings $h^{\mathrm{L}}_{ij}(\mathbf{R}')$ connecting to polarons of bilayer $i$ with those in the adjacent bilayers $j$,

$$\begin{aligned}\Delta_i\left(t,t'\right) = &\sum_{\mathbf{R}\neq 0}\mathcal{H}_{\mathrm{SOD},i}(\mathbf{R},t)G_i(t,t')\mathcal{H}_{\mathrm{SOD},i}(-\mathbf{R},t')\\ &+\sum_{j=i\pm1,\mathbf{R}'}h^{L}_{ij}(\mathbf{R}',t)G_j(t,t')h^{L}_{ji}(-\mathbf{R}',t'),\end{aligned} \tag{25.3}$$

where we employed the Bethe-lattice-like connection to the cluster Green's functions for the bilayers $i$ and adjacent bilayers $j = i\pm1$. (The monolayer #1 is treated as a bilayer with $h^A = 0$.) Using the hybridization function defined in Eq. (25.3) and the NCA solution for the cluster impurity problem, the bilayer Green's functions $G_j$ are self-consistently computed. In order to mimic the cooling effect from the coupling to degrees of freedom not included in the model, we locally add a boson bath in the form of a self-energy $(\Sigma_j)^{\mathrm{bath}}_{ab}(t,t') = g^2\delta_{ab}D(t,t';\omega_0,T)G_{j,aa}(t,t')$, which is diagonal in the layer index. Here, $D(t,t';\omega_0,T)$ is the bosonic Green's function [32] for boson frequency $\omega_0 = 0.05$ eV and temperature $T = 0.02$ eV$/k_{\mathrm{B}}$. We choose the coupling strength $g = 0.08$ eV. To describe the effect of the breathing mode, we modulate $U$, $h^A$ and $h^L$ by 5%, with the frequency $\Omega = 2.4$ THz.

Figure 25.4 presents the calculated time-dependent changes in the spectral function for $x = 0$ in panels (a-c) and for $x = 0.02$ in (e-g) for the monolayer #1 at the surface (a,e), for

the first bilayer #23 (b,f), and the second bilayer #45 (c,g). These results compare reasonably well with the experimental results that are replotted in panels (d,h). Comparing experimental and theoretical results allows a discussion of the bi- and monolayer contributions in the cleaved crystal that are probed in the experiment. In our modeling we find for $x = 0$ above $E_{\mathrm{F}}$ decaying hot electron contributions that are strong and contain a weakly oscillating contribution. For $x = 0.02$ all calculated hot electron contributions are weaker than for $x = 0$. At energies $E - E_{\mathrm{F}} < 0.1$ eV oscillatory signatures of the amplitude mode are present in all cases, although their strength varies.

In the following we concentrate on the monolayer and second bilayer since they exhibit clear phase and energy dependent changes. In the experiment, the negative changes for $x = 0$ are very pronounced at $0 < E - E_{\mathrm{F}} < -0.3$ eV and match well with the calculations in this energy interval for the monolayer. Calculations and experiment also match well in this energy range for positive changes $\Delta I_{\mathrm{PES}}$. At the phase characterized by the maximal $|\Delta I_{\mathrm{PES}} < 0|$ at high energy, these features are indicated in panels (a,d) by a yellow "$\times$" symbol, $\Delta I_{\mathrm{PES}} > 0$ indicated by a black "$\cdot$" appears at lower energy. At the opposite phase with maximal $|\Delta I_{\mathrm{PES}} < 0|$ at the lowest energy, indicated by a black "$+$" symbol, $\Delta I_{\mathrm{PES}} > 0$, marked by a yellow "$\circ$" symbol, appears at high energy. This oscillatory fine structure is found in experiment and theory for the monolayer, although at short times (when doublon/holon populations exist in the Hubbard bands), the main intensity is above $E_{\mathrm{F}}$. Considering that differential signals are discussed, these oscillations around a central energy of $E - E_{\mathrm{F}} = -180$ meV indicate a modulation of the Hubbard $U$. The fact that positive and negative changes $\Delta I_{\mathrm{PES}}$ occur at opposite phases at different energy implies that the line profile and, thus, the hopping rate varies within the oscillation cycle. In the experiment the maxima and minima in $\Delta I_{\mathrm{PES}}$ occur at 30 meV energy difference on the higher and lower energy spectral sides. In the simulations, the results differ slightly for the higher and lower energy spectral sides, probably due to the large spectral weight obtained in the calculation above $E_{\mathrm{F}}$. However, as an order of magnitude estimation we conclude on substantial changes in the hopping rates of several 10 meV.

Considering that photoemission spectroscopy is a surface sensitive technique the question of a monolayer or bilayer surface termination is relevant. Comparing panels (c,d) in Fig. 25.4, we see that also the bilayer contribution can qualitatively explain the experimental signal. In particular the time-dependent signature of the simulated bilayer behavior directly at $E_{\mathrm{F}}$ matches well with the experiment, since the photo-doping of bilayers generates in-gap states [30]. The bilayer signal at lower energy however appears to be weaker than in the experiment.

Turning to the results for the doped crystals, we find that a periodic intensity change is found at $E_{\mathrm{F}}$ for the bilayer and for the monolayer simulation, as well as in the experiment. The changes for the bilayer are however much weaker than for the monolayer and do not vary in the sign of $\Delta I$ across $E_{\mathrm{F}}$, which is clearly inconsistent with the experiment. In the simulation, the strong modification of the spectral weight at $E_F$ reflects a periodic modulation of a narrow quasi-particle band. We, therefore, conclude that for the doped case the monolayer contribution dominates.

A recent x-ray scattering study [14] reported a ratio of bilayers to monolayers in the bulk of pristine $1T$-$TaS_2$ of 2:1, i.e. 20% of the layers are monolayers. Our results for $x = 0$ are consistent with a significant bilayer contribution, as discussed above. For the doped compound, the calculated monolayer spectral function shows a much better agreement with the experimental result than the bilayer spectral function. This indicates that the contribution of monolayers in the doped system is higher than in the undoped compound, at least near the surface probed by ARPES. Apparently, the doping not only reduces the CDW fraction as concluded from LEED, see Fig. 25.1, but also hinders the formation of bilayers. Since the stacking order influences the physics in profound ways, this finding is significant. It suggests that in addition to the appearance of metallic channels between polaronically distorted domains, chemical doping trig-

gers a restructuring of the layered crystal and fundamentally changes the nature of electronic correlations.

Having drawn this conclusion we note that the match of the oscillatory spectral fine structure between experiment and theory is not perfect. The spectral changes calculated for the doped case reach considerably higher energies above $E_{\mathrm{F}}$ than the experimental spectra. We assign this difference to the construction of the model, which considers only the low-energy band(s). In the real material, additional bands are present, and may play a role in the excitation and relaxation process. Furthermore, in the experiment for $x = 0$, we observe at $E - E_{\mathrm{F}} = -0.4$ eV an additional oscillatory signature with $\Delta I > 0$. This energy agrees well with the CDW energy gap at the Brillouin zone boundary at the M-point detected in static angle-resolved PES (ARPES) [21, 35]. In time-resolved ARPES the CDW gap oscillates at the amplitude mode frequency, in agreement with the $\Omega = 2.4$ THz identified in the present work using $h\nu = 6$ eV. At this low photon energy, ARPES does not reach the M-point. Moreover, we detect the photoelectron in normal emission at $\Gamma$. Following Petersen *et al.* [21], we assign the oscillation at $-0.4$ eV to the amplitudon whose excitation coherently modifies the scattering probability leading to backfolding from M to $\Gamma$. Our modeling does not take the long-range ordered crystal lattice into account and lacks this backscattered feature.

We presented phase-resolved microscopic insights into dynamic electronic structure changes in response to the amplitude mode of the charge density wave in parent and Mo-doped $1T$-$TaS_2$. Comparing results of time-resolved photoelectron spectroscopy with real-time dynamical mean field simulations combined with parameter modulations inspired by density functional calculations, we resolved periodic variations in the Coulomb repulsion and the hopping rate. Furthermore, we were able to draw conclusions on the stacking in the material. While for the parent compound we favor a coexistence of mono- and bilayers near the surface, the Mo doping increases the monolayer fraction and, along with this restructuring, the effect of strong electronic correlations. Such an analysis of dynamic changes of the electronic structure combined with electronic structure engineering through accessible control parameters provides valuable insights into the fundamental electronic interactions governing complex materials with considerable potential for future analysis.

## Appendix: Analysis of sample homogeneity

In Fig. 25.5, we present spatially resolved ARPES measurements over a large area of a 6% Mo-doped $TaS_2$ sample using a step size of 25 $\mu$m. The raw variations in the Ta $4f$ core-level intensity across the sample are shown in Fig. 25.5(a). Normalized core-level spectra extracted from three distinct regions indicated by colored areas in Fig. 25.5(a) are plotted in the top of Fig. 25.5(b), demonstrating no significant variations across the sample surface. To further confirm the uniformity of the sample, we investigated variations in the valence band electronic structure at different positions marked by colored symbols in Fig. 25.5(a), using a photon energy of 50 eV. High statistics measurements of the Valence band spectra at normal emission, represented by EDCs at the $\Gamma$ point using a 0.06 $\mathrm{\AA}^{-1}$ integration range (bottom panel of Fig. 25.5(b)), indicate that observed spectral differences arise primarily due to slight angular offsets between measurement positions. Additionally, the homogeneity was evaluated by fitting the Ta $4f$ core-level spectra at each spatial point of the map using four peaks convoluted with a Gaussian function and a linear background. The resulting spatial variation of the binding energy for the third peak component (indicated by the gray arrow in Fig. 25.5(b)) is plotted in Fig. 25.5(c), revealing only minor variations in the uppermost region of the sample.

## Appendix: DFT band structure calculations

DFT calculations were performed with QUANTUM ESPRESSO [25] using the PBE approximation for the exchange-correlation potential [39] and norm-conserving pseudopotentials [42]. Plane waves until an energy cutoff of 100 Ry were included and a Fermi-Dirac-type smearing of 0.005 Ry was imposed. We used a lattice constant of 3.43 Å and a $6 \times 6 \times 1$ **k**-point grid for the $\sqrt{13} \times \sqrt{13}$ supercell. A vacuum of approximately 12 Å was included above the monolayer/bilayer. For calculations of the doped system, we considered a doping of 0.02/0.04/0.06 $e^-$ per $TaS_2$ unit cell, which corresponds to 0.26/0.52/0.78 $e^-$ per $\sqrt{13} \times \sqrt{13}$ supercell.

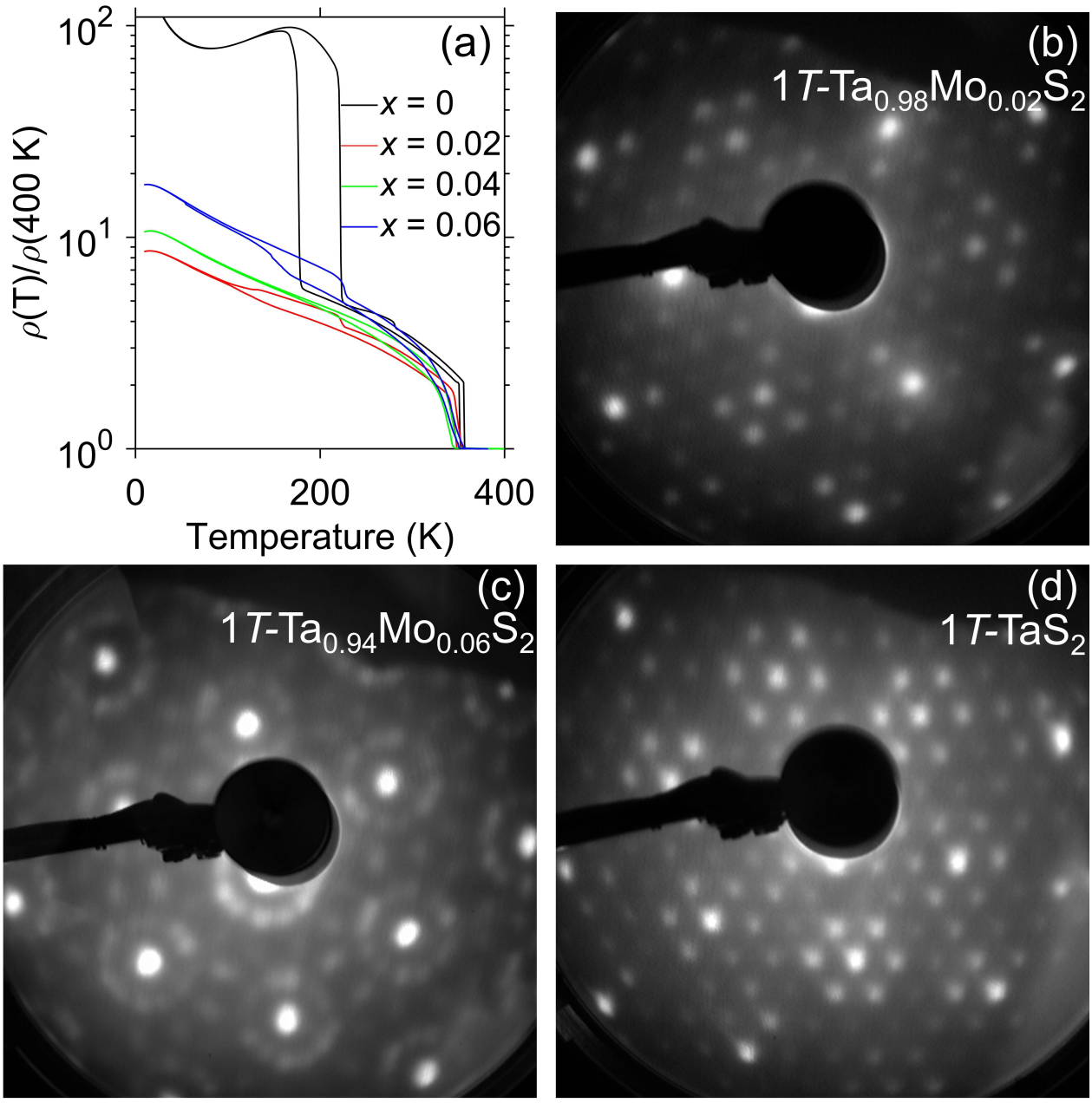


Figure 25.1: Panel (a) shows the temperature dependent electrical resistivity $\rho$ of $1T$-$Ta_{(1-x)}Mo_xS_2$ at the indicated doping level $x$. Panels (b-d) present LEED images for $x = 0.02$ (b), 0.06 (c), and the parent compound $x = 0$ (d), recorded at $T = 30$ K with an electron kinetic energy of 123 eV.

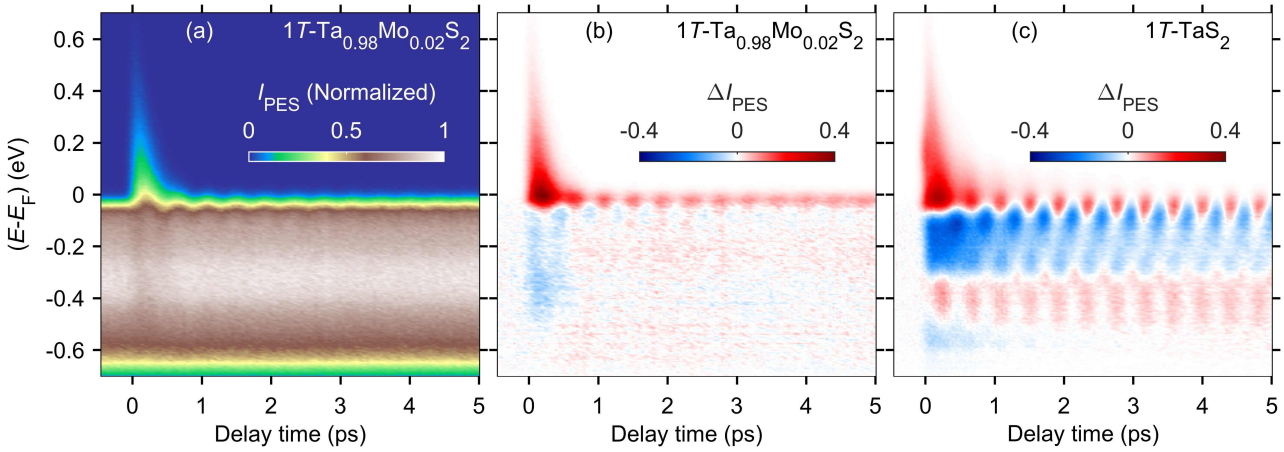


Figure 25.2: The time-dependent photoelectron intensity $I_{\mathrm{PES}}$ is depicted as a function of energy $E - E_{\mathrm{F}}$ and delay time $t$ in panel (a) for $T = 30$ K and $x = 0.02$ after normalization to the intensity maximum using a false color map. Panels (b,c) present the pump-induced change for $x = 0.02$; 0, respectively. Panels (a,b) show identical data; in (b) the static spectrum at $t < 0$ was subtracted. Positive and negative changes are indicated in red and blue color, respectively. For $x = 0$, full time-resolved spectra were previously published in Refs. [7, 25, 12].

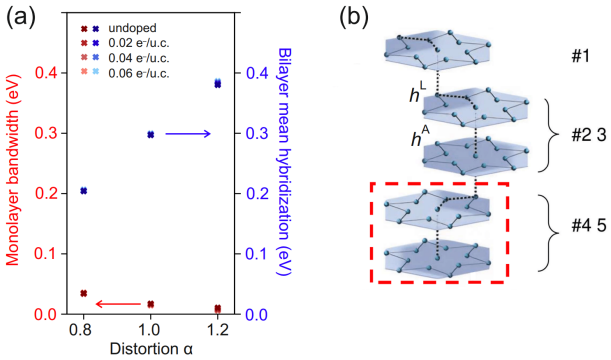


Figure 25.3: (a) Representative energy scales for mono- and bilayers of $1T$-$TaS_2$ calculated by DFT for the indicated doping. Left axis: Bandwidth for the monolayer single band as a function of the distortion $\alpha$ to simulate the influence of the breathing mode on the intralayer physics. Right axis: Calculated mean hybridization gap of the bilayer band structure for identical $\alpha$ representing the effect of the breathing mode on the interlayer physics. The interlayer energy scale is one order of magnitude larger than the intralayer one. (b) Stacking arrangements of the CDW ordered clusters located on different planes. The two-site DMFT cluster associated with a bilayer is indicated by the red box. Two hopping matrix elements $h^A$ and $h^L$ are considered, see text.

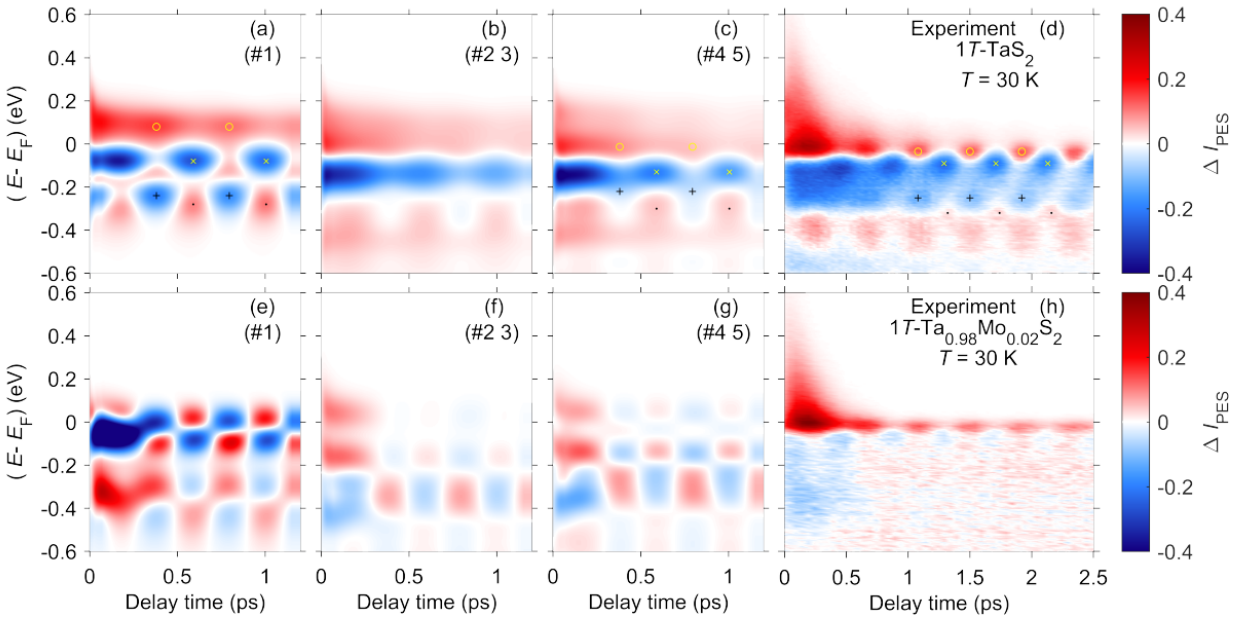


Figure 25.4: False color representation of the calculated (a-c, e-g) and measured (d,h) transient spectral changes for the monolayer at the surface #1, the 1st bilayer #2 3, and the 2nd bilayer #4 5. The changes in the calculated spectral functions reflect the relative changes between the mono- and bilayers. Experimental results are replotted from Fig. 25.2. The top panels represent $x = 0$, the bottom ones $x = 0.02$.

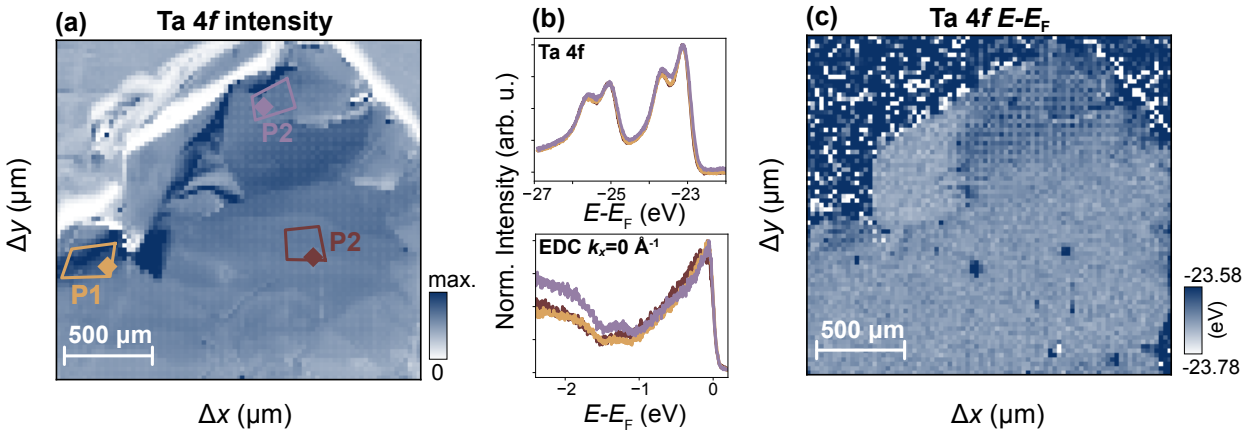


Figure 25.5: (a) Spatially resolved ARPES measurements scanning over the Ta $4f$ core levels using a photon energy of h$\nu = 80$ eV and LH-polarized light. (b) Top: Extracted core levels from the map shown in (a), integrated over small regions around three different probing spots. Bottom: Extracted EDCs at the Gamma point ($k_x = 0$ Å$^{-1}$) from fixed scans measured at the same three positions, indicated by the colored markers in (a) using a photon energy of h$\nu = 50$ eV. (c) Variations in the Ta $4f$ binding energy of the third peak component indicated by the arrow in (b), showing only small variations in the binding energy within the topmost part of the sample.

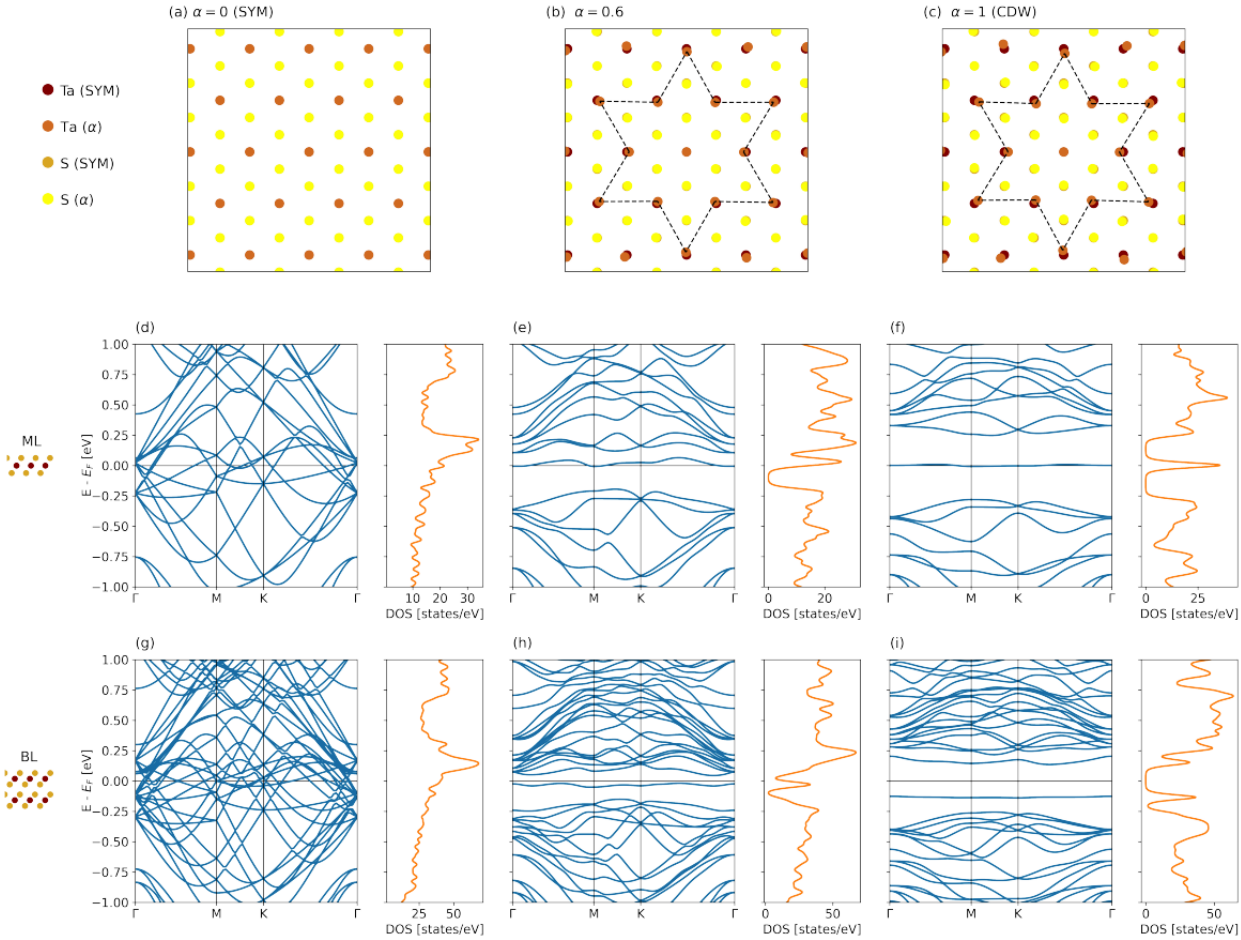


Figure 25.6: DFT calculations for monolayer and bilayer $1T$-$TaS_2$. (a)-(c) Zoom into the $\sqrt{13} \times \sqrt{13}$ supercell with a lattice constant of 3.43 Å for different percentages of displacement towards the SOD distortion, from (a) the symmetric phase $\alpha = 0$ over (b) $\alpha = 0.6$ to (c) the SOD CDW $\alpha = 1$. As a guide to the eye, the star shape of the CDW is marked via dashed lines. (d)-(f) Non-interacting band structure (blue) and density of states (DOS, orange) of the $1T$-$TaS_2$ monolayer obtained via DFT for the different percentages of distortion $\alpha$ from (a)-(c). The emergence of a single band around the Fermi level can be seen. (g)-(i) Non-interacting band structure (blue) and density of states (DOS, orange) of the $1T$-$TaS_2$ bilayer obtained via DFT for the different percentages of distortion $\alpha$ from (a)-(c).

# References


[1] H. Yang, S. Kim, M. Chhowalla, and Y. H. Lee, Nat. Phys. **13**, 931 (2017).

[7] B. Sipos, A. F. Kusmartseva, A. Akrap, H. Berger, L. Forró, and E. Tutiš, Nat. Mater. **7**, 960 (2008).

[3] C. Giannetti, M. Capone, D. Fausti, M. Fabrizio, F. Parmigiani, and D. Mihailovic, Adv. Phys. **65**, 58 (2016), https://doi.org/10.1080/00018732.2016.1194044 .

[4] A. de la Torre, D. M. Kennes, M. Claassen, S. Gerber, J. W. McIver, and M. A. Sentef, Rev. Mod. Phys. **93**, 041002 (2021).

[5] Y. Murakami, D. Golež, M. Eckstein, and P. Werner, Photo-induced nonequilibrium states in mott insulators (2023), arXiv:2310.05201 [cond-mat.str-el] .

[2] P. Fazekas and E. Tosatti, Philosophical Magazine B **39**, 229 (1979).

[7] L. Perfetti, P. A. Loukakos, M. Lisowski, U. Bovensiepen, H. Berger, S. Biermann, P. S. Cornaglia, A. Georges, and M. Wolf, Phys. Rev. Lett. **97**, 067402 (2006).

[56] T. Ritschel, J. Trinckauf, K. Koepernik, B. Büchner, M. v. Zimmermann, H. Berger, Y. I. Joe, P. Abbamonte, and J. Geck, Nat. Phys. **11**, 328 (2015), 1409.7341 .

[9] T. Ritschel, H. Berger, and J. Geck, Phys. Rev. B **98**, 195134 (2018), 1806.01944 .

[10] S.-H. Lee, J. S. Goh, and D. Cho, Phys. Rev. Lett. **122**, 106404 (2019).

[11] Y. D. Wang, W. L. Yao, Z. M. Xin, T. T. Han, Z. G. Wang, L. Chen, C. Cai, Y. Li, and Y. Zhang, Nat. Commun. **11**, 4215 (2020).

[12] J. Dong, W. Qi, D. Shin, L. Cario, Z. Chen, R. Grasset, D. Boschetto, M. Weis, P. Lample, E. Pastor, T. Ritschel, M. Marsi, A. Taleb, N. Park, A. Rubio, E. Papalazarou, and L. Perfetti, Phys. Rev. B **108**, 155145 (2023).

[25] C. J. Butler, M. Yoshida, T. Hanaguri, and Y. Iwasa, Nat. Commun. **11**, 2477 (2020), 1908.08221 .

[14] N. Hua, F. Petocchi, H. G. Bell, G. Aeppli, P. Werner, and S. Gerber, Effect of interlayer stacking on the electronic properties of $1T$-$TaS_2$, `https://doi.org/10.48550/arXiv.2503.24124`, arXiv:2503.24124.

[15] Y. Liu, R. Ang, W. J. Lu, W. H. Song, L. J. Li, and Y. P. Sun, Appl. Phys. Lett. **102**, 192602 (2013).

[24] S. Qiao, X. Li, N. Wang, W. Ruan, C. Ye, P. Cai, Z. Hao, H. Yao, X. Chen, J. Wu, Y. Wang, and Z. Liu, Phys. Rev. X **7**, 041054 (2017).

[17] W. Zhang, J. Gao, L. Cheng, K. Bu, Z. Wu, Y. Fei, Y. Zheng, L. Wang, F. Li, X. Luo, Z. Liu, Y. Sun, and Y. Yin, npj Quantum Materials **7**, 8 (2023).

[37] J. Demsar, L. Forró, H. Berger, and D. Mihailovic, Phys. Rev. B **66**, 041101 (2002).

[19] M. Eichberger, H. Schäfer, M. Krumova, M. Beyer, J. Demsar, H. Berger, G. Moriena, G. Sciaini, and R. J. D. Miller, Nature **468**, 799 (2010).

[20] N. Dean, J. C. Petersen, D. Fausti, R. I. Tobey, S. Kaiser, L. V. Gasparov, H. Berger, and A. Cavalleri, Phys. Rev. Lett. **106**, 016401 (2011).

[21] J. C. Petersen, S. Kaiser, N. Dean, A. Simoncig, H. Y. Liu, A. L. Cavalieri, C. Cacho, I. C. E. Turcu, E. Springate, F. Frassetto, L. Poletto, S. S. Dhesi, H. Berger, and A. Cavalleri, Phys. Rev. Lett. **107**, 177402 (2011).

[35] S. Hellmann, T. Rohwer, M. Kalläne, K. Hanff, C. Sohrt, A. Stange, A. Carr, M. M. Murnane, H. C. Kapteyn, L. Kipp, M. Bauer, and K. Rossnagel, Nat. Commun. **12**, 1069 (2012).

[23] C. J. Butler, M. Yoshida, T. Hanaguri, and Y. Iwasa, Phys. Rev. X **11**, 011059 (2021).

[34] J. Maklar, J. Sarkar, S. Dong, Y. A. Gerasimenko, T. Pincelli, S. Beaulieu, P. S. Kirchmann, J. A. Sobota, S. Yang, D. Leuenberger, R. G. Moore, Z.-X. Shen, M. Wolf, D. Mihailovic, R. Ernstorfer, and L. Rettig, Sci. Adv. **9**, eadi4661 (2023).

[25] I. Avigo, P. Zhou, M. Kalläne, K. Rossnagel, U. Bovensiepen, and M. Ligges, Applied Sciences **9**, 44 (2018).

[26] M. Sandhofer, I. Sklyadneva, V. Sharma, V. M. Trontl, P. Zhou, M. Ligges, R. Heid, K.-P. Bohnen, E. Chulkov, and U. Bovensiepen, J. Electron Spectros. Relat. Phenom. **195**, 278 (2014).

[27] A. Zong, X. Shen, A. Kogar, L. Ye, C. Marks, D. Chowdhury, T. Rohwer, B. Freelon, S. Weathersby, R. Li, J. Yang, J. Checkelsky, X. Wang, and N. Gedik, Sci. Adv. **4**, eaau5501 (2018).

[8] L. Stojchevska, I. Vaskivskyi, T. Mertelj, P. Kusar, D. Svetin, S. Brazovskii, and D. Mihailovic, Science **344**, 177 (2014).

[13] F. Petocchi, C. W. Nicholson, B. Salzmann, D. Pasquier, O. V. Yazyev, C. Monney, and P. Werner, Phys. Rev. Lett. **129**, 016402 (2022).

[30] F. Petocchi, J. Chen, J. Li, M. Eckstein, and P. Werner, Phys. Rev. B **107**, 165102 (2023).

[31] D. Pasquier and O. V. Yazyev, Phys. Rev. B **105**, L081106 (2022).

[32] H. Aoki, N. Tsuji, M. Eckstein, M. Kollar, T. Oka, and P. Werner, Rev. Mod. Phys. **86**, 779 (2014).

[33] H. Keiter and J. C. Kimball, Int. J. Magn. **1**, 233 (1971).

[34] M. Eckstein and P. Werner, Phys. Rev. B **82**, 115115 (2010).

[40] A. Georges, G. Kotliar, W. Krauth, and M. J. Rozenberg, Rev. Mod. Phys. **68**, 13 (1996).

[36] P. Werner, H. U. R. Strand, S. Hoshino, and M. Eckstein, Phys. Rev. B **95**, 195405 (2017).

[37] J. Chen, F. Petocchi, V. Christiansson, and P. Werner, Phys. Rev. B **109**, L201101 (2024).

[38] J. Chen, F. Petocchi, V. Christiansson, and P. Werner, Phys. Rev. B **110**, 045117 (2024).

[39] A. I. Lichtenstein and M. I. Katsnelson, Phys. Rev. B **62**, R9283 (2000).

[25] P. Giannozzi, S. Baroni, N. Bonini, M. Calandra, R. Car, C. Cavazzoni, D. Ceresoli, G. L. Chiarotti, M. Cococcioni, I. Dabo, A. D. Corso, S. de Gironcoli, S. Fabris, G. Fratesi, R. Gebauer, U. Gerstmann, C. Gougoussis, A. Kokalj, M. Lazzeri, L. Martin-Samos, N. Marzari, F. Mauri, R. Mazzarello, S. Paolini, A. Pasquarello, L. Paulatto, C. Sbraccia, S. Scandolo, G. Sclauzero, A. P. Seitsonen, A. Smogunov, P. Umari, and R. M. Wentzcovitch, J. Phys. Condens. Matter **21**, 395502 (2009).

[39] J. P. Perdew, K. Burke, and M. Ernzerhof, Phys. Rev. Lett. **77**, 3865 (1996).

[42] C. Hartwigsen, S. Goedecker, and J. Hutter, Phys. Rev. B **58**, 3641 (1998).

# 26 Filling-dependent intertwined electronic and atomic orders in the flat-band state of 1T-$TaS_2$ by Geng

Yanyan Geng [1,2,+], Haoyu Dong [1,2,+], Renhong Wang [1,2,+], Jianfeng Guo [1,2,3], Shuo Mi [1,2], Le Lei [1,2,3], Yan Li [3], Li Huang [3], Fei Pang [1,2], Rui Xu [1,2], Weiqiang Yu [1,2], Hong-Jun Gao [3], Wei Ji [1,2,*], Weichang Zhou [4,*], and Zhihai Cheng [1,2,*]

[1] Key Laboratory of Quantum State Construction and Manipulation (Ministry of Education), Renmin University of China, Beijing, 100872, People's Republic of China [2] Beijing Key Laboratory of Optoelectronic Functional Materials & Micro-nano Devices, Department of Physics, Renmin University of China, Beijing 100872, People's Republic of China

[3] Beijing National Laboratory for Condensed Matter Physics, Institute of Physics, Chinese Academy of Sciences, Beijing 100190, People's Republic of China

[4] Key Laboratory of Low-dimensional Quantum Structures and Quantum Control of Ministry of Education, School of Physics and Electronics, Institute of Interdisciplinary Studies, Hunan Normal University, Changsha 410081, People's Republic of China

**Abstract**

The delicate interplay among the complex intra-/inter-layer electron-electron and electron-lattice interactions is the fundamental prerequisite of these exotic quantum states, such as superconductivity, nematic order, and checkerboard charge order. Here we explore the filling-dependent multiple stable intertwined electronic and atomic orders of flat-band state of $1T-TaS_2$ encompassing hole order, phase orders, coexisting left- and right-chiral orders and mixed phase/chiral orders via scanning tunneling microscopy (STM). Combining first-principles calculations, the emergent electronic/atomic orders can be attributed to the weakening of electron-electron correlations and stacking-dependent interlayer interactions. Moreover, achiral intermediate ring-like clusters and nematic charge density wave (CDW) states are successfully realized in intralayer chiral domain wall and interlayer heterochiral stacking regions through chiral overlap configurations. Our study not only deepens the understanding of filling-dependent electronic/atomic orders in flat-band systems, but also offers perspectives for exploring exotic quantum states in correlated electronic systems.

The transition metal dichalcogenides (TMDs) deserve particular attention as they exhibit rich electronic states such as charge density wave (CDW) [1-3], superconductivity (SC) [4,5], quantum spin liquid [6], magnetism [7], etc. Most of these electronic states depend on the competition, coexistence or cooperation of electron-electron correlations and electron-lattice interactions and, therefore, are significantly sensitive to variations in the electronic structures [8,9]. Hole or electron doping has been an effective way to tune electronic structures. For example, CDW is very rapidly suppressed in hole Sn -doped $CsV_3Sb_5$ [10], superconductivity

occurs in electron/hole-doped twisted graphene moiré superlattice system [11,12], and superconductivity is enhanced in electron K-doped FeSe [13]. Meanwhile, precise carrier doping can also gradually modulate the internal electron-electron correlation, leading to the induction of intriguing quantum states, including checkerboard charge order [14,15], nematic phase [16], a superconducting dome [17], a correlation-driven insulating phase [18,19] and a metallic phase [20,21]. Therefore, a detailed study of the structure and properties of the doping-related electrons is a necessary prerequisite for achieving the controllability of CDW-based exotic quantum states.

Among various TMDs materials, $1T - TaS_2$ has attracted wide attention due to its abundant CDW phase [22-24]. The formation of the Star of David (SoD) in the CDW state creates a half-filled flat band, which is transformed into a Mott insulator or band insulator by electronic correlations or interlayer coupling [25-27]. Meanwhile, because of the close proximity of the various competing interactions in energy, doped electron or hole carriers can modify the flat-band filling factor and effectively modulate the electron correlation effects in CDW to achieve a rich variety of quantum states [28-30]. Prominent examples include the metallization can be realized without breaking the long-range CDW order when surface electron doping is applied [31,32], while hole doping is known to drastically suppress the transition from a nearly commensurate CDW (NCCDW) phase to a commensurate CDW (CCDW) phase [33], and superconductivity coexists with CDW [34]. Furthermore, doping not only can directly affect the interior electron-electron correlations but also induce significantly changes in the interlayer CDW stacking order [22]. Despite extensive previous studies on doping, it is still important to understand the evolution of filling-dependent electronic and atomic orders in the flat-band state based on intralayer and interlayer
interactions.
In this work, we investigate the filling-dependent intertwined electronic and atomic orders in the flat-band state and internal interlayer/intralayer interactions of $1T - TaS_2$ by STM combined with theoretical calculations. With decreasing flat-band filling factor, a variety of interleaving orders are observed: hole order, phase orders, stacking disorder and intertwined phase/chiral orders in sequence. The emergence of stable fragmentized intralayer phase domain can be attributed to the reduced electron-electron correlations, which is incapable of persisting long-range intralayer orders. The further decreased electron-electron correlations and interlayer interactions contributed to the following appearance of intralayer chiral domains and interlayer heterochiral stacking. At the intralayer chiral domain wall and interlayer heterochiral stacking regions, the intermediate ring-SoD clusters and nematic CDW states are discovered and discussed based on the transient chiral-overlapping interactions. This work provides important insights into the internal interactions and the future realization of exotic quantum states in corrected electronic materials.

### 26.0.1 Results and Discussion

electron-filled and -empty SoDs are marked by the central red and grey dots, respectively. (k-m) Simulated STM images of the three inequivalent substitution sites: site A(k), site B(l), and site C(m). (n) Structure model of the inequivalent substitution site A. Scanning parameter: (g, i) $V = -0.4$ V, $I = -100$pA; (h) $V = 0.4$ V, $I = 100$pA.

The ground CDW state of $1T$ - $TaS_2$ is characterized by the commensurate $\sqrt{13} \times \sqrt{13}$ superlattice of SoD clusters, as depicted in Fig. 1a-b. The SoD cluster is made of 12 inward-distorted outer Ta atoms and one center Ta atom, in which the twelve $5d_{z^2}$ electrons of the outer Ta atoms pair and form six occupied CDW valence bands. The remaining one unpaired electron of SoD is maximally localized at the central Ta atom to form the half-filled flat band. A relatively strong intralayer electron-electron correlations then leads to the split upper Hubbard

band (UHB) and lower Hubbard band (LHB), forming a correlated Mott insulator without considering the interlayer interaction (Fig. 1c). Recently, the important role of the interlayer stacking order has been emphasized, and the ground CCDW state of $1T-\mathrm{TaS_2}$ can be described as a trivial band insulator/conventional Mott insulator on the termination of $\mathrm{T_A/T_c}$ stacking at low temperatures [25-27]. Figure 1d presents the STM image of the ground CCDW state with the overlaid star models of SoDs.

Hole doping can effectively modify the flat-band filling factor, providing an exemplary platform to fine-tune the electronic/atomic structure and realize a wide range of intriguing electronic states. Figure 1e illustrates the schematic diagram of electronic orders and flat-band filling factors, which shows the evolution of a series of electronic orders: (i) hole order, (ii) phase orders, (iii) coexisting left- and right-chiral orders, and (iv) intertwined phase/chiral orders. Notably, the phase and chiral domains created by hole doping can reach the millimeter scale in a stable state, in contrast to the various metastable domain induced by pressure, ultrafast optical, and electrical pulses [35-39]. These emergent electronic states can be phenomenologically attributed to the competition and/or cooperation of stacking-dependent interlayer interactions and intralayer interactions of $1T-\mathrm{TaS_2}$ (Fig. 1f). In $1T-\mathrm{TaS_2}$, with the increase of hole doping, the reduction of intralayer electrons contributes to the gradually weakening of electron-electron correlation, resulting in the inability of the CCDW to maintain long-range ordering and the emergence of hole and phase/chiral domain walls (DWs). Meanwhile, hole doping is also accompanied by the gradual diminishing of
interlayer SoD interactions (T) (Fig. S1) [22], which leads to the emergence of random stacking order and interlayer heterochiral stacking.

Compared to the pristine $1T-\mathrm{TaS_2}$, the slight reduction of flat-band filling electrons results in the appearance of hole-SoDs within the CCDW superlattice, showing darker (brighter) contrast than the normal SoDs at the occupied (unoccupied) state, as shown in Figs. 1g and 1h. These hole-SoDs are clearly resolved as the darker three-petal flower shapes in the high-resolution STM image of Fig. 1i, and further schematically illustrated in Fig. 1j. To determine the origin of the three-petal flower SoD, first-principles calculations and $\mathrm{d}I/\mathrm{d}V$ spectra are performed. It can be seen that the typical $\mathrm{d}I/\mathrm{d}V$ spectra of bright triangular SoDs and dark three-petal flower SoDs show significant differences [Fig. S2]. The bright SoDs display an electron-hole symmetric gap, while the dark SoDs exhibit an electron-hole asymmetric single pronounced peak that onsets sharply above the Fermi energy. According to the first-principles simulation, the three-petal flower SoDs can be well reproduced by selecting the central (site A) or peripheral Ta (site B or C) as the Ti substitution sites as the shown in Fig. 1k-1n and Fig. S3. Since the central (site A) has the lowest doping energy (Supplementary Table I), we suggest that the three-petal flower SoDs originate from the substitution of Ti atoms for the central Ta atoms, leaving the SoDs without central Mott electrons.

phase DWs (top) and their schematic structural configurations (bottom). The constituent SoDs of phase DWs are highlighted by the dashed lines separating the two neighboring phase domains. (c,d) STM images of two typical CDW vortexes and their schematic structural configurations. (e) STM images for sublayer phase DWs. The red lines denote the phase DWs of the sublayer. (f) Arrangement of the localized states of the central Ta atoms for the three representative CDW stacking configurations: $\mathrm{T_A}, \mathrm{T_B}$, and $\mathrm{T_C}$. (g) First-principles calculations of the $\mathrm{T_A}, \mathrm{T_B}$, and $\mathrm{T_C}$ stacking configurations as a function of flat-band filling factor in $1T-\mathrm{TaS_2}$. Scanning parameter: (a, e) $V=-0.4$ V, $I=-100$pA; (b-d) $V=0.4$ V, $I=100$pA.

The obvious effect of the reduction of the flat-band filling factor is to create domains of diverse shapes and sizes separated by sharp DWs (Fig. 2a). Most DWs are formed straightly along the CCDW unit vector with a single-phase shift between two adjacent CCDW domains as shown in Fig. 2b and Figs. S4-S5. In addition, the DWs also construct the complex DW junctions including the X, Y, and so on (Figs. 2c and 2d). It is worth noting that the mosaic-

like CDW states are the stable ground state in the thermal equilibrium, which is existent in each layer and different from the metastable (by the external energy excitations) mosaic state of surface layers in pristine $1T - TaS_2$ in recent reports (Fig. S6) [37].

Interestingly, in addition to the DWs in the surface layer, there are extra but weaker domain walls within a relatively large single-domain (indicated by the red dashed lines in Fig. 2e), which is assigned as the sublayer DWs [37, 42]. These subdomains correspond to different interlayer CDW stacking configurations (Fig. 2f), resulting in different apparent contrasts in the surface-sensitive STM images. The calculation results (Fig. 2g and Fig. S7) show that the flat-band filling factor has a dramatic effect on the stability of interlayer CDW stacking configurations. In the case of a flat-band filling factor n = 1, $T_C$ stacking dominates. As the filling factor decreases, the energy of $T_C$ stacking gradually increases (Supplementary Table II). At the flat band filling factor n $=\sim 3/5$, the energies of the various stacking configurations are similar and the stacking order is random. It means that doping reduces the stacking-dependent interlayer interactions, leading to various local interlayer stacking configurations, which increases the complexity of these mosaic-like CDW states.

In $1T - TaS_2$, SoD can also be arranged into different chiral domains: L-chiral and R-chiral, as shown schematically in Figs. 3a and 3b. The SoD superlattices are rotated clockwise from the Ta atomic lattice by $-13.9°$ and $+13.9°$ in the L- and R-chiral-arranged CDW domains, respectively. In general, the lateral size of the $\sqrt{13} \times \sqrt{13}$ domain of a SoD superlattice in $1T - TaS_2$ is much larger than normal scan range of STM measurements of about a few hundred nanometers [40], and their interlayer stackings are almost exclusively preferred to the homochiral stacking even in different phase stacking configurations. Only very few works about the chiral CDW state were just reported recently with the focus on their global chiral-switching via the circularly polarized light or electrical pulse in the nanothick flakes [41,42].

At the flat band filling factor n $=\sim 3/5$, the large chiral CDW domains emergent within the mosaic-like CDW states, as shown by the marked chiral DWs to separate the R- and L-chiral domains in Figs. 3c-d and the corresponding FFT pattern. The large chiral domains are made of many small homochiral phase domains, as schematically illustrated in Fig. 3e. It is also noted that different from the DWs at low-doping-level, the DWs could not be readily resolved based on their specific local contrast. At the flat-band filling factor n $=\sim 1/3$, the fragmentized CDW states are observed, made of randomly distributed tiny phase and chiral domains, as shown in Figs. 3f and 3h. The short phase and chiral DWs are disordered and could not be clearly defined. The atomic-/SoD-resolution characterizations of these fragmented DWs were further performed, as depicted in Fig. 3g, indicating the perfect continuous atomic lattice across the DWs without any visible doping-induced atomic defects and/or dislocations.

The mirror-symmetric chiral DWs along the [110] and [211] directions of the atomic lattice are illustrated in Fig. 4a and Fig. S9. The chiral DWs along the [110] direction is mostly observed in STM images, as shown in Fig. S10, which should be relatively stable considering the complex inter-SoD interactions around the chiral DWs. Particularly, such chiral DWs easily form the intermediate ring-SoD clusters with a unique central achiral SoD as an anchor point as indicated by the black dashed circles in Fig. 4b. By variable-temperature STM, the STM image containing the ring-SoD cluster features are successfully attained at 50 K (Fig. 4c). In contrast to single chiral domains, such ring-SoD clusters are rarely observed and are found only in larger chiral domains with flat-band filling factor n $=\sim 3/5$. The ring-SoD clusters (white dashed circles) typically have a lateral size of $\sim 5 \times 5$ nm and are surrounded by chiral DWs. Interestingly, these ring-SoD clusters act as thermally excited dynamic structures that can move along the chiral DW and act as intermediate electronic states of the SoD during chiral transitions (Fig. S11). The evolution of chiral transitions via intermediate ring-SoD clusters is further visualized in Fig. 4d, which is schematically illustrated by the atomic model in Fig. 4e and Fig. S12.

Next, we concentrate on the evolution of the metastable intermediate ring-SoD clusters. The sequential in-situ STM characterizations (identified by the bright spots) provide a detailed insight into the dynamics of the chiral changes in CDW superlattices (Figs. 4f-4i). It can be seen that the two chiral domains change over time, with the R-chiral domain expanding and the L-chiral domain gradually shrinking until it eventually all transforms into a structural domain with a single R chirality (Fig. 4i). Moreover, the atomic arrangement of the CDW superlattice remains continuous and intact after the change of chirality. In $1T - TaS_2$, electron-electron correlation and e- *ph* interaction are key factors in the formation of SoD cluster. As the flat-band filling factor decreases, the number of correlated electrons reduces, leading to a weakening of electron-electron correlation. Meanwhile, the ring-SoD clusters serve as the intermediate states during chiral transitions, causing the redistribution of atoms and the renormalization of the phonon frequency. Therefore, we suggest that the appearance of the ring-SoD structure can be phenomenologically attributed to the electron-electron correlation and e-ph coupling.

In $1T-TaS_2$, the manipulation of interlayer stacking allows for the construction of customizable quantum systems exhibiting exotic physics. The models of the homochiral and heterochiral CDW units are depicted in Figs. 5a and 5c. The STM experiments can easily identify the CDW chirality of both layers by measuring the angle between the close-packed direction of SOD and the step edges, which directly visualizes the two different stacking structures of homochiral L/L and heterochiral L/R CDW stacking order as shown in Figs. 5b and 5d. At near full filling of the flat band, no obvious chiral domains are observed in both
the upper and lower layers, showing homochiral stacking (Fig. 5b), which is consistent with pristine $1T-TaS_2$ [43,44]. At half-filling of the flat band, the reduction of electron-electron correlation contributes to the appearance of chiral domains, meanwhile the weakening of interlayer interactions is accompanied by the simultaneous emergence of two different chiral domains in both the upper and the lower layers, resulting in heterochiral stacking (Fig. 5d).

In contrast to the homochiral L/L stacking configuration (Fig. 5e), a 27.8° rotational mismatch between the L- and R-layer CDWs in the heterochiral L/R stacking configuration contributes to a commensurate CDW moiré superstructure (Fig. 5f). In the CDW moiré unit cell (black diamond-shaped box in Fig. 5f), the relaxed atomic structure transforms from a $(\sqrt{13} \times \sqrt{13})$ R13.9° triangular superlattice to a larger $13 \times 13$ super-superlattice. This superstructure CDW state is energetically very unfavorable and susceptible to spontaneous symmetry breaking, inducing a redistribution of atoms into a nematic structure. We propose the possible formation of the intermediate nematic L/R structure (Fig. 5g) and the final nematic CDW configuration after structural relaxation of the superstructure generated by CDW chiral coexistence (Fig. 5h).

Real-space investigations of the nematic CDW state at heterochiral L/R stacking interfaces are presented in Fig. 5i and Fig. S13. By statistically analyzing the areas occupied by homochiral L/L (R/R) stacking structures and the areas occupied by heterochiral L/R (R/L) stacking configurations, we can roughly determine the ratio of homochirality to heterochiral to be approximately 5:5. One-dimensional stripe-like features with different orientations are observed in the heterochiral L/R stacking region, and the stripes are all along the [211] direction of the underlying atomic lattice. This can be directly evidenced by the observed CDW states around the homochiral and heterochiral stacking edges in Fig. 5j. Note that we can rule out the multiple tip effect because it would have caused discontinuity in the surrounding CDW unicells while the unicells are smoothly connected in the above observation. The detailed mechanism for the formation of the nematic CDW states needs to be further investigated in conjunction with theoretical calculations, which is beyond the scope of this paper.

### 26.0.2 Conclusion

$1T - TaS_2$ exhibits abundant physical properties and electronic structure, providing an ideal platform to investigate the CDW order and strong electron-electron correlations. In the CCDW state, the central Mott electrons of SoDs form a flat-band structure at the $E_F$. This phenomenon is attributed to the interplay between electron-electron correlations and electron-lattice interactions. The $1T - TaS_2$ in the flat-band state demonstrates diverse quantum states, including superconductivity, CDW, and insulating states. The modulation of these quantum states is crucial for advancing our understanding of correlated electronic systems. Hole doping, as a particularly effective means of regulation, not only adjusts the flat-band filling factor in $1T - TaS_2$ by altering the electron density, but also induces changes in electronic interactions. This dual effect suggests a promising avenue for research aimed at realizing quantum states.

We directly visualize the filling-dependent stable multiple intertwined orders in $1T - TaS_2$, involving hole order, phase domains, chiral domains, and mixed phase/chiral domains by STM (Fig. S14). The evolution of intralayer electron correlations and interlayer CDW stacking order with flat-band filling factor is further investigated in conjunction with DFT calculations. As the flat-band filling factor approaches 1, the system exhibits a long-range ordered CCDW structure with some hole orders. As the flat band filling factor decreases, phase and chiral domains of different shapes and sizes appear. As the flat-band filling factor further decreases, interlayer CDW stacking becomes progressively disordered, contributing to the weakening of interlayer interactions and the emergence of interlayer heterochiral stacking. The interplay of complex electron-electron correlations, electron-lattice interactions, and interlayer interactions collectively induces a redistribution of atoms into a ring-SoD and stripe-SoD ordered structures, accompanied by a change in symmetry. This modulation of the atomic structure further feeds back into the electronic structure, complicating the interactions between electronic and atomic orders. The study paves a way to realize exotic quantum states via the accurate tuning of interior interactions and flat-band filling factors in correlated materials. This approach to manipulating interactions and electronic degrees of freedom will inspire further research focus on electronic structures, properties, and applications in the field of correlated electron materials.

### 26.0.3 Methods

**Single crystal growth of Ti-doped $1T - TaS_2$.**

The high-quality $1T - Ta_{1-x}Ti_xS_2$ single-crystals were grown by chemical vapor transport (CVT) method. Ta (99.99%, Aladdin), $TaCl_5$ (99.99%, Aladdin), S (99.99%, Aladdin), and Ti (99.99%, Aladdin) powders with a nominal molar ratio of 1:0.02:2.05:x (x $=\sim 0.3\%, 0.8\%, 2.5\%, 4.2\%, 6.3\%$) were mixed thoroughly and then loaded into quartz tubes (inner diameter/outer diameter/length: 14/16/200 mm). Large $1T - Ta_{1-x}Ti_xS_2$ crystals with size up to 10 mm were collected for further characterization and measurement. X-ray diffraction (XRD) and X-ray energy dispersive spectroscopy (EDS) were employed to determine the crystal structure, morphology, and composition of as-prepared samples. The Ti-doping contents of all samples agree with their nominal molar ratio of source materials, demonstrating the controllable synthesis. In order to visualize the filling factor of the flat bands more visually for different doping concentrations, we approximate the filling factor n as the fraction.

**Scanning tunneling microscopy (STM).**

High-quality Ti-doped $1T - TaS_2$ crystals were cleaved at room temperature in ultrahigh vacuum at a base pressure of $2\times10^{-10}$ Torr, and directly transferred to the cryogen-free variable-temperature STM system (PanScan Freedom, RHK). Chemically etched W tips were used for

STM measurement in constant-current mode. The STM tips were calibrated on a clean Ag(111) surface. Gwyddion was used for STM data analysis.

**Density functional theory calculations and simulations.**

Our DFT calculations were performed using the generalized gradient approximation for the exchange-correlation potential, the projector augmented wave method and a plane-wave basis set as implemented in the Vienna ab-initio simulation package (VASP). Dispersion correction was implemented using the DFT-D3 method, with the PBE functional for the exchange potential. The effective U value of the on-site Coulomb interaction of the Ta $d$ orbitals is 2.3 eV . All our simulation cells contain a 20Å vacuum to prevent interlayer coupling between different layers. The plane-wave cutoff was set to 450 eV. A k-mesh of $5 \times 5 \times 1$ was adopted to sample the first Brillouin zone of the cell. Convergence is reached if the consecutive energy difference is within 10-5 eV for electronic iterations and the forces are less than 0.01eVÅ.

### 26.0.4 References:


1. Chen, P.; Chan, Y.-H.; Fang, X.-Y.; Zhang, Y.; Chou, M. Y.; Mo, S.-K.; Hussain, Z.; Fedorov, A.-V.; Chiang, T.-C. Charge Density Wave Transition in Single-Layer Titanium Diselenide. Nat. Commun. 2015, 6, 8943.

2. Ugeda, M. M.; Bradley, A. J.; Zhang, Y.; Onishi, S.; Chen, Y.; Ruan, W.; Ojeda-Aristizabal, C.; Ryu, H.; Edmonds, M. T.; Tsai, H.-Z.; Riss, A.; Mo, S.-K.; Lee, D.; Zettl, A.; Hussain, Z.; Shen, Z.-X.; Crommie, M. F. Characterization of Collective Ground States in Single-Layer $NbSe_2$. Nat. Phys. 2016, 12, 92-97.

3. Ryu, H.; Chen, Y.; Kim, H.; Tsai, H.-Z.; Tang, S.; Jiang, J.; Liou, F.; Kahn, S.; Jia, C.; Omrani, A. A.; Shim, J. H.; Hussain, Z.; Shen, Z.-X.; Kim, K.; Min, B. I.; Hwang, C.; Crommie, M. F.; Mo, S.-K. Persistent Charge-Density-Wave Order in Single-Layer $TaSe_2$. Nano Lett. 2018,18, 689-694.

4. Ye, J. T.; Zhang, Y. J.; Akashi, R.; Bahramy, M. S.; Arita, R.; Iwasa, Y. Superconducting Dome in a Gate-Tuned Band Insulator. Science 2012, 338, 1193-1196.

5. Rubio-Verdu, C.; Garcıa-Garcıa, A. M.; Ryu, H.; Choi, D.-J.; Zaldıvar, J.; Tang, S.; Fan, B.; Shen, Z.-X.; Mo, S.-K.; Pascual, J. I.; Ugeda, M. M. Visualization of Multifractal Superconductivity in a Two-Dimensional Transition Metal Dichalcogenide in the Weak-Disorder Regime. Nano Lett. 2020, 20, 5111-5118.

6. Chen, Y.; Ruan, W.; Wu, M.; Tang, S.; Ryu, H.; Tsai, H.-Z.; Lee, R. L.; Kahn, S.; Liou, F.; Jia, C.; Albertini, O. R.; Xiong, H.; Jia, T.; Liu, Z.; Sobota, J. A.; Liu, A. Y.; Moore, J. E.; Shen, Z.-X.; Louie, S. G.; Mo, S.-K.; et al. Strong Correlations and Orbital Texture in Single-Layer 1T-$TaSe_2$. Nat. Phys. 2020, 16, 218-224.

7. Bonilla, M.; Kolekar, S.; Ma, Y.; Diaz, H. C.; Kalappattil, V.; Das, R.; Eggers, T.; Gutierrez, H. R.; Phan, M.-H.; Batzill, M. Strong Room-Temperature Ferromagnetism in $VSe_2$ Monolayers on van der Waals Substrates. Nat. Nanotechnol. 2018, 13, 289-293.

8. Anshul, K.; Melinda, S. R.; Sean, V.; Ali, A. H.; Felix, F.; Young, I. J.; Luc, V.; Greg, J. M.; Tai, C. C.; Eduardo, Fradkin.; Jasper, V. W.; Peter, A.; Signatures of exciton condensation in a transition metal dichalcogenide. Science 2017, 358, 1314.

9. Rossnagel, K.; On the origin of charge-density waves in select layered transition-metal dichalcogenides. J Phys Condens Matter. 2011, 23, 213001.

10. Zhong, Y. G.; Liu, J. J.; Wu, X. X.; Guguchia, Z.; Yin, J.-X.; Mine, A.; Li, Y. K.; Najafzadeh, S.; Das, D.; Mielke, C.; Khasanov, R.; Luetkens, H.; Suzuki, T.; Liu, K. C.; Han, X. L.; Kondo, T.; Hu, J. P.; Shin, S.; Wang, Z. W.; Shi, X.; Yao, Y. G.; Okazaki, K. Nodeless electron pairing in $CsV_3Sb_5$ derived kagome superconductors. Nature 2023, 617, 488-492.

11. Li, C. S.; Xu, F.; Li, B. H.; Li, J. Y.; Li, G.; Watanabe, K. J.; Taniguchi, T.; Tong, B. B. Shen, J.; Lu, L.; Jia, J. F.; Wu, F. C.; Liu, X. X.; Li, T. X. Tunable superconductivity in electron- and hole-doped Bernal bilayer graphene. Nature 2024, 631, 300-306.

12. Cao, Y.; Park, J. M.; Watanabe, K. J.; Taniguchi, T.; Jarillo-Herrero, P. Pauli-limit violation and re-entrant superconductivity in moiré graphene. Nature 2021, 595, 526-531.

13. Zhang, Y.; Yang, L. X.; Xu, M.; Ye, Z. R.; Chen, F.; He, C.; Xu, H. C.; Jiang, J.; Xie, B. P.; Ying, J. J.; Wang, X. F.; Chen, X. H.; Hu, J. P.; Matsunami, M.; Kimura, S.; Feng, D. L. Nodeless superconducting gap in $AxFe_2Se_2(\ A = K, Cs)$ revealed by angle-resolved photoemission spectroscopy. Nat. Mater. 2011,10, 273-277.

14. Xintong Li, Changwei Zou, Ying Ding, Hongtao Yan, Shusen Ye, Haiwei Li, Zhenqi Hao, Lin Zhao, Xingjiang Zhou, and Yayu Wang, Evolution of Charge and Pair Density Modulations in Overdoped $Bi_2Sr_2CuO_{6+\delta}$. Phys. Rev. X 2021, 11, 011007.

15. Wise, W.; Boyer, M.; Chatterjee, K.; Kondo, T.; Takeuchi, T.; Ikuta, H.; Wang, Y. Y.; Hudson, E. W. Charge-density-wave origin of cuprate checkerboard visualized by scanning tunnelling microscopy. Nat. Phys. 2008, 4, 696-699.

16. Cao, L.; Xue, Y. C.; Wang, Y. B.; Zhang, F.-C.; Kang, J.; Gao, H.-J.; Mao, J. H.; Jiang, Y. H. Directly visualizing nematic superconductivity driven by the pair density wave in $NbSe_2$. Nat. Commun. 2024, 15, 7234.

17. Wen, C. H. P.; Xu, H. C.; Chen, C.; Huang, Z. C.; Lou, X.; Pu, Y. J.; Song, Q.; Xie, B. P.; Abdel-Hafiez, M.; Chareev, D. A.; Vasiliev, A. N.; Peng, R.; Feng, D. L. Anomalous correlation effects and unique phase diagram of electron-doped FeSe revealed by photoemission spectroscopy. Nat. Commun. 2016, 7, 10840.

18. Chen, F.; Xu, M.; Ge, Q. Q.; Zhang, Y.; Ye, Z. R.; Yang, L. X.; Jiang, J.; Xie, B. P.; Che, R. C.; Zhang, M.; Wang, A. F.; Chen, X. H.; Shen, D. W.; Hu, J. P., Feng, D. L. Electronic Identification of the Parental Phases and Mesoscopic Phase Separation of $K_xFe_{2-y}Se_2$ Superconductors. Phys. Rev. X 2011, 1, 021020.

19. Yi, M.; Lu, D. H.; Yu, R.; Riggs, S. C.; Chu, J.-H.; Lv, B.; Liu, Z. K.; Lu, M.; Cui, Y.-T.; Hashimoto, M.; Mo, S.-K.; Hussain, Z.; Chu, C. W.; Fisher, I. R.; Si, Q.; Shen, Z.-X. Observation of Temperature-Induced Crossover to an Orbital-Selective Mott Phase in $AxFe_2Se_2(\ A = K, Rb)$ Superconductors. Phys. Rev. Lett. 2013, 110, 067003.

20. Kang, Y. M.; Najmaei, S.; Liu, Z.; Bao, Y. J.; Wang, Y. M.; Zhu, X.; Halas, N. J.; Nordlander, P.; Ajayan, P. M.; Lou, J.; Fang, Z. Y. Plasmonic hot electron induced structural phase transition in a $MoS_2$ monolayer. Adv. Mater. 2014, 26, 6467-6471.

21. Lin, Y.-C.; Torsi, R.; Geohegan, D. B.; Robinson, J. A.; Xiao, K. Controllable Thin-Film Approaches for Doping and Alloying Transition Metal Dichalcogenides Monolayers. Adv. Sci. 2021, 8, 2004249.

22. Lee, S.-H.; Goh, J. S.; Cho, D. Origin of the insulating phase and first-order metal-insulator transition in 1T-TaS $_2$. Phys. Rev. Lett. 2019, 122, 106404.

23. Wilson, J. A.; Di Salvo, F. J.; Mahajan, S.; Charge-density waves in metallic, layered, transition-metal dichalcogenides. Phys. Rev. Lett. 1974, 32, 882-885.

24. Geng, Y. Y.; Lei, L.; Dong, H. Y.; Guo, J. F.; Mi, S.; Li, Y.; Huang, L.; Pang, F.; Xu, R.; Zhou, W. C.; Liu, Z.; Ji, W.; Cheng, Z. H. Hysteretic electronic phase transitions in correlated charge-density-wave state of 1T-TaS $_2$. Phys. Rev. B 2023, 107, 195401.

25. Butler, C. J.; Yoshida, M.; Hanaguri, T.; Iwasa, Y. Mottness versus unit-cell doubling as the driver of the insulating state in 1T -TaS $_2$, Nat. Commun. 2020, 11, 2477.

26. Ritschel, T.; Berger, H.; Geck, J. Stacking-driven gap formation in layered 1T -TaS $_2$, Phys. Rev. B 2018, 98, 195134.

27. Lee, J.; Jin, K. H.; Yeom, H. W. Distinguishing a Mott Insulator from a Trivial Insulator with Atomic Adsorbates, Phys. Rev. Lett. 2021, 126, 196405.

28. Wang, Z. L.; Dong, H. Y.; Zhou, W. C.; Cheng, Z. H.; Wang, S. C. Flat band in hole-doped transition metal dichalcogenide observed by angle-resolved photoemission spectroscopy. Chin. Phys. B 2023, 32, 067103.

29. Geng, Y. Y.; Guo, J. F.; Meng, F. Y.; Wang, M. Y.; Mi, S.; Huang, L.; Xu, R.; Pang, F.; Liu, K.; Wang, S. C.; Gao, H.-G.; Zhou, W. C.; Ji, W.; Lei, H. C.; Cheng, Z. H.; Correlated electrons of the flat band in charge density wave state of $4H_b - TaSe_xS_{2-x}$. Phys. Rev. B 2024, 110, 115107.

30. Bang, J.; Lee, B.; Yang, H.; Kim, S.; Wulferding, D.; Cho, D. Charge-ordered phases in the hole-doped triangular Mott insulator $4H_b - TaS_2$. Phys. Rev. B 2024, 109, 195170.

31. Lee, J.; Jin, K.-H.; Yeom, H. W. Distinguishing a Mott insulator from a trivial insulator with atomic adsorbates. Phys. Rev. Lett. 2021, 126,196405.

32. Lee, D.; Jin, K.-H.; Feng, L.; Yeom, H. W. Tunable Mott Dirac and Kagome bands engineered on 1T-TaS $_2$. Nano. Lett. 2022, 22, 7902-7909 (2022).

33. Zhang, W. H.; Gao, J. J.; Cheng, L.; Bu, K. L.; Wu, Z. X.; Fei, Y.; Zheng, Y.; Wang, L.; Li, F. S.; Luo, X.; Liu, Z.; Sun, Y. P.; Yin, Y. Visualizing the evolution from Mott insulator to Anderson insulator in Ti-doped 1T-TaS $_2$. npj Quantum Mater. 2022, 7, 8.

34. Patel, R. K.; Patra, K.; Ojha, S. K.; Kumar, S.; Sarkar, S.; Saha, A.; Bhattacharya, N.; Freeland, J. W.; Kim, J.-W.; Ryan, P. J.; Mahadevan, P.; Middey, S. Hole doping in a negative charge transfer insulator. Commun. Phys. 2022, 5, 216.

35. Cho, D.; Cheon, S.; Kim, K.-S.; Lee, S.-H.; Cho, Y.-H.; Cheong, Yeom, H. W. Nanoscale manipulation of the Mott insulating state coupled to charge order in 1T-TaS $_2$. Nat. Commun. 2016, 7, 10453.

36. Cho, D.; Gye, G.; Lee, J.; Lee, S.-H.; Wang, L. H.; Cheong S.-W.; Yeom, H. W. Correlated electronic states at domain walls of a Mott-charge-density-wave insulator 1T-TaS $_2$. Nat. Commun. 2017, 8, 392.

37. Ma, L. G.; Ye, C.; Yu, Y. J.; Lu, X. F.; Niu, X. H.; Kim, S.; Feng, D. L.; Tománek, D.; Son, Y.-W.; Chen, X. H.; Zhang, Y. B. A metallic mosaic phase and the origin of Mott-insulating state in 1T-TaS $_2$. Nat. Commun. 2016, 7, 10956.

38. Bu, K. L.; Zhang, W. H.; Fei, Y.; Wu, Z. X.; Zheng, Y.; Gao, J. J.; Luo, X.; Sun, Y.-P. Yin, Y. Possible strain induced Mott gap collapse in 1T-TaS $_2$. Commun. Phys. 2019, 2, 146.

39. Zhang J.; Lian, C.; Guan, M. X.; Ma, W.; Fu, H. X.; Guo, H. Z.; Meng, S.; Photoexcitation induced quantum dynamics of charge density wave and emergence of a collective mode in 1T-TaS $_2$. Nano Lett. 2019,19, 6027-6034.

40. Ohta S.; Kobayashi, S.; Nomura, A.; Sakata, H.; Electronic state modulation of the Star of David lattice by stacking of $\sqrt{13} \times \sqrt{13}$ domains in 1T-TaSe $_2$. Phys. Rev. B 2021, 104, 155433 (2021).

41. Jarc, G.; Mathengattil, S. Y.; Montanaro, A.; Giusti, F.; Rigoni, E. M.; Sergo, R.; Fassioli, F.; Winnerl, S.; Zilio, S. D.; Mihailovic, D.; Prelovšek, P.; Eckstein, M.; Fausti, D. Cavity-mediated thermal control of metal-to-insulator transition in 1T-TaS $_2$. Nature 2023, 622, 487.

42. Park, J. W.; Lee, J. W.; Yeom, H. W. Zoology of domain walls in quasi-2D correlated charge density wave of 1T-TaS $_2$. npj Quantum Mater. 2021, 6, 32.

43. Song, X.; Liu, L.; Chen, Y.; Yang, H.; Huang, Z.; Hou, B.; Hou, Y.; Han, X.; Yang, H.; Zhang, Q.; Zhang, T.; Zhou, J.; Huang, Y.; Zhang, Y.; Gao, H.-J.; Wang, Y. Atomic-Scale Visualization of Chiral Charge Density Wave Superlattices and Their Reversible Switching. Nat. Commun. 2022, 13, 1843.

44. Liu, L. W.; Song, X.; Dai, J. Q.; Yang, H.; Chen, Y. Y.; Huang, X. Y.; Huang, Z. P.; Ji, H. Y.; Zhang, Y.; Wu, X.; Sun, J.-T.; Zhang, Q. Z.; Zhou, J. D.; Huang, Y.; Qiao, J. S.; Ji, W.; Gao, H.-J.; Wang, Y. L. Unveiling Electronic Behaviors in Heterochiral Charge-Density-Wave Twisted Stacking Materials with 1.25 nm Unit Dependence. ACS Nano 2023, 17, 2702-2710.

45. Ravnik, J.; Vaskivskyi, Y.; Vodeb, J.; Diego, M.; Venturini, R.; Gerasimenko, Y.; Kabanov, V.; Kranjec, A.; Mihailovic, D. Chiral domain dynamics and transient interferences of mirrored superlattices in nonequilibrium electronic crystals. Sci Rep. 2023, 13(1),19622.

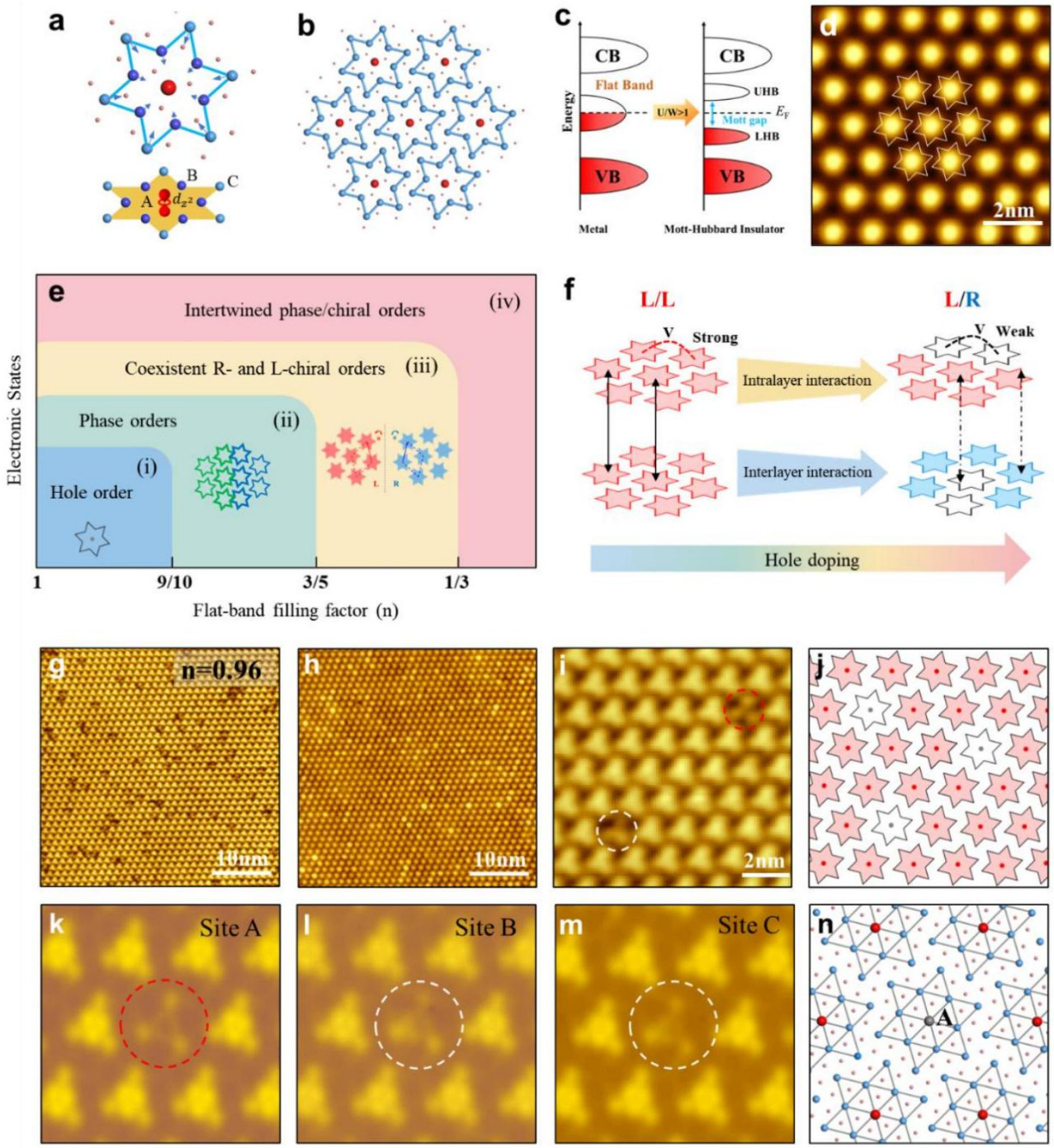


Figure 1. Structure model of filling-dependent intertwined electronic and atomic orders of $\mathbf{1}\boldsymbol{T}\mathbf{TaS_2}$. (a) Atomic models of the SoD cluster with the localized $d_{z^2}$ orbital (unpaired electron) of central Ta atom. (b) Schematic of the SoD clusters with the $\sqrt{13} \times \sqrt{13}$ periodicity. (c) Schematic band structures of correlated CDW state, in which the half-filled flat band of the localized $d_{z^2}$ orbital is split into UHB and LHB bands via electron correlations. (d) STM image of commensurate CDW state with the overlaid SoD models. (e) Schematic diagram of electronic orders and flat-band filling factors of $1T - TaS_2$. Each SoD is fully central electron-filled, corresponding to a flat-band filling factor n = 1 for $1T - TaS_2$. While each SoD is fully central electron-empty, corresponding to a flat-band filling factor n = 0 for $1T$ - $TaS_2$. (f) Schematic of the delicate interplay of the complex intralayer and interlayer interactions with the hole doping. (g-i) Large-scale occupied state (g), unoccupied state (h), high-resolution (i) STM images of hole order at the flat-band filling factor n =$\sim$ 0.96. (j) Structure model of electron-filled and -empty SoDs. The central

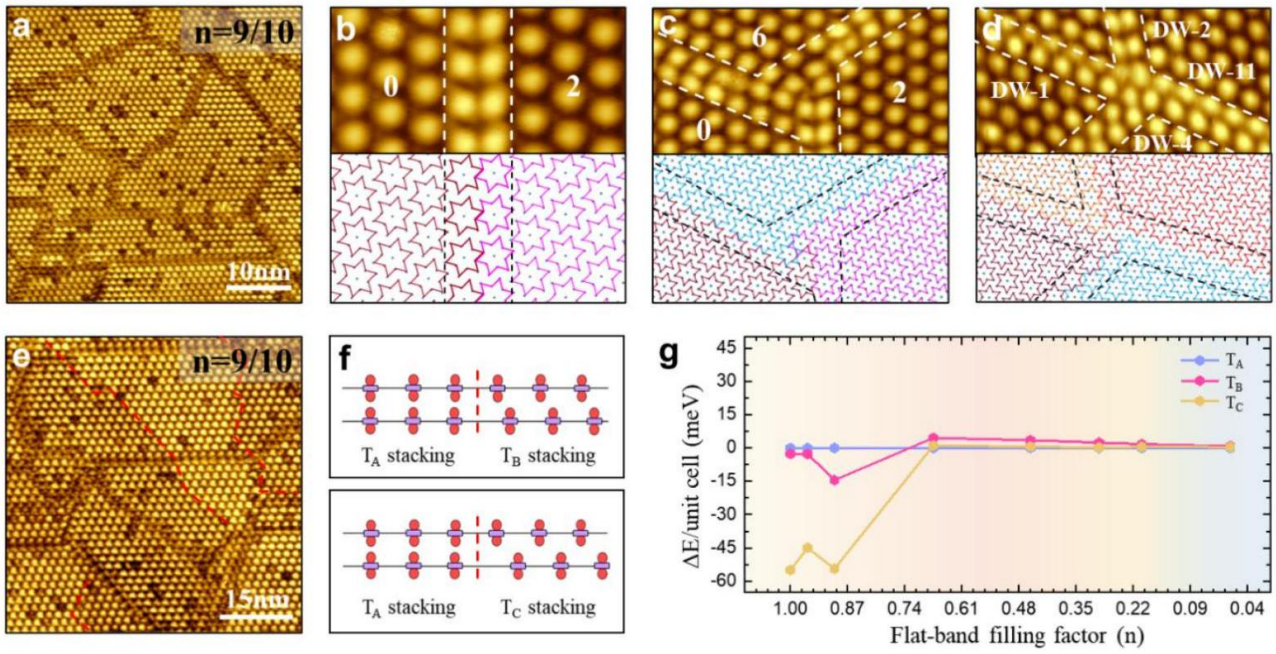


Figure 2. Emergence of phase domains at the flat-band filling factor $\mathbf{n} = \sim \mathbf{9/10}$ of $\mathbf{1}\boldsymbol{T} - \mathbf{TaS_2}$. (a) Large-scale STM images of the emergent phase domains of $1T - \mathrm{TaS_2}$. (b) STM images of the typical CDW

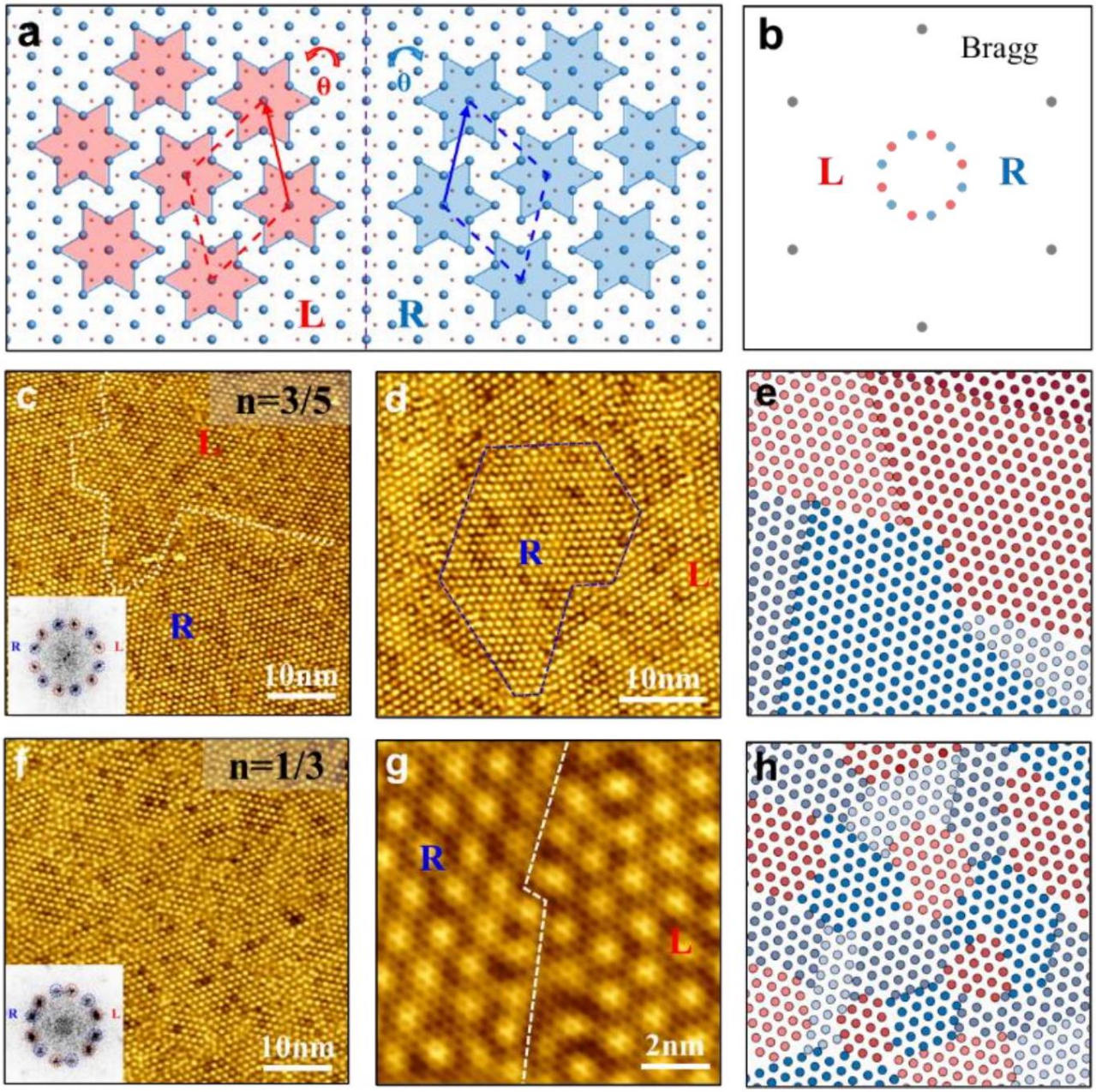


Figure 3. Filling-dependent intertwined phase and chiral orders of $\mathbf{1}\boldsymbol{T}-\mathbf{TaS_2}$. (a) Schematic of L- and R- chiral CDW domains. Unit cells of L- and R-chiral domains are shaded in red and blue, respectively. (b) Schematic FFT pattern of L- and R-chiral CDW domains with the atomic Bragg spots. (c,d) Large-scale STM images of the emergent chiral domain wall at the flat-band filling factor n = 3/5 of $1T - TaS_2$. The chiral DW is along the [110] directions of R-chiral domain and marked by blue dashed lines in (d). (e) The structural model of chiral domains. The emergent large chiral-arranged CDW domain is made of many small homochiral phase domains. (f) Large-scale STM images of intertwined chiral and phase domains at the flat-band filling factor n $=\sim 1/3$ of $1T - TaS_2$. (g) Atomic-resolution STM image of typical chiral DWs. The chiral DW is marked by white dashed lines. (h) The structural model of mixed chiral/phase domains. The fragmentized CDW state is made of randomly distributed tiny phase and chiral domain. Scanning parameter: $V = 0.4$ V, $I = 100$pA.

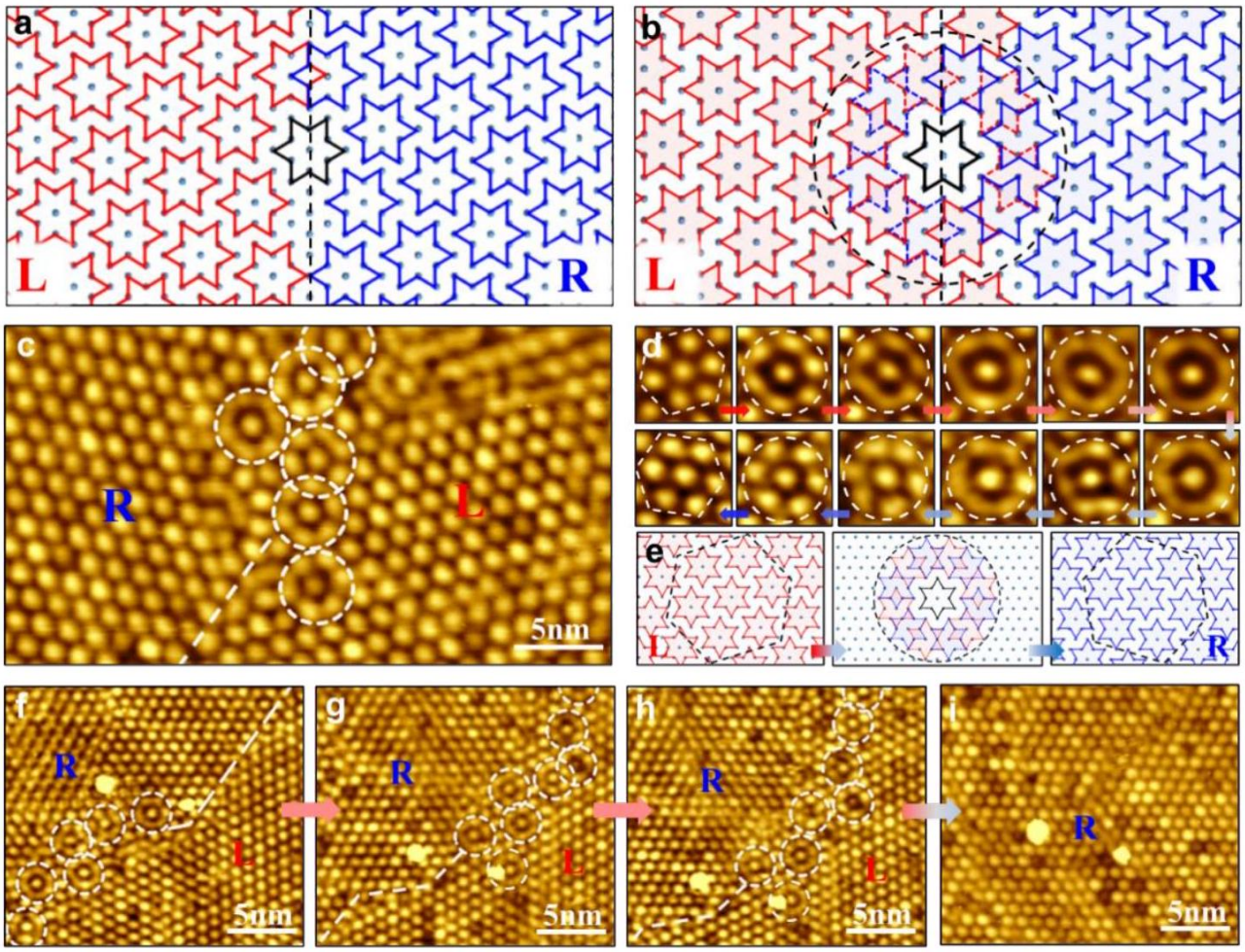


Figure 4. Emergence of intralayer ring-SoD clusters on the chiral domain wall of $\mathbf{1}\boldsymbol{T}-\mathbf{TaS_2}$. (a) Atomic structural model of chiral DW along the [110] direction. This kind of chiral DW is mostly observed in STM images, which should be relatively stable considering the complex intra-SoD interactions around the chiral domain walls. (b) Chiral SoD-overlapping model of the mirror-symmetric DW with the central achiral SoD (black star). (c) STM images of the emergent intermediate ring-SoD clusters around the chiral DWs of $1T-\mathrm{TaS_2}$. (d,e) High-resolution STM images and structural models of a series of dynamic intermediate ring-SoD clusters configurations from L-chiral SoD to R-chiral SoD, phenomenally indicating the structural evolution of SoDs and the process of chiral-switching transition. (f-i) A sequential in-situ STM images showing dynamic chiral-switching of ring-SoD clusters at the chiral DWs. The ring-SoD clusters are marked with the dashed circles. Scanning parameter: $V = 0.4$ V, $I = 100$pA.

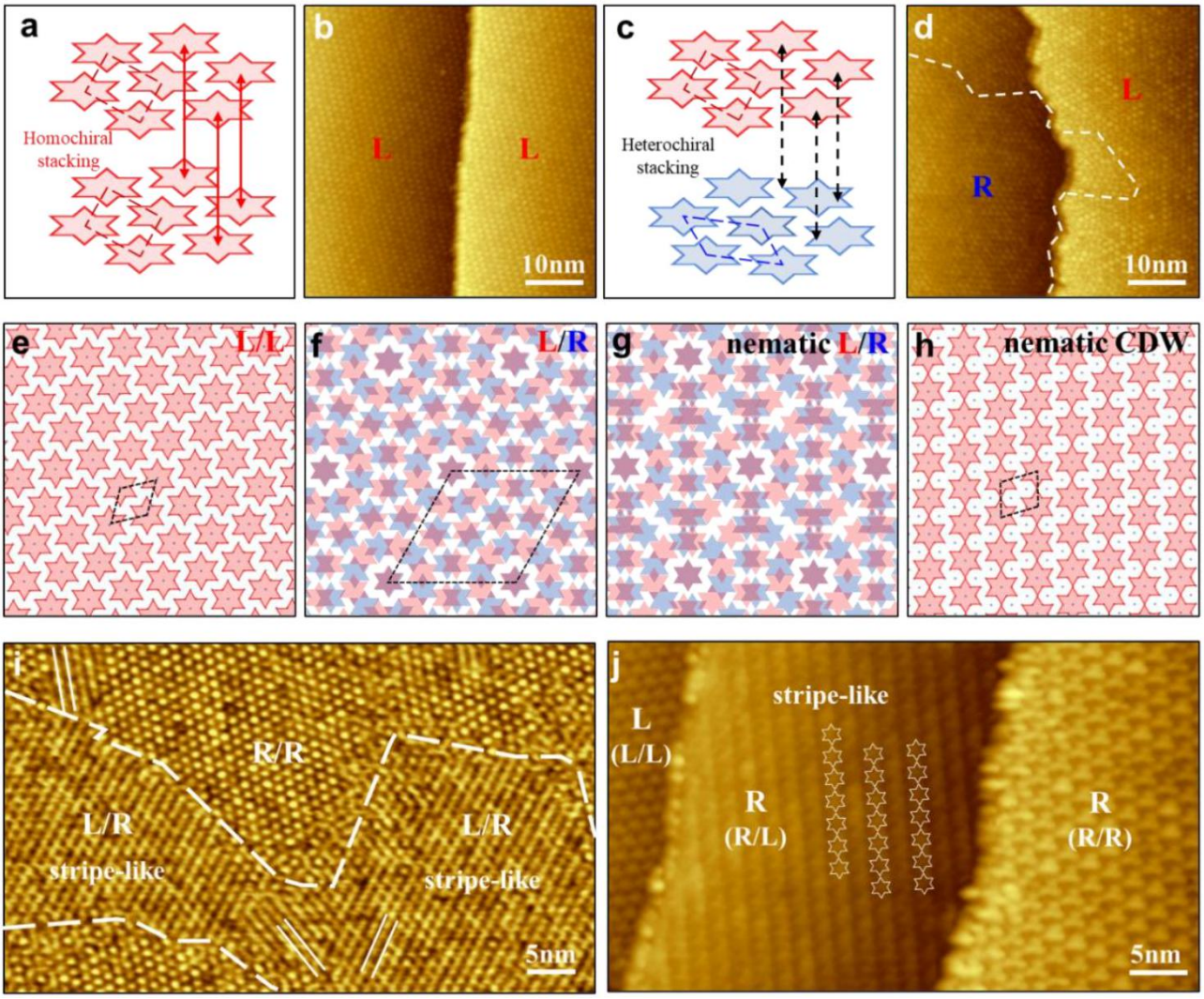


Figure 5. Interlayer heterochiral CDW stacking and the emergent nematic CDW state of $\mathbf{1}\boldsymbol{T}-\mathbf{TaS_2}$. (a,b) Schematics and STM images of step edge in homochiral CDW stacking configurations. (c,d) Schematics and STM images of step edge in heterochiral CDW stacking configurations. (e,f) Illustration of CDW superstructures for homochiral L/L and heterochiral L/R stacking. Unit cells of the CDW superstructures are outlined in black. (g) Proposed directional relaxed heterochiral stacking configurations for the observed stripe-like pattern of nematic L/R stacking. (h) Structural model of the stripe-like nematic CDW state. (i) Large-scale STM image of the chiral domain with the emergent stripe-like nematic CDW state due to heterochiral stacking configuration. (j) STM image of two step edges with respective homochiral/heterochiral stacking configurations and the accompanying stripe-like feature of nematic CDW state. Scanning parameters: $(\mathrm{b,d,j})V = -0.4$ V, $I = -100$pA; (i) $V = 0.4$ V, $I = 100$pA.

# 27 Dualistic insulator states in 1T-TaS $_2$ crystals (2023) by Wang et al.

**Authors:** Yihao Wang, Zhihao Li, Xuan Luo, Jingjing Gao, Yuyan Han, Jialiang Jiang, Jin Tang, Huanxin Ju, Tongrui Li, Run Lv, Shengtao Cui, Yingguo Yang, Yuping Sun, Junfa Zhu, Xingyu Gao, Wenjian Lu, Zhe Sun, Hai Xu, Yimin Xiong, and Liang Cao.

## 27.1 Article

(we are not sure about the reason of insulation of bulk TaS2) While the monolayer sheet is well-established as a Mott-insulator with a finite energy gap, the insulating nature of bulk $1\ \mathrm{T}-\mathrm{TaS}_2$ crystals remains ambiguous due to their varying dimensionalities(what is meant by varying dimensionalities?) and alterable interlayer coupling.

(we'll show you how you can describe layered material) In this study, we present a unique approach to unlock the intertwined two-dimensional Mott-insulator and three-dimensional band-insulator states in bulk 1T- $\mathrm{TaS}_2$ crystals by structuring a laddering stack along the out-of-plane direction.

(layers coupling gives insulation) Through modulating the interlayer coupling, the insulating nature can be switched between band-insulator and Mott-insulator mechanisms.

(some duality was found in TaS2) Our findings demonstrate the duality of insulating nature in $1\ \mathrm{T}-\mathrm{TaS}_2$ crystals.

(maybe somehow you can get something more useful from this duality) By manipulating the translational degree of freedom in layered crystals, our discovery presents a promising strategy for exploring fascinating physics, independent of their dimensionality, thereby offering a "three-dimensional" control for the era of slidetronics (materials, where properties are controlled by sliding individual atomic layers relative to one another) .

### 27.1.1 Introduction

(Mott-insulating states can be useful) The discovery of Mott-insulating states holds significant relevance for unconventional superconductors and quantum spin liquid phase (QSL), showing promise for applications in quantum computing (applications in quantum computing?) [1–4].

(people studied a lot insulating state of TaS2) The Mott-insulating state in the layered octahedral 1T- $\mathrm{TaS}_2$ crystals, first proposed four decades ago [5], has led to extensive investigations into the intertwined correlations among Mott-insulator, charge density wave (CDW), and superconducting states [6–9].

(1 layer TaS2 -> SOD+CDW) The Mott-insulating nature is widely accepted in isolated monolayer $1\ \mathrm{T}-\mathrm{TaS}_2$ due to the preserved in-plane David-stars in the commensurate CDW (C-CDW) state and the absence of interlayer coupling [10–13]. (no interlayer coupling -> MH model is applicable without any correction for other layers -> Mott state)

(something important was researched about bulk TaS2) However, in the past decade, a plot twist has emerged in understanding the insulating behavior in bulk $1\ \mathrm{T}-\mathrm{TaS}_2$ crystals.

(SOD are important and they can be aligned differently in one layer to another) Theoretical and experimental studies have introduced the concept of the band-insulator mechanism, considering the key role of the David-stars dimerization associated with specific ontop David-stars $\mathrm{T_A}$ stacking configurations (Fig. 1d) [10,13–18].

(out of plane there is still insulation) However, the theoretically predicted out-of-plane metallic state(theoretically predicted out-of-plane metallic state?) has not been observed in transport experiment [10,14–16,19].

(something is not explained for bulk TaS2) And discrepancies exist between microscopic and macroscopic properties [17,20–22].

(some band-to-Mott insulating phase transitions were predicted but most likely were not confirmed ) For instance, the recent findings of the band-to-Mott insulating phase transition (band-to-Mott insulating phase transition????) at a narrow temperature window in 1 T$-$TaS$_2$ crystals upon heating have not fully manifested in the macroscopic transport measurements yet [22,23].

(some other effects are there, this is why people are not sure about real insulating mechanism) Along with anomalies like the absence of long-range magnetic order and unexpected emergence of superconducting states [6,7,18,24–27], these complexities complicate the understanding of the physics of this system, making it challenging to reach a definitive conclusion about the insulating nature of 1 T $-$ TaS$_2$ crystals.

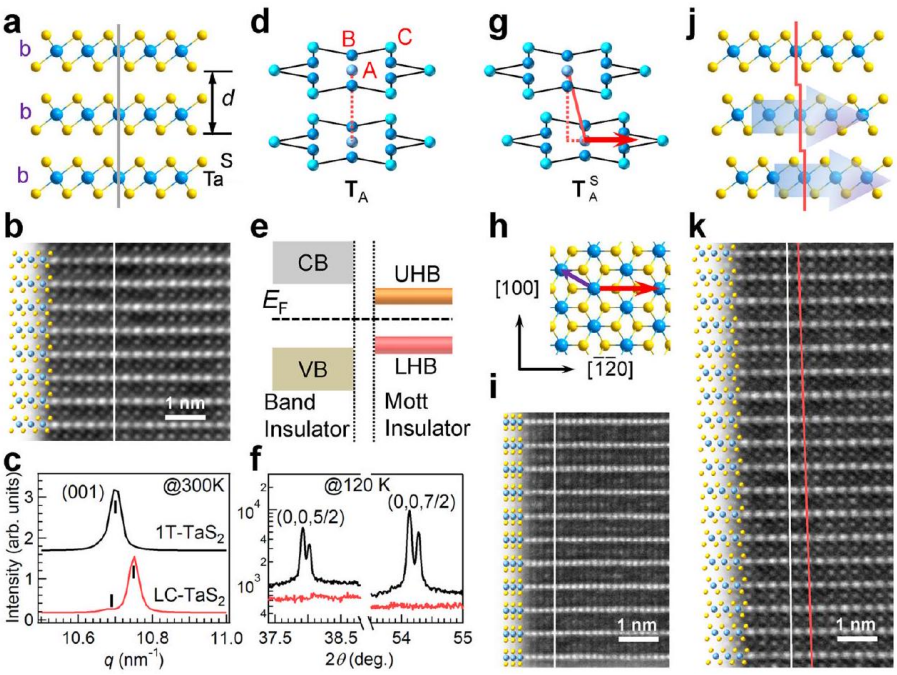


Fig. 1 | Variation in the atomic structure and insulating nature.
a Schematic side view of 1 T$-$TaS$_2$ crystals and (b) corresponding [100] cross-sectional HAADF-STEM image (HAADF-STEM image?) .
c Synchrotron-based XRD spectra(XRD spectra???) around the (001) diffraction peak collected at room temperature.
f The out-of-plane superlattice and reflections for a 1T-TaS$_2$ crystal collected at 120 K.
The peak splitting is attributed to the CuK$_{\alpha 1}$ and K$_{\alpha 2}$ X-ray split.
Illustration of (d) the David-stars T$_A$ stacking and (g) the T$^S{}_A$ stacking associated with (**j**) the laddering stack structure in LC-TaS $_2$ crystals verified by HAADF-STEM images collected along (k) [100] and (i) [120] directions.
The white vertical lines in panels (b, k, i) indicate the c-direction. The red solid line in panel (k) highlights the atomic misalignment. h Schematic top view of monolayer octahedral TaS$_2$.
The red and purple arrows indicate the [120] and [110] directions, respectively. e Schematic energy band diagrams depicting a band-insulator and a Mott-insulator.
CB, VB, UHB, and LHB denote the conduction band, valence band, upper Hubbard band, and lower Hubbard band, respectively.

(if we increase layers, inner interaction becomes more influential) As the surface-to-volume

ratio increases in layered materials, surface and interface effects gain greater significance.

(some experiment motivates us to try to generalize theory of several layers to more layers) The recent discovery of sliding ferroelectricity in two-dimensional (2D) layered homostructures, achieved by controlling the translational degrees of freedom [28–32] (is sliding ferroelectricity important?) , naturally prompts a fundamental question: Can stacking modulation be extended to the three-dimensional (3D) counterpart?

(and think again about interactions of layers) And how does lattice translation between adjacent layers in 3D layered crystals impact their electronic structures?

(we'll slight move some layers corresponding to other) In this study, we introduced a laddering stack structure (Fig. 1j) in $1\ \mathrm{T}-\mathrm{TaS_2}$ crystals by deliberately creating fractional misalignment of adjacent layers, leading to a misaligned David-stars $\mathrm{T}_{\mathrm{A}}^{\mathrm{S}}$ stacking (Fig. 1g).

(we learned something from this) This unique approach unveiled a distinct insulating state, shedding light on switching between Mott-states and band-insulating states through interlayer stacking and coupling manipulation.

(interlayer coupled -> 3D band insulator interlayer nearly not coupled -> 2D Mott insulator) With interlayer coupling, the dominance shifts towards the 3D band-insulating states, whereas interlayer decoupling, achieved through the structuring of laddering interlayer sliding, favors the prevalence of 2D Mott-insulating states.

(some "dualistic nature" can be seen from their analysis) This discovery provides compelling evidence of the dualistic insulating nature of $1\ \mathrm{T}-\mathrm{TaS_2}$ crystals.

(maybe you can apply this approach to other materials) Furthermore, extending this laddering stack structure to other layered materials with similar structural characteristics of intralayer stiffness and interlayer slipperiness opens up exciting possibilities to explore fascinating physics and intriguing properties regardless of their dimensionality.

### 27.1.2 Results

#### Laddering interlayer sliding and structural characterization

(name of device for seeing stacking) The laddering stack structure is verified using aberration-corrected high-angle annular dark-field scanning transmission electron microscopy (HAADF-STEM), as shown in Fig. 1k.

(nothing is important in this sentence, they say that this slight misalignment makes situation slightly different, and the layers are the same) ("A features X, whereas B distinguishes it from C") This unique structure features(= has) a routine sandwiched unit (=usual S–Ta–S structural unit) , whereas a periodically misaligned interlayer stacking arrangement along the out-of-plane c-direction (Fig. 1j) distinguishes it from the well-established vertical alignment of Ta-atoms between adjacent layers in $1\ \mathrm{T}-\mathrm{TaS_2}$ (bb-stacking in Fig. 1a, b and Supplementary Fig. 1) [33].

(direction of sliding is on figures) The interlayer sliding occurs along the [120] direction within the *ab*-plane guided by red arrows in Fig. 1h, g, as determined from the corresponding HAADF-STEM image (Fig. 1i).

(there is a periodicity in the perpendicular (in plane) direction) Viewing along the [100] direction, a 20-layer periodicity is discerned(=observed) from a large-scale HAADF-STEM image (see Supplementary Fig. 2) (maybe I'll see the spp later) .

([$\bar{2}$]=[-2], this is the notation)

(what are these direction??? what are these periodicity. here is just a description, it is not important, I'll ask GPT later about it)

(in another direction of the described shift there is a 40-layer periodicity) Considering the [120] direction interlayer sliding, the Ta-atoms in the upper layer are expected to align with the

Ta-atoms in the lower layer after a 40-layer periodicity, corresponding to a translational shift of ∼0.015 nm per layer.

(the same periodicity is in another direction) The 40-layer periodicity is confirmed by the HAADF-STEM image along [110] direction (Supplementary Fig. 3).

(def. of LC- $TaS_2$ stacking (with the shift)) Here, we name the crystals with octahedral coordinated $TaS_2$ units stacking in a laddering configuration as LC- $TaS_2$ (laddering configuration = LC) .

(method of measurement spacing) The interlayer spacing $d$ is determined by synchrotron-based Xray diffraction (XRD) spectroscopy at room temperature (Fig. 1c).

(results of the measurement) The scattering vector $q$ for LC- $TaS_2$ is determined to be 10.75 $nm^{-1}$, corresponding to a $d = 0.584$ nm (calculated using $d = 2\pi/q$ ).

(without shift spacing is bigger) This $d$ value is slightly smaller than 0.587 nm ($q = 10.70$ $nm^{-1}$) for 1 T − $TaS_2$[34], indicating a slight out-of-plane contraction.

(XRD gave some peak, which has a shoulder) A shoulder with a lower $q = 10.69$ $nm^{-1}$ originates from residual bb-stacking configurations. (learn XRD to understand this)

(systems tends to go out of this LC phase to 1T phase) It is not surprising that a complete transition to the metastable laddering stack structural phase remains challenging, given that local fluctuation favors the relatively more stable 1T-phase [35,36]. (or actually to 2H phase, since it is even more stable)

(how layers configuration influence SODs? use XRD) To understand the influence of laddering stack structure on interlayer dimerization, the XRD measurements were performed using $Cu_\alpha$.

(see fig. 1f for XRD diffraction) Figure 1f displays the superlattice reflections collected at 120 K, and the ( $00l$ ) indexed diffraction peaks((00$l$) indexed diffraction peaks??) are presented in Supplementary Fig. 4.

(SODs give peaks in XRD) (why SODs give peaks in XRD?) In the 1 T − $TaS_2$ crystal, interlayer dimerization associated with David-stars ordered array results in half-integer (0,0,5/2) and (0,0,7/2) reflections at ∼37.9° and ∼54.1°, consistent with previous findings [22].

(if we have shifts in layers, SODs do not pair, this is seen in XRD) The absence of these superlattice reflections in the LC-$TaS_2$ crystal implies the collapse of interlayer dimerization, either caused by the collapse of CDW states or the absence of a David-stars ordered array. (this is very expected, since layers of SODs do not overlap)

### Electron localization at the David-star center

(they did PES in NCCDW to learn something about layer influence on SODs) To understand the influence of the laddering interlayer sliding on charge redistribution within the David-stars, synchrotron-based photoemission spectroscopy (PES) was conducted at room temperature, where 1 T − $TaS_2$ is in the nearly-commensurate CDW (NC-CDW) phase.

(electrons hop within SOD) Within each David-star, there is in-plane electron transfer from outer C-/B-Ta-atoms to the central A-Ta-atoms (Fig. 1d) [37,38].

(The peak that corresponds to SOD consists of 3 peaks) The distinct corehole screening effect, resulting from unequal local electron density at specific Ta-sites, leads to further splitting of the Ta $4f_{7/2}$(why $4f_{7/2}$?) peak (Fig. 2a). (think about the explanation of this. (GPT:) Because A, B, and C Ta atoms have different electron densities, they screen a created core hole differently. Therefore their Ta 4f 7/2 electrons have slightly different measured binding energies, producing several peaks instead of one.)

(positions of peaks) Three components at ∼23.64, ∼23.10, and ∼22.97 eV with an intensity ratio of ∼6:6:1 are extracted for 1 T − $TaS_2$.

(if we go to LC phase, peaks for B and C type of Ta atoms are not changed) The binding energies (BEs) of C-Ta and B-Ta features for LC − $TaS_2$ remain unchanged, indicating the persistence of the CDW states. (I am not sure that there is such a connection btw peaks and CDW)

(peak A shifts) However, a lower BE shift of the A-Ta feature (∼0.05 eV), which is appearance seen in Supplementary Fig. 5, indicates enhanced electron density and localization at A-Ta-atoms. (connection btw shift of peak and higher electron density)

(if there are more electrons in the center, then layers are less coupled) This effect is most likely caused by interlayer decoupling [15], resulting from laddering interlayer sliding. (maybe because if there was coupling, electrons will be between layers somewhere)

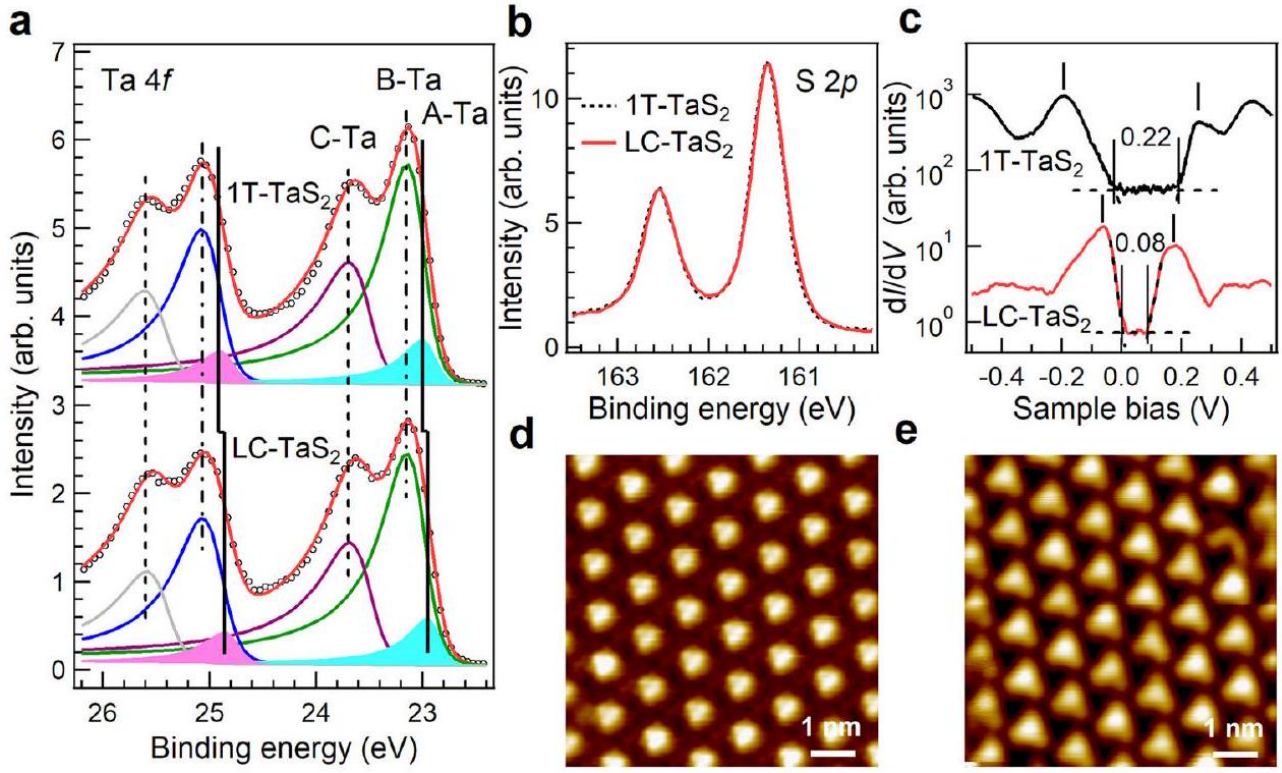


Fig. 2 | Evolution of chemical composition and electronic structures. a Ta $4f$ with corresponding fitting curves and (b) S $2p$ core-level spectra measured at room temperature using a photon energy of 240 eV. c Spatially averaged d//dV spectra with logarithmic intensity scale conducted at David-star centers for 1 T − $TaS_2$ and LC-$TaS_2$ crystals at 4.5 K. The curves are vertically shifted for clarity with zero conductance marked by horizontal dashed lines. STM images of the C-CDW phase for (d) 1 T − $TaS_2$ and (e) LC − $TaS_2$ crystals conducted at 4.5 K.

(2H phase and S vacancies are not there) An alternative explanation for the lower BE feature(=shift of A peak) , attributed to the $2H - TaS_2$ phase or $Ta^{3+}$ species associated with S-vacancy defects [39], can be ruled out based on the following evidences:

(somewhere there there is a S $2p$ peak which is not changed) (i) The S $2p$ spectral profile for LC-TaS $_2$ crystals remains almost unchanged (Fig. 2b)(what is this measurement at all?) , indicating the absence of $2H - TaS_2$.

(in 2H phase somehow there should be a shift in this speactra) Otherwise, an additional feature at ∼ 160.80eV would be detected, as we reported previously [39].

(chemical composition is the same, as they checked with some clever intensity method) (ii) The comparable intensity ratio of Ta/S for both 1 T − $TaS_2$($\sim$ 0.91) and LC − $TaS_2$($\sim$ 0.92) crystals indicates a constant chemical stoichiometry. (think one day about the way how to check the chemical composition???)

**Duality of insulating states**

(now, we'll discuss STM, STS) To further understand the influence of the laddering interlayer sliding on the properties of insulating states and CDW order presented at low temperatures, scanning tunneling microscopy/spectroscopy (STM/ STS) measurements were conducted at 4.5 K.

(typical STM results are still in LC phase) The STM images of both 1T- $TaS_2$ (Fig. 2d) and LC- $TaS_2$ (Fig. 2e) crystals reveal the well-resolved C-CDW phase accompanied by a commensurate $\sqrt{13} \times \sqrt{13}$ triangular David-star superlattice, where each bright spot corresponds to one David-star.

(CCDW in LC phase is not special) Remarkably, the long-range CDW order remains intact(=undamaged) at the surface of LC- $TaS_2$ crystals.

(why there are triangles of electrons? not balls?)

(SODs are ordered in a plane) The persistence of David-stars, along with the absence of out-of-plane superlattice reflections (Fig. 1f), implies the absence of out-of-plane ordered array of Davis-stars. (I don't understand this argument, some idea is meant here)

(d/d$V$ change a lot in LC phase) Interestingly, the profiles of the corresponding d/d$V$ spectra change dramatically (Fig. 2c).

(collect typical plots of dI/dV, I still don't understand how they look?)

(description of dI/dV plot in 1T phase) For the as-grown(as-grown?) 1 T − $TaS_2$ crystal, two distinct peaks centered at approximately -0.19 and 0.26 eV feature a peak-to-peak energy gap with $\Delta \sim 0.45$eV and an edge-to-edge energy gap of $\sim$ 0.22eV, consistent with previous experimental results [8,9,11,21,39,40].

(description of change of dI/dV plot to the LC phase) However, for the LC-$TaS_2$ crystal, two in-gap states appear at -0.06 eV and 0.18 eV, yielding a narrower energy gap of $\Delta \sim$0.24 eV and an edge-to-edge gap of $\sim$0.08 eV.

(dI/dV plot was measured a lot of times) These pronounced differences in edge-to-edge gap features between 1 T − $TaS_2$ and LC- $TaS_2$ crystals persist consistently across the surface, as shown in Supplementary Fig. 6d, f.

(there is a good theory for dI/dV in 1T phase) The $\Delta \sim 0.24$eV closely matches the theoretically predicted Mott-gap of $\sim$0.2 eV for monolayer 1 T − $TaS_2$[10], indicating that this insulating state is induced by Mott localization. (read this prediction! maybe they gave there a really good theory!)

(but if we do another experiment, then it does not match) Nevertheless, this value is smaller than the experimentally observed energy gap of $\sim$ 0.45eV in molecular beam epitaxy growth monolayer 1 T − $TaS_2$ on a graphene/SiC surface [41], implying a larger screening of Coulomb repulsion(why larger screening of Coulomb repulsion gives the bigger gap?) in a 3D structure compared to a 2D monolayer.

(now, STS was also calculated and measured, layers play role) The STS spectra with a narrow energy gap have also been theoretically stimulated and experimentally observed on the cleaved 1T- $TaS_2$ surface with specific David-stars $T_C$ stacking [13,20,21,42], suggesting their common origin of interlayer decoupling.

(def of Tc phase) Here, $T_C$ refers to the vertical alignment between A-Ta-atoms and C-Ta-atoms of the adjacent David-stars.

(some special reason should be for the bigger gap (obviously)) These findings imply that the two times larger gap of the as-grown 1T-$TaS_2$ crystal can be attributed to a distinct mechanism, for instance, band-insulating (what is this band-insulating mechanism in terms of formulas???) .

### Flat band structure and DFT calculation

(we'll again do ARPES) To gain insights into the nature of insulating states, the temperature-dependent band structures were investigated by using synchrotron-based angle-resolved PES (ARPES).

(they reproduced the established results) The results for $1\ \mathrm{T}-\mathrm{TaS}_2$ crystals are consistent with previous findings [22,43], providing a reliable reference for comparison.

(ARPES at 280K for 1T and LC phases) In the NC-CDW phase range at 280 K, both $1\ \mathrm{T}-\mathrm{TaS}_2$ and $\mathrm{LC}-\mathrm{TaS}_2$ exhibit a flat band that emerges near the Fermi level ($E_\mathrm{F}$) (Fig. 3a, d).

(ARPES at 187K for 1T and LC phases, gap increases) As the temperature decreases to 187 K, the flat bands shift away from $E_\mathrm{F}$ and center at $\sim -0.2$eV (Fig. 3b, e), resulting in an increase in the energy gap.

(ARPES of 1T and LC phases are very different in blurriness!)

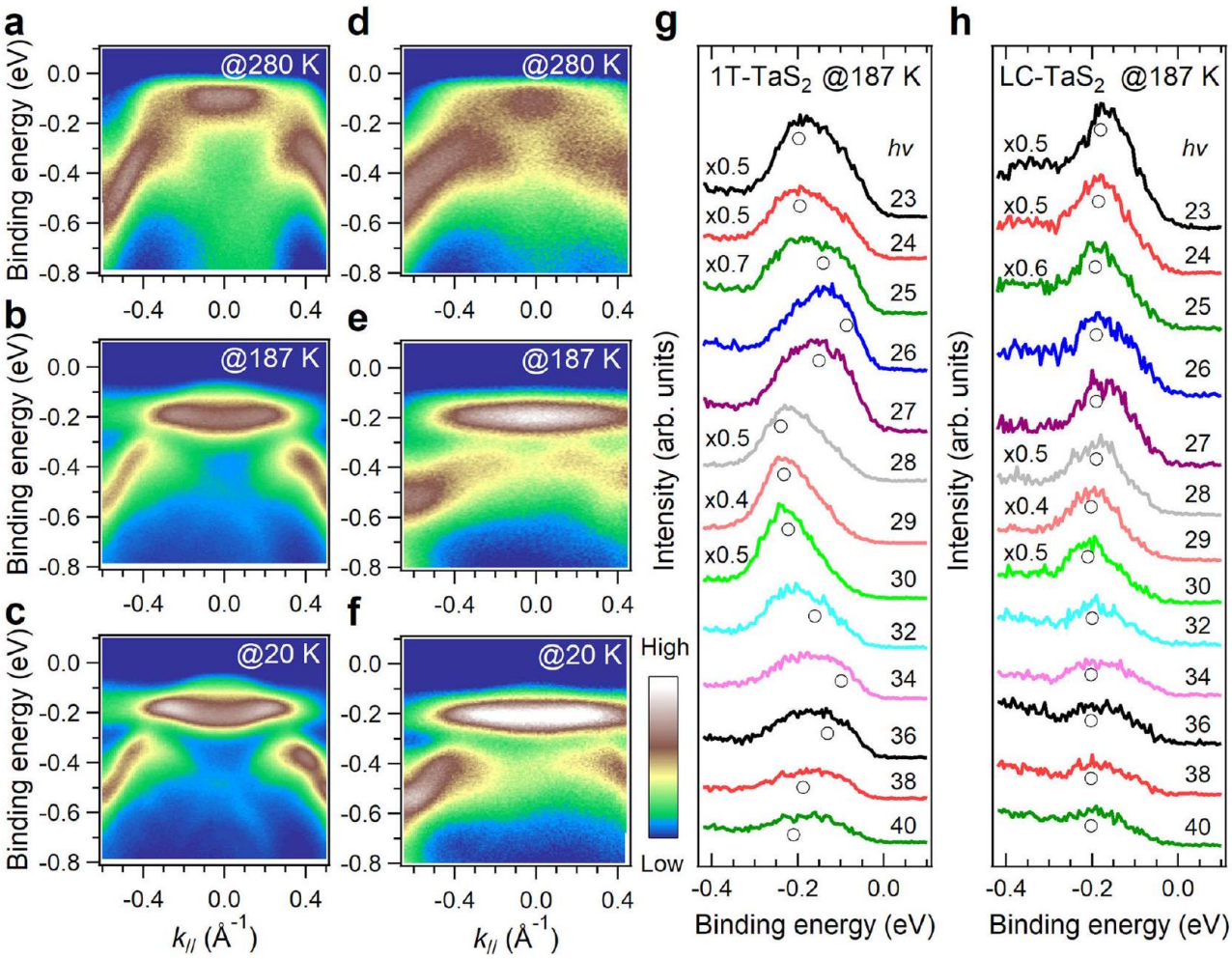


Fig. 3 | Band dispersions along the $\boldsymbol{k}_{//}$and $\boldsymbol{k}_{\mathbf{z}}$ direction in different electronic states (I don't understand these two directions and these two plots, how are they consistent one with another???) . The ARPES data taken along the $\Gamma - \mathrm{M}/k_{//}$direction (see Supplementary Fig. 7a, b) for $(\mathbf{a}-\mathbf{c})$1 T $-$ TaS$_2$ and $(\mathbf{d}-\mathbf{f})$LC $-$ TaS$_2$ at reducing temperatures of 280 K (NC-CDW phase), 187 K (C-CDW phase), and 20 K (insulating phase) with a photon energy of 22 eV .(WHY THE LC phase has such a different dispersion along vertical axes????????!!!!) (Each vertical cut through the ARPES spectrum gives an EDC, and its peak tracks the band!) Photon energy dependence of energy distribution curves (EDCs) in the C-CDW phase collected at the Γ-point and 187 K for (**g**)1 T $-$ TaS$_2$ and (h) LC-TaS$_2$. The opened circles represent the fitted band positions.

(into to some other measurements, which are not explained here) To investigate the band dispersion along the $k_{\mathrm{z}}$ direction, photon energy-dependent measurements were conducted at 187 K.

(discussion of the peak which is obtained for several photon energies) In 1T- TaS$_2$, the peak position shifts from -0.23 to -0.09 eV (Fig. 3g), whereas for LC $-$ TaS$_2$, the dominant peak at ∼-0.2 eV exhibits less photon energy dependence (Fig. 3h).

(these results are approx. the same as befores) These characteristics were similar to those reported in 1T- TaS$_2$ during a band-to-Mott insulating phase transition triggered by temperature (it is not clear what they mean by "during a band-to-Mott insulating", since it sounds like another setup, but there is a citation if you really want to learn it) [22].

(at 20K arpes is nearly the same for 1T and LC phase) In contrast, the observed characteristics in LC $-$ TaS$_2$ remain unchanged at 20 K (Fig. 3f and Supplementary Fig. 7d), indicating

the insensitivity of the electronic states to temperatures and confirming their intrinsic nature.

(somehow we conclude that layered structure is not the reason for that well-known Mott phase transition) This feature, along with a distinct interlayer distance difference between LC- and 1 $T-TaS_2$ crystals, implies that the periodic laddering stack structure is unlikely to be the structural origin for the heating-triggered surface intermediate (= at intermediate temperature range) Mott-insulator phase [22,44].

(there is another sliding, on a surface, which is irregular (not periodic), it can still be) However, the possibility of an interlayer atomic sliding confined to the surface region (5-8 layers), such as the irregular sliding observed in layered bulk $PbI_2$[45] (see this citation to understand what this sliding is) , cannot be ruled out.

(intro to DFT) Furthermore, we performed density functional theory (DFT) calculations to gain a comprehensive understanding of electronic structures in the above STS and ARPES experiments.

(we get input to DFT - the lattice - by XRD) A four-layer supercell with an ordered David-stars $T_AT_C$ stacking (Fig. 4a), identified by XRD superlattice reflections in 1 $T-TaS_2$ (Fig. 1f), was adopted.

(citations for other DFT calculations, I'll look later to them most likely) This configuration has been extensively employed in previous DFT calculations [13,14,20].

(SODs are actually random now) The absence of out-of-plane superlattice reflections in LC- $TaS_2$ crystals indicates a disordered David-stars stacking configuration (why disordered David-stars stacking ???) . (if SODs were periodic vertically, then there would be peaks in some reflection (XRD))

(disordered SODs can be QSL, but we need to check spin configuration, right now it is not clear if it is a QSL or no.)

(let's see what happens to the electronic bands when we slide the layers?) Aiming to emphasize the influence of atomic layer sliding on the alteration of the electronic structures, ${T^S}_A{T^S}_C$ stacking (Fig. 4b), integrating (="taking X and adding Y to it") David-stars $T_AT_C$ stacking with a translational shift representing disordered David-stars stacking due to broken translational symmetry along the $c$-direction, was adopted.

(they calculated band structure for $T_AT_C$ and they coincide with what was obtained before) The band structure for four layers 1T- $TaS_2$ (Fig. 4d) with David-stars $T_AT_C$ stacking is in good agreement with previous reports [14,15,46].

(they calculated band structure for ${T^S}_A{T^S}_C$ and they do not coincide with what was obtained before, they are metallic, but they'll fix it later) However, for ${T^S}_A{T^S}_C$ stacking with a translational shift of 0.053 nm, the calculated band structures using generalized gradient approximation (GGA) exhibit metallic characteristics with a conduction band crossing the $E_F$ at the L-point (Fig. 4g).

(but if you calculate more careful (with extra parameter), you'll get the insulating state again) To address this discrepancy, the Hubbard $U$ term (GGA + U) is introduced in calculations, which opens a gap (Fig. 4h), confirming its Mott-insulator nature.

(so they calculated more carefully the firs type of stacking) For comparison purposes, the GGA + U method is also employed to calculate the band structure of $T_AT_C$ stacking, as shown in Fig. 4e.

(even without U there was a gap) As expected, the limited increase in the energy gap after the introduction of the Hubbard $U$ term indicates that on-site Coulomb repulsion (= U term) is not the primary factor contributing to the energy gap for $T_AT_C$ stacking (Fig. 4c).

(in LC phase, layers are slightly closer and shifted. the closeness does not give the contribution to the spectrum) In addition, interlayer distance contraction has negligible influence on the low-energy electronic structure beyond the reduced gap (Supplementary Fig. 9)(they

did some complicated calculation to prove it, I guess) , confirming the dominant roles that laddering stack (=periodically shifted stacking) played in determining the interlayer coupling.

(see methods for details) The validity of simplifying the system to only 4 layers and employing a larger translational shift is discussed in the Methods part.

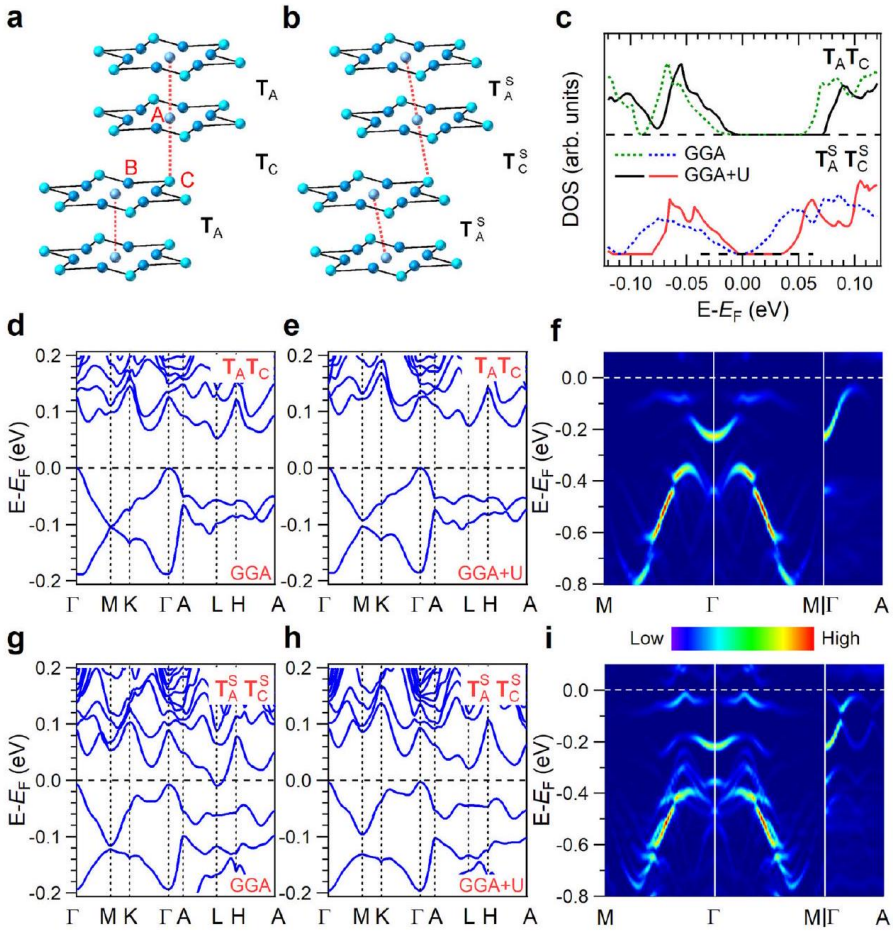


Fig. 4 | DFT calculated band structures.
Schematic diagrams illustrating (a) the $T_AT_C$ and (b) $T^S{}_AT^S{}_C$ David-stars stacking sequence.
c Density of States (DOS) for the $T_AT_C$ and $T^S{}_AT^S{}_C$ stacking.
Band structures near the $E_F$ for $T_AT_C$ stacking calculated using (d) generalized gradient approximation (GGA) and (e) GGA + U method.
Band structure for $T^S{}_AT^S{}_C$ stacking using (g) GGA and (h) GGA + U method.
Calculated unfolded band structure for (f) $T_AT_C$ and (i) $T_A^ST_C^S$ stacking using the GGA + U method.

(they calculated DOS) The density of states (DOS) represents gap opening induced by Mott-localization for the laddering stack structure (Fig. 4c). (how did they calculate DOS? it is a question about DFT method)

(GGA gives no gap, but GGA+U gives a small gap) Although GGA calculations typically underestimate the gap size [13], the DOS calculations show that the gap closes after laddering interlayer sliding, and reopens with a smaller value after introducing the Hubbard $U$ term.

(experimental results are not reproduced, but general trends are there) This trend is consistent with the STS results (Fig. 2c).

(intro to flattening of a band) The unfolded bands in the unit-cell Brillouin zone demonstrate the reduction in band dispersion along both Γ-A and $\Gamma - M$ directions.

(see fig. 1i (where the layers are shifted), it is flatten compared to 4i) Specifically, the dispersion of the flat band near -0.2 eV for $T^S{}_A T^S{}_C$ stacking (Fig. 4i) becomes flatter than that for $T_A T_C$ stacking (Fig. 4f).

(ARPES gave us results which look different, but this trend of flattening is also there) This is consistent with ARPES results at ∼187 K, where the flat band centered at $\sim -0.2$eV for $LC - TaS_2$ (Fig. 3e) is much narrower and less dispersive than that of 1 $T - TaS_2$ (Fig. 3b).

(in another direction in BZ the trends are similar) In addition, the dispersion along the Γ-A direction is reduced to ∼0.10 eV for $T^S{}_A T^S{}_C$ stacking (where is it in fig. 4i???) from $\sim 0.18$eV for $T_A T_C$ stacking. (what about extra bands in Γ-A direction?)

(repetition of the statement that there are no big contradictions) The reduced band dispersion aligns with observations from ARPES results.

(I assume that if ARPES were more precise, the exactly calculated band structures would be reproduced.)

(The bands exhibit sharper spectral features) For $LC - TaS_2$, the dominant peak at ∼ -0.2 eV exhibits less photon energy dependence (Fig. 3h).

(now, there is an ARPES of several layers) The ARPES spectra, with a detected depth of 2-3 nm for electrons with 18 eV kinetic energy, extend across three layers [47], providing multilayer information rather than characteristics of the top surface layer [22].

(bands are flat, gap in dI/dV is there, so we have a Mott insulator, since DFT predicts this ) In LC-TaS $_2$, the 2D flat bands close to $E_F$ along both the $\Gamma - A/k_z$ and $\Gamma - M/k_{//}$(think more about these parallel or perpendicular measurements, how exactly they are done? I never heard before about them) directions in the ARPES measurements and the wide energy gap determined from the STS spectra, in agreement with DFT calculations, confirms its 2D Mott-insulator nature. (why should the Mott insulator have these properties?)

(1T phase should be a 3D band insulator, not a Mott insulator, since there is a cited paper about it) On the other hand, significant band dispersion in 1 $T - TaS_2$ implies its classification as a 3D band insulator [22] (3D band insulator??) .

(note that experiment data is not fully calculated) It is noteworthy that, although DFT calculations based on $T^S{}_A T^S{}_C$ stacking generally capture the reduced band dispersion character in LC-TaS $_2$, deviations in actual band dispersion values are present.

(maybe if we take a more realistic stacking, we'll get the experimental bands?) This discrepancy may arise from alterations in the David-stars stacking sequence induced by atomic layer sliding, as illustrated in Supplementary Fig. 8, warranting further investigation.

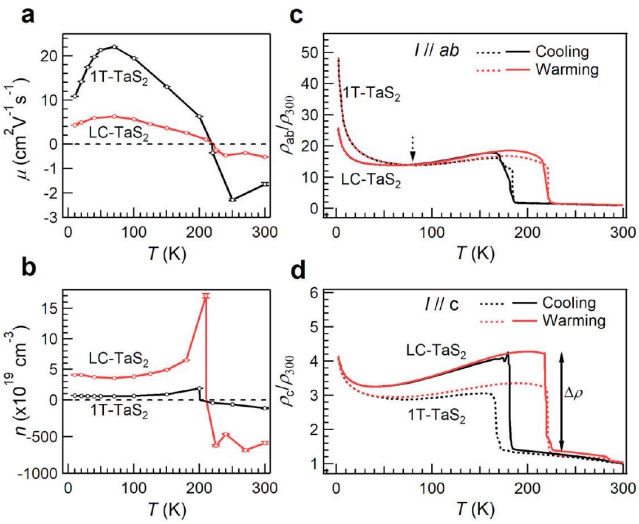


Fig. 5 | Anisotropic electrical transport properties. a The carrier mobility $\mu$ and (b) carrier concentrations $n$ determined from the Hall measurements (see Supplementary Fig. 12). The negative values in panels (**a**, **b**) correspond to the electron concentration and electron mobility, respectively. The error bars are derived from

### The effects of laddering interlayer sliding on electrical transport

(now, we'll look at el. transport) To explore the distinct macroscopic properties associated with this kind of duality of insulating states, anisotropic electrical transport measurements were conducted.

(results for $\mu$ and $n$) Figure 5a, b show the temperature dependence of the mobility $\mu$ and carrier concentration $n$, respectively.

(Hall effect theory was used for this) The values were calculated using the formulas $n = (\mathrm{e}R_{\mathrm{H}})^{-1}$ and $\mu = R_{\mathrm{H}}/\rho_{\mathrm{xx}}$, where $\rho_{\mathrm{xx}}$ (check Hall effect in the note on cond matter) and $R_{\mathrm{H}}$ represent resistivity and Hall coefficient, respectively, as shown in Supplementary Fig. 12.

(sometimes there are more electrons and sometimes more holes) The negative and positive signs denote the electron and hole carrier types, respectively. (how to understand this? revise basic cond matter)

(similar results were obtained) The obtained parameters for $1\ \mathrm{T}-\mathrm{TaS}_2$ are consistent well with the literature [48].

The sign change for both parameters corresponds to the transition from NC-CDW to C-CDW phase, as well as the gap opening observed in ARPES results (Fig. 3). (so in NCCDW he have more holes???? why???)

(in LC phase $\mu$ is way smaller) In LC-TaS $_2$, the electron localization and increased effective mass arising from the narrowing of flat bands, as revealed by ARPES, leads to a reduction in $\mu$ to $\sim$0.3 times of the value of $1\ \mathrm{T}-\mathrm{TaS}_2$. (are there formulas for this change of $\mu$ in this phase?)

($n$ is way bigger in LC phase because of the gap) Meanwhile, the $\sim$6-fold increase in $n$ for $\mathrm{LC}-\mathrm{TaS}_2$ is dominated by the narrower Mott-gap (why dominated by the narrower Mott-gap???) , as revealed by STS, although the increase in the effective mass of carriers can offset part of the contribution. (is there a theoretical derivation of $n$? it is very strange that they increase so much)

(summary of the obtained results) It is clear that the relatively large $\mu$ and small $n$ observed in intrinsic 1T- $\mathrm{TaS}_2$ crystals, are conversed into (=changed/transformed into) the lowered $\mu$ and elevated $n$ in LC- $\mathrm{TaS}_2$.

(now, let's discuss resistivity) To better understand the underlying physics of laddering interlayer sliding, we normalized the resistivity to the values of NC-CDW state at 300 K ($\rho_{300\ \mathrm{K}}$).

(normalization is done, because exactly changes in $\rho$ will give us useful info.) This helps to exclude the effects of extrinsic factors and facilitate a comparison with 1 T $-$ $TaS_2$ (Fig. 5c).

(even though LC resistivity is still there where the 1T resistivity is not there at e.g. 200K, the maximal and constant minimal its values are the same) Above 80 K, the resistivity behavior remains consistent (=qualitative temperature dependence / overall trend remains similar) even after laddering interlayer sliding, indicating unchanged in-plane David-stars configuration, although both $\mu$ and $n$ are modulated by interlayer coupling.

(at low T, LC resistivity is always smaller) Below 80 K, the weaker insulating behavior of LC- $TaS_2$ is consistent with its narrower energy gap.

(now, let's look at perpendicular direction) For electrical transport between layers, resistivity with $I//c$(electric current $I$ is parallel to the crystallographic c-axis) was measured and plotted in Fig. 5d.

(at || direction, the jump is also there, but it is bigger) The abrupt resistance jump ($\Delta\rho$) induced by the first-order NC-to-C-CDW phase transition in $\rho_{\mathrm{c}}/\rho_{\mathrm{c(300\ K)}}$ for LC $-$ $TaS_2$ is much larger (I don't see a big difference on the plot) than that for 1 T $-$ $TaS_2$.

(an idea why there is such jump: bigger mass, so harder to move, so bigger resistance) This significant increase of $\Delta\rho$ can be attributed to the reduced band dispersion along $k_{\mathrm{z}}$ and, consequently, a larger effective mass of carriers in LC-TaS $_2$ rising from the Mott-insulating mechanism. (is there a formula for it? did someone try to explain it?)

### 27.1.3 Discussion

(conclusion: bilayers dimerize in 1T phase) Upon reviewing the aforementioned results(=based on the results discussed above) , in $T_A$ stacking (Fig. 1d), the David-stars with unpaired electrons dimerize to form bilayers with an even number of electrons [8,10,11,14−16,20−22,49].

(I still don't understand the argument, why they dimerize and why all other explanations are ruled out?)

(conclusion: bilayers DO NOT dimerize in 1T phase) Conversely, in the fractional translation of $T^S{}_A$ stacking (Fig. 1g), the non-dimerization of David-stars preserves an odd number of electrons within each David-star.

(electrons do not go much outside of SOD, so they stronger interact within it) This results in an enhancement of electron density within the David-star, consequently strengthening electron-electron interactions [9,19,20,50,51]. (which formulas can be written for strengthening electron-electron?)

(electrons are mainly on each SOD, so they don't much overlap with other orbitals in other sods) Here, the laddering stack structure is expected to gradually weaken the interlayer coupling by reducing the out-of-plane wavefunction overlap integral between David-stars of adjacent layers, thus reducing out-of-plane bandwidth $t_\perp$.

(the same what was just written: electron-electron interactions increase = U increase) This reduction in $t_\perp$ leads to an increase in Coulomb repulsion $U$ due to the reduced electron screening.

(more U -> less transitions between layers) Consequently, the increased $U/t_\perp$ ratio explains the switching from a band-insulator to a Mott-insulator mechanism [52]. (I added this paper, I'll learn later how this transition happen)

(we've analyzed the translation of layers) Our discovery introduces a translational degree of freedom for precise tuning of bulk crystal properties.

(you can create some devices with this knowledge, but most likely no, I don't know why did they write this? there is no way to understand what they mean) It stands out for its simplicity, cleanliness, and seamless(without any sudden stops) integration into device fabrication processes.

(before this work, people studied sliding ferroelectricity. Now maybe you can do something more complicated. maybe no) This method opens up opportunities to investigate low-dimensional physics in layered 3D crystals [53], expanding its applications beyond the realm of sliding ferroelectricity [28,29,32].

### 27.1.4 Methods

#### Samples Preparation

(CVT -> 1T phase) High-quality 1 $T-TaS_2$ single crystals were grown by a chemical vapor transport (CVT) method [34,54,55].

(mix Ta and S) First, tantalum and sulfur power with a 1:2 molar ratio were mixed and vacuum-sealed(sealed=made tight so that air cannot get in) in the quartz tubes.

(heat, wait, cool fast) After annealing at 800 °C for 3 days, polycrystalline $TaS_2$ was obtained by quenching the quartz tubes in an ice-water mixture.

(add iodine to move them in the air to make later a crystal) Subsequently, the polycrystalline $TaS_2$ powder and iodine (as a transport agent) were vacuum-sealed in quartz tubes.

(heat and cool them at different sites) The quartz tubes were heated in a two-zone furnace for 10 days with different temperatures in the hot zone (850 °C) and cold zone (750 °C).

(cool fast) The 1T- $TaS_2$ crystals were obtained after quenching the quartz tubes in an ice-water mixture.

(put to vacuum at cold temperature) The obtained 1 $T-TaS_2$ crystals were transferred to a vacuum chamber (better than $10^{-2}$mbar ) and annealed at $150-200$ °C for 3-4 h.

(suddenly, we have a LC phase, after cool at 20 °C) The $LC-TaS_2$ crystals are obtained (why exactly the LC phase appears?) after cooling to room temperature naturally.

(store in vacuum) All collected crystals were stored in an Ar-protected glove box before further characterization.

(cut to pieces) Subsequently, the crystals were cut to pieces for electron microscopy and (synchrotron-based) XRD and PES characterization.

#### Electron microscopy

(name and parameters of the microscope) HAADF-STEM images of the cross-sectional samples were collected at room temperature on an FEI Themis Z aberration-corrected scanning transmission electron microscope operating at 300 keV with a convergence angle of 30mrad[56,57].

#### XRD measurement

(here is about figs. 1c and 1f)

(name of XRD setup and 2 parameters) The synchrotron-based XRD measurements were performed at the BL14B1 beamline of the Shanghai Synchrotron Radiation Facility (SSRF) using X-rays with a wavelength of $\lambda = 1.24$Åand grazing incident angles of 1.0°.

(some parameters) The corresponding spectra collected at room temperature are presented in scattering vector $q$ coordinates by using the equation $q = 4\pi \sin\theta/\lambda$, where $\theta$ is half of the diffraction angle. (learn XRD to understand this)

(somehow they got one parameter) The $q$ has been calibrated by measuring the synchrotron-based XRD of a lanthanum hexaboride reference sample.

(there was another XRD in another facility) Lab-based XRD characterizations were performed on a Bruker D8 diffractometer using $CuK_\alpha$ radiation to assess the quality of the obtained crystals.

(the analysis was of the same material, as we know) XRD data were also collected on 1T- and LC-TaS $_2$ crystals after cooling down to 120 K.

### Synchrotron-based PES and ARPES

(name of place of PES ) High-resolution PES was collected at the BL11U beamline of the National Synchrotron Radiation Laboratory (NSRL, China).

(cut, put to vacuum) The single crystals were cleaved(=split or cut something apart) and transferred into an ultra-high vacuum (UHV) chamber with a base pressure of $1 \times 10^{-10}$mbar.

(measure spectra) The S $2p$ and Ta $4f$ spectra were measured at normal emission and room temperature using 240 eV photon energy.

(somehow we got info about photon energies) The photon energy was calibrated using the Au $4f_{7/2}$ core-level peak (84.0 eV) of a gold foil in electrical contact with the samples.

(and fitting was also done) The least-squares peak fitting was performed employing a Shirley background and asymmetric peak profiles for $TaS_2$ species.

(name of place of ARPES ) The ARPES measurements were performed at the BL13U beamline of NSRL.

(cool, cut, measure) The single crystals, previously qualified by XRD, were cooled to 280 K, cleaved (to get a fresh surface) , and measured in situ in a UHV chamber with a base pressure of $1 \times 10^{-10}$mbar.

(cool them, measure again) The crystals were further cooled to a selective temperature and maintained for 10 min before measurement.

(somehow they got Ef) The Fermi energy was referred to as a gold foil in electrical contact with the samples.

(reminder: spend 1 day on learing ARPES)

### STM/STS measurement

(I don't know much STM, STS so there is no sense to think about it)

(name of a lab) The STM/STS measurements were conducted in an Omicron LT-STM system.

(experimental details) The obtained 1T- and LC- $TaS_2$ single crystals, qualified by XRD, were cleaved and transferred into a UHV prep-chamber with a base pressure of $5 \times 10^{-10}$mbar.

(experimental details) After degassing at approximately 100 °C for 1 h , the distinct samples were transferred to the analysis chamber with a base pressure of $1 \times 10^{-10}$mbar for STM/STS measurements.

(experimental details) STM topography images were collected in constant-current mode.

(experimental details) STS measurements were performed in constant-height mode using a standard lock-in technique ( $f = 773$ Hz, $V_{\text{r.m.s.}} = 15$mV ).

(calibration was done) The STM tip was calibrated spectroscopically on the Au(111) surface.

(T=4.5 K) All data were collected at 4.5 K.

### Transport measurement and sources of error in data fitting

(somehow they did this experiment, I don't know this)

The electrical transport measurements for freshly cleaved single crystals, cut from XRD-qualified samples, were carried out by using a physical property measurement system (PPMS, Quantum Design)(what is PPMS???) with a standard six-probe method.

(speed of change of T) The warming and cooling rates are 3 K/min.

(in plane and out of plane resistivity were measured) The in-plane and out-of-plane resistivity data for LC-TaS $_2$ are collected on two identical samples cut from one single crystal.

(fitting) While linear fittings to Hall resistivity provide satisfactory descriptions of experimental data (Supplementary Fig. 12d, e), standard fitting errors persist.

(there are errors) These errors subsequently introduced inaccuracies in related parameters, such as $\mu$ and $n$ (Fig. 5a, b).

(errors are small) Notably, the standard fitting errors for Hall coefficient were four orders of magnitudes smaller than the obtained parameters, ensuring the high reliability of both the fitting process and its related outcomes.

### DFT calculation

(name of DFT code) The first-principles calculations based on DFT were performed using the Vienna Ab initio Simulation Package (VASP) [58,59].

(names of methods in scope of DFT) The pseudopotential was described using the projector augmented wave (PAW) methods, and the exchange-correlation interaction was treated using GGA, which is parameterized by Perdew-Burke-Ernzerhof (PBE) [60]. (read this citation, it is a very well-known paper!)

(an important parameter) The on-site Coulomb repulsion $U = 2.94$eV, previously established using a self-consistent method [61], was included for the tantalum $5d$ orbitals. (In paper by Jung Kim of 2022 and there was 0.371 eV. GPT said that the meaning of them is different) (todo: think about it, why the models are different????)

(another computational parameter) The energy cutoff for the plane wave was set to 400 eV.

(some another famous method was used) The van der Waals interaction was accounted for using Grimme's DFT-D3 of the semi-empirical method [62].

(lattice grid) Brillouin zone sampling was performed using a $5 \times 5 \times 5k$-point mesh for electronic properties calculation.

(another code was used) The band unfolding was processed using the VASPKIT code [63].

(now, bands will be calculated by first principles) To examine the influence of laddering interlayer sliding on the electronic structure, first-principles calculations were performed.

(initial configuration of 1T phase) The initial assumption was made for pristine 1 $\mathrm{T-TaS_2}$ crystals, which were considered to exhibit an out-of-plane paired $\mathrm{T_A T_C}$ David-stars stacking sequence (Fig. 4a). (TA means that A atoms are on top on A, TC means that A are on top on C. they are alternate. This is what is seen in experiment, not TA TA TA..)

(def. of vectors which give this configuration) This specific stacking arrangement, characterized by stacking vectors of $\mathbf{T}_\mathrm{A} = \mathbf{c}$ and $\mathbf{T}_\mathrm{C} = 2\mathbf{a} + \mathbf{c}$ (why exactly 2a is here??? learn this convention from some paper) , has been proposed in previous experimental studies and was employed in DFT calculations [13,14,20].

(intro to sliding geometry) To simulate the interlayer sliding effect, the corresponding $\mathrm{T^S{}_A T^S{}_C}$ stacking configuration was considered (Fig. 4e).

(def. of vectors in this geometry) In this configuration, $\mathbf{T}^{\mathrm{S}}{}_{\mathrm{A}} = \delta\mathbf{a}+\mathbf{c}$ and $\mathbf{T}^{\mathrm{S}}_{\mathrm{C}} = (2+\delta)\mathbf{a}+\mathbf{c}$, with $\delta\mathbf{a}$ representing the lateral sliding distance.

(we'll not simulate all the layers) Simulating the experimentally observed 40-layer supercell structure, which contains 1560 Ta- and S-atoms, poses challenges.

(we'll simulate 4 layers) As a result, a simplified structure with a minimum of 4 layers or one $\mathrm{T}^{\mathrm{S}}{}_{\mathrm{A}}\mathrm{T}^{\mathrm{S}}{}_{\mathrm{C}}$ stacking period was adopted.

(less layers, but bigger shift) To compensate for the effects of this structural simplification, a larger sliding distance $\delta\mathbf{a}$ of 0.053 nm (1/6a) was used.

(they check different shift) The validity of this approach was verified by varying $\delta\mathbf{a}$ from 0.039 nm (1/8a) to 0.106 nm (1/3a).

(this is an unclear sentence, they mean maybe that they used some shifts to reproduce some results (maybe from DFT with 4 layers)) Supplementary Fig. 10 demonstrates that the band structures calculated with $\delta\mathbf{a} \geq 0.053$ nm$(1/6\mathbf{a})$ accurately reproduce results from the four-layer supercell structure.

(we'll also study 8 layers + different shift) To clarify the coordination effect between supercell layer numbers and sliding distance in representing experimental observation, extended calculations of eight-layer supercell structures were performed.

(if you really want, you can find results of this) Supplementary Fig. 11 illustrates the corresponding band structures for various $\delta\mathbf{a}$.

(8 layers -> a 0.039 nm shift to close the gap, 4 layers -> 0.053 nm) Notably, a 0.039 nm (1/8a) value is identified to close the gap for a larger eight-layer supercell structure, which is smaller than 0.053 nm (1/6a) for the four-layer supercell structure (Supplementary Fig. 11e).

(if you decrease sliding and increase layers -> you'll get still no gap) The observations lead to the conclusion that a sliding distance $\leq \sqrt{3}/n\mathbf{a}$ can effectively close the gap for an $n$-layer supercell structure (Supplementary Fig. 11f).

(I have no idea why gap closing is a criterion for the correct shift for the case of lower number of layers)

(sliding for 40 layers to close the gap) Therefore, it is reasonable to propose that $\sqrt{3}$ /40a sliding can close the gap in a 40-layer supercell structure, as observed experimentally. (reminder that experiment gave sliding ~0.015 nm per layer.)

(if we are using wrong U, we'll get a wrong gap) Notably, the GGA + U method has limitations regarding the accuracy of gap value in this system, given its sensitivity to the onsite $U$ value.

(hey, one can try another method, here is a citation) A potential alternative approach is the DFT+GOU method, where the self-consistent $U$ acts on the entire David-star cluster. This method may offer a more precise description of the electronic structure [19,42], warranting further theoretical investigation.

## 27.2 My Discussion

### 27.2.1 My Conclusion ans Summary

#### My Conclusion

This article has complicated sentences and details of experiments, which look not so important.

**Summary of the main results**

(GPT:) The main result of this work is that the insulating mechanism of bulk $1T$-$TaS_2$ can be strongly modified by interlayer stacking. HAADF-STEM demonstrates that LC-$TaS_2$ exhibits a laddering interlayer sliding structure, while XRD and STM show that this sliding suppresses the ordered out-of-plane David-star dimerization without destroying the in-plane David-star/CDW structure. PES indicates enhanced electron localization at the central A-Ta sites, and STS reveals a smaller insulating gap in LC-$TaS_2$. ARPES shows strongly reduced band dispersion, particularly along the out-of-plane $k_z$ direction, indicating reduced interlayer coupling. The DFT calculations qualitatively reproduce this behavior and show that, after sliding weakens the interlayer wavefunction overlap and reduces the out-of-plane bandwidth $t_\perp$, the Hubbard interaction $U$ becomes important for opening the insulating gap. Thus, the proposed physical picture is

$$\text{laddering sliding} \rightarrow \text{weaker interlayer overlap} \rightarrow \text{suppressed SoD dimerization} \rightarrow \downarrow t_\perp,$$

$$\downarrow \text{screening} \rightarrow \uparrow U/t_\perp \rightarrow \text{Mott-insulating behavior},$$

whereas strongly coupled and dimerized pristine $1T$-$TaS_2$ is interpreted as a three-dimensional band insulator. Transport measurements provide additional macroscopic evidence for this change through the reduced mobility, increased carrier concentration, and modified anisotropic resistivity of LC-$TaS_2$. Therefore, the authors describe the insulating nature of $1T$-$TaS_2$ as "dualistic": depending on the interlayer stacking and coupling, the same material can favor either a three-dimensional band-insulating or a quasi-two-dimensional Mott-insulating state.

### 27.2.2 My Main questions

**Why do the authors call the insulating nature of $1T$-$TaS_2$ "dualistic"?**

(GPT:)

The authors use the term "duality" because the same bulk $1T$-$TaS_2$ system can exhibit two different insulating mechanisms depending on the interlayer stacking and coupling. In the conventional stacking configuration, interlayer coupling and David-star dimerization favor a three-dimensional band-insulating state. In contrast, the laddering stacking configuration weakens the interlayer coupling and suppresses the interlayer dimerization, favoring a two-dimensional Mott-insulating state. Thus, the duality does not mean that the system is simultaneously a band insulator and a Mott insulator; rather, it means that two different insulating mechanisms can occur in the same material and can be controlled through the interlayer stacking.

**How did they at all create these layers?**

(??? sounds very complicated, is it? It is written in methods, but I still don't understand it)

**Why do the authors perform two different XRD experiments?**

(I missed it, I'll think later)

(GPT:) The two XRD measurements address different structural properties. Synchrotron-based XRD at room temperature (Fig. 1c) is used to determine the interlayer spacing $d$ and reveals a slight out-of-plane contraction in LC-$TaS_2$. In contrast, Cu K$\alpha$ XRD at 120 K (Fig. 1f) is used to investigate the low-temperature David-star superlattice and interlayer dimerization. The half-integer superlattice reflections $(0, 0, 5/2)$ and $(0, 0, 7/2)$ are observed in $1T$-$TaS_2$ but are absent in LC-$TaS_2$, indicating the loss of ordered interlayer David-star dimerization in the latter.

**Which theory did they confirm or disconfirm? What do we need to know about the theory after their results?**

(GPT:) The work mainly supports the idea that the insulating state of bulk $1T$-$TaS_2$ is strongly controlled by interlayer stacking, rather than being an intrinsic Mott state of every individual layer. For the conventional $T_AT_C$ stacking, interlayer David-star dimerization produces a gap already within GGA, so the authors interpret this state mainly as a three-dimensional band insulator. After introducing laddering sliding, the interlayer overlap and dimerization are reduced; GGA then gives a metallic state, while GGA+$U$ reopens a gap, which they interpret as a Mott gap. Thus, the paper supports a stacking-controlled competition between band-insulating and Mott-insulating mechanisms. It does not, however, prove that every ordinary bulk $1T$-$TaS_2$ sample is a pure band insulator, nor does it disprove Mott physics in bulk in general; previous works have reached somewhat different conclusions depending on stacking and surface termination.

**Did they fully reproduce with their calculations the experiments?**

(GPT:) No. The calculations reproduce the experiments mainly *qualitatively*. They reproduce the important trends: sliding reduces the band dispersion, especially along $\Gamma$–A/$k_z$; the shifted structure becomes metallic in GGA and insulating after adding $U$; and the resulting insulating gap is smaller than in the conventional stacking, consistently with STS. However, the calculated band dispersions do not quantitatively coincide with ARPES. The authors explicitly state that deviations in the actual dispersion values remain and suggest that the simplified stacking used in DFT may differ from the real David-star stacking. Furthermore, the calculated gap depends strongly on the chosen $U$, and the real 40-layer LC structure is replaced by a simplified four-layer model.

**Give a summary: experiment - theory - how they coinside - conclusion. What coinside, what does not coinside? (it is hard to see this in the paper, because we are given just a list of resuls, but a very little discussion is there)**

(GPT:) Experimentally, HAADF-STEM establishes the periodic laddering layer displacement; XRD shows that the ordered out-of-plane David-star dimerization is lost; STM shows that the in-plane David-star/CDW lattice nevertheless survives; PES indicates increased localization at the central A-Ta atom; STS finds a smaller insulating gap in LC-$TaS_2$; ARPES finds substantially reduced $k_z$ and in-plane band dispersion; and transport shows lower mobility and strongly modified anisotropic resistivity. The theoretical picture is that sliding decreases the interlayer wavefunction overlap and therefore $t_\perp$, suppresses dimerization and screening, and makes $U/t_\perp$ more important. DFT agrees qualitatively: conventional $T_AT_C$ stacking is already gapped without $U$, whereas shifted $T_A^ST_C^S$ stacking loses this gap in GGA and recovers a smaller gap with GGA+$U$; it also predicts flatter bands. What does *not* coincide exactly is the numerical band dispersion, the exact gap magnitude, and the true experimental stacking structure, since the calculation replaces the experimental 40-layer structure by a simplified four-layer model with an artificially enhanced sliding distance. The conclusion is therefore much stronger at the qualitative level—stacking controls the insulating mechanism—than at the level of an exact microscopic reproduction of the spectra.

**What do we need to change about how we see the physics of TaS2 after this work? (it is also hard to see)**

(GPT:) The main conceptual change is that bulk $1T$-$TaS_2$ should not simply be viewed as many independent two-dimensional Mott-insulating layers stacked together. The interlayer

degree of freedom is an active part of the low-energy physics. Depending on how David stars in adjacent layers are registered, interlayer hybridization can dimerize their electronic states and produce a three-dimensional band-insulating state; reducing this coupling can instead recover a much more two-dimensional, correlation-dominated Mott state. Thus, stacking, $t_\perp$, screening, and $U$ must be treated together when discussing bulk $1T$-$TaS_2$. This work strengthens the broader view that the apparently "layered" material can nevertheless have essential three-dimensional electronic physics.

**What exactly is potentially possible to do with these results?**

(GPT:) In principle, one could use controlled relative translation of layers as an additional tuning parameter for electronic properties: change interlayer hopping, electronic dimensionality, gap mechanism, carrier mobility, and possibly switch between correlation-dominated and hybridization-dominated states without changing chemical composition. This is the "slidetronics" idea emphasized by the authors. However, this paper does *not* demonstrate a functioning electronic device or reversible electrically controlled switching; it demonstrates that a metastable laddering structure can be prepared and that its electronic state differs strongly from ordinary $1T$-$TaS_2$. Therefore, device applications are a proposed direction rather than an experimentally established result of this work.

**double check that Rossnagel's 2011 review (and other papers) is about the layer or a bulk?**

(GPT:) Rossnagel's 2011 review is primarily about layered TMDC crystals as bulk/quasi-two-dimensional solids, not about isolated monolayers. The word "layered" there does not mean "single layer." Rossnagel discusses materials whose electronic structure is strongly anisotropic but can still contain important out-of-plane dispersion and interlayer coupling. The later $1T$-$TaS_2$ literature makes this even more explicit: bulk measurements find substantial out-of-plane dispersion and stacking-dependent electronic states.

**what is the real model for 3D band insulator?**

(GPT:) A useful minimal model is not an isolated monolayer Hubbard model but a lattice of David-star orbitals with both in-plane hopping and stacking-dependent interlayer hopping. Schematically,

$$H_0 = \sum_{\mathbf{k},l,\sigma} \epsilon_\parallel(\mathbf{k}) c^\dagger_{\mathbf{k}l\sigma} c_{\mathbf{k}l\sigma} - \sum_{\mathbf{k},l,\sigma} t_{\perp,l} \left( c^\dagger_{\mathbf{k}l\sigma} c_{\mathbf{k},l+1,\sigma} + \text{h.c.} \right).$$

For a dimerized pair of layers, the simplest limit is

$$H_{\text{dimer}} = -t_\perp \sum_\sigma (c^\dagger_{1\sigma} c_{2\sigma} + \text{h.c.}),$$

which produces bonding and antibonding states

$$E_\pm = \epsilon_\parallel(\mathbf{k}) \pm t_\perp.$$

If the bonding band is full and the antibonding band is empty without overlap, the system is a band/hybridization insulator even for $U = 0$. More realistic treatments use the full stacking-dependent electronic structure and many-body interactions.

**what about non-2D nature from Rossnagel, is it here?**

(GPT:) Yes—it is actually central to this paper. Ordinary bulk $1T$-$TaS_2$ shows substantial dispersion along $\Gamma$–A/$k_z$, meaning that the electronic states are not confined to individual layers. The LC structure reduces this $k_z$ dispersion and therefore moves the system toward a more two-dimensional electronic limit. Thus, this work gives a particularly direct illustration of the general point that a geometrically layered material does not have to be electronically two-dimensional.

**How exactly 3D band insulator in the 2D limit becomes a Mott insulator?**

(GPT:) In the dimerized three-dimensional limit, two adjacent David-star orbitals strongly hybridize through $t_\perp$. Their states split into bonding and antibonding combinations, and two electrons can fill the lower bonding state, producing a hybridization/band gap. As the layers are shifted, $t_\perp$ decreases and this bonding–antibonding splitting becomes smaller; eventually the band gap associated with dimerization collapses. At the same time, reduced interlayer screening makes electron–electron interactions relatively stronger. One then approaches effectively one localized electron per David star, and if the interaction $U$ is sufficiently large compared with the remaining bandwidth $W$ or hopping scale, the half-filled state separates into lower and upper Hubbard bands:

$$\begin{aligned} \text{large } t_\perp : &\quad \text{bonding/antibonding gap,} \\ t_\perp \downarrow: \quad \Delta_{\text{band}} \downarrow, &\qquad \frac{U}{W} \uparrow, \\ \text{2D limit} : &\quad \text{Mott gap.} \end{aligned}$$

Wang *et al.* summarize this using an increasing $U/t_\perp$ ratio, although a more complete many-body description involves both in-plane bandwidth and intersite interactions as well.

**which parameters did they use for DFT calculations? And what is the model? how do we just add U there?**

(GPT:) They use VASP with PAW pseudopotentials, PBE-GGA exchange–correlation, a plane-wave cutoff of 400 eV, DFT-D3 van der Waals corrections, a $5 \times 5 \times 5$ $k$-point mesh, and $U = 2.94$ eV applied to the Ta $5d$ orbitals. The normal structure is modeled by a four-layer $T_A T_C$ David-star supercell, with $\mathbf{T}_A = \mathbf{c}$ and $\mathbf{T}_C = 2\mathbf{a}+\mathbf{c}$. LC-$TaS_2$ is approximated by shifted $T_A^S T_C^S$ stacking with $\delta a = 0.053$ nm in the main four-layer calculation; additional four- and eight-layer calculations test other $\delta a$ values. Adding $U$ means using a DFT+$U$ energy functional in which an occupation-dependent correction is applied to the localized Ta $5d$ subspace in addition to the ordinary GGA energy. A commonly used form is schematically

$$E_{\text{DFT}+U} = E_{\text{DFT}} + \frac{U_{\text{eff}}}{2} \sum_{m,\sigma} n_{m\sigma}(1 - n_{m\sigma}),$$

but the Wang paper does not specify enough implementation details to identify this particular equation as their exact $+U$ functional. Therefore this formula should be regarded as an illustration of how DFT+$U$ works, not as an equation explicitly written in the article.

**which exactly formula they mean by DFT?**

(GPT:) "DFT" here does not refer to one special $TaS_2$ Hamiltonian written in the paper. VASP numerically solves the Kohn–Sham equations,

$$\left[ -\frac{\hbar^2 \nabla^2}{2m} + V_{\text{ion}} + V_{\text{H}}[n] + V_{\text{xc}}[n] \right] \psi_{n\mathbf{k}} = \epsilon_{n\mathbf{k}} \psi_{n\mathbf{k}},$$

self-consistently with

$$n(\mathbf{r}) = \sum_{n\mathbf{k}}^{\text{occ}} |\psi_{n\mathbf{k}}(\mathbf{r})|^2.$$

In this work, $V_{\text{xc}}$ is approximated by PBE-GGA, the ionic/core-electron problem is handled with PAW, van der Waals interactions are supplemented by DFT-D3, and for the GGA+$U$ calculations an extra local interaction correction is applied to Ta 5$d$ states. Thus, they input the atomic supercell and stacking geometry and numerically obtain the bands rather than solving a simple analytical Hubbard Hamiltonian.

**Did someone ever reproduced the experimental results of dI/dV exactly?**

(GPT:) There are theoretical calculations that reproduce the *types* of STS/$dI/dV$ spectra and the dependence of the gap on stacking rather well, but I would not say that an exact point-by-point experimental $dI/dV(V)$ curve has been reproduced. Several many-body and stacking-resolved calculations reproduce characteristic large- and small-gap spectra. But exact STS lineshapes additionally depend on surface termination, tunneling matrix elements, tip properties, lifetime broadening, temperature and defects, so "exact reproduction" is a much stronger criterion than matching the gap and major spectral peaks.

**Why don't we see a gap in 4i figure (where there are blue DFT calculations of LC phase)? Is it correct or no??**

(GPT:) Fig. 4i is not the clearest figure for judging the gap. It is an *unfolded* GGA+$U$ band structure in which the color represents spectral weight after projecting the supercell bands back into the smaller Brillouin zone. Consequently, weak "ghost" spectral weight and broad-looking features can appear close to $E_F$, and the small gap is visually difficult to identify. The direct GGA+$U$ band plot in Fig. 4h and especially the DOS in Fig. 4c are what the authors use to demonstrate reopening of the gap after adding $U$. Therefore, it is reasonable that Fig. 4i looks almost gapless; I would not use Fig. 4i alone as evidence for the magnitude of the gap. The paper itself says only that the unfolded bands reproduce the *reduced dispersion*, while the gap argument is made from Fig. 4c/h.

**why resistivity has a phase transitions at different T?**

(GPT:) There are two related effects. First, the NC-CDW $\leftrightarrow$ C-CDW transition is first order, so it exhibits thermal hysteresis: during cooling the old phase can remain metastable below the equilibrium transition temperature, whereas during warming the low-temperature phase can survive above it. Therefore the resistance jump occurs at different temperatures on cooling and warming because nucleation requires crossing an energy barrier. Second, LC-$TaS_2$ and ordinary 1$T$-$TaS_2$ have different interlayer stacking and electronic coupling, so the free energies of their CDW states are modified and their transition temperatures need not be identical. In Fig. 5, the dotted curves correspond to cooling and the solid curves to warming.

**why in 5c there are red lines in the blue line?**

(GPT:) There are several curves because Fig. 5c contains data for *two different samples* and for *two temperature sweep directions*. In the original figure, black corresponds to 1$T$-$TaS_2$ and red to LC-$TaS_2$, while dotted curves represent cooling and solid curves represent warming. The curves overlap over substantial temperature ranges because the resistivity has been normalized by each sample's own value at 300 K and because the authors find broadly similar temperature dependence above about 80 K. They separate strongly around the first-order transition because of thermal hysteresis and at low temperature because LC-$TaS_2$ has weaker insulating behavior.

**Is the interaction between several SODs in the one plane is taken into account?**

(GPT:) Yes, but only at the level provided by their periodic DFT calculation. Their supercell contains the commensurate David-star reconstruction, and because the calculation is periodic in the *ab* plane, the electronic hopping and hybridization between neighboring David-star cells are automatically included in the Kohn–Sham band structure. This is what produces the in-plane dispersion along Γ–M. However, they do *not* use an explicit many-body lattice model with a separate Hubbard interaction $U_{ij}$ between different David stars in the same plane. Their added $U = 2.94$ eV is applied locally to Ta $5d$ orbitals. Thus, in-plane coupling between SoDs is included through the DFT electronic structure, while nonlocal many-body correlations between different SoDs are not treated explicitly by this GGA+$U$ model.

### 27.2.3 What I Understood Wrongly (Maybe)

**GPT version: I am wrong at describing the two insulating mechanisms simply as "interactions between layers" versus "interactions within one layer."**

This description is too vague and misses the specific physics established in the paper. The two mechanisms are a three-dimensional band-insulating mechanism associated with interlayer David-star dimerization and a Mott-insulating mechanism associated with electron localization and strong Coulomb interactions. The authors create a laddering stack that weakens the interlayer coupling and destroys the ordered interlayer dimerization. This drives the system from a state dominated by the 3D band-insulating mechanism toward a state dominated by the 2D Mott-insulating mechanism. Thus, the distinction is not simply "interlayer interaction versus intralayer interaction," but rather band insulation produced by interlayer hybridization/dimerization versus correlation-driven Mott localization.

**GPT version: I am wrong at saying that if we have one layer, we can simply apply the Mott-Hubbard model, whereas if we have interlayer interaction, we use a different model.**

The presence of interlayer coupling does not mean that the Mott-Hubbard physics disappears or that one switches completely from one model to another. The relevant competition is controlled by the relative importance of electron correlations and interlayer hopping. In the authors' interpretation, laddering interlayer sliding reduces the overlap between electronic wavefunctions on David-stars in neighboring layers, thereby reducing the out-of-plane bandwidth $t_\perp$. Reduced screening also increases the effective Coulomb interaction $U$. Consequently, the ratio $U/t_\perp$ increases and the Mott-insulating mechanism becomes dominant. Both Coulomb interactions and interlayer coupling are therefore present in the bulk system; their relative importance changes with stacking.

**GPT version: I am wrong at describing ordinary 1T-$TaS_2$ as simply a symmetric or non-shifted stacking configuration.**

The pristine 1T-$TaS_2$ crystal considered in this paper is not adequately described as simply "non-shifted." At low temperature, the relevant David-star stacking is an ordered $T_A T_C$ sequence. In the $T_A$ configuration, neighboring David-stars are aligned in a particular way that allows interlayer dimerization, while $T_C$ represents another stacking vector in the ordered sequence. The LC-$TaS_2$ structure introduces an additional fractional lateral translation, producing the laddering $T_A^S$-type stacking. Therefore, the distinction is between specific ordered stacking sequences and the deliberately translated laddering configuration, not simply between "shifted" and "not shifted."

**GPT version: I am wrong at saying that the layer translation is approximately 0.15 nm per layer.**

The experimentally inferred translational shift is approximately 0.015 nm per layer, not 0.15 nm. The HAADF-STEM measurements reveal a 40-layer periodicity along the relevant direction, corresponding to a lateral translation of about 0.015 nm for each successive layer. The much larger value used later in the four-layer DFT model, 0.053 nm, is a computationally chosen effective translation used to compensate for replacing the experimentally observed 40-layer structure with a much smaller supercell.

**GPT version: I am wrong at saying that the XRD result simply shows that shifted layers have a smaller spacing and unshifted layers have a larger spacing.**

The experiment does show a small contraction of the average interlayer spacing: approximately 0.584 nm in LC-$TaS_2$ compared with 0.587 nm in pristine 1T-$TaS_2$. However, this should not be interpreted as a general geometrical rule that lateral shifting automatically reduces the vertical spacing. More importantly, the authors explicitly investigate whether this small change in interlayer distance is responsible for the electronic changes and conclude that its influence on the low-energy electronic structure is negligible compared with the effect of the laddering lateral translation. The central control parameter is therefore the stacking translation and the associated change in interlayer coupling, not simply the vertical spacing.

**GPT version: I am wrong at saying that the disappearance of the XRD superlattice peaks means that the David-stars are simply not paired.**

The interpretation is more precise. In pristine 1T-$TaS_2$, the half-integer out-of-plane XRD reflections are associated with an ordered array of interlayer-dimerized David-stars. Their disappearance in LC-$TaS_2$ demonstrates the collapse of this ordered out-of-plane dimerization pattern. By itself, the XRD result could in principle arise either from the disappearance of the CDW or from the loss of the ordered out-of-plane David-star array. The STM measurements subsequently show that the in-plane commensurate CDW and David-stars remain intact. Combining STM and XRD therefore allows the authors to conclude that it is specifically the out-of-plane ordered David-star dimerization that has disappeared.

**GPT version: I am wrong at saying that PES directly tells us how many electrons are inside a David-star.**

The Ta $4f$ photoemission spectrum does not simply count the number of electrons in a David-star. The different Ta sites inside the David-star have different local electronic environments and therefore different core-level binding energies. The Ta $4f_{7/2}$ spectrum can consequently be decomposed into contributions associated with the A-, B-, and C-Ta sites. In LC-$TaS_2$, the A-Ta component shifts by approximately 0.05 eV toward lower binding energy, while the B- and C-Ta features remain approximately unchanged. The authors interpret this lower-binding-energy shift as evidence of enhanced electron density and localization at the central A-Ta site.

**GPT version: I am wrong at describing the PES result as a higher density of states in the David-star.**

The PES measurement discussed here concerns a change in local electron density and core-level binding energy, not directly an increased density of states. The lower binding energy of the A-Ta core-level feature is interpreted as enhanced electron density and localization at the

central Ta atom. "Electron density" and "density of states" are different physical quantities and should not be used interchangeably here.

**GPT version: I am wrong at saying that weaker interlayer coupling means that electrons are simply "more inside the cluster," which directly makes electron-electron interaction larger.**

The qualitative direction is correct, but the mechanism should be stated more carefully. Laddering translation reduces the overlap of electronic wavefunctions between David-stars in adjacent layers and therefore decreases the out-of-plane hopping and bandwidth $t_\perp$. At the same time, weaker interlayer coupling reduces electronic screening, which increases the effective Coulomb repulsion $U$. The important quantity is therefore the increasing ratio $U/t_\perp$. It is this enhanced relative importance of Coulomb interactions compared with kinetic delocalization that favors the Mott-insulating state.

**GPT version: I am wrong at saying that the STM images are simply plots of electron density.**

STM topography is not a direct map of the total electron density. The tunneling current depends on the local density of electronic states within the energy window determined by the bias, as well as on the tip-sample distance and tunneling matrix elements. In this experiment, the periodic bright features in the STM images reveal the $\sqrt{13} \times \sqrt{13}$ commensurate CDW David-star superlattice. The important conclusion is that this in-plane long-range CDW order remains present in LC-$TaS_2$ despite the loss of ordered out-of-plane David-star dimerization.

**GPT version: I am wrong at treating the difference between the circular-looking and triangular-looking STM features as an unexplained change in the CDW structure.**

The important conclusion of Fig. 2d,e is not the precise visual shape of individual bright features. Both pristine 1T-$TaS_2$ and LC-$TaS_2$ exhibit the same commensurate $\sqrt{13} \times \sqrt{13}$ David-star superlattice and long-range in-plane CDW order. Therefore, one should not infer a fundamentally different in-plane CDW merely from the apparent difference in the shapes of the bright features in the plotted STM images.

**GPT version: I am wrong at saying that the smaller STS gap merely "supports interlayer decoupling" without identifying the insulating mechanism.**

The paper makes a stronger interpretation. Pristine 1T-$TaS_2$ exhibits a peak-to-peak gap of approximately 0.45 eV, whereas LC-$TaS_2$ exhibits in-gap states and a substantially smaller gap of approximately 0.24 eV. The latter is close to the theoretically predicted Mott gap of approximately 0.2 eV for monolayer 1T-$TaS_2$. The authors therefore interpret the LC-$TaS_2$ insulating state specifically as a Mott-localized state produced by interlayer decoupling, while attributing the much larger gap in pristine 1T-$TaS_2$ primarily to the band-insulating mechanism.

**GPT version: I am wrong at describing 1T-$TaS_2$ as the phase without a special shift and LC-$TaS_2$ as simply another phase with a shift.**

LC-$TaS_2$ is not a different crystallographic polytype analogous to 1T versus 2H. Both samples consist of octahedrally coordinated 1T-$TaS_2$ layers. "LC" denotes the laddering configuration created by fractional translations between successive 1T layers. It is therefore better to call 1T-$TaS_2$ and LC-$TaS_2$ two different stacking structures or crystal configurations within the 1T system rather than two different structural phases in the same sense as 1T and 2H.

**GPT version: I am wrong at saying that the ARPES result shows that the layer structure is not the reason for the Mott phase because the spectra do not change much.**

The ARPES results actually reveal an important change caused by the laddering stack. In pristine 1T-$TaS_2$, the electronic band near $-0.2$ eV has appreciable dispersion along $k_z$, indicating significant three-dimensional interlayer coupling. In LC-$TaS_2$, this band has much weaker photon-energy dependence and therefore substantially reduced $k_z$ dispersion. The authors interpret this reduced dispersion as evidence that laddering sliding suppresses interlayer coupling and makes the electronic structure more two-dimensional. Together with STS and DFT, this supports the classification of LC-$TaS_2$ as predominantly a 2D Mott insulator.

**GPT version: I am wrong at saying that the similarity of the 187 K and 20 K LC-$TaS_2$ spectra shows that interlayer structure is unimportant for the Mott state.**

The paper draws a different conclusion from this temperature independence. The fact that the characteristic LC-$TaS_2$ electronic structure remains essentially unchanged between 187 K and 20 K indicates that the observed state is intrinsic to the laddering configuration rather than being a temperature-induced intermediate surface state. Together with the different interlayer distances, this allows the authors to argue that their periodic laddering structure is unlikely to be the structural origin of the previously reported heating-induced intermediate Mott state. It does not imply that interlayer structure is irrelevant.

**GPT version: I am wrong at saying that the "disordered David-star stacking configuration" probably does not exist because the experiment just shows a regular shift.**

There are two different structural statements here. The atomic layers form a regular laddering structure with a well-defined periodic fractional translation, as directly observed by HAADF-STEM. However, relative to the David-star superlattice, the usual ordered out-of-plane David-star stacking and dimerization are destroyed. The absence of the corresponding XRD superlattice reflections is therefore described by the authors as a disordered David-star stacking configuration. A periodic atomic-layer translation can consequently coexist with the loss of the original ordered David-star stacking sequence.

**GPT version: I am wrong at describing the GGA calculation as possibly a tight-binding or Mott-Hubbard calculation.**

The calculation in Fig. 4 is a first-principles density-functional-theory calculation. The authors first use GGA within DFT. For the laddering $T_A^S T_C^S$ stacking, ordinary GGA predicts a metallic band crossing the Fermi level. They then use GGA+$U$, where an on-site Coulomb correction is added to the Ta $5d$ orbitals, and this opens an insulating gap. This is not the same calculation as directly solving a simple Hubbard Hamiltonian or a tight-binding model, although the Hubbard-$U$ correction is introduced to capture correlation effects that ordinary GGA does not describe adequately.

**GPT version: I am wrong at saying that the authors added the Hubbard $U$ simply because they did not like the metallic GGA result.**

The motivation is physical rather than merely fitting an unwanted result. Ordinary GGA predicts that the laddering configuration is metallic, whereas the experiments show that LC-$TaS_2$ remains insulating. Because interlayer decoupling enhances electron localization and electron-electron correlations, the authors introduce the on-site Hubbard correction through

GGA+$U$. The resulting gap is interpreted as evidence that correlations are essential for the insulating state of LC-$TaS_2$. For pristine $T_A T_C$ stacking, by contrast, adding $U$ changes the already existing gap only modestly, indicating that Coulomb repulsion is not the primary origin of that gap.

**GPT version: I am wrong at saying that the $U$ used in DFT+$U$ and the $U$ of the Hubbard model are "two purely different parameters."**

They are not identical objects in the sense that their numerical values cannot generally be transferred directly between different effective models and computational schemes, but they represent the same underlying physical concept: an effective local Coulomb repulsion. In the Hubbard model, $U$ is the interaction parameter of an effective many-body Hamiltonian. In DFT+$U$, an effective on-site Coulomb correction is added to selected localized orbitals to compensate for correlation effects poorly described by standard DFT. In this paper, the authors use $U = 2.94$ eV for the Ta $5d$ orbitals, obtained previously by a self-consistent procedure. Thus, it is better to say that the two $U$'s are related effective descriptions of Coulomb repulsion but are defined within different theoretical frameworks and should not automatically be numerically identified.

**GPT version: I am wrong at saying that first-principles calculations are something different that the authors suddenly switch to after DFT.**

The DFT calculations discussed in the paper are themselves first-principles calculations. "First-principles" or "ab initio" describes the general computational approach, while DFT is the specific theoretical framework being used. The authors use VASP with the PAW method, PBE-GGA exchange-correlation functional, DFT-D3 van der Waals correction, and, where required, an on-site Hubbard $U$ correction. Therefore, the Methods section is continuing the description of the same DFT calculations rather than introducing an unrelated new type of calculation.

**GPT version: I am wrong at saying that the calculations do not reproduce the experimental results.**

The agreement is partial rather than absent. The calculated density of states reproduces the experimentally observed trend that laddering sliding closes the original gap and that including Hubbard $U$ reopens a smaller Mott gap. The calculations also reproduce the reduction of band dispersion observed by ARPES: the bands near $-0.2$ eV become flatter, and the dispersion along the out-of-plane direction decreases. However, the authors explicitly state that there are quantitative deviations between calculated and experimental band dispersions, probably because the actual David-star stacking sequence is more complicated than the simplified computational structure. Thus, the correct statement is that the calculations reproduce the principal experimental trends but not the detailed spectra quantitatively.

**GPT version: I am wrong at saying that ARPES looks different from the calculation mainly because ARPES has large errors.**

The paper does not attribute the disagreement primarily to experimental error. Instead, the authors suggest that the discrepancy may originate from differences between the simplified David-star stacking sequence used in the DFT calculations and the actual stacking sequence produced by atomic-layer sliding. Therefore, the disagreement is potentially a limitation of the structural model used in the calculation rather than simply uncertainty or noise in ARPES.

**GPT version: I am wrong at saying that flatter bands by themselves mean that the system is a Mott insulator.**

A flatter band means a smaller bandwidth and therefore reduced kinetic energy or hopping, which can make electron correlations more important. However, flatness alone does not prove a Mott-insulating state. In this paper, the Mott interpretation of LC-$TaS_2$ comes from several observations taken together: reduced in-plane and out-of-plane band dispersion, a smaller insulating gap consistent with the expected Mott gap, enhanced localization at the central Ta atom, the failure of ordinary GGA to produce an insulating laddering structure, and the opening of a gap when the Hubbard $U$ correction is included.

**GPT version: I am wrong at describing carrier mobility simply as how fast the electrons are moving.**

Carrier mobility is not the carrier velocity itself. It measures how strongly the average drift velocity responds to an applied electric field, conventionally through $v_{\mathrm{d}} = \mu E$. A smaller mobility therefore means that carriers acquire a smaller drift velocity for the same applied field. In LC-$TaS_2$, the mobility is strongly reduced, which the authors associate with enhanced localization, narrower bands, and an increased effective carrier mass.

**GPT version: I am wrong at saying that because $n$ is larger, $\mu$ should automatically be smaller.**

Carrier concentration $n$ and mobility $\mu$ are not constrained to vary inversely with one another. In the simple Hall analysis used in the paper,

$$n = \frac{1}{eR_H}, \qquad \mu = \frac{R_H}{\rho_{xx}}.$$

Both quantities depend on the measured Hall coefficient, but mobility also depends on the longitudinal resistivity. Therefore, an increase in $n$ does not mathematically require a decrease in $\mu$. In this experiment, both changes happen simultaneously for physical reasons: the narrower Mott gap increases the carrier concentration, while stronger localization and the larger effective mass reduce the mobility.

**GPT version: I am wrong at saying that the similar normalized resistivities above approximately 80 K mean that the two configurations simply have the same resistivity.**

The curves shown in Fig. 5c are normalized by their values at 300 K, so their similarity should not be interpreted as equality of the absolute resistivities. The authors use the normalized behavior to compare the temperature dependence while reducing the influence of extrinsic factors. Their conclusion is that above approximately 80 K the normalized resistivity evolves similarly in the two structures, consistent with the preservation of the in-plane David-star configuration, whereas below 80 K LC-$TaS_2$ shows weaker insulating behavior consistent with its narrower gap.

**GPT version: I am wrong at explaining the larger out-of-plane resistance jump simply by saying that electrons are more localized and therefore the resistivity is larger.**

The authors make a more specific connection. Laddering interlayer sliding reduces the electronic dispersion along $k_z$. A smaller dispersion corresponds to a larger effective mass for

out-of-plane carrier motion. This enhanced effective mass, associated with the Mott-insulating mechanism in LC-$TaS_2$, is used to explain the much larger normalized resistance jump across the NC-CDW to C-CDW transition for current flowing along the $c$ direction.

**GPT version: I am wrong at saying that if $U$ increases, this causes less interlayer hopping.**

The causal relation in the authors' discussion goes primarily in the opposite direction. Laddering translation reduces the overlap between wavefunctions on neighboring David-stars and therefore reduces the interlayer hopping and out-of-plane bandwidth $t_\perp$. The reduced interlayer coupling also weakens electronic screening, which increases the effective Coulomb interaction $U$. Thus both effects increase the ratio $U/t_\perp$, favoring Mott localization. It is not simply that a larger $U$ directly causes the interlayer hopping to become smaller.

**GPT version: I am wrong at saying that the David-stars do not dimerize in ordinary 1T-$TaS_2$.**

The paper's interpretation is the opposite. In the ordered $T_A$ stacking associated with pristine 1T-$TaS_2$, David-stars containing unpaired electrons dimerize between neighboring layers, forming bilayers with an even number of electrons. This interlayer dimerization is central to the three-dimensional band-insulator picture. In the fractionally translated $T_A^S$ configuration of LC-$TaS_2$, this dimerization is suppressed, preserving an odd number of electrons per David-star and enhancing the importance of electron-electron correlations.

**GPT version: I am wrong at saying that the DFT somehow takes into account essentially every interaction automatically.**

DFT does not automatically contain every relevant many-body interaction exactly. Standard GGA treats exchange and correlation approximately and, in this system, actually predicts a metallic state for the laddering configuration. The authors have to introduce an additional Hubbard-$U$ correction to describe the stronger local Coulomb correlations. They also add a DFT-D3 correction to account for van der Waals interactions. The need for these additional ingredients illustrates precisely that the basic DFT approximation does not automatically capture all relevant physics.

**GPT version: I am wrong at concluding that because both calculated configurations have a gap after GGA+$U$, stacking is not important for the gap.**

This is one of the most important corrections to my summary. The paper demonstrates that stacking is crucial for determining the *mechanism* of the insulating gap. In pristine $T_AT_C$ stacking, a gap already exists in GGA without Hubbard $U$, and introducing $U$ produces only a limited additional increase. This indicates that the gap is predominantly associated with the three-dimensional band-insulating mechanism generated by interlayer coupling and David-star dimerization. In the laddering $T_A^ST_C^S$ structure, however, GGA predicts a metallic state; an insulating gap appears only after the Hubbard $U$ correction is introduced. This identifies the LC-$TaS_2$ state as predominantly Mott insulating. Therefore, the important result is not merely whether a gap exists, but *why* the gap exists in each stacking configuration.

**GPT version: I am wrong at saying that after reading the whole paper there is no clear main conclusion.**

The paper actually has a rather specific central conclusion. Pristine bulk 1T-$TaS_2$ with strong interlayer coupling and David-star dimerization is predominantly a three-dimensional

band insulator. Introducing a periodic laddering translation weakens interlayer wavefunction overlap, destroys the ordered interlayer David-star dimerization, narrows the electronic bands, enhances localization and effective Coulomb interactions, and converts the dominant insulating mechanism toward a two-dimensional Mott-insulating state. The authors therefore demonstrate that the insulating mechanism of bulk 1T-$TaS_2$ can be switched by manipulating the translational degree of freedom between its layers.

This is what the authors mean by the "dualistic insulating nature" of 1T-$TaS_2$: the same bulk layered material can exhibit insulating behavior dominated either by three-dimensional band physics or by two-dimensional Mott physics depending on its interlayer stacking and coupling.

**GPT version: I am wrong at saying that the final result shows that stacking is unimportant for the gap.**

Stacking is in fact the control knob at the center of the paper. The laddering translation weakens interlayer coupling by reducing the out-of-plane wavefunction overlap between David-stars. This reduces $t_\perp$ and simultaneously enhances the effective $U$ through reduced screening. The resulting increase of $U/t_\perp$ changes the dominant insulating mechanism from a 3D band insulator to a 2D Mott insulator. The existence of an insulating gap in both cases therefore does not make stacking irrelevant; rather, the striking result is that stacking determines the microscopic origin and character of that gap.

# 28 Distinguishing a Mott Insulator from a Trivial Insulator with Atomic Adsorbates by Lee, Jin, Woong Yeom (2021)

**Abstract**

(electronic systems are complicated) In an electronic system with various interactions intertwined, revealing the origin of its many-body ground state is challenging and a direct experimental way to verify the correlated nature of an insulator has been lacking.

(we'll distinguish Mott insulator, from a trivial band insulator) Here we demonstrate a way to unambiguously distinguish a paradigmatic correlated insulator, a Mott insulator, from a trivial band insulator based on their distinct chemical behavior for a surface adsorbate using 1T-$TaS_2$, which has been debated between a spin-frustrated Mott insulator or a spin-singlet trivial insulator.

We start from the observation of different sizes of spectral gaps on different surface terminations and show that potassium adatoms on these two surface layers behave in totally different ways.

This can be straightforwardly understood from distinct properties of a Mott and a band insulators due to the fundamental difference of a half and a full-filled orbital involved respectively.

(we did a good job and maybe you can use it somewhere in experiments) This work not only solves an outstanding problem in this particularly interesting material but also provides a simple touchstone to identify the correlated ground state of electrons experimentally.

*Introduction.*—When a material has strong interactions in various degrees of freedom, such as charge, spin, orbital, lattice, disorder, and topology, our understanding of the system's ground state and phase evolution is largely limited, and intriguing quantum phenomena emerge. The competition of a few different interactions often makes it truly challenging to identify the origin

of the material's ground state, such as the high-temperature superconductivity [1], which would be crucial to control its macroscopic properties and functionalize the material. For a simple but paradigmatic example, the Mott insulating state is driven by strong on-site Coulomb interaction of electrons ($U$) for a material with a half-filled electron band, which would otherwise form a metallic state [2]. This state is usually distinguished by the existence of an energy gap in spectroscopy against the theoretical prediction of a gapless state without the inclusion of $U$ [2]. However, there has been no direct experimental way to verify the half-filled insulating state and distinguish it from a band insulator with a full-filled electron band. The situation becomes more complicated when there exist competing insulating states of different origins, such as the charge or spin density wave states. In this Letter, we introduce a simple but powerful method to straightforwardly distinguish a Mott insulator from a band insulator based on the chemical difference in a half and a full-filled electronic orbital.

As a critical example to show the limitation in distinguishing a Mott insulator under various different interactions, we take a layered transition metal dichalcogenide $1T$-$TaS_2$. This material has been assumed widely as a Mott insulator with a coexisting charge-density-wave state [10, 4, 5, 6, 7, 8, 28, 9, 11, 16, 13, 25, 15, 16, 17, 18, 19, 20, 21, 22, 23, 24, 25, 26] but there exist a few other degrees of freedom to be considered. It undergoes a characteristic series of phase transitions from a metal to a commensurate charge-density-wave (CCDW) phase through a nearly commensurate charge-density-wave (NCCDW) phases [27]. A common unit cell of CDW phases has 13 Ta atoms distorted into a David-star(DS)-shape cluster to form a $\sqrt{13} \times \sqrt{13}$ superstructure [27]. 13 $5d$ electrons of a unit cell, one from each Ta atom, form 6 full-filled and one half-filled band with its electron localized strongly on the central Ta atom. The system exhibits a metal-insulator transition accompanying the NCCDW-CCDW transition and the strong localization of the half-filled electron, a very small bandwidth to amplify $U$, provides a natural ground of a Mott insulator model [10]. The model prevailed the scene for more than three decades [10, 4, 5, 6, 7, 8, 28, 9, 11, 16, 13, 25, 15, 16, 17, 18, 19, 20, 21, 22, 23, 24, 25, 26] and fueled the recent proposal of a quantum spin liquid state to explain the absence of a magnetic ordering down to a very low temperature [19, 21].

However, the Mott insulator model is seriously challenged by a few recent band structure calculations [28, 29, 30]. Very importantly, the above model ignores the interlayer hopping of electrons, which can crucially affect the bandwidth. The experiments seem to favor a bilayer stacking order, the layers within the bilayer stacked without a lateral translation [33, 34, 35, 32, 31] [a $\mathbf{T}_\mathrm{A}$ stacking, Fig. 28.1(a)] and each bilayer unit stacked with a translation of a half unit cell [34, 32] [a $\mathbf{T}_\mathrm{C}$ stacking, Fig. 28.1(b)], where half-filled Ta $5d_{z^2}$ electrons within bilayers form a spin-singlet state to lead to a trivial bonding-antibonding energy gap against the Mott insulator model. In our point of view, while tracking the intriguing interlayer ordering is very important, this situation manifests the weakness of the current method to verify a Mott insulating state, which relies crucially on the band structure calculation.

*Methods.*—$1T$-$TaS_2$ single crystal was cleaved in high vacuum and K atoms were deposited in a ultra high vacuum at room temperature. STM images were obtained at 4.4 K by a constant-current mode with a sample bias of -600 ($\mathbf{T}_\mathrm{C}$) or -800 meV ($\mathbf{T}_\mathrm{A}$) depending on the terminations [36]. A lock-in technique with a modulation of 1 kHz was utilized for $dI/dV$ measurements. After the measurements on the adsorption behavior, K adatoms were removed by through mild electric field applied by an STM tip in order to determine the layer stacking [36].

First-principles calculations were performed using the projected augmented plane-wave method implemented in the Vienna *ab initio* simulation package [37, 38] and the generalized gradient approximation for the exchange and correlation potential [39]. Spin-orbit coupling was also included. Electronic wave functions were expanded in plane waves with an energy cutoff of 400 eV. The isolated and K-adsorbed $TaS_2$ layers were considered within supercell geometries

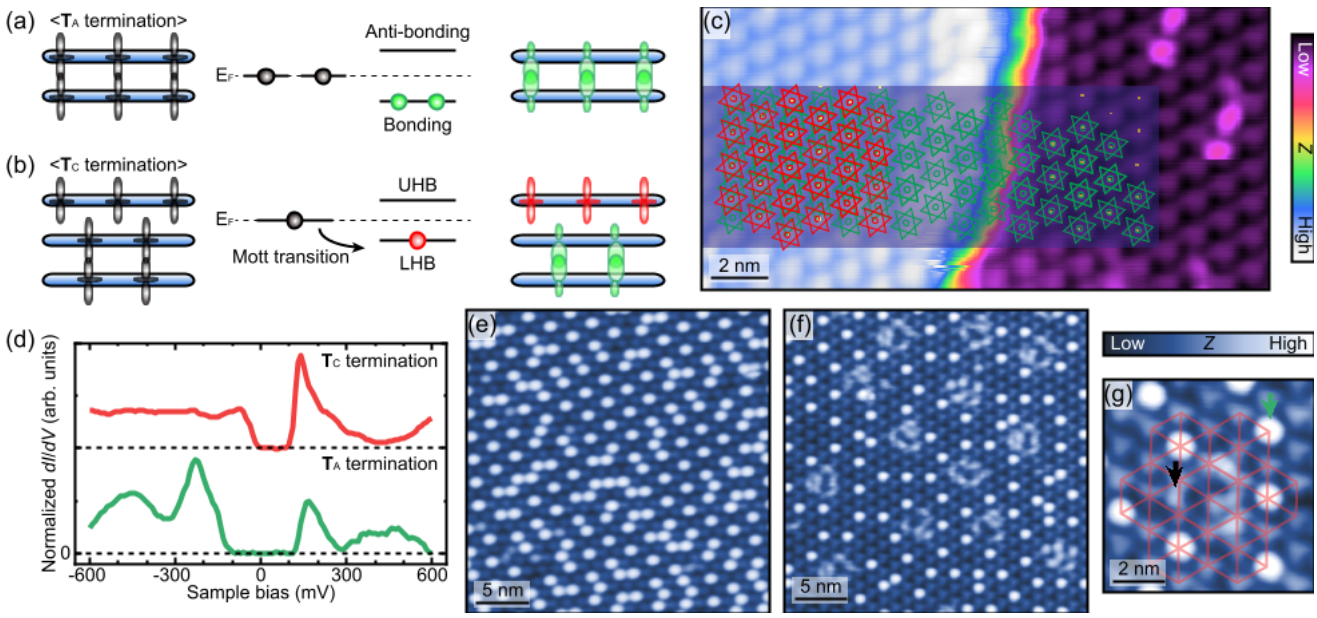


Figure 28.1: Distinct adsorption behaviors of K atoms on different surface terminations of 1$T$-$TaS_2$. (a) and (b) Orbital schematics for inter- ($\mathbf{T}_A$) and intra- ($\mathbf{T}_C$) bilayer terminations. Left (right) panels are those without (with) interlayer coupling. Note that only unpaired $d_{z^2}$ orbitals at the center of CDW unit cells are illustrated. Green and red colors represent the paired and unpaired electrons, respectively, after the interlayer coupling. (c) Determination of the $\mathbf{T}_C$ stacking of two neighboring surface layers across a single layer step. Yellow dots overlaid on the image indicate the center of the DS, obtained from the numerical process. (d) Normalized $dI/dV$ spectra of neighboring surface layers with different terminations without K adatoms; red (green) spectrum from the $\mathbf{T}_C$ ($\mathbf{T}_A$) termination in the left (right) part of (c). (e) and (f) STM images of $\mathbf{T}_C$- and $\mathbf{T}_A$-terminated surfaces with K adatoms. The adatom coverage is 0.38 and 0.33 per DS unit cell in (e) and (f), respectively. (g) An enlarged STM image of (f). While all adatoms in (e) are adsorbed at the DS center, they have two adsorption sites in (f) as shown with black (a site between DS unit cells) and green (one on the center) arrows in (g).

where the interlayer spacing was 20 Å. Geometries were relaxed until the forces on each atom were less than 0.01 eV $\text{Å}^{-1}$. We used a 7×7×1 and 3×3×1 **k**-point grid to sample the entire Brillouin zone for the pristine and K-adsorbed 1$T$-$TaS_2$ system, respectively.

*Different surface terminations with distinct adsorption behavior.*—The bilayer stacking would manifest itself as the existence of two distinct, inter- and intra-bilayer, terminations ($\mathbf{T}_A$ and $\mathbf{T}_C$ terminations, respectively) on the cleaved surface [Figs. 28.1(a) and 28.1(b)]. Indeed, a very recent STM experiment observed both terminations but with different sizes of the band gap [32]. However, the nature of each band gap is unclear. We pick up two neighboring surface layers separated by a single-layer-height step [Figs. 28.1(c) and 28.1(d)] and assign accurately the centers of DS clusters through the numerical processing of the STM images and compared them quantitatively between the neighboring layer. The top layer corresponds to the $\mathbf{T}_C$ termination, which inevitably requests the bottom one as $\mathbf{T}_A$ based on the alternative $\mathbf{T}_A$-$\mathbf{T}_C$ stacking order at low temperature [34, 32]. They both exhibit insulating tunneling spectra [the normalized differential tunneling conductance ($dI/dV$)] but with different band gaps of 250 and 400 meV as shown in Fig. 28.1(d), which is quantitatively consistent with the recent STM results [32, 36].

These two terminations are sharply contrasted by a simple electron-donating adsorbate of K as illustrated in the STM images of Figs. 28.1(e)-28.1(g). The most apparent is that the adsorption behaviors of K atoms are distinct on different terminations. On the $\mathbf{T}_C$ termination

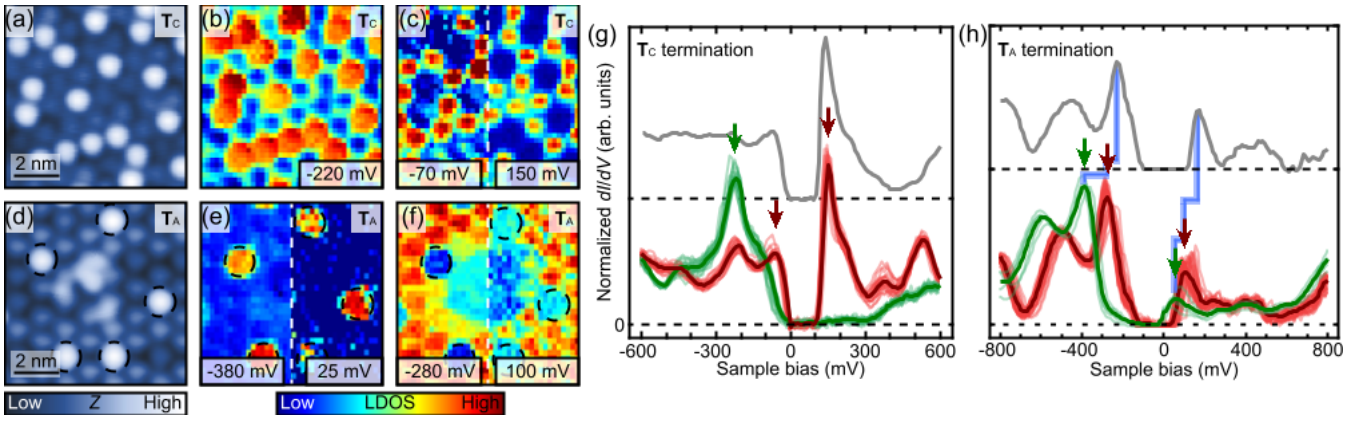


Figure 28.2: Electronic states of K adatoms on two different layers. (a) A STM image of the $\mathbf{T}_{\mathrm{C}}$-terminated surface. (b) and (c) Corresponding LDOS maps at three different biases indicated. (d)-(f) Similar images of the $\mathbf{T}_{\mathrm{A}}$-terminated surface. (g) and (h) Normalized $dI/dV$ spectra obtained on the $\mathbf{T}_{\mathrm{C}}$- and $\mathbf{T}_{\mathrm{A}}$-terminated surfaces. Red (green) spectra are obtained at the center of the bare (K-adsorbed) CDW unit cells in (a) and (d). Thick and dark spectra are the average of them. Biases for (b), (c), (e), and (f) are marked with arrows. The spectra of the pristine sample without adsorbates are plotted in grey for the comparison.

[Fig. 28.1(e)], all K atoms sit on the center of a DS cluster as reported recently [40], and the surface unit cells bifurcate into two groups, DS with and without K adatom at their center. On the other hand, we observe two different adsorbate configurations on the $\mathbf{T}_{\mathrm{A}}$ termination. The bright ones are at the center of the DS clusters as on the $\mathbf{T}_{\mathrm{C}}$ termination, but there exist off-centered adsorbates [medium contrast protrusions in Figs. 28.1(f) and 28.1(g)] mostly between neighboring DS clusters. The off-centered adsorbates are metastable configurations, which are prone to hop and easily perturbed by STM tips. The distinct adsorption behavior of the neighboring terraces is uniformly observed over different areas surfaces and in different cleavages.

*Distinct electronic states of different surface terminations with adsorbates.*—The difference between two different terminations becomes more evident in the spectroscopic measurements. The DS clusters with central K adsorbates exhibit strong local density of states (LDOS) at different energies, -220 meV on the $\mathbf{T}_{\mathrm{C}}$ [Figs. 28.2(a) and 28.2(b)], and 25 and -380 meV on the $\mathbf{T}_{\mathrm{A}}$ termination [Figs. 28.2(d) and 28.2(e)] as shown in the LDOS maps. The corresponding spectra reveal more important details. The DS clusters without K on the $\mathbf{T}_{\mathrm{C}}$ termination show no change of the LDOS while those with K have a single strong LDOS peak at -220 meV replacing the two peaks defining the energy gap at the Fermi level [Fig. 28.2(g)] [36]. This is natural for a Mott insulator since the half-filled electron in a unit cell with a K adsorbate would be fully saturated by the electron from the adsorbate. Since the full-filled electron orbital is strongly localized, the neighboring bare unit cells would have little doping effect [Figs. 28.2(c) and 28.2(g)]. In stark contrast, on the $\mathbf{T}_{\mathrm{A}}$ termination, the two LDOS peaks defining the band gap are rigidly shifted to lower energies for the DS clusters without an adsorbate and to even lower energy for those with K [Fig. 28.2(h)] [36]. This straightforwardly indicates that the K adsorbates dope the system. The rigid shift upon doping is what is expected in a band insulator. The doping effect is stronger on the DS cluster with K adsorbate and weaker on those without [see their LDOS maps in Figs. 28.2(e) and 28.2(f)].

*DFT calculations with a single and a bilayer model.*—All experimental results are well explained by the DFT calculations with an isolated single and a bilayer layer model for the $\mathbf{T}_{\mathrm{C}}$ and $\mathbf{T}_{\mathrm{A}}$ termination, respectively. The validity of the single-layer model can be confirmed by a trilayer model [36] and is easily understood from a marginal overlap of half-filled $d_{z^2}$ electrons

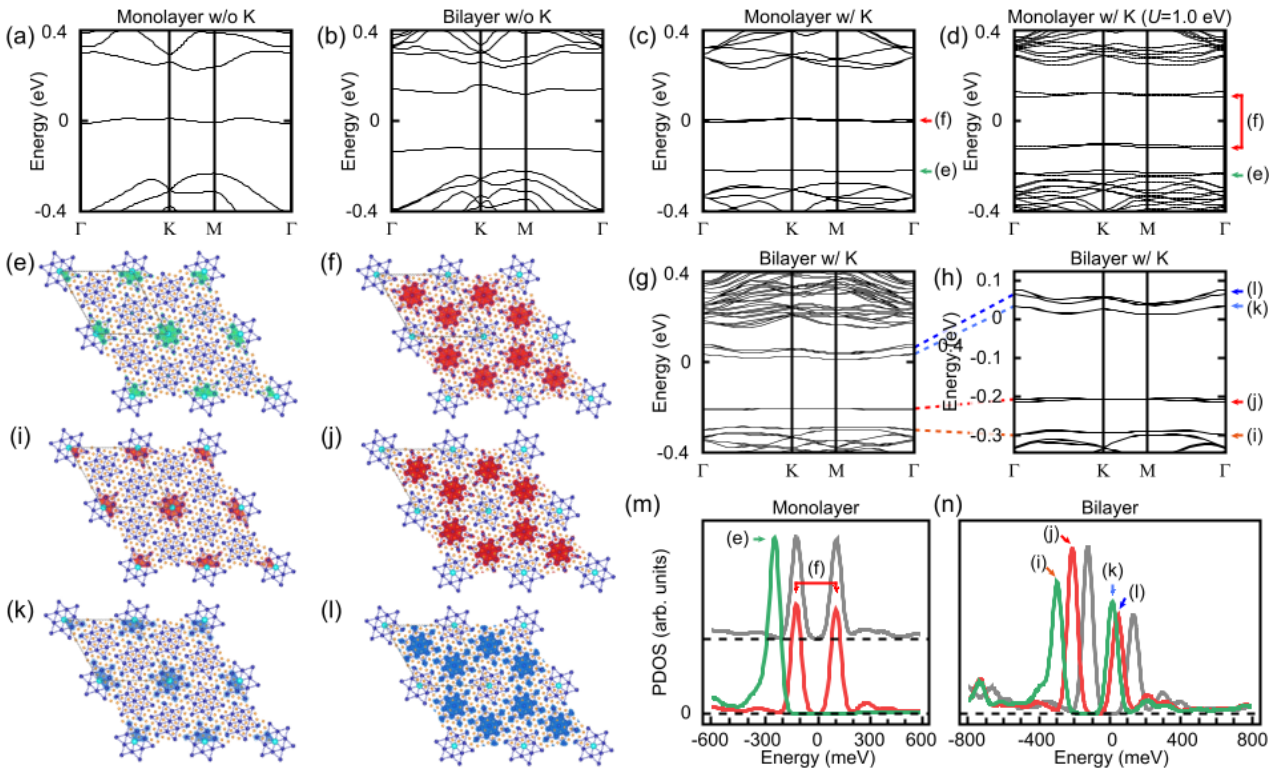


Figure 28.3: Electronic band structures and local density of states calculated for K-adsorbed $1T$-$TaS_2$. (a) and (b) Band structures of the monolayer and bilayer ($\mathbf{T}_A$-stacked) $1T$-$TaS_2$, respectively. (c) and (d) Band structures of a monolayer with K adatoms in a $(\sqrt{3}\times\sqrt{3})R30°$ superstructure without and with the on-site Coulomb repulsion $U$, respectively. (e) and (f) Spatial distributions of electrons within the bands marked in (c) and (d). (g) A band structure of a bilayer $1T$-$TaS_2$ in the $\mathbf{T}_A$ stacking with K adatoms in the same superstructure as in (c). (h) An enlargement of (g) near the Fermi level. (i)-(l) Electron spatial distributions of the bands marked in (h). (m) $5d_{z^2}$ partial density of states for the K adsorption on the monolayer, and (n) on the bilayer $1T$-$TaS_2$. Gray, red, and green plots represent the PDOS in the pristine layer, and the bare and the K-adsorbed DS unit cells in the K-adsorbed layer. Each of the PDOS peaks corresponds to bands indicated in (d) or (h) whose spatial distributions are shown in (e), (f), or (i)-(l). Blue, orange, and cyan atoms in (e), (f), and (i)-(l) represent Ta, S, and K, respectively. See the Supplemental Material [36] for the side views of the charge distribution.

between the top and the second layer. Even before any calculation, the difference of the electronic system is obvious. In contrast to the single layer with half-filled electrons, there exist an even number of $d_{z^2}$ electrons in a double-layer unit cell, which would form an interlayer bonding on each unit cell to fall into a simple band insulator [Fig. 28.1(a)]. These result in totally different single-particle band structures, a metallic band at the Fermi level [Fig. 28.3(a)] and insulating bonding-antibonding bands [Fig. 28.3(b)] in a single and a double layer, respectively. As well known, introducing electron correlation $U$ in the single layer would open a Mott gap but does not affect substantially the bonding-antibonding bands [36].

The K adsorption on both terminations is modeled with a periodic occupation of 1/3 of DS clusters, which results in a $(\sqrt{3}\times\sqrt{3})R30°$ superstructure. As detailed previously, on the $\mathbf{T}_C$ termination, this superstructure is highly favored due to the dipole-dipole interaction of adsorbates [40]. When K atoms are deposited, its $4s$ electron forms a strong local bonding with $d_{z^2}$ electron at the center of the DS [Fig. 28.3(e)] and a full-filled band at -200 meV [Fig. 28.3(c)]. The electrons in the bare DS clusters are almost intact [Fig. 28.3(f)] with their partially-filled band remaining at the Fermi level [Fig. 28.3(c)] or Mott Hubbard bands [Fig. 28.3(d)] when

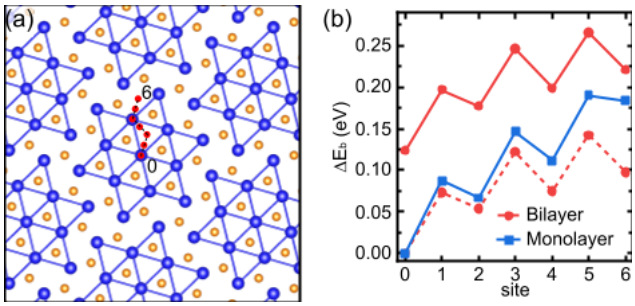


Figure 28.4: Adsorption energies of K adatoms on different terminations. (a) Representative adsorption sites of K, and (b) their relative binding energies ($\Delta E_b$) to the most stable site of a monolayer (blue). Those on a $\mathbf{T}_\mathrm{A}$-stacked bilayer (red) are shifted for the comparison (dashed red line).

$U$ is excluded or included, respectively. The corresponding partial density of states [PDOS, Fig. 28.3(m)] reproduce well the spectroscopic data [36], two distinct spectra on a K-adsorbed and a bare DS cluster, as mentioned above [Fig. 28.2(g)]. On the $\mathbf{T}_\mathrm{A}$ termination, in clear contrast, the 4$s$ electron is donated to the $d_{z^2}$ bands to shift them rigidly. There exist different amounts of shifts for the DS clusters with and without K adsorbates, a larger shift for the former, as observed in the experiment, giving rise to basically two sets of bands with wave functions on different unit cells [Figs. 28.3(g), 28.3(h), and 28.3(i)-28.3(l)]. The inclusion of $U$ does not affect the overall band structure but only increases the band gap marginally (∼15 meV) [36]. The PDOS changes [Fig. 28.3(n)] match excellently with the experimental data [Fig. 28.2(h)] [36].

*Details of the adsorption behavior.*—As we mentioned above, the difference of the surface termination appears not only in spectroscopy but also in the adsorbate distribution as the existence of the minor adsorption sites on the $\mathbf{T}_\mathrm{A}$ termination. This can also be explained within the DFT calculations. In principle, there are 28 symmetrically inequivalent adsorption sites in a DS cluster [40]. We first exclude those on top of surface sulfur atoms, which are energetically unfavored. The adsorption energy is found to be minimized at the DS center but depends on the termination as -2.85 and -2.73 eV on $\mathbf{T}_\mathrm{C}$ and $\mathbf{T}_\mathrm{A}$ termination, respectively. A larger adsorption energy gain is expected on the $\mathbf{T}_\mathrm{C}$ termination due to the localized half-filled electrons as discussed above. As shown for 7 representative sites [Fig. 28.4(a)] with different distances from the center, the adsorption energy increases rather linearly with the distance from the center [Fig. 28.4(b)]. We note the relatively large difference of the adsorption energy between the site 5 and 6 on the $\mathbf{T}_\mathrm{A}$ than the $\mathbf{T}_\mathrm{C}$ termination. Note also that the energy difference between the site 6 and the most stable site (site 0) is much large on the $\mathbf{T}_\mathrm{C}$ termination. Thus, the adatom migration to a more stable sites toward the center of a DS cluster is much easier on the $\mathbf{T}_\mathrm{C}$ termination. These adsorption-energy landscapes qualitatively explain the absence/presence of adsorbates on the site 6 in the experiment on the $\mathbf{T}_\mathrm{C}/\mathbf{T}_\mathrm{A}$ termination [36]. While the difference in the adsorbate distribution is easily observable in the topographic imaging, its origin is not as fundamental as the spectroscopic difference on different terminations. However, roughly speaking, the origin of the difference can be traced back to the stronger bonding of the electron-donating adsorbate on the Mott insulator due to the half-filled electron. Combining all the experimental and theoretical result consistently, we introduce that the adsorption of monovalent adsorbates can be a direct and unique touchstone to distinguish a Mott insulator from a band insulator or other types of insulators based on filled orbitals.

# Part XV
# Appendix

## .1 Appendix

### .1.1 Literature

# Bibliography

# References

## .2 References from Generally Main Articles

**References from Configurational Electronic States in Layered Transition Metal Dichalcogenides by Vodeb, Kabanov et al.**


1. Stojchevska, L. et al. Ultrafast switching to a stable hidden quantum state in an electronic crystal. Science (80-. ). 344, 177-180 (2014).

2. Cho, D. et al. Nanoscale manipulation of the Mott insulating state coupled to charge order in 1T-TaS2. Nat. Commun. 7, 1-6 (2016).

3. Cho, D. et al. Correlated electronic states at domain walls of a Mott-charge-density-wave insulator 1T-TaS2. Nat. Commun. 8, 1-6 (2017).

4. Ma, L. et al. A metallic mosaic phase and the origin of Mott-insulating state in 1T-TaS 2. 1-8 (2016). doi:10.1038/ncomms10956

5. Vaskivskyi, I. et al. Fast electronic resistance switching involving hidden charge density wave
states. Nat. Commun. 7, 1-6 (2016).

6. Vaskivskyi, I. et al. Controlling the metal-to-insulator relaxation of the metastable hidden quantum state in 1T-TaS 2. 1-7 (2015).

7. Han, T. T. et al. Exploration of metastability and hidden phases in correlated electron crystals visualized by femtosecond optical doping and electron crystallography. (2015).

8. Withers, R. L. & Wilson, J. A. An examination of the formation and characteristics of chargedensity waves in inorganic materials with special reference to the two- and one-dimensional transition- metal chalcogenides. J. Phys. C Solid State Phys. 19, 4809-4845 (1986).

9. Wilson, J. A., Di Salvo, F. J. & Mahajan, S. Charge-density waves and superlattices in the metallic layered transition metal dichalcogenides. Adv. Phys. 24, 117-201 (1975).

10. Rossnagel, K. On the origin of charge-density waves in select layered transition-metal dichalcogenides. Journal of Physics Condensed Matter 23, (2011).

11. Sipos, B. et al. From Mott state to superconductivity in-1T-TaS2. Nat. Mater. 7, 960-965 (2008).

12. Li, L. J. et al. Fe-doping-induced superconductivity in the charge-density-wave system 1T-TaS 2. Epl 97, (2012).

13. Ang, R. et al. Superconductivity and bandwidth-controlled Mott metal-insulator transition in 1T-TaS2-xSex. Phys. Rev. B - Condens. Matter Mater. Phys. 88, 1-5 (2013).

14. Friend, R. H., Frindt, R. F., Grant, A. J., Yoffe, A. D. & Jerome, D. Electrical conductivity and charge density wave formation in 4 Hb TaS2 under pressure. J. Phys. C Solid State Phys. (1977). doi:10.1088/0022-3719/10/7/011

15. Joe, Y. I. et al. Emergence of charge density wave domain walls above the superconducting dome in 1T-TiSe 2. Nat. Phys. 10, 421-425 (2014).

16. Kusmartseva, A. F., Sipos, B., Berger, H., Forró, L. & Tutiš, E. Pressure Induced Superconductivity in Pristine 1T-TiSe2. Phys. Rev. Lett. 103, 2-5 (2009).

17. Liu, Y. et al. Nature of charge density waves and superconductivity in 1T-TaSe2-xTex. Phys. Rev. B 94, 1-8 (2016).

18. Luo, H. et al. Differences in Chemical Doping Matter: Superconductivity in Ti1-xTaxSe2 but Not in Ti1-xNbxSe2. Chem. Mater. 28, 1927-1935 (2016).

19. Morosan, E. et al. Multiple electronic transitions and superconductivity in Pdx TiSe2. Phys. Rev. B - Condens. Matter Mater. Phys. 81, 1-5 (2010).

20. Suderow, H., Tissen, V. G., Brison, J. P., Martínez, J. L. & Vieira, S. Pressure induced effects on the fermi surface of superconducting 2H-NbSe2. Phys. Rev. Lett. (2005). doi:10.1103/PhysRevLett.95.117006

21. Wagner, K. E. et al. Tuning the charge density wave and superconductivity in Cux TaS2. Phys. Rev. B - Condens. Matter Mater. Phys. 78, 1-6 (2008).

22. Grüner, G. Density waves in solids. Density Waves in Solids (2018). doi:10.1201/9780429501012

23. McMillan, W. L. Landau theory of CDW in transition-metal dichalcogenides. Phys. Rev. B 12, 1187 (1975).

24. Hellmann, S. et al. Time-domain classification of charge-density-wave insulators. Nat. Commun. (2012). doi:10.1038/ncomms2078

25. Kogar, A. et al. Signatures of exciton condensation in a transition metal dichalcogenide. Science (80-. ). 358, 1314-1317 (2017).

26. Johannes, M. D. & Mazin, I. I. Fermi surface nesting and the origin of charge density waves in metals. Phys. Rev. B - Condens. Matter Mater. Phys. 77, 1-8 (2008).

27. Kiss, T. et al. Charge-order-maximized momentum-dependent superconductivity. Nat. Phys. 3, 720-725 (2007).

28. Yao, H., Robertson, J. A., Kim, E. A. & Kivelson, S. A. Theory of stripes in quasi-twodimensional rare-earth tellurides. Phys. Rev. B - Condens. Matter Mater. Phys. 74, 1-7 (2006).

29. Varma, C. M. & Simons, A. L. Strong-coupling theory of charge-density-wave transitions. Phys. Rev. Lett. (1983). doi:10.1103/PhysRevLett.51.138

30. McMillan, W. L. Microscopic model of charge-density waves in 2H-TaSe2. Phys. Rev. B 16, 643-650 (1977).

31. Eiter, H.-M. et al. Alternative route to charge density wave formation in multiband systems. 16 (2012). doi:10.1073/pnas. 1214745110

32. Zhu, X., Cao, Y., Zhang, J., Plummer, E. W. & Guo, J. Classification of charge density waves based on their nature. 112, 2367-2371 (2015).

33. Lee, P. A., Rice, T. M. & Anderson, P. W. Conductivity from charge or spin density waves. Solid State Commun. (1993). doi:10.1016/0038-1098(93)90284-T

34. Di Salvo, F. J., Wilson, J. A., Bagley, B. G. & Waszczak, J. V. Effects of doping on chargedensity waves in layer compounds. Phys. Rev. B 12, 2220-2235 (1975).

35. DiSalvo, F. J. & Fleming, R. M. Search for a sliding charge density wave in layered compounds. Solid State Commun. (1980). doi:10.1016/0038-1098(80)90874-1

36. Ma, Y., Hou, Y., Lu, C., Li, L. & Petrovic, C. Possible origin of nonlinear conductivity and large dielectric constant in the commensurate charge-density-wave phase of 1T-TaS2. Phys. Rev. B 97, 1-9 (2018).

37. Fazekas, P. & Tosatti, E. Electrical, structural and magnetic properties of pure and doped 1TTaS2. Philos. Mag. B Phys. Condens. Matter; Stat. Mech. Electron. Opt. Magn. Prop. (1979). doi:10.1080/13642817908245359

38. Gerasimenko, Y. A., Vaskivskyi, I. & Mihailovic, D. Long range electronic order in a metastable state created by ultrafast topological transformation. arXiv:1704.08149 [cond-mat] (2017).

39. Rossnagel, K. & Smith, N. V. Spin-orbit coupling in the band structure of reconstructed 1TTaS2. Phys. Rev. B - Condens. Matter Mater. Phys. 73, 1-3 (2006).

40. Ritschel, T. et al. Orbital textures and charge density waves in transition metal dichalcogenides. Nat. Phys. 11, 328-331 (2015).

41. Svetin, D., Vaskivskyi, I., Brazovskii, S. & Mihailovic, D. Three-dimensional resistivity and switching between correlated electronic states in 1T-TaS2. Sci. Rep. 7, 1-10 (2017).

42. Clerc, F. et al. Lattice-distortion-enhanced electron-phonon coupling and Fermi surface nesting in 1T-Ta S2. Phys. Rev. B - Condens. Matter Mater. Phys. 74, 1-7 (2006).

43. Zhang, Q., Gan, L. Y., Cheng, Y. & Schwingenschlögl, U. Spin polarization driven by a charge-density wave in monolayer 1T- TaS2. Phys. Rev. B - Condens. Matter Mater. Phys. 90, 1-5 (2014).

44. Gerasimenko, Y. A., Vaskivskyi, I. & Mihailovic, D. Dual vortex charge order in a metastable state created by an ultrafast topological transition in 1T-TaS2. arXiv:1704.08149v2 (2017).

45. Karpov, P. & Brazovskii, S. Modeling of networks and globules of charged domain walls observed in pump and pulse induced states. Sci. Rep. 8, 1-4 (2018).

46. Fujisawa, Y. et al. Appearance of a domain structure and its electronic states in iron doped 1TTaS2observed using scanning tunneling microscopy and spectroscopy. J. Phys. Soc. Japan 86, 80-83 (2017).

47. Dai, H., Chen, H. & Lieber, C. M. Weak pinning and hexatic order in a doped two-dimensional charge-density-wave system. Phys. Rev. Lett. (1991). doi:10.1103/PhysRevLett.66.3183

48. Wu, X. L. & Lieber, C. M. Direct characterization of charge-density-wave defects in titaniumdoped TaSe2 by scanning tunneling microscopy. Phys. Rev. B (1990). doi:10.1103/PhysRevB.41.1239

49. Qiao, S. et al. Mottness collapse in 1T-TaS2-xSex transition-metal dichalcogenide: An interplay between localized and itinerant orbitals. Phys. Rev. X 7, 1-10 (2017).

50. Yan, S. et al. Influence of Domain Walls in the Incommensurate Charge Density Wave State of Cu Intercalated 1T-TiSe2. Phys. Rev. Lett. 118, 1-5 (2017).

51. Gerasimenko, Y. et al. Ultrafast jamming of electrons into an amorphous entangled state. arXiv (2018).

52. Rossnagel, K., Rotenberg, E., Koh, H., Smith, N. V & Kipp, L. Continuous tuning of electronic correlations by alkali adsorption on layered 1T-TaS2. Phys. Rev. Lett. 95, 1-4 (2005).

53. Rossnagel, K. Suppression and emergence of charge-density waves at the surfaces of layered 1T-TiSe2and 1T-TaS2by in situ Rb deposition. New J. Phys. 12, (2010).

54. Hollander, M. J. et al. Electrically driven reversible insulator-metal phase transition in 1TTaS2. Nano Lett. 15, 1861-1866 (2015).

55. Li, L. J. et al. Controlling many-body states by the electric-field effect in a two-dimensional material. Nature 529, 185-189 (2016).

56. Zhu, C. et al. Light-Tunable 1T-TaS2 Charge-Density-Wave Oscillators. ACS Nano 12, 11203-11210 (2018).

57. Zong, A. et al. Ultrafast manipulation of mirror domain walls in a charge density wave. Sci. Adv. 4, 1-7 (2018).

58. Sun, K. et al. Hidden CDW states and insulator-to-metal transition after a pulsed femtosecond laser excitation in layered chalcogenide 1T-TaS2-xSex. Sci. Adv. 4, 1-8 (2018).

59. Wu, D. et al. Ultrabroadband photosensitivity from visible to terahertz at room temperature. Sci. Adv. 4, 1-7 (2018).

60. Zheng, S., Liu, F., Zhu, C., Liu, Z. & Fan, H. J. Room-temperature electrically driven phase transition of two-dimensional 1T-TaS2layers. Nanoscale 9, 2436-2441 (2017).

61. Yoshida, M., Suzuki, R., Zhang, Y., Nakano, M. & Iwasa, Y. Memristive phase switching in two-dimensional 1T-TaS2 crystals. Sci. Adv. 1, e1500606-e1500606 (2015).

62. Chatterjee, U. et al. Emergence of coherence in the charge-density wave state of 2H − NbSe2. Nat. Commun. 6, 1-7 (2015).

63. Nakanishi, K. & Shiba, H. Domain-Like Incommensurate Charge-Density-Wave States and Collective Modes. J. Phys. Soc. Japan (1978). doi:10.1143/JPSJ.45.1147

64. Nakanishi, K. & Shiba, H. Theory of Three-Dimensional Orderings of Charge-Density Waves in IT-TaX2(X: S, Se). J. Phys. Soc. Japan (1984). doi:10.1143/JPSJ.53.1103

65. Tosatti, E. & Fazekas, P. ON THE NATURE OF THE LOW-TEMPERATURE PHASE OF 1T-TaS2 Jz. 1-5 (1976).

66. Fazekas, P. & Tosatti, E. Charge carrier localization in pure and doped 1T-TaS2. Phys. $B + C$ (1980). doi:10.1016/0378-4363(80)90229-6

67. Mertelj, T., Kabanov, V. V. & Mihailovic, D. Charged particles on a two-dimensional lattice subject to anisotropic jahn-teller interactions. Phys. Rev. Lett. 94, 13-16 (2005).

68. Mertelj, T., Kabanov, V. V, Mena, J. M. & Mihailovic, D. Self-organization of charged particles on a two-dimensional lattice subject to anisotropic Jahn-Teller-type interaction and three-dimensional Coulomb repulsion. Phys. Rev. B - Condens. Matter Mater. Phys. 76, 1-9 (2007).

69. Rademaker, L., Van Den Brink, J., Zaanen, J. & Hilgenkamp, H. Exciton condensation in strongly correlated electron bilayers. Phys. Rev. B - Condens. Matter Mater. Phys. 88, 1-21 (2013).

70. Dobrosavljević, V., Tanasković, D. & Pastor, A. A. Glassy Behavior of Electrons Near MetalInsulator Transitions. Phys. Rev. Lett. 90, 4 (2003).

71. Brazovskii, S. Modeling of Evolution of a Complex Electronic System to an Ordered Hidden State: Application to Optical Quench in 1T-TaS2. J. Supercond. Nov. Magn. 28, 1349-1353 (2015).

72. Fazio, R. & Van der Zant, H. Quantum phase transitions and vortex dynamics in superconducting networks. Phys. Rep. 355, 235-334 (2001).

73. Rammal, R., Lubensky, T. C. & Toulouse, G. Superconducting networks in a magnetic field. Phys. Rev. B (1983). doi:10.1103/PhysRevB.27.2820

74. Gurevich, A., Kadyrov, E. & Larbalestier, D. C. Dynamic Matching of Vortex Lattice in Superconducting Multilayers. Phys. Rev. Lett. 77, 4078-4081 (1996).

75. Harada, K. et al. Direct observation of vortex dynamics in superconducting films with regular arrays of defects. Science (80-. ). 274, 1167-1170 (1996).

76. Martín, J. I., Vélez, M., Nogués, J. & Schuller, I. K. Flux pinning in a superconductor by an
array of submicrometer magnetic dots. Phys. Rev. Lett. (1997).
doi:10.1103/PhysRevLett.79.1929

77. Morgan, D. J. & Ketterson, J. B. Asymmetric flux pinning in a regular array of magnetic dipoles. Phys. Rev. Lett. 80, 3614-3617 (1998).

78. Welp, U. et al. Superconducting transition and vortex pinning in Nb films patterned with nanoscale hole arrays. Phys. Rev. B 66, 212507 (2002).

79. Lobb, C. J., Abraham, D. W. & Tinkham, M. Theoretical interpretation of resistive transition data from arrays of superconducting weak links. Phys. Rev. B 27, 150-157 (1983).

80. Teitel, S. & Jayaprakash, C. Phase transtions in frustrated two-dimensional XY models. Phys. Rev. B 27, 598-601 (1983).

81. Rademaker, L., Pramudya, Y., Zaanen, J. & Dobrosavljević, V. Influence of long-range interactions on charge ordering phenomena on a square lattice. Phys. Rev. E - Stat. Nonlinear, Soft Matter Phys. 88, 1-8 (2013).

82. Teitel, S. & Jayaprakash, C. Josephson-junction arrays in transverse magnetic fields. Phys. Rev. Lett. (1983). doi:10.1103/PhysRevLett.51.1999

83. Straley, J. P. & Barnett, G. M. Phase diagram for a Josephson network in a magnetic field. Phys. Rev. B (1993). doi:10.1103/PhysRevB.48.3309

84. Minnhagen, P. The two-dimensional Coulomb gas, vortex unbinding, and superfluidsuperconducting films. Rev. Mod. Phys. (1987). doi:10.1103/RevModPhys.59.1001

85. Lee, S. J., Kim, B. & Lee, J. Infinite ground state degeneracy and glassy dynamics in the frustrated XY model and lattice Coulomb gas with f = 1/6. in Physica A: Statistical Mechanics and its Applications (2002). doi:10.1016/S0378-4371(02)01232-3

86. Lee, S. J., Lee, J. R. & Kim, B. Patterns of Striped Order in the Classical Lattice Coulomb Gas. Phys. Rev. Lett. 88, 4 (2002).

87. Kolahchi, M. R. & Fazli, H. Behavior of a Josephson-junction array with golden mean frustration. Phys. Rev. B - Condens. Matter Mater. Phys. 62, 9089-9094 (2000).

88. Kolahchi, M. R. Ground state of uniformly frustrated josephson-junction arrays at irrational frustration. Phys. Rev. B - Condens. Matter Mater. Phys. 59, 9569-9572 (1999).

89. Gupta, P. & Teitel, S. Phase diagram of the two-dimensional lattice Coulomb gas. Phys. Rev. B - Condens. Matter Mater. Phys. 55, 2756-2759 (1997).

90. Reichhardt, C., Olson, C. & Nori, F. Commensurate and incommensurate vortex states in
superconductors with periodic pinning arrays. Phys. Rev. B - Condens. Matter Mater. Phys. 57, 7937-7943 (1998).

91. Reichhardt, C. & Grønbech-Jensen, N. Critical currents and vortex states at fractional matching fields in superconductors with periodic pinning. Phys. Rev. B - Condens. Matter Mater. Phys. 63, 1-10 (2001).

92. Pokrovsky, V. L. & Uimin, G. V. On the properties of monolayers of adsorbed atoms. J. Phys. C Solid State Phys. 11, 3535-3549 (1978).

93. Shinjo, K. & Sasada, T. Commensurate Structures of Ionic Adlayer with Repulsive Long Range Interaction. J. Phys. Soc. Japan 54, 1469-1476 (1985).

94. Cocho, G., Pérez-Pascual, R. & Rius, J. L. Minimal-energy configuration of charged particles in a square lattice. *EPL* (1986). doi:10.1209/0295-5075/2/7/001

95. Arce, H., Mochán, W. L. & Cocho, G. Minimum energy configurations of atoms adsorbed on a lattice. Surf. Sci. 294, 108-115 (1993).

96. Arce, H., Mochán, W. L. & Gutiérrez, J. J. Minimum energy 2D patterns of atoms adsorbed on a hexagonal lattice. Surf. Sci. 348, 379-386 (1996).

97. Diehl, R. D. & McGrath, R. Structural studies of alkali metal adsorption and coadsorption on metal surfaces. Surf. Sci. Rep. (1996). doi:10.1016/0167-5729(95)00010-0

98. Van Blaaderen, A., Ruel, R. & Wiltzius, P. Template-directed colloidal crystallization. Nature (1997). doi:10.1038/385321a0

99. Kagawa, F. et al. Charge-cluster glass in an organic conductor. Nat. Phys. 9, 419-422 (2013).

100. Mahmoudian, S., Rademaker, L., Ralko, A., Fratini, S. & Dobrosavljević, V. Glassy Dynamics in Geometrically Frustrated Coulomb Liquids without Disorder. Phys. Rev. Lett. 115, 1-5 (2015).

101. Hu, J. & Westervelt, R. Commensurate-incommensurate transitions in magnetic bubble arrays with periodic line pinning. Phys. Rev. B - Condens. Matter Mater. Phys. 55, 771-774 (1997).

102. Bak, P., Mukamel, D., Villain, J. & Wentowska, K. Commensurate-incommensurate transitions in rare-gas monolayers adsorbed on graphite and in layered charge-density-wave systems. Phys. Rev. B 19, 1610-1613 (1979).

103. Villain, J. Commensurate-incommensurate transition of krypton monolayers on graphite: A low temperature theory. Surf. Sci. (1980). doi:10.1016/0039-6028(80)90115-6

104. Zhou, Y., Kanoda, K. & Ng, T. K. Quantum spin liquid states. Rev. Mod. Phys. 89, 1-50
(2017).

105. Debenedetti, P. G. & Stillinger, F. H. Supercooled liquids and the glass transition. Nature 410, 259-267 (2001).

106. Alexandrov, A. S. & Mott, N. F. Polarons and Bipolarons. (World Scientific, 1995).

107. ALPS. Available at: http://alps.comp-phys.org/.

108. M. Troyer, B. Ammon, and E. Heeb: Lecture Notes in Com-puter Science1505(1998) 191.

109. B. Bauer, L. Carr, H. G. Evertz, A. Feiguin, J. Freire, S. Fuchs, L. Gamper, J. Gukelberger, E. Gull, S. Guertler, et al., Journal of Statistical Mechanics: Theory and Experiment 2011, P05001 (2011).

110. A. F. Albuquerque, F. Alet, P. Corboz, P. Dayal, A. Feiguin, S. Fuchs, L. Gamper, E. Gull, S. G □ urtler, A. Honecker, et al., Journal of Magnetism and Magnetic Materials 310, 1187 (2007).

111. Dai, Z., Xue, Q., Gong, Y., Slough, C. G. & Coleman, R. V. Scanning-probe-microscopy studies of superlattice structures and density-wave structures in $2H-NbSe2, 2H-TaSe2$, and 2 H TaS2 induced by Fe doping. Phys. Rev. B 48, 14543-14555 (1993).

112. Tatlock, G. J. & Acrivos, J. V. In situ intercalation of TaS2 in the electron microscope. Philos. Mag. B Phys. Condens. Matter; Stat. Mech. Electron. Opt. Magn. Prop. 38, 81-93 (1978).

113. Clark, W. B. & Williams, P. M. Charge density waves in intercalated IT-TaS2. Philos. Mag. 35, 883-899 (1977).

114. Coleman, R. V. et al. Scanning tunnelling microscopy of charge-density waves in transition metal chalcogenides. Advances in Physics 37, (1988).

115. Pettenkofer, C., Jaegermann, W. & Parkinson, B. A. Copper intercalation in 1T-TaS2. Surf. Sci. 251-252, 583-586 (1991).

116. Parsons, C. Polypharmacy and inappropriate medication use in patients with dementia: an underresearched problem. Therapeutic Advances in Drug Safety 8, 31-46 (2017).

117. Hotta, C. & Furukawa, N. Strong coupling theory of the spinless charges on triangular lattices: Possible formation of a gapless charge-ordered liquid. Phys. Rev. B - Condens. Matter Mater. Phys. 74, 10-13 (2006).

118. Schmalian, J. & Wolynes, P. G. Stripe glasses: self-generated randomness in a uniformly frustrated system. Phys. Rev. Lett. 85, 836-839 (2000).

119. Westfahl, H., Schmalian, J. & Wolynes, P. G. Self-generated randomness, defect wandering,
and viscous flow in stripe glasses. Phys. Rev. B 64, 174203 (2001).

120. Alexandrov, A.S. and Bratkovsky, A.M., 2000. Alexandrov and Bratkovsky reply. Physical Review Letters, 84(9), pp. 2043.

121. Mattheiss, L. F. Band structures of transition-metal-dichalcogenide layer compounds. Phys. Rev. B 8, 3719-3740 (1973).

122. Benda, J. A. Optical, electrical-transport, and heat-capacity studies of the solid solutions TixTa1-xS2, ZrxTa1-xS2, and TixNb1-xSe2. Phys. Rev. B (1974). doi:10.1103/PhysRevB.10.1409

**References from SI to "Configurational Electronic States in TMDCs"**

1. Villain, J. Theory of one- and two-dimensional magnets with an easy magnetization plane. II. The planar, classical, two-dimensional magnet. J. Phys. 36, 581-590 (1975).

2. Alexandrov, A. S. & Mott, N. F. Polarons and Bipolarons. (World Scientific, 1995).

3. Hukushima Koji & Nemoto Koji. Exchange Monte Carlo Method and Application to Spin Glass Simulations. Journal of the Physical Society of Japan 65, 1604-1608 (1996).

4. Spijkerman, A., de Boer, J. L., Meetsma, A., Wiegers, G. A. & van Smaalen, S. X-ray crystalstructure refinement of the nearly commensurate phase of in-dimensional superspace. Phys. Rev. B - Condens. Matter Mater. Phys. 56, 13757-13767(1997).

5. Ma, Y., Hou, Y., Lu, C., Li, L. & Petrovic, C. Possible origin of nonlinear conductivity and large dielectric constant in the commensurate charge-density-wave phase of 1T-Ta$S_2$. Phys. Rev. B 97, 1-9 (2018).

6. Bittner, E., Nußbaumer, A. & Janke, W. Make life simple: Unleash the full power of the parallel tempering algorithm. Phys. Rev. Lett. 101, 1-4 (2008).

7. Hamze, F., Dickson, N. & Karimi, K. Robust Parameter Selection for Parallel Tempering. 21, 603-615 (2010).

8. Fiore, C. E. First-order phase transitions: A study through the parallel tempering method. Phys. Rev. E - Stat. Nonlinear, Soft Matter Phys. 78, 1-5 (2008).

9. Rossnagel, K. Suppression and emergence of charge-density waves at the surfaces of layered 1T-TiSe2and 1T-Ta$S_2$by in situ Rb deposition. New J. Phys. 12, (2010).

**References from 2D transition metal dichalcogenides by Manzeli, Ovchinnikov**

1. Radisavljevic, B., Radenovic, A., Brivio, J., Giacometti, V. & Kis, A. Single-layer $MoS_2$ transistors. Nat. Nanotechnol. 6, 147-150 (2011).

2. Splendiani, A. et al. Emerging photoluminescence in monolayer $MoS_2$. Nano Lett. 10, 1271-1275 (2010).

3. Mak, K. F., Lee, C., Hone, J., Shan, J. & Heinz, T. F. Atomically thin $MoS_2$ : a new direct-gap semiconductor. Phys. Rev. Lett. 105, 136805 (2010).

4. Dickinson, R. G. & Pauling, L. The crystal structure of molybdenite. J. Am. Chem. Soc. 45, 1466-1471 (1923).

5. Wilson, J. A. & Yoffe, A. D. The transition metal dichalcogenides discussion and interpretation of the observed optical, electrical and structural properties. Adv. Phys. 18, 193-335 (1969).

6. Frindt, R. F. & Yoffe, A. D. Physical properties of layer structures: optical properties and photoconductivity of thin crystals of molybdenum disulphide. Proc. R. Soc. A 273, 69-83 (1963).

7. Joensen, P., Frindt, R. F. & Morrison, S. R. Singlelayer $MoS_2$. Mater. Res. Bull. 21, 457-461 (1986).

8. Tenne, R., Margulis, L., Genut, M. & Hodes, G. Polyhedral and cylindrical structures of tungsten disulfide. Nature 360, 444-446 (1992).

9. Feldman, Y., Wasserman, E., Srolovitz, D. J. & Tenne, R. High-rate, gas-phase growth of $MoS_2$ nested inorganic fullerenes and nanotubes. Science 267, 222-225 (1995).

10. Koppens, F. H. L. et al. Photodetectors based on graphene, other two-dimensional materials and hybrid systems. Nat. Nanotechnol. 9, 780-793 (2014).

11. Xu, X., Yao, W., Xiao, D. & Heinz, T. F. Spin and pseudospins in layered transition metal dichalcogenides. Nat. Phys. 10, 343-350 (2014).

12. Mak, K. F. & Shan, J. Photonics and optoelectronics of 2D semiconductor transition metal dichalcogenides. Nat. Photonics 10, 216-226 (2016).

13. Hill, H. M., Rigosi, A. F., Rim, K. T., Flynn, G. W. & Heinz, T. F. Band alignment in $MoS_2/WS_2$ transition metal dichalcogenide heterostructures probed by scanning tunneling microscopy and spectroscopy. Nano Lett. 16, 4837-4837 (2016).

14. Zhu, Z. Y., Cheng, Y. C. & Schwingenschlögl, U. Giant spin-orbit-induced spin splitting in two-dimensional transition-metal dichalcogenide semiconductors. Phys. Rev. B 84, 153402 (2011).

15. Andor, K. et al. k.p theory for two-dimensional transition metal dichalcogenide semiconductors. 2D Mater. 2, 2053-1583 (2015).

16. Xiao, D., Liu, G.-B., Feng, W., Xu, X. & Yao, W. Coupled spin and valley physics in monolayers of $MoS_2$ and
other group-VI dichalcogenides. Phys. Rev. Lett. 108, 196802 (2012).

17. Pulkin, A. & Yazyev, O. V. Spin- and valley-polarized transport across line defects in monolayer $MoS_2$. Phys. Rev. B 93, 041419 (2016).

18. Habe, T. & Koshino, M. Spin-dependent refraction at the atomic step of transition-metal dichalcogenides. Phys. Rev. B 91, 201407 (2015).

19. Peierls, S. R. E. Quantum Theory of Solids (Clarendon Press, 1955).

20. Frohlich, H. On the theory of superconductivity: the one-dimensional case. Proc. R. Soc. A 223, 305 (1954).

21. Chan, S.-K. & Heine, V. Spin density wave and soft phonon mode from nesting Fermi surfaces. J. Phys. F Met. Phys. 3, 795-809 (1973).

22. Lomer, W. M. Electronic structure of chromium group metals. Proc. Phys. Soc. 80, 489-496 (1962).

23. Wilson, J. A., Di Salvo, F. J. & Mahajan, S. Chargedensity waves in metallic, layered, transition-metal dichalcogenides. Phys. Rev. Lett. 37, C4-139-C4-150 (1974).

24. Wilson, J. A., Di Salvo, F. J. & Mahajan, S. Chargedensity waves and superlattices in the metallic layered transition metal dichalcogenides. Adv. Phys. 50, 1171-1248 (2010).

25. Moncton, D. E., Axe, J. D. & Di Salvo, F. J. Neutron scattering study of the charge-density wave transitions in $2H - TaSe_2$ and $2H - NbSe_2$. Phys. Rev. B 16, 801-819 (1977).

26. Di Salvo, J., Francis, J. & Rice, T. M. Charge-density waves in transition-metal compounds. Phys. Today 32, 32-38 (1979).

27. Revolinsky, E., Spiering, G. A. & Beerntsen, D. J. Superconductivity in the niobium-selenium system. J. Phys. Chem. Solids 26, 1029-1034 (1965).

28. Perfetti, L., Gloor, T. A., Mila, F., Berger, H. & Grioni, M. Unexpected periodicity in the quasi-two-dimensional Mott insulator $1\ T - TaS_2$ revealed by angle-resolved photoemission. Phys. Rev. B 71, 153101 (2005).

29. Sipos, B. et al. From Mott state to superconductivity in 1T-$TaS_2$. Nat. Mater. 7, 960-965 (2008).

30. Calandra, M. 2D materials: charge density waves go nano. Nat. Nanotechnol. 10, 737-738 (2015).

31. Calandra, M., Mazin, I. I. & Mauri, F. Effect of dimensionality on the charge-density wave in few-layer $2H - NbSe_2$. Phys. Rev. B 80, 241108 (2009).

32. Xi, X. et al. Strongly enhanced charge-density-wave order in monolayer $NbSe_2$. Nat. Nanotechnol. 10, 765-769 (2015).

33. Ugeda, M. M. et al. Characterization of collective ground states in single-layer $NbSe_2$. Nat. Phys. 12, 92-97 (2016).

34. Ge, Y. & Liu, A. Y. Effect of dimensionality and spinorbit coupling on charge-density-wave transition in 2H-TaSe $_2$. Phys. Rev. B 86, 104101 (2012).

35. Yu, Y. et al. Gate-tunable phase transitions in thin flakes of 1T-TaS. Nat. Nanotechnol. 10, 270-276 (2015).

36. Hovden, R. et al. Atomic lattice disorder in charge-density-wave phases of exfoliated dichalcogenides (1T-TaS2). Proc. Natl Acad. Sci. USA 113, 11424 (2016).

37. Albertini, O. R. et al. Zone-center phonons of bulk, few-layer, and monolayer 1T- $TaS_2$ : detection of the commensurate charge density wave phase through Raman scattering. Phys. Rev. B 93, 214109 (2016).

38. Sugawara, K. et al. Unconventional charge-densitywave transition in monolayer 1T-TiSe $_2$. ACS Nano 10, 1341-1345 (2016).

39. Chen, P. et al. Dimensional effects on the charge density waves in ultrathin films of TiSe $_2$. Nano Lett. 16, 6331-6336 (2016).

40. Kohn, W. Excitonic phases. Phys. Rev. Lett. 19, 439-442 (1967).

41. Jérome, D., Rice, T. M. & Kohn, W. Excitonic insulator. Phys. Rev. 158, 462-475 (1967).

42. Guillamón, l. et al. Superconducting density of states and vortex cores of $2H - NbS_2$. Phys. Rev. Lett. 101, 166407 (2008).

43. Valla, T. et al. Charge-density-wave-induced modifications to the quasiparticle self-energy in 2H-TaSe $_2$. Phys. Rev. Lett. 85, 4759-4762 (2000).

44. Nagata, S. et al. Superconductivity in the layered compound $2H - TaS_2$. J. Phys. Chem. Solids 53, 1259-1263 (1992).

45. Freitas, D. C. et al. Strong enhancement of superconductivity at high pressures within the charge-density-wave states of $2H - TaS_2$ and $2H - TaSe_2$. Phys. Rev. B 93, 184512 (2016).

46. Kusmartseva, A. F., Sipos, B., Berger, H., Forró, L. & Tutiš, E. Pressure induced superconductivity in pristine 1T-TiSe $_2$. Phys. Rev. Lett. 103, 236401 (2009).

47. Morosan, E. et al. Superconductivity in $Cu_xTiSe_2$. Nat. Phys. 2, 544-550 (2006).

48. Wagner, K. E. et al. Tuning the charge density wave and superconductivity in $Cu_xTaS_2$. Phys. Rev. B 78, 104520 (2008).

49. Yang, J. J. et al. Charge-orbital density wave and superconductivity in the strong spin-orbit coupled IrTe $_2$ :Pd. Phys. Rev. Lett. 108, 116402 (2012).

50. Kosterlitz, J. M. & Thouless, D. J. Ordering, metastability and phase transitions in two-dimensional systems. J. Phys. C Solid State Phys. 6, 1181-1203 (1973).

51. Xi, X. et al. Ising pairing in superconducting $NbSe_2$ atomic layers. Nat. Phys. 12, 139-143 (2016).

52. Lu, J. M. et al. Evidence for two-dimensional Ising superconductivity in gated $MoS_2$. Science 350, 1353-1357 (2015).

53. He, W.-Y., Zhou, B. T., He, J. J., Zhang, T. & Law, K. T. Nodal topological superconductivity in monolayer $NbSe_2$. Preprint at ArXiv https://arxiv.org/ abs/1604.02867 (2016).

54. Sharma, G. & Tewari, S. Yu-Shiba-Rusinov states and topological superconductivity in Ising paired superconductors. Phys. Rev. B 94, 094515 (2016).

55. Zhou, B. T., Yuan, N. F. Q., Jiang, H.-L. & Law, K. T. Ising superconductivity and Majorana fermions in transition-metal dichalcogenides. Phys. Rev. B 93, 180501 (2016).

56. Ye, J. T. et al. Superconducting dome in a gate-tuned band insulator. Science 338, 1193-1196 (2012).

57. Costanzo, D., Jo, S., Berger, H. & Morpurgo, A. F. Gate-induced superconductivity in atomically thin $MoS_2$ crystals. Nat. Nanotechnol. 11, 339-344 (2016).

58. Shi, W. et al. Superconductivity series in transition metal dichalcogenides by ionic gating. Sci. Rep. 5, 12534 (2015).

59. Jo, S., Costanzo, D., Berger, H. & Morpurgo, A. F. Electrostatically induced superconductivity at the surface of $WS_2$. Nano Lett. 15, 1197-1202 (2015).

60. Hasan, M. Z. & Kane, C. L. Colloquium: topological insulators. Rev. Mod. Phys. 82, 3045-3067 (2010).

61. Qi, X.-L. & Zhang, S.-C. Topological insulators and superconductors. Rev. Mod. Phys. 83, 1057-1110 (2011).

62. Qian, X., Liu, J., Fu, L. & Li, J. Quantum spin Hall effect in two-dimensional transition metal dichalcogenides. Science 346, 1344-1347 (2014).

63. Bernevig, B. A., Hughes, T. L. & Zhang, S.-C. Quantum spin Hall effect and topological phase transition in HgTe quantum wells. Science 314, 1757-1761 (2006).

64. Konig, M. et al. Quantum spin Hall insulator state in HgTe quantum wells. Science 318, 766-770 (2007).

65. Knez, I., Du, R.-R. & Sullivan, G. Evidence for helical edge modes in inverted InAs/GaSb quantum wells. Phys. Rev. Lett. 107, 136603 (2011).
66. Sabater, C. et al. Topologically protected quantum transport in locally exfoliated bismuth at room temperature. Phys. Rev. Lett. 110, 176802 (2013).

66. Drozdov, I. K. et al. One-dimensional topological edge states of bismuth bilayers. Nat. Phys. 10, 664-669 (2014).

67. Ali, M. N. et al. Large, non-saturating magnetoresistance in $WTe_2$. Nature 514, 205-208 (2014).

68. Pletikosić, I., Ali, M. N., Fedorov, A. V., Cava, R. J. & Valla, T. Electronic structure basis for the extraordinary magnetoresistance in $WTe_2$. Phys. Rev. Lett. 113, 216601 (2014).

69. Soluyanov, A. A. et al. Type-II Weyl semimetals. Nature 527, 495-498 (2015).

70. Wang, Z. et al. $MoTe_2$ : a type-II Weyl topological metal. Phys. Rev. Lett. 117, 056805 (2016).

71. Sun, Y., Wu, S.-C., Ali, M. N., Felser, C. & Yan, B. Prediction of Weyl semimetal in orthorhombic $MoTe_2$. Phys. Rev. B 92, 161107 (2015).

72. Bruno, F. Y. et al. Observation of large topologically trivial Fermi arcs in the candidate type-II Weyl semimetal $WTe_2$. Phys. Rev. B 94, 121112 (2016).

73. Tamai, A. et al. Fermi arcs and their topological character in the candidate type-II Weyl semimetal $MoTe_2$. Phys. Rev. X 6, 031021 (2016).

74. Huang, Y.-Preparation, S. Electrical and modulation optical properties of $2H - MoSe_2$. Chin. J. Phys. 22, 43-53 (1984).

75. Schäfer, H. Chemical transport reactions. (Academic Press, 1964).

76. Benameur, M. M. et al. Visibility of dichalcogenide nanolayers. Nanotechnology 22, 125706 (2011).

77. Novoselov, K. S. et al. Two-dimensional atomic crystals. Proc. Natl Acad. Sci. USA 102, 10451-10453 (2005).

78. Coleman, J. N. et al. Two-dimensional nanosheets produced by liquid exfoliation of layered materials. Science 331, 568-571 (2011).

79. Nicolosi, V., Chhowalla, M., Kanatzidis, M. G., Strano, M. S. & Coleman, J. N. Liquid exfoliation of layered materials. Science 340, 1226419 (2013).

80. Dines, M. B. Lithium intercalation via $n$-Butyllithium of the layered transition metal dichalcogenides. Mater. Res. Bull. 10, 287-291 (1975).

81. Eda, G. et al. Photoluminescence from chemically exfoliated $MoS_2$. Nano Lett. 11, 5111-5116 (2011).

82. Zeng, Z. et al. Single-layer semiconducting nanosheets: high-yield preparation and device fabrication. Angew. Chem. Int. Ed. 50, 11093-11097 (2011).

83. Gordon, R. A., Yang, D., Crozier, E. D., Jiang, D. T. & Frindt, R. F. Structures of exfoliated single layers of $WS_2, MoS_2$, and $MoSe_2$ in aqueous suspension. Phys. Rev. B 65, 125407 (2002).

84. Kappera, R. et al. Phase-engineered low-resistance contacts for ultrathin $MoS_2$ transistors. Nat. Mater. 13, 1128-1134 (2014).

85. Joyce, B. A. Molecular beam epitaxy. Rep. Prog. Phys. 48, 1637-1697 (1985).

86. Koma, A. & Yoshimura, K. Ultrasharp interfaces grown with van der waals epitaxy. Surf. Sci. 174, 556-560 (1986).

87. Ohuchi, F. S., Shimada, T., Parkinson, B. A., Ueno, K. & Koma, A. Growth of $MoSe_2$ thin-films with Van der Waals epitaxy. J. Cryst. Growth 111, 1033-1037 (1991).

88. Ohuchi, F. S., Parkinson, B. A., Ueno, K. & Koma, A. Van der Waals epitaxial growth and characterization of $MoSe_2$ thin films on $SnS_2$. J. Appl. Phys. 68, 2168-2175 (1990).

89. Koma, A. Van der Waals epitaxy for highly latticemismatched systems. J. Cryst. Growth 201-202, 236-241 (1999).

90. Dumcenco, D. et al. Large-area epitaxial monolayer $MoS_2$. ACS Nano 9, 4611-4620 (2015).

91. Lehtinen, O. et al. Atomic scale microstructure and properties of Se-deficient two-dimensional $MoSe_2$. ACS Nano 9, 3274-3283 (2015).

92. Roy, A. et al. Structural and electrical properties of $MoTe_2$ and $MoSe_2$ grown by molecular beam epitaxy. ACS Appl. Mater. Interfaces 8, 7396-7402 (2016).

93. Ugeda, M. M. et al. Giant bandgap renormalization and excitonic effects in a monolayer transition metal dichalcogenide semiconductor. Nat. Mater. 13, 1091-1095 (2014).

94. Barja, S. et al. Charge density wave order in 1D mirror twin boundaries of single-layer $MoSe_2$. Nat. Phys. 12, 751-756 (2016).

95. Aretouli, K. E. et al. Epitaxial 2D $SnSe_2$/2D$WSe_2$ van der Waals heterostructures. ACS Appl. Mater. Interfaces 8, 23222-23229 (2016).

96. Xenogiannopoulou, E. et al. High-quality, large-area $MoSe_2$ and $MoSe_2/Bi_2Se_3$ heterostructures on AIN(0001)/Si(111) substrates by molecular beam epitaxy. Nanoscale 7, 7896-7905 (2015).

97. Vishwanath, S. et al. Comprehensive structural and optical characterization of MBE grown $MoSe_2$ on graphite, CaF2 and graphene. 2D Mater. 2, 024007 (2015).

98. Zhan, Y., Liu, Z., Najmaei, S., Ajayan, P. M. & Lou, J. Large-area vapor-phase growth and characterization of $MoS_2$ atomic layers on a $SiO_2$ substrate. Small 8, 966-971 (2012).

99. Liu, K.-K. et al. Growth of large-area and highly crystalline $MoS_2$ thin layers on insulating substrates. Nano Lett. 12, 1538-1544 (2012).

100. Shi, Y. et al. Van der Waals epitaxy of $MoS_2$ layers using graphene as growth templates. Nano Lett. 12, 2784-2791 (2012).

101. Lee, Y.-H. et al. Synthesis of large-area $MoS_2$ atomic layers with chemical vapor deposition. Adv. Mater. 24, 2320-2325 (2012).

102. Najmaei, S. et al. Vapor phase growth and grain boundary structure of molybdenum disulfide atomic layers. Nat. Mater. 12, 754-759 (2013).

103. van der Zande, A. M. et al. Grains and grain boundaries in highly crystalline monolayer molybdenum disulphide. Nat. Mater. 12, 554-561 (2013).

104. Zou, X., Liu, Y. & Yakobson, B. I. Predicting dislocations and grain boundaries in two-dimensional metaldisulfides from the first principles. Nano Lett. 13, 253-258 (2012).

105. Najmaei, S. et al. Electrical transport properties of polycrystalline monolayer molybdenum disulfide. ACS Nano 8, 7930-7937 (2014).

106. Chung, J.-W., Dai, Z. R. & Ohuchi, F. S. WS $_2$ thin films by metal organic chemical vapor deposition. J. Cryst. Growth 186, 137-150 (1998).

107. Dumcenco, D. et al. Large-area $MoS_2$ grown using $H_2$ S as the sulphur source. 2D Mater. 2, 044005 (2015).

108. Eichfeld, S. M. et al. Highly scalable, atomically thin $WSe_2$ grown via metal-organic chemical vapor deposition. ACS Nano 9, 2080-2087 (2015).

109. Kang, K. et al. High-mobility three-atom-thick semiconducting films with wafer-scale homogeneity. Nature 520, 656-660 (2015).

110. Wang, X. et al. Chemical vapor deposition growth of crystalline monolayer $MoSe_2$. ACS Nano 8, 5125-5131 (2014).

111. Xia, J. et al. CVD synthesis of large-area, highly crystalline $MoSe_2$ atomic layers on diverse substrates and application to photodetectors. Nanoscale 6, 8949-8955 (2014).

112. Chang, Y.-H. et al. Monolayer $MoSe_2$ grown by chemical vapor deposition for fast photodetection. ACS Nano 8, 8582-8590 (2014).

113. Gao, Y. et al. Large-area synthesis of high-quality and uniform monolayer $WS_2$ on reusable Au foils. Nat. Commun. 6, 8569 (2015).

114. Kobayashi, Y. et al. Growth and optical properties of high-quality monolayer $WS_2$ on graphite. ACS Nano 9, 4056-4063 (2015).

115. McCreary, K. M., Hanbicki, A. T., Jernigan, G. G., Culbertson, J. C. & Jonker, B. T. Synthesis of large-area $WS_2$ monolayers with exceptional photoluminescence. Sci. Rep. 6, 19159 (2016).

116. Okada, M. et al. Direct chemical vapor deposition growth of $WS_2$ atomic layers on hexagonal boron nitride. ACS Nano 8, 8273-8277 (2014).

117. Tan, H. et al. Ultrathin 2D photodetectors utilizing chemical vapor deposition grown $WS_2$ with graphene electrodes. ACS Nano 10, 7866-7873 (2016).

118. Tanabe, I. et al. Band structure characterization of $WS_2$ grown by chemical vapor deposition. Appl. Phys. Lett. 108, 252103 (2016).

119. Zhang, Y. et al. Controlled growth of high-quality monolayer $WS_2$ layers on sapphire and imaging its grain boundary. ACS Nano 7, 8963-8971 (2013).

120. Chen, J. et al. Chemical vapor deposition of large-sized hexagonal $WSe_2$ crystals on dielectric substrates. Adv. Mater. 27, 6722-6727 (2015).

121. Liu, B. et al. Chemical vapor deposition growth of monolayer $WSe_2$ with tunable device characteristics and growth mechanism study. ACS Nano 9, 6119-6127 (2015).

122. Yoshida, M. et al. Gate-optimized thermoelectric power factor in ultrathin $WSe_2$ single crystals. Nano Lett. 16, 2061-2065 (2016).

123. Keyshar, K. et al. Chemical vapor deposition of monolayer rhenium disulfide ($ReS_2$). Adv. Mater. 27, 4640-4648 (2015).

124. He, X. et al. Chemical vapor deposition of high-quality and atomically layered $ReS_2$. Small 11, 5423-5429 (2015).

125. Hafeez, M., Gan, L., Li, H., Ma, Y. & Zhai, T. Large-area bilayer $ReS_2$ film/multilayer $ReS_2$ flakes synthesized by chemical vapor deposition for high performance photodetectors. Adv. Funct. Mater. 26, 4551-4560 (2016).

126. Hafeez, M., Gan, L., Li, H., Ma, Y. & Zhai, T. Chemical vapor deposition synthesis of ultrathin hexagonal $ReSe_2$ flakes for anisotropic raman property and optoelectronic application. Adv. Mater. 28, 8296-8301 (2016).

127. Naylor, C. H. et al. Monolayer single-crystal 1 $T' - MoTe_2$ grown by chemical vapor deposition exhibits weak antilocalization effect. Nano Lett. 16, 4297-4304 (2016).

128. Zhou, J. et al. Large-area and high-quality 2D transition metal telluride. Adv. Mat. 29, 1603471 (2017).

129. Duan, X. et al. Lateral epitaxial growth of twodimensional layered semiconductor heterojunctions. Nat. Nanotechnol. 9, 1024-1030 (2014).

130. Huang, C. et al. Lateral heterojunctions within monolayer $MoSe_2 - WSe_2$ semiconductors. Nat. Mater. 13, 1096-1101 (2014).

131. Gong, Y. et al. Vertical and in-plane heterostructures from $WS_2/MoS_2$ monolayers. Nat. Mater. 13, 1135-1142 (2014).

132. Li, M.-Y. et al. Epitaxial growth of a monolayer $WSe_2 - MoS_2$ lateral $p - n$ junction with an atomically sharp interface. Science 349, 524-528 (2015).

133. Yu, H., Kutana, A. & Yakobson, B. I. Carrier delocalization in two-dimensional coplanar $p - n$ junctions of graphene and metal dichalcogenides. Nano Lett. 16, 5032-5036 (2016).

134. Kaasbjerg, K., Thygesen, K. S. & Jacobsen, K. W. Phonon-limited mobility in n-type single-layer $MoS_2$ from first principles. Phys. Rev. B 85, 115317 (2012).

135. Kaasbjerg, K., Thygesen, K. S. & Jauho, A.-P. Acoustic phonon limited mobility in two-dimensional semiconductors: deformation potential and piezoelectric scattering in monolayer $MoS_2$ from first principles. Phys. Rev. B 87, 235312 (2013).

136. Zhang, W., Huang, Z., Zhang, W. & Li, Y. Twodimensional semiconductors with possible high room temperature mobility. Nano Res. 7, 1731-1737 (2014).

137. Li, X. et al. Intrinsic electrical transport properties of monolayer silicene and $MoS_2$ from first principles. Phys. Rev. B 87, 115418 (2013).

138. Ma, N. & Jena, D. Charge scattering and mobility in atomically thin semiconductors. Phys. Rev. X4, 011043 (2014).

139. Fivaz, R. & Mooser, E. Mobility of charge carriers in semiconducting layer structures. Phys. Rev. 163, 743-755 (1967).

140. Radisavljevic, B. & Kis, A. Mobility engineering and a metal-insulator transition in monolayer $MoS_2$. Nat. Mater. 12, 815-820 (2013).

141. Baugher, B. W. H., Churchill, H. O. H., Yang, Y. & Jarillo-Herrero, P. Intrinsic electronic transport properties of high-quality monolayer and bilayer $MoS_2$. Nano Lett. 13, 4212-4216 (2013).

142. Yu, Z. et al. Realization of room-temperature phononlimited carrier transport in monolayer $MoS_2$ by dielectric and carrier screening. Adv. Mater. 28, 547-552 (2016).

143. Chamlagain, B. et al. Mobility improvement and temperature dependence in $MoSe_2$ field-effect transistors on parylene-c substrate. ACS Nano 8, 5079-5088 (2014).

144. Cui, X. et al. Multi-terminal transport measurements of $MoS_2$ using a van der Waals heterostructure device platform. Nat. Nanotechnol. 10, 534-540 (2015).

145. Bertolazzi, S., Krasnozhon, D. & Kis, A. Nonvolatile memory cells based on $MoS_2$/graphene heterostructures. ACS Nano 7, 3246-3252 (2013).

146. Iqbal, M. W. et al. High-mobility and air-stable singlelayer $WS_2$ field-effect transistors sandwiched between chemical vapor deposition-grown hexagonal BN films. Sci. Rep. 5, 10699 (2015).

147. Xu, S. et al. Universal low-temperature Ohmic contacts for quantum transport in transition metal dichalcogenides. 2D Mater. 3, 021007 (2016).

148. Ovchinnikov, D., Allain, A., Huang, Y.-S., Dumcenco, D. & Kis, A. Electrical transport properties of single-layer $WS_2$. ACS Nano 8, 8174-8181 (2014).

149. Fallahazad, B. et al. Shubnikov-de Haas oscillations of high-mobility holes in monolayer and bilayer $WSe_2$ : Landau level degeneracy, effective mass, and negative compressibility. Phys. Rev. Lett. 116, 086601 (2016).

150. Schwierz, F. Graphene transistors. Nat. Nanotechnol. 5, 487-496 (2010).

151. Wu, Y. et al. State-of-the-art graphene high-frequency electronics. Nano Lett. 12, 3062-3067(2012).

152. Yoon, Y., Ganapathi, K. & Salahuddin, S. How good can monolayer $MoS_2$ transistors be? Nano Lett. 11, 3768-3773 (2011).

153. Krasnozhon, D., Lembke, D., Nyffeler, C., Leblebici, Y. &Kis, A.$MoS_2$ transistors operating at gigahertz frequencies. Nano Lett. 14, 5905-5911 (2014).

154. Krasnozhon, D., Dutta, S., Nyffeler, C., Leblebici, Y. & Kis, A. High-frequency, scaled $MoS_2$ transistors. IEEE Int. Electron Devices Meet. http://dx.doi.org/10.1109/ IEDM. 2015.7409781 (2015).

155. Cheng, R. et al. Few-layer molybdenum disulfide transistors and circuits for high-speed flexible electronics. Nat. Commun. 5, 5143 (2014).

156. Chang, H.-Y. et al. Large-area monolayer $MoS_2$ for flexible low-power RF nanoelectronics in the GHz regime. Adv. Mater. 28, 1818-1823 (2015).

157. Sun, L. et al. $12-$GHz thin-film transistors on transferrable silicon nanomembranes for highperformance flexible electronics. Small 6, 2553-2557 (2010).

158. Wang, C. et al. Self-aligned, extremely high frequency III-V metal-oxide-semiconductor field-effect transistors on rigid and flexible substrates. Nano Lett. 12, 4140-4145 (2012).

159. Bertolazzi, S., Brivio, J. & Kis, A. Stretching and breaking of ultrathin $MoS_2$. ACS Nano 5, 9703-9709 (2011).

160. Ni, Z. H. et al. Uniaxial strain on graphene: raman spectroscopy study and band-gap opening. ACS Nano 2, 2301-2305 (2008).

161. Pereira, V. M., Castro Neto, A. H. & Peres, N. M. R. Tight-binding approach to uniaxial strain in graphene. Phys. Rev. B 80, 045401 (2009).

162. Johari, P. & Shenoy, V. B. Tuning the electronic properties of semiconducting transition metal dichalcogenides by applying mechanical strains. ACS Nano 6, 5449-5456 (2012).

163. Yue, Q. et al. Mechanical and electronic properties of monolayer $MoS_2$ under elastic strain. Phys. Lett. A 376, 1166-1170 (2012).

164. Shi, H., Pan, H., Zhang, Y.-W. & Yakobson, B. I. Quasiparticle band structures and optical properties of strained monolayer $MoS_2$ and $WS_2$. Phys. Rev. B 87, 155304 (2013).

165. Dong, L., Namburu, R. R., O'Regan, T. P., Dubey, M. & Dongare, A. M. Theoretical study on strain-induced variations in electronic properties of monolayer $MoS_2$. J. Mater. Sci. 49, 6762-6771 (2014).

166. Ghorbani-Asl, M., Borini, S., Kuc, A. & Heine, T. Straindependent modulation of conductivity in single-layer transition-metal dichalcogenides. Phys. Rev. B 87, 235434 (2013).

167. Harada, N., Sato, S. & Yokoyama, N. Computational study on electrical properties of transition metal dichalcogenide field-effect transistors with strained channel. J. Appl. Phys. 115, 034505 (2014).

168. Horzum, S. et al. Phonon softening and direct to indirect band gap crossover in strained single-layer $MoSe_2$. Phys. Rev. B 87, 125415 (2013).

169. Lu, P., Wu, X., Guo, W. & Zeng, X. C. Strain-dependent electronic and magnetic properties of $MoS_2$ monolayer, bilayer, nanoribbons and nanotubes. Phys. Chem. Chem. Phys. 14, 13035-13040 (2012).

170. Scalise, E., Houssa, M., Pourtois, G., Afanas'ev, V. V. & Stesmans, A. First-principles study of strained 2D $MoS_2$. Phys. E 56, 416-421 (2014).

171. Wang, L., Kutana, A. & Yakobson, B. I. Many-body and spin-orbit effects on direct-indirect band gap transition of strained monolayer $MoS_2$ and $WS_2$ : direct-indirect band gap transition in strained monolayer $MoS_2$ and $WS_2$. Ann. Phys. 526, L7-L12 (2014).

172. Kumar, A. & Ahluwalia, P. K. Mechanical strain dependent electronic and dielectric properties of twodimensional honeycomb structures of $MoX_2(X = S, Se, Te)$. Phys. B (Amsterdam, Neth.) 419, 66-75 (2013).

173. Bhattacharyya, S., Pandey, T. & Singh, A. K. Effect of strain on electronic and thermoelectric properties of few layers to bulk $MoS_2$. Nanotechnology 25, 465701 (2014).

174. Zhu, L. et al. Thermal conductivity of biaxial-strained $MoS_2$ : sensitive strain dependence and size-dependent reduction rate. Nanotechnology 26, 465707 (2015).

175. Rostami, H., Roldán, R., Cappelluti, E., Asgari, R. & Guinea, F. Theory of strain in single-layer transition metal dichalcogenides. Phys. Rev. B 92, 195402 (2015).

176. Cheiwchanchamnangij, T., Lambrecht, W. R. L., Song, Y. & Dery, H. Strain effects on the spin-orbitinduced band structure splittings in monolayer $MoS_2$ and graphene. Phys. Rev. B 88, 155404 (2013).

177. Koskinen, P., Fampiou, I. & Ramasubramaniam, A. Density-functional tight-binding simulations of curvature-controlled layer decoupling and band-gap tuning in bilayer $MoS_2$. Phys. Rev. Lett. 112, 186802 (2014).

178. Sengupta, A., Ghosh, R. K. & Mahapatra, S. Performance analysis of strained monolayer $MoS_2$ MOSFET. IEEE Trans. Electron. Devices 60, 2782-2787 (2013).

179. Mohammad Tabatabaei, S., Noei, M., Khaliji, K., Pourfath, M. & Fathipour, M. A first-principles study on the effect of biaxial strain on the ultimate performance of monolayer $MoS_2$-based double gate field effect transistor. J. Appl. Phys. 113, 163708 (2013).

180. Feng, J., Qian, X., Huang, C.-W. & Li, J. Strainengineered artificial atom as a broad-spectrum solar energy funnel. Nat. Photonics 6, 866-872 (2012).

181. Kumar, H., Er, D., Dong, L., Li, J. & Shenoy, V. B. Elastic deformations in 2D van der waals heterostructures and their impact on optoelectronic properties: predictions from a multiscale computational approach. Sci. Rep. 5, 10872 (2015).

182. Sharma, M., Kumar, A., Ahluwalia, P. K. & Pandey, R. Strain and electric field induced electronic properties of two-dimensional hybrid bilayers of transition-metal dichalcogenides. J. Appl. Phys. 116, 063711 (2014).

183. Yu, S. et al. Strain-engineering the anisotropic electrical conductance in $ReS_2$ monolayer. Appl. Phys. Lett. 108, 191901 (2016).

184. Manzeli, S., Allain, A., Ghadimi, A. & Kis, A. Piezoresistivity and strain-induced band gap tuning in atomically thin $MoS_2$. Nano Lett. 15, 5330-5335 (2015).

185. Zhu, H. et al. Observation of piezoelectricity in freestanding monolayer $MoS_2$. Nat. Nanotechnol. 10, 151-155 (2015).

186. Lloyd, D. et al. Band gap engineering with ultralarge biaxial strains in suspended monolayer $MoS_2$. Nano Lett. 16, 5836-5841 (2016).

187. Li, H. et al. Optoelectronic crystal of artificial atoms in strain-textured molybdenum disulphide. Nat. Commun. 6, 7381 (2015).

188. Conley, H. J. et al. Bandgap engineering of strained monolayer and bilayer $MoS_2$. Nano Lett. 13, 3626-3630 (2013).

189. He, K., Poole, C., Mak, K. F. & Shan, J. Experimental demonstration of continuous electronic structure tuning via strain in atomically thin $MoS_2$. Nano Lett. 13, 2931-2936 (2013).

190. Zhu, C. R. et al. Strain tuning of optical emission energy and polarization in monolayer and bilayer $MoS_2$. Phys. Rev. B 88, 121301 (2013).

191. Castellanos-Gomez, A. et al. Local strain engineering in atomically thin $MoS_2$. Nano Lett. 13, 5361-5366 (2013).

192. Plechinger, G. et al. Control of biaxial strain in singlelayer molybdenite using local thermal expansion of the substrate. 2D Mater. 2, 015006 (2015).

193. Hui, Y. Y. et al. Exceptional tunability of band energy in a compressively strained trilayer $MoS_2$ sheet. ACS Nano 7, 7126-7131 (2013).

194. Liu, Z. et al. Strain and structure heterogeneity in $MoS_2$ atomic layers grown by chemical vapour deposition. Nat. Commun. 5, 5246 (2014).

195. Rice, C. et al. Raman-scattering measurements and first-principles calculations of strain-induced phonon shifts in monolayer $MoS_2$. Phys. Rev. B 87, 081307 (2013).

196. Desai, S. B. et al. Strain-induced indirect to direct bandgap transition in multilayer $WSe_2$. Nano Lett. 14, 4592-4597 (2014).

197. Island, J. O. et al. Precise and reversible band gap tuning in single-layer $MoSe_2$ by uniaxial strain. Nanoscale 8, 2589-2593 (2016).

198. Duerloo, K.-A. N., Ong, M. T. & Reed, E. J. Intrinsic piezoelectricity in two-dimensional materials. J. Phys. Chem. Lett. 3, 2871-2876 (2012).

199. Blonsky, M. N., Zhuang, H. L., Singh, A. K. & Hennig, R. G. Ab-initio prediction of piezoelectricity in two-dimensional materials. ACS Nano 9, 9885-9891 (2015).

200. Wu, W. et al. Piezoelectricity of single-atomic-layer $MoS_2$ for energy conversion and piezotronics. Nature 514, 470-474 (2014).

201. Kanda, Y. Piezoresistance effect of silicon. Sens. Actuators Phys. 28, 83-91 (1991).

202. Smith, A. D. et al. Electromechanical piezoresistive sensing in suspended graphene membranes. Nano Lett. 13, 3237-3242 (2013).

203. Huang, M., Pascal, T. A., Kim, H., Goddard, W. A. & Greer, J. R. Electronic-mechanical coupling in graphene from in situ nanoindentation experiments and multiscale atomistic simulations. Nano Lett. 11, 1241-1246 (2011).

204. Petersen, K. E. Silicon as a mechanical material. Proc. IEEE 70, 420-457 (1982).

205. Solomon, P. M. et al. Pathway to the piezoelectronic transduction logic device. Nano Lett. 15, 2391-2395 (2015).

206. Newns, D., Elmegreen, B., Liu, X. H. & Martyna, G. A low-voltage high-speed electronic switch based on piezoelectric transduction. J. Appl. Phys. 111, 084509 (2012).

207. Wu, W. et al. Piezophototronic effect in single-atomiclayer $MoS_2$ for strain-gated flexible optoelectronics. Adv. Mater. 28, 8463-8468 (2016).

208. Pu, J. et al. Highly flexible $MoS_2$ thin-film transistors with ion gel dielectrics. Nano Lett. 12, 4013-4017 (2012).

209. Chang, H.-Y. et al. High-performance, highly bendable $MoS_2$ transistors with high-K dielectrics for flexible low-power systems. ACS Nano 7, 5446-5452 (2013).

210. Lee, G.-H. et al. Flexible and transparent $MoS_2$ fieldeffect transistors on hexagonal boron nitride-graphene heterostructures. ACS Nano 7, 7931-7936 (2013).

211. Akinwande, D., Petrone, N. & Hone, J. Twodimensional flexible nanoelectronics. Nat. Commun. 5, 5678 (2014).

212. Yoon, J. et al. Highly flexible and transparent multilayer $MoS_2$ transistors with graphene electrodes. Small 9, 3295-3300 (2013).

213. Pu, J. et al. Fabrication of stretchable $MoS_2$ thin-film transistors using elastic ion-gel gate dielectrics. Appl. Phys. Lett. 103, 023505 (2013).

214. Shen, T., Penumatcha, A. V. & Appenzeller, J. Strain engineering for transition metal dichalcogenides based field effect transistors. ACS Nano 10, 4712-4718 (2016).

215. Tsai, M.-Y. et al. Flexible $MoS_2$ field-effect transistors for gate-tunable piezoresistive strain sensors. ACS Appl. Mater. Interfaces 7, 12850-12855 (2015).

216. Pu, J. et al. Highly flexible and high-performance complementary inverters of large-area transition metal dichalcogenide monolayers. Adv. Mater. 28, 4111-4119 (2016).

217. Feng, J. et al. Identification of single nucleotides in $MoS_2$ nanopores. Nat. Nanotechnol. 10, 1070-1076 (2015).

218. Feng, J. et al. Electrochemical reaction in single layer $MoS_2$ : nanopores opened atom by atom. Nano Lett. 15, 3431-3438 (2015).

219. Schmidt, H. et al. Transport properties of monolayer $MoS_2$ grown by chemical vapor deposition. Nano Lett. 14, 1909-1913 (2014).

**References from On the origin of charge-density waves in select layered transition-metal dichalcogenides by Rossnagel**

[1] Peierls R E 1955 Quantum Theory of Solids (Oxford: Clarendon) pp 108-12
Peierls R E 1991 More Surprises in Theoretical Physics (Princeton, NJ: Princeton University Press) pp 27-30
[2] Fröhlich H 1954 Proc. R. Soc. A 233296
[3] Overhauser A W 1968 Phys. Rev. 167691
Overhauser A W 1971 Phys. Rev. B 33173
Overhauser A W 1978 Adv. Phys. 27353
[4] Kohn W 1968 Many Body Physics ed C DeWitt and R Balian (New York: Gordon and Breach) p 353
[5] Halperin B I and Rice T M 1968 Solid State Phys. 21115 Halperin B I and Rice T M 1968 Rev. Mod. Phys. 40755
[6] Chan S-K and Heine V 1973 J. Phys. F: Met. Phys. 3795
[7] Tosatti E 1975 Festkörperprobleme (Advances in Solid State Physics vol 15) ed H J Queisser (Braunschweig: Vieweg) p 113
[8] Friedel J 1977 Electron-Phonon Interactions and Phase Transitions ed T Riste (New York: Plenum) p 1
[9] Morosan E, Zandbergen H W, Dennis B S, Bos J W G, Onose Y, Klimczuk T, Ramirez A P, Ong N P and Cava R J 2006 Nature Phys. 2544
[10] Kiss T, Yokoya T, Chainani A, Shin S, Hanaguri T, Nohara M and Takagi H 2007 Nature Phys. 3720
[11] Cercellier H et al 2007 Phys. Rev. Lett. 99146403
[12] Sipos B, Kusmartseva A F, Akrap A, Berger H, Forró L and Tutiš E 2008 Nat. Mater. 7960
[13] Johannes M D and Mazin I I 2008 Phys. Rev. B 77165135
[14] Schmitt F et al 2008 Science 3211649
[15] Yusupov R, Mertelj T, Kabanov V V, Brazovskii S, Kusar P, Chu J-H, Fisher I R and Mihailovic D 2010 Nature Phys. 6681
[16] Hellmann S et al 2010 Phys. Rev. Lett. 105187401
[17] Eichberger M, Schäfer H, Krumova M, Beyer M, Demsar J, Berger H, Moriena G, Sciaini G and Miller R J D 2010 Nature 468799
[18] Wilson J A, Di Salvo F J and Mahajan S 1975 Adv. Phys. 24117
[19] Friend R H and Jérome D 1979 J. Phys. C: Solid State Phys. 121441
[20] Di Salvo F J and Rice T M 1979 Phys. Today 3232
[21] Klipstein P C, Friend R H and Yoffe A D 1985 Phil. Mag. B 52611
[22] Withers R L and Wilson J A 1986 J. Phys. C: Solid State Phys. 194809
[23] Motizuki K (ed) 1986 Structural Phase Transitions in Layered Transition Metal Compounds (Dordrecht: Reidel)
[24] Whangbo M-H and Canadell E 1992 J. Am. Chem. Soc. 1149587
[25] Grüner G 2000 Density Waves in Solids (Cambridge, MA: Perseus)
[26] Brouet V, Yang W L, Zhou X J, Hussain Z, Ru N, Shin K Y, Fisher I R and Shen Z X 2004 Phys. Rev. Lett. 93126405
[27] Brouet V et al 2008 Phys. Rev. B 77235104
[28] Grüner G 1988 Rev. Mod. Phys. 601129
[29] Gabovich A M, Voitenko A I and Ausloos M 2002 Phys. Rep. 367583
[30] Aruga T 2002 J. Phys.: Condens. Matter 148393
[31] Littlewood P B 1983 Crit. Rev. Solid State Mater. Sci. 11229
[32] Fawcett E 1988 Rev. Mod. Phys. 60209
[33] Altmann S L 1994 Band Theory of Solids: An Introduction from the Point of View of

Symmetry (Oxford: Clarendon) chapter 12
[34] Rice M J and Strässler S 1973 Solid State Commun. 13125
[35] Allender D, Bray J W and Bardeen J 1974 Phys. Rev. B 9119
[36] Littlewood P B and Heine V 1981 J. Phys. C: Solid State Phys. 142943
[37] Tosatti E 1995 Electronic Surface and Interface States on Metallic Systems ed E Berthel and M Donath (Singapore: World Scientific) p 67
[38] Tosatti E 1980 Modern Trends in the Theory of Condensed Matter ed A Pekalski and J Przystawa (Berlin: Springer) p 501
[39] McMillan W L 1977 Phys. Rev. B 16643
Riste T (ed) 1977 Electron-Phonon Interactions and Phase Transitions (New York: Plenum) p 142
[40] Haas C 1978 Solid State Commun. 26709
[41] Inglesfield J E 1980 Physica B 99238
[42] Huntley D J, DiSalvo F J and Rice T M 1978 J. Phys. C: Solid State Phys. 11 L767
[43] Fehlner W R and Loly P D 1974 Solid State Commun. 14653
[44] Rice T M and Scott G K 1975 Phys. Rev. Lett. 35120
[45] Myron H W, Rath J and Freeman A J 1977 Phys. Rev. B 15885
[46] Doran N J, Riccó B, Schreiber M, Titterington D and Wexler G 1978 J. Phys. C: Solid State Phys. 11699
[47] Yoshida Y and Motizuki K 1980 J. Phys. Soc. Japan 49898
[48] Motizuki K and Ando E 1983 J. Phys. Soc. Japan 522849
[49] Doran N J, Wexler G, Heine V and Ricco B 1977 Nuovo Cimento B 38544
[50] Varma C M and Weber W 1977 Phys. Rev. Lett. 391049
[51] Yoshida Y and Motizuki K 1982 J. Phys. Soc. Japan 512107
[52] Doran N J 1978 J. Phys. C: Solid State Phys. 11 L959
[53] Rice M J and Gartstein Y N 2005 J. Phys.: Condens. Matter 174615
[54] Neuenschwander J and Wachter P 1990 Phys. Rev. B 4112693
[55] Gaby J H, DeLong B, Brown F C, Kirby R D and Lévy F 1981 Solid State Commun. 391167
[56] Wilson J A, Di Salvo F J and Mahajan S 1974 Phys. Rev. Lett. 32882
[57] Dai Z, Xue Q, Gong Y, Slough C G and Coleman R V 1993 Phys. Rev. B 4814543
[58] Tatlock G J 1976 Commun. Phys. 187
[59] Bayliss S C, Ghorayeb A M and Guy D R P 1984 J. Phys. C: Solid State Phys. 17 L533
[60] DiSalvo F J, Moncton D E, Wilson J A and Mahajan S 1976 Phys. Rev. B 141543
[61] Scruby C B, Williams P M and Parry G S 1975 Phil. Mag. 31255
[62] Brouwer R and Jellinek F 1980 Physica B 9951
[63] Spijkerman A, de Boer J L, Meetsma A, Wiegers G A and van Smaalen S 1997 Phys. Rev. B 5613757
[64] Fung K K, Steeds J W and Eades J A 1980 Physica B +C 9947
[65] Tanda S, Sambongi T, Tani T and Tanaka S 1984 J. Phys. Soc. Japan 53476
[66] Nakanishi K and Shiba H 1984 J. Phys. Soc. Japan 531103
[67] Fazekas P and Tosatti E 1979 Phil. Mag. B 39229
Fazekas P and Tosatti E 1980 Physica B 99183
[68] Dardel B, Grioni M, Malterre D, Weibel P, Baer Y and Lévy F 1992 Phys. Rev. B 451462
Dardel B, Grioni M, Malterre D, Weibel P, Baer Y and Lévy F 1992 Phys. Rev. B 467407
[69] Moncton D E, Axe J D and DiSalvo F J 1977 Phys. Rev. B 16801
[70] Fleming R M, Moncton D E, McWhan D B and DiSalvo F J 1980 Phys. Rev. Lett. 45576
[71] DiSalvo F J, Moncton D E and Waszczak J V 1976 Phys. Rev. B 144321
[72] McMillan W L 1975 Phys. Rev. B 121187
McMillan W L 1976 Phys. Rev. B 141496

Riste T (ed) 1977 Electron-Phonon Interactions and Phase Transitions (New York: Plenum) p 137
[73] Nakanishi K and Shiba H 1977 J. Phys. Soc. Japan 431839 Nakanishi K and Shiba H 1978 J. Phys. Soc. Japan 441465 Shiba H and Nakanishi K 1986 Structural Phase Transitions in Layered Transition Metal Compounds ed K Motizuki (Dordrecht: Reidel) p 175
[74] Withers R L and Bursill L A 1982 Phys. Rev. B 261469
[75] Smith N V, Kevan S D and DiSalvo F J 1985 J. Phys. C: Solid State Phys. 183175
[76] Enomoto H, Ozaki H, Suzuki M, Fujii T and Yamaguchi M 1991 J. Vac. Sci. Technol. B 91022
[77] Pillo Th, Hayoz J, Naumović D, Berger H, Perfetti L, Gavioli L, Taleb-Ibrahimi A, Schlapbach L and Aebi P 2001 Phys. Rev. B 64245105
[78] Gasparov L V, Brown K G, Wint A C, Tanner D B, Berger H, Margaritondo G, Gaál R and Forró L 2002 Phys. Rev. B 66094301
[79] Aiura Y et al 2004 Phys. Rev. B 69245123
[80] Wang C, Giambattista B, Slough C G, Coleman R V and Subramanian M A 1990 Phys. Rev. B 428890
[81] Liu R, Olson C G, Tonjes W C and Frindt R F 1998 Phys. Rev. Lett. 805762
[82] Liu R, Tonjes W C, Greanya V A, Olson C G and Frindt R F 2000 Phys. Rev. B **615212**
[83] Demsar J, Forró L, Berger H and Mihailovic D 2002 Phys. Rev. B 66 041101(R)
[84] Rossnagel K, Rotenberg E, Koh H, Smith N V and Kipp L 2005 Phys. Rev. B 72 121103(R)
[85] Borisenko S V et al 2008 Phys. Rev. Lett. 100196402
[86] Rossnagel K, Kipp L and Skibowski M 2001 Phys. Rev. B 65235101
[87] Kidd T E, Miller T, Chou M Y and Chiang T-C 2002 Phys. Rev. Lett. 88226402
[88] Qian D, Hsieh D, Wray L, Morosan E, Wang N L, Xia Y, Cava R J and Hasan M Z 2007 Phys. Rev. Lett. 98117007
[89] Zhao J F et al 2007 Phys. Rev. Lett. 99146401
[90] Machida Y, Hanashima T, Ohkubo K, Yamawaki K, Tanaka M and Sasaki S 2004 J. Phys. Soc. Japan 733064
[91] Holt M, Zschack P, Hong H, Chou M Y and Chiang T-C 2001 Phys. Rev. Lett. 863799
[92] Bovet M, van Smaalen S, Berger H, Gaal R, Forró L, Schlapbach L and Aebi P 2003 Phys. Rev. B 67125105
[93] Krasovskii E E 2007 private communication
[94] Reshak A H and Auluck S 2005 Physica B 358158
[95] Reshak A H and Auluck S 2003 Phys. Rev. B 68245113
[96] Shiino O et al 2000 Physica B 284-288 1673
[97] Harper J M E, Geballe T H and DiSalvo F J 1977 Phys. Rev. B 152943
[98] Craven R A, Di Salvo F J and Hsu F S L 1978 Solid State Commun. 2539
[99] Ruzicka B, Degiorgi L, Berger H, Gaál R and Forró L 2001 Phys. Rev. Lett. 864136
[100] Hambourger P D and Di Salvo F J 1980 Physica B 99173
[101] Lieth R M A and Terhell J C J M 1977 Preparation and Crystal Growth of Materials with Layered Structures ed R M A Lieth (Dordrecht: Reidel) p 141
[102] Ashcroft N W and Mermin N D 1976 Solid State Physics (Fort Worth: Saunders)
[103] Naito M and Tanaka S 1982 J. Phys. Soc. Japan 51219
[104] Zwick F, Berger H, Vobornik I, Margaritondo G, Forró L, Beeli C, Onellion M, Panaccione G, Taleb-Ibrahimi A and Grioni M 1998 Phys. Rev. Lett. 811058
[105] Pillo T, Hayoz J, Berger H, Grioni M, Schlapbach L and Aebi P 1999 Phys. Rev. Lett. 833494
[106] Pillo Th, Hayoz J, Berger H, Fasel R, Schlapbach L and Aebi P 2000 Phys. Rev. B 624277
[107] Aebi P, Pillo T, Berger H and Lévy F 2001 J. Electron Spectrosc. Relat. Phenom.

117/118 433
[108] Bovet M, Popović D, Clerc F, Koitzsch C, Probst U, Bucher E, Berger H, Naumović D and Aebi P 2004 Phys. Rev. B 69125117
[109] Arita M et al 2004 Physica B 351265
[110] Perfetti L, Gloor T A, Mila F, Berger H and Grioni M 2005 Phys. Rev. B 71153101
[111] Clerc F, Battaglia C, Bovet M, Despont L, Monney C, Cercellier H, Garnier M G and Aebi P 2006 Phys. Rev. B 74155114
[112] Clerc F, Battaglia C, Cercellier H, Monney C, Berger H, Despont L, Garnier M G and Aebi P 2007 J. Phys.: Condens. Matter 19355002
[113] Inosov D S, Zabolotnyy V B, Evtushinsky D V, Kordyuk A A, Büchner B, Follath R, Berger H and Borisenko S V 2008 New J. Phys. 10125027
[114] Inosov D S, Evtushinsky D V, Zabolotnyy V B, Kordyuk A A, Büchner B, Follath R, Berger H and Borisenko S V 2009 Phys. Rev. B 79125112
[115] Pillo Th, Hayoz J, Berger H, Lévy F, Schlapbach L and Aebi P 2000 Phys. Rev. B **61**16213
[116] Rasch J C E, Stemmler T, Müller B, Dudy L and Manzke R 2008 Phys. Rev. Lett. 101237602
[117] Mattheiss L F 1973 Phys. Rev. B 83719
[118] Rossnagel K and Smith N V 2006 Phys. Rev. B 73073106
[119] Rossnagel K and Smith N V 2007 Phys. Rev. B 76073102
[120] Barnett R L, Polkovnikov A, Demler E, Yin W-G and Ku W 2006 Phys. Rev. Lett. 96026406
[121] Abate E and Asdente M 1965 Phys. Rev. 140 A1303
[122] Herman F and Skillman S 1963 Atomic Structure Calculations (Englewood Cliffs, NJ: Prentice-Hall)
[123] Harrison W A 2004 Elementary Electronic Structure revised edn (Singapore: World Scientific)
[124] Voit J, Perfetti L, Zwick F, Berger H, Margaritondo G, Grüner G, Höchst H and Grioni M 2000 Science 290501
[125] Grioni M, Ast C R, Pacilé D, Papagno M, Berger H and Perfetti L 2005 New J. Phys. 7106
[126] Doran N J and Woolley A M 1981 J. Phys. C: Solid State Phys. 144257
[127] Anderson O, Manzke R and Skibowski M 1985 Phys. Rev. Lett. 552188
[128] van Wezel J, Nahai-Williamson P and Saxena S S 2010 Phys. Rev. B 81165109
[129] van Wezel J, Nahai-Williamson P and Saxena S S 2010 Europhys. Lett. 8947004
[130] van Wezel J, Nahai-Williamson P and Saxena S S 2010 Phys. Status Solidi b 247592
[131] Thompson A H 1976 Comm. Solid State Phys. 7125
[132] Di Salvo F J 1977 Electron-Phonon Interactions and Phase Transitions ed T Riste (New York: Plenum) p 107
[133] Wertheim G K, Di Salvo F J and Chiang S 1976 Phys. Rev. B 135476
[134] Coleman R V, Giambattista B, Hansma P K, Johnson A, McNairy W W and Slough C G 1988 Adv. Phys. 37559
[135] Hughes H P 1977 J. Phys. C: Solid State Phys. 10 L319
[136] Suzuki N, Yamamoto A and Motizuki K 1984 Solid State Commun. 491039
[137] Wilson J A and Mahajan S 1977 Commun. Phys. 223
[138] Wilson J A 1977 Solid State Commun. 22551 Wilson J A 1978 Phys. Status Solidi b 8611
[139] Monney C et al 2009 Phys. Rev. B 79045116
[140] Monney C et al 2010 Phys. Rev. B 81155104
[141] McMillan W C 1968 Phys. Rev. 167331
[142] Inglesfield J E 1980 J. Phys. C: Solid State Phys. 1317

**References from Theoretical Model of Non-equil Amorph St in 1TTaS2 by Vodeb**

# References


[1] A. Spijkerman, J.L. de Boer, A. Meetsma, G.A. Wiegers, S. van Smaalen, X-ray crystal-structure refinement of the nearly commensurate phase of 1 t- tas 2 in (3+ 2)-dimensional superspace, Physical review B **56**(21), 13757 (1997)

[2] P. Fazekas, E. Tosatti, Electrical, structural and magnetic properties of pure and doped 1t-tas2, Philosophical Magazine B **39**(3), 229 (1979)

[3] K. Rossnagel, N. Smith, Spin-orbit coupling in the band structure of reconstructed 1 t-tas 2, Physical Review B **73**(7), 073106 (2006)

[4] R. Withers, J. Wilson, An examination of the formation and characteristics of charge-density waves in inorganic materials with special reference to the two-and one-dimensional transition-metal chalcogenides, Journal of Physics C: Solid State Physics **19**(25), 4809 (1986)

[5] B. Sipos, A.F. Kusmartseva, A. Akrap, H. Berger, L. Forró, E. Tutiš, From mott state to superconductivity in 1T-TaS2, Nature materials **7**(12), 960 (2008)

[6] A. Thompson, R. Gamble, J. Revelli, Transitions between semiconducting and metallic phases in 1-t tas2, Solid State Communications **9**(13), 981 (1971)

[7] M. Klanjšek, A. Zorko, J. Mravlje, Z. Jagličić, P.K. Biswas, P. Prelovšek, D. Mihailovic, D. Arčon, et al., A high-temperature quantum spin liquid with polaron spins, Nature Physics (2017)

[8] S. Brazovskii, Modeling of evolution of a complex electronic system to an ordered hidden state: Application to optical quench in 1T-TaS2, Journal of Superconductivity and Novel Magnetism **28**(4), 1349 (2015)

[9] L. Stojchevska, I. Vaskivskyi, T. Mertelj, P. Kusar, D. Svetin, S. Brazovskii, D. Mihailovic, Ultrafast switching to a stable hidden quantum state in an electronic crystal, Science **344**(6180), 177 (2014)

[10] P. Karpov, S. Brazovskii, Modeling of networks and globules of charged domain walls observed in pump and pulse induced states, Scientific reports **8**(1), 4043 (2018)

[11] G. Wellein, H. Fehske, Polaron band formation in the holstein model, Physical Review B **56**(8), 4513 (1997)

[12] J. Bonča, S. Trugman, I. Batistić, Holstein polaron, Physical Review B **60**(3), 1633 (1999)

[13] H. De Raedt, A. Lagendijk, Numerical calculation of path integrals: the small-polaron model, Physical Review B **27**(10), 6097 (1983)

[14] A.S. Davydov, Solitons in molecular systems, Physica Scripta **20**(3-4), 387 (1979)

[15] E. Jeckelmann, S.R. White, Density-matrix renormalization-group study of the polaron problem in the holstein model, Physical Review B **57**(11), 6376 (1998)

[16] X. Li, J.C. Tully, H.B. Schlegel, M.J. Frisch, Ab initio ehrenfest dynamics, The Journal of chemical physics **123**(8), 084106 (2005)

[17] G. Donati, D.B. Lingerfelt, A. Petrone, N. Rega, X. Li, "watching" polaron pair formation from first-principles electron–nuclear dynamics, The Journal of Physical Chemistry A **120**(37), 7255 (2016)

[18] M. Polkehn, P. Eisenbrandt, H. Tamura, I. Burghardt, Quantum dynamical studies of ultrafast charge separation in nanostructured organic polymer materials: Effects of vibronic interactions and molecular packing, International Journal of Quantum Chemistry **118**(1), e25502 (2018)

[19] M.H. Beck, A. Jäckle, G. Worth, H.D. Meyer, The multiconfiguration time-dependent hartree (mctdh) method: a highly efficient algorithm for propagating wavepackets, Physics reports **324**(1), 1 (2000)

[20] H. Wang, M. Thoss, Multilayer formulation of the multiconfiguration time-dependent hartree theory, The Journal of chemical physics **119**(3), 1289 (2003)

[21] Y. Tanimura, R. Kubo, Time evolution of a quantum system in contact with a nearly gaussian-markoffian noise bath, Journal of the Physical Society of Japan **58**(1), 101 (1989)

[22] L. Chen, Y. Zhao, Y. Tanimura, Dynamics of a one-dimensional holstein polaron with the hierarchical equations of motion approach, The journal of physical chemistry letters **6**(15), 3110 (2015)

[23] A. Petrone, D.B. Lingerfelt, D.B. Williams-Young, X. Li, Ab initio transient vibrational spectral analysis, The journal of physical chemistry letters **7**(22), 4501 (2016)

[24] A. Petrone, J.J. Goings, X. Li, Quantum confinement effects on optical transitions in nanodiamonds containing nitrogen vacancies, Physical Review B **94**(16), 165402 (2016)

[25] J.L. Stein, M.I. Steimle, M.W. Terban, A. Petrone, S.J. Billinge, X. Li, B.M. Cossairt, Cation exchange induced transformation of inp magic-sized clusters, Chemistry of Materials **29**(18), 7984 (2017)

[26] Y. Gerasimenko, I. Vaskivskyi, J. Ravnik, J. Vodeb, V.V. Kabanov, D. Mihailovic, Ultrafast jamming of electrons into an amorphous entangled state, arXiv preprint arXiv:1803.00255 (2018)

[27] K. Rossnagel, On the origin of charge-density waves in select layered transition-metal dichalcogenides, Journal of Physics: Condensed Matter **23**(21), 213001 (2011)

[28] A.S. Alexandrov, N.F. Mott, *Polarons & bipolarons* (World Scientific, 1995)

[29] Monte carlo code. https://github.com/JakaVodeb\Physics/MonteCarloSimulatedAnnealing. Accessed: 2018-09-20

[30] S.J. Lee, B. Kim, J. Lee, Infinite ground state degeneracy and glassy dynamics in the frustrated xy model and lattice coulomb gas with f= 16, Physica A: Statistical Mechanics and its Applications **315**(1), 314 (2002)

[31] L. Rademaker, Y. Pramudya, J. Zaanen, V. Dobrosavljević, Influence of long-range interactions on charge ordering phenomena on a square lattice, Physical Review E **88**(3), 032121 (2013)

[32] V. Pokrovsky, G. Uimin, On the properties of monolayers of adsorbed atoms, Journal of Physics C: Solid State Physics **11**(16), 3535 (1978)

**References from Controll magn frustr 1T-TaS2 via Coul engin by Chen**

# References


[1] Leon Balents, "Spin liquids in frustrated magnets," Nature **464**, 199–208 (2010).

[2] P. A. Lee, "An end to the drought of quantum spin liquids," Science **321**, 1306–1307 (2008).

[3] C. Broholm, R. J. Cava, S. A. Kivelson, D. G. Nocera, M. R. Norman, and T. Senthil, "Quantum spin liquids," Science **367**, eaay0668 (2020).

[4] Yi Zhou, Kazushi Kanoda, and Tai-Kai Ng, "Quantum spin liquid states," Rev. Mod. Phys. **89**, 025003 (2017).

[5] Lucile Savary and Leon Balents, "Quantum spin liquids: a review," Reports on Progress in Physics **80**, 016502 (2016).

[6] Alexei Kitaev, "Anyons in an exactly solved model and beyond," Annals of Physics **321**, 2–111 (2006).

[7] P. W. Anderson, "The resonating valence bond state in la2cuo4 and superconductivity," Science **235**, 1196–1198 (1987).

[8] Z. A. Kelly, M. J. Gallagher, and T. M. McQueen, "Electron doping a kagome spin liquid," Phys. Rev. X **6**, 041007 (2016).

[9] David Aasen, Roger S. K. Mong, Benjamin M. Hunt, David Mandrus, and Jason Alicea, "Electrical probes of the non-abelian spin liquid in kitaev materials," Phys. Rev. X **10**, 031014 (2020).

[10] Tian-Heng Han, Joel S. Helton, Shaoyan Chu, Daniel G. Nocera, Jose A. Rodriguez-Rivera, Collin Broholm, and Young S. Lee, "Fractionalized excitations in the spin-liquid state of a kagome-lattice antiferromagnet," Nature **492**, 406–410 (2012).

[11] M. Fu, T. Imai, T.-H. Han, and Y. S. Lee, "Evidence for a gapped spin-liquid ground state in a kagome heisenberg antiferromagnet," Science **350**, 655–658 (2015).

[12] B J Powell and Ross H McKenzie, "Quantum frustration in organic mott insulators: from spin liquids to unconventional superconductors," Reports on Progress in Physics **74**, 056501 (2011).

[13] Sean K. Takahashi, Jiaming Wang, Alexandre Arsenault, Takashi Imai, Mykola Abramchuk, Fazel Tafti, and Philip M. Singer, "Spin excitations of a proximate kitaev quantum spin liquid realized in $cu_2iro_3$," Phys. Rev. X **9**, 031047 (2019).

[14] M. R. Norman, "Colloquium: Herbertsmithite and the search for the quantum spin liquid," Rev. Mod. Phys. **88**, 041002 (2016).

[15] Hidenori Takagi, Tomohiro Takayama, George Jackeli, Giniyat Khaliullin, and Stephen E. Nagler, "Concept and realization of kitaev quantum spin liquids," Nature Reviews Physics **1**, 264–280 (2019).

[16] Y. Shimizu, K. Miyagawa, K. Kanoda, M. Maesato, and G. Saito, "Spin liquid state in an organic mott insulator with a triangular lattice," Phys. Rev. Lett. **91**, 107001 (2003).

[17] Minoru Yamashita, Norihito Nakata, Yuichi Kasahara, Takahiko Sasaki, Naoki Yoneyama, Norio Kobayashi, Satoshi Fujimoto, Takasada Shibauchi, and Yuji Matsuda, "Thermal-transport measurements in a quantum spin-liquid state of the frustrated triangular magnet $\kappa$-(BEDT-TTF)2cu2(CN)3," Nature Physics **5**, 44–47 (2008).

[18] T. Itou, A. Oyamada, S. Maegawa, M. Tamura, and R. Kato, "Quantum spin liquid in the spin-1/2 triangular antiferromagnet $\mathrm{Etme_3Sb[Pd(dmit)_2]_2}$," Phys. Rev. B **77**, 104413 (2008).

[19] Takayuki Isono, Hiromichi Kamo, Akira Ueda, Kazuyuki Takahashi, Motoi Kimata, Hiroyuki Tajima, Satoshi Tsuchiya, Taichi Terashima, Shinya Uji, and Hatsumi Mori, "Gapless quantum spin liquid in an organic spin-1/2 triangular-lattice $\kappa - \mathrm{h_3(cat\text{-}edt\text{-}ttf)_2}$," Phys. Rev. Lett. **112**, 177201 (2014).

[20] J. S. Helton, K. Matan, M. P. Shores, E. A. Nytko, B. M. Bartlett, Y. Yoshida, Y. Takano, A. Suslov, Y. Qiu, J.-H. Chung, D. G. Nocera, and Y. S. Lee, "Spin dynamics of the spin-1/2 kagome lattice antiferromagnet $\mathrm{zncu_3(OH)_6cl_2}$," Phys. Rev. Lett. **98**, 107204 (2007).

[21] Lei Ding, Pascal Manuel, Sebastian Bachus, Franziska Grußler, Philipp Gegenwart, John Singleton, Roger D. Johnson, Helen C. Walker, Devashibhai T. Adroja, Adrian D. Hillier, and Alexander A. Tsirlin, "Gapless spin-liquid state in the structurally disorder-free triangular antiferromagnet $\mathrm{naybo_2}$," Phys. Rev. B **100**, 144432 (2019).

[22] Mitchell M. Bordelon, Eric Kenney, Chunxiao Liu, Tom Hogan, Lorenzo Posthuma, Marzieh Kavand, Yuanqi Lyu, Mark Sherwin, N. P. Butch, Craig Brown, M. J. Graf, Leon Balents, and Stephen D. Wilson, "Field-tunable quantum disordered ground state in the triangular-lattice antiferromagnet NaYbO2," Nature Physics **15**, 1058–1064 (2019).

[23] Peng-Ling Dai, Gaoning Zhang, Yaofeng Xie, Chunruo Duan, Yonghao Gao, Zihao Zhu, Erxi Feng, Zhen Tao, Chien-Lung Huang, Huibo Cao, Andrey Podlesnyak, Garrett E. Granroth, Michelle S. Everett, Joerg C. Neuefeind, David Voneshen, Shun Wang, Guotai Tan, Emilia Morosan, Xia Wang, Hai-Qing Lin, Lei Shu, Gang Chen, Yanfeng Guo, Xingye Lu, and Pengcheng Dai, "Spinon fermi surface spin liquid in a triangular lattice antiferromagnet $\mathrm{naybse_2}$," Phys. Rev. X **11**, 021044 (2021).

[19] K. T. Law and Patrick A. Lee, "1t-TaS2 as a quantum spin liquid," Proceedings of the National Academy of Sciences **114**, 6996–7000 (2017).

[25] H. Murayama, Y. Sato, T. Taniguchi, R. Kurihara, X. Z. Xing, W. Huang, S. Kasahara, Y. Kasahara, I. Kimchi, M. Yoshida, Y. Iwasa, Y. Mizukami, T. Shibauchi, M. Konczykowski, and Y. Matsuda, "Effect of quenched disorder on the quantum spin liquid state of the triangular-lattice antiferromagnet $1t - \mathrm{tas_2}$," Phys. Rev. Research **2**, 013099 (2020).

[26] Samuel Mañas-Valero, Benjamin Huddart, Tom Lancaster, Eugenio Coronado, and Francis Pratt, "Multiple Quantum Spin Liquid Phases in 1T-TaS2," arXiv e-prints , arXiv:2007.15905 (2020), arXiv:2007.15905 [cond-mat.str-el] .

[27] Yi Chen, Wei Ruan, Meng Wu, Shujie Tang, Hyejin Ryu, Hsin-Zon Tsai, Ryan Lee, Salman Kahn, Franklin Liou, Caihong Jia, Oliver R. Albertini, Hongyu Xiong, Tao Jia, Zhi Liu, Jonathan A. Sobota, Amy Y. Liu, Joel E. Moore, Zhi-Xun Shen, Steven G. Louie, Sung-Kwan Mo, and Michael F. Crommie, "Strong correlations and orbital texture in single-layer 1t-TaSe2," Nature Physics **16**, 218–224 (2020).

[28] F. Guinea, M. I. Katsnelson, and A. K. Geim, "Energy gaps and a zero-field quantum hall effect in graphene by strain engineering," Nature Physics **6**, 30–33 (2009).

[29] Changsong Xu, Junsheng Feng, Mitsuaki Kawamura, Youhei Yamaji, Yousra Nahas, Sergei Prokhorenko, Yang Qi, Hongjun Xiang, and L. Bellaiche, "Possible kitaev quantum spin liquid state in 2d materials with $s = 3/2$," Phys. Rev. Lett. **124**, 087205 (2020).

[30] J. M. B. Lopes dos Santos, N. M. R. Peres, and A. H. Castro Neto, "Graphene bilayer with a twist: Electronic structure," Phys. Rev. Lett. **99**, 256802 (2007).

[31] Eva Y. Andrei, Dmitri K. Efetov, Pablo Jarillo-Herrero, Allan H. MacDonald, Kin Fai Mak, T. Senthil, Emanuel Tutuc, Ali Yazdani, and Andrea F. Young, "The marvels of moiré materials," Nature Reviews Materials **6**, 201–206 (2021).

[32] Guangze Chen and J. L. Lado, "Tunable moire spinons in magnetically encapsulated twisted van der waals quantum spin liquids," Phys. Rev. Research **3**, 033276 (2021).

[33] H. Gonzalez-Herrero, J. M. Gomez-Rodriguez, P. Mallet, M. Moaied, J. J. Palacios, C. Salgado, M. M. Ugeda, J.-Y. Veuillen, F. Yndurain, and I. Brihuega, "Atomic-scale control of graphene magnetism by using hydrogen atoms," Science **352**, 437–441 (2016).

[34] Lucile Savary and Leon Balents, "Disorder-induced quantum spin liquid in spin ice pyrochlores," Phys. Rev. Lett. **118**, 087203 (2017).

[35] Guangze Chen and J. L. Lado, "Impurity-induced resonant spinon zero modes in dirac quantum spin liquids," Phys. Rev. Research **2**, 033466 (2020).

[36] Debdeep Jena and Aniruddha Konar, "Enhancement of carrier mobility in semiconductor nanostructures by dielectric engineering," Phys. Rev. Lett. **98**, 136805 (2007).

[37] M. Rösner, E. Şaşıoğlu, C. Friedrich, S. Blügel, and T. O. Wehling, "Wannier function approach to realistic coulomb interactions in layered materials and heterostructures," Phys. Rev. B **92**, 085102 (2015).

[38] Archana Raja, Andrey Chaves, Jaeeun Yu, Ghidewon Arefe, Heather M. Hill, Albert F. Rigosi, Timothy C. Berkelbach, Philipp Nagler, Christian Schüller, Tobias Korn, Colin Nuckolls, James Hone, Louis E. Brus, Tony F. Heinz, David R. Reichman, and Alexey Chernikov, "Coulomb engineering of the bandgap and excitons in two-dimensional materials," Nature Communications **8** (2017), 10.1038/ncomms15251.

[39] M. Rösner, C. Steinke, M. Lorke, C. Gies, F. Jahnke, and T. O. Wehling, "Two-dimensional heterojunctions from nonlocal manipulations of the interactions," Nano Letters **16**, 2322–2327 (2016).

[40] A. Steinhoff, M. Florian, M. Rösner, G. Schönhoff, T. O. Wehling, and F. Jahnke, "Exciton fission in monolayer transition metal dichalcogenide semiconductors," Nature Communications **8**, 1166 (2017).

[41] M. Iqbal Bakti Utama, Hans Kleemann, Wenyu Zhao, Chin Shen Ong, Felipe H. da Jornada, Diana Y. Qiu, Hui Cai, Han Li, Rai Kou, Sihan Zhao, Sheng Wang, Kenji Watanabe, Takashi Taniguchi, Sefaattin Tongay, Alex Zettl, Steven G. Louie, and Feng Wang, "A dielectric-defined lateral heterojunction in a monolayer semiconductor," Nature Electronics **2**, 60–65 (2019).

[42] C. Steinke, T. O. Wehling, and M. Rösner, "Coulomb-engineered heterojunctions and dynamical screening in transition metal dichalcogenide monolayers," Phys. Rev. B **102**, 115111 (2020).

[43] Lutz Waldecker, Archana Raja, Malte Rösner, Christina Steinke, Aaron Bostwick, Roland J. Koch, Chris Jozwiak, Takashi Taniguchi, Kenji Watanabe, Eli Rotenberg, Tim O. Wehling, and Tony F. Heinz, "Rigid band shifts in two-dimensional semiconductors through external dielectric screening," Phys. Rev. Lett. **123**, 206403 (2019).

[44] Erik G. C. P. van Loon, Malte Schüler, Daniel Springer, Giorgio Sangiovanni, Jan M. Tomczak, and Tim O. Wehling, "Coulomb engineering of two-dimensional mott materials," (2020), arXiv:2001.01735 [cond-mat.str-el] .

[45] C. Steinke, D. Mourad, M. Rösner, M. Lorke, C. Gies, F. Jahnke, G. Czycholl, and T. O. Wehling, "Noninvasive control of excitons in two-dimensional materials," Phys. Rev. B **96**, 045431 (2017).

[46] Felipe H. da Jornada, Lede Xian, Angel Rubio, and Steven G. Louie, "Universal slow plasmons and giant field enhancement in atomically thin quasi-two-dimensional metals," Nature Communications **11**, 1013 (2020).

[47] Zhihao Jiang, Stephan Haas, and Malte Rösner, "Plasmonic waveguides from coulomb-engineered two-dimensional metals," 2D Materials **8**, 035037 (2021).

[48] M. Rösner and J. L. Lado, "Inducing a many-body topological state of matter through coulomb-engineered local interactions," Phys. Rev. Research **3**, 013265 (2021).

[49] D. Soriano, A. N. Rudenko, M. I. Katsnelson, and M. Rösner, "Environmental screening and ligand-field effects to magnetism in CrI3 monolayer," npj Computational Materials **7** (2021), 10.1038/s41524-021-00631-4.

[18] Doohee Cho, Sangmo Cheon, Ki-Seok Kim, Sung-Hoon Lee, Yong-Heum Cho, Sang-Wook Cheong, and Han Woong Yeom, "Nanoscale manipulation of the mott insulating state coupled to charge order in 1t-TaS2," Nature Communications **7** (2016), 10.1038/ncomms10453.

[51] Shuang Qiao, Xintong Li, Naizhou Wang, Wei Ruan, Cun Ye, Peng Cai, Zhenqi Hao, Hong Yao, Xianhui Chen, Jian Wu, Yayu Wang, and Zheng Liu, "Mottness collapse in $1\mathrm{T}-\mathrm{tas}_{2-x}\mathrm{se}_x$ transition-metal dichalcogenide: An interplay between localized and itinerant orbitals," Phys. Rev. X **7**, 041054 (2017).

[52] Marie Kratochvilova, Adrian D. Hillier, Andrew R. Wildes, Lihai Wang, Sang-Wook Cheong, and Je-Geun Park, "The low-temperature highly correlated quantum phase in the charge-density-wave 1T-$TaS_2$ compound," npj Quantum Mater. **2**, 42 (2017).

[53] Viliam Vaňo, Mohammad Amini, Somesh C. Ganguli, Guangze Chen, Jose L. Lado, Shawulienu Kezilebieke, and Peter Liljeroth, "Artificial heavy fermions in a van der waals heterostructure," Nature **599**, 582–586 (2021).

[31] Y. D. Wang, W. L. Yao, Z. M. Xin, T. T. Han, Z. G. Wang, L. Chen, C. Cai, Yuan Li, and Y. Zhang, "Band insulator to mott insulator transition in 1t-TaS2," Nature Communications **11** (2020), 10.1038/s41467-020-18040-4.

[55] K. Rossnagel and N. V. Smith, "Spin-orbit coupling in the band structure of reconstructed $1t-\mathrm{tas}_2$," Phys. Rev. B **73**, 073106 (2006).

[56] Diego Pasquier and Oleg V. Yazyev, "Ab initio theory of magnetism in two-dimensional $1t-\mathrm{tas}_2$," Phys. Rev. B **105**, L081106 (2022).

[57] Kimio Ohno, "Some remarks on the pariser-parr-pople method," Theoretica chimica acta **2**, 219–227 (1964).

[58] L. V. Keldysh, Pis'ma Zh. Eksp. Teor. Fiz. **29**, 716 (1979).

[59] Yann in 't Veld, Malte Schüler, Tim O Wehling, Mikhail I Katsnelson, and Erik G C P van Loon, "Bandwidth renormalization due to the intersite coulomb interaction," Journal of Physics: Condensed Matter **31**, 465603 (2019).

[60] Thomas Ayral, Silke Biermann, Philipp Werner, and Lewin Boehnke, "Influence of fock exchange in combined many-body perturbation and dynamical mean field theory," Phys. Rev. B **95**, 245130 (2017).

[61] E Kamil, J Berges, G Schönhoff, M Rösner, M Schüler, G Sangiovanni, and T O Wehling, "Electronic structure of single layer 1t-NbSe2: interplay of lattice distortions, non-local exchange, and mott–hubbard correlations," Journal of Physics: Condensed Matter **30**, 325601 (2018).

[62] José M. Pizarro, Severino Adler, Karim Zantout, Thomas Mertz, Paolo Barone, Roser Valentí, Giorgio Sangiovanni, and Tim O. Wehling, "Deconfinement of mott localized electrons into topological and spin–orbit-coupled dirac fermions," npj Quantum Materials **5** (2020), 10.1038/s41535-020-00277-3.

[63] Simeng Yan, David A. Huse, and Steven R. White, "Spin-liquid ground state of the s = 1/2 kagome heisenberg antiferromagnet," Science **332**, 1173–1176 (2011).

[64] Shijie Hu, W. Zhu, Sebastian Eggert, and Yin-Chen He, "Dirac spin liquid on the spin-1/2 triangular heisenberg antiferromagnet," Phys. Rev. Lett. **123**, 207203 (2019).

[65] Giuseppe Carleo and Matthias Troyer, "Solving the quantum many-body problem with artificial neural networks," Science **355**, 602–606 (2017).

[66] Kenny Choo, Titus Neupert, and Giuseppe Carleo, "Two-dimensional frustrated $J_1-J_2$ model studied with neural network quantum states," Phys. Rev. B **100**, 125124 (2019).

[67] S. M. Giampaolo, G. Gualdi, A. Monras, and F. Illuminati, "Characterizing and quantifying frustration in quantum many-body systems," Phys. Rev. Lett. **107**, 260602 (2011).

[68] Reinhold Egger and Karsten Flensberg, "Emerging dirac and majorana fermions for carbon nanotubes with proximity-induced pairing and spiral magnetic field," Physical Review B **85** (2012), 10.1103/physrevb.85.235462.

[69] Guangze Chen, Maryam Khosravian, Jose L Lado, and Aline Ramires, "Designing spin-textured flat bands in twisted graphene multilayers via helimagnet encapsulation," 2D Materials **9**, 024002 (2022).

[70] Bernd Braunecker, George I. Japaridze, Jelena Klinovaja, and Daniel Loss, "Spin-selective peierls transition in interacting one-dimensional conductors with spin-orbit interaction," Physical Review B **82** (2010), 10.1103/physrevb.82.045127.

[26] We can perform a change of basis to Eq. (10.6): $d^\dagger_{i,\uparrow} = \cos\theta c^\dagger_{i,\uparrow} + i\sin\theta c^\dagger_{i,\downarrow}$ and $d^\dagger_{i,\downarrow} = i\sin\theta c^\dagger_{i,\uparrow} + \cos\theta c^\dagger_{i,\downarrow}$. This does not change the $V_{ij}$ term, and the Hamiltonian becomes Eq. 10.1 with only changes in the $U$ term. The resulting $\tilde{t}_{ij}$ after integrating out $V_{ij}$ is thus given by Eq. 10.3. Transforming back to the original basis results in Eq. (10.7).

[72] V. V. Mazurenko, A. N. Rudenko, S. A. Nikolaev, D. S. Medvedeva, A. I. Lichtenstein, and M. I. Katsnelson, "Role of direct exchange and dzyaloshinskii-moriya interactions in magnetic properties of graphene derivatives: $c_2F$ and $c_2H$," Phys. Rev. B **94**, 214411 (2016).

[73] Anders C. Riis-Jensen, Jiong Lu, and Kristian S. Thygesen, "Electrically controlled dielectric band gap engineering in a two-dimensional semiconductor," Phys. Rev. B **101**, 121110 (2020).

[74] Yu Saito, Jingyuan Ge, Kenji Watanabe, Takashi Taniguchi, and Andrea F. Young, "Independent superconductors and correlated insulators in twisted bilayer graphene," Nature Physics **16**, 926–930 (2020).

[75] M. Schüler, M. Rösner, T. O. Wehling, A. I. Lichtenstein, and M. I. Katsnelson, "Optimal hubbard models for materials with nonlocal coulomb interactions: Graphene, silicene, and benzene," Phys. Rev. Lett. **111**, 036601 (2013).

[76] E. G. C. P. van Loon, M. Schüler, M. I. Katsnelson, and T. O. Wehling, "Capturing nonlocal interaction effects in the hubbard model: Optimal mappings and limits of applicability," Phys. Rev. B **94**, 165141 (2016).

[77] Diego Pasquier and Oleg V. Yazyev, "Ab initio theory of magnetism in two-dimensional $1t-\mathrm{tas}_2$," Phys. Rev. B **105**, L081106 (2022).

[78] Diego Pasquier and Oleg V. Yazyev, "Charge density wave phase, mottness, and ferromagnetism in monolayer $1t-\mathrm{nbse}_2$," Phys. Rev. B **98**, 045114 (2018).

[79] Yuki Nakata, Katsuaki Sugawara, Ryota Shimizu, Yoshinori Okada, Patrick Han, Taro Hitosugi, Keiji Ueno, Takafumi Sato, and Takashi Takahashi, "Monolayer 1t-NbSe2 as a mott insulator," NPG Asia Materials **8**, e321–e321 (2016).

[80] Mengke Liu, Joshua Leveillee, Shuangzan Lu, Jia Yu, Hyunsue Kim, Cheng Tian, Youguo Shi, Keji Lai, Chendong Zhang, Feliciano Giustino, and Chih-Kang Shih, "Monolayer 1t-NbSe 2 as a 2d-correlated magnetic insulator," Science Advances **7** (2021), 10.1126/sciadv.abi6339.

[81] Wei Wang, Bosen Wang, Zhibin Gao, Gang Tang, Wen Lei, Xiaojun Zheng, Huan Li, Xing Ming, and Carmine Autieri, "Charge density wave instability and pressure-induced superconductivity in bulk $1t-\mathrm{Nbs}_2$," Phys. Rev. B **102**, 155115 (2020).

[82] Wei Wang, Chen Si, Wen Lei, Feng Xiao, Yunhui Liu, Carmine Autieri, and Xing Ming, "Stacking order and coulomb correlation effect in the layered charge density wave phase of $1t-\mathrm{Nbs}_2$," Phys. Rev. B **105**, 035119 (2022).

[83] Wei Ruan, Yi Chen, Shujie Tang, Jinwoong Hwang, Hsin-Zon Tsai, Ryan L. Lee, Meng Wu, Hyejin Ryu, Salman Kahn, Franklin Liou, Caihong Jia, Andrew Aikawa, Choongyu Hwang, Feng Wang, Yongseong Choi, Steven G. Louie, Patrick A. Lee, Zhi-Xun Shen, Sung-Kwan Mo, and Michael F. Crommie, "Evidence for quantum spin liquid behaviour in single-layer 1t-TaSe2 from scanning tunnelling microscopy," Nature Physics **17**, 1154–1161 (2021).

[84] J. M. Pizarro, M. Rösner, R. Thomale, R. Valentí, and T. O. Wehling, "Internal screening and dielectric engineering in magic-angle twisted bilayer graphene," Phys. Rev. B **100**, 161102 (2019).

[85] T. M. R. Wolf, J. L. Lado, G. Blatter, and O. Zilberberg, "Electrically tunable flat bands and magnetism in twisted bilayer graphene," Phys. Rev. Lett. **123**, 096802 (2019).

[86] Fengnian Xia, Han Wang, and Yichen Jia, "Rediscovering black phosphorus as an anisotropic layered material for optoelectronics and electronics," Nature Communications **5** (2014), 10.1038/ncomms5458.

[87] Brian Kiraly, Elze J. Knol, Klara Volckaert, Deepnarayan Biswas, Alexander N. Rudenko, Danil A. Prishchenko, Vladimir G. Mazurenko, Mikhail I. Katsnelson, Philip Hofmann, Daniel Wegner, and Alexander A. Khajetoorians, "Anisotropic two-dimensional screening at the surface of black phosphorus," Phys. Rev. Lett. **123**, 216403 (2019).

**References from Ab initio theory of magn in 2D 1T-TaS2 by Pasquier**

## References

[1] Y. Cao, V. Fatemi, S. Fang, K. Watanabe, T. Taniguchi, E. Kaxiras, and P. Jarillo-Herrero, Nature **556**, 43 (2018).

[2] Y. Cao, V. Fatemi, A. Demir, S. Fang, S. L. Tomarken, J. Y. Luo, J. D. Sanchez-Yamagishi, K. Watanabe, T. Taniguchi, E. Kaxiras, *et al.*, Nature **556**, 80 (2018).

[3] B. Sipos, A. F. Kusmartseva, A. Akrap, H. Berger, L. Forró, and E. Tutiš, Nature Materials **7**, 960 (2008).

[4] P. Darancet, A. J. Millis, and C. A. Marianetti, Physical Review B **90**, 045134 (2014).

[5] D. Pasquier and O. V. Yazyev, Physical Review B **98**, 045114 (2018).

[6] Y. Chen, W. Ruan, M. Wu, S. Tang, H. Ryu, H.-Z. Tsai, R. Lee, S. Kahn, F. Liou, C. Jia, *et al.*, Nature Physics **16**, 218 (2020).

[7] J. A. Wilson, F. Di Salvo, and S. Mahajan, Advances in Physics **24**, 117 (1975).

[8] A. C. Neto, Physical Review Letters **86**, 4382 (2001).

[9] K. Rossnagel, Journal of Physics: Condensed Matter **23**, 213001 (2011).

[10] S. Manzeli, D. Ovchinnikov, D. Pasquier, O. V. Yazyev, and A. Kis, Nature Reviews Materials **2**, 17033 (2017).

[11] D. Pasquier and O. V. Yazyev, Physical Review B **100**, 201103 (2019).

[12] P. Fazekas and E. Tosatti, Physica B+ C **99**, 183 (1980).

[13] D. Pasquier and O. V. Yazyev, 2D Materials **6**, 025015 (2019).

[14] K. T. Law and P. A. Lee, Proceedings of the National Academy of Sciences **114**, 6996 (2017).

[15] P. W. Anderson, Materials Research Bulletin **8**, 153 (1973).

[16] P. Fazekas and E. Tosatti, Philosophical Magazine B **39**, 229 (1979).

[17] L. Perfetti, T. Gloor, F. Mila, H. Berger, and M. Grioni, Physical Review B **71**, 153101 (2005).

[18] W.-Y. He, X. Y. Xu, G. Chen, K. T. Law, and P. A. Lee, Physical Review Letters **121**, 046401 (2018).

[19] S. Mañas-Valero, B. M. Huddart, T. Lancaster, E. Coronado, and F. L. Pratt, npj Quantum Materials **6**, 1 (2021).

[20] W. Ruan, Y. Chen, S. Tang, J. Hwang, H.-Z. Tsai, R. Lee, M. Wu, H. Ryu, S. Kahn, F. Liou, *et al.*, arXiv preprint arXiv:2009.07379 (2020).

[21] N. S. Fedorova, C. Ederer, N. A. Spaldin, and A. Scaramucci, Physical Review B **91**, 165122 (2015).

[22] N. S. Fedorova, A. Bortis, C. Findler, and N. A. Spaldin, Physical Review B **98**, 235113 (2018).

[23] P. Giannozzi, S. Baroni, N. Bonini, M. Calandra, R. Car, C. Cavazzoni, D. Ceresoli, G. L. Chiarotti, M. Cococcioni, I. Dabo, *et al.*, Journal of physics: Condensed matter **21**, 395502 (2009).

[24] J. P. Perdew and W. Yue, Physical Review B **33**, 8800 (1986).

[25] J. P. Perdew, K. Burke, and M. Ernzerhof, Physical Review Letters **77**, 3865 (1996).

[26] N. Marzari, D. Vanderbilt, A. De Vita, and M. Payne, Physical Review Letters **82**, 3296 (1999).

[27] P. E. Blöchl, Physical Review B **50**, 17953 (1994).

[28] A. Dal Corso, Computational Materials Science **95**, 337 (2014).

[29] D. C. Miller, S. D. Mahanti, and P. M. Duxbury, Physical Review B **97**, 045133 (2018).

[30] S. Yi, Z. Zhang, and J.-H. Cho, Physical Review B **97**, 041413 (2018).

[31] C. Tresca and M. Calandra, 2D Materials **6**, 035041 (2019).

[32] K. Penc, H. Shiba, F. Mila, and T. Tsukagoshi, Physical Review B **54**, 4056 (1996).

[33] Z. Huang, D. Liu, A. Mansikkamäki, V. Vieru, N. Iwahara, and L. F. Chibotaru, Physical Review Research **2**, 033430 (2020).

[34] K. Seo, V. N. Kotov, and B. Uchoa, Physical review letters **122**, 246402 (2019).

[35] L. Perfetti, P. A. Loukakos, M. Lisowski, U. Bovensiepen, M. Wolf, H. Berger, S. Biermann, and A. Georges, New Journal of Physics **10**, 053019 (2008).

[36] T. Grover, N. Trivedi, T. Senthil, and P. A. Lee, Physical Review B **81**, 245121 (2010).

[37] N. D. Mermin and H. Wagner, Physical Review Letters **17**, 1133 (1966).

[38] J. L. Lado and J. Fernández-Rossier, 2D Materials **4**, 035002 (2017).

[39] A. Cuccoli, V. Tognetti, and R. Vaia, Physical Review B **52**, 10221 (1995).

[40] A. Cuccoli, V. Tognetti, P. Verrucchi, and R. Vaia, Physical Review B **51**, 12840 (1995).

[41] S. A. Owerre, Canadian Journal of Physics **91**, 542 (2013).

[42] A. S. Ngankeu, S. K. Mahatha, K. Guilloy, M. Bianchi, C. E. Sanders, K. Hanff, K. Rossnagel, J. A. Miwa, C. Breth Nielsen, M. Bremholm, and P. Hofmann, Physical Review B **96**, 195147 (2017).

[43] C. Butler, M. Yoshida, T. Hanaguri, and Y. Iwasa, Nature Communications **11**, 2477 (2020).

[44] J. Lee, K.-H. Jin, and H. W. Yeom, Physical Review Letters **126**, 196405 (2021).

[45] T. Ritschel, H. Berger, and J. Geck, Physical Review B **98**, 195134 (2018).

[46] S.-H. Lee, J. S. Goh, and D. Cho, Physical Review Letters **122**, 106404 (2019).

**References from From Mott state to superconductivity in** $1\,\mathrm{T}-\mathrm{TaS}_2$ **by Sipos, Kusamartseva et al.**

1. Bednorz, J. G. & Müller, K. A. Possible high $T_c$ superconductivity in the Ba-La-Cu-O system. Zeitschrift für Physik B 64, 189-193 (1986).

2. Lee, P. A., Nagaosa, N. & Wen, X.-G. Doping a Mott insulator: Physics of high-temperature superconductivity. Rev. Mod. Phys. 78, 17-76 (2006).

3. Carlson, E., Emery, V., Kiveslon, S. & Ograd, D. The Physics of Conventional and Unconventional Superconductors (Springer, 2003).

4. Gabovich, A. M., Voitenko, A. I., Annett, J. F. & Ausloos, M. Charge- and spin-density wave superconductors. Supercond. Sci. Tech. 14, R1-R27 (2001).

5. Grosche, F. M. et al. Superconductivity on the threshold of magnetism in $CePd_2Si_2$ and CeIn. J. Phys. Condens. Matter 13, 2845-2860 (2001).

6. Takada, K. et al. Superconductivity in two-dimensional $CoO_2$ layers. Nature 422, 53-55 (2003).

7. Morosan, E. et al. Superconductivity in $Cu_xTiSe_2$. Nature Phys. 2, 544-550 (2006).

8. Friend, R. H. & Yoffe, A. D. Electronic properties of intercalation complexes of the transition metal dichalcogenides. Adv. Phys. 36, 1-94 (1987).

9. Wilson, J. A., Di Salvo, F. J. & Mahajan, S. Charge density waves and superlattices in metallic layered transition-metal dichalcogenides. Adv. Phys. 24, 117-201 (1975).

10. Thomson, R. E., Burk, B., Zettl, A. & Clarke, J. Scanning tunneling microscopy of the charge-density-wave structure in 1T-$TaS_2$. Phys. Rev. B 49, 16899-16916 (1994).

11. Fazekas, P. & Tosatti, E. Charge carrier localization in pure and doped 1T-$TaS_2$. Physica B & C 99, 183-187 (1980).

12. Fazekas, P. & Tosatti, E. Electrical, structural and magnetic-properties of pure and doped 1T-$TaS_2$. Phil. Mag. B 39, 229-244 (1979).

13. Perfetti, L., Gloor, T. A., Mila, F., Berger, H. & Grioni, M. Unexpected periodicity in the quasi-two-dimensional Mott insulator 1T-$TaS_2$ revealed by angle-resolved photoemission. Phys. Rev. B 71, 153101 (2005).

14. Bourbonnais, C. & Jrome, D. Advances in Synthetic Metals (Elsevier, 1999).

15. Ramirez, A. $C_{60}$ and its superconductivity. Supercond. Rev. 1, 1-101 (1994).

16. Zhou, O. et al. Structural and electronic properties of $(NH_3) \times K_3C_6$ 0. Phys. Rev. B 52, 483-489 (1995).

17. Ishiguro, T., Yamaji, K. & Saito, G. Organic Superconductors (Springer, 1998).

18. Nam, M.-S., Ardavan, A., Blundell, S. J. & Schlueter, J. A. Fluctuating superconductivity in organic molecular metals close to the Mott transition. Nature 449, 584-587 (2007).

19. Rossnagel, K. & Smith, N. V. Spin-orbit coupling in the band structure of reconstructed 1T-$TaS_2$ Phys. Rev. B 73, 073106 (2006).

20. Zwick, F. et al. Spectral consequences of broken phase coherence in 1T-$TaS_2$. Phys. Rev. Lett. 81, 1058-1061 (1998).

21. Pillo, T. et al. Interplay between electron-electron interaction and electron-phonon coupling near the Fermi surface of 1T-$TaS_2$. Phys. Rev. B 62, 4277-4287 (2000).

22. Wilson, J. A. Questions concerning the form taken by the charge density wave and the accompanying periodic-structural distortions in $2H-TaSe_2$, and closely related materials. Phys. Rev. B 17, 3880-3898 (1978).

23. Bovet, M. et al. Interplane coupling in the quasi-two-dimensional 1T-$TaS_2$. Phys. Rev. B 67, 125105 (2003).

24. Di Salvo, F. J., Wilson, J. A., Bagley, B. G. & Waszczak, J. V. Effects of doping on charge density waves in layer compounds. Phys. Rev. B 12, 2220-2235 (1975).

25. Mutka, H., Zuppiroli, L., Molinié, P. & Bourgoin, J. C. Charge-density waves and localization in electron-irradiated 1T-$TaS_2$. Phys. Rev. B 23, 5030-5037 (1981).

26. Tani, T., Osada, T. & Tanaka, S. The pressure effect on the CDW-transition temperatures in 1T- $TaS_2$. Solid State Commun. 22, 269-272 (1977).

27. Spijkerman, A., de Boer, J. L., Meetsma, A., Wiegers, G. A. & van Smaalen, S. X-ray crystal-structure refinement of the nearly commensurate phase of $1\ T - TaS_2$ in $(\ 3 + 2\ )$-dimensional superspace. Phys. Rev. B 56, 13757-13767 (1997).

**References from Quantum jamming transition to a correlated electron glass in $1T-TaS_2$ by Gerasimenko, Vaskivskyi, Litskevich, Ravnik, Vodeb, Diego, Kabanov, Mihailovic (2019)**

1. Zurek, W. Cosmological experiments in superfluid helium? Nature 317, 505 (1985).

2. Cavalleri, A. et al. Femtosecond structural dynamics in $VO_2$ during an ultrafast solid-solid phase transition. Phys. Rev. Lett. 87, 237401 (2001).

3. Nasu, K., Ping, H. & Mizouchi, H. Photoinduced structural phase transitions and their dynamics. J. Phys. Condens. Mat. 13, R693-R721 (2001).

4. Iwai, S. et al. Photoinduced melting of a stripe-type charge-order and metallic domain formation in a layered BEDT-TTF-based organic salt. Phys. Rev. Lett. 98, 097402 (2007).

5. Schmitt, F. et al. Transient electronic structure and melting of a charge density wave in $TbTe_3$. Science 321, 1649-1652 (2008).

6. Yusupov, R. et al. Coherent dynamics of macroscopic electronic order through a symmetry breaking transition. Nat. Phys. 6, 681-684(2010).

7. Kosterlitz, J. M. & Thouless, D. J. Ordering, metastability and phase transitions in two-dimensional systems. J. Phys. C 6, 1181-1203 (1973).

8. Anderson, P. W. Through the glass lightly. Science 267, 1615-1616 (1995).

9. Mitrano, M. et al. Possible light-induced superconductivity in $K_3C_{60}$ at high temperature. Nature 530, 461-464 (2016).

10. Giannetti, C. et al. Ultrafast optical spectroscopy of strongly correlated materials and high-temperature superconductors: a non-equilibrium approach. Adv. Phys. 65, 58-238 (2016).

11. Koshihara, S. et al. Photoinduced valence instability in the organic molecular compound tetrathiafulvalene-p-chloranil (TTF-CA). Phys. Rev. B 42, 6853-6856 (1990).

12. Fausti, D. et al. Light-induced superconductivity in a stripe-ordered cuprate. Science 331, 189-191 (2011).

13. Stojchevska, L. et al. Ultrafast switching to a stable hidden quantum state in an electronic crystal. Science 344, 177-180 (2014).

14. Zhang, J. et al. Cooperative photoinduced metastable phase control in strained manganite films. Nat. Mater. 15, 956-960 (2016).

15. Basov, D. N., Averitt, R. D. & Hsieh, D. Towards properties on demand in quantum materials. Nat. Mater. 16, 1077-1088 (2017).

16. Gerasimenko, Y. A., Karpov, P., Vaskivskyi, I., Brazovskii, S. & Mihailovic, D. Intertwined chiral charge orders and topological stabilization of the light-induced state of a prototypical transition metal dichalcogenide. npj Quantum Mater. 4, 32 (2019).

17. Ravnik, J., Vaskivskyi, I., Mertelj, T. & Mihailović, D. Real-time observation of the coherent transition to a metastable emergent state in 1T- $TaS_2$. Phys. Rev. B 97, 075304 (2018).

18. Nakanishi, K. & Shiba, H. Domain-like incommensurate charge-density-wave states and the first-order incommensurate-commensurate transitions in layered tantalum dichalcogenides. I. 1T-polytype. J. Phys. Soc. Jpn 43, 1839 (1977).

19. Tosatti, E. & Fazekas, P. On the nature of the low-temperature phase of 1T- $TaS_2$. J. Phys. Colloques 37, C4-165-168 (1976).

20. Rossnagel, K. On the origin of charge-density waves in select layered transition-metal dichalcogenides. J. Phys. Condens. Mat. 23, 213001 (2011).

21. Ritschel, R. et al. Orbital textures and charge density waves in transition metal dichalcogenides. Nat. Phys. 11, 328-331 (2015).

22. Sipos, B. et al. From Mott state to superconductivity in 1T-$TaS_2$. Nat. Mater. 7, 960-965 (2008).

23. Klanjsek, M. et al. A high-temperature quantum spin liquid with polaron spins. Nat. Phys. 13, 1130-1134 (2017).

24. Han, T.-R. T. et al. Exploration of metastability and hidden phases in correlated electron crystals visualized by femtosecond optical doping and electron crystallography. Sci. Adv. 1, e1400173 (2015).

25. Torquato, S. & Stillinger, F. H. Local density fluctuations, hyperuniformity, and order metrics. Phys. Rev. E 68, 411131-4111325 (2003).

26. Torquato, S. Hyperuniformity and its generalizations. Phys. Rev. E 94, 022122 (2016).

27. Ma, Z. & Torquato, S. Random scalar fields and hyperuniformity. J. Appl. Phys. 121, 244904 (2016).

28. Lesanovsky, Y. & Garrahan, J. P. Out-of-equilibrium structures in strongly interacting Rydberg gases with dissipation. Phys. Rev. A 90, 011603 (2014).

29. Jiao, Y. et al. Avian photoreceptor patterns represent a disordered hyperuniform solution to a multiscale packing problem. Phys. Rev. E 89, 022721 (2014).

30. Getzin, S. et al. Discovery of fairy circles in Australia supports selforganization theory. Proc. Natl Acad. Sci. USA 113, 3551-3556 (2016).

31. Torquato, S., Scardicchio, A. & Zachary, C. E. Point processes in arbitrary dimension from fermionic gases, random matrix theory, and number theory. J. Stat. Mech. Theory Exp. 2008, P11019 (2008).

32. Karpov, P. & Brazovskii, S. Modeling of networks and globules of charged domain walls observed in pump and pulse induced states. Sci. Rep. 8, 4043 (2018).

33. Dean, N. et al. Polaronic conductivity in the photoinduced phase of 1T- $TaS_2$. Phys. Rev. Lett. 106, 016401 (2011).

34. Havlin, S. & Ben-Avraham, D. Diffusion in disordered media. Adv. Phys. 51, 187 (2002).

35. Burov, S., Metzler, R. & Barkai, E. Aging and nonergodicity beyond the Khinchin theorem. Proc. Natl Acad. Sci. USA 107, 13228 (2010).

36. Shklovskii, B. I. & Efros, A. L. Electronic Properties of Doped Semiconductors Vol. 45 (Springer, 1984).

37. Wang, Z. et al. Disorder induced power-law gaps in an insulator-metal Mott transition. Proc. Natl Acad. Sci. USA 115, 11198-11202 (2018).

38. Hellmann, S. et al. Time-domain classification of charge-density-wave insulators. Nat. Comms. 3, 1069 (2012).

39. Cho, D. et al. Nanoscale manipulation of the Mott insulating state coupled to charge order in 1T-TaS. Nat. Comms. 7, 10956 (2016).

40. Ma, L. et al. A metallic mosaic phase and the origin of Mott-insulating state in 1T- $TaS_2$. Nat. Commun. 7, 10453 (2016).

41. Svetin, D., Vaskivskyi, I., Brazovskii, S. & Mihailovic, D. Three-dimensional resistivity switching between correlated electronic states in 1T-$TaS_2$. Sci. Rep. 7, 46048 (2017).

42. Mishima, O., Calvert, L. D. & Whalley, E. 'Melting ice I' at 77 K and 10 kbar: a new method of making amorphous solids. Nature 310, 393-395 (1984).

43. Miroshnichenko, A. E., Flach, S. & Kivshar, Y. S. Fano resonances in nanoscale structures. Rev. Mod. Phys. 82, 2257-2298 (2010).

44. De Roeck, W. & Imbrie, J. Z. Many-body localization: stability and instability. Phil. Trans. R. Soc. A 375, 20160422 (2017).

45. Mahmoudian, S., Rademaker, L., Ralko, A., Fratini, S. & Dobrosavljević, V. Glassy dynamics in geometrically frustrated Coulomb liquids without disorder. Phys. Rev. Lett. 115, 025701 (2015).

46. Smith, A., Knolle, J., Kovrizhin, D. L. & Moessner, R. Disorder-free localization. Phys. Rev. Lett. 118, 266601 (2017).

47. Nandkishore, R. & Huse, D. A. Many-body localization and thermalization in quantum statistical mechanics. Ann. Rev. Cond. Mat. Phys. 6, 15-38 (2015).

48. Rademaker, L., Pramudya, Y., Zaanen, J. & Dobrosavljević, V. Influence of long-range interactions on charge ordering phenomena on a square lattice. Phys. Rev. E 88, 032121 (2013).

49. Hanaguri, T. et al. A 'checkerboard' electronic crystal state in lightly hole-doped $Ca_{2-x}Na_xCuO_2Cl_2$. Nature 430, 1001-1005 (2004).

50. Schmalian, J. & Wolynes, P. Stripe glasses: self-generated randomness in a uniformly frustrated system. Phys. Rev. Lett. 85, 836-839 (2000).

51. Metropolis, N. et al. Equation of state calculations by fast computing machines. J. Chem. Phys. 21, 1087 (1953).

52. Mertelj, T., Kabanov, V. V. & Mihailović, D. Charged particles on a two-dimensional lattice subject to anisotropic Jahn-Teller interactions. Phys. Rev. Lett. 94, 147003 (2005).

53. Hukushima, K. & Nemoto, K. Exchange Monte Carlo method and application to spin glass simulations. J. Phys. Soc. Jpn 65, 1604-1608 (1996).

[1] Ravnik, J., Vaskivskyi, I., Mertelj, T., Mihailovic, D. Real-time observation of the coherent transition to a metastable emergent state in 1T-TaS. Phys. Rev. B 97, 075304 (2018).
[2] Stojchevska, L. et al. Ultrafast Switching to a Stable Hidden Quantum State in an Electronic Crystal. Science 344, 177-180 (2014).
[3] Lifshitz, I. M. and Slyozov, V. V. The kinetics of precipitation from supersaturated solid solutions. J. Phys. Chem. Solids 19, 35 (1961).
[4] Allen, S. M. and Cahn, J. W. A macroscopic theory for antiphase boundary motion and its application to antiphase domain coarsening. Acta Metall. Mater. 27, 1085 (1979).
[5] Burov, S., Metzler, R., Barkai, E. Aging and nonergodicity beyond the Khinchin theorem. Proc. Natl. Acad. Sci. 107, 13228 (2010).

[6] Thomson, R. E., Burk, B., Zettl, A., Clarke, J. Scanning tunneling microscopy of the charge-density-wave structure in 1T-$TaS_2$. Phys. Rev. B 49, 16899 (1994).
[7] Torquato, S. and Stillinger, F. H. Local density fluctuations, hyperuniformity and order metrics. Phys. Rev. E 68, 041113 (2003).
[8] Zachary, C. E. and Torquato, S. Hyperuniformity in point patterns and two-phase random heterogeneous media. J. Stat. Mech. 12, P12015 (2009).
[9] Dreyfus, R. et al. Diagnosing hyperuniformity in two-dimensional, disordered, jammed packings of soft spheres. Phys. Rev. E 91, 012302 (2015).
[10] Valdes, L. Resistivity measurements on germanium for transistors. Proc. I.R.E. 42, 420 (1954).
[11] Shafarman, W. N., Koon, D. W. and Castner, T. G. dc conductivity of arsenic-doped silicon near the metal-insulator transition. Phys. Rev. B 40, 1216 (1989).
[12] Inada, R., Onuki, Y., Tanuma, S. Hall effect of 1T-$TaS_2$ and 1T-$TaSe_2$. Physica B 99, 188 (1980).
[13] Vodeb, J., Kabanov, V. V., Gerasimenko, Ya. A., Venturini, R., Ravnik, J., van Midden, M., Zupanic, E., Sutar, P. and Mihailovic, D. Correlated Configurational States and a Quantum Charge Liquid in Layered Metallic Dichalcogenides. arXiv:1901.02232 (2019).
[14] Karpov, P., Brazovskii, S. Modeling of networks and globules of charged domain walls observed in pump and pulse induced states. Sci. Rep. 8, 4043 (2018).
[15] Bittner, E., Nußbaumer, A. and Janke, W. Make life simple: Unleash the full power of the parallel tempering algorithm. Phys. Rev. Lett. 101, 130603 (2008)
[16] Hamze, F., Dickson, N. and Karimi, K. Robust parameter selection for parallel tempering. Int. J. Mod. Phys. C 21, 603-615 (2010)
[17] Fiore, C. E. First-order phase transitions: A study through the parallel tempering method. Phys. Rev. E 78041109 (2008)
[18] Pokrovsky, V. and Uimin, G. On the properties of monolayers of adsorbed atoms. J. Phys. C 11, 3535 (1978).
[19] Rademaker, L., Pramudya, Y., Zaanen, J. and Dobrosavljević, V. Influence of long-range interactions on charge ordering phenomena on a square lattice. Phys. Rev. E 88, 032121 (2013).
[20] Lee, S. J., Kim, B. and Lee, J. Infinite ground state degeneracy and glassy dynamics in the frustrated XY model and lattice Coulomb gas with $f = 1/6$. Physica A 315, 314-320 (2002).
[21] Gruner, G. Density waves in solids. Addison-Wesley (1994).
[22] Torquato, S. Hyperuniformity and its generalizations. Phys. Rev. E 94, 022122 (2016).
[23] Torquato, S., Scardicchio, A., Zachary, C. E. Point processes in arbitrary dimension from fermionic gases, random matrix theory, and number theory. J. Stat. Mech. Theory Exp. P11019 (2008).
[24] Ma, Z., Torquato, S. Random scalar fields and hyperuniformity. J. Appl. Phys. 121, 244904 (2017).
[25] Gerasimenko, Ya. A., Vaskivskyi, I., Mihailović, D. Dual vortex charge order in a metastable state created by an ultrafast topological transition in 1T-TaS 2. arXiv:1704.08149v2 (2017).
[26] Perfetti, L. et al. Femtosecond dynamics of electronic states in the Mott insulator 1T-$TaS_2$ by time resolved photoelectron spectroscopy. New Journal of Physics 10, 053019 (2008).
[27] Skolimowski, J., Gerasimenko, Ya., Zitko, R. Mottness collapse without metallization in the domain wall of the triangularlattice Mott insulator 1T-TaS2. Phys. Rev. Lett. 122, 036802 (2019).
[28] Thygesen, K. S. Calculating excitons, plasmons, and quasiparticles in 2D materials and van der Waals heterostructures. 2D Materials 4, 022004 (2017).
[29] http://scikit-image.org/docs/dev/api/skimage.feature.html#skimage.feature.blob_log

**References from Spin-orbit coupling in the band structure of reconstructed 1T-Ta$S_2$ by Rossnagel, Smith (2006)**

[1] P. Fazekas and E. Tosatti, Philos. Mag. B 39, 229 (1979); W. Geertsma, C. Haas, R. Huisman, and F. Jellinek, Solid State Commun. 10, 75 (1972).
[2] N. V. Smith, S. D. Kevan, and F. J. DiSalvo, J. Phys. C 18, 3175 (1985).
[3] L. F. Mattheiss, Phys. Rev. B 8, 3719 (1973).
[4] E. Abate and M. Asdente, Phys. Rev. 140, A1303 (1965).
[5] F. Herman and S. Skillman, Atomic Structure Calculations (Prentice-Hall, Englewood Cliffs, NJ, 1963).
[6] R. Brouwer and F. Jellinek, Physica B & C 99, 51 (1980).
[7] V. Heine, Phys. Rev. 153, 673 (1967).
[8] R. Manzke, O. Anderson, and M. Skibowski, J. Phys. C 21, 2399 (1988); F. Zwick, H. Berger, I. Vobornik, G. Margaritondo, L. Forró, C. Beeli, M. Onellion, G. Panaccione, A. Taleb-Ibrahimi,
and M. Grioni, Phys. Rev. Lett. 81, 1058 (1998); Y. Aiura, I. Hase, K. Yagi-Watanabe, H. Bando, K. Ozawa, K. Tanaka, R. Kitagawa, S. Maruyama, T. Iwase, Y. Nishihara, K. Horiba, O. Shiino, M. Oshima, M. Nakatake, M. Kubota, and K. Ono, Phys. Rev. B 69, 245123 (2004).
[9] Th. Pillo, J. Hayoz, D. Naumovic, H. Berger, L. Perfetti, L. Gavioli, A. Taleb-Ibrahimi, L. Schlapbach, and P. Aebi, Phys. Rev. B 64, 245105 (2001).
[10] M. Bovet, S. van Smaalen, H. Berger, R. Gaal, L. Forró, L. Schlapbach, and P. Aebi, Phys. Rev. B 67, 125105 (2003).
[11] L. Perfetti, T. A. Gloor, F. Mila, H. Berger, and M. Grioni, Phys. Rev. B 71, 153101 (2005).
[12] F. Clerc, M. Bovet, H. Berger, L. Despont, C. Koitzsch, O. Gallus, L. Patthey, M. Shi, J. Krempasky, M. G. Garnier, and P. Aebi, J. Phys.: Condens. Matter 16, 3271 (2004).

**References from Dualistic insulator states in 1T-TaS $_2$ crystals (2023) by Wang et al.**

1. Lee, P. A., Nagaosa, N. & Wen, X.-G. Doping a Mott insulator: physics of high-temperature superconductivity. Rev. Mod. Phys. 78, 17-85 (2006).

2. Neupert, T., Denner, M. M., Yin, J.-X., Thomale, R. & Hasan, M. Z. Charge order and superconductivity in kagome materials. Nat. Phys. 18, 137-143 (2022).

3. Nie, L. et al. Charge-density-wave-driven electronic nematicity in a kagome superconductor. Nature 604, 59-64 (2022).

4. Persky, E. et al. Magnetic memory and spontaneous vortices in a van der Waals superconductor. Nature 607, 692-696 (2022).

5. Fazekas, P. & Tosatti, E. Electrical, structural and magnetic properties of pure and doped 1T-TaS2. Philos. Mag. B 39, 229-244 (1979).

6. Sipos, B. et al. From Mott state to superconductivity in 1T-TaS $_2$. Nat. Mater. 7, 960-965 (2008).

7. Dong, Q. et al. Structural phase transition and superconductivity hierarchy in 1 $T-TaS_2$ under pressure up to 100 GPa. npj Quantum Mater. 6, 20 (2021).

8. Ma, L. et al. A metallic mosaic phase and the origin of Mottinsulating state in 1T- $TaS_2$. Nat. Commun. 7, 10956 (2016).

9. Cho, D. et al. Nanoscale manipulation of the Mott insulating state coupled to charge order in 1T-TaS $_2$. Nat. Commun. 7, 10453 (2016).

10. Darancet, P., Millis, A. J. & Marianetti, C. A. Three-dimensional metallic and two-dimensional insulating behavior in octahedral tantalum dichalcogenides. Phys. Rev. B 90, 045134 (2014).

11. Wen, C. et al. Roles of the narrow electronic band near the fermi level in $1\ \mathrm{T} - \mathrm{TaS}_2$-telated layered materials. Phys. Rev. Lett. 126, 256402 (2021).

12. Vaňo, V. et al. Artificial heavy fermions in a van der Waals heterostructure. Nature 599, 582-586 (2021).

13. Petocchi, F. et al. Mott versus hybridization gap in the lowtemperature phase of $1\ \mathrm{T} - \mathrm{TaS}_2$. Phys. Rev. Lett. 129, 016402 (2022).

14. Lee, S.-H., Goh, J. S. & Cho, D. Origin of the insulating phase and first-order metal-insulator transition in $1\ \mathrm{T} - \mathrm{TaS}_2$. Phys. Rev. Lett. 122, 106404 (2019).

15. Ritschel, T. et al. Orbital textures and charge density waves in transition metal dichalcogenides. Nat. Phys. 11, 328-331 (2015).

16. Ritschel, T., Berger, H. & Geck, J. Stacking-driven gap formation in layered 1T- $\mathrm{TaS}_2$. Phys. Rev. B 98, 195134 (2018).

17. Lee, J., Jin, K.-H. & Yeom, H. W. Distinguishing a Mott Insulator from a trivial insulator with atomic adsorbates. Phys. Rev. Lett. 126, 196405 (2021).

18. Li, C.-K., Yao, X.-P., Liu, J. & Chen, G. Fractionalization on the surface: Is type-II terminated $1\ \mathrm{T} - \mathrm{TaS}_2$ surface an anomalously realized spin liquid? Phys. Rev. Lett. 129, 017202 (2022).

19. Shin, D. et al. Identification of the Mott insulating charge density wave state in 1T- $\mathrm{TaS}_2$. Phys. Rev. Lett. 126, 196406 (2021).

20. Butler, C. J., Yoshida, M., Hanaguri, T. & Iwasa, Y. Mottness versus unit-cell doubling as the driver of the insulating state in $1\ \mathrm{T} - \mathrm{TaS}_2$. Nat. Commun. 11, 2477 (2020).

21. Wu, Z. et al. Effect of stacking order on the electronic state of $1\mathrm{TTaS}_2$. Phys. Rev. B 105, 035109 (2022).

22. Wang, Y. D. et al. Band insulator to Mott insulator transition in $1\mathrm{TTaS}_2$. Nat. Commun. 11, 4215 (2020).

23. Martino, E. et al. Preferential out-of-plane conduction and quasione-dimensional electronic states in layered 1T- $\mathrm{TaS}_2$.npj 2D Mater. Appl. 4, 7 (2020).

24. Klanjšek, M. et al. A high-temperature quantum spin liquid with polaron spins. Nat. Phys. 13, 1130-1134 (2017).

25. Kratochvilova, M. et al. The low-temperature highly correlated quantum phase in the charge-density-wave $1\ \mathrm{T} - \mathrm{TaS}_2$ compound. npj Quantum Mater. 2, 42 (2017).

26. Mañas-Valero, S., Huddart, B. M., Lancaster, T., Coronado, E. & Pratt, F. L. Quantum phases and spin liquid properties of $1\ \mathrm{T} - \mathrm{TaS}_2$. npj Quantum Mater. 6, 69 (2021).

27. Law, K. T. & Lee, P. A. 1 T − $TaS_2$ as a quantum spin liquid. Proc. Natl Acad. Sci. USA 114, 6996-7000 (2017).

28. Yasuda, K., Wang, X., Watanabe, K., Taniguchi, T. & Jarillo-Herrero, P. Stacking-engineered ferroelectricity in bilayer boron nitride. Science 372, 1458-1462 (2021).

29. Vizner Stern, M. et al. Interfacial ferroelectricity by van der Waals sliding. Science 372, 1462-1466 (2021).

30. Wang, X. et al. Interfacial ferroelectricity in rhombohedral-stacked bilayer transition metal dichalcogenides. Nat. Nanotechnol. 17, 367-371 (2022).

31. Wu, M. & Li, J. Sliding ferroelectricity in 2D van der Waals materials: related physics and future opportunities. Proc. Natl Acad. Sci. USA 118, e2115703118 (2021).

32. Deb, S. et al. Cumulative polarization in conductive interfacial ferroelectrics. Nature 612, 465-469 (2022).

33. Hovden, R. et al. Atomic lattice disorder in charge-density-wave phases of exfoliated dichalcogenides (1T-$TaS_2$). Proc. Natl Acad. Sci. USA 113, 11420-11424 (2016).

34. Liu, Y. et al. Superconductivity induced by Se-doping in layered charge-density-wave system 1T- $TaS_{2-x}Se_x$. Appl. Phys. Lett. 102, 192602 (2013).

35. Eda, G. et al. Coherent atomic and electronic heterostructures of single-layer $MoS_2$. ACS Nano 6, 7311-7317 (2012).

36. Yin, X. et al. Tunable inverted gap in monolayer quasi-metallic MoS2 induced by strong charge-lattice coupling. Nat. Commun. 8, 486 (2017).

37. Pollak, R. A. & Hughes, H. P. Charge density density wave phase transitions observed by X-ray photoemission. J. Phys. Colloq. 37, C4-151-155 (1976).

38. Hughes, H. P. & Scarfe, J. A. Site specific photohole screening in a charge density wave. Phys. Rev. Lett. 74, 3069-3072 (1995).

39. Wang, Z. et al. Surface-limited superconducting phase transition on 1T- $TaS_2$. ACS Nano 12, 12619-12628 (2018).

40. Zhu, X.-Y. et al. Realization of a metallic state in 1 T − $TaS_2$ with persisting long-range order of a charge density wave. Phys. Rev. Lett. 123, 206405 (2019).

41. Lin, H. et al. Scanning tunneling spectroscopic study of monolayer 1T- $TaS_2$ and 1T-$TaSe_2$. Nano Res. 13, 133-137 (2020).

42. Dong, J. et al. Electronic dispersion, correlations and stacking in the photoexcited state of 1T-TaS2. 2D Mater. 10, 045001 (2023).

43. Yu, Y. et al. Gate-tunable phase transitions in thin flakes of 1T-$TaS_2$. Nat. Nanotechnol. 10, 270-276 (2015).

44. Dong, J. et al. Dynamics of electronic states in the insulating intermediate surface phase of 1 T − $TaS_2$. Phys. Rev. B 108, 155145 (2023).

45. Cha, S. et al. Order-disorder phase transition driven by interlayer sliding in lead iodides. Nat. Commun. 14, 1981 (2023).

46. Zhang, W. & Wu, J. Stacking order and driving forces in the layered charge density wave phase of 1 $\mathrm{T}-\mathrm{MX}_2(\mathrm{M}=\mathrm{Nb}, \mathrm{Ta}$ and $\mathrm{X}=\mathrm{S}, \mathrm{Se})$. Mater. Res. Express 10, 046302 (2023).

47. Seah, M. P. & Dench, W. A. Quantitative electron spectroscopy of surfaces: a standard data base for electron inelastic mean free paths in solids. Surf. Interface Anal. 1, 2-11 (1979).

48. Inada, R., Ōnuki, Y. & Tanuma, S. Hall effect of 1 $\mathrm{T}-\mathrm{TaS}_2$. Phys. Lett. A 69, 453-456 (1979).

49. Stahl, Q. et al. Collapse of layer dimerization in the photo-induced hidden state of 1 $\mathrm{T}-\mathrm{TaS}_2$. Nat. Commun. 11, 1247 (2020).

50. Kim, J.-J., Yamaguchi, W., Hasegawa, T. & Kitazawa, K. Observation of Mott localization gap using low temperature scanning tunneling spectroscopy in commensurate $1T-\mathrm{TaS}_2$. Phys. Rev. Lett. 73, 2103-2106 (1994).

51. Cho, D., Cho, Y.-H., Cheong, S.-W., Kim, K.-S. & Yeom, H. W. Interplay of electron-electron and electron-phonon interactions in the low-temperature phase of 1 $\mathrm{T}-\mathrm{TaS}_2$. Phys. Rev. B 92, 085132 (2015).

52. Kancharla, S. S. & Okamoto, S. Band insulator to Mott insulator transition in a bilayer Hubbard model. Phys. Rev. B 75, 193103 (2007).

53. Wang, J., Cheng, F., Sun, Y., Xu, H. & Cao, L. Stacking engineering in layered homostructures: transitioning from 2D to 3D architectures. Phys. Chem. Chem. Phys. 26, 7988-8012 (2024).

54. Bu, K. et al. Possible strain induced Mott gap collapse in 1 $\mathrm{T}-\mathrm{TaS}_2$. Commun. Phys. 2, 146 (2019).

55. Shen, S. et al. Single-water-dipole-layer-driven reversible charge order transition in 1T-$\mathrm{TaS}_2$. Nano Lett. 20, 8854-8860 (2020).

56. Wang, W. et al. Electrical manipulation of skyrmions in a chiral magnet. Nat. Commun. 13, 1593 (2022).

57. Tang, J. et al. Magnetic skyrmion bundles and their current-driven dynamics. Nat. Nanotechnol. 16, 1086-1091 (2021).

58. Kresse, G. & Furthmüller, J. Efficient iterative schemes for ab initio total-energy calculations using a plane-wave basis set. Phys. Rev. B 54, 11169-11186 (1996).

59. Kresse, G. & Joubert, D. From ultrasoft pseudopotentials to the projector augmented-wave method. Phys. Rev. B 59, 1758-1775 (1999).

60. Perdew, J. P., Burke, K. & Ernzerhof, M. Generalized gradient approximation made simple. Phys. Rev. Lett. 77, 3865-3868 (1996).

61. Boix-Constant, C. et al. Out-of-plane transport of 1 $\mathrm{T}-\mathrm{TaS}_2$/ graphenebased van der Waals heterostructures. ACS Nano 15, 11898-11907 (2021).

62. Grimme, S., Ehrlich, S. & Goerigk, L. Effect of the damping function in dispersion corrected density functional theory. J. Comput. Chem. 32, 1456-1465 (2011).

63. Wang, V., Xu, N., Liu, J.-C., Tang, G. & Geng, W.-T. VASPKIT: a userfriendly interface facilitating high-throughput computing and analysis using VASP code. Comput. Phys. Commun. 267, 108033 (2021).

**References from Mottness collapse without metallisation in the domain walls of something**

# References


[1] E. Tosatti and P. Fazekas, "On the nature of the low-temperature phase of 1T-$TaS_2$," J. de Physique Colloques **37 (C4)**, 165 (1976).

[2] P. Fazekas and E. Tosatti, "Electrical, structural and magnetic properties of pure and doped 1T-$TaS_2$," Philos. Mag. B **39**, 229 (1979).

[3] P. Fazekas and E. Tosatti, "Charge carrier localization in pure and doped 1T-$TaS_2$," Physica B **99**, 183 (1980).

[4] R. E. Thomson, U. Walter, E. Ganz, J. Clarke, A. Zettl, P. Rauch, and F. J. DiSalvo, "Local charge-density-wave structure in 1T-$TaS_2$ determined by scanning tunneling microscopy," Phys. Rev. B **38**, 10734 (1988).

[5] P. W. Anderson, "Resonating valence bonds: a new kind of insulator?" Mater. Res. Bull. **8**, 153 (1973).

[6] Martin Klanjšek, Andrej Zorko, Rok Žitko, Jernej Mravlje, Zvonko Jagličić, Pabitra Kumar Biswas, Peter Prelovšek, Dragan Mihailovic, and Denis Arčon, "A new high-temperature quantum spin liquid with polaron spins," Nat. Phys. **13**, 1130 (2017).

[7] K. T. Law and P. A. Lee, "1T-$TaS_2$ as a quantum spin liquid," Proc. Natl. Acad. Sci. USA **114**, 6996 (2017).

[8] M. Kratochvilova, A. D. Hillier, A. R. Wildes, L. Wang, S.-W. Cheong, and J. G. Park, "The low-temperature highly correlated quantum phase in the charge-density-wave in 1$T$-$TaS_2$," Npj Quantum Mater. **2**, 42 (2017).

[9] A. Ribak, I. Silber, C. Baines, K. Chashka, Z. Salman, Y. Dagan, and A. Kanigel, "Gapless excitations in the ground state of 1T-$TaS_2$," Phys. Rev. B **96**, 195131 (2017).

[10] Y. J. Yu, Y. Xu, L. P. He, M. Kratochvilova, Y. Y. Huang, J. M. Ni, L. Wang, S.-W. Cheong, Je-Geun Park, and S. Y. Li, "Heat transport study of the spin liquid candidate 1$T$-$TaS_2$," Phys. Rev. B **96**, 081111(R) (2017).

[11] Y. Liu, R. Ang, W. J. Lu, W. H. Song, L. J. Li, and Y. P. Sun, "Superconductivity induced by Se-doping in layered charge-density-wave system 1T-$TaS_{2-x}Se_x$," Appl. Phys. Lett. **102**, 192602 (2013).

[12] L. J. Li, W.J. Lu, X.D. Zhu, L.S. Ling, Z. Qu, and Y. P. Sun, "Fe-doping–induced superconductivity in the charge-density-wave system 1T-$TaS_2$," European Physics Letters **97**, 67005 (2012).

[13] B. Sipos, A. F. Kusmartseva, A. Akrap, H. Berger, L. Forró, and E. Tutis, "From Mott state to superconductivity in 1T-$TaS_2$," Nat. Mater. **7**, 960 (2008).

[14] L. Stojchevska, I. Vaskivskyi, T. Mertelj, P. Kušar, D. Svetin, S. Brazovskii, and D. Mihailović, "Ultrafast switching to a stable hidden topologically protected quantum state in an electronic crystal," Science **344**, 177 (2014).

[15] M. Yoshida, R. Suzuki, Y. Zhang, M. Nakano, and Y. Iwasa, "Memristive phase switching in two-dimensional 1T-$TaS_2$ crystals," Sci. Adv. **1**, e1500606 (2015).

[16] I. Vaskivskyi, I. A. Mihailović, S. Brazovskii, J. Gospodarič, T. Mertelj, D. Svetin, P. Sutar, and D. Mihailovic, "Fast electronic resistance switching involving hidden charge density wave states," Nat. Commun. **7**, 11442 (2015).

[17] L. Ma, C. Ye, Y. Yu, X. F. Lu, X. Niu, S. Kim, D. Feng, D. Tománek, Y.-W. Son, X. H. Chen, and Y. Zhang, "A metallic mosaic phase and the origin of Mott-insulating state in 1T-$TaS_2$," Nat. Comms. **7**, 10956 (2016).

[18] D. Cho et al., "Nanoscale manipulation of the Mott insulating state coupled to charge order in 1T-$TaS_2$," Nat. Commun. **7**, 10453 (2016).

[19] D. Svetin, I. Vaskivskyi, Brazovskii S, and D. Mihailovic, "Three-dimensional resistivity and switching between correlated electronic states in 1T-$TaS_2$," Sci. Reports **7**, 46048 (2017).

[20] Yaroslav A. Gerasimenko, Igor Vaskivskyi, and Dragan Mihailovic, "Dual vortex charge order in a metastable state created by an ultrafast topological transition in 1T-$TaS_2$," arxiv:1704.08149 (2017).

[21] Yaroslav Gerasimenko, Igor Vaskivskyi, Jan Ravnik, Jaka Vodeb, Viktor V. Kabanov, and Dragan Mihailovic, "Ultrafast jamming of electrons into an amorphous entangled state," arxiv:1803.00255 (2018).

[22] Y. I. Joe, X. M. Chen, P. Ghaemi, K. D. Finkelstein, G. A. de La Peña, Y. Gan, J. C. T. Lee, S. Yuan, J. Geck, G. J. MacDougall, T. C. Chiang, S. L. Cooper, E. Fradkin, and P. Abbamonte, "Emergence of charge density wave domain walls above the superconducting dome in 1T-$TiSe_2$," Nat. Phys. **10**, 421 (2014).

[23] Shichao Yan, Davide Iaia, Emilia Morosan, Eduardo Fradkin, Peter Abbamonte, and Vidya Madhavan, "Influence of domain walls in the incommensurate charge density wave state of Cu intercalated 1T-$TiSe_2$," Phys. Rev. Lett. **118**, 106405 (2017).

[24] S. Qiao, X. Li, N. Wang, W. Ruan, C. Ye, P. Cai, Z. Hao, H. Yao, X. Chen, J. Wu, Y. Wang, and Z. Liu, "Orbital-driven Mottness collapse in 1T-$TaS_{2-x}Se_x$ transition metal dichalcogenide," Phys. Rev. X **7**, 041054 (2017).

[25] Doohee Cho, Gyeongcheol Gye, Jinwon Lee, Sung-Hoon Lee, Lihai Wang, Sang-Wook Cheong, and Han Woong Yeom, "Correlated electronic states at domain walls of a Mott-charge-density-wave insulator 1T-$TaS_2$," Nat. Comm. **8**, 392 (20176).

[26] K. Rossnagel, "On the origin of charge-density waves in select layered transition-metal dichalcogenides," J. Phys.: Condens. Matter **23**, 213001 (2011).

[27] P. Darancet, A. J. Millis, and C. A. Marianetti, "Three-dimensional metallic and two-dimensional insulating behavior in octahedral tantalum dichalcogenides," Phys. Rev. B **90**, 045134 (2014).

[28] Ju-Jin Kim, W. Yamaguchi, T. Hasegawa, and K. Kitazawa, "Observation of Mott localization gap using low temperature scanning tunneling spectroscopy in commensuare 1T-$TaS_2$," Phys. Rev. Lett. **73**, 2103 (1994).

[36] L. Perfetti, P. A. Loukakos, M. Lisowski, U. Bovensiepen, H. Berger, S. Biermann, P. S. Cornaglia, A. Georges, and M. Wolf, "Time evolution of the electronic structure of 1T-$TaS_2$ through the insulator-metal transition," Phys. Rev. Lett. **97**, 067402 (2006).

[30] L. Perfetti, P. A. Loukakos, M. Lisowski, U. Bovensiepen, M. Wolf, H. Berger, S. Biermann, and A. Georges, "Femtosecond dynamics of electronic states in the Mott insulator 1T-$TaS_2$ by time resolved photoelectron spectroscopy," New J. Phys. **10**, 053019 (2008).

[31] M. Ligges, I. Avigo, D. Golež, H. U. R. Strand, L. Stojchevska, M. Malläne, K. Rossnagel, M. Eckstein, P. Werner, and U. Bovensiepen, "Ultrafast doublon dynamics in photoexcited 1T-$TaS_2$," arXiv:1702.05300 (2017).

[32] P. Karpov and S. Brazovskii, "Modeling of networks and globules of charged domain walls observed in pump and pulse induced states," Scientific Reports **8**, 4043 (2018).

[33] Masatoshi Imada, Atsushi Fujimori, and Yoshinori Tokura, "Metal-insulator transitions," Rev. Mod. Phys. **70**, 1039 (1998).

[34] F. Gebhardt, *The Mott metal-insulator transition* (Springer, Berlin, 1997).

[35] K. Aryanpour, W. E. Pickett, and R. T. Scalettar, "Dynamical mean-field study of the Mott transition in the half-filled hubbard model on a triangular lattice," Phys. Rev. B **74**, 085117 (2006).

[36] L. Perfetti, T. A. Gloor, F. Mila, H. Berger, and M. Grioni, "Unexpected periodicity in the quasi-two-dimensional Mott insulator $1T$-$TaS_2$ revealed by angle-resolved photoemission," Phys. Rev. B **71**, 153101 (2005).

[37] J. K. Freericks, H. R. Krishnamurthy, Y. Ge, A. Y. Liu, and Th. Pruschke, "Theoretical description of time-resolved pump/probe photoemission in $TaS_2$: a single-band DFT+DMFT(NRG) study within the quasiequilibrium approximation," Phys. Status Solidi B **256**, 948 (2009).

[38] T. Yoshioka, A. Koga, and N. Kawakami, "Quantum phase transitions in the Hubbard model on a triangular lattice," Phys. Rev. Lett. **103**, 036401 (2009).

[39] Tomonori Shirakawa, Takami Tohyama, Jure Kokalj, Sigetoshi Sota, and Seiji Yunoki, "Ground-state phase diagram of the triangular lattice Hubbard model by the density-matrix renormalization group method," Phys. Rev. B **96**, 205130 (2017).

[40] Antoine Georges, Gabriel Kotliar, Werner Krauth, and Marcelo J. Rozenberg, "Dynamical mean-field theory of strongly correlated fermion systems and the limit of infinite dimensions," Rev. Mod. Phys. **68**, 13 (1996).

[41] M. Potthoff and W. Nolting, "Surface metal-insulator transition in the Hubbard model," Phys. Rev. B **59**, 2549 (1999).

[42] M. Potthoff and W. Nolting, "Metallic surface of a Mott insulator–Mott insulating surface of a metal," Phys. Rev. B **60**, 7834 (1999).

[43] M. Potthoff and W. Nolting, "Dynamical mean-field study of the Mott transition in thin films," Eur. Phys. J. B **8**, 555 (1999).

[44] J. K. Freericks, "Dynamical mean-field theory for strongly correlated inhomogeneous multilayered nanostructures," Phys. Rev. B **70**, 195342 (2004).

[45] J. Freericks, *Transport in Multilayered Nanostructures: The Dynamical Mean-field Theory Approach* (Imperial College Press, London, 2006).

[46] S. Okamoto and A. J. Millis, "Spatial inhomogeneity and strong correlation physics: A dynamical mean-field study of a model mott-insulator–band-insulator heterostructure," Phys. Rev. B **70**, 241104(R) (2004).

[47] R. W. Helmes, T. A. Costi, and A. Rosch, "Kondo Proximity Effect: How Does a Metal Penetrate into a Mott Insulator?" Phys. Rev. Lett. **101**, 066802 (2008).

[48] M. Jiang, G. G. Batrouni, and R. T. Scalettar, "Density of states and magnetic correlations at a metal-Mott insulator interface," Phys. Rev. B **86**, 195117 (2012).

[49] Juho Lee and Chuck-Hou Yee, "Interfaces in coexisting metals and Mott insulators," Phys. Rev. B **95**, 205126 (2017).

[50] P. Bakalov, D. Nasr Esfahani, L. Covaci, F. M. Peeters, J. Tempere, and J.-P. Locquet, "Electric-field-driven Mott metal-insulator transition in correlated thin films: An inhomogeneous dynamical mean-field theory approach," Phys. Rev. B **93**, 165112 (2016).

[51] Antoine Georges and Werner Krauth, "Numerical solution of the $d = \infty$ Hubbard model: Evidence for a Mott transition," Phys. Rev. Lett. **69**, 1240 (1992).

[52] X. Y. Zhang, M. J. Rozenberg, and G. Kotliar, "Mott transition in the d=$\infty$ Hubbard model at zero temperature," Phys. Rev. Lett. **70**, 1666 (1993).

[53] P. Werner and A. J. Millis, "Doping-driven Mott transition in the one-band Hubbard model," Phys. Rev. B **75**, 085108 (2007).

[54] R. Žitko, D. Hansen, E. Perepelitsky, J. Mravlje, A. Georges, and B. S. Shastry, "Extremely correlated Fermi liquid theory meets dynamical mean-field theory: Analytical insights into the doping-driven Mott transition," Phys. Rev. B **88**, 235132 (2013).

[55] D. E. Logan and M. R. Galpin, "Mott insulators and the doping-induced Mott transition within DMFT: exact results for the one-band Hubbard model," J. Phys.: Condens. Matter **28**, 025601 (2016).

[56] T. Ritschel, J. Trinckauf, K. Koepernik, B. Buchner, M. von Zimmermann, H. Berger, Y. I. Joe, P. Abbamonte, and J. Geck, "Orbital textures and charge density waves in transition metal dichalcogenides," Nature Phys. **11**, 328 (2015).

[1] Volker Heine, " $s-d$ interaction in transition metals," Phys. Rev. 153, 673-682 (1967).

[2] K. Rossnagel and N. V. Smith, "Spin-orbit coupling in the band structure of reconstructed 1T-TaS $_2$," Phys. Rev. B 73, 073106 (2006).

[3] L. Ma, C. Ye, Y. Yu, X. F. Lu, X. Niu, S. Kim, D. Feng, D. Tománek, Y.-W. Son, X. H. Chen, and Y. Zhang, "A metallic mosaic phase and the origin of Mott-insulating state in 1T-$TaS_2$," Nat. Comms. 7, 10956 (2016).

[4] R. W. Helmes, T. A. Costi, and A. Rosch, "Kondo Proximity Effect: How Does a Metal Penetrate into a Mott Insulator?" Phys. Rev. Lett. 101, 066802 (2008).

[5] P. Bakalov, D. Nasr Esfahani, L. Covaci, F. M. Peeters, J. Tempere, and J.-P. Locquet, "Electric-field-driven Mott metalinsulator transition in correlated thin films: An inhomogeneous dynamical mean-field theory approach," Phys. Rev. B 93, 165112 (2016).

[6] Juho Lee and Chuck-Hou Yee, "Interfaces in coexisting metals and Mott insulators," Phys. Rev. B 95, 205126 (2017).

[7] H. Ishida and A. Liebsch, "Embedding approach for dynamical mean-field theory of strongly correlated heterostructures," Phys. Rev. B 79, 045130 (2009).

[8] H. Ishida and A. Liebsch, "Cluster dynamical mean-field study of strongly correlated heterostructures: Correlation-induced reduction of proximity effect," Phys. Rev. B 82, 045107 (2010).

[9] M. Settnes, S. R. Power, J. Lin, D. H. Petersen, and A.-P. Jauho, "Patched green's function techniques for two-dimensional systems: Electronic behavior of bubbles and perforations in graphene," Phys. Rev. B 91, 125408 (2014).

[10] M. M. Odashima, B. G. Prado, and E. Vernek, "Pedagogical introduction to equilibrium Green's functions: condensedmatter examples with numerical implementations," Rev. Bras. Ens. Fis. 39, 1303 (2017).

[11] K. G. Wilson, "The renormalization group: Critical phenomena and the Kondo problem," Rev. Mod. Phys. 47, 773 (1975).

[12] Ralf Bulla, Theo Costi, and Thomas Pruschke, "The numerical renormalization group method for quantum impurity systems," Rev. Mod. Phys. 80, 395 (2008).

**References from Emergent quantum phenomena in two-dimensional 1T-TaS $_2$ by Chen, Sun, Chen**

1. Wilson JA, Di Salvo FJ, Mahajan S (1975) Charge-density waves and superlattices in the metallic layered transition metal dichalcogenides. Advances in Physics 24:117-201. https://doi.org/10.1080/00018737500101391

2. Grüner G (1988) The dynamics of charge-density waves. Rev Mod Phys 60:1129-1181. https://doi.org/10.1103/RevModPhys.60.1129

3. Rossnagel K (2011) On the origin of charge-density waves in select layered transition-metal dichalcogenides. J Phys: Condens Matter 23:213001. https://doi.org/10.1088/0953-8984/23/21/213001

4. Eichberger M, Schäfer H, Krumova M, Beyer M, Demsar J, Berger H, Moriena G, Sciaini G, Miller RJD (2010) Snapshots of cooperative atomic motions in the optical suppression of charge density waves. Nature 468:799-802. https://doi.org/10.1038/nature09539

5. Voiry D, Mohite A, Chhowalla M (2015) Phase engineering of transition metal dichalcogenides. Chem Soc Rev 44:2702-2712. https://doi.org/10.1039/C5CS00151J

6. Han GH, Duong DL, Keum DH, Yun SJ, Lee YH (2018) van der Waals Metallic Transition Metal Dichalcogenides. Chem Rev 118:6297-6336. https://doi.org/10.1021/acs.chemrev.7b00618

7. Qian X, Liu J, Fu L, Li J (2014) Quantum spin Hall effect in two-dimensional transition metal dichalcogenides. Science 346:1344-1347. https://doi.org/10.1126/science. 1256815

8. Wu S, Fatemi V, Gibson QD, Watanabe K, Taniguchi T, Cava RJ, Jarillo-Herrero P (2018) Observation of the quantum spin Hall effect up to 100 kelvin in a monolayer crystal. Science 359:76-79. https://doi.org/10.1126/science.aan6003

9. Chen P, Pai WW, Chan Y-H, Sun W-L, Xu C-Z, Lin D-S, Chou MY, Fedorov A-V, Chiang T-C (2018) Large quantum-spin-Hall gap in single-layer 1T' $WSe_2$. Nat Commun 9:2003. https://doi.org/10.1038/s41467-018-04395-2

10. Sipos B, Kusmartseva AF, Akrap A, Berger H, Forró L, Tutiš E (2008) From Mott state to superconductivity in 1T-$TaS_2$. Nature Mater 7:960-965. https://doi.org/10.1038/nmat2318

11. Morosan E, Zandbergen HW, Dennis BS, Bos JWG, Onose Y, Klimczuk T, Ramirez AP, Ong NP, Cava RJ (2006) Superconductivity in $Cu_xTiSe_2$. Nature Phys 2:544-550. https://doi.org/10.1038/nphys360

12. Chen P, Chan Y-H, Fang X-Y, Zhang Y, Chou MY, Mo S-K, Hussain Z, Fedorov A-V, Chiang T-C (2015) Charge density wave transition in single-layer titanium diselenide. Nat Commun 6:8943. https://doi.org/10.1038/ncomms9943

13. Gao Q, Chan Y, Wang Y, Zhang H, Jinxu P, Cui S, Yang Y, Liu Z, Shen D, Sun Z, Jiang J, Chiang TC, Chen P (2023) Evidence of high-temperature exciton condensation in a two-dimensional semimetal. Nat Commun 14:994. https://doi.org/10.1038/s41467-023-36667-x

14. Gao Q, Chan Y, Jiao P, Chen H, Yin S, Tangprapha K, Yang Y, Li X, Liu Z, Shen D, Jiang S, Chen P (2024) Observation of possible excitonic charge density waves and metal-insulator transitions in atomically thin semimetals. Nat Phys 20:597-602. https://doi.org/10.1038/s41567-023-02349-0

15. Kogar A, Rak MS, Vig S, Husain AA, Flicker F, Joe YI, Venema L, MacDougall GJ, Chiang TC, Fradkin E, Van Wezel J, Abbamonte P (2017) Signatures of exciton condensation in a transition metal dichalcogenide. Science 358:1314-1317. https://doi.org/10.1126/science.aam6432

16. Ribak A, Skiff RM, Mograbi M, Rout PK, Fischer MH, Ruhman J, Chashka K, Dagan Y, Kanigel A (2020) Chiral superconductivity in the alternate stacking compound 4Hb-$TaS_2$. Sci Adv 6: 9480. https://doi.org/10.1126/sciadv.aax9480

17. Achari A, Bekaert J, Sreepal V, Orekhov A, Kumaravadivel P, Kim M, Gauquelin N, Balakrishna Pillai P, Verbeeck J, Peeters FM, Geim AK, Milošević MV, Nair RR (2022) Alternating Superconducting and Charge Density Wave Monolayers within Bulk 6R-$TaS_2$. Nano Lett 22:6268-6275. https://doi.org/10.1021/acs.nanolett.2c01851

18. Yang HF, He KY, Koo J, Shen SW, Zhang SH, Liu G, Liu YZ, Chen C, Liang AJ, Huang K, Wang

    MX, Gao JJ, Luo X, Yang LX, Liu JP, Sun YP, Yan SC, Yan BH, Chen YL, Xi X, Liu ZK (2022) Visualization of Chiral Electronic Structure and Anomalous Optical Response in a Material with Chiral Charge Density Waves. Phys Rev Lett 129:156401. https://doi.org/10.1103/PhysRevLett.129.156401

19. Almoalem A, Gofman R, Nitzav Y, Mangel I, Feldman I, Koo J, Mazzola F, Fujii J, Vobornik I, Sánchez-Barriga J, Clark OJ, Plumb NC, Shi M, Yan B, Kanigel A (2024) Charge transfer and spinvalley locking in 4 Hb- $TaS_2$. npj Quantum Mater 9:36. https://doi.org/10.1038/s41535-024-00646-2

20. Camerano L, Mastrippolito D, Pierucci D, Dai J, Tallarida M, Ottaviano L, Profeta G, Bisti F (2025) Darkness in interlayer and charge density wave states of $2H - TaS_2$. Phys Rev B 111: 121112. https://doi.org/10.1103/PhysRevB.111.L121112

21. Lazar P, Martincová J, Otyepka M (2015) Structure, dynamical stability, and electronic properties of phases in $TaS_2$ from a high-level quantum mechanical calculation. Phys Rev B 92:224104. https://doi.org/10.1103/PhysRevB.92.224104

22. Lin H, Huang W, Zhao K, Lian C, Duan W, Chen X, Ji S-H (2018) Growth of atomically thick transition metal sulfide filmson graphene/6H-SiC(0001) by molecular beam epitaxy. Nano Res 11:4722-4727. https://doi.org/10.1007/s12274-018-2054-4

23. Lin H, Huang W, Zhao K, Qiao S, Liu Z, Wu J, Chen X, Ji S-H (2020) Scanning tunneling spectroscopic study of monolayer 1T- $TaS_2$ and 1T-TaSe $_2$. Nano Res 13:133-137. https://doi.org/10.1007/s12274-019-2584-4

24. Wang X, Liu H, Wu J, Lin J, He W, Wang H, Shi X, Suenaga K, Xie L (2018) Chemical Growth of $1\ T - TaS_2$ Monolayer and Thin Films: Robust Charge Density Wave Transitions and High Bolometric Responsivity. Advanced Materials 30:1800074. https://doi.org/10.1002/adma. 201800074

25. Sanders CE, Dendzik M, Ngankeu AS, Eich A, Bruix A, Bianchi M, Miwa JA, Hammer B, Khajetoorians AA, Hofmann P (2016) Crystalline and electronic structure of single-layer $TaS_2$. Phys Rev B 94:081404. https://doi.org/10.1103/PhysRevB.94.081404

26. Li H, Li Y, Aljarb A, Shi Y, Li L-J (2018) Epitaxial Growth of Two-Dimensional Layered Transition-Metal Dichalcogenides: Growth Mechanism, Controllability, and Scalability. Chem Rev 118:6134-6150. https://doi.org/10.1021/acs.chemrev.7b00212

27. Chhowalla M, Shin HS, Eda G, Li L-J, Loh KP, Zhang H (2013) The chemistry of two-dimensional layered transition metal dichalcogenide nanosheets. Nature Chem 5:263-275. https://doi.org/10.1038/nchem. 1589

28. Nakata Y, Sugawara K, Chainani A, Oka H, Bao C, Zhou S, Chuang P-Y, Cheng C-M, Kawakami T, Saruta Y, Fukumura T, Zhou S, Takahashi T, Sato T (2021) Robust charge-density wave strengthened by electron correlations in monolayer 1T-TaSe $_2$ and 1T-NbSe $_2$. Nat Commun 12:5873.

https://doi.org/10.1038/s41467-021-26105-1

29. Fu W, Chen Y, Lin J, Wang X, Zeng Q, Zhou J, Zheng L, Wang H, He Y, He H, Fu Q, Suenaga K, Yu T, Liu Z (2016) Controlled Synthesis of Atomically Thin 1T-TaS $_2$ for Tunable Charge Density Wave Phase Transitions. Chem Mater 28:7613-7618. https://doi.org/10.1021/acs.chemmater.6b02334

30. Chen H, Wang F-H, Gao Q, Gao X-J, Chen Z, Huang Y, Law KT, Xu XY, Chen P (2025) Spectroscopic Evidence for Possible Quantum Spin Liquid Behavior in a Two-Dimensional Mott Insulator. Phys Rev Lett 134:066402. https://doi.org/10.1103/PhysRevLett.134.066402

31. Di Salvo FJ, Wilson JA, Bagley BG, Waszczak JV (1975) Effects of doping on charge-density waves in layer compounds. Phys Rev B 12:2220-2235.

https://doi.org/10.1103/PhysRevB.12.2220
32. Scruby CB, Williams PM, Parry GS (1975) The role of charge density waves in structural transformations of 1T $TaS_2$. Philosophical Magazine 31:255-274. https://doi.org/10.1080/14786437508228930
33. Thomson RE, Walter U, Ganz E, Clarke J, Zettl A, Rauch P, DiSalvo FJ (1988) Local chargedensity-wave structure in $1\ T - TaS_2$ determined by scanning tunneling microscopy. Phys Rev B 38:10734-10743. https://doi.org/10.1103/PhysRevB.38.10734
34. Mott NF (1968) Metal-Insulator Transition. Rev Mod Phys 40:677-683. https://doi.org/10.1103/RevModPhys. 40.677
35. Fazekas P, Tosatti E (1979) Electrical, structural and magnetic properties of pure and doped 1T-$TaS_2$. Philosophical Magazine B 39:229-244. https://doi.org/10.1080/13642817908245359
36. Ritschel T, Trinckauf J, Koepernik K, Büchner B, Zimmermann MV, Berger H, Joe YI, Abbamonte P, Geck J (2015) Orbital textures and charge density waves in transition metal dichalcogenides. Nature Phys 11:328-331. https://doi.org/10.1038/nphys3267
37. Lee S-H, Goh JS, Cho D (2019) Origin of the Insulating Phase and First-Order Metal-Insulator Transition in 1T- $TaS_2$. Phys Rev Lett 122:106404. https://doi.org/10.1103/PhysRevLett.122.106404
38. Wen C, Gao J, Xie Y, Zhang Q, Kong P, Wang J, Jiang Y, Luo X, Li J, Lu W, Sun Y-P, Yan S (2021) Roles of the Narrow Electronic Band near the Fermi Level in $1\ T - TaS_2-$ Related Layered Materials. Phys Rev Lett 126:256402. https://doi.org/10.1103/PhysRevLett.126.256402
39. Butler CJ, Yoshida M, Hanaguri T, Iwasa Y (2020) Mottness versus unit-cell doubling as the driver of the insulating state in 1T-$TaS_2$. Nat Commun 11:2477. https://doi.org/10.1038/s41467-020-16132-9
40. Lee J, Jin K-H, Yeom HW (2021) Distinguishing a Mott Insulator from a Trivial Insulator with Atomic Adsorbates. Phys Rev Lett 126:196405. https://doi.org/10.1103/PhysRevLett.126.196405
41. Anderson PW (1973) Resonating valence bonds: A new kind of insulator? Materials Research
Bulletin 8:153-160. https://doi.org/10.1016/0025-5408(73)90167-0

42. Yoshida M, Suzuki R, Zhang Y, Nakano M, Iwasa Y (2015) Memristive phase switching in twodimensional 1T-$TaS_2$ crystals. Sci Adv 1:e1500606. https://doi.org/10.1126/sciadv.1500606

43. Zhao Y, Nie Z, Hong H, Qiu X, Han S, Yu Y, Liu M, Qiu X, Liu K, Meng S, Tong L, Zhang J (2023) Spectroscopic visualization and phase manipulation of chiral charge density waves in 1T-$TaS_2$. Nat Commun 14:2223. https://doi.org/10.1038/s41467-023-37927-6

44. Lee D, Jin K-H, Liu F, Yeom HW (2022) Tunable Mott Dirac and Kagome Bands Engineered on 1T-$TaS_2$. Nano Lett 22:7902-7909. https://doi.org/10.1021/acs.nanolett.2c02866

45. Luo X, Obeysekera D, Won C, Sung SH, Schnitzer N, Hovden R, Cheong S-W, Yang J, Sun K, Zhao L (2021) Ultrafast Modulations and Detection of a Ferro-Rotational Charge Density Wave Using Time-Resolved Electric Quadrupole Second Harmonic Generation. Phys Rev Lett 127:126401. https://doi.org/10.1103/PhysRevLett.127.126401

46. Liu G, Qiu T, He K, Liu Y, Lin D, Ma Z, Huang Z, Tang W, Xu J, Watanabe K, Taniguchi T, Gao L, Wen J, Liu J-M, Yan B, Xi X (2023) Electrical switching of ferro-

rotational order in nanometrethick 1 T − $TaS_2$ crystals. Nat Nanotechnol 18:854-860. https://doi.org/10.1038/s41565-023-01403-5

47. Hollander MJ, Liu Y, Lu W-J, Li L-J, Sun Y-P, Robinson JA, Datta S (2015) Electrically Driven Reversible Insulator-Metal Phase Transition in 1T-TaS $_2$. Nano Lett 15:1861-1866. https://doi.org/10.1021/n1504662b

48. Zong A, Shen X, Kogar A, Ye L, Marks C, Chowdhury D, Rohwer T, Freelon B, Weathersby S, Li R, Yang J, Checkelsky J, Wang X, Gedik N (2018) Ultrafast manipulation of mirror domain walls in a charge density wave. Sci Adv 4: 5501. https://doi.org/10.1126/sciadv.aau5501

49. Stahl Q, Kusch M, Heinsch F, Garbarino G, Kretzschmar N, Hanff K, Rossnagel K, Geck J, Ritschel T (2020) Collapse of layer dimerization in the photo-induced hidden state of 1T-TaS $_2$. Nat Commun 11:1247. https://doi.org/10.1038/s41467-020-15079-1

50. Kumar V, Singh B, Kumar P (2025) Hidden Quantum State and Signature of Mott Transition in 2D 1T-TaS $_2$. Physica Rapid Research Ltrs 19:2500056. https://doi.org/10.1002/pssr. 202500056

51. Vaskivskyi I, Gospodaric J, Brazovskii S, Svetin D, Sutar P, Goreshnik E, Mihailovic IA, Mertelj T, Mihailovic D (2015) Controlling the metal-to-insulator relaxation of the metastable hidden quantum state in 1T-TaS $_2$. Sci Adv 1:1500168. https://doi.org/10.1126/sciadv. 1500168

52. Sun K, Sun S, Zhu C, Tian H, Yang H, Li J (2018) Hidden CDW states and insulator-to-metal transition after a pulsed femtosecond laser excitation in layered chalcogenide 1T-$TaS_{2-x}Se_x$. Sci Adv 4: 9660. https://doi.org/10.1126/sciadv.aas9660

53. Wen W, Dang C, Xie L (2019) Photoinduced phase transitions in two-dimensional charge-densitywave 1T-TaS $_2$. Chinese Phys B 28:058504. https://doi.org/10.1088/1674-1056/28/5/058504

54. De La Torre A, Wang Q, Masoumi Y, Campbell B, Riffle JV, Balasundaram D, Vora PM, Ruff JPC, Fiete GA, Hollen SM, Plumb KW (2025) Dynamic phase transition in 1 T − $TaS_2$ via a thermal quench. Nat Phys. https://doi.org/10.1038/s41567-025-02938-1

55. Gao Q, Chen H, Lu W, Chan Y, Chen Z, Huang Y, Liu Z, Chen P (2025) Orbital textures and evolution of correlated insulating state in monolayer 1T phase transition metal dichalcogenides. Nat Commun 16:3784. https://doi.org/10.1038/s41467-025-59228-w

56. Yang Q, Shi W, Zhong Z, Li X, Li Y, Meng X, Wang J, Chu J, Huang H (2024) Current-Driven to Thermally Driven Multistep Phase Transition of Charge Density Wave Order in 1T-TaS $_2$. Nano Lett 24:16417-16425. https://doi.org/10.1021/acs.nanolett.4c05302

57. Yu Y, Yang F, Lu XF, Yan YJ, Cho Y-H, Ma L, Niu X, Kim S, Son Y-W, Feng D, Li S, Cheong S-W, Chen XH, Zhang Y (2015) Gate-tunable phase transitions in thin flakes of 1T-TaS $_2$. Nature Nanotech 10:270-276. https://doi.org/10.1038/nnano.2014.323

58. Ramos SLLM, Plumadore R, Boddison-Chouinard J, Hla SW, Guest JR, Gosztola DJ, Pimenta MA, Luican-Mayer A (2019) Suppression of the commensurate charge density wave phase in ultrathin 1 T − $TaS_2$ evidenced by Raman hyperspectral analysis. Phys Rev B 100:165414. https://doi.org/10.1103/PhysRevB.100.165414

59. Ang R, Tanaka Y, Ieki E, Nakayama K, Sato T, Li LJ, Lu WJ, Sun YP, Takahashi T (2012) Real-Space Coexistence of the Melted Mott State and Superconductivity in Fe-Substituted 1T- $TaS_2$. Phys Rev Lett 109:176403. https://doi.org/10.1103/PhysRevLett.109.176403

60. Ang R, Miyata Y, Ieki E, Nakayama K, Sato T, Liu Y, Lu WJ, Sun YP, Takahashi T (2013) Superconductivity and bandwidth-controlled Mott metal-insulator transition in 1T-TaS $_{2-x}Se_x$. Phys Rev B 88:115145. https://doi.org/10.1103/PhysRevB.88.115145

61. Kivelson SA, Bindloss IP, Fradkin E, Oganesyan V, Tranquada JM, Kapitulnik A, Howald C (2003) How to detect fluctuating stripes in the high-temperature superconductors. Rev Mod Phys 75:1201-1241. https://doi.org/10.1103/RevModPhys.75.1201

62. Merino J, McKenzie RH (2001) Superconductivity Mediated by Charge Fluctuations in Layered Molecular Crystals. Phys Rev Lett 87:237002. https://doi.org/10.1103/PhysRevLett.87.237002

63. Lee PA, Nagaosa N, Wen X-G (2006) Doping a Mott insulator: Physics of high-temperature superconductivity. Rev Mod Phys 78:17-85. https://doi.org/10.1103/RevModPhys.78.17

64. Kratochvilova M, Hillier AD, Wildes AR, Wang L, Cheong S-W, Park J-G (2017) The lowtemperature highly correlated quantum phase in the charge-density-wave 1T-TaS $_2$ compound. npj Quant Mater 2:42. https://doi.org/10.1038/s41535-017-0048-1

65. Qiao S, Li X, Wang N, Ruan W, Ye C, Cai P, Hao Z, Yao H, Chen X, Wu J, Wang Y, Liu Z (2017) Mottness Collapse in $1\ T - TaS_{2-x}Se_x$ Transition-Metal Dichalcogenide: An Interplay between Localized and Itinerant Orbitals. Phys Rev X 7:041054. https://doi.org/10.1103/PhysRevX.7.041054

66. Rossnagel K, Smith NV (2006) Spin-orbit coupling in the band structure of reconstructed 1T- $TaS_2$. Phys Rev B 73:073106. https://doi.org/10.1103/PhysRevB.73.073106

67. Perfetti L, Gloor TA, Mila F, Berger H, Grioni M (2005) Unexpected periodicity in the quasi-twodimensional Mott insulator 1T- $TaS_2$ revealed by angle-resolved photoemission. Phys Rev B 71:153101. https://doi.org/10.1103/PhysRevB.71.153101

68. Wang YD, Yao WL, Xin ZM, Han TT, Wang ZG, Chen L, Cai C, Li Y, Zhang Y (2020) Band insulator to Mott insulator transition in 1T-TaS $_2$. Nat Commun 11:4215. https://doi.org/10.1038/s41467-020-18040-4

69. Ritschel T, Berger H, Geck J (2018) Stacking-driven gap formation in layered 1T-TaS $_2$. Phys Rev B 98:195134. https://doi.org/10.1103/PhysRevB.98.195134

70. Ligges M, Avigo I, Golež D, Strand HUR, Beyazit Y, Hanff K, Diekmann F, Stojchevska L, Kalläne M, Zhou P, Rossnagel K, Eckstein M, Werner P, Bovensiepen U (2018) Ultrafast Doublon Dynamics in Photoexcited 1T-TaS $_2$. Phys Rev Lett 120:166401. https://doi.org/10.1103/PhysRevLett.120.166401

71. Sato H, Arita M, Utsumi Y, Mukaegawa Y, Sasaki M, Ohnishi A, Kitaura M, Namatame H, Taniguchi M (2014) Conduction-band electronic structure of 1 T - $TaS_2$ revealed by angle-resolved inverse-photoemission spectroscopy. Phys Rev B 89:155137. https://doi.org/10.1103/PhysRevB.89.155137

72. Wu Z, Bu K, Zhang W, Fei Y, Zheng Y, Gao J, Luo X, Liu Z, Sun Y-P, Yin Y (2022) Effect of stacking order on the electronic state of 1 T − $TaS_2$. Phys Rev B 105:035109. https://doi.org/10.1103/PhysRevB.105.035109

73. Ma L, Ye C, Yu Y, Lu XF, Niu X, Kim S, Feng D, Tománek D, Son Y-W, Chen XH, Zhang Y (2016) A metallic mosaic phase and the origin of Mott-insulating state in 1T-$TaS_2$. Nat Commun 7:10956. https://doi.org/10.1038/ncomms10956

74. Zhang W, Wu Z, Bu K, Fei Y, Zheng Y, Gao J, Luo X, Liu Z, Sun Y-P, Yin Y (2022) Reconciling the bulk metallic and surface insulating state in 1T- $TaSe_2$. Phys Rev B 105:035110. https://doi.org/10.1103/PhysRevB.105.035110

75. Tian N, Huang Z, Jang BG, Guo S, Yan Y-J, Gao J, Yu Y, Hwang J, Tang C, Wang M, Luo X, Sun YP, Liu Z, Feng D-L, Chen X, Mo S-K, Kim M, Son Y-W, Shen D, Ruan W, Zhang Y (2024) Dimensionality-driven metal to Mott insulator transition in two-dimensional 1T-$TaSe_2$. National Science Review 11:144. https://doi.org/10.1093/nsr/nwad144

76. Perfetti L, Georges A, Florens S, Biermann S, Mitrovic S, Berger H, Tomm Y, Höchst H, Grioni M (2003) Spectroscopic Signatures of a Bandwidth-Controlled Mott Transition at the Surface of 1 T-$TaSe_2$. Phys Rev Lett 90:166401. https://doi.org/10.1103/PhysRevLett.90.166401

77. Straub M, Petocchi F, Witteveen C, Kugler FB, Hunter A, Alexanian Y, Gatti G, Mandloi S, Polley C, Carbone G, Osiecki J, Von Rohr FO, Georges A, Baumberger F, Tamai A (2025) Nature of

    Metallic and Insulating Domains in the Charge-Density-Wave System 1T- $TaSe_2$. Phys Rev Lett 135:096501. https://doi.org/10.1103/pbyw-mzfy

78. Vaňo V, Amini M, Ganguli SC, Chen G, Lado JL, Kezilebieke S, Liljeroth P (2021) Artificial heavy fermions in a van der Waals heterostructure. Nature 599:582-586. https://doi.org/10.1038/s41586-021-04021-0

79. Tian Q, Ding C, Qiu X, Meng Q, Wang K, Yu F, Mu Y, Wang C, Sun J, Zhang Y (2024) Electronic structures and Mott state of epitaxial $TaS_2$ monolayers. Sci China Phys Mech Astron 67:256811. https://doi.org/10.1007/s11433-023-2328-1

80. Balents L (2010) Spin liquids in frustrated magnets. Nature 464:199-208. https://doi.org/10.1038/nature08917

81. Law KT, Lee PA (2017) 1T-$TaS_2$ as a quantum spin liquid. Proc Natl Acad Sci USA 114:6996-7000. https://doi.org/10.1073/pnas. 1706769114

82. Pal S, Roy SB (2022) Understanding the magnetic response of the Quantum Spin Liquid compound 1T-$TaS_2$. Physica B: Condensed Matter 643:414121. https://doi.org/10.1016/j.physb.2022.414121

83. Ribak A, Silber I, Baines C, Chashka K, Salman Z, Dagan Y, Kanigel A (2017) Gapless excitations in the ground state of 1 T − $TaS_2$. Phys Rev B 96:195131. https://doi.org/10.1103/PhysRevB.96.195131

84. Murayama H, Sato Y, Taniguchi T, Kurihara R, Xing XZ, Huang W, Kasahara S, Kasahara Y, Kimchi I, Yoshida M, Iwasa Y, Mizukami Y, Shibauchi T, Konczykowski M, Matsuda Y (2020) Effect of quenched disorder on the quantum spin liquid state of the triangular-lattice antiferromagnet 1T- $TaS_2$. Phys Rev Research 2:013099. https://doi.org/10.1103/PhysRevResearch.2.013099

85. Klanjšek M, Zorko A, Žitko R, Mravlje J, Jagličić Z, Biswas PK, Prelovšek P, Mihailovic D, Arčon D (2017) A high-temperature quantum spin liquid with polaron spins. Nature Phys 13:1130-1134. https://doi.org/10.1038/nphys4212

86. Yu YJ, Xu Y, He LP, Kratochvilova M, Huang YY, Ni JM, Wang L, Cheong S-W, Park J-G, Li SY (2017) Heat transport study of the spin liquid candidate 1T- $TaS_2$. Phys Rev B 96:081111. https://doi.org/10.1103/PhysRevB.96.081111

87. Tang E, Fisher MPA, Lee PA (2013) Low-energy behavior of spin-liquid electron spectral functions. Phys Rev B 87:045119. https://doi.org/10.1103/PhysRevB.87.045119

88. Ruan W, Chen Y, Tang S, Hwang J, Tsai H-Z, Lee RL, Wu M, Ryu H, Kahn S, Liou F, Jia C, Aikawa A, Hwang C, Wang F, Choi Y, Louie SG, Lee PA, Shen Z-X, Mo S-K, Crommie MF (2021) Evidence for quantum spin liquid behaviour in single-layer 1T-$TaSe_2$ from scanning tunnelling microscopy. Nat Phys 17:1154-1161. https://doi.org/10.1038/s41567-021-01321-0

89. He W-Y, Lee PA (2023) Electronic density of states of a U (1) quantum spin liquid with spinon

Fermi surface. I. Orbital magnetic field effects. Phys Rev B 107:195155. https://doi.org/10.1103/PhysRevB.107.195155

90. Zhang Q, He W-Y, Zhang Y, Chen Y, Jia L, Hou Y, Ji H, Yang H, Zhang T, Liu L, Gao H-J, Jung TA, Wang Y (2024) Quantum spin liquid signatures in monolayer 1T-$NbSe_2$. Nat Commun 15:2336. https://doi.org/10.1038/s41467-024-46612-1

91. Chen Y, He W-Y, Ruan W, Hwang J, Tang S, Lee RL, Wu M, Zhu T, Zhang C, Ryu H, Wang F, Louie SG, Shen Z-X, Mo S-K, Lee PA, Crommie MF (2022) Evidence for a spinon Kondo effect in cobalt atoms on single-layer 1T-$TaSe_2$. Nat Phys 18:1335-1340. https://doi.org/10.1038/s41567-022-01751-4

92. Bu K, Zhang W, Fei Y, Wu Z, Zheng Y, Gao J, Luo X, Sun Y-P, Yin Y (2019) Possible strain induced Mott gap collapse in 1T-$TaS_2$. Commun Phys 2:146. https://doi.org/10.1038/s42005-019-0247-0

93. Chen Y, Ruan W, Wu M, Tang S, Ryu H, Tsai H-Z, Lee RL, Kahn S, Liou F, Jia C, Albertini OR, Xiong H, Jia T, Liu Z, Sobota JA, Liu AY, Moore JE, Shen Z-X, Louie SG, Mo S-K, Crommie MF (2020) Strong correlations and orbital texture in single-layer 1T-$TaSe_2$. Nat Phys 16:218-224. https://doi.org/10.1038/s41567-019-0744-9

94. Hellmann S, Rohwer T, Kalläne M, Hanff K, Sohrt C, Stange A, Carr A, Murnane MM, Kapteyn HC, Kipp L, Bauer M, Rossnagel K (2012) Time-domain classification of charge-density-wave insulators. Nat Commun 3:1069. https://doi.org/10.1038/ncomms2078

**References from Two-dimensional Fröhlich int in TMDC monolayers**

# References

[1] Branimir Radisavljevic, Aleksandra Radenovic, Jacopo Brivio, V. Giacometti, and Andras Kis, "Single-layer MoS2 transistors," Nature nanotechnology **6**, 147–50 (2011), arXiv:0402594v3 [arXiv:cond-mat] .

[2] Qing Hua Wang, Kourosh Kalantar-Zadeh, Andras Kis, Jonathan N Coleman, and Michael S Strano, "Electronics and optoelectronics of two-dimensional transition metal dichalcogenides," Nature Nanotechnology **7**, 699–712 (2012).

[9] Deep Jariwala, Vinod K. Sangwan, Lincoln J. Lauhon, Tobin J. Marks, and Mark C. Hersam, "Emerging device applications for semiconducting two-dimensional transition metal dichalcogenides," ACS Nano **8**, 1102–1120 (2014), arXiv:1402.0047 .

[4] Rudren Ganatra and Qing Zhang, "Few-layer MoS2: A promising layered semiconductor," ACS Nano **8**, 4074–4099 (2014).

[5] Gianluca Fiori, Francesco Bonaccorso, Giuseppe Iannaccone, Tomás Palacios, Daniel Neumaier, Alan Seabaugh, Sanjay K. Banerjee, and Luigi Colombo, "Electronics based on two-dimensional materials," Nature Nanotechnology **9**, 768–779 (2014).

[6] Galan Moody, Chandriker Kavir Dass, Kai Hao, Chang-Hsiao Chen, Lain-Jong Li, Akshay Singh, Kha Tran, Genevieve Clark, Xiaodong Xu, Gunnar Berghäuser, Ermin Malic, Andreas Knorr, and Xiaoqin Li, "Intrinsic homogeneous linewidth and broadening mechanisms of excitons in monolayer transition metal dichalcogenides," Nature Communications **6**, 8315 (2015).

[7] Haining Wang, Changjian Zhang, and Farhan Rana, "Ultrafast dynamics of defect-assisted electron-hole recombination in monolayer MoS2," Nano Letters **15**, 339–345 (2015), arXiv:1409.4518 .

[8] Hongyan Shi, Rusen Yan, Simone Bertolazzi, Jacopo Brivio, Bo Gao, Andras Kis, Debdeep Jena, Huili Grace Xing, and Libai Huang, "Exciton dynamics in suspended monolayer and few-layer MoS2 2D crystals," ACS Nano **7**, 1072–1080 (2013).

[9] Stefano Baroni, Stefano De Gironcoli, Andrea Dal Corso, and Paolo Giannozzi, "Phonons and related crystal properties from density-functional perturbation theory," Reviews of Modern Physics **73**, 515–562 (2001), arXiv:0012092v1 [arXiv:cond-mat] .

[10] Peter Vogl, "Microscopic theory of electron-phonon interaction in insulators or semiconductors," Physical Review B **13**, 694–704 (1976).

[11] Sankar Das Sarma and Bruce A. Mason, "Optical phonon interaction effects in layered semiconductor structures," Annals of Physics **163**, 78–119 (1985).

[12] Nobuya Mori and Tsuneya Ando, "Electronoptical-phonon interaction in single and double heterostructures," Physical Review B **40**, 6175–6188 (1989).

[13] Jelena Sjakste, Nathalie Vast, Matteo Calandra, and Francesco Mauri, "Wannier interpolation of the electron-phonon matrix elements in polar semiconductors: Polar-optical coupling in GaAs," Physical Review B - Condensed Matter and Materials Physics **92**, 054307 (2015), arXiv:1508.06172 .

[14] Thibault Sohier, Matteo Calandra, and Francesco Mauri, "Density-functional calculation of static screening in two-dimensional materials: The long-wavelength dielectric function of graphene," Physical Review B - Condensed Matter and Materials Physics **91**, 165428 (2015), arXiv:1503.02530v1 .

[15] Leonid V. Keldysh, "Coulomb interaction in thin semiconductor and semimetal films," JETP Letters **29**, 658–661 (1979).

[16] Pierluigi Cudazzo, Ilya V. Tokatly, and Angel Rubio, "Dielectric screening in two-dimensional insulators: Implications for excitonic and impurity states in graphane," Physical Review B - Condensed Matter and Materials Physics **84**, 085406 (2011), arXiv:1104.3346 .

[17] Tim O. Wehling, Ersoy Sasioglu, Christoph Friedrich, Alexander I. Lichtenstein, Mikhail I. Katsnelson, and Stefan Blügel, "Strength of effective coulomb interactions in graphene and graphite," Physical Review Letters **106**, 236805 (2011), arXiv:1101.4007 .

[18] Timothy C. Berkelbach, Mark S. Hybertsen, and David R. Reichman, "Theory of neutral and charged excitons in monolayer transition metal dichalcogenides," Physical Review B - Condensed Matter and Materials Physics **88**, 045318 (2013), arXiv:1305.4972 .

[19] Alexander Steinhoff, M. Rösner, Frank Jahnke, Tim O. Wehling, and Christopher Gies, "Influence of excited carriers on the optical and electronic properties of MoS2," Nano Letters **14**, 3743–3748 (2014).

[20] Kristen Kaasbjerg, Kristian S. Thygesen, and Karsten W. Jacobsen, "Phonon-limited mobility in n-type single-layer MoS 2 from first principles," Physical Review B - Condensed Matter and Materials Physics **85**, 115317 (2012), arXiv:1201.5284 .

[21] Xiaodong Li, Jeffrey T. Mullen, Zhenghe Jin, Kostyantyn M. Borysenko, M. Buongiorno Nardelli, and Ki Wook Kim, "Intrinsic electrical transport properties of monolayer silicene and MoS2 from first principles," Physical Review B - Condensed Matter and Materials Physics **87**, 115418 (2013), arXiv:arXiv:1301.7709v1 .

[22] Zhenghe Jin, Xiaodong Li, Jeffrey T. Mullen, and Ki Wook Kim, "Intrinsic transport properties of electrons and holes in monolayer transition-metal dichalcogenides," Physical Review B - Condensed Matter and Materials Physics **90**, 045422 (2014), arXiv:1406.4569 .

[23] Mark Danovich, Igor Aleiner, Neil D. Drummond, and Vladimir Fal'ko, "Fast relaxation of photo-excited carriers in 2D transition metal dichalcogenides," arXiv , 13–16 (2015), arXiv:1510.06288 .

[24] Thibault Sohier, *Electrons and phonons in graphene : electron-phonon coupling, screening and transport in the field effect setup*, Phd thesis, Universite Pierre et Marie Curie, Paris VI (2015).

[25] Paolo Giannozzi, Stefano Baroni, Nicola Bonini, Matteo Calandra, Roberto Car, Carlo Cavazzoni, Davide Ceresoli, Guido L Chiarotti, Matteo Cococcioni, Ismaila Dabo, Andrea Dal Corso, Stefano de Gironcoli, Stefano Fabris, Guido Fratesi, Ralph Gebauer, Uwe Gerstmann, Christos Gougoussis, Anton Kokalj, Michele Lazzeri, Layla Martin-Samos, Nicola Marzari, Francesco Mauri, Riccardo Mazzarello, Stefano Paolini, Alfredo Pasquarello, Lorenzo Paulatto, Carlo Sbraccia, Sandro Scandolo, Gabriele Sclauzero, Ari P Seitsonen, Alexander Smogunov, Paolo Umari, and Renata M Wentzcovitch, "QUANTUM ESPRESSO: a modular and open-source software project for quantum simulations of materials." Journal of Physics: Condensed Matter **21**, 395502 (2009), arXiv:0906.2569 .

[26] I. E. Castelli et al. in preparation (2016), see http://www.materialscloud.org/sssp.

[27] Nina V. Podberezskaya, Svetlana A. Magarill, Natal'ya V. Pervukhina, and Stanislav V. Borisov, "Crystal chemistry of dichalcogenides MX2," Journal of Structural Chemistry **42**, 654–681 (2001).

[28] Thomas Brumme, Matteo Calandra, and Francesco Mauri, "First-principles theory of field-effect doping in transition-metal dichalcogenides: Structural properties, electronic structure, Hall coefficient, and electrical conductivity," Physical Review B - Condensed Matter and Materials Physics **91**, 155436 (2015), arXiv:1501.07223 .

[29] Alejandro Molina-Sánchez and Ludger Wirtz, "Phonons in single-layer and few-layer MoS2 and WS2," Physical Review B - Condensed Matter and Materials Physics **84**, 155413 (2011), arXiv:1109.5499 .

[30] Jaroslav Tóbik and Andrea Dal Corso, "Electric fields with ultrasoft pseudo-potentials: Applications to benzene and anthracene," Journal of Chemical Physics **120**, 9934–9941 (2004), arXiv:0403291 [cond-mat] .

[31] Eric K. Yu, Derek A. Stewart, and Sandip Tiwari, "Ab initio study of polarizability and induced charge densities in multilayer graphene films," Physical Review B - Condensed Matter and Materials Physics **77**, 195406 (2008).

[32] Christoph Freysoldt, Philipp Eggert, Patrick Rinke, Arno Schindlmayr, and Matthias Scheffler, "Screening in two dimensions: GW calculations for surfaces and thin films using the repeated-slab approach," Physical Review B - Condensed Matter and Materials Physics **77**, 235428 (2008), arXiv:0801.1714 .

[33] Debdeep Jena and Aniruddha Konar, "Enhancement of carrier mobility in semiconductor nanostructures by dielectric engineering," Physical Review Letters **98**, 136805 (2007), arXiv:0707.2244 .

[34] Andor Kormányos, Guido Burkard, Martin Gmitra, Jaroslav Fabian, Viktor Zólyomi, Neil D Drummond, and Vladimir Fal'ko, "K · P Theory for Two-Dimensional Transition Metal Dichalcogenide Semiconductors," 2D Materials **2**, 022001 (2015), arXiv:1410.6666 .

**References from Origin of Dist Insul Dom in 1T-TaS2 by Yang**

## References

[1] J. S. Alden, A. W. Tsen, P. Y. Huang, R. Hovden, L. Brown, J. Park, D. A. Muller, and P. L. McEuen, Proceedings of the National Academy of Sciences **110**, 11256 (2013).

[51] T. Ritschel, J. Trinckauf, K. Koepernik, B. Büchner, M. v. Zimmermann, H. Berger, Y. Joe, P. Abbamonte, and J. Geck, Nature Physics **11**, 328 (2015).

[3] V. Vaňo, M. Amini, S. C. Ganguli, G. Chen, J. L. Lado, S. Kezilebieke, and P. Liljeroth, Nature **599**, 582 (2021).

[4] X. Zhao, P. Song, C. Wang, A. C. Riis-Jensen, W. Fu, Y. Deng, D. Wan, L. Kang, S. Ning, J. Dan, *et al.*, Nature **581**, 171 (2020).

[5] T. Ritschel, J. Trinckauf, G. Garbarino, M. Hanfland, M. v. Zimmermann, H. Berger, B. Büchner, and J. Geck, Physical Review B **87**, 125135 (2013).

[16] P. Fazekas and E. Tosatti, Philosophical Magazine B **39**, 229 (1979).

[7] B. Sipos, A. F. Kusmartseva, A. Akrap, H. Berger, L. Forró, and E. Tutiš, Nature Materials **7**, 960 (2008).

[8] L. Stojchevska, I. Vaskivskyi, T. Mertelj, P. Kusar, D. Svetin, S. Brazovskii, and D. Mihailovic, Science **344**, 177 (2014).

[9] Y. Yu, F. Yang, X. F. Lu, Y. J. Yan, Y.-H. Cho, L. Ma, X. Niu, S. Kim, Y.-W. Son, D. Feng, *et al.*, Nature Nanotechnology **10**, 270 (2015).

[10] Y. A. Gerasimenko, I. Vaskivskyi, M. Litskevich, J. Ravnik, J. Vodeb, M. Diego, V. Kabanov, and D. Mihailovic, Nature Materials **18**, 1078 (2019).

[30] J. Ravnik, M. Diego, Y. Gerasimenko, Y. Vaskivskyi, I. Vaskivskyi, T. Mertelj, J. Vodeb, and D. Mihailovic, Nature Communications **12**, 2323 (2021).

[12] G. Liu, T. Qiu, K. He, Y. Liu, D. Lin, Z. Ma, Z. Huang, W. Tang, J. Xu, K. Watanabe, *et al.*, Nature Nanotechnology , 1 (2023).

[64] G. Jarc, S. Y. Mathengattil, A. Montanaro, F. Giusti, E. M. Rigoni, R. Sergo, F. Fassioli, S. Winnerl, S. Dal Zilio, D. Mihailovic, *et al.*, Nature **622**, 487 (2023).

[14] J. A. Wilson, F. Di Salvo, and S. Mahajan, Advances in Physics **24**, 117 (1975).

[15] P. W. Anderson, Materials Research Bulletin **8**, 153 (1973).

[14] K. T. Law and P. A. Lee, Proceedings of the National Academy of Sciences **114**, 6996 (2017).

[17] Y. Wang, W. Yao, Z. Xin, T. Han, Z. Wang, L. Chen, C. Cai, Y. Li, and Y. Zhang, Nature Communications **11**, 4215 (2020).

[18] P. Darancet, A. J. Millis, and C. A. Marianetti, Physical Review B **90**, 045134 (2014).

[46] S.-H. Lee, J. S. Goh, and D. Cho, Physical Review Letters **122**, 106404 (2019).

[20] F. Petocchi, C. W. Nicholson, B. Salzmann, D. Pasquier, O. V. Yazyev, C. Monney, and P. Werner, Physical Review Letters **129**, 016402 (2022).

[21] G. Grüner, Reviews of Modern Physics **60**, 1129 (1988).

[43] C. Butler, M. Yoshida, T. Hanaguri, and Y. Iwasa, Nature Communications **11**, 2477 (2020).

[23] S.-H. Lee and D. Cho, Nature Communications **14**, 5735 (2023).

[44] J. Lee, K.-H. Jin, and H. W. Yeom, Physical Review Letters **126**, 196405 (2021).

[25] Z. Wu, K. Bu, W. Zhang, Y. Fei, Y. Zheng, J. Gao, X. Luo, Z. Liu, Y.-P. Sun, and Y. Yin, Physical Review B **105**, 035109 (2022).

[26] C. Butler, M. Yoshida, T. Hanaguri, and Y. Iwasa, Physical Review B **107**, L161107 (2023).

[27] W.-Y. He and P. A. Lee, Physical Review B **107**, 195155 (2023).

[28] W.-Y. He and P. A. Lee, Physical Review B **107**, 195156 (2023).

[29] D. Cho, Y.-H. Cho, S.-W. Cheong, K.-S. Kim, and H. W. Yeom, Physical Review B **92**, 085132 (2015).

[30] I. Lutsyk, K. Szalowski, P. Krukowski, P. Dabrowski, M. Rogala, W. Kozlowski, M. Le Ster, M. Piskorski, D. A. Kowalczyk, W. Rys, *et al.*, Nano Research **16**, 11528 (2023).

[52] D. Cho, G. Gye, J. Lee, S.-H. Lee, L. Wang, S.-W. Cheong, and H. W. Yeom, Nature Communications **8**, 392 (2017).

[32] I.-W. Lyo and P. Avouris, Science **245**, 1369 (1989).

[54] J. W. Park, J. Lee, and H. W. Yeom, Communications Materials **4**, 99 (2023).

[34] T. Ishiguro and H. Sato, Physical Review B **44**, 2046 (1991).

[35] C. Wittneven, R. Dombrowski, M. Morgenstern, and R. Wiesendanger, Physical Review Letters **81**, 5616 (1998).

[36] G. Kresse and J. Furthmüller, Physical Review B **54**, 11169 (1996).

[37] G. Kresse and D. Joubert, Physical Review B **59**, 1758 (1999).

[38] P. E. Blöchl, Physical Review B **50**, 17953 (1994).

[39] J. P. Perdew, K. Burke, and M. Ernzerhof, Physical Review Letters **77**, 3865 (1996).

[40] S. L. Dudarev, G. A. Botton, S. Y. Savrasov, C. J. Humphreys, and A. P. Sutton, Physical Review B **57**, 1505 (1998).

[41] A. Tkatchenko and M. Scheffler, Physical Review Letters **102**, 073005 (2009).

[42] M. Lawler, K. Fujita, J. Lee, A. Schmidt, Y. Kohsaka, C. K. Kim, H. Eisaki, S. Uchida, J. Davis, J. Sethna, *et al.*, Nature **466**, 347 (2010).

[43] T. Nakashizu, T. Sekine, K. Uchinokura, and E. Matsuura, Physical Review B **29**, 3090 (1984).

**References from Dynamic phase transition into a mixed-CDW state in 1T-$TaS_2$ via a thermal quench by de la Torre et al.**

## References

[1] A.H. Thompson, R.F. Gamble, and J.F. Revelli, "Transitions between semiconducting and metallic phases in 1-t tas2," Solid State Communications **9**, 981–985 (1971).

[27] J.A. Wilson, F.J. Di Salvo, and S. Mahajan, "Charge-density waves and superlattices in the metallic layered transition metal dichalcogenides," Advances in Physics **24**, 117–201 (1975).

[16] P Fazekas and E Tosatti, "Electrical, structural and magnetic properties of pure and doped 1t-tas2," Philosophical Magazine B **39**, 229–244 (1979).

[9] B. Sipos, A. F. Kusmartseva, A. Akrap, H. Berger, L. Forró, and E. Tutiš, "From mott state to superconductivity in 1t-tas2," Nature Materials **7**, 960–965 (2008).

[5] Albert Spijkerman, Jan L. de Boer, Auke Meetsma, Gerrit A. Wiegers, and Sander van Smaalen, "X-ray crystal-structure refinement of the nearly commensurate phase of $1t-\mathrm{tas}_2$ in $(3+2)$-dimensional superspace," Phys. Rev. B **56**, 13757–13767 (1997).

[6] Alfred Zong, Xiaozhe Shen, Anshul Kogar, Linda Ye, Carolyn Marks, Debanjan Chowdhury, Timm Rohwer, Byron Freelon, Stephen Weathersby, Renkai Li, Jie Yang, Joseph Checkelsky, Xijie Wang, and Nuh Gedik, "Ultrafast manipulation of mirror domain walls in a charge density wave," Science Advances **4**, eaau5501 (2018).

[7] Bryan T. Fichera, Anshul Kogar, Linda Ye, Bilal Gökce, Alfred Zong, Joseph G. Checkelsky, and Nuh Gedik, "Second harmonic generation as a probe of broken mirror symmetry," Phys. Rev. B **101**, 241106 (2020).

[8] Xiangpeng Luo, Dimuthu Obeysekera, Choongjae Won, Suk Hyun Sung, Noah Schnitzer, Robert Hovden, Sang-Wook Cheong, Junjie Yang, Kai Sun, and Liuyan Zhao, "Ultrafast modulations and detection of a ferro-rotational charge density wave using time-resolved electric quadrupole second harmonic generation," Phys. Rev. Lett. **127**, 126401 (2021).

[9] H. F. Yang, K. Y. He, J. Koo, S. W. Shen, S. H. Zhang, G. Liu, Y. Z. Liu, C. Chen, A. J. Liang, K. Huang, M. X. Wang, J. J. Gao, X. Luo, L. X. Yang, J. P. Liu, Y. P. Sun, S. C. Yan, B. H. Yan, Y. L. Chen, X. Xi, and Z. K. Liu, "Visualization of chiral electronic structure and anomalous optical response in a material with chiral charge density waves," Phys. Rev. Lett. **129**, 156401 (2022).

[10] B. Campbell, J. V. Riffle, A. de la Torre, Q. Wang, K. W. Plumb, and S. M. Hollen, "Nanoscale electronic inhomogeneities in $1t$-tas$_2$," Phys. Rev. Mater. **8**, 034002 (2024).

[11] D. Sept and J. A. Tuszyński, "Inhomogeneous nucleation in first-order phase transitions," Phys. Rev. E **50**, 4906–4910 (1994).

[12] K Binder, "Theory of first-order phase transitions," Reports on Progress in Physics **50**, 783 (1987).

[13] David W. Oxtoby, "Nucleation of first-order phase transitions," Accounts of Chemical Research **31**, 91–97 (1998).

[14] Björn Salzmann, Elina Hujala, Catherine Witteveen, Baptiste Hildebrand, Helmuth Berger, Fabian O. von Rohr, Christopher W. Nicholson, and Claude Monney, "Observation of the metallic mosaic phase in $1t-TaS_2$ at equilibrium," Phys. Rev. Mater. **7**, 064005 (2023).

[15] Yan Zhao, Zhengwei Nie, Hao Hong, Xia Qiu, Shiyi Han, Yue Yu, Mengxi Liu, Xiaohui Qiu, Kaihui Liu, Sheng Meng, Lianming Tong, and Jin Zhang, "Spectroscopic visualization and phase manipulation of chiral charge density waves in 1t-tas2," Nature Communications **14**, 2223 (2023).

[16] Suk Hyun Sung, Noah Schnitzer, Steve Novakov, Ismail El Baggari, Xiangpeng Luo, Jiseok Gim, Nguyen M. Vu, Zidong Li, Todd H. Brintlinger, Yu Liu, Wenjian Lu, Yuping Sun, Parag B. Deotare, Kai Sun, Liuyan Zhao, Lena F. Kourkoutis, John T. Heron, and Robert Hovden, "Two-dimensional charge order stabilized in clean polytype heterostructures," Nature Communications **13**, 413 (2022).

[17] Samra Husremović, Berit H. Goodge, Matthew P. Erodici, Katherine Inzani, Alberto Mier, Stephanie M. Ribet, Karen C. Bustillo, Takashi Taniguchi, Kenji Watanabe, Colin Ophus, Sinéad M. Griffin, and D. Kwabena Bediako, "Encoding multistate charge order and chirality in endotaxial heterostructures," Nature Communications **14**, 6031 (2023).

[18] Samuel Mañas-Valero, Benjamin M. Huddart, Tom Lancaster, Eugenio Coronado, and Francis L. Pratt, "Quantum phases and spin liquid properties of 1t-tas2," npj Quantum Materials **6**, 69 (2021).

[19] Emil S Bozin, M Abeykoon, S Conradson, Gianguido Baldinozzi, P Sutar, and D Mihailovic, "Crystallization of polarons through charge and spin ordering transitions in 1t-tas2," Nature Communications **14**, 7055 (2023).

[20] Quirin Stahl, Maximilian Kusch, Florian Heinsch, Gaston Garbarino, Norman Kretzschmar, Kerstin Hanff, Kai Rossnagel, Jochen Geck, and Tobias Ritschel, "Collapse of layer dimerization in the photo-induced hidden state of 1t-tas2," Nature Communications **11**, 1247 (2020).

[21] L. Stojchevska, I. Vaskivskyi, T. Mertelj, P. Kusar, D. Svetin, S. Brazovskii, and D. Mihailovic, "Ultrafast switching to a stable hidden quantum state in an electronic crystal," Science **344**, 177–180 (2014).

[22] Igor Vaskivskyi, Jan Gospodaric, Serguei Brazovskii, Damjan Svetin, Petra Sutar, Evgeny Goreshnik, Ian A. Mihailovic, Tomaz Mertelj, and Dragan Mihailovic, "Controlling the metal-to-insulator relaxation of the metastable hidden quantum state in 1t-tas<sub>2</sub>," Science Advances **1**, e1500168 (2015).

[23] Matthew J Hollander, Yu Liu, Wen-Jian Lu, Li-Jun Li, Yu-Ping Sun, Joshua A Robinson, and Suman Datta, "Electrically driven reversible insulator–metal phase transition in 1t-tas2," Nano letters **15**, 1861–1866 (2015).

[24] Liguo Ma, Cun Ye, Yijun Yu, Xiu Fang Lu, Xiaohai Niu, Sejoong Kim, Donglai Feng, David Tománek, Young-Woo Son, Xian Hui Chen, *et al.*, "A metallic mosaic phase and the origin of mott-insulating state in 1t-tas2," Nature communications **7**, 10956 (2016).

[25] Doohee Cho, Sangmo Cheon, Ki-Seok Kim, Sung-Hoon Lee, Yong-Heum Cho, Sang-Wook Cheong, and Han Woong Yeom, "Nanoscale manipulation of the mott insulating state coupled to charge order in 1 t-tas2," Nature communications **7**, 10453 (2016).

[26] Rok Venturini, Anže Mraz, Igor Vaskivskyi, Yevhenii Vaskivskyi, Damjan Svetin, Tomaž Mertelj, Leon Pavlovič, Jing Cheng, Genyu Chen, Priyanthi Amarasinghe, Syed B. Qadri, Sudhir B. Trivedi, Roman Sobolewski, and Dragan Mihailovic, "Ultraefficient resistance switching between charge ordered phases in 1T-TaS2 with a single picosecond electrical pulse," Applied Physics Letters **120**, 253510 (2022).

[27] Adam W. Tsen, Robert Hovden, Dennis Wang, Young Duck Kim, Junichi Okamoto, Katherine A. Spoth, Yu Liu, Wenjian Lu, Yuping Sun, James C. Hone, Lena F. Kourkoutis, Philip Kim, and Abhay N. Pasupathy, "Structure and control of charge density waves in two-dimensional 1t-tas<sub>2</sub>," Proceedings of the National Academy of Sciences **112**, 15054–15059 (2015).

[30] Yaroslav A. Gerasimenko, Petr Karpov, Igor Vaskivskyi, Serguei Brazovskii, and Dragan Mihailovic, "Intertwined chiral charge orders and topological stabilization of the light-induced state of a prototypical transition metal dichalcogenide," npj Quantum Materials **4**, 32 (2019).

[29] Julian Maklar, Jit Sarkar, Shuo Dong, Yaroslav A. Gerasimenko, Tommaso Pincelli, Samuel Beaulieu, Patrick S. Kirchmann, Jonathan A. Sobota, Shuolong Yang, Dominik Leuenberger, Robert G. Moore, Zhi-Xun Shen, Martin Wolf, Dragan Mihailovic, Ralph Ernstorfer, and Laurenz Rettig, "Coherent light control of a metastable hidden state," Science Advances **9**, eadi4661 (2023).

[30] Jan Ravnik, Michele Diego, Yaroslav Gerasimenko, Yevhenii Vaskivskyi, Igor Vaskivskyi, Tomaz Mertelj, Jaka Vodeb, and Dragan Mihailovic, "A time-domain phase diagram of metastable states in a charge ordered quantum material," Nature communications **12**, 2323 (2021).

[26] Masaro Yoshida, Ryuji Suzuki, Yijin Zhang, Masaki Nakano, and Yoshihiro Iwasa, "Memristive phase switching in two-dimensional 1t-tas<sub>2</sub> crystals," Science Advances **1**, e1500606 (2015).

[32] H. Mutka, L. Zuppiroli, P. Molinié, and J. C. Bourgoin, "Charge-density waves and localization in electron-irradiated $1t - \mathrm{Tas}_2$," Phys. Rev. B **23**, 5030–5037 (1981).

[33] Wenhao Zhang, Jingjing Gao, Li Cheng, Kunliang Bu, Zongxiu Wu, Ying Fei, Yuan Zheng, Li Wang, Fangsen Li, Xuan Luo, Zheng Liu, Yuping Sun, and Yi Yin, "Visualizing the evolution from mott insulator to anderson insulator in ti-doped 1t-tas2," npj Quantum Materials **7** (2022), 10.1038/s41535-021-00415-5.

[34] Björn Salzmann, Elina Hujala, Catherine Witteveen, Baptiste Hildebrand, Helmuth Berger, Fabian O. von Rohr, Christopher W. Nicholson, and Claude Monney, "Observation of the metallic mosaic phase in $1t{-}\mathrm{TaS}_2$ at equilibrium," Phys. Rev. Mater. **7**, 064005 (2023).

[35] Kai Sun, Shuaishuai Sun, Chunhui Zhu, Huanfang Tian, Huaixin Yang, and Jianqi Li, "Hidden cdw states and insulator-to-metal transition after a pulsed femtosecond laser excitation in layered chalcogenide 1t-tas2-xsex," Science Advances **4**, eaas9660 (2018).

[36] Frank Y. Gao, Zhuquan Zhang, Zhiyuan Sun, Linda Ye, Yu-Hsiang Cheng, Zi-Jie Liu, Joseph G. Checkelsky, Edoardo Baldini, and Keith A. Nelson, "Snapshots of a light-induced metastable hidden phase driven by the collapse of charge order," Science Advances **8**, eabp9076 (2022).

[37] Pierre-Adrien Mante, Chin Shen Ong, Daniel Finkelstein Shapiro, Arkady Yartsev, Oscar Grånäs, and Olle Eriksson, "Photo-induced hidden phase of 1t-tas2 with tunable lifetime," (2022), arXiv:2203.13509 [cond-mat.mtrl-sci] .

[38] Alberto de la Torre, Dante M. Kennes, Martin Claassen, Simon Gerber, James W. McIver, and Michael A. Sentef, "Colloquium: Nonthermal pathways to ultrafast control in quantum materials," Rev. Mod. Phys. **93**, 041002 (2021).

[39] D. Mihailovic, D. Svetin, I. Vaskivskyi, R. Venturini, B. Lipovšek, and A. Mraz, "Ultrafast non-thermal and thermal switching in charge configuration memory devices based on 1T-TaS2," Applied Physics Letters **119**, 013106 (2021).

[43] Anze Mraz, Rok Venturini, Damjan Svetin, Vitomir Sever, Ian Aleksander Mihailovic, Igor Vaskivskyi, Bojan Ambrozic, Goran Dražić, Maria D'Antuono, Daniela Stornaiuolo, Francesco Tafuri, Dimitrios Kazazis, Jan Ravnik, Yasin Ekinci, and Dragan Mihailovic, "Charge configuration memory devices: Energy efficiency and switching speed," Nano Letters **22**, 4814–4821 (2022).

[41] T. R. Devidas, Jonathan T. Reichanadter, Shannon C. Haley, Matan Sterenberg, Joel E. Moore, Jeffrey B. Neaton, James G. Analytis, Beena Kalisky, and Eran Maniv, "Spontaneous conducting boundary channels in $1\text{t-tas}_2$," (2024), arXiv:2405.02036 [cond-mat.str-el] .

[42] Jan Ravnik, Igor Vaskivskyi, Tomaz Mertelj, and Dragan Mihailovic, "Real-time observation of the coherent transition to a metastable emergent state in 1 t- ta s 2," Physical Review B **97**, 075304 (2018).

[43] DN Basov, RD Averitt, and D Hsieh, "Towards properties on demand in quantum materials," Nature materials **16**, 1077–1088 (2017).

[44] Satoshi Tanda, Takashi Sambongi, Toshiro Tani, and Shoji Tanaka, "X-ray study of charge density wave structure in 1t-tas2," Journal of the Physical Society of Japan **53**, 476–479 (1984).

[45] Kerstin Haupt, Maximilian Eichberger, Nicolas Erasmus, Andrea Rohwer, Jure Demsar, Kai Rossnagel, and Heinrich Schwoerer, "Ultrafast metamorphosis of a complex charge-density wave," Phys. Rev. Lett. **116**, 016402 (2016).

[46] Francesco Petocchi, Christopher W. Nicholson, Bjoern Salzmann, Diego Pasquier, Oleg V. Yazyev, Claude Monney, and Philipp Werner, "Mott versus hybridization gap in the low-temperature phase of $1t-\mathrm{tas}_2$," Phys. Rev. Lett. **129**, 016402 (2022).

[47] Y. D. Wang, W. L. Yao, Z. M. Xin, T. T. Han, Z. G. Wang, L. Chen, C. Cai, Yuan Li, and Y. Zhang, "Band insulator to mott insulator transition in 1t-tas2," Nature Communications **11**, 4215 (2020).

[48] T. Ritschel, H. Berger, and J. Geck, "Stacking-driven gap formation in layered $1\text{t-tas}_2$," Phys. Rev. B **98**, 195134 (2018).

[49] Sung-Hoon Lee, Jung Suk Goh, and Doohee Cho, "Origin of the insulating phase and first-order metal-insulator transition in $1t-\mathrm{tas}_2$," Phys. Rev. Lett. **122**, 106404 (2019).

[43] CJ Butler, Masaro Yoshida, Tetsuo Hanaguri, and Yoshihiro Iwasa, "Mottness versus unit-cell doubling as the driver of the insulating state in 1 t-tas2," Nature communications **11**, 2477 (2020).

[51] T Ritschel, J Trinckauf, K Koepernik, B Büchner, M v Zimmermann, H Berger, YI Joe, P Abbamonte, and J Geck, "Orbital textures and charge density waves in transition metal dichalcogenides," Nature physics **11**, 328–331 (2015).

[52] Doohee Cho, Gyeongcheol Gye, Jinwon Lee, Sung-Hoon Lee, Lihai Wang, Sang-Wook Cheong, and Han Woong Yeom, "Correlated electronic states at domain walls of a mott-charge-density-wave insulator 1 t-tas2," Nature communications **8**, 392 (2017).

[53] Jae Whan Park, Jinwon Lee, and Han Woong Yeom, "Zoology of domain walls in quasi-2d correlated charge density wave of 1t-tas2," npj Quantum Materials **6**, 32 (2021).

[54] Jae Whan Park, Jinwon Lee, and Han Woong Yeom, "Stacking and spin order in a van der waals mott insulator 1t-tas2," Communications Materials **4**, 99 (2023).

[55] L. Perfetti, T. A. Gloor, F. Mila, H. Berger, and M. Grioni, "Unexpected periodicity in the quasi-two-dimensional mott insulator $1t-\mathrm{tas}_2$ revealed by angle-resolved photoemission," Phys. Rev. B **71**, 153101 (2005).

[56] Ju-Jin Kim, W. Yamaguchi, T. Hasegawa, and K. Kitazawa, "Observation of mott localization gap using low temperature scanning tunneling spectroscopy in commensurate $1t-\mathrm{Tasa}_2$," Phys. Rev. Lett. **73**, 2103–2106 (1994).

[57] Doohee Cho, Yong-Heum Cho, Sang-Wook Cheong, Ki-Seok Kim, and Han Woong Yeom, "Interplay of electron-electron and electron-phonon interactions in the low-temperature phase of $1t-\mathrm{tas}_2$," Phys. Rev. B **92**, 085132 (2015).

[58] Junde Liu, Pei Liu, Liu Yang, Sung-Hoon Lee, Mojun Pan, Famin Chen, Jierui Huang, Bei Jiang, Mingzhe Hu, Yuchong Zhang, Zhaoyang Xie, Gang Wang, Mengxue Guan, Wei Jiang, Huaixin Yang, Jianqi Li, Chenxia Yun, Zhiwei Wang, Sheng Meng, Yugui Yao, Tian

Qian, and Xun Shi, "Nonvolatile optical control of interlayer stacking order in 1t-tas2," (2024), arXiv:2405.02831 [cond-mat.mtrl-sci] .

[59] Zhiyuan Sun and Andrew J. Millis, "Transient trapping into metastable states in systems with competing orders," Phys. Rev. X **10**, 021028 (2020).

[60] Yasamin Masoumi Sefidkhani, Alberto de la Torre, and Gregory A. Fiete, "Metastability in coexisting competing orders," (2024), arXiv:2411.17871 [cond-mat.str-el] .

[61] W. L. McMillan, "Landau theory of charge-density waves in transition-metal dichalcogenides," Phys. Rev. B **12**, 1187–1196 (1975).

[62] Lorenzo Del Re, Michele Fabrizio, and Erio Tosatti, "Nonequilibrium and nonhomogeneous phenomena around a first-order quantum phase transition," Phys. Rev. B **93**, 125131 (2016).

[63] Corinna Burri, Nelson Hua, Dario Ferreira Sanchez, Wenxiang Hu, Henry G. Bell, Rok Venturini, Shih-Wen Huang, Aidan G. McConnell, Faris Dizdarevic, Anze Mraz, Damjan Svetin, Benjamin Lipovsek, Marko Topic, Dimitrios Kazazis, Gabriel Aeppli, Daniel Grolimund, Yasin Ekinci, Dragan Mihailovic, and Simon Gerber, "Non-destructive imaging of bulk electrical 'hidden' state switching in a 1t-tas2 cryo-memory device," (2024), arXiv:2411.04830 [cond-mat.str-el] .

[64] Giacomo Jarc, Shahla Yasmin Mathengattil, Angela Montanaro, Francesca Giusti, Enrico Maria Rigoni, Rudi Sergo, Francesca Fassioli, Stephan Winnerl, Simone Dal Zilio, Dragan Mihailovic, *et al.*, "Cavity-mediated thermal control of metal-to-insulator transition in 1t-tas2," Nature **622**, 487–492 (2023).

[65] Anushya Chandran, Amir Erez, Steven S. Gubser, and S. L. Sondhi, "Kibble-zurek problem: Universality and the scaling limit," Phys. Rev. B **86**, 064304 (2012).

[66] Kai Du, Xiaochen Fang, Choongjae Won, Chandan De, Fei-Ting Huang, Wenqian Xu, Hoydoo You, Fernando J. Gómez-Ruiz, Adolfo del Campo, and Sang-Wook Cheong, "Kibble–zurek mechanism of ising domains," Nature Physics (2023), 10.1038/s41567-023-02112-5.

[67] Han Wu, Lei Chen, Paul Malinowski, Bo Gyu Jang, Qinwen Deng, Kirsty Scott, Jianwei Huang, Jacob P. C. Ruff, Yu He, Xiang Chen, Chaowei Hu, Ziqin Yue, Ji Seop Oh, Xiaokun Teng, Yucheng Guo, Mason Klemm, Chuqiao Shi, Yue Shi, Chandan Setty, Tyler Werner, Makoto Hashimoto, Donghui Lu, Turgut Yilmaz, Elio Vescovo, Sung-Kwan Mo, Alexei Fedorov, Jonathan D. Denlinger, Yaofeng Xie, Bin Gao, Junichiro Kono, Pengcheng Dai, Yimo Han, Xiaodong Xu, Robert J. Birgeneau, Jian-Xin Zhu, Eduardo H. da Silva Neto, Liang Wu, Jiun-Haw Chu, Qimiao Si, and Ming Yi, "Reversible non-volatile electronic switching in a near-room-temperature van der waals ferromagnet," Nature Communications **15** (2024), 10.1038/s41467-024-46862-z.

**References from Non-equilibrium quantum domain reconfiguration dynamics in a two-dimensional electronic crystal: experiments and quantum simulations by Vodeb et al.**

1. Kibble, T. W. B. Topology of cosmic domains and strings. J. Phys. Math. Gen. 9, 1387-1398 (1976).

2. Zurek, W. H. Cosmological experiments in superfluid helium? Nature 317, 505-508 (1985).

3. Monaco, R., Mygind, J., Aaroe, M., Rivers, R. J. & Koshelets, V. P. Zurek-Kibble Mechanism for the Spontaneous Vortex Formation in Nb − Al/Al ox /Nb Josephson Tunnel Junctions: New Theory and Experiment. Phys. Rev. Lett. 96, 180604 (2006).

4. Pitaevskii. Physical Kinetics. (Butterworth-Heinemann, 1981).

5. Baldan, A. Review Progress in Ostwald ripening theories and their applications to nickel-base superalloys Part I: Ostwald ripening theories. J. Mater. Sci. 37, 2171-2202 (2002).

6. Kosterlitz, J. M. & Thouless, D. J. Ordering, metastability and phase transitions in two-dimensional systems. J. Phys. C Solid State Phys. 6, 1181-1203 (1973).

7. Gerasimenko, Y. A. et al. Quantum jamming transition to a correlated electron glass in 1T-TaS2. Nat. Mater. 18, 1078-1083 (2019).

8. Lifshitz, I. M. & Kagan, Yu. Quantum Kinetics of Phase Transitions at Temperatures Close to Absolute Zero. Sov. Phys. JETP 35, (1972).

9. Leggett, A. J. et al. Dynamics of the dissipative two-state system. Rev. Mod. Phys. 59, 1-85 (1987).

10. Mraz, A. et al. Charge Configuration Memory Devices: Energy Efficiency and Switching Speed. Nano Lett. 22, 4814-4821 (2022).

11. Villain, J. & Bak, P. Two-dimensional ising model with competing interactions : floating phase, walls and dislocations. J. Phys. 42, 657-668 (1981).

12. Villain, J. Commensurate-incommensurate transition of krypton monolayers on graphite: A low temperature theory. Surf. Sci. 97, 219-242 (1980).

13. McMillan, W. L. Theory of discommensurations and the commensurate-incommensurate charge-densitywave phase transition. Phys. Rev. B 14, 1496-1502 (1976).

14. Park, J. W., Lee, J. & Yeom, H. W. Zoology of domain walls in quasi-2D correlated charge density wave of 1T-TaS2. Npj Quantum Mater. 6, 32 (2021).

15. Daley, A. J. et al. Practical quantum advantage in quantum simulation. Nature 607, 667-676 (2022).

16. Arute, F. et al. Quantum supremacy using a programmable superconducting processor. Nature vol. 574 (2019).

17. Meng, Z. et al. Atomic Bose-Einstein condensate in twisted-bilayer optical lattices. Nature (2023) doi:10.1038/s41586-023-05695-4.

18. Tan, W. L. et al. Domain-wall confinement and dynamics in a quantum simulator. Nat. Phys. 17, 742-747 (2021).

19. Chudnovsky, E. M. & Gunther, L. Quantum Tunneling of Magnetization in Small Ferromagnetic Particles. Phys. Rev. Lett. 60, 661-664 (1988).

20. Kleemann, W. Universal Domain Wall Dynamics in Disordered Ferroic Materials. Annu. Rev. Mater. Res. 37, 415-448 (2007).

21. Stamp, P. C. E., Chudnovsky, E. M. & Barbara, B. QUANTUM TUNNELING OF MAGNETIZATION IN SOLIDS. Int. J. Mod. Phys. B 06, 1355-1473 (1992).

22. Braun, H.-B., Kyriakidis, J. & Loss, D. Macroscopic quantum tunneling of ferromagnetic domain walls. Phys. Rev. B 56, 8129-8137 (1997).

23. Hong, K. & Giordano, N. Evidence for domain wall tunnelling in a quasi-one dimensional ferromagnet. J. Phys. Condens. Matter 8, L301-L306 (1996).

24. Coppinger, F. et al. Single Domain Switching Investigated Using Telegraph Noise Spectroscopy: Possible Evidence for Macroscopic Quantum Tunneling. Phys. Rev. Lett. 75, 3513-3516 (1995).

25. Wernsdorfer, W. et al. Macroscopic Quantum Tunneling of Magnetization of Single Ferrimagnetic Nanoparticles of Barium Ferrite. Phys. Rev. Lett. 79, 4014-4017 (1997).

26. Awschalom, D. D., Smyth, J. F., Grinstein, G., DiVincenzo, D. P. & Loss, D. Macroscopic quantum tunneling in magnetic proteins. Phys. Rev. Lett. 68, 3092-3095 (1992).

27. Friedman, J. R., Sarachik, M. P., Tejada, J. & Ziolo, R. Macroscopic Measurement of Resonant Magnetization Tunneling in High-Spin Molecules. Phys. Rev. Lett. 76, 3830-3833 (1996).

28. Thomas, L. et al. Macroscopic quantum tunnelling of magnetization in a single crystal of nanomagnets. Nature 383, 145-147 (1996).

29. Barbara, B. et al. Quantum tunnelling in magnetic particles, layers and multilayers. Phys. Scr. T49A, 268273 (1993).

30. Uehara, M. & Barbara, B. Noncoherent quantum effects in the magnetization reversal of a chemically disordered magnet : SmCo3.5Cu1.5. J. Phys. 47, 235-238 (1986).

31. Tejada, J., Zhang, X. X. & Chudnovsky, E. M. Quantum relaxation in random magnets. Phys. Rev. B 47, 14977-14987 (1993).

32. Vitale, S., Cavalleri, A., Cerdonio, M., Maraner, A. & Prodi, G. A. Thermal equilibrium noise with $1/f$ spectrum in a ferromagnetic alloy: Anomalous temperature dependence. J. Appl. Phys. 76, 6332-6334 (1994).

33. Arnaudas, J. I., Del Moral, A., De La Fuente, C., Ciria, M. & De Groot, P. A. J. Mesoscopic spin tunneling in the hard-random-axis-magnet amorphous alloy Tb 2 Fe. Phys. Rev. B 50, 547-550 (1994).

34. Wigner, E. On the Interaction of Electrons in Metals. Phys. Rev. 46, 1002-1011 (1934).

35. Bozin, E. S. et al. Crystallization of polarons through charge and spin ordering transitions in 1T-TaS2. Nat. Commun. 14, 7055 (2023).

36. Alexandrov, A. S. & Mott, N. F. Polarons & bipolarons. (World Scientific, 1995).

37. Fazekas, P. & Tosatti, E. Electrical, structural and magnetic properties of pure and doped 1T-TaS 2. Philos. Mag. B 39, 229-244 (1979).

38. Vodeb, J. et al. Configurational electronic states in layered transition metal dichalcogenides. New J. Phys. 21, 083001 (2019).

39. Ravnik, J. et al. A time-domain phase diagram of metastable states in a charge ordered quantum material. Nat. Commun. 12, 2323 (2021).

40. Stojchevska, L. et al. Ultrafast switching to a stable hidden quantum state in an electronic crystal. Science 344, 177-180 (2014).

41. Vaskivskyi, I. et al. Fast electronic resistance switching involving hidden charge density wave states. Nat. Commun. 7, 11442 (2016).

42. Mraz, A. et al. Manipulation of fractionalized charge in the metastable topologically entangled state of a doped Wigner crystal. Nat. Commun. 14, 8214 (2023).

43. Gerasimenko, Y. A., Karpov, P., Vaskivskyi, I., Brazovskii, S. & Mihailovic, D. Intertwined chiral charge orders and topological stabilization of the light-induced state of a prototypical transition metal dichalcogenide. Npj Quantum Mater. 4, 32 (2019).

44. Kranjec, A. et al. Electronic Dislocation Dynamics in Metastable Wigner Crystal States. Symmetry 14, 926 (2022).

45. Mihailovic, D. et al. Femtosecond data storage, processing, and search using collective excitations of a macroscopic quantum state. Appl. Phys. Lett. 80, 871-873 (2002).

46. Salgado, R. et al. Low-frequency noise spectroscopy of charge-density-wave phase transitions in vertical quasi-2D 1T-$TaS_2$ devices. Appl. Phys. Express 12, 037001 (2019).

47. Whiticar, A. M. et al. Probing flux and charge noise with macroscopic resonant tunneling. Phys. Rev. B 107, 075412 (2023).

48. Feynman, R. P. Simulating physics with computers. Int. J. Theor. Phys. 21, 467-488 (1982).

49. Ma, L. et al. A metallic mosaic phase and the origin of Mott-insulating state in 1T-TaS2. Nat. Commun. 7, 10956 (2016).

50. Cho, D. et al. Nanoscale manipulation of the Mott insulating state coupled to charge order in 1T-TaS2. Nat. Commun. 7, 10453 (2016).

51. Vaskivskyi, I. et al. Controlling the metal-to-insulator relaxation of the metastable hidden quantum state in 1T-TaS 2. Sci. Adv. 1, e1500168 (2015).

52. Laulhé, C. et al. Ultrafast Formation of a Charge Density Wave State in $1\ T - TaS2$ : Observation at Nanometer Scales Using Time-Resolved X-Ray Diffraction. Phys. Rev. Lett. 118, 247401 (2017).

53. Hänggi, P., Talkner, P. & Borkovec, M. Reaction-rate theory: fifty years after Kramers. Rev. Mod. Phys. 62, 251-341 (1990).

54. Grabert, H., Olschowski, P. & Weiss, U. Quantum decay rates for dissipative systems at finite temperatures. Phys. Rev. B 36, 1931-1951 (1987).

55. Ritschel, T. et al. Orbital textures and charge density waves in transition metal dichalcogenides. Nat. Phys. 11, 328-331 (2015).

56. Boixo, S. et al. Computational multiqubit tunnelling in programmable quantum annealers. Nat. Commun. 7, 1-7 (2016).

57. Boixo, S. et al. Evidence for quantum annealing with more than one hundred qubits. Nat. Phys. 10, 218224 (2014).

58. Boixo, S., Albash, T., Spedalieri, F. M., Chancellor, N. & Lidar, D. A. Experimental signature of programmable quantum annealing. Nat. Commun. 4, 1-8 (2013).

59. Denchev, V. S. et al. What is the computational value of finite-range tunneling? Phys. Rev. X 6, 1-19 (2016).

60. De Gennes, P. G. Collective motions of hydrogen bonds. Solid State Commun. 1, 132-137 (1963).

61. Lagnese, G., Surace, F. M., Kormos, M. & Calabrese, P. False vacuum decay in quantum spin chains. Phys. Rev. B 104, L201106 (2021).

62. Balducci, F., Gambassi, A., Lerose, A., Scardicchio, A. & Vanoni, C. Localization and Melting of Interfaces in the Two-Dimensional Quantum Ising Model. Phys. Rev. Lett. 129, 120601 (2022).

63. QPU-Specific Characteristics - D-Wave System Documentation documentation. https://docs.dwavesys.com/docs/latest/doc_physical_properties.html#doc-qpu-characteristics.

64. Amin, M. H. S., Averin, D. V. & Nesteroff, J. A. Decoherence in adiabatic quantum computation. Phys. Rev. A 79, 022107 (2009).

65. Drummond, N. D. & Needs, R. J. Phase Diagram of the Low-Density Two-Dimensional Homogeneous Electron Gas. Phys. Rev. Lett. 102, 126402 (2009).

66. Kustov, S., Liubimova, I. & Salje, E. K. H. Domain Dynamics in Quantum-Paraelectric SrTiO 3. Phys. Rev. Lett. 124, 016801 (2020).

67. Van Voorhis, T. et al. The Diabatic Picture of Electron Transfer, Reaction Barriers, and Molecular Dynamics. Annu. Rev. Phys. Chem. 61, 149-170 (2010).

68. Shank, E. A., Cecconi, C., Dill, J. W., Marqusee, S. & Bustamante, C. The folding cooperativity of a protein is controlled by its chain topology. Nature 465, 637-640 (2010).

69. Coleman, S. Fate of the false vacuum: Semiclassical theory. Phys. Rev. D 15, 2929-2936 (1977).

70. Linde, A. Inflationary Cosmology. in Inflationary Cosmology (eds. Lemoine, M., Martin, J. & Peter, P.) vol. 738 1-54 (Springer Berlin Heidelberg, 2008).

71. Ng, K. L., Opanchuk, B., Thenabadu, M., Reid, M. & Drummond, P. D. Fate of the False Vacuum: Finite Temperature, Entropy, and Topological Phase in Quantum Simulations of the Early Universe. PRX Quantum 2, 010350 (2021).

**Supplementary References from Non-equilibrium quantum domain reconfiguration dynamics in a two-dimensional electronic crystal: experiments and quantum simulations by Vodeb et al.**

1. Stojchevska, L. et al. Ultrafast switching to a stable hidden quantum state in an electronic crystal. Science 344, 177-180 (2014).

2. Ma, L. et al. A metallic mosaic phase and the origin of Mott-insulating state in 1T-TaS 2. Nat. Commun. 7, 1-8 (2016).

3. Cho, D. et al. Nanoscale manipulation of the Mott insulating state coupled to charge order in 1TTaS2. Nat. Commun. 7, 1-6 (2016).

4. Vaskivskyi, I. et al. Fast electronic resistance switching involving hidden charge density wave states. Nat. Commun. 7, 1-6 (2016).

5. Vaskivskyi, I. et al. Controlling the metal-to-insulator relaxation of the metastable hidden quantum state in 1T-TaS 2. Sci. Adv. 1, e1500168 (2015).

6. Yu, Y. et al. Gate-tunable phase transitions in thin flakes of 1T-TaS2. Nat. Nanotechnol. 10, 270276 (2015).

7. Cho, D. et al. Correlated electronic states at domain walls of a Mott-charge-density-wave insulator 1T-TaS2. Nat. Commun. 8, 1-6 (2017).

8. Cho, D., Cho, Y. H., Cheong, S. W., Kim, K. S. & Yeom, H. W. Interplay of electron-electron and electron-phonon interactions in the low-temperature phase of 1T-TaS2. Phys. Rev. B - Condens. Matter Mater. Phys. 92, 1-5 (2015).

9. Gerasimenko, Y. A., Karpov, P., Vaskivskyi, I., Brazovskii, S. & Mihailovic, D. Intertwined chiral charge orders and topological stabilization of the light-induced state of a prototypical transition metal dichalcogenide. Npj Quantum Mater. 4, 32 (2019).

10. Suzuki, A., Koizumi, M. & Doyama, M. Thermal evidences for successive CDW phase transitions in 1T-TaS2. Solid State Commun. 53, 201-203 (1985).

11. Núñez-Regueiro, M. D., Lopez-Castillo, J. M. & Ayache, C. Thermal conductivity of 1T-TaS2 and 2H-TaSe2. Phys. Rev. Lett. 55, 1931-1934 (1985).

12. Ravnik, J. et al. A time-domain phase diagram of metastable states in a charge ordered quantum material. Nat. Commun. 12, 2323 (2021).

13. Elliott, S. R. A.c. conduction in amorphous chalcogenide and pnictide semiconductors. Adv. Phys. 36, 135-217 (1987).

14. Karpov, P. & Brazovskii, S. Modeling of networks and globules of charged domain walls observed in pump and pulse induced states. Sci. Rep. 8, 1-7 (2018).

15. Mihailovic, D. et al. Ultrafast non-thermal and thermal switching in charge configuration memory devices based on 1T-TaS2. Appl. Phys. Lett. 119, (2021).

16. Vodeb, J. et al. Configurational electronic states in layered transition metal dichalcogenides. New J. Phys. 21, (2019).

17. Alexandrov, A. S. & Mott, N. F. Polarons and Bipolarons. (WORLD SCIENTIFIC, 1996). doi:10.1142/2784.

18. Vodeb, J. et al. Theoretical Modeling of the Non-equilibrium Amorphous State in 1T-TaS2. J. Supercond. Nov. Magn. (2019) doi:10.1007/s10948-019-5028-1.

19. Balducci, F., Gambassi, A., Lerose, A., Scardicchio, A. & Vanoni, C. Localization and Melting of Interfaces in the Two-Dimensional Quantum Ising Model. Phys. Rev. Lett. 129, 120601 (2022).

20. Daley, A. J. et al. Practical quantum advantage in quantum simulation. Nature 607, 667-676 (2022).

21. Vodeb, J. et al. Configurational electronic states in layered transition metal dichalcogenides. New J. Phys. 21, 083001 (2019).

22. Gerasimenko, Y. A. et al. Quantum jamming transition to a correlated electron glass in 1T-TaS2. Nat. Mater. 18, 1078-1083 (2019).

23. Grabert, H., Olschowski, P. & Weiss, U. Quantum decay rates for dissipative systems at finite temperatures. Phys. Rev. B 36, 1931-1951 (1987).

24. Leggett, A. J. et al. Dynamics of the dissipative two-state system. Rev. Mod. Phys. 59, 1-85 (1987).

25. Amin, M. H. S. & Averin, D. V. Macroscopic Resonant Tunneling in the Presence of Low Frequency Noise. Phys. Rev. Lett. 100, 197001 (2008).

26. Amin, M. H. S., Love, P. J. & Truncik, C. J. S. Thermally Assisted Adiabatic Quantum Computation. Phys. Rev. Lett. 100, 060503 (2008).

27. Amin, M. H. S., Averin, D. V. & Nesteroff, J. A. Decoherence in adiabatic quantum computation. Phys. Rev. A 79, 022107 (2009).

28. Amin, M. H. S., Truncik, C. J. S. & Averin, D. V. Role of single-qubit decoherence time in adiabatic quantum computation. Phys. Rev. A 80, 022303 (2009).

29. Knysh, S. Zero-temperature quantum annealing bottlenecks in the spin-glass phase. Nat. Commun. 7, 12370 (2016).

30. Isakov, S. V. et al. Understanding Quantum Tunneling through Quantum Monte Carlo Simulations. Phys. Rev. Lett. 117, 180402 (2016).

31. QPU-Specific Characteristics - D-Wave System Documentation documentation. https://docs.dwavesys.com/docs/latest/doc_physical_properties.html#doc-qpu-characteristics.

32. Salgado, R. et al. Low-frequency noise spectroscopy of charge-density-wave phase transitions in vertical quasi-2D 1T-$TaS_2$ devices. Appl. Phys. Express 12, 037001 (2019).

33. Whiticar, A. M. et al. Probing flux and charge noise with macroscopic resonant tunneling. Phys. Rev. B 107, 075412 (2023).

34. D-Wave Systems Inc. Technical Description of the D-Wave Quantum Processing Unit. Tech. Descr. -Wave Quantum Process. Unit (2021).

35. Boothby, K., Bunyk, P., Raymond, J. & Roy, A. Next-Generation Topology of D-Wave Quantum Processors. Preprint at http://arxiv.org/abs/2003.00133 (2020).

36. Dattani, N., Szalay, S. & Chancellor, N. Pegasus: The second connectivity graph for large-scale quantum annealing hardware. Preprint at http://arxiv.org/abs/1901.07636 (2019).

37. Vodeb, J., Non-equilibrium quantum domain reconfiguration dynamics in a two-dimensional electronic crystal versus a quantum annealer, Embedding a triangular lattice on D-Wave, 10.5281/zenodo.11061074, 2024

**References from First principles investigation of screened Coulomb interaction and electronic structure of low-temperature phase $TaS_2$ by Jung Kim, Yong Jeong, Joon Han (2022)**


1. Imada, M., Fujimori, A., and Tokura, Y. (1998). Metal-insulator transitions. Rev. Mod. Phys. 70, 1039-1263. https://doi.org/10.1103/RevModPhys.70.1039.

2. van Loon, E., Rösner, M., Schönhoff, G., Katsnelson, M.I., and Wehling, T.O. (2018). Competing Coulomb and electron-phonon interactions in $NbS_2$. npj Quant Mater 3, 1-8. https://doi.org/10.1038/s41535-018-0105-4.

3. Zhang, Y., Lu, H., Zhu, X., Tan, S., Feng, W., Liu, Q., Zhang, W., Chen, Q., Liu, Y., Luo, X., et al. (2018). Emergence of Kondo lattice behavior in a van der Waals itinerant ferromagnet, $Fe_3GeTe_2$. Sci. Adv. 4, eaao6791. https://doi.org/10.1126/sciadv.aao6791.

4. Kim, H.-S., Haule, K., and Vanderbilt, D. (2019). Mott metal-insulator transitions in pressurized layered trichalcogenides. Phys. Rev. Lett. 123, 236401. https://doi.org/10.1103/PhysRevLett.123.236401.

5. Kang, S., Kim, K., Kim, B.H., Kim, J., Sim, K.I., Lee, J.-U., Lee, S., Park, K., Yun, S., Kim, T., et al. (2020). Coherent many-body exciton in van der Waals antiferromagnet $NiPS_3$. Nature 583, 785-789. https://doi.org/10.1038/s41586-020-2520-5.

6. van Loon, E., Schüler, M., Springer, D., Sangiovanni, G., Tomczak, J.M., and Wehling, T.O. (2020). Coulomb engineering of two-dimensional Mott materials. Preprint at arXiv. https://doi.org/10.48550/arXiv.2001.01735.

7. Vaňo, V., Amini, M., Ganguli, S.C., Chen, G., Lado, J.L., Kezilebieke, S., and Liljeroth, P. (2021). Artificial heavy fermions in a van der Waals heterostructure. Nature 599, 582-586. https://doi.org/10.1038/s41586-021-04021-0.

8. Kim, T.J., Ryee, S., and Han, M.J. (2022). $Fe_3GeTe_2$ : a site-differentiated Hund metal. npj Comput. Mater. 8, 245. https://doi.org/10.1038/s41524-022-00937-x.

9. Kiem, D.H., Jeong, M.Y., Yoon, H., and Han, M.J. (2022). Strain engineering and the hidden role of magnetism in monolayer $VTe_2$. Nanoscale 14, 10009-10015. https://doi.org/10.1039/D2NR03026H.

10. Cao, Y., Fatemi, V., Demir, A., Fang, S., Tomarken, S.L., Luo, J.Y., Sanchez-Yamagishi, J.D., Watanabe, K., Taniguchi, T., Kaxiras, E.,et al. (2018). Correlated insulator behaviour at half-filling in magic-angle graphene superlattices. Nature 556, 80-84. https://doi.org/10.1038/nature26154.

11. Cao, Y., Fatemi, V., Fang, S., Watanabe, K., Taniguchi, T., Kaxiras, E., and Jarillo-Herrero, P. (2018). Unconventional superconductivity in magic-angle graphene superlattices. Nature 556, 43-50. https://doi.org/10.1038/nature26160.

12. Yankowitz, M., Chen, S., Polshyn, H., Zhang, Y., Watanabe, K., Taniguchi, T., Graf, D., Young, A.F., and Dean, C.R. (2019). Tuning superconductivity in twisted bilayer graphene. Science 363, 1059-1064. https://doi.org/10.1126/science.aav1910.

13. Burg, G.W., Zhu, J., Taniguchi, T., Watanabe, K., MacDonald, A.H., and Tutuc, E. (2019). Correlated insulating states in twisted double bilayer graphene. Phys. Rev. Lett. 123, 197702. https://doi.org/10.1103/PhysRevLett.123.197702.

14. Liu, X., Hao, Z., Khalaf, E., Lee, J.Y., Ronen, Y., Yoo, H., Haei Najafabadi, D., Watanabe, K., Taniguchi, T., Vishwanath, A., and Kim, P. (2020). Tunable spin-polarized correlated states in twisted double bilayer graphene. Nature 583, 221-225. https://doi.org/10.1038/s41586-020-2458-7.

15. Shen, C., Chu, Y., Wu, Q., Li, N., Wang, S., Zhao, Y., Tang, J., Liu, J., Tian, J., Watanabe, K., et al. (2020). Correlated states in twisted double bilayer graphene. Nat. Phys. 16, 520-525.https://doi.org/10.1038/s41567-020-0825-9.

16. Cao, Y., Rodan-Legrain, D., Rubies-Bigorda, O., Park, J.M., Watanabe, K., Taniguchi, T., and Jarillo-Herrero, P. (2020). Tunable correlated states and spin-polarized phases in twisted bilayer-bilayer graphene. Nature 583, 215-220. https://doi.org/10.1038/s41586-020-2260-6.

17. Wang, L., Shih, E.-M., Ghiotto, A., Xian, L., Rhodes, D.A., Tan, C., Claassen, M., Kennes, D.M., Bai, Y., Kim, B., et al. (2020). Correlated electronic phases in twisted bilayer transition metal dichalcogenides. Nat. Mater. 19,861-866. https://doi.org/10.1038/s41563-020-0708-6.

18. Xu, S., Al Ezzi, M.M., Balakrishnan, N., Garcia-Ruiz, A., Tsim, B., Mullan, C., Barrier, J., Xin, N., Piot, B.A., Taniguchi, T., et al. (2021). Tunable van Hove singularities and correlated states in twisted monolayer-bilayer graphene. Nat. Phys. 17, 619-626. https://doi.org/10.1038/s41567-021-01172-9.

19. Dagotto, E. (1994). Correlated electrons in high-temperature superconductors. Rev. Mod. Phys. 66, 763-840. https://doi.org/10.1103/RevModPhys.66.763.

20. Dagotto, E. (2005). Complexity in strongly correlated electronic systems. Science 309, 257-262. https://doi.org/10.1126/science.1107559.

21. Lee, P.A., Nagaosa, N., and Wen, X.-G. (2006). Doping a Mott insulator: physics of high-temperature superconductivity. Rev. Mod. Phys. 78, 17-85. https://doi.org/10.1103/RevModPhys.78.17.

22. Scalapino, D.J. (2012). A common thread: the pairing interaction for unconventional superconductors. Rev. Mod. Phys. 84, 1383-1417. https://doi.org/10.1103/RevModPhys.84.1383.

23. Zhou, Y., Kanoda, K., and Ng, T.-K. (2017). Quantum spin liquid states. Rev. Mod. Phys. 89, 025003. https://doi.org/10.1103/Rev ModPhys.89.025003.

24. Norman, M. (2016). Colloquium: herbertsmithite and the search for the quantum spin liquid. Rev. Mod. Phys. 88, 041002. https://doi.org/10.1103/RevMod Phys.88.041002.

25. Varma, C.M. (2020). Colloquium: linear in temperature resistivity and associated mysteries including high temperature superconductivity. Rev. Mod. Phys. 92, 031001. https://doi.org/10.1103/RevMod Phys.92.031001.

26. Salamon, M.B., and Jaime, M. (2001). The physics of manganites: structure and transport. Rev. Mod. Phys. 73, 583-628. https://doi.org/10.1103/RevModPhys.73.583.

27. Ayral, T., Biermann, S., Werner, P., and Boehnke, L. (2017). Influence of Fock exchange in combined many-body perturbation and dynamical mean field

theory. Phys. Rev. B 95, 245130. https://doi. org/10.1103/PhysRevB.95.245130.

28. In 't Veld, Y., Schüler, M., Wehling, T.O., Katsnelson, M.I., and van Loon, E.G.C.P. (2019). Bandwidth renormalization due to the intersite Coulomb interaction. J. Phys. Condens. Matter 31, 465603. https://doi.org/10.1088/1361-648X/ab36fe.

29. Wigner, E. (1934). On the interaction of electrons in metals. Phys. Rev. 46, 1002-1011. https://doi.org/10.1103/PhysRev.46.1002.

30. Wigner, E. (1938). Effects of the electron interaction on the energy levels of electrons in metals. Trans. Faraday Soc. 34, 678-685. https://doi.org/10.1039/TF9383400678.

31. Lee, P.A., and Fukuyama, H. (1978). Dynamics of the charge-density wave. II. Long-range Coulomb effects in an array of chains. Phys. Rev. B 17, 542-548. https://doi.org/10.1103/PhysRevB.17.542.

32. Ayral, T., Biermann, S., and Werner, P. (2013). Screening and nonlocal correlations in the extended Hubbard model from self-consistent combined GW and dynamical mean field theory. Phys. Rev. B 87, 125149. https://doi.org/10.1103/PhysRevB.87.125149.

33. Yu, S.-L., and Li, J.-X. (2012). Chiral superconducting phase and chiral spin-density-wave phase in a Hubbard model on the kagome lattice. Phys. Rev. B 85, 144402. https://doi.org/10.1103/PhysRevB.85.144402.

34. Kiesel, M.L., and Thomale, R. (2012). Sublattice interference in the kagome Hubbard model. Phys. Rev. B 86, 121105. https://doi.org/10.1103/PhysRevB.86.121105.

35. Kiesel, M.L., Platt, C., and Thomale, R. (2013). Unconventional Fermi surface instabilities in the kagome hubbard model. Phys. Rev. Lett. 110, 126405. https://doi.org/10.1103/ PhysRevLett.110.126405.

36. Wang, W.-S., Li, Z.-Z., Xiang, Y.-Y., and Wang, Q.-H. (2013). Competing electronic orders on kagome lattices at van Hove filling. Phys. Rev. B 87, 115135. https://doi.org/10.1103/PhysRevB.87.115135.

37. Jeong, M.Y., Yang, H.-J., Kim, H.S., Kim, Y.B., Lee, S., and Han, M.J. (2022). Crucial role of out-of-plane Sb $p$ orbitals in Van Hove singularity formation and electronic correlations in the superconducting kagome metal $CsV_3Sb_5$. Phys. Rev. B 105, 235145. https://doi.org/10. 1103/PhysRevB.105.235145.

38. Rösner, M., Steinke, C., Lorke, M., Gies, C., Jahnke, F., and Wehling, T.O. (2016). Two-dimensional heterojunctions from nonlocal manipulations of the interactions. Nano Lett. 16, 2322-2327. https://doi.org/10.1021/acs. nanolett.5b05009.

39. Raja, A., Chaves, A., Yu, J., Arefe, G., Hill, H.M., Rigosi, A.F., Berkelbach, T.C., Nagler, P., Schüller, C., Korn, T., et al. (2017). Coulomb engineering of the bandgap and excitons in two-dimensional materials. Nat. Commun. 8, 15251. https://doi.org/10.1038/ncomms15251.

40. Steinhoff, A., Florian, M., Rösner, M., Schönhoff, G., Wehling, T.O., and Jahnke, F.(2017). Exciton fission in monolayer transition metal dichalcogenide semiconductors. Nat. Commun. 8, 1166. https://doi.org/10.1038/s41467-017-01298-6.

41. Steinke, C., Wehling, T.O., and Rösner, M. (2020). Coulomb-engineered heterojunctions and dynamical screening in transition metal dichalcogenide monolayers. Phys. Rev. B 102, 115111. https://doi.org/10.1103/PhysRevB. 102.115111.

42. Sipos, B., Kusmartseva, A.F., Akrap, A., Berger, H., Forró, L., and Tutiš, E. (2008). From Mott state to superconductivity in 1 T − $TaS_2$. Nat. Mater. 7, 960-965. https://doi.org/10. 1038/nmat2318.

43. Ang, R., Wang, Z.C., Chen, C.L., Tang, J., Liu, N., Liu, Y., Lu, W.J., Sun, Y.P., Mori, T., and Ikuhara, Y. (2015). Atomistic origin of an ordered superstructure induced superconductivity in layered chalcogenides. Nat. Commun. 6, 6091. https://doi.org/10. 1038/ncomms7091.

44. Yu, Y., Yang, F., Lu, X.F., Yan, Y.J., Cho, Y.-H., Ma, L., Niu, X., Kim, S., Son, Y.-W., Feng, D., et al. (2015). Gate-tunable phase transitions in thin flakes of 1 T − $TaS_2$. Nat. Nanotechnol. 10, 270-276. https://doi.org/10.1038/nnano. 2014.323.

45. Wang, Y.D., Yao, W.L., Xin, Z.M., Han, T.T., Wang, Z.G., Chen, L., Cai, C., Li, Y., and Zhang, Y. (2020). Band insulator to Mott insulator transition in 1 T − $TaS_2$. Nat. Commun. 11, 4215. https://doi.org/10.1038/s41467-020-18040-4.

46. Wilson, J.A., Di Salvo, F.J., and Mahajan, S. (1975). Charge-density waves and superlattices in the metallic layered transition metal dichalcogenides. Adv. Phys. 24, 117-201. https://doi.org/10.1080/ 00018737500101391.

47. Fazekas, P., and Tosatti, E. (1979). Electrical, structural and magnetic properties of pure and doped 1T-TaS $_2$. Phil. Mag. B 39, 229-244. https://doi.org/10.1080/13642817908245359.

48. Giambattista, B., Slough, C.G., McNairy, W.W., and Coleman, R.V. (1990). Scanning tunneling microscopy of atoms and charge-density waves in 1T- $TaS_2$, 1T- $TaSe_2$, and 1T-$VSe_2$. Phys. Rev. B 41, 10082-10103. https://doi.org/10.1103/PhysRevB.41.10082.

49. Liu, A.Y. (2009). Electron-phonon coupling in compressed 1 T − $TaS_2$ : stability and superconductivity from first principles. Phys. Rev. B 79, 220515. https://doi.org/10.1103/PhysRevB.79.220515.

50. Ge, Y., and Liu, A.Y. (2010). First-principles investigation of the charge-density-wave instability in 1T-TaSe $_2$. Phys. Rev. B 82, 155133. https://doi.org/10.1103/PhysRevB.82.155133.

51. Law, K.T., and Lee, P.A. (2017). 1 T − $TaS_2$ as a quantum spin liquid. Proc. Natl. Acad. Sci. USA 114, 6996-7000. https://doi.org/10. 1073/pnas. 1706769114.

52. Ribak, A., Silber, I., Baines, C., Chashka, K., Salman, Z., Dagan, Y., and Kanigel, A. (2017). Gapless excitations in the ground state of 1T-$TaS_2$. Phys. Rev. B 96, 195131. https://doi.org/10.1103/PhysRevB.96.195131.

53. Klanjšek, M., Zorko, A., Žitko, R., Mravlje, J., Jagličić, Z., Biswas, P., Prelovšek, P., Mihailovic, D., and Arčon, D. (2017). A high-temperature quantum spin liquid with polaron spins. Nat. Phys. 13, 1130-1134. https://doi.org/10.1038/nphys4212.

54. Lin, H.C., Wang, C.K., Tung, Y.C., Chiu, F.Y., Su, Y.P., Wu, J., Chen, X., and Ji, S.-H. (2020). Scanning tunneling spectroscopic study of monolayer 1 T − $TaS_2$ and 1 T − $TaSe_2$. Nano Res. 40, 133-145. https://doi.org/10.1007/s12274-019-2584-4.

55. Darancet, P., Millis, A.J., and Marianetti, C.A. (2014). Three-dimensional metallic and two-dimensional insulating behavior in octahedral tantalum dichalcogenides. Phys. Rev. B 90, 045134. https://doi.org/10.1103/PhysRevB. 90.045134.

56. Yu, X.-L., Liu, D.-Y., Quan, Y.-M., Wu, J., Lin, H.-O., Chang, K., and Zou, L.-J. (2017). Electronic correlation effects and orbital density wave in the layered compound 1T-$TaS_2$. Phys. Rev. B 96, 125138. https://doi.org/10.1103/PhysRevB.96.125138.

57. Lee, S.-H., Goh, J.S., and Cho, D. (2019). Origin of the insulating phase and first-order metal-insulator transition in 1 T − $TaS_2$. Phys. Rev. Lett. 122, 106404. https://doi.org/10. 1103/PhysRevLett.122.106404.

58. Petocchi, F., Nicholson, C.W., Salzmann, B., Pasquier, D., Yazyev, O.V., Monney, C., and Werner, P. (2022). Mott versus hybridization gap in the low-temperature phase of 1T-TaS2. Preprint at arXiv. https://doi.org/10.48550/arXiv.2202.01285.

59. Butler, C.J., Yoshida, M., Hanaguri, T., and Iwasa, Y. (2020). Mottness versus unit-cell doubling as the driver of the insulating state in 1T-TaS2. Nat. Commun. 11, 2477. https://doi.org/10.1038/s41467-020-16132-9.

60. Lee, J., Jin, K.-H., and Yeom, H.W. (2021). Distinguishing a Mott insulator from a trivial insulator with atomic adsorbates. Phys. Rev. Lett. 126, 196405. https://doi.org/10.1103/PhysRevLett.126.196405.

61. Nicholson, C.W., Petocchi, F., Salzmann, B., Witteveen, C., Rumo, M., Kremer, G., von Rohr, F.O., Werner, P., and Monney, C. (2022). Modified interlayer stacking and insulator to correlated-metal transition driven by uniaxial strain in 1T-TaS2. Preprint at arXiv. https://doi.org/10.48550/arXiv:2204.05598.

62. Fuhrmann, A., Heilmann, D., and Monien, H. (2006). From Mott insulator to band insulator: a dynamical mean-field theory study. Phys. Rev. B 73, 245118. https://doi.org/10.1103/PhysRevB.73.245118.

63. Chen, G., Rösner, M., and Lado, J.L. (2022). Controlling magnetic frustration in 1T-TaS2 via Coulomb engineered long-range interactions. Preprint at arXiv. https://doi.org/10.48550/arXiv:2201.07826.

64. Si, Q., and Smith, J.L. (1996). Kosterlitz-thouless transition and short range spatial correlations in an extended hubbard model. Phys. Rev. Lett. 77, 3391-3394. https://doi.org/10.1103/PhysRevLett.77.3391.

65. Smith, J.L., and Si, Q. (2000). Spatial correlations in dynamical mean-field theory. Phys. Rev. B 61, 5184-5193. https://doi.org/10.1103/PhysRevB.61.5184.

66. Sun, P., and Kotliar, G. (2002). Extended dynamical mean-field theory and GW method. Phys. Rev. B 66, 085120. https://doi. org/10.1103/PhysRevB.66.085120.

67. Biermann, S., Aryasetiawan, F., and Georges, A. (2003). First-principles approach to the electronic structure of strongly correlated systems: combining the GW approximation and dynamical mean-field theory. Phys. Rev. Lett. 90, 086402. https://doi.org/10.1103/PhysRevLett.90.086402.

68. Sun, P., and Kotliar, G. (2004). Many-Body approximation scheme beyond GW. Phys. Rev. Lett. 92, 196402. https://doi.org/10. 1103/PhysRevLett.92.196402.

69. Chen, J., Petocchi, F., and Werner, P. (2022). Causal versus local GW+EDMFT scheme and application to the triangular-lattice extended Hubbard model. Phys. Rev. B 105, 085102. https://doi.org/10.1103/PhysRevB.105.085102.

70. Mattheiss, L.F. (1973). Band structures of transition-metal-dichalcogenide layer compounds. Phys. Rev. B 8, 3719-3740. https://doi.org/10.1103/PhysRevB.8.3719.

71. Smith, N.V., Kevan, S.D., and DiSalvo, F.J. (1985). Band structures of the layer compounds 1 T − $TaS_2$ and 2H − $TaSe_2$ in the presence of commensurate charge-density waves. J. Phys. C Solid State Phys. 18, 3175-3189. https://doi.org/10.1088/0022-3719/18/16/013.

72. Yan-Bin, Q., Yan-Ling, L., Guo-Hua, Z., Zhi, Z., and Xiao-Ying, Q. (2007). Anisotropic properties of $TaS_2$. Chin. Phys. 16, 3809-3814. https://doi.org/10.1088/1009-1963/16/12/042.

73. Tosatti, E., and Fazekas, P. (1976). On the nature of the low-temperature phase of 1T-$TaS_2$. J. Phys. Colloq. 37, C4-C168. https://doi.org/10.1051/jphyscol:1976426.

74. Brouwer, R., and Jellinek, F. (1980). The lowtemperature superstructures of 1 T − $TaSe_2$ and 2H- $TaSe_2$. Phys. B+C 99, 51-55. https://doi.org/10.1016/0378-4363(80)90209-0.

75. Perfetti, L., Georges, A., Florens, S., Biermann, S., Mitrovic, S., Berger, H., Tomm, Y., Höchst, H., and Grioni, M. (2003). Spectroscopic signatures of a bandwidthcontrolled Mott transition at the surface of 1T- $TaSe_2$. Phys. Rev. Lett. 90, 166401. https://doi.org/10.1103/PhysRevLett.90.166401.

76. Perfetti, L., Loukakos, P.A., Lisowski, M., Bovensiepen, U., Berger, H., Biermann, S., Cornaglia, P.S., Georges, A., and Wolf, M. (2006). Time evolution of the electronic structure of 1 T − $TaS_2$ through the insulatormetal transition. Phys. Rev. Lett. 97, 067402. https://doi.org/10.1103/PhysRevLett.97.067402.

77. Marzari, N., and Vanderbilt, D. (1997). Maximally localized generalized Wannier functions for composite energy bands. Phys. Rev. B 56, 12847-12865. https://doi.org/10.1103/PhysRevB.56.12847.

78. Souza, I., Marzari, N., and Vanderbilt, D. (2001). Maximally localized Wannier functions for entangled energy bands. Phys. Rev. B 65, 035109. https://doi.org/10.1103/PhysRevB. 65.035109.

79. Pasquier, D., and Yazyev, O.V. (2022). Ab initio theory of magnetism in two-dimensional 1T-$TaS_2$. Phys. Rev. B 105, L081106. https://doi.org/10.1103/PhysRevB. 105.L081106.

80. Ryee, S., Sémon, P., Han, M.J., and Choi, S. (2020). Nonlocal Coulomb interaction and spin-freezing crossover as a route to valenceskipping charge order. npj Quantum Materials 5, 2397. https://doi.org/10.1038/s41535-020-0221-9.

81. Hüser, F., Olsen, T., and Thygesen, K.S. (2013). How dielectric screening in twodimensional crystals affects the convergence of excited-state calculations: monolayer $MoS_2$. Phys. Rev. B 88, 245309. https://doi. org/10.1103/PhysRevB.88.245309.

82. Ugeda, M.M., Bradley, A.J., Shi, S.-F., da Jornada, F.H., Zhang, Y., Qiu, D.Y., Ruan, W., Mo, S.-K., Hussain, Z., Shen, Z.-X., et al. (2014). Giant bandgap renormalization and excitonic effects in a monolayer transition metal dichalcogenide semiconductor. Nat. Mater. 13, 1091-1095. https://doi.org/10.1038/nmat4061.

83. Kim, T.J., Ryee, S., Han, M.J., and Choi, S. (2020). Dynamical mean-field study of Vanadium diselenide monolayer ferromagnetism. 2D Mater. 7, 035023. https://doi.org/10.1088/2053-1583/ab8b48.

84. Boix-Constant, C., Mañas-Valero, S., Córdoba, R., Baldoví, J.J., Rubio, A., and Coronado, E. (2021). Out-of-Plane transport of 1 T − $TaS_2$/ graphene-based van der Waals heterostructures. ACS Nano 15, 11898-11907. https://doi.org/10.1021/acsnano.1c03012.

85. Karbalaee Aghaee, A., Belbasi, S., and Hadipour, H. (2022). Ab initio calculation of the effective Coulomb interactions in $MX_2$ (M=Ti, V, Cr, Mn, Fe, Co, Ni; X= S, Se, Te): intrinsic magnetic ordering and Mott phase. Phys. Rev. B 105, 115115. https://doi.org/10.1103/PhysRevB.105.115115.

86. Kamil, E., Berges, J., Schönhoff, G., Rösner, M., Schüler, M., Sangiovanni, G., and Wehling, T.O. (2018). Electronic structure of single layer 1 T − $NbSe_2$ : interplay of lattice distortions, non-local exchange, and Mott-Hubbard correlations. J. Phys. Condens. Matter 30, 325601. https://doi.org/10.1088/1361-648X/aad215.

87. Miyake, T., Nakamura, K., Arita, R., and Imada, M. (2010). Comparison of ab initiolow-energy models for LaFePO, LaFeAsO, $BaFe_2As_2$, LiFeAs, FeSe, and FeTe: electron correlation and covalency. J. Phys. Soc. Jpn. 79, 044705. https://doi.org/10.1143/JPSJ.79.044705.

88. Nakata, Y., Sugawara, K., Chainani, A., Oka, H., Bao, C., Zhou, S., Chuang, P.-Y., Cheng, C.-M., Kawakami, T., Saruta, Y., et al. (2021). Robust charge-density wave strengthened by electron correlations in monolayer 1 T − $TaSe_2$ and 1T-$NbSe_2$. Nat. Commun. 12, 5873. https://doi.org/10.1038/s41467-021-26105-1.

89. Jarrell, M., and Gubernatis, J.E. (1996). Bayesian inference and the analytic continuation of imaginary-time quantum Monte Carlo data. Phys. Rep. 269, 133-195. https://doi.org/10.1016/0370-1573(95) 00074-7.

90. Sim, J.-H., and Han, M.J. (2018). Maximum quantum entropy method. Phys. Rev. B 98, 205102. https://doi.org/10.1103/PhysRevB.98.205102.

91. Yoon, H., Sim, J.-H., and Han, M.J. (2018). Analytic continuation via domain knowledge free machine learning. Phys. Rev. B 98, 245101. https://doi.org/10.1103/PhysRevB.98.245101.

92. Ritschel, T., Berger, H., and Geck, J. (2018). Stacking-driven gap formation in layered 1T-$TaS_2$. Phys. Rev. B 98, 195134. https://doi.org/10.1103/PhysRevB.98.195134.

93. Mañas-Valero, S., Huddart, B.M., Lancaster, T., Coronado, E., and Pratt, F.L. (2021). Quantum phases and spin liquid properties of 1T-TaS2. npj Quantum Mater 6, 1-9. https://doi.org/10.1038/s41535-021-00367-w.

94. Kresse, G., and Hafner, J. (1993). Ab initio molecular dynamics for open-shell transition metals. Phys. Rev. B 48, 13115-13118. https://doi.org/10.1103/PhysRevB.48.13115.

95. Kresse, G., and Furthmüller, J. (1996). Efficiency of ab-initio total energy calculations for metals and semiconductors using a plane-wave basis set. Comput. Mater. Sci. 6, 15-50. https://doi.org/10.1016/0927-0256(96)00008-0.

96. Choi, S., Semon, P., Kang, B., Kutepov, A., and Kotliar, G. (2019). ComDMFT: a massively parallel computer package for the electronic structure of correlated-electron systems. Comput. Phys. Commun. 244, 277-294. https://doi.org/10.1016/j.cpc.2019.07.003.

97. Nakamura, K., Yoshimoto, Y., Nomura, Y., Tadano, T., Kawamura, M., Kosugi, T., Yoshimi, K., Misawa, T., and Motoyama, Y. (2021). RESPACK: an ab initio tool for derivation of effective low-energy model of material. Comput. Phys. Commun. 261, 107781. https://doi.org/10.1016/j.cpc.2020.107781.

98. Perdew, J.P., Burke, K., and Ernzerhof, M. (1996). Generalized gradient approximation made simple. Phys. Rev. Lett. 77, 3865-3868. https://doi.org/10.1103/PhysRevLett.77.3865.

**References from Orbital-driven Mottness collapse in 1T-$TaS_{2-x}Se_x$ transition metal dichalcogenide by Qiao et al. (2016)**

# References

[1] B. Sipos, A. F. Kusmartseva, A. Akrap, H. Berger, L. Forro, and E. Tutis, Nat. Mater. **7**, 960 (2008).

[2] E. Morosan, H. W. Zandbergen, B. S. Dennis, J. W. G. Bos, Y. Onose, T. Klimczuk, A. P. Ramirez, N. P. Ong, and R. J. Cava, Nat. Phys. **2**, 544 (2006).

[3] R. Ang, Y. Tanaka, E. Ieki, K. Nakayama, T. Sato, L. J. Li, W. J. Lu, Y. P. Sun, and T. Takahashi, Phys. Rev. Lett. **109**, 176403 (2012).

[4] L. J. Li, W. J. Lu, X. D. Zhu, L. S. Ling, Z. Qu, and Y. P. Sun, Europhys. Lett. **97**, 67005 (2012).

[5] Y. Yu, F. Yang, X. F. Lu, Y. J. Yan, Y.-H. Cho, L. Ma, X. Niu, S. Kim, Y.-W. Son, D. Feng, S. Li, S.-W. Cheong, X. H. Chen, and Y. Zhang, Nat. Nanotech. **10**, 270 (2015).

[6] R. Ang, Y. Miyata, E. Ieki, K. Nakayama, T. Sato, Y. Liu, W. J. Lu, Y. P. Sun, and T. Takahashi, Phys. Rev. B **88**, 115145 (2013).

[7] Y. Liu, R. Ang, W. J. Lu, W. H. Song, L. J. Li, and Y. P. Sun, Appl. Phys. Lett. **102**, 192602 (2013).

[8] R. Ang, Z. C. Wang, C. L. Chen, J. Tang, N. Liu, Y. Liu, W. J. Lu, Y. P. Sun, T. Mori, and Y. Ikuhara, Nat. Commun. **6**, 6091 (2015).

[9] J. A. Wilson, F. J. DiSalvo, and S. Mahajan, Adv. Phys. **24**, 117 (1975).

[10] C. B. Scruby, P. M. Williams, and G. S. Parry, Philos. Mag. **31**, 255 (1975).

[11] P. Fazekas and E. Tosatti, Philos. Mag. B **39**, 229 (1979).

[12] P. Fazekas and E. Tosatti, Physica B **99**, 183 (1980).

[13] B. Dardel, M. Grioni, D. Malterre, P. Weibel, Y. Baer, and F. Levy, Phys. Rev. B **45**, 1462 (1992).

[14] B. Dardel, M. Grioni, D. Malterre, P. Weibel, Y. Baer, and F. Levy, Phys. Rev. B **46**, 7407 (1992).

[15] J.-J. Kim, W. Yamaguchi, T. Hasegawa, and K. Kitazawa, Phys. Rev. Lett. **73**, 2103 (1994).

[16] X. L. Wu and C. M. Lieber, Science **243**, 1703 (1989).

[17] E. Lahoud, O. N. Meetei, K. B. Chaska, A. Kanigel, and N. Trivedi, Phys. Rev. Lett. **112**, 206402 (2014).

[18] K. Aryanpour, W. E. Pickett, and R. T. Scalettar, Phys. Rev. B **74**, 085117 (2006).

[19] L. Perfetti, P. A. Loukakos, M. Lisowski, U. Bovensiepen, H. Berger, S. Biermann, P. S. Cornaglia, A. Georges, and M. Wolf, Phys. Rev. Lett. **97**, 067402 (2006).

[20] H. Mutka, L. Zuppiroli, P. Molinie, and J. C. Bourgoin, Phys. Rev. B **23**, 5030 (1981).

[21] M. Bovet, S. vanSmaalen, H. Berger, R. Gaal, L. Forro, L. Schlapbach, and P. Aebi, Phys. Rev. B **67**, 125105 (2003).

[22] K. Rossnagel and N. V. Smith, Phys. Rev. B **73**, 073106 (2006).

[23] P. Xu, J. O. Piatek, P.-H. Lin, B. Sipos, H. Berger, L. Forro, H. M. Ronnow, and M. Grioni, Phys. Rev. B **81**, 172503 (2010).

[24] D. Cho, Y.-H. Cho, S.-W. Cheong, K.-S. Kim, and H. W. Yeom, Phys. Rev. B **92**, 085132 (2015).

[25] T. Ritschel, J. Trinckauf, K. Koepernik, B. Buchner, M. v. Zimmermann, H. Berger, Y. I. Joe, P. Abbamonte, and J. Geck, Nat. Phys. **11**, 328 (2015).

[26] C. Ye, P. Cai, R. Yu, X. Zhou, W. Ruan, Q. Liu, C. Jin, and Y. Wang, Nat. Commun. **4**, 1365 (2013).

[27] G. Kresse and J. Hafner, Phys. Rev. B **47**, 558 (1993).

[28] G. Kresse and J. Hafner, Phys. Rev. B **49**, 14251 (1994).

[29] G. Kresse and J. Furthmuller, Comput. Mater. Sci. **6**, 15 (1996).

[30] G. Kresse and J. Furthmuller, Phys. Rev. B **54**, 11169 (1996).

[31] J. P. Perdew, K. Burke, and M. Ernzerhof, Phys. Rev. Lett. **77**, 3865 (1996).

[32] G. Kresse and D. Joubert, Phys. Rev. B **59**, 1758 (1999).

[33] N. Marzari and D. Vanderbilt, Phys. Rev. B **56**, 12847 (1997).

[34] I. Souza, N. Marzari, and D. Vanderbilt, Phys. Rev. B **65**, 035109 (2001).

[35] A. A. Mostofi, J. R. Yates, Y.-S. Lee, I. Souza, D. Vanderbilt, and N. Marzari, Comput. Phys. Commun. **178**, 685 (2008).

[36] A. I. Liechtenstein, V. I. Anisimov, and J. Zaanen, Phys. Rev. B **52**, R5467 (1995).

[37] S. L. Dudarev, G. A. Botton, S. Y. Savrasov, C. J. Humphreys, and A. P. Sutton, Phys. Rev. B **57**, 1505 (1998).

[38] F. J. F. Jellinek and J. Less, J. Less-Common Met. **4**, 9 (1962).

[39] H. W. Myron and A. J. Freeman, Phys. Rev. B **11**, 2735 (1975).

[40] A. M. Woolley and G. Wexler, J. Phys. C: Solid State Phys. **10**, 2601 (1977).

[41] P. Darancet, A. J. Millis, and C. A. Marianetti, Phys. Rev. B **90**, 045134 (2014).

[42] N. V. Smith, S. D. Kevan, and F. J. DiSalvo, J. Phys. C: Solid State Phys. **18**, 3175 (1985).

[43] F. Zwick, H. Berger, I. Vobornik, G. Margaritondo, L. Forro, C. Beeli, M. Onellion, G. Panaccione, A. Taleb-Ibrahimi, and M. Grioni, Phys. Rev. Lett. **81**, 1058 (1998).

[44] F. Clerc, C. Battaglia, M. Bovet, L. Despont, C. Monney, H. Cercellier, M. G. Garnier, and P. Aebi, Phys. Rev. B **74**, 155114 (2006).

[45] L. Ma, C. Ye, Y. Yu, X. F. Lu, X. Niu, S. Kim, D. Feng, D. Tomanek, Y.-W. Son, X. H. Chen, and Y. Zhang, Nat. Commun. **7**, 10956 (2016).

[46] D. Cho, S. Cheon, K.-S. Kim, S.-H. Lee, Y.-H. Cho, S.-W. Cheong, and H. W. Yeom., Nat. Commun. **7**, 10453 (2016).

[47] L. Perfetti, A. Georges, S. Florens, S. Biermann, S. Mitrovic, H. Berger, Y. Tomm, H. Hochst, and M. Grioni, Phys. Rev. Lett. **90**, 166401 (2003).

[48] L. Perfetti, P. A. Loukakos, M. Lisowski, U. Bovensiepen, M. Wolf, H. Berger, S. Biermann, and A. Georges, New J. Phys. **10**, 053019 (2008).

[49] J. K. Freericks, H. R. Krishnamurthy, Y. Ge, A. Y. Liu, and T. Pruschke, Phys. Status. Solidi. B **246**, 948 (2009).

**References from Quantum billiards with correlated electrons confined in triangular transition metal dichalcogenide monolayer nanostructures (2021) by Ravnik et al.**

1. Heller, E. J. Bound-state eigenfunctions of classically chaotic hamiltonian systems: scars of periodic orbits. Phys. Rev. Lett. 53, 1515-1518 (1984).

2. Casati, G. & Prosen, T. Mixing property of triangular billiards. Phys. Rev. Lett. 83, 4729-4732 (1999).

3. Marcus, C. M., Rimberg, A. J., Westervelt, R. M., Hopkins, P. F. & Gossard, A. C. Conductance fluctuations and chaotic scattering in ballistic microstructures. Phys. Rev. Lett. 69, 506-509 (1992).

4. Wilkinson, P. B. et al. Observation of 'scarred' wavefunctions in a quantum well with chaotic electron dynamics. Nat. Nanotechnol. 380, 608-610 (1996).

5. Linke, H., Christensson, L., Omling, P. & Lindelof, P. Stability of classical electron orbits in triangular electron billiards. Phys. Rev. B-Condens. Matter Mater. Phys. 56, 1440-1446 (1997).

6. Fromhold, T. M. et al. Magnetotunneling spectroscopy of a quantum well in the regime of classical chaos. Phys. Rev. Lett. 72, 2608-2611 (1994).

7. Ponomarenko, L. A. et al. Chaotic dirac billiard in graphene quantum dots. Science 320, 356-358 (2008).

8. Crook, R. et al. Imaging fractal conductance fluctuations and scarred wave functions in a quantum billiard. PRL 91, 730-734 (2003).

9. Cabosart, D. et al. Recurrent quantum scars in a mesoscopic graphene ring. Nano Lett. 17, 1-6 (2017).

10. Ho, W. W., Choi, S., Pichler, H. & Lukin, M. D. Periodic orbits, entanglement, and quantum many-body scars in constrained models: matrix product state approach. Phys. Rev. Lett. 122, 040603 (2019).

11. Turner, C. J., Michailidis, A. A., Abanin, D. A., Serbyn, M. & Papić, Z. Weak ergodicity breaking from quantum many-body scars. Nat. Phys. 14, 745-749 (2018).

12. Vodeb, J. et al. Configurational electronic states in layered transition metal dichalcogenides. N. J. Phys. 21, 083001 (2019).

13. Wilson, J. A., Disalvo, F. J. & Mahajan, S. Charge-density waves and superlattices in metallic layered transition-metal dichalcogenides. Adv. Phys. 24, 117-201 (1975).

14. Sipos, B., Berger, H., Forro, L., Tutis, E. & Kusmartseva, A. F. From Mott state to superconductivity in 1T-TaS2. Nat. Mater. 7, 960-965 (2008).

15. Fazekas, P. & Tosatti, E. Charge carrier localization in pure and doped 1t-TaS2. Phys. B C. 99, 183-187 (1980).

16. Klanjsek, M. et al. A high-temperature quantum spin liquid with polaron spins. Nat. Phys. 13, 1130-1134 (2017).

17. Karpov, P. & Brazovskii, S. Modeling of networks and globules of charged domain walls observed in pump and pulse induced states. Sci. Rep. 8, 1-7 (2018).

18. Hall, J., Ehlen, N., Berges, J., Loon, E. van & ACS, C. van E. Environmental control of charge density wave order in monolayer 2H-TaS2. ACS Appl. Nano 13, 10210-10220 (2019).

19. Bardeen, J. Classical versus quantum models of charge-density-wave depinning in quasi-one-dimensional metals. Phys. Rev. B, Condens. matter 39, 3528-3532 (1989).

20. Miller, J. H., Wijesinghe, A., Tang, Z. & Guloy, A. Coherent quantum transport of charge density waves. PRB 87, 115127 (2013).

21. Miller, J. H., Wijesinghe, A. I., Tang, Z. & Guloy, A. M. Correlated quantum transport of density wave electrons. PRL 108, 036404 (2012).

22. Ravnik, J. et al. A time-domain phase diagram of metastable states in a charge ordered quantum material. Nat. Commun. 12, 2323 (2021).

23. Ravnik, J., Vaskivskyi, I. & Gerasimenko, Y. Strain-Induced metastable topological networks in laser-fabricated TaS2 polytype heterostructures for nanoscale devices. ACS Appl. Nano 2, 3743-3751 (2019).

24. Wang, Z. et al. Surface-limited superconducting phase transition on 1T -TaS2. ACS Nano 12, 12619-12628 (2018).

25. Shimada, T., Ohuchi, F. S. & Parkinson, B. A. Work function and photothreshold of layered metal dichalcogenides. Jpn. J. Appl. Phys. 33, 2696-2698 (1994).

26. Ma, L. et al. A metallic mosaic phase and the origin of Mott-insulating state in 1T-TaS2. Nature. Communications 7, 1-8 (2016).

27. Cho, D. et al. Correlated electronic states at domain walls of a Mott-chargedensity-wave insulator 1 T -TaS 2. Nature. Communications 8, 392 (2017).

28. Gerasimenko, Y. A., Karpov, P., Vaskivskyi, I., Brazovskii, S. & Mihailovic, D. Intertwined chiral charge orders and topological stabilization of the lightinduced state of a prototypical transition metal dichalcogenide. npj Quant. Mater. 4, 1-9 (2019).

29. Stahl, Q. et al. Collapse of layer dimerization in the photo-induced hidden state of 1T-TaS2. Nature. Communications 11, 1-7 (2020).

30. Cho, D. et al. Nanoscale manipulation of the Mott insulating state coupled to charge order in 1T-TaS2. Nat Commun. 7, 10453 (2016).

31. Rossnagel, K. On the origin of charge-density waves in select layered transition-metal dichalcogenides. J. Phys.-Condens. Matter 23, 213001 (2011).

32. Ryu, H. et al. Persistent charge-density-wave order in single-layer TaSe2. ACS Appl. Nano 18, 689-694 (2018).

33. Samajdar, R. & Jain, S. R. Nodal domains of the equilateral triangle billiard. J. Phys. A: Math. Theor. 47, 195101-195123 (2014).

34. Bernien, H. et al. Probing many-body dynamics on a 51-atom quantum simulator. Nature 551, 579-584 (2017).

35. Vignolle, B. et al. Quantum oscillations and the Fermi surface of hightemperature cuprate superconductors. Comptes Rendus Physique. 12, 446-460 (2011).

36. Mihailovic, D. et al. Application of the polaron-transport theory to sigma (omega) in Tl2Ba2Ca1-xGdxCu2O8, YBa2Cu3O7- d, and La2-xSrxCuO4. Phys. Rev. B, Condens. matter 42, 7989-7993 (1990).

37. Mertelj, T., Demsar, J., Podobnik, B., Poberaj, I. & Mihailovic, D. Photoexcited carrier relaxation in YBaCuO by picosecond resonant Raman spectroscopy. Phys. Rev. B 55, 6061-6069 (1997).

38. Hoffman, J. E. et al. Imaging quasiparticle interference in Bi2Sr2CaCu2O8+d. Science 297, 1148-1151 (2002).

From SM:

1. Wang, Z. et al. Surface-Limited Superconducting Phase Transition on 1T-TaS2. Acs Nano 12, 12619-12628 (2018).

2. Ravnik, J., Vaskivskyi, I. & Gerasimenko, Y. Strain-Induced Metastable Topological Networks in Laser-Fabricated TaS2 Polytype Heterostructures for Nanoscale Devices. ACS Applied Nano 2, 3743-3751 (2019).

3. Hall, J., Ehlen, N., Berges, J., Loon, E. van & ACS, C. van E. Environmental Control of Charge Density Wave Order in Monolayer 2H-TaS2. ACS Applied Nano 13, 10210-10220 (2019).

4. Ma, L. et al. A metallic mosaic phase and the origin of Mott-insulating state in 1T-TaS2. Nature Communications 7, 1-8 (2016).

5. Vodeb, J. et al. Configurational electronic states in layered transition metal dichalcogenides. New J Phys 21, 083001 (2019).

**References from Ab initio theory of magn in 2D 1T-TaS2 by Pasquier**

# References


[1] Y. Cao, V. Fatemi, S. Fang, K. Watanabe, T. Taniguchi, E. Kaxiras, and P. Jarillo-Herrero, Nature **556**, 43 (2018).

[2] Y. Cao, V. Fatemi, A. Demir, S. Fang, S. L. Tomarken, J. Y. Luo, J. D. Sanchez-Yamagishi, K. Watanabe, T. Taniguchi, E. Kaxiras, *et al.*, Nature **556**, 80 (2018).

[3] B. Sipos, A. F. Kusmartseva, A. Akrap, H. Berger, L. Forró, and E. Tutiš, Nature Materials **7**, 960 (2008).

[4] P. Darancet, A. J. Millis, and C. A. Marianetti, Physical Review B **90**, 045134 (2014).

[5] D. Pasquier and O. V. Yazyev, Physical Review B **98**, 045114 (2018).

[6] Y. Chen, W. Ruan, M. Wu, S. Tang, H. Ryu, H.-Z. Tsai, R. Lee, S. Kahn, F. Liou, C. Jia, *et al.*, Nature Physics **16**, 218 (2020).

[7] J. A. Wilson, F. Di Salvo, and S. Mahajan, Advances in Physics **24**, 117 (1975).

[8] A. C. Neto, Physical Review Letters **86**, 4382 (2001).

[9] K. Rossnagel, Journal of Physics: Condensed Matter **23**, 213001 (2011).

[10] S. Manzeli, D. Ovchinnikov, D. Pasquier, O. V. Yazyev, and A. Kis, Nature Reviews Materials **2**, 17033 (2017).

[11] D. Pasquier and O. V. Yazyev, Physical Review B **100**, 201103 (2019).

[12] P. Fazekas and E. Tosatti, Physica B+ C **99**, 183 (1980).

[13] D. Pasquier and O. V. Yazyev, 2D Materials **6**, 025015 (2019).

[14] K. T. Law and P. A. Lee, Proceedings of the National Academy of Sciences **114**, 6996 (2017).

[15] P. W. Anderson, Materials Research Bulletin **8**, 153 (1973).

[16] P. Fazekas and E. Tosatti, Philosophical Magazine B **39**, 229 (1979).

[17] L. Perfetti, T. Gloor, F. Mila, H. Berger, and M. Grioni, Physical Review B **71**, 153101 (2005).

[18] W.-Y. He, X. Y. Xu, G. Chen, K. T. Law, and P. A. Lee, Physical Review Letters **121**, 046401 (2018).

[19] S. Mañas-Valero, B. M. Huddart, T. Lancaster, E. Coronado, and F. L. Pratt, npj Quantum Materials **6**, 1 (2021).

[20] W. Ruan, Y. Chen, S. Tang, J. Hwang, H.-Z. Tsai, R. Lee, M. Wu, H. Ryu, S. Kahn, F. Liou, *et al.*, arXiv preprint arXiv:2009.07379 (2020).

[21] N. S. Fedorova, C. Ederer, N. A. Spaldin, and A. Scaramucci, Physical Review B **91**, 165122 (2015).

[22] N. S. Fedorova, A. Bortis, C. Findler, and N. A. Spaldin, Physical Review B **98**, 235113 (2018).

[23] P. Giannozzi, S. Baroni, N. Bonini, M. Calandra, R. Car, C. Cavazzoni, D. Ceresoli, G. L. Chiarotti, M. Cococcioni, I. Dabo, *et al.*, Journal of physics: Condensed matter **21**, 395502 (2009).

[24] J. P. Perdew and W. Yue, Physical Review B **33**, 8800 (1986).

[25] J. P. Perdew, K. Burke, and M. Ernzerhof, Physical Review Letters **77**, 3865 (1996).

[26] N. Marzari, D. Vanderbilt, A. De Vita, and M. Payne, Physical Review Letters **82**, 3296 (1999).

[27] P. E. Blöchl, Physical Review B **50**, 17953 (1994).

[28] A. Dal Corso, Computational Materials Science **95**, 337 (2014).

[29] D. C. Miller, S. D. Mahanti, and P. M. Duxbury, Physical Review B **97**, 045133 (2018).

[30] S. Yi, Z. Zhang, and J.-H. Cho, Physical Review B **97**, 041413 (2018).

[31] C. Tresca and M. Calandra, 2D Materials **6**, 035041 (2019).

[32] K. Penc, H. Shiba, F. Mila, and T. Tsukagoshi, Physical Review B **54**, 4056 (1996).

[33] Z. Huang, D. Liu, A. Mansikkamäki, V. Vieru, N. Iwahara, and L. F. Chibotaru, Physical Review Research **2**, 033430 (2020).

[34] K. Seo, V. N. Kotov, and B. Uchoa, Physical review letters **122**, 246402 (2019).

[35] L. Perfetti, P. A. Loukakos, M. Lisowski, U. Bovensiepen, M. Wolf, H. Berger, S. Biermann, and A. Georges, New Journal of Physics **10**, 053019 (2008).

[36] T. Grover, N. Trivedi, T. Senthil, and P. A. Lee, Physical Review B **81**, 245121 (2010).

[37] N. D. Mermin and H. Wagner, Physical Review Letters **17**, 1133 (1966).

[38] J. L. Lado and J. Fernández-Rossier, 2D Materials **4**, 035002 (2017).

[39] A. Cuccoli, V. Tognetti, and R. Vaia, Physical Review B **52**, 10221 (1995).

[40] A. Cuccoli, V. Tognetti, P. Verrucchi, and R. Vaia, Physical Review B **51**, 12840 (1995).

[41] S. A. Owerre, Canadian Journal of Physics **91**, 542 (2013).

[42] A. S. Ngankeu, S. K. Mahatha, K. Guilloy, M. Bianchi, C. E. Sanders, K. Hanff, K. Rossnagel, J. A. Miwa, C. Breth Nielsen, M. Bremholm, and P. Hofmann, Physical Review B **96**, 195147 (2017).

[43] C. Butler, M. Yoshida, T. Hanaguri, and Y. Iwasa, Nature Communications **11**, 2477 (2020).

[44] J. Lee, K.-H. Jin, and H. W. Yeom, Physical Review Letters **126**, 196405 (2021).

[45] T. Ritschel, H. Berger, and J. Geck, Physical Review B **98**, 195134 (2018).

[46] S.-H. Lee, J. S. Goh, and D. Cho, Physical Review Letters **122**, 106404 (2019).

**References from Imaging of electrically controlled van der Waals layer stacking in 1T-TaS2**

# References


[1] V. B. Rao, *Switch-level timing simulation of MOS VLSI circuits* (KAP, 1989).

[2] K. Boahen, Neuromorphic microchips, Sci. Am. **16**, 20 (2006).

[3] J. J. Yang *et al.*, Memristive devices for computing, Nat. Nanotechnol. **8**, 13 (2013).

[4] V. Garcia and M. Bibes, Ferroelectric tunnel junctions for information storage and processing, Nat. Commun. **5**, 4289 (2014).

[5] N. Maciel, E. Marques, L. Naviner, Y. Zhou, and H. Cai, Magnetic tunnel junction applications, Sensors **20**, 121 (2020).

[6] M. L. Gallo and A. Sebastian, An overview of phase-change memory device physics, J. Phys. D: Appl. Phys. **53**, 213002 (2020).

[7] D. S. Holmes *et al.*, Energy-efficient superconducting computing—power budgets and requirements, TAS **23**, 1701610 (2013).

[7] Q. H. Wang *et al.*, Electronics and optoelectronics of two-dimensional transition metal dichalcogenides, Nat. Nanotechnol. **7**, 699 (2012).

[9] D. Jariwala *et al.*, Emerging device applications for semiconducting two-dimensional transition metal dichalcogenides, ACS Nano **8**, 1102 (2014).

[10] Y. Liu *et al.*, Van der Waals heterostructures and devices, Nat. Rev. Mater. **1**, 16042 (2016).

[11] K. S. Novoselov *et al.*, Electric field effect in atomically thin carbon films, Phys. Rev. Lett **404**, 3824 (2000).

[12] Z. Wang *et al.*, Strong interface-induced spin-orbit interaction in graphene on $WS_2$, Nat. Commun. **6**, 8339 (2015).

[13] Y. Cao *et al.*, Correlated insulator behaviour at half-filling in magic-angle graphene superlattices, Nature **556**, 80 (2018).

[14] D. M. Kennes *et al.*, Moiré heterostructures as a condensed-matter quantum simulator, Nat. Phys. **17**, 155 (2021).

[27] J. A. Wilson *et al.*, Charge-density waves and superlattices in the metallic layered transition metal dichalcogenides, Adv. Phys. **24**, 117 (1975).

[10] P. Fazekas and E. Tosatti, Electrical, structural and magnetic properties of pure and doped $1T$-$TaS_2$, Philos. Mag. B: Phys. Cond. Matter **39**, 229 (1979).

[9] B. Sipos *et al.*, From Mott state to superconductivity in $1T$-$TaS_2$, Nat. Mater. **7**, 960 (2008).

[18] L. J. Li *et al.*, Fe-doping–induced superconductivity in the charge-density-wave system $1T$-$TaS_2$, EPL **97**, 67005 (2012).

[4] M. Klanjšek *et al.*, A high-temperature quantum spin liquid with polaron spins, Nat. Phys. **13**, 1130 (2017).

[19] K. T. Law and P. A. Lee, $1T$-$TaS_2$ as a quantum spin liquid, PNAS **114**, 6996 (2017).

[21] E. Tosatti and P. Fazekas, On the nature of the low-temperature phase of $1T$-$TaS_2$, J. de Phys. Colloq. **37**, C4 (1976).

[22] C. B. Scruby *et al.*, The role of charge density waves in structural transformations of $1T$-$TaS_2$, Philos. Mag. **31**, 255 (1975).

[23] L. Stojchevska *et al.*, Ultrafast switching to a stable hidden quantum state in an electronic crystal, Science **344**, 177 (2014).

[24] I. Vaskivskyi *et al.*, Controlling the metal-to-insulator relaxation of the metastable hidden quantum state in $1T$-$TaS_2$, Sci. Adv. **1**, e1500168 (2015).

[25] M. J. Hollander *et al.*, Electrically driven reversible insulator–metal phase transition in $1T$-$TaS_2$, Nano Lett. **15**, 1861 (2015).

[26] M. Yoshida *et al.*, Memristive phase switching in two-dimensional $1T$-$TaS_2$ crystals, Sci. Adv. **1**, e1500606 (2015).

[27] I. Vaskivskyi *et al.*, Fast electronic resistance switching involving hidden charge density wave states, Nat. Commun. **7**, 11442 (2016).

[18] D. Cho *et al.*, Nanoscale manipulation of the Mott insulating state coupled to charge order in $1T$-$TaS_2$, Nat. Commun. **7**, 10453 (2016).

[41] L. Ma *et al.*, A metallic mosaic phase and the origin of Mott-insulating state in $1T$-$TaS_2$, Nat. Commun. **7**, 10956 (2016).

[30] Y. A. Gerasimenko *et al.*, Intertwined chiral charge orders and topological stabilization of the light-induced state of a prototypical transition metal dichalcogenide, npj Quantum Mater. **4**, 32 (2019).

[35] Q. Stahl *et al.*, Collapse of layer dimerization in the photo-induced hidden state of $1T$-$TaS_2$, Nat. Commun. **11**, 1247 (2020).

[32] D. Mihailovic *et al.*, Ultrafast non-thermal and thermal switching in charge configuration memory devices based on $1T$-$TaS_2$, Appl. Phys. Lett. **119**, 013106 (2021).

[33] A. De La Torre *et al.*, Colloquium: Nonthermal pathways to ultrafast control in quantum materials, Rev. Mod. Phys. **93**, 041002 (2021).

[34] Y. A. Gerasimenko *et al.*, Quantum jamming transition to a correlated electron glass in $1T$-$TaS_2$, Nat. Mater. **18**, 1078 (2019).

[35] J. Vodeb *et al.*, Configurational electronic states in layered transition metal dichalcogenides, New J. Phys. **21**, 083001 (2019).

[13] L. Perfetti *et al.*, Time evolution of the electronic structure of $1T$-$TaS_2$ through the insulator-metal transition, Phys. Rev. Lett. **97**, 067402 (2006).

[37] J. Ravnik *et al.*, Real-time observation of the coherent transition to a metastable emergent state in $1T$-$TaS_2$, Phys. Rev. B **97**, 075304 (2018).

[38] A. Zong *et al.*, Ultrafast manipulation of mirror domain walls in a charge density wave, Sci. Adv. **4**, eaau5501 (2018).

[39] T. Danz *et al.*, Ultrafast nanoimaging of the order parameter in a structural phase transition, Science **371**, 371 (2021).

[40] J. Maklar *et al.*, Coherent light control of a metastable hidden state, Sci. Adv. **9**, eadi4661 (2023).

[41] J. Liu *et al.*, Nonvolatile optical control of interlayer stacking order in $1T$-$TaS_2$, arXiv:2405.02831.

[42] N. Hua *et al.*, unpublished.

[43] A. Mraz *et al.*, Charge configuration memory devices: energy efficiency and switching speed, Nano Lett. **22**, 4814 (2022).

[44] R. Venturini *et al.*, Ultraefficient resistance switching between charge ordered phases in $1T$-$TaS_2$ with a single picosecond electrical pulse, Appl. Phys. Lett. **120**, 253510 (2022).

[45] Y. Nitzav *et al.*, Emergence of a Fermi-surface in the current-driven hidden state of $1T$-$TaS_2$, arXiv:2407.05535.

[46] D. Svetin *et al.*, Three-dimensional resistivity and switching between correlated electronic states in $1T$-$TaS_2$, Sci. Rep. **7**, 46048 (2017).

[47] N. D'Anna *et al.*, Non-destructive X-ray imaging of patterned delta-layer devices in silicon, Adv. Electron. Mater. **9**, 2201212 (2023).

[48] M. G. Masteghin *et al.*, Benchmarking of X-ray fluorescence microscopy with ion beam implanted samples showing detection sensitivity of hundreds of atoms, Small Methods , e2301610 (2024).

[49] I. Vaskivskyi *et al.*, A high-efficiency programmable modulator for extreme ultraviolet light with nanometre feature size based on an electronic phase transition, Nat. Photon. **18**, 458 (2024).

[33] T. Ishiguro and H. Sato, Electron microscopy of phase transformations in $1T$-$TaS_2$, Phys. Rev. B **44**, 2046 (1991).

[51] C. Laulhé *et al.*, X-ray study of femtosecond structural dynamics in the 2D charge density wave compound $1T$-$TaS_2$, Physica B: Cond. Matter **460**, 100 (2015).

[52] R. Salgado *et al.*, Low-frequency noise spectroscopy of charge-density-wave phase transitions in vertical quasi-2D $1T$-$TaS_2$ devices, APEX **12** (2019).

[53] W. Sun *et al.*, Understanding memristive switching via in situ characterization and device modeling, Nat. Commun. **10**, 3453 (2019).

[54] T. R. Devidas *et al.*, Spontaneous conducting boundary channels in $1T$-$TaS_2$, arXiv:2405.02036.

[55] T. H. Gilani and D. Rabchuk, Electrical resistivity of gold thin film as a function of film thickness, Can. J. Phys. **96**, 272 (2018).

[56] A. M. Stoneham, The theory of defects in solids, Contemp. Phys. **20**, 535 (1979).

[57] D. Svetin *et al.*, Transitions between photoinduced macroscopic quantum states in $1T$-$TaS_2$ controlled by substrate strain, Appl. Phys. Express **7**, 103201 (2014).

[58] P. Salev *et al.*, Local strain inhomogeneities during electrical triggering of a metal–insulator transition revealed by X-ray microscopy, Proc. Natl. Acad. Sci. U.S.A. **121**, e2317944121 (2024).

[59] D. B. McWhan, G. Aeppli, J. P. Remeika, and S. Nelson, Time-resolved X-ray scattering study of $BaTiO_3$, J. Phys. C: Solid State Phys. **18**, L307 (1985).

[60] A. Singer *et al.*, Nonequilibrium phase precursors during a photoexcited insulator-to-metal transition in $V_2O_3$, Phys. Rev. Lett. **120**, 207601 (2018).

[61] B. S. Mun *et al.*, Role of joule heating effect and bulk-surface phases in voltage-driven metal-insulator transition in $VO_2$ crystal, Appl. Phys. Lett. **103**, 061902 (2013).

[62] U. Celano *et al.*, Three-dimensional observation of the conductive filament in nanoscaled resistive memory devices, Nano Lett. **14**, 2401 (2014).

[63] A. K. J. Toh and V. Ng, Tomographic imaging using conductive atomic force microscopy, Mater. Charact. **186**, 111783 (2022).

[64] T. Wei *et al.*, Three-dimensional reconstruction of conductive filaments in $HfO_x$-based memristor, Adv. Mater. **35**, 2209925 (2023).

[65] P. R. Willmott *et al.*, The Materials Science beamline upgrade at the Swiss Light Source, J. Synchrotron Rad. **20**, 667 (2013).

[66] D. Grolimund, A. Scheidegger, J. van der Veen, and R. Abela, Layout of the microXAS beamline at SLS, PSI Sci. Rep. **4**, 139 (2002).

[67] V. Solé *et al.*, A multiplatform code for the analysis of energy-dispersive X-ray fluorescence spectra, Spectrochim. Acta Part B At. Spectrosc. **62**, 63 (2007).

[68] A. Thompson, *X-ray Data Booklet* (LBNL, UC, 2001).

[69] F. Jellinek, The system tantalum-sulfur, J. Less-Common Met. **4**, 9 (1962).

[70] P. Virtanen *et al.*, SciPy 1.0: fundamental algorithms for scientific computing in Python, Nat. Methods **17**, 261 (2020).

[71] M. Graf *et al.*, X-ray studies of nanoporous gold: Powder diffraction by large crystals with small holes, Phys. Rev. Mater. **1**, 076003 (2017).

[31] Y. D. Wang *et al.*, Band insulator to Mott insulator transition in $1T$-$TaS_2$, Nat. Commun. **11**, 4215 (2020).

[73] F. I. Givens and G. E. Fredericks, Thermal expansion of $NbSe_2$ and $TaS_2$, Phys. Chem. Solids **38**, 13634365 (1977).

[74] O. Sezerman *et al.*, Thermal expansion of $1T$-$TaS_2$ and 2H-$NbSe_2$, Solid State Communications **36**, 737 (1980).

[75] D. R. P. Guy *et al.*, High pressure investigation of the CDW phase diagram of $1T$-$TaS_2$, in *Charge Density Waves in Solids*, Vol. 217 (1985) pp. 80–83.

[76] A. Suzuki *et al.*, Thermal evidences for successive CDW phase transitions in $1T$-$TaS_2$, Solid State Commun. **53**, 201 (1985).

[77] M. D. Nunez-Regueiro *et al.*, Thermal conductivity of $1T$-$TaS_2$ and $1H$-$TaSe_2$, Phys. Rev. Lett. **55**, 1931 (1985).

**References from Dynamical control of Coulomb interactions and Hubbard bands in monolayer 1T-$TaS_2$ by Notter, Aichhorn, Galler**

## References

[1] Y. Saito, T. Nojima, and Y. Iwasa, Nature Reviews Materials **2**, 1 (2016).

[2] D. Lin, S. Li, J. Wen, H. Berger, L. Forró, H. Zhou, S. Jia, T. Taniguchi, K. Watanabe, X. Xi, *et al.*, Nature communications **11**, 2406 (2020).

[3] W. Ruan, Y. Chen, S. Tang, J. Hwang, H.-Z. Tsai, R. L. Lee, M. Wu, H. Ryu, S. Kahn, F. Liou, *et al.*, Nature Physics **17**, 1154 (2021).

[4] M. Klanjsek, A. Zorko, R. Zitko, J. Mravlje, Z. Jaglicic, P. Biswas, P. Prelovsek, D. Mihailovic, and D. Arcon, Nature Physics **13**, 1130 (2017).

[5] H. H. Sønsteby, E. Skaar, Ø. S. Fjellvåg, J. E. Bratvold, H. Fjellvåg, and O. Nilsen, Nature communications **11**, 2872 (2020).

[6] A. Frano, E. Schierle, M. W. Haverkort, Y. Lu, M. Wu, S. Blanco-Canosa, U. Nwankwo, A. V. Boris, P. Wochner, G. Cristiani, H. U. Habermeier, G. Logvenov, V. Hinkov, E. Benckiser, E. Weschke, and B. Keimer, Phys. Rev. Lett. **111**, 106804 (2013).

[7] J. R. Schaibley, H. Yu, G. Clark, P. Rivera, J. S. Ross, K. L. Seyler, W. Yao, and X. Xu, Nature Reviews Materials **1**, 1 (2016).

[8] T. Cao, G. Wang, W. Han, H. Ye, C. Zhu, J. Shi, Q. Niu, P. Tan, E. Wang, B. Liu, *et al.*, Nature communications **3**, 887 (2012).

[9] E. Y. Andrei and A. H. MacDonald, Nature materials **19**, 1265 (2020).

[10] L. Wang, E.-M. Shih, A. Ghiotto, L. Xian, D. A. Rhodes, C. Tan, M. Claassen, D. M. Kennes, Y. Bai, B. Kim, K. Watanabe, T. Taniguchi, X. Zhu, J. Hone, A. Rubio, A. N. Pasupathy, and C. R. Dean, Nature Materials **19**, 861 (2020).

[11] Y. Cao, V. Fatemi, A. Demir, S. Fang, S. L. Tomarken, J. Y. Luo, J. D. Sanchez-Yamagishi, K. Watanabe, T. Taniguchi, E. Kaxiras, R. C. Ashoori, and P. Jarillo-Herrero, Nature **556**, 80 (2018).

[12] M. Straub, F. Petocchi, C. Witteveen, F. B. Kugler, A. Hunter, Y. Alexanian, G. Gatti, S. Mandloi, C. Polley, G. Carbone, J. Osiecki, F. O. von Rohr, A. Georges, F. Baumberger, and A. Tamai, Phys. Rev. Lett. **135**, 096501 (2025).

[13] F. Petocchi, C. W. Nicholson, B. Salzmann, D. Pasquier, O. V. Yazyev, C. Monney, and P. Werner, Physical Review Letters **129**, 016402 (2022).

[14] D. Shin, N. Tancogne-Dejean, J. Zhang, M. S. Okyay, A. Rubio, and N. Park, Phys. Rev. Lett. **126**, 196406 (2021).

[15] Y. Chen, W. Ruan, M. Wu, S. Tang, H. Ryu, H.-Z. Tsai, R. Lee, S. Kahn, F. Liou, C. Jia, O. R. Albertini, H. Xiong, T. Jia, Z. Liu, J. A. Sobota, A. Y. Liu, J. E. Moore, Z.-X. Shen, S. G. Louie, S.-K. Mo, and M. F. Crommie, Nature Physics **16**, 218 (2020).

[16] Y. Nakata, K. Sugawara, R. Shimizu, Y. Okada, P. Han, T. Hitosugi, K. Ueno, T. Sato, and T. Takahashi, NPG Asia Materials **8**, 321 (2016).

[17] P. Darancet, A. J. Millis, and C. A. Marianetti, Phys. Rev. B **90**, 045134 (2014).

[18] L. Perfetti, P. A. Loukakos, M. Lisowski, U. Bovensiepen, M. Wolf, H. Berger, S. Biermann, and A. Georges, New Journal of Physics **10**, 053019 (2008).

[19] L. Perfetti, A. Georges, S. Florens, S. Biermann, S. Mitrovic, H. Berger, Y. Tomm, H. Höchst, and M. Grioni, Phys. Rev. Lett. **90**, 166401 (2003).

[20] B. Dardel, M. Grioni, D. Malterre, P. Weibel, Y. Baer, and F. Lévy, Phys. Rev. B **45**, 1462 (1992).

[21] R. Claessen, B. Burandt, H. Carstensen, and M. Skibowski, Phys. Rev. B **41**, 8270 (1990).

[22] P. Fazekas and E. Tosatti, Philosophical Magazine B **39**, 229 (1979).

[23] N. Hua, F. Petocchi, H. G. Bell, G. Aeppli, P. Werner, and S. Gerber, arXiv preprint arXiv:2503.24124 (2025).

[24] Y. Wang, Z. Li, X. Luo, J. Gao, Y. Han, J. Jiang, J. Tang, H. Ju, T. Li, R. Lv, *et al.*, Nature Communications **15**, 3425 (2024).

[25] C. Butler, M. Yoshida, T. Hanaguri, and Y. Iwasa, Nature communications **11**, 2477 (2020).

[26] M. Vandelli, A. Galler, A. Rubio, A. I. Lichtenstein, S. Biermann, and E. A. Stepanov, npj Quantum Materials **9**, 19 (2024).

[27] A. Wietek, R. Rossi, F. Šimkovic, M. Klett, P. Hansmann, M. Ferrero, E. M. Stoudenmire, T. Schäfer, and A. Georges, Phys. Rev. X **11**, 041013 (2021).

[28] X. Wu, F. Ming, T. S. Smith, G. Liu, F. Ye, K. Wang, S. Johnston, and H. H. Weitering, Phys. Rev. Lett. **125**, 117001 (2020).

[29] X. Cao, T. Ayral, Z. Zhong, O. Parcollet, D. Manske, and P. Hansmann, Phys. Rev. B **97**, 155145 (2018).

[30] W.-Y. He, X. Y. Xu, G. Chen, K. T. Law, and P. A. Lee, Phys. Rev. Lett. **121**, 046401 (2018).

[31] Z.-Y. Liu, S. Qiao, Q.-Y. Tang, W.-H. Ling, Zi-Heng Zhang, H.-N. Xia, X. Liao, W.-H. Mao, J.-T. Lü, B. Huang, and Y.-S. Fu, Nano Lett. **21**, 7005 (2021).

[32] L. E. P. López, A. Vaitsi, V. Sleziona, F. Schulz, M. Wolf, and M. Müller, arXiv preprint arXiv:2505.20541 (2025).

[33] J. Jayabalan, J. Chen, F. Petocchi, F. K. Diekmann, N. Najafianpour, P. Zhou, W. Schnelle, G.-R. Siemann, P. Hofmann, T. Wehling, *et al.*, arXiv preprint arXiv:2504.19961 (2025).

[34] J. Maklar, J. Sarkar, S. Dong, Y. A. Gerasimenko, T. Pincelli, S. Beaulieu, P. S. Kirchmann, J. A. Sobota, S. Yang, D. Leuenberger, *et al.*, Science advances **9**, eadi4661 (2023).

[35] S. Hellmann, T. Rohwer, M. Kalläne, K. Hanff, C. Sohrt, A. Stange, A. Carr, M. Murnane, H. Kapteyn, L. Kipp, *et al.*, Nature communications **3**, 1069 (2012).

[36] L. Perfetti, P. A. Loukakos, M. Lisowski, U. Bovensiepen, H. Berger, S. Biermann, P. S. Cornaglia, A. Georges, and M. Wolf, Phys. Rev. Lett. **97**, 067402 (2006).

[37] J. Demsar, L. Forró, H. Berger, and D. Mihailovic, Phys. Rev. B **66**, 041101 (2002).

[39] J. P. Perdew, K. Burke, and M. Ernzerhof, Phys. Rev. Lett. **77**, 3865 (1996).

[39] G. Kresse and J. Furthmüller, Physical Review B **54**, 11169 (1996).

[40] G. Pizzi, V. Vitale, R. Arita, S. Blügel, F. Freimuth, G. Géranton, M. Gibertini, D. Gresch, C. Johnson, T. Koretsune, J. Ibañez-Azpiroz, H. Lee, J.-M. Lihm, D. Marchand, A. Marrazzo, Y. Mokrousov, J. Mustafa, Y. Nohara, Y. Nomura, L. Paulatto, S. Ponce, T. Ponweiser, J. Qiao, L. Thøgersen, P. Vàzquez-Montejo, Q. Wu, M. Zacchigna, Z. Zhu, M. Zwiebler, F. Giustino, J. P. Perdew, N. Marzari, D. Vanderbilt, I. Souza, A. A. Mostofi, and J. R. Yates, Journal of Physics: Condensed Matter **32**, 165902 (2020).

[41] F. Aryasetiawan, M. Imada, A. Georges, G. Kotliar, S. Biermann, and A. I. Lichtenstein, Phys. Rev. B **70**, 195104 (2004).

[42] T. Kotani, Journal of Physics: Condensed Matter **12**, 2413 (2000).

[43] M. Springer and F. Aryasetiawan, Phys. Rev. B **57**, 4364 (1998).

[44] A. A. Mostofi, J. R. Yates, Y.-S. Lee, I. Souza, D. Vanderbilt, and N. Marzari, Computer Physics Communications **178**, 685 (2008).

[45] Y. Nomura, M. Kaltak, K. Nakamura, C. Taranto, S. Sakai, A. Toschi, R. Arita, K. Held, G. Kresse, and M. Imada, Phys. Rev. B **86**, 085117 (2012).

[46] A. Kutepov, K. Haule, S. Y. Savrasov, and G. Kotliar, Phys. Rev. B **82**, 045105 (2010).

[47] M. Wallerberger, A. Hausoel, P. Gunacker, A. Kowalski, N. Parragh, F. Goth, K. Held, and G. Sangiovanni, Computer Physics Communications **235**, 388 (2019).

[48] J. Kaufmann and K. Held, Computer Physics Communications **282**, 108519 (2023).

[49] V. I. Anisimov, I. V. Solovyev, M. A. Korotin, M. T. Czyżyk, and G. A. Sawatzky, Phys. Rev. B **48**, 16929 (1993).

From SM:

[1] Kresse, G.; Hafner, J. Ab initio molecular dynamics for liquid metals. Physical Review B 1993, 47, 558-561. [2] Kresse, G.; Furthmüller, J. Efficient iterative schemes for ab initio total-energy calculations using a plane-wave basis set. Physical Review B 1996, 54, 11169-11186. [3] Kresse, G.; Furthmüller, J. Efficiency of ab-initio total energy calculations for metals and semiconductors using a plane-wave basis set. Computational Materials Science 1996, 6, 15-50. [4] Perdew, J. P.; Burke, K.; Ernzerhof, M. Generalized Gradient Approximation Made Simple. Physical Review Letters 1996, 77, 3865-3868. [5] Blöchl, P. E. Projector augmented-wave method. Physical Review B 1994, 50, 17953-17979. [6] Kresse, G.; Joubert, D. From ultrasoft pseudopotentials to the projector augmented-wave method. Physical Review B 1999, 59,

1758-1775. [7] Pizzi, G. et al. Wannier90 as a community code: new features and applications. Journal of Physics: Condensed Matter 2020, 32, 165902. [8] Mostofi, A. A.; Yates, J. R.; Lee, Y.-S.; Souza, I.; Vanderbilt, D.; Marzari, N. wannier90: A tool for obtaining maximally-localised Wannier functions. Computer Physics Communications 2008, 178, 685-699. [9] Aryasetiawan, F.; Imada, M.; Georges, A.; Kotliar, G.; Biermann, S.; Lichtenstein, A. I. Frequency-dependent local interactions and low-energy effective models from electronic structure calculations. Phys. Rev. B 2004, 70, 195104. [10] Kotani, T. Ab initio random-phase-approximation calculation of the frequency-dependent effective interaction between 3d electrons: Ni, Fe, and MnO. Journal of Physics: Condensed Matter 2000, 12, 2413. [11] Springer, M.; Aryasetiawan, F. Frequency-dependent screened interaction in Ni within the random-phase approximation. Phys. Rev. B 1998, 57, 4364-4368. [12] Kaltak, M. Merging GW with DMFT. PhD thesis, University of Vienna 2015, [13] Wallerberger, M.; Hausoel, A.; Gunacker, P.; Kowalski, A.; Parragh, N.; Goth, F.; Held, K.; Sangiovanni, G. w2dynamics: Local one- and two-particle quantities from dynamical mean field theory. Computer Physics Communications 2019, 235, 388-399. [14] Boehnke, L.; Hafermann, H.; Ferrero, M.; Lechermann, F.; Parcollet, O. Orthogonal polynomial representation of imaginarytime Green's functions. Physical Review B 2011, 84. [15] Kaufmann, J.; Held, K. ana_cont: Python package for analytic continuation. Computer Physics Communications 2023, 282, 108519. [16] Gubernatis, J. E.; Jarrell, M.; Silver, R. N.; Sivia, D. S. Quantum Monte Carlo simulations and maximum entropy: Dynamics from imaginary-time data. Physical Review B 1991, 44, 6011-6029. [17] Sandvik, A. W. Stochastic method for analytic continuation of quantum Monte Carlo data. Physical Review B 1998, 57, 10287-10290. [18] Bergeron, D.; Tremblay, A.-M. S. Algorithms for optimized maximum entropy and diagnostic tools for analytic continuation. Physical Review E 2016, 94. [19] Kraberger, G. J.; Triebl, R.; Zingl, M.; Aichhorn, M. Maximum entropy formalism for the analytic continuation of matrixvalued Green's functions. Physical Review B 2017, 96. [20] Momma, K.; Izumi, F. VESTA 3 for three-dimensional visualization of crystal, volumetric and morphology data. Journal of Applied Crystallography 2011, 44, 1272-1276.

s

**References from Distinguishing a Mott Insulator from a Trivial Insulator with Atomic Adsorbates by Lee et al.**

# References

[1] B. Keimer, S. A. Kivelson, M. R. Norman, S. Uchida, and J. Zaanen, *From quantum matter to high-temperature superconductivity in copper oxides,* Nature **518**, 179 (2015).

[2] N. F. Mott, *Metal-Insulator Transition,* Rev. Mod. Phys. **40**, 677 (1968).

[3] P. Fazekas and E. Tosatti, *Electrical, structural and magnetic properties of pure and doped* $1\mathrm{T}-\mathrm{TaS}_2$*,* Philos. Mag. B **39**, 229 (1979).

[4] B. Giambattista, C. G. Slough, W. W. McNairy, and R. V. Coleman, *Scanning tunneling microscopy of atoms and charge-density waves in* $1T-\mathrm{TaS}_2$*,* $1T-\mathrm{TaSe}_2$*, and* $1T-\mathrm{VSe}_2$*,* Phys. Rev. B **41**, 10082 (1990).

[5] J.-J. Kim, W. Yamaguchi, T. Hasegawa, and K. Kitazawa, *Observation of Mott Localization Gap Using Low Temperature Scanning Tunneling Spectroscopy in Commensurate* $1T-\mathrm{TaS}_2$*,* Phys. Rev. Lett. **73**, 2103 (1994).

[6] J.-J. Kim, I. Ekvall, and H. Olin, *Temperature-dependent scanning tunneling spectroscopy of* $1T-\mathrm{TaS}_2$*,* Phys. Rev. B **54**, 2244 (1996).

[7] F. F.Zwick *et al.*, *Spectral Consequences of Broken Phase Coherence in* $1T-TaS_2$, Phys. Rev. Lett. **81**, 1058 (1998).

[8] T. Pillo *et al.*, *Interplay between electron-electron interaction and electron-phonon coupling near the Fermi surface of* $1T-TaS_2$, Phys. Rev. B **62**, 4277 (2000).

[9] K. Rossnagel, E. Rotenberg, H. Koh, N. V. Smith, and L. Kipp, *Continuous Tuning of Electronic Correlations by Alkali Adsorption on Layered* $1T-TaS_2$, Phys. Rev. Lett. **95**, 126403 (2005).

[10] B. Sipos *et al.*, *From Mott state to superconductivity in* $1T-TaS_2$, Nat. Mater. **7**, 960 (2008).

[11] P. Xu *et al.*, *Superconducting phase in the layered dichalcogenide* $1T-TaS_2$ *upon inhibition of the metal-insulator transition,* Phys. Rev. B **81**, 172503 (2010).

[12] R. Ang *et al.*, *Real-Space Coexistence of the Melted Mott State and Superconductivity in Fe-Substituted* $1T-TaS_2$, Phys. Rev. Lett. **109**, 176403 (2012).

[13] R. Ang *et al.*, *Superconductivity and bandwidth-controlled Mott metal-insulator transition in* $1T$*-*$TaS_{2-x}Se_x$, Phys. Rev. B **88**, 115145 (2013).

[14] L. Stojchevska *et al.*, *Ultrafast Switching to a Stable Hidden Quantum State in an Electronic Crystal,* Science **344**, 177 (2014).

[15] E. Lahoud, O. N. Meetei, K. B. Chaska, A. Kanigel, and N. Trivedi, *Emergence of a Novel Pseudogap Metallic State in a Disordered 2D Mott Insulator,* Phys. Rev. Lett. **112**, 206402 (2014).

[16] R. Ang *et al.*, *Atomistic origin of an ordered superstructure induced superconductivity in layered chalcogenides,* Nat. Commun. **6**, 6091 (2015).

[17] D. Cho, Y.-H. Cho, S.-W. Cheong, K.-S. Kim, and H. W. Yeom, *Interplay of electron-electron and electron-phonon interactions in the low-temperature phase of* $1T-TaS_2$, Phys. Rev. B **92**, 085132 (2015).

[18] D. Cho *et al.*, *Nanoscale manipulation of the Mott insulating state coupled to charge order in* $1T-TaS_2$, Nat. Commun. **7**, 10453 (2016).

[19] K. T. Law and P. A. Lee, $1T-TaS_2$ *as a quantum spin liquid,* Proc. Natl. Acad. Sci. **114**, 6996 (2017).

[20] D. Cho *et al.*, *Correlated electronic states at domain walls of a Mott-charge-density-wave insulator* $1T-TaS_2$, Nat. Commun. **8**, 392 (2017).

[21] A. Ribak *et al.*, *Gapless excitations in the ground state of* $1T-TaS_2$, Phys. Rev. B **96**, 195131 (2017).

[22] M. Ligges *et al.*, *Ultrafast Doublon Dynamics in Photoexcited* $1T$-$TaS_2$, Phys. Rev. Lett. **120**, 166401 (2018).

[23] I. Lutsky *et al.*, *Electronic structure of commensurate, nearly commensurate, and incommensurate phases of* $1T-TaS_2$ *by angle-resolved photoelectron spectroscopy, scanning tunneling spectroscopy, and density functional theory,* Phys. Rev. B **98**, 195425 (2018).

[24] J. Skolimowski, Y. Gerasimenko, and R. Žitko, *Mottness collapse without metallization in the domain wall of the triangular-lattice Mott insulator* $1T-\mathrm{TaS}_2$, Phys. Rev. Lett. **122**, 036802 (2019).

[25] J. W. Park, G. Y. Cho, J. Lee, and H. W. Yeom, *Emergent honeycomb network of topological excitations in correlated charge density wave,* Nat. Commun. **10**, 4038 (2019).

[26] L. Cheng *et al.*, *Renormalization of the Mott gap by lattice entropy: The case of 1T*-$\mathrm{TaS}_2$, Phys. Rev. Res. **2**, 023064 (2020).

[27] J. A. Wilson, F. J. Di Salvo, and S. Mahajan, *Charge-density waves and superlattices in the metallic layered transition metal dichalcogenides,* Adv. Phys. **24**, 117 (1975).

[28] T. Ritschel *et al.*, *Orbital textures and charge density waves in transition metal dichalcogenides,* Nat. Phys. **11**, 328 (2015).

[29] T. Ritschel, H. Berger, and J. Geck, *Stacking-driven gap formation in layered 1T*-$\mathrm{TaS}_2$, Phys. Rev. B **98**, 195134 (2018).

[30] S.-H. Lee, J. S. Goh, and D. Cho, *Origin of the Insulating Phase and First-Order Metal-Insulator Transition in* $1T-\mathrm{TaS}_2$, Phys. Rev. Lett. **122**, 106404 (2019).

[31] Y. D. Wang *et al.*, *Band insulator to Mott insulator transition in 1T-*$TaS_2$, Nat. Commun. **11**, 4215 (2020).

[32] C. J. Butler, M. Yoshida, T. Hanaguri, and Y. Iwasa, *Mottness versus unit-cell doubling as the driver of the insulating state in* $1T-\mathrm{TaS}_2$, Nat. Commun. **11**, 2477 (2020).

[33] T. Ishiguro and H. Sato, *Electron microscopy of phase transformations in 1T*-$\mathrm{TaS}_2$, Phys. Rev. B **44**, 2046 (1991).

[34] G. von Witte *et al.*, *Surface structure and stacking of the commensurate* $(\sqrt{13}\times\sqrt{13})R13.9^\circ$ *charge density wave phase of* $1T-\mathrm{TaS}_2(0001)$, Phys. Rev. B **100**, 155407 (2019).

[35] W. Stahl *et al.*, *Collapse of layer dimerization in the photo-induced hidden state of 1T-*$TaS_2$, Nat. Commun. **11**, 1247 (2020).

[36] See the Supplemental Material at [URL will be given by the publisher] for the details, which includes Refs. [18, 41, 31, 32].

[37] P. E. Blöchl, *Projector augmented-wave method,* Phys. Rev. B **50**, 17953 (1994).

[38] G. Kresse, and J. Furthmüller, *Efficient iterative schemes for ab initio total-energy calculations using a plane-wave basis set,* Phys. Rev. B **54**, 11169 (1996).

[39] J. P. Perdew, K. Burke, and M. Ernzerhof, *Generalized Gradient Approximation Made Simple,* Phys. Rev. Lett. **77**, 3865 (1996).

[40] J. Lee *et al.*, *Honeycomb-Lattice Mott Insulator on Tantalum Disulphide,* Phys. Rev. Lett. **125**, 096403 (2020).

[41] L. Ma *et al.*, *A metallic mosaic phase and the origin of Mott-insulating state in 1T-*$TaS_2$, Nat. Commun. **7**, 10956 (2016).

## .3 References from Main Articles about Experiments

**References from Orbital textures and charge density waves in transition metal dichalcogenides by Ritschel, Trinckauf, Koepernik, Büchner, Zimmermann, Berger, Joe, Abbamonte, Geck**

# References


[1] Grüner, G. *Density waves in solids*, vol. 89 (Addison-Wesley Reading, MA, 1994).

[2] Chang, J. *et al.* Direct observation of competition between superconductivity and charge density wave order in $YBa_2Cu_3O_{6.67}$. *Nat Phys* **8**, 871–876 (2012).

[3] Ghiringhelli, G. *et al.* Long-range incommensurate charge fluctuations in $(Y, Nd)Ba_2Cu_3O_{6+x}$. *Science* **337**, 821–825 (2012).

[4] da Silva Neto, E. H. *et al.* Ubiquitous interplay between charge ordering and high-temperature superconductivity in cuprates. *Science* **343**, 393–396 (2014).

[5] de la Cruz, C. *et al.* Magnetic order close to superconductivity in the iron-based layered $LaO_{1-x}F_xFeAs$ systems. *Nature* **453**, 899–902 (2008).

[6] Mühlbauer, S. *et al.* Skyrmion lattice in a chiral magnet. *Science* **323**, 915–919 (2009).

[7] Wang, Q. H., Kalantar-Zadeh, K., Kis, A., Coleman, J. N. & Strano, M. S. Electronics and optoelectronics of two-dimensional transition metal dichalcogenides. *Nature nanotechnology* **7**, 699–712 (2012).

[8] Chhowalla, M. *et al.* The chemistry of two-dimensional layered transition metal dichalcogenide nanosheets. *Nature chemistry* **5**, 263–275 (2013).

[9] Sipos, B. *et al.* From mott state to superconductivity in $1T$-$TaS_2$. *Nat Mater* **7**, 960–965 (2008).

[10] Fazekas, P. & Tosatti, E. Electrical, structural and magnetic properties of pure and doped $1T$-$TaS_2$. *Philos. Mag. B* **39**, 229–244 (1979).

[11] Hellmann, S. *et al.* Ultrafast melting of a charge-density wave in the mott insulator $1T$-$TaS_2$. *Phys. Rev. Lett.* **105**, 187401 (2010).

[12] Petersen, J. C. *et al.* Clocking the melting transition of charge and lattice order in $1T$-$TaS_2$ with ultrafast extreme-ultraviolet angle-resolved photoemission spectroscopy. *Phys. Rev. Lett.* **107**, 177402 (2011).

[13] Perfetti, L. *et al.* Time evolution of the electronic structure of $1T$-$TaS_2$ through the insulator-metal transition. *Phys. Rev. Lett.* **97**, 067402 (2006).

[14] Wu, X. L. & Lieber, C. M. Hexagonal domain-like charge density wave phase of $1T$-$TaS_2$ determined by scanning tunneling microscopy. *Science* **243**, 4899 (1989).

[15] Spijkerman, A., de Boer, J. L., Meetsma, A., Wiegers, G. A. & van Smaalen, S. X-ray crystal-structure refinement of the nearly commensurate phase of $1T$-$TaS_2$ in (3 + 2)-dimensional superspace. *Phys. Rev. B* **56**, 13757–13767 (1997).

[16] Ang, R. *et al.* Real-space coexistence of the melted mott state and superconductivity in fe-substituted $1T$-$TaS_2$. *Phys. Rev. Lett.* **109**, 176403 (2012).

[17] Tanda, S., Sambongi, T., Tani, T. & Tanaka, S. X-ray study of charge density wave structure in $1T$-$TaS_2$. *Journal of the Physical Society of Japan* **53**, 476–479 (1984).

[18] Nakanishi, K. & Shiba, H. Theory of three-dimensional orderings of charge-density waves in $1T$-$TaX_2$ (X: S, Se). *Journal of the Physical Society of Japan* **53**, 1103–1113 (1984).

[19] Bovet, M. *et al.* Interplane coupling in the quasi-two-dimensional $1T$-$TaS_2$. *Phys. Rev. B* **67**, 125105 (2003).

[20] Darancet, P., Millis, A. J. & Marianetti, C. A. Three-dimensional metallic and two-dimensional insulating behavior in octahedral tantalum dichalcogenides. *Phys. Rev. B* **90**, 045134 (2014).

[21] Damascelli, A., Hussain, Z. & Shen, Z.-X. Angle-resolved photoemission studies of the cuprate superconductors. *Rev. Mod. Phys.* **75**, 473–541 (2003).

[22] Ku, W., Berlijn, T. & Lee, C.-C. Unfolding first-principles band structures. *Phys. Rev. Lett.* **104**, 216401 (2010).

[23] Rossnagel, K. On the origin of charge-density waves in select layered transition-metal dichalcogenides. *J. Phys.: Condens. Matter* **23**, 213001 (2011).

[24] Pillo, T. *et al.* Remnant fermi surface in the presence of an underlying instability in layered $1T$-$TaS_2$. *Phys. Rev. Lett.* **83**, 3494–3497 (1999).

[25] Stojchevska, L. *et al.* Ultrafast switching to a stable hidden quantum state in an electronic crystal. *Science* **344**, 177–180 (2014).

[26] Koepernik, K. & Eschrig, H. Full-potential nonorthogonal local-orbital minimum-basis band-structure scheme. *Phys. Rev. B* **59**, 1743–1757 (1999).

[27] Brouwer, R. *Incommensurability in crystal structures.* Ph.D. thesis, Rijksuniversiteit Groningen (Netherlands) (1978).

[28] Rossnagel, K., Rotenberg, E., Koh, H., Smith, N. V. & Kipp, L. Continuous tuning of electronic correlations by alkali adsorption on layered $1T$-$TaS_2$. *Phys. Rev. Lett.* **95**, 126403 (2005).

## .4 References from Main Articles about Applications

**References from Charge Configuration Memory Devices: Energy Efficiency and Switching Speed by Mraz et al. (2022)**

(1) Holmes, D. S.; Kadin, A. M.; Johnson, M. W. Superconducting Computing in Large-Scale Hybrid Systems. Computer 2015, 48, 3442.
(2) Soloviev, I. I.; et al. Beyond Moore's technologies: operation principles of a superconductor alternative. Beilstein J. Nanotechnol. 2017, 8, 2689-2710.
(3) Janod, E.; et al. Resistive Switching in Mott Insulators and Correlated Systems. Adv. Funct. Mater. 2015, 25, 6287-6305.
(4) Tafuri, F., Ed. Fundamentals and Frontiers of the Josephson Effect; Springer Series in Materials Science, Vol. 286; Springer Nature, 2019; pp 632-648.
(5) Holmes, D. S.; Ripple, A. L.; Manheimer, M. A. Energy-Efficient Superconducting Computing-Power Budgets and Requirements. IEEE Trans. Appl. Supercond. 2013, 23, 1701610-1701610.

(6) Vaskivskyi, I.; et al. Fast electronic resistance switching involving hidden charge density wave states. Nat. Commun. 2016, 7, 11442.
(7) Mihailovic, D.; et al. Ultrafast non-thermal and thermal switching in charge configuration memory devices based on 1T$TaS_2$. Appl. Phys. Lett. 2021, 119, 013106.
(8) Stojchevska, L.; et al. Ultrafast Switching to a Stable Hidden Quantum State in an Electronic Crystal. Science 2014, 344, 177-180.
(9) Gerasimenko, Y. A.; Karpov, P.; Vaskivskyi, I.; Brazovskii, S.; Mihailovic, D. Intertwined chiral charge orders and topological stabilization of the light-induced state of a prototypical transition metal dichalcogenide. npj Quantum Mater. 2019, 4, 32.
(10) Ritschel, T.; et al. Orbital textures and charge density waves in transition metal dichalcogenides. Nat. Phys. 2015, 11, 328-331.
(11) Stahl, Q.; et al. Collapse of layer dimerization in the photoinduced hidden state of $1\ T - TaS_2$. Nat. Commun. 2020, 11, 1247.
(12) Zhu, X.; Li, A. J.; Stewart, G. R.; Hebard, A. F. Detection of charge density wave phase transitions at $1\ T - TaS_2/GaAs^2$ interfaces. Appl. Phys. Lett. 2017, 110, 181603.
(13) Tsen, A. W.; et al. Structure and control of charge density waves in two-dimensional 1T-$TaS_2$. Proc. Natl. Acad. Sci. U. S. A. 2015, 112, 15054-15059.
(14) Perfetti, L.; et al. Femtosecond dynamics of electronic states in the Mott insulator $1\ T - TaS_2$ by time resolved photoelectron spectroscopy. New J. Phys. 2008, 10, 053019.
(15) Michaelson, H. B. The work function of the elements and its periodicity. J. Appl. Phys. 1977, 48, 4729-4733.
(16) Cho, D.; Cho, Y.-H.; Cheong, S.-W.; Kim, K.-S.; Yeom, H. W. Interplay of electron-electron and electron-phonon interactions in the low-temperature phase of $1\ T - TaS2$. Phys. Rev. B 2015, 92, 085132.
(17) Vaskivskyi, I.; et al. Controlling the metal-to-insulator relaxation of the metastable hidden quantum state in $1\ T - TaS_2$. Sci. Adv. 2015, 1, No. e1500168.
(18) Tanda, S.; Sambongi, T.; Tani, T.; Tanaka, S. X-Ray Study of Charge Density Wave Structure in 1T-$TaS_2$. J. Phys. Soc. Jpn. 1984, 53, 476-479.
(19) Wang, Y. D.; et al. Band insulator to Mott insulator transition in 1T-$TaS_2$. Nat. Commun. 2020, 11, 4215.
(20) Cho, D.; et al. Nanoscale manipulation of the Mott insulating state coupled to charge order in 1T-$TaS_2$. Nat. Commun. 2016, 7, 10453.
(21) Venturini, R. Ultra-Efficient Resistance Switching between Charge Ordered Phases in 1T-$TaS_2$ with a Single Picosecond Electrical Pulse. arXiv 2022, 2202.13831.
(22) Anders, S.; et al. European roadmap on superconductive electronics - status and perspectives. Phys. C Supercond. 2010, 470, 2079-2126.
(23) Ravnik, J.; Vaskivskyi, I.; Mertelj, T.; Mihailovic, D. Real-time observation of the coherent transition to a metastable emergent state in 1T-$TaS_2$. Phys. Rev. B 2018, 97, 075304.
(24) Landauer, R. Irreversibility and Heat Generation in the Computing Process. IBM journal 1961, 5, 183.
(25) Grezes, C.; et al. Ultra-low switching energy and scaling in electric-field-controlled nanoscale magnetic tunnel junctions with high resistance-area product. Appl. Phys. Lett. 2016, 108, 012403.
(26) Cheng, C. H.; Chin, A.; Yeh, F. S. Ultralow Switching Energy Ni/$GeO_x$/HfON/TaN RRAM. IEEE Electron Device Lett. 2011, 32, 366-368.
(27) Wang, L.; et al. Voltage-Controlled Magnetic Tunnel Junctions for Processing-In-Memory Implementation. IEEE Electron Device Lett. 2018, 39, 440-443.
(28) Liu, B.; et al. Multi-level phase-change memory with ultralow power consumption and resistance drift. Sci. Bull. 2021, 66, 22172224.

(29) Loke, D.; et al. Breaking the Speed Limits of Phase-Change Memory. Science 2012, 336, 1566-1569.
(30) Ding, K.; et al. Phase-change heterostructure enables ultralow noise and drift for memory operation. Science 2019, 366, 210-215.
(31) Pi, S.; et al. Memristor crossbar arrays with 6 -nm half-pitch and 2-nm critical dimension. Nat. Nanotechnol. 2019, 14, 35-39.
(32) Xu, W.; Min, S.-Y.; Hwang, H.; Lee, T.-W. Organic core-sheath nanowire artificial synapses with femtojoule energy consumption. Sci. Adv. 2016, 2, No. e1501326.
(33) Havel, V.; et al. Ultrafast switching in $Ta_2O_5$-based resistive memories. In 2016 IEEE Silicon Nanoelectronics Workshop (SNW) 82-83; IEEE, 2016; DOI: 10.1109/SNW.2016.7577995.
(34) Torrezan, A. C.; Strachan, J. P.; Medeiros-Ribeiro, G.; Williams, R. S. Sub-nanosecond switching of a tantalum oxide memristor. Nanotechnology 2011, 22, 485203.
(35) Lee, S.; Sohn, J.; Jiang, Z.; Chen, H.-Y.; Philip Wong, H.-S. Metal oxide-resistive memory using graphene-edge electrodes. Nat. Commun. 2015, 6, 8407.
(36) Ando, K.; et al. Spin-transfer torque magnetoresistive randomaccess memory technologies for normally off computing (invited). J. Appl. Phys. 2014, 115, 172607.
(37) Jan, G.; et al. Demonstration of Ultra-Low Voltage and Ultra Low Power STT-MRAM designed for compatibility with 0x node embedded LLC applications. In 2018 IEEE Symposium on VLSI Technology 65-66; IEEE, 2018.
(38) Rehm, L.; et al. Sub-nanosecond switching in a cryogenic spintorque spin-valve memory element with a dilute permalloy free layer. Appl. Phys. Lett. 2019, 114, 212402.
(39) Khalili Amiri, P.; et al. Electric-Field-Controlled Magnetoelectric RAM: Progress, Challenges, and Scaling. IEEE Trans. Magn. 2015, 51, 1-7.
(40) Zhao, Q.-Y.; et al. A compact superconducting nanowire memory element operated by nanowire cryotrons. Supercond. Sci. Technol. 2018, 31, 035009.
(41) McCaughan, A. N.; Toomey, E.; Schneider, M.; Berggren, K. K.; Nam, S. W. A kinetic-inductance-based superconducting memory element with shunting and sub-nanosecond write times. Supercond. Sci. Technol. 2019, 32, 015005.
(42) Konno, G.; Yamanashi, Y.; Yoshikawa, N. Fully Functional Operation of Low-Power 64-kb Josephson-CMOS Hybrid Memories. IEEE Trans. Appl. Supercond. 2017, 27, 1-7.
(43) Krivorotov, I. N.; et al. Ultrafast spin torque memory based on magnetic tunnel junctions with combined in-plane and perpendicular polarizers. In 70th Device Research Conference 211-212; IEEE, 2012.
(44) Pickett, M. D.; Stanley Williams, R. Sub-100 fJ and subnanosecond thermally driven threshold switching in niobium oxide crosspoint nanodevices. Nanotechnology 2012, 23, 215202.
(45) Clerc, S.; et al. A 0.32 V, 55 fJ per bit access energy, CMOS 65 nm bit-interleaved SRAM with radiation Soft Error tolerance. In 2012 IEEE International Conference on IC Design & Technology 1-4; IEEE, 2012; DOI: 10.1109/ICICDT.2012.6232860.
(46) Wang, K. L.; Alzate, J. G.; Khalili Amiri, P. Low-power nonvolatile spintronic memory: STT-RAM and beyond. J. Phys. Appl. Phys. 2013, 46, 074003.
(47) Dieny, B.; et al. Opportunities and challenges for spintronics in the microelectronics industry. Nat. Electron. 2020, 3, 446-459.
(48) Stupakiewicz, A.; Szerenos, K.; Afanasiev, D.; Kirilyuk, A.; Kimel, A. V. Ultrafast nonthermal photo-magnetic recording in a transparent medium. Nature 2017, 542, 71-74.
(49) Dayton, I. M.; et al. Experimental Demonstration of a Josephson Magnetic Memory Cell With a Programmable $\pi$-Junction. IEEE Magn. Lett. 2018, 9, 1-5.
(50) Takeshita, Y.; et al. High-Speed Memory Driven by SFQ Pulses Based on $0-\pi$ SQUID. IEEE Trans. Appl. Supercond. 2021, 31, 1-6.

(51) Tanaka, M.; et al. Josephson-CMOS Hybrid Memory With Nanocryotrons. IEEE Trans. Appl. Supercond. 2017, 27, 1-4.
(52) Van Duzer, T.; et al. 64-kb Hybrid Josephson-CMOS 4 K RAM With 400 ps Access Time and 12 mW Read Power. IEEE Trans. Appl. Supercond. 2013, 23, 1700504-1700504.
(53) Tolpygo, S. K. Superconductor digital electronics: Scalability and energy efficiency issues (Review Article). Low Temp. Phys. 2016, 42, 361-379.
(54) Enomoto, H.; Kawano, T.; Kawaguchi, M.; Takano, Y.; Sekizawa, K. Van der Waals Growth of Thin $TaS_2$ on Layered Substrates by Chemical Vapor Transport Technique. Jpn. J. Appl. Phys. 2004, 43, L123-L126.
(55) Sanders, C. E.; et al. Crystalline and electronic structure of single-layer TaS 2. Phys. Rev. B 2016, 94, 081404.
(56) Wang, X.; et al. Chemical Growth of $1T - TaS_2$ Monolayer and Thin Films: Robust Charge Density Wave Transitions and High Bolometric Responsivity. Adv. Mater. 2018, 30, 1800074.
(57) Zhao, Q.-Y.; McCaughan, A. N.; Dane, A. E.; Berggren, K. K.; Ortlepp, T. A nanocryotron comparator can connect single-fluxquantum circuits to conventional electronics. Supercond. Sci. Technol. 2017, 30, 044002.
(58) Mraz, A.; Kabanov, V. V.; Mihailovic, D. Nanocryotron-driven Charge Configuration Memory. arXiv 2022, 2203.14586.
(59) Mukhanov, O. A.; Kirichenko, A. F.; Filippov, T. V.; Sarwana, S. Hybrid Semiconductor-Superconductor Fast-Readout Memory for Digital RF Receivers. IEEE Trans. Appl. Supercond. 2011, 21, 797800.
(60) Joshi, J.; et al. Charge density wave activated excitons in $TiSe_2 - MoSe_2$ heterostructures. APL Mater. 2022, 10, 011103.

**References from Possible origin of nonlinear conductivity and large dielectric constant in the commensurate charge-density-wave phase of $1T - TaS_2$ by Ma, Hou, Lu, Li, Petrovic (2017)**

[1] G. Gruner, Rev. Mod. Phys. 60, 1129 (1988).
[2] P. Monceau, Adv. Phys. 61, 325 (2012).
[3] C.-W. Chen, J. Choe, and E. Morosan, Rep. Prog. Phys. 79, 084505 (2016).
[4] M. E. Itkis, F. Ya. Nad, and P. Monceau, J. Phys.: Condens. Matter 2, 8327 (1990).
[5] J.-P. Pouget, Comptes Rendus Physique 17, 332 (2016).
[6] F. Ya. Nad and P. Monceau, Phys. Rev. B 46, 7413 (1992).
[7] G. Gruner, A. Zawadowski, and P. M. Chaikin, Phys. Rev. Lett. 46, 511 (1981).
[8] I. G. Gorlova, S. G. Zybtsev, and V. Ya Pokrovskii, JETP Lett. 100, 256 (2014).
[9] D. Staresinic, K. Biljakovic, W. Brutting, K. Hosseini, P. Monceau, H. Berger, and F. Levy, Phys. Rev. B 65, 165109 (2002).
[10] D. Staresinic, P. Lunkenheimer, J. Hemberger, K. Biljakovic, and A. Loidl, Phys. Rev. Lett. 96, 046402 (2006).
[11] M. E. Itkis, F. Ya. Nad, S. V. Zaitsev-Zotov, and F. Levy, Solid State Commun. 71, 895 (1989).
[12] V. Nasretdinova and S. Zaitsev-Zotov, Physica B (Amsterdam, Neth.) 407, 1874 (2012).
[13] F. J. Di Salvo, J. A. Wilson, B. G. Bagley, and J. V. Waszczak, Phys. Rev. B 12, 2220 (1975).
[14] J. A. Wilson, F. J. Di Salvo, and S. Mahajan, Adv. Phys. 24, 117 (1975).
[15] A. A. Sinchenko, P. Lejay, and P. Monceau, Phys. Rev. B 85, 241104(R) (2012).
[16] S. Uchida, K. Tanabe, and S. Tanaka, Solid State Commun. 27, 637 (1978).
[17] I. Vaskivskyi, I. A. Mihailovic, S. Brazovskii, J. Gospodaric, T. Mertelj, D. Svetin, P. Sutar, and D. Mihailovic, Nat. Commun. 7, 11442 (2016), and the Supplementary Information.

[18] J. Chang, E. Blackburn, A. T. Holmes, N. B. Christensen, J. Larsen, J. Mesot, R. Liang, D. A. Bonn, W. N. Hardy, A. Watenphul, M. V. Zimmermann, E. M. Forgan, and S. M. Hayden, Nat. Phys. 8, 871 (2012).
[19] M. G. Velarde, W. Ebeling, and A. P. Chetverikov, C. R. Mec. 340, 910 (2012).
[20] R. Comin, R. Sutarto, F. He, E. H. da Silva Neto, L. Chauviere, A. Frano, R. Liang, W. N. Hardy, D. A. Bonn, Y. Yoshida, H. Eisaki, A. J. Achkar, D. G. Hawthorn, B. Keimer, G. A. Sawatzky, and A. Damascelli, Nat. Mater. 14, 796 (2015).
[21] M. Yoshida, R. Suzuki, Y. J. Zhang, M. Nakano, and Y. Iwasa, Sci. Adv. 1, e1500606 (2015); M. Yoshida, T. Gokuden, R. Suzuki, M. Nakano, and Y. Iwasa, Phys. Rev. B 95, 121405(R) (2017).
[22] M. J. Hollander, Y. Liu, W. J. Lu, L. J. Li, Y. P. Sun, J. A. Robinson, and S. Datta, Nano Lett. 15, 1861 (2015).
[23] H. Mutka, L. Zuppiroli, P. Molinie, and J. C. Bourgoin, Phys. Rev. B 23, 5030 (1981).
[24] A. Ubaldini and E. Giannini, J. Cryst. Growth 401, 878 (2014).
[25] A. A. Sinchenko, P. Lejay, O. Leynaud, and P. Monceau, Phys. Rev. B 93, 235141 (2016).
[26] Y. Huang, B. F. Hu, T. Dong, A. F. Fang, P. Zheng, and N. L. Wang, Phys. Rev. B 86, 205123 (2012).
[27] F. J. Di Salvo and J. E. Graebner, Solid State Commun. 23, 825 (1977).
[28] P. D. Hambourger and F. J. Di Salvo, Solid State Commun. 35, 405 (1980).
[29] B. Dardel, M. Grioni, D. Malterre, P. Weibel, Y. Baer, and F. Levy, Phys. Rev. B 45, 1462 (1992).
[30] J.-J. Kim, W. Yamaguchi, T. Hasegawa, and K. Kitazawa, Phys. Rev. Lett. 73, 2103 (1994).
[31] L. Perfetti, P. A. Loukakos, M. Lisowski, U. Bovensiepen, H. Berger, S. Biermann, P. S. Cornaglia, A. Georges, and M. Wolf, Phys. Rev. Lett. 97, 067402 (2006).
[32] B. Burk, R. E. Thomson, A. Zettl, and J. Clarke, Phys. Rev. Lett. 66, 3040 (1991).
[33] D. Cho, G. Gye, J. Lee, S.-H. Lee, L. Wang, S.-W. Cheong, and H. W. Yeom, Nat. Commun. 8, 392 (2017).
[34] R. Rajaraman, Phys. Rep. C 21, 227 (1975).
[35] I. V. Krive and A. S. Rozhavsky, Solid State Commun. 55, 691 (1985).
[36] P. Lunkenheimer, S. Krohns, S. Riegg, S. G. Ebbinghaus, A. Reller, and A. Loidl, Eur. Phys. J.: Spec. Top. 180, 61 (2010).
[37] S. R. Elliott, Adv. Phys. 36, 135 (1987).
[38] Y. C. Ma, C. Lu, X. Wang, X. Du, L. Li, and C. Petrovic, J. Phys.: Condens. Matter 28, 395901 (2016).
[39] T. Ivek, T. Vuletic, S. Tomic, A. Akrap, H. Berger, and L. Forro, Phys. Rev. B. 78, 035110 (2008).
[40] P. Lunkenheimer and A. Loidl, Phys. Rev. Lett. 91, 207601 (2003).
[41] A. K. Jonscher, Nature (London) 267, 673 (1977).
[42] R. J. Cava, R. M. Fleming, P. B. Littlewood, E. A. Rietman, L. F. Schneemeyer, and R. G. Dunn, Phys. Rev. B 30, 3228 (1984).
[43] A. Fischer, P. Pahner, B. Lussem, K. Leo, R. Scholz, T. Koprucki, K. Gartner, and A. Glitzky, Phys. Rev. Lett. 110, 126601 (2013).
[44] N. Croitoru and C. Popescu, Phys. Status Solidi A 3, 1047 (1970).
[45] M. J. Cohen and A. J. Heeger, Phys. Rev. B 16, 688 (1977).
[46] J. B. Balaguru Rayappan, S. A. Cecil Raj, and N. Lawrence, Physica B (Amsterdam, Neth.) 405, 3172 (2010).
[47] A. V. Inyushkin, A. N. Taldenkov, and V. V. Florentiev, Synth. Met. 19, 843 (1987).
[48] M. D. Nunnez-Regueiro, J. M. Lopez-Castillo, and C. Ayache, Phys. Rev. Lett. 55, 1931 (1985).

[49] As thermal conductivity $\kappa$ of $1T - TaS_2$ below $T = 100$ K is absent, the value $\kappa$ of $TaS_3$ is taken as a reference. Moreover, the anisotropy of the thermal conductivity of $1T - TaS_2$ should be considered: it is acceptable that $d/S$ and $\kappa$ in the $ab$ plane (cleaved surface) would be remarkably different from the case of the $\|c$ axis. For our measurement's configuration, the heat flow along the $c$ axis is remarkable for the large ratio of contact area/thickness; hence at low frequencies the heating of the substrate as a whole contributes greatly to removing the Joule heating. That is, as most of the heating power flows into the sapphire substrate, the relaxation time $\tau_{SH}$ (of the sample and the substrate as a whole) is enhanced significantly. Thus the conductivity under dc bias mainly gives a chordal contribution. Nevertheless, the thermal relaxation effects could be neglected above 10 kHz , though systematic research work on the thermal properties of $1T - TaS_2$ is still necessary.
[50] P. B. Littlewood, Phys. Rev. B 36, 3108 (1987).
[51] W.-y. Wu, L. Mihaly, and G. Gruner, Solid State Commun. 55, 663 (1985).
[52] I. G. Austin and N. F. Mott, Adv. Phys. 18, 41 (1969).
[53] N. Dean, J. C. Petersen, D. Fausti, R. I. Tobey, S. Kaiser, L. V. Gasparov, H. Berger, and A. Cavalleri, Phys. Rev. Lett. 106, 016401 (2011).
[54] S. V. Zaitsev-Zotov and V. E. Minakova, Phys. Rev. Lett. 97, 266404 (2006).
[55] S. Brazovskii, C. Brun, Z.-Z. Wang, and P. Monceau, Phys. Rev. Lett. 108, 096801 (2012).
[56] M. J. Rice, A. R. Bishop, J. A. Krumhansl, and S. E. Trullinger, Phys. Rev. Lett. 36, 432 (1976).
[57] B. Horovitz and J. A. Krumhansl, Phys. Rev. B 29, 2109 (1984).
[58] T. Matsuura, J. Hara, K. Inagaki, M. Tsubota, T. Hosokawa, and S. Tanda, Europhys. Lett. 109, 27005 (2015).
[59] J. H. Miller, C. Ordonez, and E. Prodan, Phys. Rev. Lett. 84, 1555 (2000).
[60] K. Inagaki, M. Tsubota, and S. Tanda, Phys. Rev. B 81, 113101 (2010).
[61] A. Rojo-Bravo, V. L. R. Jacques, and D. Le Bolloch, Phys. Rev. B 94, 201120 (2016).
[62] S. Krohns, P. Lunkenheimer, Ch. Kant, A. V. Pronin, H. B. Brom, A. A. Nugroho, M. Diantoro, and A. Loidl, Appl. Phys. Lett. 94, 122903 (2009).
[63] T. B. Adams, D. C. Sinclair, and A. R. West, Phys. Rev. B 73, 094124 (2006).
[64] A. S. Rozhavsky, Yu. V. Pershin, and A. S. Kovalev, Low Temp. Phys. 23, 996 (1997).

**References from Fast electronic resistance switching involving hidden CDW states by Vaskivskyi et al.**

1. Ichikawa, H. et al. Transient photoinduced 'hidden' phase in a manganite. Nat. Mater. 10, 101-105 (2011).

2. Stojchevska, L. et al. Ultrafast switching to a stable hidden quantum state in an electronic crystal. Science 344, 177-180 (2014).

3. Nasu, K. Photoinduced Phase Transitions (World Scientific Publishing Company Incorporated, 2004).

4. Tokura, Y. Photoinduced phase transition: a tool for generating a hidden state of matter. J. Phys. Soc. Jpn 75, 011001 (2006).

5. Vaskivskyi, I. et al. Controlling the metal to insulator relaxation of the metastable hidden quantum state in 1T-$TaS_2$. Sci. Advances 1, e1500168 (2015).

6. Monceau, P. Electronic crystals: an experimental overview. Adv. Phys. 61, 325-581 (2012).

7. Hollander, M. J. et al. Electrically driven reversible insulator-metal phase transition in 1T-$TaS_2$. Nano Lett. 15, 1861-1866 (2015).

8. Brazovskii, S. et al. Plastic sliding of charge density waves: X-ray space resolvedstudies versus theory of current conversion. Phys. Rev. B 61, 10640-10650 (2000).

9. Holmes, D. S., Ripple, A. L. & Manheimer, M. A. Energy-efficient superconducting computing; power budgets and requirements. IEEE Trans. Appl. Supercond. 23, 1701610-1701610 (2015).

10. Wilson, J., DiSalvo, F. & Mahajan, S. Charge-density waves and superlattices in metallic layered transition-metal dichalcogenides. Adv. Phys. 24, 117-201 (1975).

11. Rossnagel, K. On the origin of charge-density waves in select layered transition-metal dichalcogenides. J. Phys. Condens. Matter 23, 213001 (2011).

12. Cario, L., Corraze, B., Meerschaut, A. & Chauvet, O. Dielectric breakdown and current switching effect in the incommensurate layered compound (LaS)1.196VS2. Phys. Rev. B 73, 155116 (2006).

13. Asamitsu, A., Tomioka, Y., Kuwahara, H. & Tokura, Y. Current switching of resistive states in magnetoresistive manganites. Nature 388, 50-52 (1997).

14. Yang, J. J., Strukov, D. B. & Stewart, D. R. Memristive devices for computing. Nat. Nanotechnol. 8, 13-24 (2013).

15. Lee, P. A. & Rice, T. M. Electric field depinning of charge density waves. Phys. Rev. B 19, 3970-3980 (1979).

16. Gruner, G., Zawadowski, A. & Chaikin, P. M. Nonlinear conductivity and noise due to charge-density-wave depinning in Nb Se3. Phys. Rev. Lett. 46, 511-515 (1981).

17. Mihaly, G. & Beauchene, P. Sliding charge density waves without damping: possible Fröhlich superconductivity in blue bronze. Solid State Commun. 63, 911-914 (1987).

18. Cho, D. et al. Nanoscale manipulation of the Mott insulating state coupled to charge order in 1T-$TaS_2$. Nat Commun. 7, 10453 (2016).

19. Ma, L. et al. A metallic mosaic phase and the origin of Mott-insulating state in 1T-$TaS_2$. Nat Commun. 7, 10956 (2016).

20. Nakanishi, K. & Shiba, H. Domain-like incommensurate charge-density-wave states and the first-order incommensurate-commensurate transitions in layered tantalum dichalcogenides. I. 1T-polytype. J. Phys. Soc. Jpn 43, 1839 (1977).

21. Fazekas, P. & Tosatti, E. Charge carrier localization in pure and doped 1T-TaS2. Phys. B & C 99, 183-187 (1980).

22. Eichberger, M. et al. Snapshots of cooperative atomic motions in the optical suppression of charge density waves. Nature 468, 799-802 (2010).

23. Yoshida, M., Suzuki, R., Zhang, Y., Nakano, M. & Iwasa, Y. Memristive phase switching in two-dimensional 1T-$TaS_2$ crystals. Science Adv. 1, e1500606 (2015).

24. Kent, A. D. & Worledge, D. C. A new spin on magnetic memories. Nat. Nanotechnol. 10, 187-191 (2015).

25. Loke, D. et al. Breaking the speed limits of phase-change memory. Science 336, 1566-1569 (2012).

26. Sawa, A. Resistive switching in transition metal oxides. Mater. Today 11, 28-36 (2008).

27. Waser, R. & Aono, M. Nanoionics-based resistive switching memories. Nat. Mater. 6, 833-840 (2007).

28. Welnic, W. Unravelling the interplay of local structure and physical properties in phase-change materials. Nat. Mater. 5, 56-62 (2005).

29. Yoshida, M. et al. Controlling charge-density-wave states in nano-thick crystals of 1T-$TaS_2$. Sci. Rep. 4, 7302-7307 (2014).

30. Wong, H. S. P. et al. Phase change memory. Proc. IEEE 98, 2201-2227 (2010).

31. Wong, H. S. P. & Salahuddin, S. Memory leads the way to better computing. Nat. Nanotechnol. 10, 191-194 (2015).

32. DiSalvo, F., Wilson, J., Bagley, B. & Waszczak, J. Effects of doping on charge-density waves in layer compounds. Phys. Rev. B 12, 2220-2235 (1975).

**References from Chiral domain dynamics and transient interferences of mirrored superlattices in nonequilibrium electronic crystals by Ravnik et al.**

1. Vodeb, J. et al. Configurational electronic states in layered transition metal dichalcogenides. New J. Phys. 21, 083001 (2019).

2. Coleman, R. et al. Scanning tunnelling microscopy of charge-density waves in transition metal chalcogenides. Adv. Phys. 37, 559 (1988).

3. Hall, J. et al. Environmental control of charge density wave order in monolayer 2H-TaS2. ACS Nano 13, 10210 (2019).

4. McMillan, W. Landau theory of charge-density waves in transition-metal dichalcogenides. Phys. Rev. B 12, 1187 (1975).

5. Villain, J. Commensurate-incommensurate transition of krypton monolayers on graphite: A low temperature theory. Surf. Sci. 97, 219 (1980).

6. Bak, P. Commensurate phases, incommensurate phases and the devil's staircase. Rep. Prog. Phys. 45, 587 (1982).

7. Wilson, J. A., Di Salvo, F. & Mahajan, S. Charge-density waves and superlattices in the metallic layered transition metal dichalcogenides. Adv. Phys. 24, 117 (1975).

8. Li, W. & Naik, G.V. Reorganization of CDW stacking in 1T-TaS2 by an in-plane electrical bias. APL Mater. 9, 18 (2021).

9. Gao, J., Zhang, W., Si, J., Luo, X., Yan, J., Jiang, Z., Wang, W., Lv, H., Tong, P., Song, W. et al. Chiral charge density waves induced by Ti-doping in 1T-TaS2. Appl. Phys. Lett. 118, 256 (2021).

10. Liu, G., Qiu, T., He, K., Liu, Y., Lin, D., Ma, Z., Huang, Z., Tang, W., Xu, J., Watanabe, K. et al. Electrical switching of ferro-rotational order in nanometre-thick 1T-TaS2 crystals. Nat. Nanotechnol. 1, 1-7 (2023).

11. Ohta, S., Kobayashi, S., Nomura, A. & Sakata, H. Electronic state modulation of the Star of David lattice by stacking of $13 \times 13$ domains in 1T- TaSe2. Phys. Rev. B 104, 155433 (2021).

12. Zong, A., Shen, X., Kogar, A., Ye, L., Marks, C., Chowdhury, D., Rohwer, T., Freelon, B., Weathersby, S., Li, R. et al. Ultrafast manipulation of mirror domain walls in a charge density wave. Sci. Adv. 4, eaau5501 (2018).

13. Bardeen, J. Tunneling theory of charge-density-wave depinning. Phys. Rev. Lett. 45, 1978 (1980).

14. Miller, J. Jr., Wijesinghe, A., Tang, Z. & Guloy, A. Correlated quantum transport of density wave electrons. Phys. Rev. Lett. 108, 036404 (2012).

15. Vodeb, J., Diego, M., Vaskivskyi, Y., Gerasimenko, Y., Kabanov, V. & Mihailovic, D. Emergent False Vacuum Decay Processes in a Two-Dimensional Electronic Crystal: Experiment vs. Simulations on a Noisy Superconducting Quantum Processor. arXiv Preprint arXiv:2103.07343 (2021).

16. Sohrt, C., Stange, A., Bauer, M. & Rossnagel, K. How fast can a Peierls-Mott insulator be melted?. Faraday Discuss. 171, 243 (2014).

17. Scruby, C., Williams, P. & Parry, G. The role of charge density waves in structural transformations of 1T TaS2. Philos. Mag. 31, 255 (1975).

18. Sipos, B., Kusmartseva, A. F., Akrap, A., Berger, H., Forró, L. & Tutivs, E. From Mott state to superconductivity in 1T-TaS 2. Nat. Mater. 7, 960 (2008).

19. Stojchevska, L. et al. Ultrafast switching to a stable hidden quantum state in an electronic crystal. Science 344, 177 (2014).

20. Ma, L. et al. A metallic mosaic phase and the origin of Mott-insulating state in 1T-TaS 2. Nat. Commun. 7, 10956 (2016).

21. Cho, D. et al. Nanoscale manipulation of the Mott insulating state coupled to charge order in 1T-TaS 2. Nat. Commun. 7, 10453 (2016).

22. Gerasimenko, Y. A., Karpov, P., Vaskivskyi, I., Brazovskii, S. & Mihailovic, D. Intertwined chiral charge orders and topological stabilization of the light-induced state of a prototypical transition metal dichalcogenide. Npj Quantum Mater. 4, 1 (2019).

23. Ravnik, J., Vaskivskyi, I., Mertelj, T. & Mihailovic, D. Ultrafast jamming of electrons into an amorphous entangled state. Phys. Rev. B 97, 075304 (2018).

24. Ravnik, J. et al. A time-domain phase diagram of metastable states in a charge ordered quantum material. Nat. Commun. 12, 1 (2021).

25. Stahl, Q. et al. Collapse of layer dimerization in the photo-induced hidden state of 1T-TaS 2. Nat. Commun. 11, 1(2020).

26. Le Guyader, L. et al. Stacking order dynamics in the quasi-two-dimensional dichalcogenide 1 T-TaS2 probed with MeV ultrafast electron diffraction. Struct. Dyn. 4, 044020 (2017).

27. Gerasimenko, Y. A. et al. Quantum jamming transition to a correlated electron glass in 1T-TaS 2. Nat. Mater. 18, 1078 (2019).

28. Park, J. W., Lee, J. & Yeom, H. W. Zoology of domain walls in quasi-2D correlated charge density wave of 1T-TaS 2. Npj Quantum Mater. 6, 1 (2021).

29. Karpov, P. & Brazovskii, S. Modeling of networks and globules of charged domain walls observed in pump and pulse induced states. Sci. Rep. 8, 4043 (2018).

30. Ritschel, T., Trinckauf, J., Koepernik, K., Büchner, B., Zimmermann, M.V., Berger, H., Joe, Y., Abbamonte, P. & Geck, J. Orbital textures and charge density waves in transition metal dichalcogenides. Nat. Phys. 11, 328 (2015).

31. Ravnik, J., Vaskivskyi, Y., Vodeb, J., Aupivc, P., Vaskivskyi, I., Golevz, D., Gerasimenko, Y., Kabanov, V. & Mihailovic, D. Quantum billiards with correlated electrons confined in triangular transition metal dichalcogenide monolayer nanostructures. Nat. Commun. 12, 1 (2021).

32. Yazyev, O. V. & Louie, S. G. Topological defects in graphene: Dislocations and grain boundaries. Phys. Rev. B 81, 195420 (2010).

33. Machida, Y. et al. Observation of soft phonon modes in 1 T-TaS2 by means of X-ray thermal diffuse scattering. J. Phys. Soc. Jpn. 73, 3064 (2004).

34. Ziebeck, K., Dorner, B., Stirling, W. & Schollhorn, R. Kohn anomaly in the 1T2 phase of TaS2. J. Phys. F Met. Phys. 7, 1139 (1977).

From SM of this article:

[1] J. Ravnik, M. Diego, Y. Gerasimenko, Y. Vaskivskyi, I. Vaskivskyi, T. Mertelj, J. Vodeb, and D. Mihailovic, Nature Communications 12, 1 (2021).
[2] Y. A. Gerasimenko, I. Vaskivskyi, M. Litskevich, J. Ravnik, J. Vodeb, M. Diego, V. Kabanov, and D. Mihailovic, Nature Materials 18, 1078 (2019).
[3] Q. Stahl, M. Kusch, F. Heinsch, G. Garbarino, N. Kretzschmar, K. Hanff, K. Rossnagel, J. Geck, and T. Ritschel, Nature Communications 11, 1 (2020).
[4] T. Ritschel, J. Trinckauf, K. Koepernik, B. Büchner, M. v Zimmermann, H. Berger, Y. Joe, P. Abbamonte, and J. Geck, Nature Physics 11, 328 (2015).
[5] L. Ma, C. Ye, Y. Yu, X. F. Lu, X. Niu, S. Kim, D. Feng, D. Tománek, Y.-W. Son, X. H. Chen, and others, Nature Communications 7, 10956 (2016).
[6] D. Cho, S. Cheon, K.-S. Kim, S.-H. Lee, Y.-H. Cho, S.-W. Cheong, and H. W. Yeom, Nature Communications 7, 10453 (2016).
[7] F. Di Salvo, D. Moncton, J. Wilson, and S. Mahajan, Physical Review B 14, 1543 (1976).
[8] J. Villain, Surface Science 97, 219 (1980).
[9] J. Vodeb, V. V. Kabanov, Y. A. Gerasimenko, I. Vaskivskyi, J. Ravnik, and D. Mihailovic, Journal of Superconductivity and Novel Magnetism 32, 3057 (2019).
[10] J. Vodeb, V. V. Kabanov, Y. A. Gerasimenko, J. Ravnik, M. A. van Midden, E. Zupanic, P. Sutar, D. Mihailovic, and others, New Journal of Physics 21, 083001 (2019).
[11] R. Brouwer and F. Jellinek, Physica B+ C 99, 51 (1980).
[12] C. Sohrt, A. Stange, M. Bauer, and K. Rossnagel, Faraday Discussions 171, 243 (2014).
[13] L. Stojchevska, I. Vaskivskyi, T. Mertelj, P. Kusar, D. Svetin, S. Brazovskii, and D. Mihailovic, Science 344, 177 (2014).

**References from A charge-density-wave oscillator based on an integrated tantalum disulfide-boron nitride- graphene device operating at room temperature by Liu, Debnath, Pope, Salguero, Lake, Balandin (2016)**

1. Grüner, G. Density Waves in Solids (Addison-Wesley, 1994).

2. Rossnagel, K. On the origin of charge-density waves in select layered transitionmetal dichalcogenides. J. Phys. Condens. Matter 23, 213001-213024 (2011).

3. Brown, S. & Grüner, G. Charge and spin density waves. Sci. Am. 270, 50-56 (1994).

4. Thorne, R. E. Charge-density-wave conductors. Phys. Today 49, 42-47 (1996).

5. Porer, M. et al. Non-thermal separation of electronic and structural orders in a persisting charge density wave. Nature Mater. 13, 857-861 (2014).

6. Wilson, J. A., Di Salvo, F. J. & Mahajan, S. Charge-density waves and superlattices in the metallic layered transition metal dichalcogenides. Phys. Rev. Lett. 32, 882-885 (1974).

7. Sipos, B. et al. From Mott state to superconductivity in 1T- $TaS_2$. Nature Mater. 7, 960-965 (2008).

8. Stojchevska, L. et al. Ultrafast switching to a stable hidden quantum state in an electronic crystal. Science 344, 177-180 (2014).

9. Manzke, R., Buslaps, T., Pfalzgraf, B., Skibowski, M. & Anderson, O. On the phase transitions in 1T-TaS $_2$. Europhys. Lett. 8, 195-200 (1989).

10. Yu, Y. et al. Gate-tunable phase transitions in thin flakes of 1T- $TaS_2$. Nature Nanotech. 10, 270-276 (2015).

11. Yoshida, M. et al. Controlling charge-density-wave states in nano-thick crystals of 1T-$TaS_2$. Sci. Rep. 4, 7302 (2014).

12. Joe, Y. I. et al. Emergence of charge density wave domain walls above the superconducting dome in 1T-TiSe $_2$. Nature Phys. 10, 421-425 (2014).

13. Samnakay, R. et al. Zone-folded phonons and the commensurateincommensurate charge-density-wave transition in 1T- $TaSe_2$ thin films. Nano Lett. 15, 2965-2973 (2015).

14. Hollander, M. J. et al. Electrically driven reversible insulator-metal phase transition in 1T-TaS $_2$. Nano Lett. 15, 1861-1866 (2015).

15. Xi, X. et al. Strongly enhanced charge-density-wave order in monolayer $NbSe_2$. Nature Nanotech. 10, 765-769 (2015).

16. Tsen, A. W. et al. Structure and control of charge density waves in twodimensional 1T-TaS $_2$. Proc. Natl Acad. Sci. USA 112, 15054-15059 (2016).

17. Yoshida, M., Suzuki, R., Zhang, Y., Nakano, M. & Iwasa, Y. Memristive phase switching in two-dimensional 1T- $TaS_2$ crystals. Sci. Adv. 1, e1500606 (2015).

18. Wang, L. et al. One-dimensional electrical contact to a two-dimensional material. Science 342, 614-617 (2013).

19. Doganov, R. A. et al. Transport properties of pristine few-layer black phosphorus by van der Waals passivation in an inert atmosphere. Nature Commun. 6, 6647 (2014).

20. Cao, Y.-F. et al. Transport and capacitance properties of charge density wave in few-layer $2H - TaS_2$ devices. Chinese Phys. Lett. 31, 077203-077206 (2014).

21. Rhea, R. W. Oscillator Design and Computer Simulation (McGraw-Hill, 1997).

22. Razavi, B. A study of phase noise in CMOS oscillator. IEEE J. Solid State Circ. 31, 331-343 (1996).

23. Stolyarov, M. A., Liu, G., Rumyantsev, S. L., Shur, M. & Balandin, A. A. Suppression of $1/f$ noise in near-ballistic h-BN-graphene-h-BN heterostructure field-effect transistors. Appl. Phys. Lett. 107, 023106 (2015).

24. Novoselov, K. S. et al. Electric field effect in atomically thin carbon films. Science 22, 666-669 (2004).

25. Lin, Y.-M. et al. Wafer-scale graphene integrated circuit. Science 332, 1294-1297 (2011).

26. Wu, Y. et al. High-frequency, scaled graphene transistors on diamond-like carbon. Nature 472, 74-78 (2011).

27. Balandin, A. A. Thermal properties of graphene and nanostructured carbon materials. Nature Mater. 10, 569-581 (2011).

28. Jo, I. et al. Thermal conductivity and phonon transport in suspended few-layer hexagonal boron nitride. Nano Lett. 13, 550-554 (2013).

29. Perfetti, L. et al. Femtosecond dynamics of electronic states in the Mott insulator $1T-TaS_2$ by time resolved photoelectron spectroscopy. New J. Phys. 10, 053019 (2008).

30. Kumar, S. et al. Local temperature redistribution and structural transition during joule-heating-driven conductance switching in $VO_2$. Adv. Mater. 25, 6128-6132 (2013).

31. Zimmers, A. et al. Role of thermal heating on the voltage induced insulatormetal transition in $VO_2$. Phys. Rev. Lett. 110, 056601 (2013).

32. Brockman, J. S. et al. Subnanosecond incubation times for electric-field-induced metallization of a correlated electron oxide. Nature Nanotech. 9, 453-458 (2014).

33. Horowitz, P. & Hill, W. The Art of Electronics (Cambridge Univ. Press, 1989).

34. Hoppensteadt, F. C. & Izhikevich, E. M. Pattern recognition via synchronization in phase-locked loop neural networks. IEEE Trans. Neural Netw. 11, 734-738 (2000).

35. Nikonov, D. E. et al. Coupled-oscillator associative memory array operation for pattern recognition. IEEE J. Explor. Solid State Comput. Dev. Circ. 1, 85-93 (2015).

36. Rahman, M. H. & Hamid, M. A. K. Solid-state oscillator using a $VO_2$ polyconductor film as a circuit element. Int. J. Electron. 42, 65-72 (1977).

37. Fisher, B. Voltage oscillations in switching $VO_2$ needles. J. Appl. Phys. 49, 5339-5341 (1978).

38. Lee, Y. K. et al. Metal-insulator transition-induced electrical oscillation in vanadium dioxide thin film. Appl. Phys. Lett. 92, 162903 (2008).

39. Leroy, J. et al. High-speed metal-insulator transition in vanadium dioxide films induced by an electrical pulsed voltage over nano-gap electrodes. Appl. Phys. Lett. 100, 213507 (2012).

40. Shukla, N. et al. Synchronized charge oscillations in correlated electron systems. Sci. Rep. 4, 4964 (2014).

41. Joushaghani, A. et al. Voltage-controlled switching and thermal effects in $VO_2$ nano-gap junctions. Appl. Phys. Lett. 104, 221904 (2014).

42. Wang, Y. et al. Electrical oscillation in Pt/$VO_2$ bilayer strips. J. Appl. Phys. 117, 064502 (2015).

43. Yang, Z., Ko, C. & Ramanathan, S. Oxide electronics utilizing ultrafast metalinsulator transitions. Annu. Rev. Mater. Res. 41, 337-367 (2011).

44. Pergament, A. et al. Vanadium dioxide: metal-insulator transition, electrical switching and oscillations. A review of state of the art and recent progress. Preprint at http://arxiv.org/abs/1601.06246 (2016).

45. Cavalleri, A. et al. Evidence for a structurally-driven insulator-to-metal transition in $VO_2$ : a view from the ultrafast timescale. Phys. Rev. B 70, 161102(R) (2004).

46. Petersen, J. C. et al. Clocking the melting transition of charge and lattice order in $1\ T - TaS_2$ with ultrafast extreme-ultraviolet angle-resolved photoemission spectroscopy. Phys. Rev. Lett. 107, 177402 (2011).

47. Paik, H. et al. Transport properties of ultra-thin $VO_2$ films on (001) $TiO_2$ grown by reactive molecular-beam epitaxy. Appl. Phys. Lett. 107, 163101 (2015).

48. Quackenbush, N. F. et al. Nature of the metal insulator transition in ultrathin epitaxial vanadium dioxide. Nano Lett. 13, 4857-4861 (2013).